Transactions of the ASME®

Journal of Engineering for Gas Turbines and Power

Published Quarterly by The American Society of Mechanical Engineers

VOLUME 121 • NUMBER 3 • JULY 1999

TECHNICAL PAPERS

Gas Turbines: Aircraft Engine

Gas Turbines: Coal, Biomass, and Alternative Fuels

Gas Turbines: Combustion and Fuels

Gas Turbines: Controls and Diagnostics

Gas Turbines: Cycle Innovations

(Contents continued on outside back cover)

This journal is printed on acid-free paper, which exceeds the ANSI Z39.48-1992 specification for permanence of paper and library materials. ∞™
♻ 85% recycled content, including 10% post-consumer fibers.

Technical Editor
H. D. NELSON (2001)

Associate Technical Editors
Advanced Energy Systems
M. J. MORAN (1999)
G. REISTAD (2002)
Fuels and Combustion Technologies
S. GOLLAHALLI (2001)
Gas Turbine (Review Chair)
D. WISLER (2001)
Gas Turbine
D. COOKE (1999)
M. MIGNOLET (2002)
J. PETERS (1999)
Internal Combustion Engines
D. ASSANIS (1999)
Nuclear
R. DUFFEY (2001)
Power
D. LOU (2002)

BOARD ON COMMUNICATIONS
Chairman and Vice President
R. K. SHAH

OFFICERS OF THE ASME
President, **R. E. NICKELL**
Executive Director, **D. L. BELDEN**
Treasurer, **J. A. MASON**

PUBLISHING STAFF
Managing Director, Engineering
CHARLES W. BEARDSLEY
Director, Technical Publishing
PHILIP DI VIETRO
Managing Editor, Technical Publishing
CYNTHIA B. CLARK
Managing Editor, Transactions
CORNELIA MONAHAN
Production Coordinator
COLIN MCATEER
Production Assistant
MARISOL ANDINO

Transactions of the ASME, Journal of Engineering for Gas Turbines and Power (ISSN 0742-4795) is published quarterly (Jan., April, July, Oct.) for $215.00 per year by The American Society of Mechanical Engineers, Three Park Avenue, New York, NY 10016. Periodicals postage paid at New York, NY and additional mailing offices. POSTMASTER: Send address changes to Transactions of the ASME, Journal of Engineering for Gas Turbines and Power, c/o THE AMERICAN SOCIETY OF MECHANICAL ENGINEERS, 22 Law Drive, Box 2300, Fairfield, NJ 07007-2300.

CHANGES OF ADDRESS must be received at Society headquarters seven weeks before they are to be effective. Please send old label and new address.

PRICES: To members, $40.00, annually: to nonmembers, $215.00. Add $40.00 for postage to countries outside the United States and Canada.

STATEMENT from By-Laws. The Society shall not be responsible for statements or opinions advanced in papers or . . . printed in its publications (B7.1, par. 3).

COPYRIGHT © 1999 by The American Society of Mechanical Engineers. Authorization to photocopy material for internal or personal use under circumstances not falling within the fair use provisions of the Copyright Act is granted by ASME to libraries and other users registered with the Copyright Clearance Center (CCC) Transactional Reporting Service provided that the base fee of $3.00 per article is paid directly to CCC, Inc., 222 Rosewood Dr., Danvers, MA 01923. Request for special permission or bulk copying should be addressed to Reprints/Permission Department.

INDEXED by Applied Mechanics Reviews and Engineering Information, Inc. Canadian Goods & Services Tax Registration #126148048

Downloaded 03 Jun 2010 to 171.66.16.159. Redistribution subject to ASME license or copyright; see http://www.asme.org/terms/Terms_Use.cfm

Gas Turbines: Manufacturing Materials and Metallurgy

Gas Turbines: Structures and Dynamics

Internal Combustion Engines

ANNOUNCEMENTS

A Parametric Starting Study of an Axial-Centrifugal Gas Turbine Engine Using a One-Dimensional Dynamic Engine Model and Comparisons to Experimental Results: Part I—Model Development and Facility Description[1]

A. K. Owen

A. Daugherty

U. S. Army Vehicle Propulsion Directorate,
NASA Lewis Research Center,
MS 77-6, 21000 Brookpark Road,
Cleveland, OH 44135-3191

D. Garrard
Sverdrup Technology, Inc./AEDC Group,
1099 Avenue C,
Arnold AFB, TN 37389-9013

H. C. Reynolds

R. D. Wright

General Electric Corporation,
Lynn, MA 01910

A generic one-dimensional gas turbine engine model, developed at the Arnold Engineering Development Center, has been configured to represent the gas generator of a General Electric axial-centrifugal gas turbine engine in the six kg/sec airflow class. The model was calibrated against experimental test results for a variety of initial conditions to insure that the model accurately represented the engine over the range of test conditions of interest. These conditions included both assisted (with a starter motor) and unassisted (altitude windmill) starts. The model was then exercised to study a variety of engine configuration modifications designed to improve its starting characteristics, and, thus, quantify potential starting improvements for the next generation of gas turbine engines. This paper discusses the model development and describes the test facilities used to obtain the calibration data. The test matrix for the ground level testing is also presented. A companion paper presents the model calibration results and the results of the trade-off study.

Introduction

There has been a continuing effort on the part of gas turbine engine manufacturers to improve performance. This improved performance has manifested itself not only as higher efficiencies and as improved reliability but also as reduced engine weight. This drive for improved performance, exemplified by the Integrated high performance turbine engine technology (IHPTET) program, results in higher-pressure ratio compressors containing more highly loaded stages. A result of this effort is a greater difficulty in engine starting. Previously, this difficulty has been overcome by using higher power starting systems to meet the increased torque requirements. However, for small aircraft with self-contained systems such as commuter aircraft and helicopters, this requirement for larger starting systems has begun to impact the overall aircraft payloads and costs.

In 1995, the General Electric Corporation (GE) suggested a cooperative program with the NASA Lewis Research Center (LeRC) and the US Army Vehicle Propulsion Directorate (VPD). The purpose of the program was to study the start sequence of small gas turbine engines and to explore methods for reducing required starter power. The proposed program was funded and implemented beginning in the summer of 1995. Ground level testing of the selected engine system was conducted at the General Electric Corporate Research and Development (CR&D) Center. Altitude testing of the engine system was conducted at the Lewis Research Center (LeRC). Model development was conducted at the Arnold Engineering Development Center (AEDC), and analytical trade-off studies using the AEDC model were conducted at both General Electric (Lynn) and at the LeRC. The experimental vehicle selected for this program was the gas generator section of the GE CT7-5.

Both ground level and simulated altitude condition engine testing were divided into baseline, model calibration, and experimental trade-off testing. Baseline testing insured the engine, configured in this program as a gas generator core, operated similarly to its standard turboprop configuration. This was done by adjustments to the compressor bleed and exhaust area. Repeatable starting procedures for cold, cool, and hot starts were developed, insuring that pre-start thermal conditions would be precisely controlled. Calibration testing provided engine-starting sensitivity to the variations in certain engine operational parameters including fuel schedule, stator vane settings, bleed schedules, and starter power.

The final phase of the experimental testing consisted of modifying these operational parameters in an attempt to improve the starting characteristics of the engine. While the scope and purpose of both ground level and altitude testing were the same, differences in the nature of the starting process required different approaches

---

[1] The research reported herein was performed by the U.S. Army Vehicle Propulsion directorate, the NASA Lewis Research Center, General Electric Aircraft Engines, the General Electric Corporate Research and Development Center, and the Arnold Engineering Development Center (AEDC), Air Force Material Command. Funding was provided by NASA's Advanced Subsonic Technology program and by GE Internal Research and Development under Space Act Agreement No. FA-103, Large Engine Technology Contract (LET) No. NASA-26617 Task Order 54 and Interagency Agreement C-71064-E. Further reproduction is authorized to satisfy the needs of the U. S. Government.

Contributed by the International Gas Turbine Institute (IGTI) of THE AMERICAN SOCIETY OF MECHANICAL ENGINEERS for publication in the ASME JOURNAL OF ENGINEERING FOR GAS TURBINES AND POWER. Paper presented at the International Gas Turbine and Aeroengine Congress and Exhibition, Stockholm, Sweden, June 2–5, 1998; ASME Paper 98-GT-470.

Manuscript received by IGTI March 24, 1998; final revision received by the ASME Headquarters March 23, 1999. Associate Technical Editor: R. Kielb.

to experimental testing. The ground level test matrix also included various steady-state operating points from ground idle to 90 percent of design speed.

Ground level testing occurred at the GE CR&D Center in the fall of 1995. Simulated altitude testing occurred at the LeRC in the fall of 1996. The test matrix used for this altitude testing was based on the results of the ground data calibrated simulation. Post altitude-testing calibration was done using the results of the altitude testing. Model calibration occurred at GE, the LeRC, and the AEDC.

The program was initiated with four goals in mind. First, the development of a transient engine model that reliably represented a gas turbine engine for use in detailed analytical studies of the start sequence was desired. Second, the program was structured to acquire sufficient experimental results to validate the effectiveness of many of the proposed changes to the start sequence. Third, the development of protocols to conduct starting modification studies was desired. Finally, the development of methodologies to determine the most cost-effective approaches to improving the start sequence was a program goal.

This cooperative program approach brought the strengths and complementary interests of the contributing organizations together to produce an effective research program. LeRC and AEDC created and validated the ATEC model to test data. GE and LeRC used this model to study starting improvement concepts. GE did extensive analysis of the experimental results and, with its extensive understanding of the CT7 core, developed appropriate strategies for improved starting. Validation testing verified concept improvement effectiveness for risk reduction in future concept development. The combined interests and strengths of all contributors made the program successful and productive. The model development effort and the experimental program are discussed in this paper. The results of the model calibration and analytical trade-off studies are presented in Part II of this article.

Modeling Techniques

The Aerodynamic Turbine Engine Code (ATEC) model and simulation solves the one-dimensional Euler equations with source terms within a given domain of interest (Garrard, 1995). The overall system under consideration is separated into individual, elemental control volumes, as sketched in Fig. 1. The following governing equations are derived by the application of mass, momentum, and energy conservation to the elemental control volume:

$$\frac{\partial \mathbf{U}}{\partial t} + \frac{\partial \mathbf{F}}{\partial x} = \mathbf{G},$$

where

$$\mathbf{U} = \begin{bmatrix} A\rho \\ \rho A u \\ AE \end{bmatrix}$$

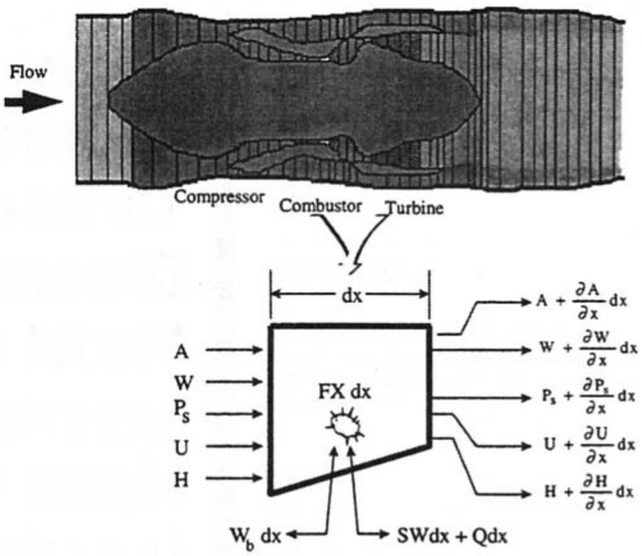

Fig. 1 System discretization into elemental control volumes

$$\mathbf{F} = \begin{bmatrix} \rho A u \\ \rho A u^2 + AP \\ u(AE + AP) \end{bmatrix}$$

$$\mathbf{G} = \begin{bmatrix} -W_{Bx} \\ FX_x \\ Q_x + SW_x - H_{Bx} \end{bmatrix}$$

The specific flow variables are density ρ, static pressure P, total energy per unit volume E, and the axial flow velocity, u. The cross-sectional area of the flow path is defined as A. The source term for the conservation of mass equation is the bleed flow rate distribution W_{Bx}. Compressor bleeds and turbine cooling bleeds are added through W_{Bx}. The conservation of momentum equation source term is FX_x, which is the axial force distribution acting on the control volume. This term is used to represent the blade forces in such components as the compressor and turbine, and it is used to implement wall friction losses. The conservation of energy equation source terms include the energy addition or extraction rate due to heat transfer or combustion into the control volume fluid, Qx, the shaft work distribution applied to the control volume, SWx, and the enthalpy change due to the bleed flow distribution, HBx.

Compressor Model. To provide compressor and turbine stage force ($FXdx$) and shaft work (SWx) inputs to the momentum and energy equations, sets of steady-state stage characteristics must be

Nomenclature

Δ = difference
ρ = density
Θ = longwell loading parameter
Γ = torque
ω = shaft rotational speed
A = cross-sectional area
C = metal specific heat
E = total energy
FX = distributed blade force
H = total enthalpy
I = rotational moment of inertia
k = thermal conductivity
m = mass of metal
N = engine shaft rotor speed
P = pressure
q = heat flux
Q = distributed heat addition
SW = distributed shaft work
t = time
T = temperature
TFF = turbine flow function
U = axial velocity
V = radial velocity, combustor volume
W = mass flow rate
WDF = turbine work done factor
x = axial coordinate

Subscripts

B, b = bleed
c = combustor
eff = effective
f = fuel
N = maximum node number
s = static
t = total
x = axial coordinate
0 = free stream station
2 = compressor inlet station
3 = compressor exit station
4 = combustor exit station
5 = turbine exit station

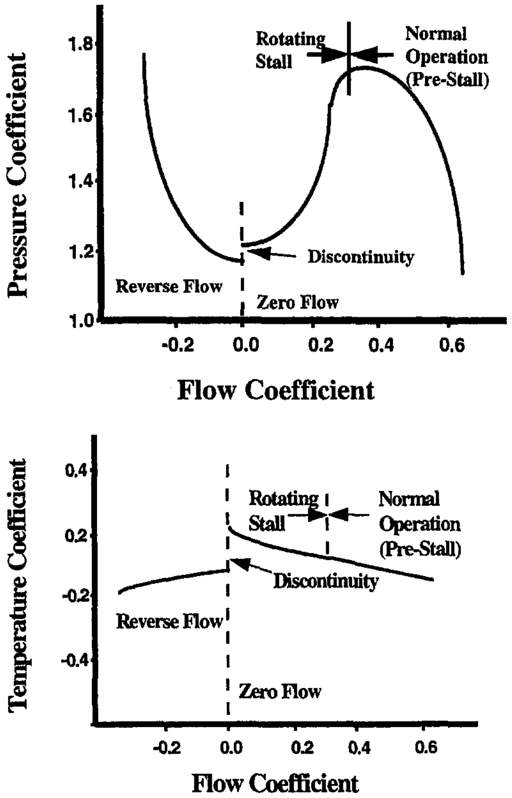

Fig. 2 Typical compressor pressure and temperature stage characteristics used in ATEC

provided. A generic set of compressor pressure and temperature characteristics is shown in Fig. 2. Note that post-stall operation is allowed. With the steady-state total pressure ratio and temperature ratio at an assumed steady flow rate, the model uses the steady-state conservation equations to compute the appropriate control volume forces and shaft work. These values are then used in the time dependent Euler equations as the necessary values of the forces in the momentum equation and shaft work in the energy equation. To provide a dynamic stage characteristic, a first order time lag on the stage forces has been incorporated into the modeling technique in the post-stall region only (Davis, 1986).

Combustor Model. The combustor heat addition (Q_x) to the energy equation uses a set of steady-state combustion efficiency maps. The combustion efficiency is given as a function of the Longwell Loading Parameter, θ (Longwell et al., 1955), where

$$\theta = \frac{P_4^{1.8} T_3 V_c}{W_4}.$$

A representative map of combustion efficiency as a function of Longwell loading parameter for lines of constant combustor equivalency ratio is shown in Fig. 3. Pressure loss in the combustor is based on a one-dimensional, constant cross-sectional area analysis of the combustor stagnation pressure loss due to the energy release, as given by Oates, 1988.

Turbine Model. Consistent with the approach taken to formulate and construct the compressor model, turbine performance characteristics are defined which have a particular format. The turbine stage forces and shaft work are determined from a set of turbine performance characteristics as sketched in Fig. 4. The turbine flow function is

$$\mathrm{TFF} = \frac{W_4 \sqrt{T_{t4}}}{P_{t4}}.$$

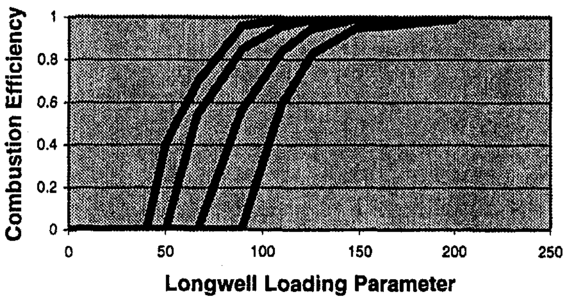

Fig. 3 Combustion efficiency as a function of Longwell loading parameter for lines of constant combustor equivalency ratio increasing left to right

For flow conditions in which the turbine stage nozzle is not choked, a given value of turbine flow function explicitly defines a value for the turbine work done factor (WDF):

$$\mathrm{WDF} = \frac{h_4 - h_5}{T_{t4}}.$$

Once the turbine work done factor is known for the given inlet flow conditions and rotor speed, the turbine stage exit temperature is found. Given the total temperature ratio across the turbine, the second plot shown in Fig. 4 is used to obtain the total pressure ratio across the turbine stage. At this point, sufficient information has been obtained about the turbine to obtain the steady-state blade forces and shaft work terms required to integrate the Euler equations to the next point in time.

For flow conditions in which the turbine stage nozzle is choked, a given value of turbine flow function can not be used to explicitly define the turbine work done factor. In the one-dimensional ATEC representation of the engine, the physical blockage of the nozzles is not modeled. The engine is typically modeled using the overall

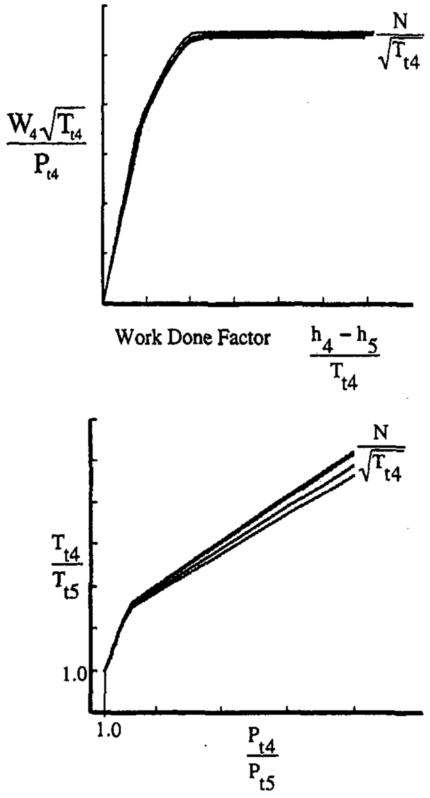

Fig. 4 Typical turbine performance specification curves

flow passage geometry with no reduction in area made for blading. The mass flow through the turbine, however, can not exceed the limit given by the turbine flow function. The total temperature and total pressure ratio across the choked turbine stage is calculated by assuming that the downstream, rather than upstream, total pressure is known from the previous time step. The solution is iterated until convergence of exit total temperature, inlet mass flow function, and total pressure ratio is obtained. Steady-state blade forces and shaft work for the turbomachinery source terms are then calculated to use in the integration of the Euler equations to the next point in time.

Rotor Dynamics Model. Although not directly tied to a source term calculation, the rotor dynamics play an important function in the transient operation of a gas turbine engine. For both the compressor and turbine models, the rotor rotational speed determines where, on the given operational maps, the operating condition is located.

The rotor rotational speed is given as part of the initial conditions. Once the time integration process is started, the change in rotational speed is given by

$$\frac{d\omega}{dt} = \frac{1}{I}(\Gamma_t - \Gamma_c - \Gamma_v - \Gamma_p + \Gamma_s),$$

where I is the rotor polar moment of inertia, ω is the shaft rotational speed, Γ_t is the torque produced by the turbine, Γ_c is the torque required by the compressor, Γ_v is the torque required to account for viscous losses, Γ_p is the torque required to satisfy any customer power requirements, and Γ_s is the net torque produced by the starter and delivered to the rotor.

The rotor dynamics model is integrated into the overall simulation at the end of the time marching routine. To begin a new time step, it is assumed that the rotor rotational speed is known either from the initial conditions or from the previous time step. During the calculation of source terms for the current time step, the rotor rotational speed is held constant. Given the changes in source terms that occur during the current time step, a new flow field solution is determined by the flow solver routine. With the new flow field variables, the change in rotor speed is determined using the above equation. With the new value for rotor rotational speed, the simulation moves on to the next time step.

The rotor dynamics model works with torque rather than power due to the requirements at zero speed. If power, which is the torque divided by the rotor speed, is used during an engine starting process, the initial rotor speed of zero will result in power requirements being indeterminate. Rather than basing the change in rotor speed on a power balance, the rotor dynamics model tracks the torque level as given by the starter motor and other interacting components.

Heat Transfer Model. During normal engine operation, heat transfer processes occur throughout the engine. The effects of this heat transfer on the gas turbine engine operation can be significant (Crawford et al., 1985). During steady-state operation, however, the heat transfer effects are implicitly built into the component performance maps. Since the ATEC simulation is based upon steady-state performance maps, the heat transfer does not have to be considered and modeled to match the steady state operation.

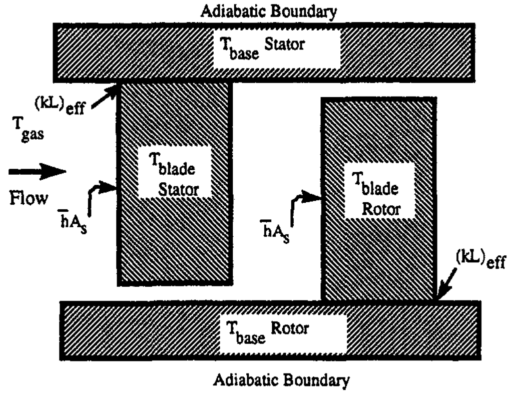

Fig. 5 Axial compressor heat transfer model

Frequently, however, the engine is not operated at the conditions for which the steady-state performance maps were developed (MacCullum et al., 1985). The ATEC model and simulation considers the effects of the heat transfer within the compressor, combustor, and turbine components. It is assumed that the overall engine operates adiabatically with the surroundings. The heat transfer source terms for each of the components are calculated using standard heat transfer engineering correlations (Sissom et al., 1972). In the compressor, the heat can be convected from the air to the stator blades and then conducted to the outer engine casing. In a rotor row, the heat is likewise convected from the air to the rotor blading and then conducted to the rotor. To represent the convective and conductive flow paths, a simple representation of the system is used and is sketched in Fig. 5. The heat transfer model tracks four temperatures. They are the rotor and stator blade temperatures and the base metal temperatures for the respective blades. The convective heat transfer rate from a blade to the air is given by

$$\mathring{q}_{b-a} = \bar{h}A_s(T_{\text{blade}} - T_{\text{gas}}),$$

where T_{gas} is the average total temperature of the air flow through the compressor stage. The conductive heat transfer rate from the blade to the base is given by

$$\mathring{q}_{b-b} = (kL)_{\text{eff}}(T_{\text{base}} - T_{\text{blade}}),$$

where $(kL)_{\text{eff}}$ is a measure of the potential for conduction heat transfer. It is a combination of the thermal conductivity of the blade material and the overall length across which the conduction occurs. Given these two heat transfer rates, the metal temperatures are calculated using

$$T^n_{\text{blade}} = T^{n-1}_{\text{blade}} + \frac{(\mathring{q}_{b-b} - \mathring{q}_{b-a})}{m_{\text{blade}}C_{\text{blade}}}\Delta t$$

$$T^n_{\text{base}} = T^{n-1}_{\text{base}} - \frac{\mathring{q}_{b-b}}{m_{\text{base}}C_{\text{base}}}\Delta t.$$

The combustor and turbine heat transfer models are similar to the compressor model. The combustor model tracks the combustor liner temperature, the combustor liner airflow temperature, and a case temperature. The turbine heat transfer model builds on the compressor model by adding heat transfer to the internal cooling flow. It is assumed in the models that the Biot modulus of the respective metal parts is sufficiently small to warrant the assumption of equal temperature throughout the metal masses. The average convective heat transfer coefficient is provided as a user input, rather than being calculated.

Control Model. The control system was modeled as a digital representation of the hydromechanical fuel control system. Both the control and its model schedule the ratio of fuel flow divided by compressor exit static pressure ($Wf/P3$). In the model, this ratio was input as a set of tables with $Wf/P3$ supplied versus inlet temperature, throttle angle, and engine speed. Also included as model inputs were minimum and maximum fuel flow rates and fuel manifold fill time (set to 4.3 s). Several other equations are required to obtain closure of the equation set. These include the ideal gas equation of state and the isentropic flow relationships. A constant ratio of specific heats is also assumed.

The model is formulated as an initial condition boundary value problem. Initial conditions for the dependent variables (ρA, ρAu, AE) are provided by an internal calculation routine that assumes steady-state flow conditions. The major inputs for the ATEC simulation include the corrected rotational speed of the rotor, the exit boundary condition type and magnitude, and fuel flow rate. A set of initial conditions for each control volume entrance is calculated using steady-state flow physics and pre-stall compressor stage characteristics. These routines develop steady-state initial condition sets of data from which the time dependent model solutions are initiated. Upon specification of boundary conditions, the simulation is ready for time marching.

The time dependent flow field within the system of interest is obtained by solving the time dependent system of equations using either an explicit or an implicit numerical approach. Both simulations use a flux-difference splitting scheme based upon characteristic theory (Kneile et al., 1995) expressed in both an explicit and implicit formulation to solve for the face fluxes. The explicit numerical solver uses a first order Euler method to integrate the solution from the current time step to the next time step. The implicit numerical solver uses a first order Runge-Kutta scheme for the time integration.

Test Facilities

Ground Level Starting Facility and Data Acquisition/Reduction. The engine was installed and tested in a ground level test cell at the General Electric CR&D Center (cell X7) which was configured specifically to accept the CT7-5 for this test. One hundred and thirty eight low range pressure transducers were installed on the engine, providing data for measuring engine overall and individual component starting operating characteristics. Included were inlet temperatures, pressures, and airflow, flow path outer static pressures at each compressor stage, compressor bleed airflow, pressure and temperature rakes at axial compressor and centrifugal compressor exits, starter pressures, fuel pressure, vane geometry location, combustor pressure drop, and turbine exit pressure and temperature rakes.

Control modifications were made to allow variations in the normal engine fuel, bleed, and variable geometry schedules. The baseline operating characteristics were defined with the standard hydromechanical fuel control. The fuel control was then replaced with an electronic fuel control. The variable geometry and intercompressor bleed valve actuation system was replaced with four independently scheduled actuators.

All instrumented parameters were recorded at a rate of 100 samples/second, providing a bandwidth of approximately 40 Hz. This bandwidth was high enough to resolve any surge events during the start sequence. The PC-based data acquisition system used at the CR&D facility was designed and assembled by GE.

Altitude Starting Facility and Data Acquisition/Reduction. At the end of the ground level testing at the GE CR&D facility, the engine was moved and installed in the Engine Components Research Laboratory 2B (ECRL-2B). This facility is capable of testing engines up to the 12 kg/sec flow class and at simulated altitudes from ground level to 7600 meters. Inlet temperature is not controlled. Additional facility detail is provided in, "The Engine Components Research Laboratory" (1993). Altitude testing began late in 1996.

For all tests, 281 instrumented parameters were recorded at 1 Hz/channel using a steady-state data acquisition system. In addition, 96 of these instrumented parameters were sampled using a dynamic data acquisition system at a rate of 100 samples/second/channel. Data error bands were no more than 4.6 percent for all instrumented parameters (including hysteresis, residual zero, sensitivity, nonrepeatability, and nonlinearity). Additional detail is provided in Owen, 1995.

Engine Test Matrix for Model Calibration

Ground Level Starting Test Matrix. Baseline testing (1) insured the gas generator configuration operated in a manner similar to it's operation when configured as a turboprop and (2) acquired detailed data describing engine operation. To insure that the operation was similar to that of a turboprop, a number of starts were done with varying nozzle exit areas. Start times and engine ground idle operating conditions were compared to standard CT7-5 engine operation and the exit area was set to match the engine operating conditions.

Table 1 Ground level sensitivity study test matrix

Operational Parameter	Variation
Engine Thermal State	Cold, Cool, Hot
Start Bleed	0 to 3.5% Increase
Fuel Acceleration Schedule	0 to 15% Enrichment
Inlet Guide Vane Schedule	± 12%
Stator Vanes (SV) 1 & 2 Schedule	± 12% SV1 ± 16% SV2
Starter Power	0 to 50% Reduction

The sensitivity of the engine starting characteristics was studied by changing or adjusting the operating characteristics of each of the engine components. This study matrix is shown in Table 1. Percentage changes shown are for the normal operating range and, for the variable geometry, represent the limits of safe travel without rotor gauges to monitor stress levels. The bleed increase represents an attempt to move the compressor away from the stall line, allowing a starting fuel flow rate increase to increase energy available for extraction by the turbine during the start. Data were recorded with each of these changes, as well as at the normal setting or configuration, establishing the effect of each change on engine and component operation. The model was then run both in a normal configuration and with the changes incorporated. Differences between engine operation and model predictions were noted and component definitions in the model were modified to accurately reflect engine operation.

The resulting model, used in the trade off studies, matched the overall engine starting characteristics well for a cold start. Additional tuning was required to improve the model representation of hot starts and component representation. Post stall characteristics, not currently available, are also needed to improve model simulation of starts with stalls.

Altitude Test Matrix. The altitude test matrix was principally designed to provide calibration points and engine sensitivities over the entire engine Mach number and altitude operational envelope, as shown in Fig. 6. It was structured using results from the ground testing and from the preliminary simulation trade study. Note that this preliminary study used the simulation calibrated to ground level starts only. Here, assisted starts (triangles) represent air starts

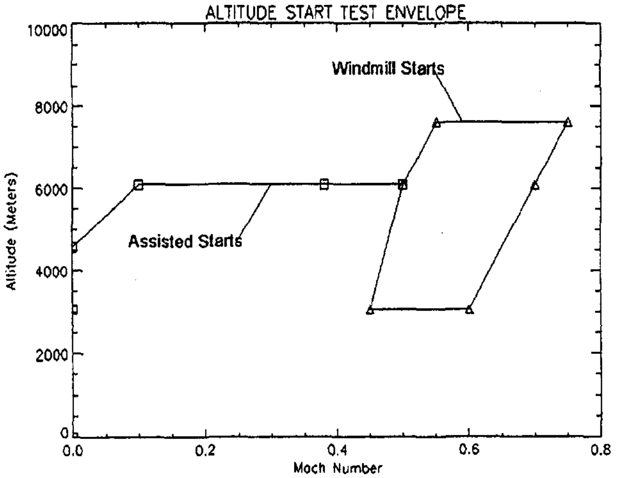

Fig. 6 Altitude test program altitude/mach number range

Table 2 Altitude sensitivity study test matrix

Variable	Variations
Engine Thermal State	Cold, Cool, Hot
Start Bleed	15% & 25% Reduction
Fuel Acceleration Schedule	4% & 8% Enrichment
Inlet Guide Vane Schedule	± 12%
Stator Vanes 1 & 2 Schedule	± 12% SV1 ± 16% SV2
Turbine Exit Area	%
Minimum Fuel Flow	4% & 8% Enrichment
Auxiliary Power	Disconnect

that are starter assisted. The upper Mach number windmill boundary represents the limit for normal operation of this engine. The lower limit is a simulation estimate of the Mach number at which a successful unassisted start can be made. Over 160 altitude starts were accomplished, both starter assisted and windmill. The matrix used for the altitude sensitivity studies is presented in Table 2. Notice an interesting difference between the ground level study matrix and the altitude study matrix. Where the ground level studies called for an increase in bleed, the altitude windmill studies, using the ground level calibrated model, indicated a bleed reduction is more appropriate.

Only engine sensitivities to variables easily modified in the test cell were studied during the preliminary evaluation of concepts for improved starting. Unfortunately, it was not possible to disconnect the auxiliary loads from the system during the test phase.

The following paragraphs indicate how the preliminary simulation was used to guide the development of the preliminary test matrix. A plot of the predicted difference between the torque provided by the engine during a windmill start and the torque required for a successful windmill start and a barely unsuccessful windmill start is shown in Fig. 7. The torque provided by the engine includes ram air effects plus the torque provided by the combustor and turbine. Theses torques are countered by the viscous losses, parasite drag, and compressor drag. Both starts are at a simulated altitude of 3000 meters and are plotted against engine speed. The simulation results were obtained before the altitude testing and used the simulation before it was calibrated to the altitude starts. As can be seen in Fig. 7, there exists a predicted minimum torque imbalance at about 38 percent of design speed. This was a predicted critical speed and during the preliminary studies, this is the point where simulated starts either failed or succeeded. It can be inferred from Fig. 7 that windmill air starting speeds can be reduced if this minimum torque imbalance can be increased—either by reducing required torque or by increasing torque available. Thus, the preliminary simulation studies were designed to assess what modifications to various engine components or their operating schedules would maximize this predicted minimum torque.

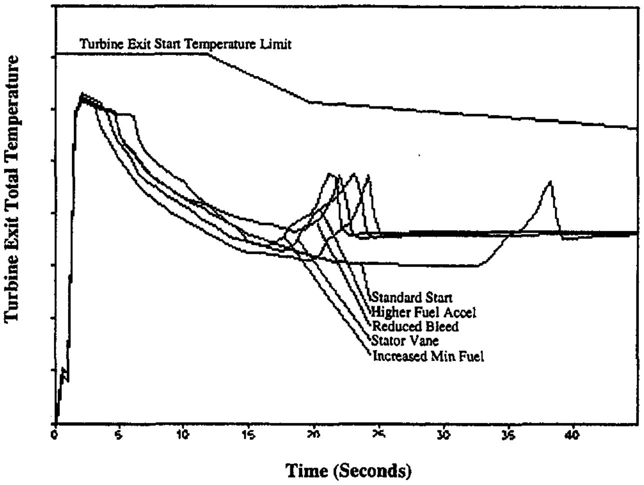

Fig. 8 Turbine exit total temperature for the selected starting conditions

Two other considerations were important for this study. They were the restriction of maximum turbine exit temperature and the compressor stall/surge line. Turbine exit temperature for the starting conditions selected for study and the manufacturer temperature limit are shown in Fig. 8. The compressor operating line during the minimum predicted successful starting Mach number versus the compressor stall/surge limit, as determined from the ground start test program, is shown in Fig. 9. As can be seen from these plots, the simulation indicated that the engine would operate safely away from the temperature and stall lines during the proposed test matrix and, indeed, this proved to be the case.

Some comments should be made to clarify the reasons for selecting the parameters varied during the altitude starting test program. Enriching the minimum fuel flow or the acceleration schedule is an attempt to increase the torque provided by the turbine. The normal fuel control logic has a set minimum starting fuel flow, insuring an adequate minimum of fuel for combustion during the very early part of the start sequence. Later in the start sequence, the fuel control transitions to an acceleration schedule specifying fuel provided as a function of compressor inlet temperature, engine speed, and compressor exit pressure. Notice that the start schedule is enriched only in the region of minimum predicted torque imbalance. The acceleration schedule is not enriched in the area of low speeds to minimize the possibility of over-

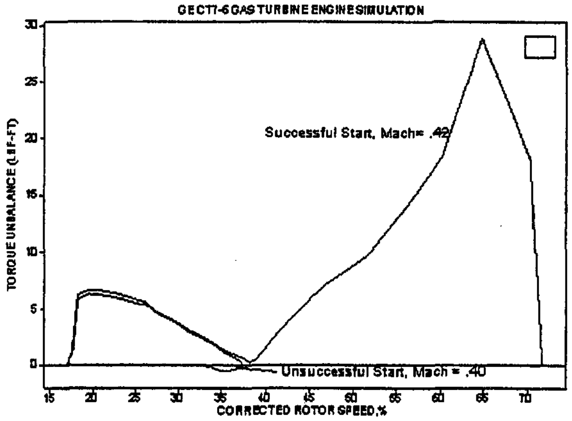

Fig. 7 Engine torque balance for successful and unsuccessful altitude start test cases as a function of corrected rotor speed

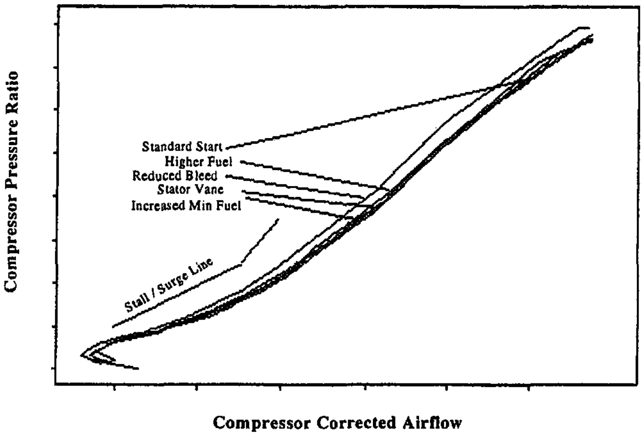

Fig. 9 Compressor operating line for various engine operating conditions at the minimum successful starting mach number

temperatures at low speeds (indeed, the fuel control is providing the programmed minimum fuel here) and the amount of enrichment is reduced at the higher speeds where it is not required and may aggravate peak starting temperatures. The selected 4 percent and 8 percent enrichments were chosen to provide adequate enrichment of the standard fuel schedule. During testing, the fuel enrichment was increased to 16 percent to enhance the effects of enriched fuel schedule on the engine starting capabilities.

Modifications of the inlet guide vane and stator vane stages 1 and 2 positions are an attempt to reduce the torque required for a successful start as well as increasing windmill speeds required for fuel and combustion systems. These changes also effected compressor stall/surge line. The test vehicle did not contain rotor strain gauges for stress monitoring, thus requiring conservative limits in the magnitudes of the changes.

The reduction in start bleed is an attempt to reduce the required starting torque. The magnitude of the changes was selected in an attempt to invoke a change large enough to be measurable and yet small enough to minimize the reduction in surge margin. Turbine area variation indicated the effect of changing the power extracted in the turbine by altering the overall pressure change across the turbine.

The engine thermal state, cold, cool, and hot, could have a major effect on the ability of the engine to successfully complete a start, requiring its inclusion in the study.

Summary

A generic one-dimensional gas turbine engine model, developed at the Arnold Engineering Development Center, has been configured to represent the gas generator of a General Electric axial-centrifugal gas turbine engine in the six kg/s airflow class. This paper has described the various component models and the numerical algorithm used in the simulation development. The test facilities used to obtain the calibration data have also been discussed. The test matrix for both the ground level and altitude testing was presented. A companion paper presents the model calibration results and the results of the trade-off study.

Acknowledgments

The Aerodynamic Turbine Engine Code (ATEC) was developed under the direction of the Joint Dynamic Airbreathing Propulsion Simulations (JDAPS) partnership (Davis et al., 1995). JDAPS is a partnership of government, university, and industry. The JDAPS partnership was formed for the purpose of developing and applying turbine engine and component numerical simulations to aid in the understanding of turbine engine behavior.

References

"The Engine Components Research Laboratory," Aeropropulsion Facilities and Experiments Division, Lewis Research Center, August 1993.

Crawford, R. A., and Burwell, A. E., 1985, "Quantitative Evaluation of Transient Heat Transfer on Axial Flow Compressor Stability," AIAA 85-1352.

Davis, M. W., Jr., Owen, A. K., O'Brien, W. F., and Cousins, W. T., 1995, "Joint Dynamic Airbreathing Propulsion Simulations Partnership JDAPS," ASME Paper 95-GT-143.

Davis, M. W., 1986, "A Stage-by-Stage Post-Stall Compressor System Modeling Technique: Methodology, Validation, and Application," Ph.D. dissertation, Virginia Polytechnical Institute and State University, Blacksburg, VA.

Garrard, G. D., 1995, "ATEC: The Aerodynamic Turbine Engine Code for the Analysis of Transient and Dynamic Gas Turbine Engine System Operations," Ph.D. dissertation, University of Tennessee, TN.

Longwell, J. P., and Weiss, M. A., 1955, "High Temperature Reaction Rates in Hydrocarbon Combustion," *Ind. Eng. Chem.*, Vol. 47, pp. 1634–1637.

Oates, G. C., 1988, *Aerothermodynamics of Gas Turbine and Rocket Propulsion, AIAA Education Series,* J. S. Przemieniecki, Series Editor-in-Chief, American Institute of Aeronautics and Astronautics, Washington, DC, pp. 218–220.

Owen, A. K., 1995, "Comparisons Between Unsteady Aerodynamic Events in a Gas Turbine Generator and an Identical Compressor Rig," presented at the AGARD 85th PEP, Derby, England, May 8–12, 1995.

Sissom, L. E., and Pitts, D. R., 1972, *Elements of Transport Phenomena,* McGraw-Hill, Inc., New York, pp. 118–121.

A Parametric Starting Study of an Axial-Centrifugal Gas Turbine Engine Using a One-Dimensional Dynamic Engine Model and Comparisons to Experimental Results: Part II—Simulation Calibration and Trade-Off Study[1]

A. K. Owen

A. Daugherty

U.S. Army Vehicle Propulsion Directorate,
NASA Lewis Research Center,
MS 77-6, 21000 Brookpark Road,
Cleveland, OH 44135-3191

D. Garrard

Sverdrup Technology, Inc./AEDC Group,
1099 Avenue C,
Arnold AFB, TN 37389-9013

H. C. Reynolds

R. D. Wright

General Electric Corporation,
Lynn, MA 01910

A generic one-dimensional gas turbine engine model, developed at the Arnold Engineering Development Center, has been configured to represent the gas generator of a General Electric axial-centrifugal gas turbine engine in the six-kg/sec airflow class. The model was calibrated against experimental test results for a variety of initial conditions to insure that the model accurately represented the engine over the range of test conditions of interest. These conditions included both assisted (with a starter motor) and unassisted (altitude windmill) starts. The model was then exercised to study a variety of engine configuration modifications designed to improve its starting characteristics and thus quantify potential starting improvements for the next generation of gas turbine engines. This paper presents the model calibration results and the results of the trade-off study. A companion paper discusses the model development and describes the test facilities used to obtain the calibration data.

Introduction

In a companion paper, presented as Part 1, the objectives, justification, and approach of the small gas turbine engine starting improvement study have been described. Given that the *Aerodynamic Turbine Engine Code* (ATEC) was used in the study, the Part 1 paper also documented the mathematical models and the numerical methods employed in the simulation. The Part 1 paper concluded with a discussion of the planned test matrices for both the sea-level starting tests and the altitude starting tests. This paper documents the result of the model calibration studies. The trade-off studies used to look at ways to improve the starting characteristics of the gas turbine engine are also discussed.

Given the importance of the ATEC simulation to the overall project objectives, considerable effort was expended ensuring that the simulation results agreed with the test data. As noted in an earlier paper on ATEC (Garrard, 1995), one of the most difficult tasks in the development of any mathematical model is ensuring that the actual system has been modeled correctly. If a model is not sufficiently detailed, then any conclusions made about the actual system based on the model results may be incorrect (Fishbach et al., 1975). As such, the calibration of computational fluid dynamics (CFD) programs in general has been a very active research topic in the recent past. As more and more dependence is placed on CFD calculations, the sources of errors in the computational algorithms must be fully understood. It is important that CFD programs be tested by comparing them to appropriate data sets to ensure their validity and to define their applicable range. Any shortfalls in the CFD model must be fully understood before it can be applied with confidence.

The ATEC model and simulation, based on the one-dimensional, inviscid Euler equations, is a CFD program. The one-dimensionality of the program, however, means that it can not be expected to provide the detailed surface and flow field properties that are required to fully simulate a gas turbine engine. This, of course, is not the purpose of the ATEC simulation. Rather, ATEC provides a "moderately" detailed simulation that can be used to identify the important factors which influence the bulk flow within the overall gas turbine engine, and hence its operation. The development of detailed component and sub-component level simulations can then be focused on the critical parameters.

The purpose of this paper is to present the results of the calibration effort. The calibration effort was conducted to demonstrate that the ATEC model and simulation could match the gas turbine engine starting operation. Calibration results are presented for the ground level, starter assisted starting and the windmill starting occurring at altitude flight conditions. For both cases, the simulation results are compared to actual test data obtained during the

---

[1] The research reported herein was performed by the U.S. Army Vehicle Propulsion directorate, the NASA Lewis Research Center, General Electric Aircraft Engines, the General Electric Corporate Research and Development Center, and the Arnold Engineering Development Center (AEDC), Air Force Materiel Command. Funding was provided by NASA's Advanced Subsonic Technology program and by GE Internal Research and Development under Space Act Agreement No. FA-103, Large Engine Technology Contract (LET) No. NASA-26617 Task Order 54 and Interagency Agreement C-71064-E. Further reproduction is authorized to satisfy the needs of the U.S. Government.

Contributed by the International Gas Turbine Institute (IGTI) of THE AMERICAN SOCIETY OF MECHANICAL ENGINEERS for publication in the ASME JOURNAL OF ENGINEERING FOR GAS TURBINES AND POWER. Paper presented at the International Gas Turbine and Aeroengine Congress and Exhibition, Stockholm, Sweden, June 2–5, 1998; ASME Paper 98-GT-471.

Manuscript received by IGTI March 24, 1998; final revision received by the ASME Headquarters March 23, 1999. Associate Technical Editor: R. Kielb.

experimental portion of the program. The paper concludes by presenting some results from the trade-off study. Several possible options were considered to improve the starting characteristics of the gas turbine engine.

Model Calibration

The ATEC model requires detailed information describing the operation of the major components of the gas turbine engine to be simulated. Much of the information required to model the General Electric (GE) CT-7 engine was provided by the engineering staff of the General Electric Aircraft Engines Lynn, MA facility. However, some specifics of engine operation, particularly in the starting range, were not available. This information was acquired from the ground level testing that occurred at the GE Corporate Research and Development (CR&D) Center and the altitude testing that occurred at the NASA Lewis Research Center (LeRC). Comparisons between model predictions and actual engine operations provided a database to modify component characteristics in the starting region. These are discussed in this section.

Initially, the simulation did not accurately describe the actual engine performance. Indeed, it deviated substantially from the test article. There were three reasons for this:

1 As was previously mentioned, little information exists in the very low speed range of engine operation. The initial assumptions concerning turbine performance, for example, were in error.
2 The engine had a substantial number of operating hours on it. Thus, component performance was somewhat less than that of a nominal engine, which the provided information described.
3 Lastly, this code was used to describe a transient event, the engine start. The engine description provided, of course, was steady-state information. As such, transient variations not normally described and perhaps not well understood were not included in the information describing the engine operation.

When approaching this model calibration effort, one must understand the operational nature of the system. For example, the engine fuel schedule is determined partially from the compressor outlet conditions. Thus, if the simulation's model of the compressor is inaccurate, the start time will be incorrect because the simulated fuel flow is not correct. However, since compressor operation at any given engine speed is a function of airflow through the engine (a variable controlled largely, but not entirely, by the turbine throat area) an incorrect fuel setting may be the result of the turbine parameters and not the compressor description. Thus, modification of any part of the engine description used by the simulation should be made with care to insure the proper variable is changed.

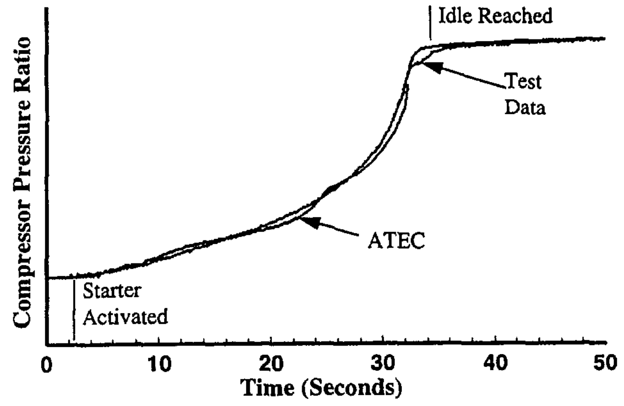

Fig. 2 Compressor pressure ratio as a function of time for the gas turbine engine ground level starting calibration study

Ground Level Starting Calibration. Baseline and sensitivity testing at the General Electric Corporate Research and Development Center provided a database to modify engine component representations to match start times and turbine temperatures. As noted above, the ATEC simulation of the CT7 core was initially based on a "nominal" engine. Data for the combustor efficiency map were obtained from an engine that used a combustor similar to that of the CT7. Turbine performance maps were obtained from the CT7 design database for the higher speeds and extrapolated to the lower speeds as needed. Because of the criticality of the compressor performance to the overall start process, an initial map of compressor performance was not developed. Compressor performance maps were generated only after test data were acquired. Additional detail of the ground level calibration effort is reported in Garrard et al. (1997).

A sample compressor stage pressure ratio map is shown in Fig. 1. Although the ATEC simulation has the ability to represent the compression system in post-stall operation, program objectives limited the simulation to operating only in the normal, pre-stall regime. As such, the ground level calibration was limited to simulating only the starts in which the engine was at ambient thermal conditions. It was shown by the test data that starts occurring with the engine metal temperatures elevated due to previous starts resulted in the compression system operating in stall during part of the speed transient.

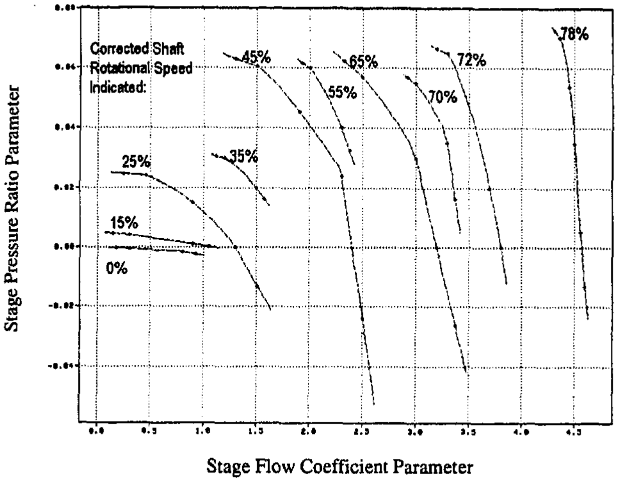

Fig. 1 Map of stage 1 compressor total pressure parameter as a function of inlet flow parameter

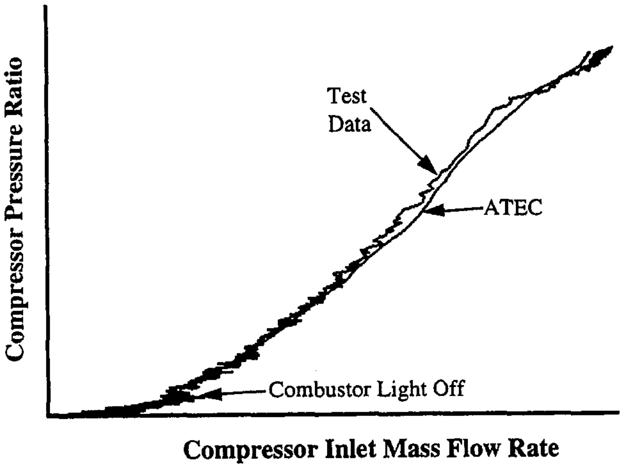

Fig. 3 Compressor pressure ratio as a function of percent design compressor corrected air flow rate for the gas turbine engine ground level starting calibration study

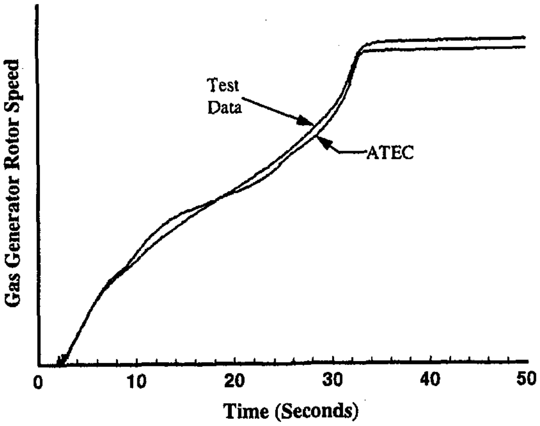

Fig. 4 Gas generator shaft corrected rotational speed as a function of time for the gas turbine engine ground level starting calibration study

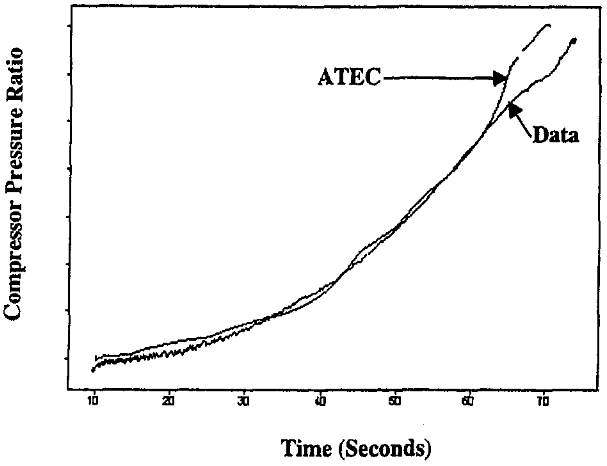

Fig. 6 Compressor total pressure ratio as a function of engine shaft corrected rotational speed

The results of the model calibration are presented in Figs. 2 through 4. The compressor total pressure ratio as a function of time is shown for both the simulation and test data in Fig. 2. The compressor pressure ratio is shown as a function of the percent design corrected airflow rate in Fig. 3. The gas generator shaft rotational speed as a function of time is shown in Fig. 4. The simulation results matched the test results closely, with approximately a ten percent difference that occurred during the highly dynamic portion of the start near the time that the engine reached idle speed.

Initial Altitude Starting Calibration. After the completion of altitude testing at the LeRC, the simulation calibration was adjusted to reflect the measured engine starting performance. The approach used to calibrate the simulation was to start at the front of the engine and to modify inputs from front-to-rear. While this appeared to be a straightforward approach, it was not. It cannot be stressed strongly enough that the model is of an engine system. As such, the modification of one parameter can have unforeseen consequences on the simulation performance. For example, compressor performance is governed not only by the compressor maps but by the turbine performance, which sets the engine mass flow throughout the start.

A typical engine windmill start (normal engine configuration) at approximately 3000 meters and the original model simulation of a start with the same boundary conditions is shown in Figs. 5 through 11. The engine gas generator shaft rotational speed as a function of time is shown in Fig. 5. The compressor total pressure ratio as a function of engine shaft corrected rotational speed is shown in Fig. 6. The compressor total temperature ratio as a function of corrected engine speed is shown in Fig. 7. The engine inlet airflow rate as a function of corrected engine rotational speed is shown in Fig. 8. The scatter present in the experimental data is attributable to the measurement uncertainties inherent with measuring small mass flow rates with a venturi. The fuel flow rate as a function of corrected engine speed is shown in Fig. 9. The

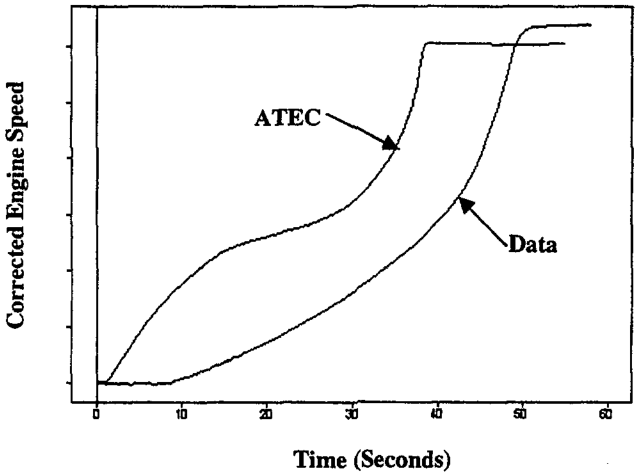

Fig. 5 Engine gas generator shaft rotational speed as a function of time

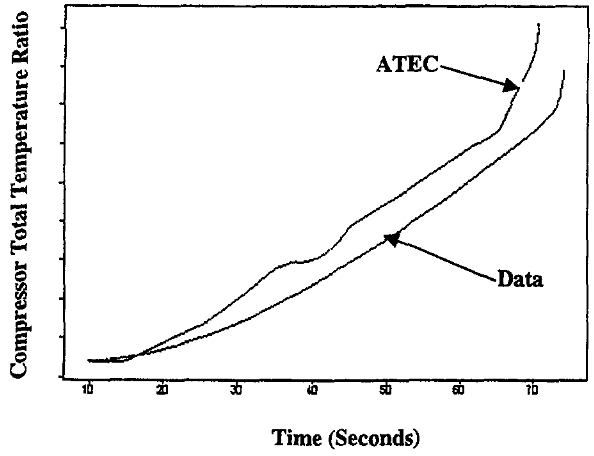

Fig. 7 Compressor total temperature ratio as a function of corrected engine speed

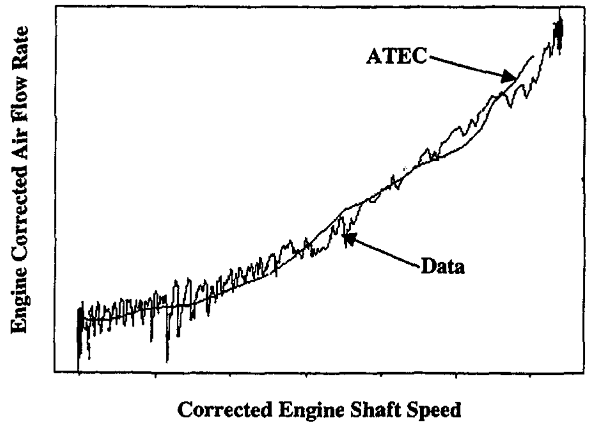

Fig. 8 Engine inlet airflow rate as a function of corrected engine rotational speed

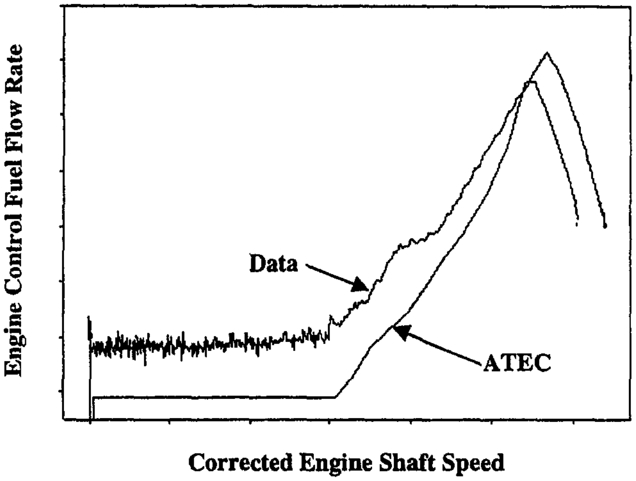

Fig. 9 Fuel flow rate as a function of corrected engine speed

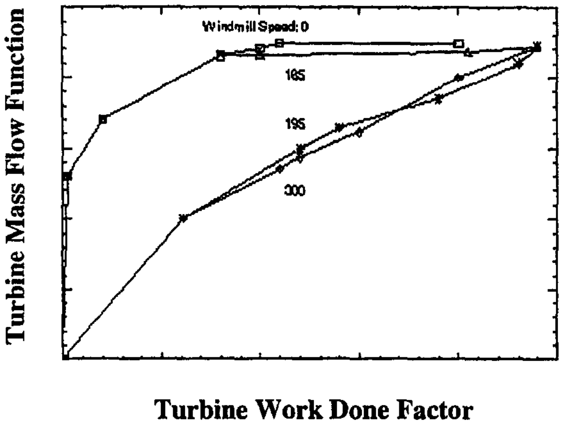

Fig. 12 Turbine flow function as a function of turbine work done factor

combustion efficiency as a function of the Longwell Loading Parameter (Longwell, 1955) is shown in Fig. 10. Finally, the turbine work done factor as a function of the corrected turbine speed is shown in Fig. 11.

Many parameters, such as compressor pressure ratio versus compressor corrected speed, closely match the actual engine performance over much of the start, and the original engine simulation starts in about the same time as the test. However, many parameters, such as compressor temperature rise, do not accurately reflect the engine operation, and it is obvious that the model did not represent the start accurately. Additional calibration to altitude windmill starting conditions, in addition to calibration to ground level starts, was needed. The testing that was accomplished at the LeRC was the first information available for the engine that could be used for this type of calibration.

Recalibration Using Windmill Start Test Results. The most obvious discrepancy between the simulated start and the experimental test data is in the rate of acceleration of the simulated start versus the experimental start. As is apparent in Fig. 4, the experimental data shows a start that begins slowly and continues to increase its rate of acceleration until on-speed conditions are reached. In contrast, the simulated start begins rapidly and slows in its rate of acceleration until about 38 percent corrected speed, where it rapidly begins to increase its rate of acceleration until on-speed conditions are reached. This inflection point is important because it represents the point where the simulation indicated was critical during windmill altitude starts during the preliminary altitude trade-off studies. This occurs near the point when the fuel flow comes off the minimum flow value and on to the acceleration schedule, as shown in Fig. 9. Figure 11 presents the turbine work done factor as a function of corrected turbine speed. This was far higher than the measured value. Even after the model was calibrated, this value remained high.

Figure 11 also provides some indication of why the predicted start was much more rapid in the early portion of the start and why such a simulation calibration can be difficult. For the first 25 seconds of the start and including the windmill time, the gas generator turbine speed was below 300 RPM. This is the minimum

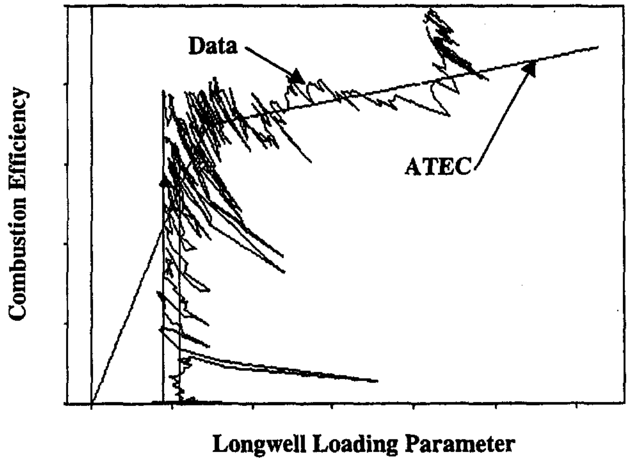

Fig. 10 Combustion efficiency as a function of the Longwell loading parameter

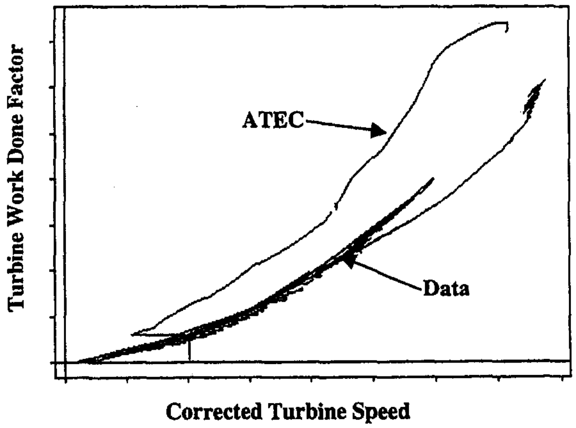

Fig. 11 Turbine work done factor as a function of corrected turbine speed

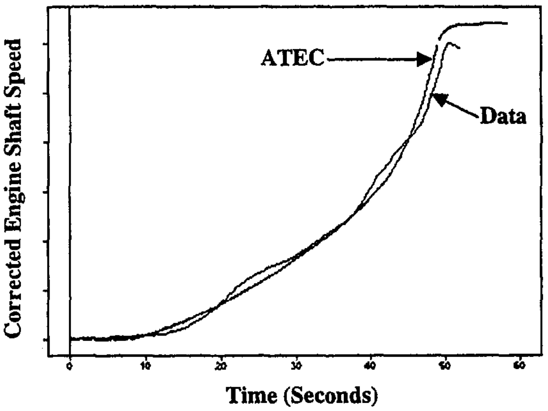

Fig. 13 Engine corrected shaft rotational speed as a function of time for both simulation and test data

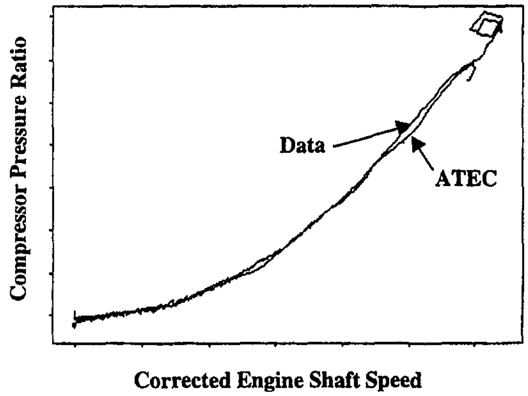

Fig. 14 Compressor total pressure ratio as a function of corrected engine speed for both simulation and test data

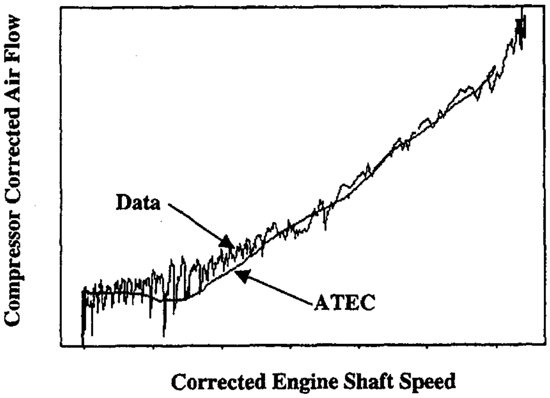

Fig. 16 Compressor corrected inlet air flow rate as a function of corrected engine speed for both simulation and test data

turbine speed for which turbine performance information was available. Thus, prior to the actual altitude testing, it was not possible to predict engine operation in this low speed range with any confidence. Indeed, this low speed range was not accurately simulated. Considerable effort was made to generate turbine maps that resulted in a reasonable representation of the start.

The resulting low speed (turbine corrected speeds of 0, 165, 195, and 200) turbine map is shown in Fig. 12. Turbine flow function is plotted on the ordinate and the turbine work done factor is plotted on the abscissa. Notice a line plotted near the turbine windmill speed (turbine corrected speed = 195 RPM). This line was used to adjust the windmill speed to be near constant. Another line was generated at a lower speed (165 RPM). This line was used to control the low speed acceleration rate of the engine by adjusting the speed it represented. Neither of these two lines was available from previously acquired data. While the resulting simulation of the start does reasonably reflect the engine start, it is unclear whether these added turbine operation lines are accurate. The authors feel that transient effects, such as heat transfer, that are largely not quantified in this low speed regime may play a large part in the robustness of the start. Nonetheless, the start is well simulated by the final calibrated simulation.

Calibration of the compressor was straightforward. Overall compressor performance was, for the most part, set by uniformly varying the performance of each stage. While the overall simulation performance compared well with the test, individual stage static pressures (the only available inter-stage parameter) did not compare well with the test. There are two reasons for this. One is that it was not possible to obtain true stage performance data. Secondly, the simulation does not account for swirl, which was present and does effect static pressures.

Combustor efficiency versus Longwell loading parameter is shown in Fig. 10. This was modified, as were the other components, to reduce combustor efficiency. Scatter in the data made it difficult to accurately assess the actual curve. The simulation is extremely sensitive to this parameter, particularly in the very early start sequence, when efficiencies are low.

The turbine performance and the final calibrated simulation of that performance are compared in Fig. 11. The turbine work done factor as a function of corrected turbine speed is shown in Fig. 11. Clearly, the turbine performance reflects the actual engine operation more closely than the combustor performance, but considerable room for improvement remains. Turbine performance was adjusted in several speed ranges to accurately represent the start. It was fabricated in the low speed range (0 to 300 RPM turbine speed) because no information existed there. Between 300 RPM and 650 RPM, performance was degraded by approximately 95 percent to slow the start. Above 650 RPM, performance was degraded in such a way that final engine airflow and ground idle speed were accurately represented.

The final 3000 meter calibrated model results are shown in Figs. 13 through 19. This calibration was done after testing, of course, and was not used in the simulation studies that helped structure the altitude testing. Figure 13 shows the simulation calibrated engine speed as a function of time compared to the experimental results. While the simulation does not exactly follow the experimental results, it much more closely reflects the actual start. The compressor pressure ratio as a function of compressor corrected speed is shown in Fig. 14. The compressor temperature rise as a function of compressor corrected speed is shown in Fig. 15. Corrected airflow as a function of corrected compressor speed is shown in

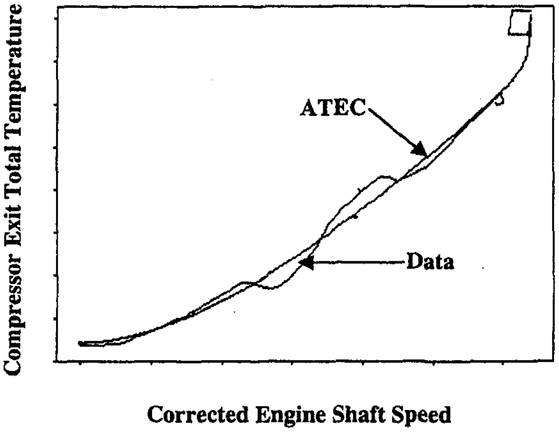

Fig. 15 Compressor exit total temperature as a function of corrected engine speed for both simulation and test data

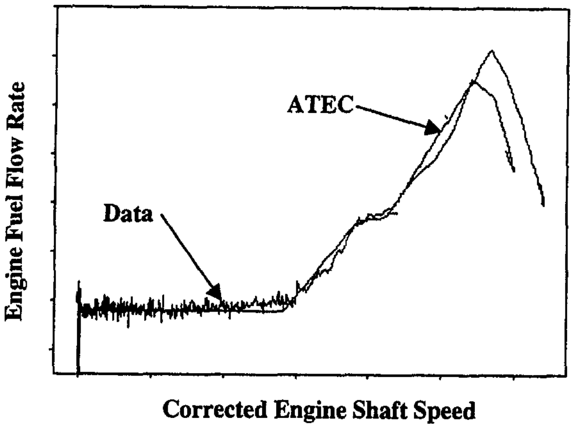

Fig. 17 Engine fuel flow rate as a function of corrected engine speed for both simulation and test data

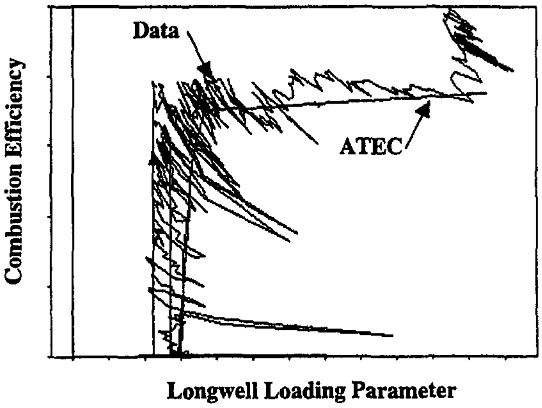

Fig. 18 Combustion efficiency as a function of the Longwell loading parameter for both simulation and test data

Fig. 16. Fuel flow rate as a function of corrected engine speed is presented in Fig. 17. Combustion efficiency as a function of Longwell Loading parameter is shown in Fig. 18. Finally, turbine work done factor as a function of corrected turbine speed is presented in Fig. 19.

The overall result is a simulation that is calibrated not only overall, but also on a component level, for altitude engine starts.

Ground Level Tradeoff Studies

Once the model was calibrated to adequately represent the engine, the objective was to use it to explore ways to improve the engine start capabilities. For ground level (and assisted altitude) starts, this improved starting was defined as reaching ground idle in the nominal time (or less) with less starter power and a minimal peak temperature increase.

Ground Level Simulation Study Matrix. For ground level model studies, modification to the engine start scheduling and characteristics were made to improve the engine start. Then, the model starter power was reduced to produce the baseline engine start time. The following modifications were made to the engine:

1 The Stage 1 and/or 2 stator vanes (SV) were closed to reduce the required compressor power and increase the stall margin. Then, the fuel schedule was increased in the region of low acceleration.
2 The compressor start bleed flow rate was increased to increase compressor stall margin and raise the fuel schedule in the region of low acceleration.
3 Closing stage 1 and 2 stator vanes and increasing start bleed with an appropriate fuel schedule modification were combined.
4 The compressor stage characteristics were modified to simulate stall improvements from casing treatment, and the fuel schedule was modified.
5 Fuel and ignition were introduced earlier during the start sequence. This resulted in higher accelerations early in the start sequence. Another result was higher combustion efficiency later in the start due to the higher combustor temperatures.
6 Combustor volume was increased to increase combustor efficiency and turbine output power. Compressor stall margin must also be increased to provide a successful stall free-start.
7 The viscous drag (and resulting starter power requirements) was reduced by heating the lubricating oil. Engine starter power requirements are often dictated by cold day viscous drag characteristics.
8 The rotor polar moment of inertia was reduced consistent with potential future low rotor inertia advances, and, thus, reducing power requirements.

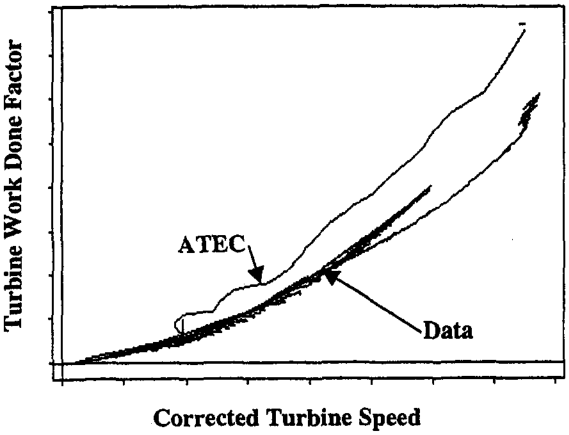

Fig. 19 Turbine work done factor as a function of corrected turbine speed for both simulation and test data

Table 1 Ground level test matrix

	Stator Vane 1	Stator Vane 2	Bleed	Accel Fuel	Ignition Speed
1	closed	nominal	nominal	+4%	nominal
2	closed	closed	nominal	+5%	nominal
3	nominal	nominal	+3.5%	+11%	nominal
4	nominal	nominal	nominal	Nominal	early
5	closed	closed	+3.5%	+15%	nominal
6	closed	closed	+3.5%	+13%	early
7	closed	closed	nominal	Nominal	nominal

When the fuel schedule was raised, it was only increased in the region of low acceleration rates to provide increased turbine power. The peak turbine exit temperature was not increased, since it occurred later in the start sequence where the acceleration rates were already high.

Comparison of Engine Test and Simulation Results. After completing the concept model studies, a test program was conducted to validate the model study results with engine test data. Only modifications that could be made without major disassembly of the engine (parameters 1 through 6 above) were considered for test validation. A summary of the ground level test matrix is shown in Table 1.

A direct comparison of the improvements predicted by the model and the ground level test results are shown in Table 2. "Starter power reduction" is the percent reduced power required to bring the engine to ground idle in the same time period as a "baseline" engine configuration. Discrepancies between model predictions and test results are apparent. These differences may result from the compressor stage maps that were used in the model. Individual stage characteristics were calculated, rather than mea-

Table 2 Percent starter power reduction

Case	Model Prediction	Test Results	Test Turbine Exit Temperature Increase (C)
1	-4%	0%	+11.1
2	-5%	0%	0
3	-8%	-24%	+9.4
4	-19%	0%	0
5	+7%	-38%	+50.0
6	---	-20%	+44.4
7	---	+16%	-5.6

Table 3 Minimum steady state starting mach numbers

Altitude (m)	Mach Number	Steady State RPM
3000	0.42	7550
4500	0.43	7450
6000	0.59	8475
7600	0.73	9750

sured, using the design point information and stage static pressures measured during the baseline testing. Thus, the model could not accurately predict compressor operation when the stages were rematched. The greatest disparity occurred for case 5, where both stator vanes and the bleed schedule have been altered.

Based on the results of the ground level testing, the following conclusions can be made for ground level starts: (1) initial thermal condition has a major influence on engine starting; (2) combustor efficiency also has a strong influence on compressor start operating line; and (3) for ground starting, increasing compressor start bleed increases the stall margin, allowing an increase in start fuel (in the slow acceleration speed regions) and the greatest reduction in required starter power.

Altitude Tradeoff Studies

As was mentioned before, initial trade-off studies used the ground level calibrated simulation. The work effort was conducted for two specific reasons. First, it was desirable to assess which modifications in the start sequence would provide the greatest opportunity for improving the start sequence. Second, it provided guidance in developing an efficient plan for the altitude start tests. As mentioned earlier, to meet both criteria, engine hardware and model modifications were restricted to modifications that could be implemented during the testing phase of the program. Additional studies exploring more extensive changes, such as blade redesigns, are anticipated. Finally, a standard protocol was developed for the trade-off study. For this protocol, individual parameters were varied from a standard initial condition (SC). The effectiveness in the change was assessed by establishing both the time to on-speed at the standard condition and the minimum Mach number for successful start.

Simulation Study Matrix. The study matrix for the analytical conceptual study ranged from minimum Mach numbers of 0.31 at 3000 meters and 0.70 at 7600 meters to maximum Mach numbers of 0.6 at 3000 meters to 0.75 at 7600 meters. All starts were at the standard altitude conditions. Initial engine configuration for the model was the desired Mach number, windmilling at 12000 RPM, fuel manifold full, and "warm" (oil temperature 30C).

The standard conditions (SC) set an engine windmill speed of 12000 RPM. This was higher than the predicted windmill speed (and starting Mach number) required for combustor light off. This allowed a clearer comparison of the differences between the parameters varied during the start study, but did not accurately portray the minimum starting Mach number for a given configuration operating without fuel pump delivery restraints. For the standard configuration, minimum steady RPM starting Mach numbers and steady state windmilling RPM at those Mach numbers predicted by the model are given in Table 3.

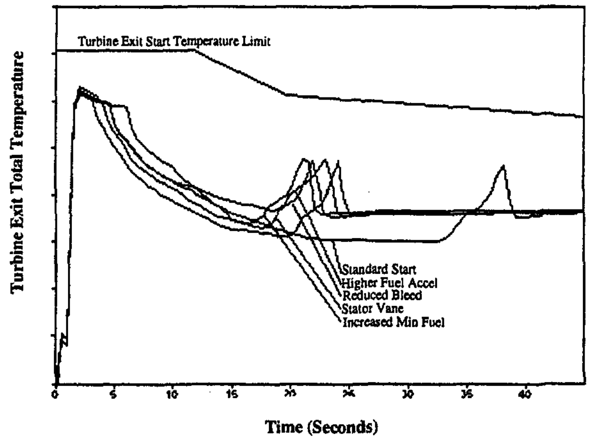

Fig. 21 Turbine exit temperature for the selected starting conditions

Since the minimum successful starting Mach number rises with altitude, the steady state windmill RPM increases, which is reflected in the results shown in Table 3. The parameters varied during the altitude simulation study are given in Table 2 of Part 1.

Preliminary Trade Study Model Results—Normal Start. The predicted torque imbalance for the engine for a successful (Mach = 0.42) and an unsuccessful (Mach = 0.4) start, both at 3000 meters, are shown in Fig. 20. The predicted turbine exit temperature for those starts is shown in Fig. 21. These particular simulations were run with a steady state engine speed as the boundary condition. This would be a restart with the aircraft gliding at a steady speed and the engine windmilling in a steady-state condition. The information shown in these figures provide some insight into the nature of the windmill restart problem. To improve windmill-starting characteristics, minimum torque imbalance must be improved, either by reducing required torque or by increasing the torque available. Accomplishing this can be difficult due to the complex relationships in a gas turbine system, but two limits are of primary importance to any desired system modification: compressor stall/surge and turbine over-temperature. Plotted in Fig. 21, in addition to the predicted turbine exit start temperature, is the limiting turbine temperature. In Fig. 22, a low speed stall/surge line, acquired during ground level testing is plotted against the compressor operating line. Clearly, the simulation

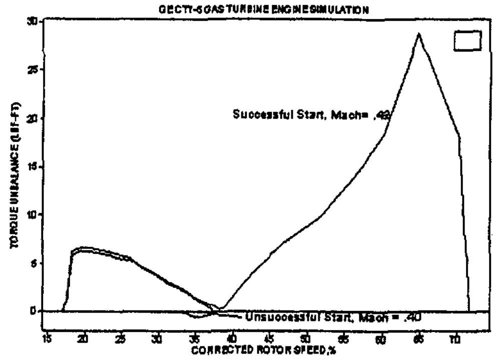

Fig. 20 Engine torque balance for successful and unsuccessful altitude start test cases as a function of corrected rotor speed

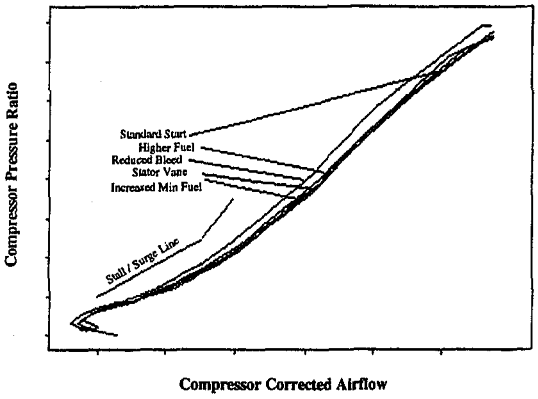

Fig. 22 Compressor operating line for various engine operating conditions at the minimum successful starting mach number

Table 4 Windmill restart mach number improvement at 3000 meters

Variable	Preliminary Model Predictions	Test Results	
Aux Power Disconnected	0.22	NA	
Minimum Fuel Enrichment, 8%	0.20	~0	
Stator Vane 1, 12% Closed	0.20	~0	
Minimum Fuel Enrichment, 4%	0.11	~0	
Stator Vane 1, 6% Closed	0.10	~0	
StartBleed, 25% Closed	0.07	0.04	
Accel Schedule Enrichment, 8%	0.07	~.0.02	

predicts considerable margin for both temperature and stall during the windmill start sequence.

Preliminary Parametric Study. For the purposes of the preliminary study, combinations of variables were not considered. Modifications of the fuel schedule are likely to affect both the turbine exit temperature and the engine acceleration rate. Modifications to the Inlet Guide Vane (IGV), SV, and bleed schedules, which are normally configured at a constant position for the start, may also affect the engine peak temperatures or surge margin. The effects of the closed SV and the 25 percent bleed reduction are also shown in Fig. 22. It is clear that the simulation predicted that the magnitude of these proposed modifications was small enough to not exceed any engine start limits. However, all of these changes will result in stage rematching. Recall that the information on compressor operation (in the form of stage characteristics) input to the model included only design point performance, with estimated individual stage characteristics. Therefore, the predicted rematching results will likely be in error.

Other proposed modifications have a much more benign effect on engine operation. One is a reduction on starting drag torques (viscous effects and auxiliary drives). An attempt to increase the power available from the turbine (changes in turbine exit area) was also considered. Increasing the lubricating oil temperature by only 10 degrees Celsius resulted in only a small change in the starting times. However, this is very dependent on initial oil temperature; start times would increase in very cold conditions. Reducing auxiliary power extraction may not be practical for most turboprop/turbofan applications, since this power provides lube oil, fuel, and electrical power for current engine configurations. Nonetheless, warming the lubricating oil at high altitudes might provide a noticeable improvement in start times. Also, the use of electrical accessories or an air turbine to provide fuel, oil and electrical services during emergencies might be a viable approach to improving air start capabilities.

The results of these preliminary parametric studies are presented in Table 4. This table shows the reduction in minimum starting Mach number for standard start conditions. Configuration changes other than those shown in the table resulted in only minimum reduction in starting Mach number at an altitude of 3000 meters.

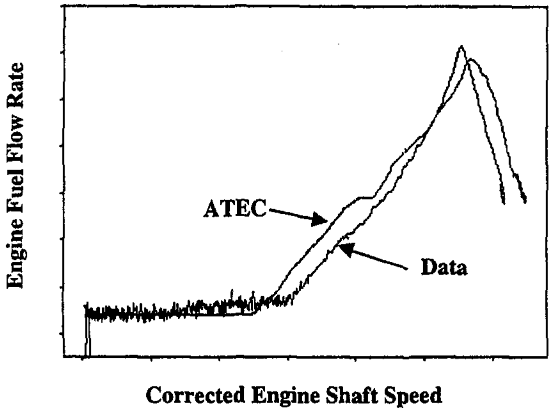

Fig. 24 Engine fuel flow rate as a function of engine corrected shaft speed

Comparison of Engine Test and Preliminary Simulation Results. The results of the altitude testing at the Lewis Research Center for engine windmill starts at 3000 meters are shown in Table 4. As has been mentioned before, the principal goal of the program was the acquisition of data for simulation calibration, with only a reduced set of test points taken to validate improved starting concepts. Overall, the tests results indicated that only reduced start bleed and fuel enrichment had noticeable effects on starting performance.

A number of differences existed between the simulation matrix and the actual tests. Minimum fuel enrichments were 3.1 percent and 5.6 percent. The start bleed reduction was 22.5 percent and the fuel acceleration schedule was 16 percent instead of 8 percent. The overall test results indicate that the engine is much less sensitive to modifications designed to improve starting than the simulation would suggest.

A "best combination" consisting of an increased fuel acceleration fuel schedule and reduced starter bleed was tested. This combination had the effect of reducing the time to idle (normally in the range of 45 to 50 sec.) by about 25 sec. This combination was allowable because of the substantial compressor and turbine margins available.

Comparison of Engine Test and Altitude Simulation Results. Following the successful calibration of the engine model to the standard 3000 meter altitude start, the model was evaluated against

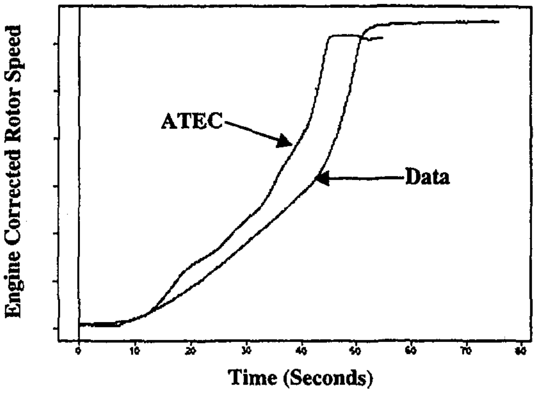

Fig. 23 Engine corrected rotor speed as a function of time for the calibrated altitude start case

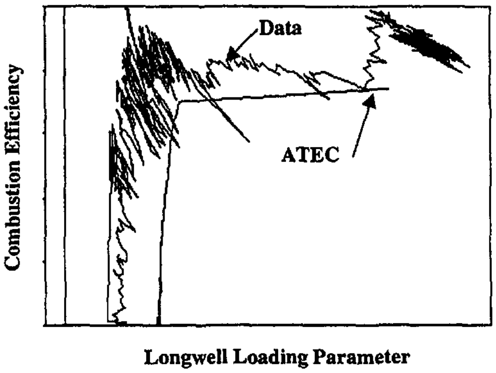

Fig. 25 Combustion efficiency as a function of Longwell loading parameter

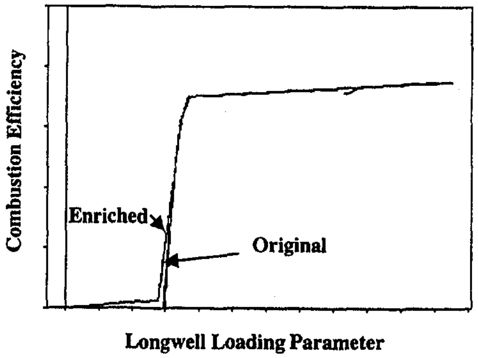

Fig. 26 Combustion efficiency as a function of Longwell loading parameter comparison

two of the experimental starts from the test program to assess if the calibrated model more accurately reflected actual variations in starting parameters. The two selected starts were a bleed-closed start and an enriched fuel schedule start.

Figures 23 through 25 present a few results from the bleed-closed start. Shown in Fig. 23 is a plot of engine speed as a function of time for both the experimental test and the simulation. The simulation predicts a start that is approximately 5 sec. faster than the actual experimental result. This correctly predicts that a reduced bleed improves the engine starting capability.

However, a closer inspection of component performances indicates that additional component tuning is required. This is clearly shown in Fig. 24, fuel flow as a function of engine speed, and Fig. 25, combustion efficiency as a function of the Longwell loading parameter. The increased fuel flow shows that predicted compressor performance is better than the test vehicle. On the other hand, the measured combustion efficiency is much better than the model predicts. A closer inspection of the acceleration rate as given in Fig. 24 shows that the windmill torque balance needs modifications also.

The initial attempt to simulate the enriched fuel start was unsuccessful. Combustion efficiencies never exceeded zero. To allow a successful start, the combustion efficiency at low Longwell loading parameters was improved. Comparison with the original calibrated combustion efficiency and the revised combustion efficiency is shown in Fig. 26. A 0.833 percentage reduction in Longwell loading parameter at the 0 percent, 10 percent, and 20 percent efficiency lines were taken. This was important for about 5 sec. early in the start sequence.

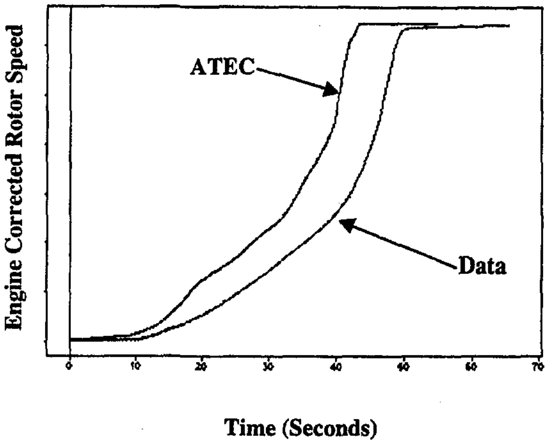

Fig. 27 Corrected engine shaft speed as a function of time for the modified altitude start case

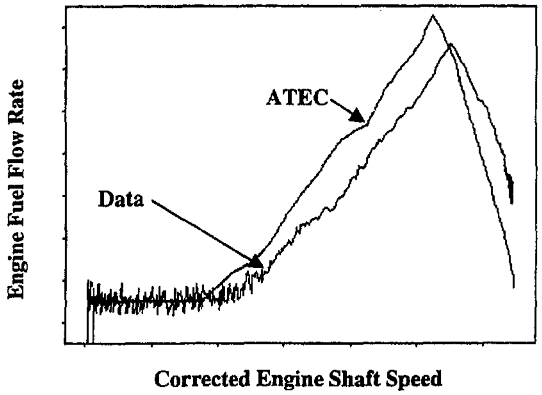

Fig. 28 Engine fuel flow rate as a function of corrected engine shaft speed for the modified altitude start case

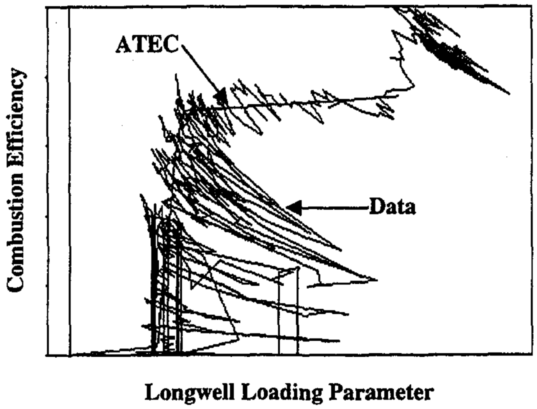

Fig. 29 Combustion efficiency as a function of the Longwell loading parameter for the modified altitude start case

Figures 27 through 29 show the results of the start as compared with the experimental results. Again, the calibrated engine simulation over-predicted the effectiveness of the engine modifications with respect to the experimental results. However, it did correctly indicate improved starting for this modification. Figure 27 shows the simulation predicting a start that is approximately 8 sec. faster than the experimental result. This is due, in large part, to the substantially higher fuel flow predicted by the simulation (Fig. 28). Finally, it is clear that the modification of the combustion efficiency to allow a successful start falls within the experimental error of the measured data (Fig. 29).

These results indicate that, while the simulation was improved by this preliminary calibration process, additional tuning of the simulation will be required.

Summary and Conclusions

1 A one-dimensional dynamic gas turbine engine model, ATEC, was configured to represent the gas generator of the General Electric CT7-5 and was used to explore improved starting methods.
2 The model indicated that, for ground starting, early ignition provided the greatest improvement in starting followed by a combination of increased bleed and a higher fuel flow.
3 Ground level testing indicated that the most substantial improvement in starting was increased bleed, higher fuel flow, and variable geometry rescheduling to control the operating line location.
4 Model altitude windmill restarts indicate the most effective method of improving restart capability is to reduce required

torque (removal of auxiliary power). However, this option was not confirmed due to the inability to implement this change in the test cell.

5 Test results indicate that only reduced start bleed and an increased fuel acceleration schedule will improve windmill starting capabilities. Improved starting was predicted using the simulation; however, the magnitudes of the improvement were underpredicted.

6 The model was considerably more sensitive to configuration changes in inlet guide vane, stator vane, and minimum fuel flow enrichment than the engine test results indicate is appropriate.

7 A successful engine simulation for use in starting studies requires accurate information for each engine component, reflecting component operation across the operating range of interest. It is difficult to calibrate in the windmill/low speed range where little or no information exists. This region is important for starting studies.

8 Additional model calibration will be required to insure the simulation accurately reflects the engine.

Acknowledgments

The authors thank the engineering and technical staffs of both the GE CR&D Center and NASA LeRC for their superior assistance. Partial funding of this effort came from NASA's Advanced Subsonics Technology Program directed by Mr. Pete Batterton. A special thanks to Mr. Peter Montgomery of Sverdrup Technology, Inc. (AEDC Group) for his assistance in the altitude model calibration.

This program is a part of JDAPS dynamic engine modeling efforts.

References

Garrard, D., Davis, M., Jr., Hale, A., Chalk, J., and Savelle, S., 1997, "Analysis of Gas Turbine Engine Operability with the Aerodynamic Turbine Engine Code," ISABE 97-7034.

Garrard, G. D., Davis, M. W., Jr., and Hale, A. A., 1995, "Recent Advances in Gas Turbine Engine Dynamic Models Developed Through JDAPS," ASME Paper 95-GT-146.

Fishbach, L. H., and Caddy, M. J., 1975, "NNEP: The Navy NASA Engine Program (NASA)," NASA TM-X-71857.

Longwell, J. P., and Weiss, M. A., 1955, "High Temperature Reaction Rates in Hydrocarbon Combustion," *Ind. Eng. Chem.*, Vol. 47, pp. 1634–1637.

Combined Biomass and Black Liquor Gasifier/Gas Turbine Cogeneration at Pulp and Paper Mills

E. D. Larson

T. G. Kreutz

Center for Energy and Environmental Studies,
Princeton University,
Princeton, NJ

S. Consonni

Departimento di Energetica,
Politecnico di Milano,
Milan, Italy

Kraft pulp and paper mills generate large quantities of black liquor and byproduct biomass suitable for gasification. These fuels are used today for onsite cogeneration of heat and power in boiler/steam turbine systems. Gasification technologies under development would enable these fuels to be used in gas turbines. This paper reports results of detailed full-load performance modeling of pulp-mill cogeneration systems based on gasifier/gas turbine technologies and, for comparison, on conventional steam-turbine cogeneration technologies. Pressurized, oxygen-blown black liquor gasification, the most advanced of proposed commercial black liquor gasifier designs, is considered, together with three alternative biomass gasifier designs under commercial development (high-pressure air-blown, low-pressure air-blown, and low-pressure indirectly-heated). Heavy-duty industrial gas turbines of the 70-MW_e and 25-MW_e class are included in the analysis. Results indicate that gasification-based cogeneration with biomass-derived fuels would transform a typical pulp mill into a significant power exporter and would also offer possibilities for net reductions in emissions of carbon dioxide relative to present practice.

Introduction

As discussed elsewhere (Consonni et al., 1998; Larson and Raymond, 1997a), the kraft pulp and paper industry in North America is faced with the need to retire much of its black liquor and biomass-fueled steam turbine cogeneration capacity during the next 5 to 20 years. This presents a unique economic opportunity to introduce gas turbine-based cogeneration systems. The biomass and black liquor gasification technologies needed to enable the use of gas turbines are under active development by companies around the world and are likely to be commercially available within the paper industry's time frame for retiring existing systems (Larson and Raymond, 1997b). Long-term economics appear favorable for gasifier/gas turbine technology using black liquor (Larson et al., 1998) or biomass (Weyerhaeuser et al., 1995).

This paper presents results of performance modeling of integrated black liquor and biomass-gasifier/gas turbine-combined cycle cogeneration systems for pulp and paper mills. Cogeneration systems at such mills are designed firstly to meet process steam demands and recover pulping chemicals from black liquor, the lignin-rich byproduct from the wood digestion stage in kraft pulping. Black liquor is burned today in Tomlinson recovery boilers to generate steam and an inorganic smelt from which pulping chemicals are reconstituted. A variety of fuels, including bark, other biomass residues, and fossil fuels, are used as supplemental fuels at kraft pulp mills today, because the black liquor by itself is typically insufficient to provide all process steam requirements. For simplicity, here we consider the use of only black liquor and byproduct biomass as cogeneration fuels at a kraft mill.

Consonni et al. (1998) modeled the performance of three alternative black liquor gasifier/gas turbine cogeneration technologies and considered the use of a biomass boiler to generate additional steam when steam derived from black liquor was insufficient. The present work extends the analysis of Consonni et al. by considering gasification of the biomass rather than combustion. Three biomass gasifier designs are considered. Since the focus of the present work is on biomass, only one black liquor gasifier (pressurized, oxygen-blown) is considered. The black liquor gasifier is coupled with a 70-MW_e class gas turbine. The biomass gasifiers are coupled with 25-MW_e or 70-MW_e class turbines. Heat recovery steam generators (HRSGs) use exhaust heat from each turbine to raise steam that is delivered to a common steam turbine (Fig. 1, lower). The black liquor flow rate is set to meet the fuel-gas demands of the 70-MW_e class turbine, and is thus constant regardless of the design of the biomass portion of the plant. A minimum biomass fuel rate is established by the fuel demands of the biomass-coupled turbine. Higher biomass rates are considered to allow for supplementary firing of the biomass-coupled turbine's HRSG when greater amounts of process steam are needed than can be provided by the gas turbine exhaust alone (see Fig. 1, lower). Results from a parallel analysis with a Tomlinson recovery boiler substituted for the black liquor gasifier/gas turbine/HRSG system are also included (Fig. 1, upper).

Calculating Performance

The approach used to calculate cogeneration performance follows that described by Consonni et al. (1998), who also describe details of the modeling of the two black liquor conversion systems considered here (oxygen gasifier and Tomlinson furnace). The discussion of methodology here is restricted to key issues relating specifically to modeling the use of biomass in gasifier/gas turbine systems.

Biomass Gasification. A variety of relatively large scale biomass gasification technologies are at various advanced stages of development (Weyerhaeuser et al., 1995; Williams and Larson, 1996; Larson and Raymond, 1997b). Three gasifier/gas cleanup designs are considered here: (i) atmospheric-pressure air-blown fluidized-bed gasification with wet scrubbing, e.g, the technology

---

Contributed by the International Gas Turbine Institute (IGTI) of THE AMERICAN SOCIETY OF MECHANICAL ENGINEERS for publication in the ASME JOURNAL OF ENGINEERING FOR GAS TURBINES AND POWER. Paper presented at the International Gas Turbine and Aeroengine Congress and Exhibition, Stockholm, Sweden, June 2–5, 1998; ASME Paper 98-GT-339.

Manuscript received by IGTI March 18, 1998; final revision received by the ASME Headquarters March 23, 1999. Associate Technical Editor: R. Kielb.

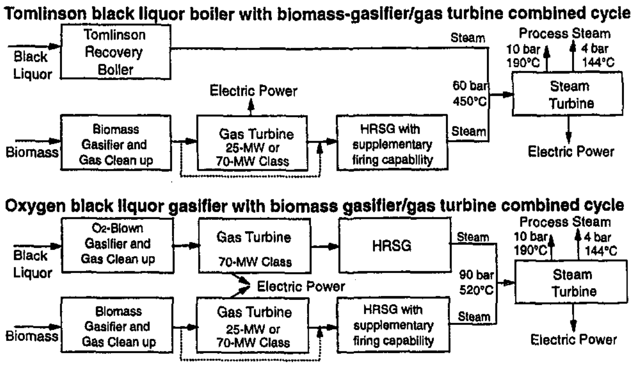

Fig. 1 Block representation of cogeneration systems modeled

under development by TPS (Waldheim and Carpentieri, 1998); (ii) pressurized air-blown fluidized-bed gasification with hot-gas cleanup, e.g., the technology under development by Carbona (Salo et al., 1998); and (iii) atmospheric-pressure indirectly-heated gasification with wet scrubbing, specifically the Battelle Columbus Laboratory (BCL) technology licensed for North American applications to FERCO (Paisley and Anson, 1997).

The assumed biomass gasifier feedstock in the modeling here is a mixture of pulpwood harvesting and thinning residuals and sawmill waste, with an initial moisture content of 50 percent. The waste bark and hog fuel generated at a typical kraft pulp mill converting logs into pulp amounts to some 0.25 dry tonnes of biomass per air-dry tonne of pulp product (0.25 t_{db}/t_p). Many mills may have access to much more biomass. One detailed study around a Weyerhaeuser pulp mill in North Carolina identified a sustainable supply of up to 3 t_{db}/t_p at reasonable cost in the form of harvest residues and self and externally generated mill residuals (Weyerhaeuser et al., 1995).

Table 1 gives the detailed biomass composition (in the table caption), as well as modeled performance of alternative gasifiers. (The overall model includes drying of the biomass from 50 percent to 20 percent moisture content before gasification.) Empirical gasifier performance estimates given by Weyerhaeuser et al. (1995) have been used as a guide for the expected performance of the air blown gasifier designs, supplemented by discussions with developers of these designs (specifically TPS and Carbona). BCL technology developers have been consulted in arriving at the performance results for the third design. The gasifier heat/mass balances in Table 1 reflect reasonable values of gasification temperatures, carbon conversions, cold-gas efficiencies, heat losses, and product gas heating values. Gas compositions have been allowed to vary somewhat from published values in order to close the heat/mass balances, because small changes in gas composition alone have relatively little impact on calculated overall cycle performance (Hughes and Larson, 1998). For additional discussion of the three biomass gasifier designs considered here, see Weyerhaeuser, et al. (1995), Craig and Mann (1996), Consonni and Larson (1996) and Larson and Raymond (1997b).

Table 1 Modeled performance of alternative biomass gasifiers. The feedstock in all cases is biomass with 20 percent moisture content with the following composition (dry mass basis): 50.2 percent carbon, 5.4 percent hydrogen, 34.4 percent oxygen, 0.2 percent nitrogen, and 4 percent ash. Its higher heating value is 20.47 MJ/dry kg.

	Low-Pressure Indirect-Heat	Low-Pressure Air-blown	High-Pressure Air-blown
Gasifier T, °C	865	920	850
Gasifier P, bar	1.50	1.34	19.8
Gasifier inputs			
Air, t/t dry biomass	0.0	1.48	1.80
Air temperature, °C	—	266	343
Steam t/t dry biomass	0.0	0.0	0.024[a]
Recycle gas, t/t dry bio.	0.06	0.0	0.0
Heat loss, % biomass HHV	2.9	1.21	0.97
Carbon conv. to gas, %[b]	70.1	96.9	97.4
Cold gas efficiency, % HHV	72.4	79.0	82.8
Clean gas			
Mass, t/t dry biomass	0.82	2.44	3.09
HHV, MJ/kg	18.1	6.47	5.48
Volume %			
Ar	0.0	0.468	0.433
CH_4	13.045	3.375	0.052
CO	39.236	21.333	24.394
CO_2	13.083	12.480	5.245
H_2	29.428	16.599	15.504
H_2O	0.432	4.826	15.504
C_2H_4	4.316	1.238	0.502
C_2H_6	0.259	0.126	0.0
N_2	0.182	39.248	38.366
NH_3	0.0	0.307	0.0

(a) Steam conditions are 26.9 bar, 441°C.

(b) Carbon in fuel gas divided by carbon into gasifier. The value for the indirectly heated gasifier appears abnormally low because, unlike the air-blown designs, char is oxidized in a separate vessel from that which generates the fuel gas. Thus, the carbon from the char is not reflected in the carbon conversion figure for the indirectly-heated gasifier.

Turbomachinery Assumptions. The accurate modeling of actual commercial gas turbines is an important feature of the process modeling software used. Turbines with the characteristics of the Siemens KWU 64.3a and the ABB GT-10 are simulated here

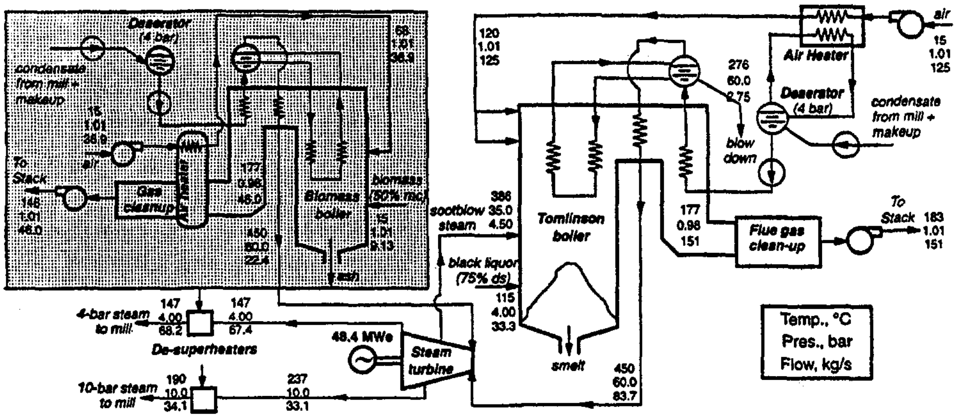

Fig. 2 Heat/mass balance for Tomlinson black liquor boiler with supplemental biomass boiler (shaded area) when delivering 16.3 GJ/*tp* process steam. Adapted from Consonni, et al., (1998).

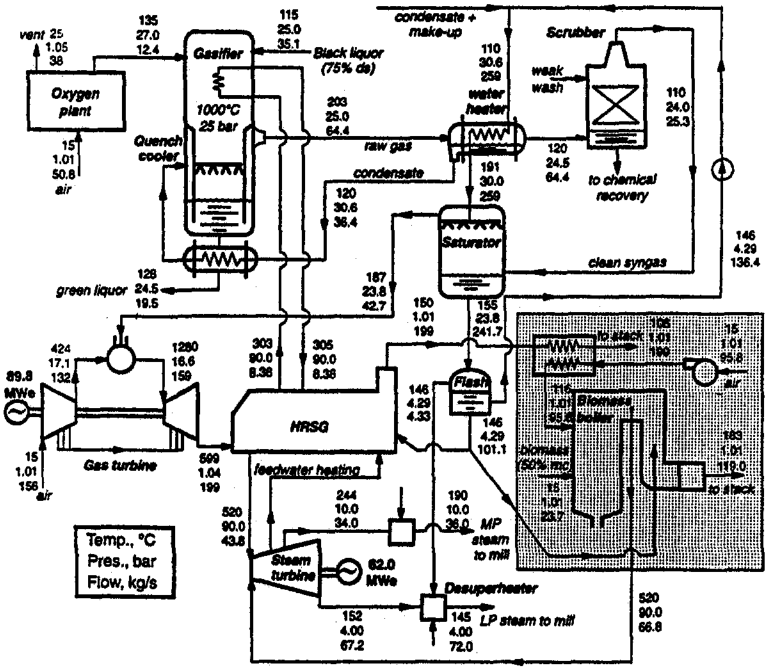

Fig. 3 Heat/mass balance for oxygen-blown black liquor gasifier/gas turbine with supplemental biomass boiler (shaded area) when delivering 16.3 GJ/*tp* process steam. Adapted from Consonni et al. (1998).

to represent state-of-the-art 70-MW$_e$ class and 25-MW$_e$ class industrial turbines. These two power output classes were selected because the requisite fuel delivery falls within the range of black liquor or biomass fuel that is, or could be made, available at many pulp mills in North America. A 70-MW$_e$ class machine is integrated with the black liquor gasifier (Fig. 1, lower). Because it is expected that atmospheric-pressure biomass gasification systems, particularly air-blown designs, will be more competitive at smaller scale than pressurized systems (Larson and Raymond, 1997a), the atmospheric-pressure gasifiers are coupled with the smaller of the two turbines. The atmospheric-pressure indirectly heated gasifier is also modeled with the larger turbine, as is the pressurized air-blown gasifier.

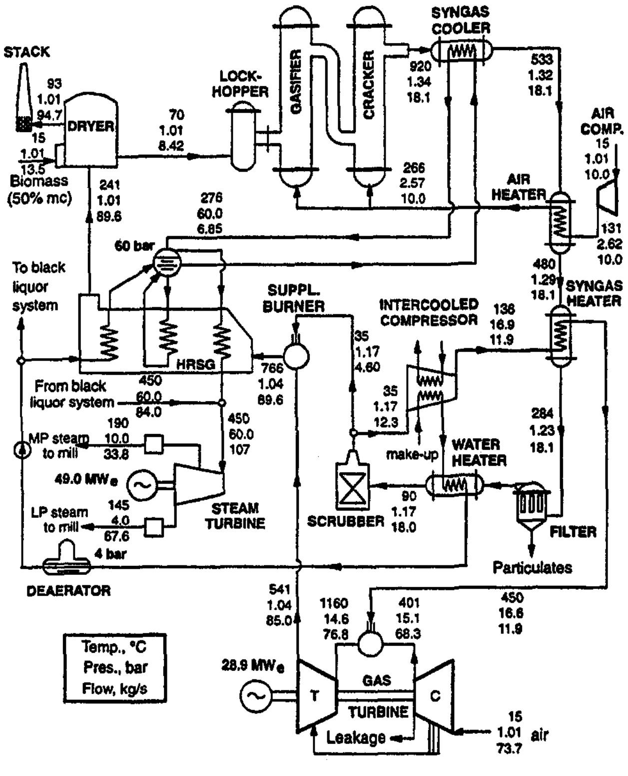

Fig. 4 Heat/mass balance for biomass-gasifier/gas turbine portion of a full cogeneration system that includes a Tomlinson black liquor boiler (see Fig. 2). The biomass gasifier is a low-pressure air-blown design and is fueling a 25-MW$_e$ class turbine. The complete (biomass plus black liquor) system delivers 16.3 GJ/*tp* of process steam.

A single steam turbine is used in all cases, with steam being generated from heat sources derived from both black liquor and biomass (Fig. 1). A range of total process steam demand is considered. Either a single-extraction back-pressure or a double-extraction condensing turbine is used depending on the level of process steam required[1]. (The back-pressure turbine is the paper industry standard today.) Process steam is delivered at 10 bar and 4 bar in a mass ratio of 1:2.

Plant Integration. To reduce the complexity of the required modeling, heat integration within the biomass sub-section of a full plant has been done independently of that within the black liquor processing sub-section. Figures 2 and 3 (adapted from Consonni et al., 1998) show illustrative heat and mass balances (for a particular process steam demand) for the two black liquor processing systems considered. A supplemental biomass boiler included in the mass balances is shown in the shaded areas of these figures. For the simulations reported in this paper, these shaded sections were, in essence, replaced by alternative biomass-gasifier/gas turbine-HRSG systems. For each of the three biomass gasifiers considered here, Figs. 4–6 show illustrative heat and mass balances for the biomass sub-sections for a particular level of process steam demand. Steam delivered from the black liquor sub-section is indicated in these figures. This steam is combined with the steam

---

[1] The performance estimates in this paper are for new cogeneration systems. In some practical situations, it may be feasible to continue to use an existing steam turbine by making minor modifications to it (e.g., increasing steam admission area) while replacing only the steam generating systems at a mill. In such cases, performance would be different from results in this paper.

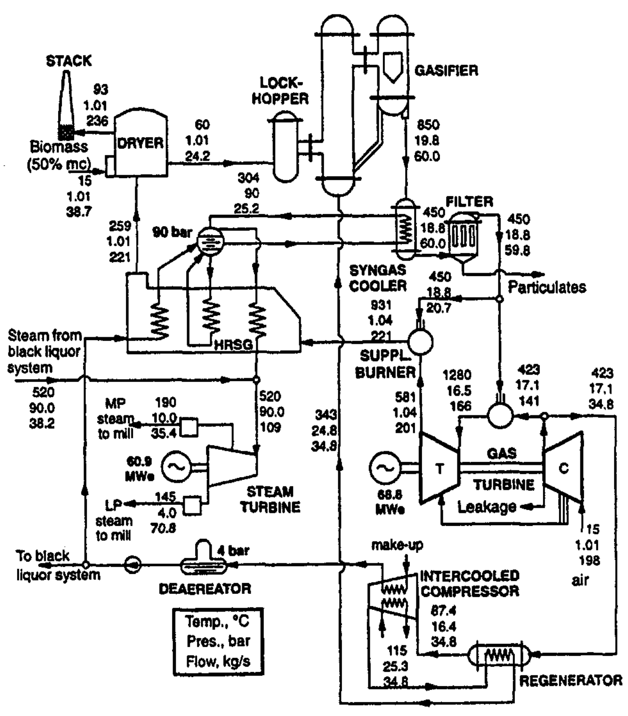

Fig. 5 Heat/mass balance for biomass-gasifier/gas turbine portion of a full cogeneration system that includes a black liquor gasifier/gas turbine (see Fig. 3). The biomass gasifier is a high-pressure air-blown design and is fueling a 70-MW$_e$ class turbine. The complete (biomass plus black liquor) system delivers 16.3 GJ/*tp* of process steam.

generated in the biomass sub-section and the combined flow is delivered to the steam turbine.

Within each sub-section, efforts have been made to optimize the heat integration among components to maximize efficiency within practical cost (and material) constraints. Heat exchanger networks have been designed following two guidelines. First, high-temperature gas streams transfer heat only to water or steam-water mixtures (evaporators); the high heat transfer coefficients guarantee acceptable heat exchanger metal temperatures. Second, to the extent possible in practice, heat is transferred across relatively small temperature differences and between flows having similar thermal capacities, which reduces irreversibilities.

Results and Discussion

Overall Performance Overall calculated performance is summarized in Fig. 7, which shows power output per metric tonne of pulp product (kWh/t_p) for different levels of process steam production (GJ/t_p) for each of the technology configurations simulated (upper set of curves) and the corresponding biomass fuel requirements per tonne of pulp (t_{db}/t_p) (lower set of curves).

For reference, Fig. 7 includes results from Consonni et al. (1998) for the two cases when biomass is burned in a boiler rather than being gasified. In these cases, process steam is delivered through a back-pressure turbine, so power output increases with increasing process steam demand. For the cases involving gasification of biomass, the minimum power output point represents the maximum process steam delivery possible without supplemental firing of the gas turbine HRSG. For any one of these systems, process steam demand levels to the right of the minimum power point require greater biomass consumption to enable supplemental firing of the HRSG. Process steam is delivered through a back-pressure turbine in these cases. The right end point represents the situation in which there is just sufficient oxygen in the exhaust of the biomass-coupled turbine to enable complete combustion of the amount of supplemental fuel required to generate the particular process steam demand. (This curve could extend further to the right, e.g., by introducing additional fresh combustion air, but this is not considered here.) To the left of the minimum power point, no supplemental firing is required. Biomass consumption remains constant (to meet the fuel demands of the gas turbine), and lower process steam demands enable a condensing turbine to be used to generate additional power. The left end-point represents the case when all of the steam generated in the biomass portion of the plant is condensed. (The curve could extend further to the left by condensing additional steam, but this is not considered here.)

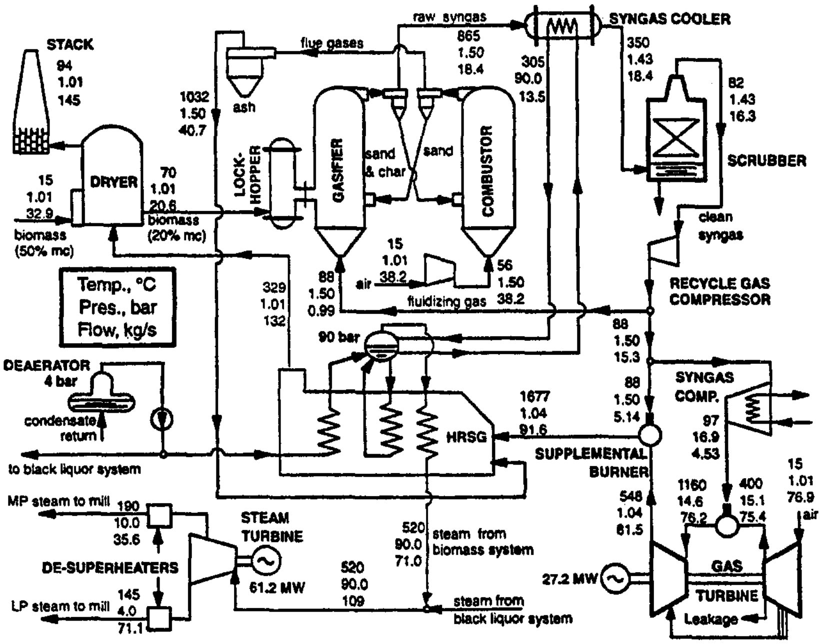

Fig. 6 Heat/mass balance for biomass-gasifier/gas turbine portion of a full cogeneration system that includes a black liquor gasifier (see Fig. 3). The biomass gasifier is a low-pressure indirectly-heated design and is fueling a 25-MW$_e$ class turbine. The complete (biomass plus black liquor) system delivers 16.3 GJ/*tp* of process steam.

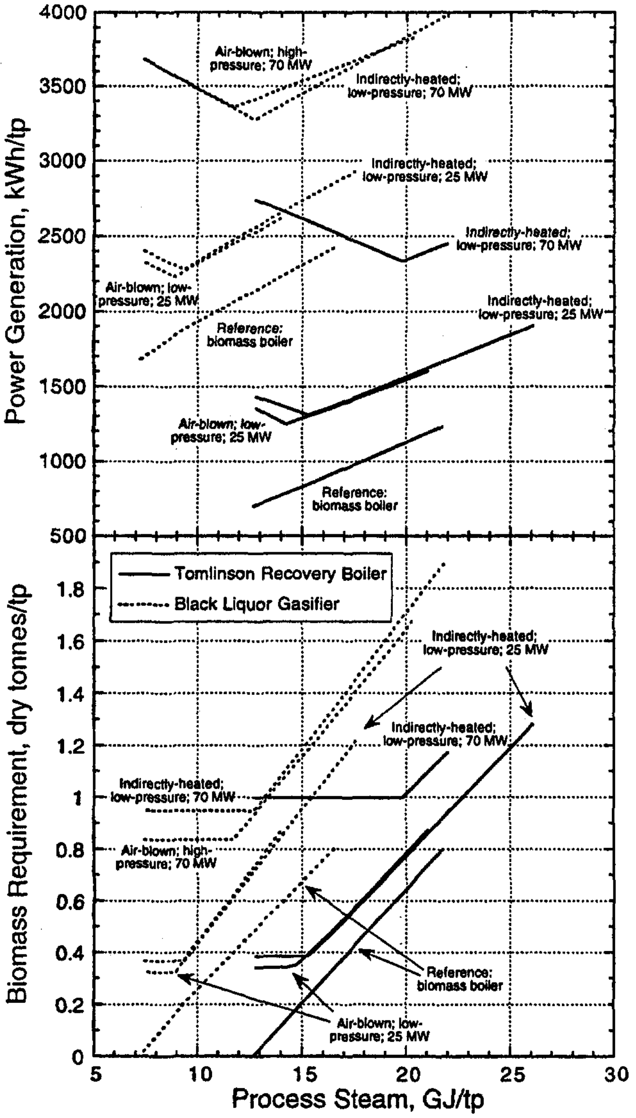

Fig. 7 Electric power generation and biomass fuel consumption for all cogeneration systems considered in this paper. In all cases, the black liquor consumption is 25 GJ/t_p. The two "reference" cases are from Consonni et al. (1998).

Among the cases involving the Tomlinson boiler (solid lines in Fig. 7), the case when biomass is burned in a boiler provides the lowest power output for a given process steam demand. On the other hand, biomass fuel requirements are also lowest, because a boiler/steam turbine converts a larger fraction of input fuel to steam than does a biomass-gasifier/gas turbine-HRSG arrangement. However, the two gasifier systems using the 25-MW_e class turbine (which have roughly comparable performance) consume relatively modest additional amounts of biomass (especially at larger process steam demand levels), while delivering considerably more electrical power. With the 70-MW_e class turbine, much more power is generated than in the reference (biomass boiler) case. The additional biomass required to accomplish this varies considerably with the level of process steam demand.

The results for the cases involving the black liquor gasifier (dashed lines in Fig. 7) parallel those for the set of Tomlinson cases. Power production is considerably higher, however, due to the more efficient conversion of black liquor to electricity. Biomass consumption is also higher in large part because in these cases steam delivered from the black liquor processing section of the plant is lower than with Tomlinson black liquor processing. The performance for one additional biomass gasifier is also included: the high-pressure air-blown design with a 70-MW_e class turbine. This case produces a comparable amount of power as the indirectly-heated gasifier coupled to a 70-MW_e class turbine, but consumes less biomass for a given process steam demand, reflecting the higher efficiency of the pressurized gasification system.

Mill-Specific Performance Comparisons. The above are general comparisons among alternative plant configurations. Now consider a mill-specific example. For concreteness, process steam and power demands representative of a typical present day U.S. mill are considered—16.3 GJ/t_p and 656 kWh/t_p (net of the cogeneration plant). (Consonni et al. (1998) give process energy demand data that helps put these figures in international perspective.) Detailed heat and mass balances for plant configurations delivering 16.3 GJ/t_p of process steam are shown in Fig. 2 and 3 for the reference cases involving biomass use in boilers. Figures 4–6 show heat and mass balances for the biomass sub-section for three of the configurations involving biomass gasification.

Table 2, which summarizes the performance of all systems, highlights the much greater power generation levels achievable with gasification. Biomass-gasifier/gas turbine systems coupled with a Tomlinson boiler (left half of Table 2) would produce 50 percent to 180 percent more power than the reference Tomlinson plus biomass boiler. When coupled with black liquor gasification (right half of Table 2), then power production is 230 percent to 320 percent more than the case using the Tomlinson and biomass boiler.

With one exception, the contribution of the steam cycle to total power production is approximately the same for all systems using a Tomlinson boiler (left half of Table 2) and for all systems using the black liquor gasifier (right half of Table 2), because process steam demand is fixed[2]. In the one case where this is not true (Tomlinson plus indirectly heated gasifier with 70-MW_e class turbine), the steam cycle involves a condensing steam turbine rather than a back-pressure turbine.

The last row in Table 2 bears on a situation in which the mill might be considering replacing an existing Tomlinson-based cogeneration system. A baseline alternative in this situation might be the installation of a new Tomlinson recovery boiler with a biomass boiler to augment steam delivery to a back-pressure steam turbine. If the mill has an opportunity to export power, then one of the other plant configurations in Table 2 might be adopted. Each generates more power than the baseline configuration, but each requires more biomass fuel as well. Dividing the incremental power generated by the incremental biomass consumed gives a measure of the marginal fuel cost associated with the increased power production. The high incremental efficiencies in Table 2 indicate that marginal fuel costs would be low. Investment and operating/maintenance costs would obviously also be considered in any full evaluation of alternative cogeneration options (Larson et al., 1998).

Greenhouse Gas Emissions Reductions. Assuming the black liquor and solid biomass energy resources at a pulp mill are derived from renewably produced wood, the use of these energy resources contributes little or no net emissions to the atmosphere of carbon dioxide, the most important of the greenhouse gases; CO_2 released in converting the feedstocks into power and heat is reabsorbed by new plant growth. To the extent that the use of these carbon-neutral resources can reduce the use of fossil fuels, net reductions in CO_2 emissions would result. The potential reductions in CO_2 emissions can be quantified using the above performance estimates. Consider a pulp mill with a production rate of 1300 t_p/day and process steam and power demands of 16.3 GJ/t_p and 656 kWh/t_p. (These are, approximately, the characteristics of the mill considered in Table 2.) For five powerhouse technology configurations, Fig. 8 shows the total power generated at the

---

[2] Steam turbine power is higher for the cases involving black liquor gasification because of the higher steam generating pressure that can be used.

Table 2 Summary comparison of alternative black liquor plus biomass cogeneration technologies for a pulp mill with a fixed process steam demand of 16.3 GJ/admt (GJ per air-dry metric tonne of pulp product). On a mass basis, half the process steam is delivered at 10-bar pressure and half at 4-bar.

Black liquor system >	Tomlinson Recovery Boiler plus:				O_2 Black Liquor Gasifier, 70-MW class g.t. plus:				
Biomass system >	Boiler[a]	Low-P air –blown gasifier	Indirectly-heated gasifier		Boiler[a]	Low-P air-blown gasifier	High-P air-blown gasifier	Indirectly heated gasifier	
MW class of biomass g.t. >	---	25	25	70	---	25	70	25	70
Mill output, t_p/day	1241				1307				
Process steam,[b] GJ/t_p	16.3				16.3				
Black liquor, tds/t_p	1.74				1.74				
GJ/tds, HHV	14.363				14.363				
GJ/t_p, HHV	25.0				25.0				
Biomass, t_{db}/t_p	0.318	0.469	0.45	0.997	0.783	---	1.277	1.108	1.315
GJ/t_{db}, HHV	20.00[a]	20.47	20.4	20.47	20.00[a]	---	20.47	20.47	20.47
GJ/t_p, HHV	6.36	9.60	9.35	20.41	15.66	---	26.14	22.27	26.92
% direct to steam[c]	100	27.3	16.0	0.0	100	(d)	34.6	66.5	28.0
Power generation, MWe									
Black liquor gas turbine	---	---	---	---	89.75	---	89.75	89.75	89.75
Biomass gas turbine	---	28.85	26.0	70.80	---	---	68.75	27.21	70.80
Steam cycle	48.4	48.99	48.8	70.50	62.00	---	60.88	61.19	60.89
Auxiliaries, MW_e	1.64	8.09	4.75	10.10	19.77	---	23.19	23.79	28.48
Net power generated									
MW_e	46.76	69.75	70.1	131.2	132.03	---	196.2	154.3	193.0
kWh/t_p	904	1349	1356	2537	2424	---	3603	2834	3543
Fraction total fuel HHV to:									
Electricity	0.104	0.140	0.14	0.201	0.215	---	0.254	0.216	0.246
Process steam	0.520	0.471	0.47	0.359	0.401	---	0.318	0.346	0.313
Electricity + steam	0.624	0.611	0.61	0.560	0.616	---	0.572	0.561	0.559
Power/steam ratio	0.20	0.30	0.30	0.56	0.54	---	0.80	0.62	0.78
Excess power available[e]									
MW_e	12.8	35.8	36.2	97.3	96.3	---	160.5	118.6	157.2
kWh/t_p	248	693	700	1881	1768	---	2947	2178	2887
Incremental Efficiency, % HHV[f]	---	49	54	42	59	---	49	44	46

(a) The results in this column are from Consonni, et al. (1998), where biomass with slightly different heating value and composition were used.

(b) Process steam is counted at 2.315 GJ/tonne for 10-bar steam and 2.276 GJ/tonne for 4-bar steam.

(c) This is the percentage of the biomass input that is used directly to raise steam for delivery to the steam turbine. It is 100% for the two biomass bioler cases. For the biomass gasifier cases, it corresponds to the percentage of the clean syngas production that is directed to supplementary firing of the HRSG.

(d) In this case, the amount of oxygen in the gas turbine exhaust flow is insufficient for complete combustion of the amount of supplementary-firing fuel that would be required to deliver a process steam demand of 16.3 GJ/t_p.

(e) This is power available in excess of the mill's assumed process requirements of 656 kWh/t_p.

(f) The numerator of the incremental efficiency is the amount of power produced (kWh) by a gasification-based system (any of the last 8 columns in the table) in excess of that consumed by the Tomlinson + biomass boiler system (column 1). The denominator is the HHV of the fuel consumed by the gasification-based system in excess of that consumed by the Tomlinson + biomass boiler system.

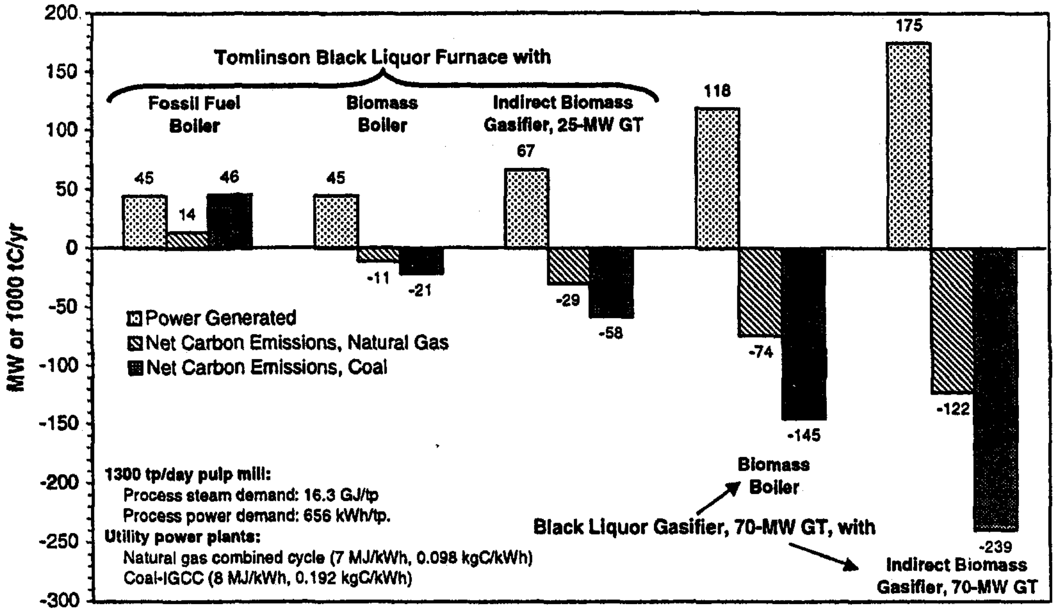

Fig. 8 Power generation and net carbon emissions for five cogeneration plant configurations at a kraft pulp mill producing 1300 t_p/day. The carbon emission estimates assume that power generated at the mill in excess of that needed for pulp production would be sold and would eliminate an equivalent amount of power produced by a utility from fossil fuels (natural gas or coal).

powerhouse while meeting process steam demand. Also shown for each case are two estimates of net annual carbon emissions from the mill. These emissions are calculated assuming that any power generated in excess of process needs is exported to a utility grid where it eliminates the need to generate an equivalent amount of power from natural gas or from coal (both cases are shown in Fig. 8). The first three sets of bars are for configurations involving a Tomlinson furnace for black liquor processing. The last two sets of bars are for cases with gasification of black liquor.

The first set of bars assumes fossil fuel (natural gas or coal) is used in a boiler to augment steam production from the Tomlinson furnace. All steam expands through a back-pressure turbine before being delivered to the process. The positive carbon emissions are due to the use of fossil fuel at the mill. The second set of bars assumes a biomass boiler is used in place of the fossil fuel boiler. Power production is the same as the first case, but carbon emissions are slightly negative now because carbon-neutral biomass has replaced the fossil fuels, and sale of some power to the grid eliminates a small amount of fossil-derived utility power. The third set of bars assumes a biomass gasifier/gas turbine (with supplementary firing of the HRSG) is used in place of the biomass boiler. The greater amount of power generated enables larger amounts of fossil-derived utility electricity to be eliminated, leading to larger negative carbon emissions. This trend is maintained in moving to the last two bars—greater and greater amounts of power are generated from carbon-neutral fuels, leading to more and more negative carbon emissions.

Conclusions

The gas turbine-based cogeneration systems modeled here would permit kraft pulp and paper mills to produce far more power from self-generated renewable fuels than is the case today. In 1994, the U.S. pulp and paper industry produced some 48 million tonnes of kraft pulp (AFPA, 1995) and in the process consumed 1.15 EJ of black liquor and 0.4 EJ of biomass (AFPA, 1996). Assuming cogeneration facilities today generate 900 kWh/t_p from these fuels, as modeled here (Table 2, left-hand column), total biomass-derived power generation in the kraft industry is some 43 billion kWh/year. The total paper industry (kraft and other products) burns fossil fuels to generate additional power and also purchases power.

On average, the present level of self-generated black liquor and biomass fuels would be sufficient to generate about 1350 kWh/t_p, or 450 kWh/t_p in excess of present systems if used in cogeneration systems that include a Tomlinson boiler and a coupled biomass gasifier (e.g., see Table 2, second column, for which the ratio of black liquor-to-biomass energy is approximately 1.15/0.4). At a production level of 48 million t_p/year, kraft mills could produce some 65 billion kWh/year and eliminate nearly half of the 51 billion kWh that the total industry purchased in 1994 (AFPA, 1996).

Electricity generation at kraft mills would be increased even more by the introduction of black liquor gasification. Because less process steam would be generated from the black liquor (compared to Tomlinson processing of the liquor), additional biomass residues would need to be used to meet steam demand. If the energy contribution of residues were raised to approximately that of the black liquor and both fuels were used in gasifier/gas turbine systems, total power generation might reach 3600 kWh/admt (e.g., Table 2, third column from right), corresponding to 173 billion kWh at the 1994 kraft pulp production level (or over 20,000 MW of installed capacity). This would be some 130 billion kWh above the estimated present kraft industry electricity production from black liquor and biomass. If this additional (carbon-neutral) power were to displace electricity that would otherwise be generated from fossil fuels, carbon emissions would be reduced by 13 or 25 million tonnes per year, depending on whether natural gas or coal generated electricity were dispaced. For comparison, carbon emissions from fossil fuel combustion in all U.S. industry in 1990 was 275 million tonnes (Watson et al., 1996).

The economics of adopting gasifier-based cogeneration systems have not been discussed here, but they will be driven largely by the relative cost of purchased fuels and value of electricity sales and by relative capital investment requirements for competing systems. Preliminary cost studies, e.g., see Larson, et al. (1998) and Weyerhaeuser, et al., (1995), suggest that once gasification-based powerhouse technologies reach commercially mature cost levels, they will compete well against boiler-based technologies.

Acknowledgments

For cost-shared contributions to this work, the authors thank the Weyerhaeuser Company. For financial support, we thank the Office of Industrial Technologies of the U.S. Department of Energy and The Energy, The W. Alton Jones, and The Geraldine R. Dodge Foundations. For additional financial support, S. Consonni thanks the Italian National Research Council.

References

AFPA, 1995, Paper, Paperboard & Wood Pulp, 1995 Stats., data through 1994, report, American Forest & Paper Assoc., Wash., DC.

AFPA, 1996, Fact Sheet on 1994 Energy Use in the US Pulp & Paper Ind., report, American Forest & Paper Assoc., Wash., DC.

Consonni, S., and Larson, E. D., 1996, "Gas Turbine Combined Cycles, Part A: Technologies and Performance Modeling, and Part B: Performance Calculations and Economic Assessment," ASME JOURNAL OF ENGINEERING FOR GAS TURBINES AND POWER, Vol. 118, pp. 507–525.

Consonni, S., Larson, E. D., Kreutz, T. G., and Berglin, N., 1998, "Black Liquor Gasifier/Gas Turbine Cogeneration," ASME JOURNAL OF ENGINEERING FOR GAS TURBINES AND POWER, Vol. 120, No. 3, pp. 442–449.

Craig, K. R., and Mann, M. K., 1996, "Cost and Performance Analysis of Biomass-Based Integrated Gasification Combined-Cycle (BIGCC) Power Systems," NREL/TP-430-21657; Nat'l. Renewable Energy Lab. Golden, CO.

Hughes, W. E. M., and Larson, E. D., 1998, "Effect of Fuel Moisture Content on Biomass-IGCC Performance," ASME JOURNAL OF ENGINEERING FOR GAS TURBINES AND POWER, Vol. 120, No. 3, pp. 455–459.

Larson, E. D., Consonni, S., and Kreutz, T. G., 1998, "Preliminary Economics of Black-Liquor Gasifier/Gas Turbine Cogeneration at Pulp and Paper Mills," ASME Paper 98-GT-346.

Larson, E. D., and Raymond, D., 1997a, "Commercializing Black Liquor and Biomass Gasifier/Gas Turbine Technology," *Tappi Journal,* Vol. 80, No. 12. pp. 50–57.

Larson, E. D., and Raymond, D., (organizers), 1997b, "Report on Workshop on Commercialization of Black Liquor and Biomass Gasification for Gas Turbine Applications in the Pulp and Paper Industry," Center for Energy & Environmental Studies, Princeton University, Princeton, NJ.

Paisley, M., and Anson, D., 1997, "Gasification for Gas Turbine Based Power Generation," ASME Paper 97-GT-5.

Salo, K., Horvath, A., and Patel, J., 1998, "Pressurized Gasification of Biomass," ASME Paper 98-GT-349.

Waldheim, L., and Carpentieri, E., 1998, "Update on the Progress of the Brazilian Wood BIG-GT Demonstration Project," ASME Paper 98-GT-472.

Watson, R. T., Zinyowera, M. C., and Moss, R. H., eds., 1996, "Climate Change 1995: Impacts, Adaptations and Mitigation of Climate Change: Scientific-Technical Analyses," contribution of Working Group II to the Second Assessment Report of the Intergovernmental Panel on Climate Change, Cambridge Univ. Press, Cambridge, MA, p. 654.

Weyerhaeuser Co., Stone & Webster, Amoco Oil, and Carolina Power & Light, 1995, "New Bern Biomass to Energy Project Phase I Feasibility Study," published by Nat'l. Renewable Energy Lab. (Golden, CO) and Electric Power Research Inst. (Palo Alto, CA).

Williams, R. H. and Larson, E. D., 1996, "Biomass-Gasifier/Gas Turbine Power Generating Technology," *Biomass and Bioenergy,* Vol. 10, No. 2/3, pp. 149–166.

R. A. Newby

T. E. Lippert

M. A. Alvin

G. J. Burck

Z. N. Sanjana

Westinghouse Electric Corporation,
Science and Technology Center,
1310 Beulah Road,
Pittsburgh, PA 15235

Status of Westinghouse Hot Gas Filters for Coal and Biomass Power Systems

Several advanced, coal and biomass-based combustion turbine power generation technologies using solid fuels (IGCC, PFBC, Topping-PFBC, HIPPS) are currently under development and demonstration. A key developing technology in these power generation systems is the hot gas filter. These power generation technologies must utilize highly reliable and efficient hot gas filter systems if their full thermal efficiency and cost potential is to be realized. This paper reviews the recent test and design progress made by Westinghouse in the development and demonstration of hot gas ceramic barrier filters toward the goal of reliability. The objective of this work is to develop and qualify, through analysis and testing, practical hot gas ceramic barrier filter systems that meet the performance and operational requirements for these applications.

Introduction

The high-temperature particulate filter is a key component in developing, coal-based and biomass-based combustion turbine power generation systems, such as Integrated Gasification Combined-Cycle (IGCC), Pressurized Fluidized-Bed Combustion (PFBC), Topping-PFBC, and advanced PC-fired boiler power plants (High Performance Power Systems—HIPPS), that are currently supported by DOE/FETC (Federal Energy Technology Center) and DOE/NREL (National Renewable Energy Laboratory). In these applications, the hot gas particulate filter protects downstream heat exchange equipment, gas cleaning equipment, and gas turbine components from particle fouling and erosion effects, and cleans the gas to meet particulate emission requirements. The power plant benefits because of lower-cost downstream components, improved energy efficiency, lower maintenance, and the elimination of additional and expensive flue gas treatment systems.

IGCC Systems. In IGCC systems, the hot gas particulate filter operates in reducing gas conditions (i.e., presence of H_2, CH_4, CO, CO_2, H_2S, COS, HCl, NH_3, higher-hydrocarbons, alkali vapors, etc.), high system pressure of 11.4–25.2 bara (150 to 350 psig) and at operating temperatures usually determined by the method of fuel gas sulfur removal, i.e., in-gasifier desulfurization, external hot fuel gas desulfurization, or conventional cold fuel gas desulfurization. Typically, these filter temperatures range around 899°C (1650°F) for in-gasifier desulfurization, 480 to 665°C (900 to 1230°F) for external hot fuel gas desulfurization, and 260 to 540°C (500 to 1000°F) for cold fuel gas desulfurization.

In gasification applications, conventional cold fuel gas desulfurization has been demonstrated as effective in cleaning the fuel gas to meet turbine and environmental requirements. However, with this cold fuel gas desulfurization process, power plant energy efficiency is reduced, and higher capital costs are incurred. Incorporating a hot particulate filter upstream of the cold gas desulfurization process reduces heat exchanger cost, provides for dry ash handling, and reduces maintenance costs. This technology has been demonstrated at both the Demkolec IGCC plant and at the PSI, Wabash River IGCC plant (Zon, 1996; Breton and Stultz, 1996).

Hot fuel gas desulfurization concepts (in-gasifier and external) have also been proposed that utilize reactive solid sorbents to remove gas phase sulfur, and hot gas filters to collect the ash and sorbent particles. This approach in IGCC provides for higher energy efficiency and lower cost of electricity.

IGCC systems may utilize air-blown or oxygen-blown entrained or fluid bed gasifiers. Specific operating conditions of the hot gas particulate filter will vary depending on these choices. In general, hot gas filter pilot plant test experience suggests that gasifier ash/char is noncohesive with relatively high flow resistance. Thus, the potential for fines re-entrainment and high filter pressure drop are reduced by selecting a relatively low filter operating face velocity. Since the filter treats only the fuel gas component of the total gas flow, the choice of a low filter face velocity does not adversely impact economics. Typically, for a 100 MW_e IGCC system, the filter is required to treat a fuel gas flow of only about 2.8 m^3/s (6,000 acfm) if the gasifier is oxygen-blown, and about 5.7 m^3/s (12,000 acfm) if air-blown. Inlet dust loadings to the filter also vary widely, ranging from <1000 ppmw to greater than 10,000 ppmw.

PFBC Systems. Bubbling-bed PFBC technology is being demonstrated at commercial scale in Europe and Japan. Currently, these plants utilize high efficiency cyclones to remove about 95 percent of the ash from the expansion gas and a "ruggedized" gas turbine tolerates the high ash carried over from the upstream cyclones. Stack gas cleaning with conventional baghouse fabric filter or ESP technology is used to meet environmental requirements. Economic and performance improvements in these bubbling-bed PFBC plants could be realized with the application of hot gas particulate filters. Both the secondary cyclones and stack gas ESPs could be eliminated, reducing equipment costs and providing lower system pressure losses. The clean expansion gas provided by the hot gas filter would also permit a wider selection of conventional gas turbines with potentially higher performance and lower cost.

The applicability of hot gas particulate filters to PFBC technology was recently demonstrated at the American Electric Power Tidd PFBC, 70 MWe Clean Coal Demonstration Plant. In this project, a 10 MWe hot gas filter slipstream was operated for approximately 6,000 hrs. over a range of conditions and configurations (Hoffman, 1995). The Tidd PFBC demonstration project was completed in March 1995. For these bubbling-bed PFBC applications, the hot gas filter operates at a temperature of about

---

Contributed by the International Gas Turbine Institute (IGTI) of The American Society of Mechanical Engineers for publication in the ASME Journal of Engineering for Gas Turbines and Power. Paper presented at the International Gas Turbine and Aeroengine Congress and Exhibition, Stockholm, Sweden, June 2–5, 1998; ASME Paper 98-GT-340.

Manuscript received by IGTI March 18, 1998; final revision received by the ASME Headquarters March 23, 1999. Associate Technical Editor: R. Kielb.

860°C (1580°F) and system pressure of about 13.1 bara (175 psig) (conditions typical of the Tidd PFBC plant). Inlet dust loadings to the filter were initially estimated to be about 500 to 1000 ppm with mass-mean particle diameter ranging from 1.5 to 3 μm. However, it was subsequently demonstrated in the Tidd PFBC filter slipstream that more reliable filter performance is achieved by eliminating the PFBC primary cyclone. Filter inlet particle loading increased to about 18,000 ppm and particle mass mean diameter increased to 27 μm.

For commercial applications typical of the 70 MWe Tidd PFBC demonstration unit, the filter must treat up to 26.7 m^3/s (56,600 acfm) of expansion gas flow. Scale-up to about 310 MWe would require filtering over 75.5 m^3/s (160,000 acfm) gas flow. For these commercial scale systems, multiple filter vessels are required.

An alternative to bubbling-bed PFBC is circulating-bed PFBC (PCFB). In this process the hot gas filter is exposed to higher operating temperatures, 871–890°C (1600–1650°F) and higher inlet particle loading. Although the inlet particle loading is high, it contains a significant coarse fraction (mass-mean generally >15 μm), which helps mitigate the effect of the higher mass loading. For a 75 MWe commercial scale circulating-bed PFBC plant, gas flow to the filter is approximately 33.0 m^3/s (70,000 acfm). At this scale multiple vessels with modular filter subassemblies are required.

Topping-PCFB is being developed and planned for demonstration and commercialization. In this advanced power plant, higher turbine inlet temperatures are achieved by partially oxidizing and devolatilizing the coal in a carbonizer unit, producing a fuel gas. The char produced is transferred to, and burned in a circulating-PFBC unit with high excess air. The hot (870°C, 1600°F) vitiated air produced is used to combust the hot fuel gas to raise the combustion gas temperature to as high as 1288°C (2350°F) (Robertson et al., 1989). With Topping-PFBC, two parallel hot gas filter systems are required. One filter is used to collect the ash, char, and sorbent carried over from the carbonizer unit with the hot fuel gas. The second filter is used to remove ash and sorbent particles carried over with the hot vitiated air leaving the circulating-bed PFBC unit. Both filter systems operate at high temperatures (665 to 870°C; 1200 to 1600°F) and high inlet particle loading. A 95 MWe Topping-PFBC plant produces a hot fuel gas flow to the carbonizer filter of about 3.8 m^3/s (8,000 acfm) and hot vitiated air flow to the CPFB filter of approximately 30.2 m^3/s (64,000 acfm).

Westinghouse Hot Gas Filter System

The Westinghouse hot gas filter design, schematically shown in Fig. 1, consists of stacked arrays of filter elements supported from a common tubesheet structure. In this design, the arrays are formed by attaching individual candle elements (Item 1) to a common plenum section (Item 2). All the dirty gas filtered through the candles comprising this single array is collected in the common plenum section and discharged through a pipe to the clean side of the tubesheet structure. Each array of filter elements is cleaned from a single pulse nozzle source. The individual plenum assemblies (or arrays) are stacked vertically from a common support structure (pipe), forming a filter cluster (Item 3). The individual clusters are supported from a common, high alloy tubesheet structure and expansion assembly (Item 4) that spans the pressure vessel and divides the vessel into its "clean" and "dirty" gas sides. Each cluster attaches to the tubesheet structure by a specially designed split ring assembly. The cluster is free to grow down at temperatures. The plenum discharge pipes ducting the filtered gas to the clean gas side of the tubesheet structure are contained within the cluster support pipe and terminate at the tubesheet. Each discharge pipe contains an eductor section. Separate pulse nozzles are positioned over each eductor section. The eductors assist pulse cleaning. During cleaning, the pulse gas is contained within and ducted down the discharge pipe and pressurizes the respective plenum section.

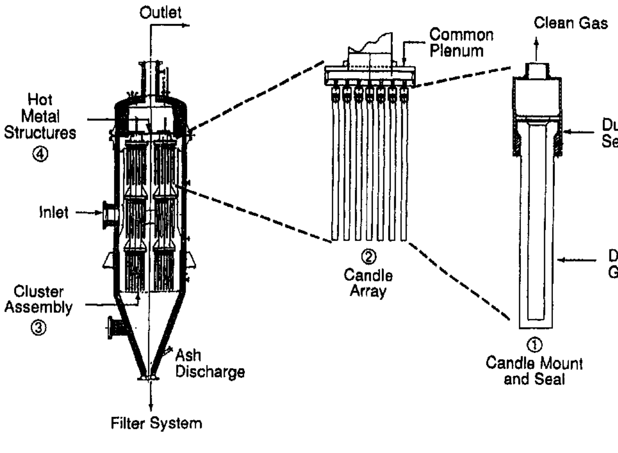

Fig. 1 Westinghouse candle filter system design

The plenum assembly and cluster (stacked plenums) form the basic modules needed for constructing large filter systems indicative of utility power generation requirements. The scale-up approach is as follows:

—increasing plenum diameter (more filter elements per array)
—increasing the number of plenums per cluster
—increasing the vessel diameter to hold more clusters

In general, vessel diameter will be limited by the tubesheet structure and the desire to shop fabricate the pressure vessel.

Clay bonded silicon carbide (SiC) candle filters are commercially available. The structure of these elements is mainly a coarse-grained SiC bonded by a clay-based binder. Each element is provided with a fine grained SiC or aluminosilicate fiber outer skin that serves as the filtration surface.

Alternate, oxide-based ceramic materials are also being developed for ceramic barrier filter application. Candle filter elements have been constructed using a homogeneous structure that is an alumina/mullite (A/M) matrix containing a small percentage of amorphous (glass) phase.

Over the past several years, Westinghouse working with DOE and various suppliers, have helped to develop and qualify alternative, advanced ceramic filter materials and candle elements. This development has included both dense and lightweight monolithic, vapor infiltrated and Sol-Gel fiber reinforced and filament wound constructions. Laboratory and field evaluation of these and other materials are being conducted to identify, characterize and compare their respective chemical and thermal stability for IGCC and PFBC applications. The status of testing of commercial and advanced ceramic candle filters has been recently reviewed (Alvin et al., 1997).

Westinghouse Hot Gas Filter Test Results

The Westinghouse hot gas filter system development is being supported through key sub-pilot, pilot and demonstration programs, as listed in Table 1. This testing has included approximately 3,500 hours of operation in reducing gas environments (gasification) and 12,000 hours in combustion (oxidizing) conditions. In addition to this field experience, over 25,000 hours of test experience has been compiled in Westinghouse sub-scale, high-temperature, high-pressure hot gas filter simulators.

Entrained Gasification. A sub-pilot scale hot gas filter was integrated with a 15 tpd Texaco entrained, oxygen-blown gasifier. The facility is located in Montebello California. The filter test program was conducted from April 1989 through August 1992 and test results were previously reported (Lippert et al., 1993). Filter testing was in support of a base program that was focused on evaluating hot desulfurization technologies. In this testing, the

Table 1 Westinghouse IGCC and PFBC hot gas cleaning testing experience

Application	Facility	Pressure bara (psig)	Temperature Range °C (°F)	Flow m3/s (ACFM)	Dust Load (ppmw)	Test Hours
Gasification (IGCC)	KRW Fluid Bed Coal Gasifier PDU	10.0-16.9 (131-231)	566 (1050)	0.024-0.14 (50-300)	1,000-25,000	1300
	Texaco Entrained Coal Gasifier Pilot	25.2 (350)	538-760 (1000-1400)	0.024-0.05 (50-110)	300-25,000	700
	IGT Fluid Bed Biomass Gasifier	14.5-18.9 (195-260)	538-899 (1000-1650)	0.06 (125)	1,000-2,500	50
	SPPC, Pinon Pine IGCC Fluid Bed Gasifier (95 $\mathrm{MW_e}$)	18.9 (260)	538 (1000)	6.3 (13,391)	18,000	Startup end-1997
Combustion (PFBC)	SCS Wilsonville Transport Gasifier/ Combustor	14.8-25.2 (200-350)	371-816 (700-1500)	0.47-0.80 (1000-1700)	4,000-40,000	1800 *(Continuing)*
	AEP Tidd, Bubbling-PFBC (10 MWe)	10.3 (135)	649-816 (1200-1500)	3.5 (7,500)	600-10,000	5,800
	FW Karhula, Circulating-Bed PCFB Pilot	12.0 (160)	843-899 (1550-1650)	1.45 (3,070)	4,000-18,000	3,676
Topping-PFBC and HIPPS	FWDC Livingston Test Facility Fluid-Bed Carbonizer	11.4-14.8 (150-200)	593-816 (1100-1500)	0.047-0.094 (100-200)	5,000-35,000	400 (700)*
	Circulating-Bed Combustor	11.4-14.8 (150-200)	593-927 (1100-1700)	0.24-0.47 (500-1000)	5,000-35,000	900 (700)*
	HIPPS Fluid-Bed Pyrolyzer	5.2-9.3 (60-120)	649-760 (1200-1400)	0.047-0.094 (100-200)	40,000-130,000	500 *(Continuing)*
	SCS/PSDF Circulating-Bed Combustor (7$\mathrm{MW_t}$)	14.8-25.2 (200-350)	649-899 (1200-1650)	0.94 (2,000)	11,000	Startup 1998

**Integrated Operation, 1995*

filter was used to protect the external sulfur sorbent beds from ash plugging. This work showed that in the entrained gasification application, stable pressure drop operation can be achieved but the ceramic barrier filter system must be sized and designed for relatively low face velocity of <2 cm/s (<4 ft/min) and high operating pressure drop of >0.2 bar (>3 psi). The potential for particle re-entrainment is a key consideration in selecting the hot gas filter design and operating conditions.

Biomass Fluid Bed Gasification Testing. A 14 candle-element hot gas filter system was integrated and operated with the Institute of Gas Technology's (IGT) RENUGAS biomass gasification process. The RENUGAS process is a pressurized fluidized bed, air or oxygen-blown gasifier. The development and operation of IGT's 10 ton per day process development unit (PDU) is described by Wiant et al. (1993) and Lau et al. (1993). The testing program at IGT utilized bagasse and alfalfa feed and was conducted in support of the DOE/NREL Biomass Power Program, and specifically the Biomass Gasification Facility Demonstration in Paia, Hawaii.

The IGT/PDU included a tar cracker that was first operated and characterized. It was concluded from this work that the majority of the oil and tar from the RENUGAS process would not crack within the pores of the filter elements if the filter temperature is maintained below 815°C (1500°F), but above the condensation temperature of the highest boiling-point components (approximately 510°C (950°F)).

The hot gas filter testing was conducted in two, one week test campaigns resulting in about 50 operational hours at representative conditions. A summary of the testing conditions is given in Table 2. Test Series 1 was conducted with the full 14-element complement of candle elements. In this test series, the upstream cyclone was disabled to increase particle size and solids loading to the filter unit. Inlet particle analysis showed a 10.8 micron mass-mean. This short duration test showed no operational issues, with stable baseline pressure drop. Visual inspection, following testing, confirmed filter integrity and high collection efficiency.

Test series 2 was conducted utilizing ten candle elements, with the upstream cyclone fully operational. Particle analysis showed that the mass-mean size, 3.8 microns, now entering the filter decreased significantly compared to Test Series 1. Initially, in Test Series 2, steady filter pressure drop characteristics were observed, but in the latter portion of this testing, a steady rise in the baseline pressure drop was observed, likely reflecting re-entrainment because of the smaller particle mean size. Post test inspection con-

Table 2 Biomass fluid bed gasifier hot gas filter test summary

	Test 1	Test 2
Feed Stock	Bagasse	Bagasse
Filter Pressure bara (psig)	18.9 (260)	14.5-17.9 (195 to 245)
Filter Gas Temperature °C (°F)	860-899 (1580 to 1650)	538-666 (1000 to 1230)
No. of Candle Elements	14	10
Dust Loading, ppmw	2900	980 to 2500
Operating Hours	21	30
Outlet Dust Loading	Not Detectable	Not Detectable
Alkali, ppmv	--	0.7 to 1.0

Table 3 SPPC-pinon pine hot gas filter design basis

Gas Environment:	Reducing
Gas Flow, kg/hr (lb/hr):	139,741 (307,800)
Pressure, bara (psig):	18.9 (260)
Gas Temperature, °C (°F):	544 (1011)
Inlet Dust Loading, ppmw:	18,400 ppm
Max. Pressure Drop, bar (psi):	0.62 (9)

firmed the filter integrity and no dust was found in the clean gas side. These test results show that better performance will be achieved with larger mean particle sizes, thus eliminating the need for the upstream cyclone.

This 14-element hot gas filter test unit has now been removed from the IGT test site and installed as a slip stream off the DOE 100 ton per day Biomass Gasification Facility (BGF) located in Paia, Hawaii. Westinghouse is the prime contractor for the DOE Hawaiian Biomass Gasification Commercialization Program. The program facilitates the commercialization of pressurized biomass gasification combined cycle power plants. The first step in the program is the technology verification phase which will result in the accumulation of 1500 hours of testing at the Paia, Hawaii site. The tests at nominal commercial operating pressure and temperatures are required to demonstrate that the biomass feed system, gasifier and hot gas filter units will work as an integrated system and that the technology is ready for commercial demonstration.

The BGF has been modified to operate at pressures up to 300 psig and at throughputs of up to 100 tons per day of dry bagasse. The Westinghouse hot gas filter system is installed in a slipstream that will filter approximately one tenth of the bagasse product gas flow from the gasifier. By the end of 1997, approximately 150 hours of operation on Bagasse was completed. Additional testing is planned.

Sierra Pacific, Pinon Pine IGCC Project. Westinghouse has designed and supplied the hot gas filter system for the Department of Energy's Clean Coal Technology Demonstration, Pinon Pine IGCC project. The coal gasification process uses the KRW fluid bed gasifier technology, owned by The M.W. Kellogg Co., who specified and purchased the filter. The final filter design evolved to satisfy the project requirements of both The M.W. Kellogg Co. and the Sierra Pacific Power Co. The plant is located at the Sierra Pacific Power Company's Tracy station near Reno, Nevada. The plant will gasify approximately 880 tons/day of coal using the KRW air-blown gasification process to generate about 95 MWe. The plant is scheduled to begin commercial operation on coal in 1998. The gasification island portion of the plant has undergone shakedown in preparation for coal operation and has initiated component startup testing. The filter system has been subjected to initial performance characterization.

Table 3 summarizes the design basis for the hot gas filter system. The filter unit is schematically shown in Fig. 2. The filter vessel holds 784 candle elements, arrayed on four clusters. Each cluster contains 187 candles distributed over four plenums.

For commercial operation, the Filter is designed for maintainability. Access into the filter body is provided by four, 91 cm (36 inch) diameter manways. Two diametrically opposite manways are positioned between clusters to access the top level of plenums. Similarly, two diametrically opposite manways are positioned between clusters to access the lower middle level of plenums. Platforms were designed to bolt to the manway flanges to provide staging for personnel to stand inside the vessel for in-situ service work. Below each manway a set of vertically oriented rails are provided. Ladders treads are strung between the rails to provide access to the lower plenum service area. Personnel climb down the ladder and work off a second platform. The arrangement is illustrated in Fig. 3. At any given platform location, all filters for two adjacent plenums are accessible by rotating the associated cluster. Such rotation is accomplished by entering the vessel head above the tubesheet, disengaging the cluster top flange from the tubesheet and with standard manual rigging attached between the vessel head and cluster top flange, lifting and rotating the cluster.

The first application of the maintenance hardware was demonstrated at the initial filter installation. Four teams of boiler makers were trained. They worked simultaneously inside the filter vessel and accomplished assembly of all the 748 candle elements, demonstrating the overall approach to maintainability. Commissioning of the gasification island was initiated in December 1997, and full operation anticipated by first quarter 1998.

Pressurized Fluidized Bed Combustion. Westinghouse has conducted hot gas filter testing at three different PFBC facilities: the American Electric Power (AEP) 70 MWe Tidd-PFBC demonstration plant located in Brilliant Ohio, the Foster Wheeler (for-

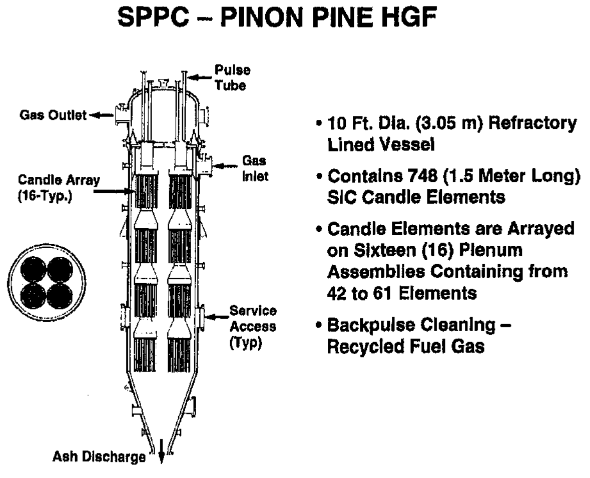

Fig. 2 SPPC—pinon pine HGF

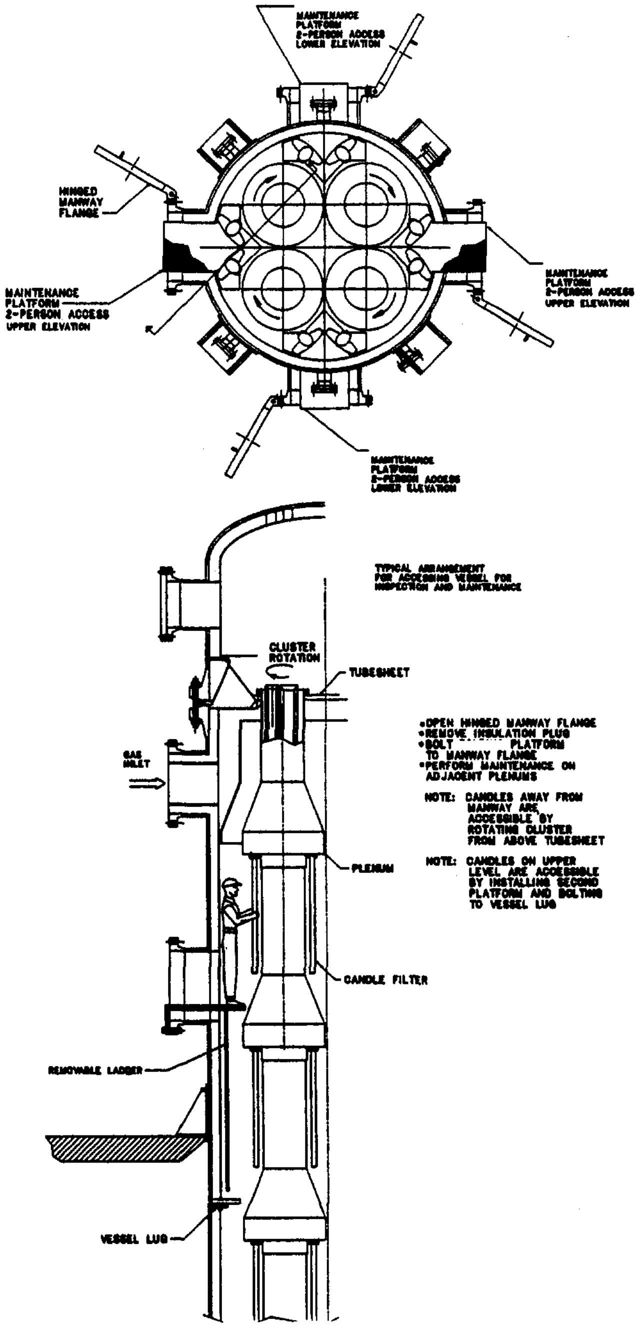

Fig. 3 Hot gas filter maintenance features

mally Ahlstrom) 10 MWt circulating PCFB facility located in Karhula, Finland, and the Foster Wheeler Development Corp. (FWDC) test facility in Livingston, NJ. Testing at the AEP/TIDD plant has been completed and results were previously reported (Hoffman, 1995).

Karhula PCFB Testing. The hot gas filter testing conducted at the Foster Wheeler Karhula 10 MWt PCFB Facility is divided into the following three test periods:

1 Nov. 1992 through June 1994
2 Nov. 1995 through Oct. 1996
3 April 1997–continuing

Table 4 summarizes the cumulative testing hours and coals used. A description of the Karhula facility and results from the earlier Nov. 1992 through June 1994 testing have been reported (Lippert et al., 1995). A summary of the Nov. 1995 through Oct. 96 and April 1997 (continuing) testing is given below.

The 1995/96, testing that included 1166 hours of coal operation was divided into three segments as summarized in Table 5. In Test Segments 1 and 2, with Linwood Limestone in combination with the Sparta coal, ash bridging was experienced in the filter array leading to damaged, and some broken, filter elements. Subsequent evaluations that included ash, coal, and sorbent analysis concluded that the ash bridging could have been the result of a higher than desired fraction of limestone fines entering the hot gas filter unit due to initial sizing of the limestone feed. To further evaluate the ash bridging experienced in Segments 1 and 2, the original Linwood Limestone was resized. Both resized Linwood and an alternative (Iowa Industrial) Limestone were utilized in separate test runs in segment 3. The Iowa Limestone had been used in the 92/94 testing without incident.

The segment 3 testing included periodic shutdown and inspections between runs. The sequence of testing, sorbent used, and results of the inspections are summarized in Table 6. Operation with the Iowa Limestone was clearly more favorable than either the original or resized Linwood Limestones. The resized Linwood did appear to do better than the original Linwood Limestone. However, particle size measurements showed that the fines fraction entering the hot gas filter unit with the resized Linwood sorbent was not significantly different from the original Linwood Limestone. Inspection following this 626 hour test segment confirmed that there were no failed candles and no evidence of dust penetrating to the clean gas side. Throughout the 1166 hours of the 1995/96 testing, the filter operating pressure drop remained stable, even with the ash bridging that occurred in segment 2. Filter cleaning cycles ranged from 20 to 30 minutes.

The objectives of the 1997 testing are to evaluate the PCFB boiler emissions and hot gas filter ash characteristics using the coal and sorbent currently anticipated for the DOE PCFB Clean Coal Demonstration Plant planned for the City of Lakeland, Florida at their McIntosh Unit 4 Station, and in addition, continue the filter material qualification testing. The filter testing is planned in two separate test segments. The first test segment has been completed

Table 4 Westinghouse hot gas filter test coals at Foster Wheeler Circulating-bed PFBC—Karhula, Finland

Coal	Hours (Oct. '92 - Feb. '94)	Hours (Nov. '95 - Oct. 96)	Hours April '97
Illinois No. 6	306		
Iowa Rawhide	61		
Newland	300		
Kentucky	270		
Black Thunder	804		
Bituminous	170		
Pennsylvania	135		
Sparta		1166	
E. Kentucky			454
Total Coal (Period)	2046	1166	454
Total Coal (Cumulative)		3212	3666

Table 5 Summary of Karhula filter operation (Nov. '95–Oct '96)

Parameter	Segment 1	Segment 2	Segment 3
Coal	Illinois #6 (Sparta)	Illinois #6 (Sparta)	Illinois #6 (Sparta)
Sorbent	Linwood Limestone	Linwood Limestone	Linwood Limestone Iowa Limestone Resized Linwood
No. of Active Elements	112	112	128
Operating Hours (Coal)	153	387	626
Filter Temperature °C (°F)	441-456 (826 - 853)	437-460 (818 - 860)	448-460 (838 - 860)
Filter Pressure, bara	10.7 - 11.1	10.6 - 11.3	10.5 - 10.7
Inlet Dust Loading, ppmw	12000 - 13000	12000 - 15500	11000 - 12500
Pulse Interval, min.	30	15 - 30	30
Pressure Drop After Cleaning, mbar	90 - 123	79 - 157	61 - 87

and focused on ash characterization, Table 7. Inspections of the filter were conducted following approximately 100 hours of operation and again at the end of the 454 hour test segment. No evidence of ash bridging was detected at either inspection. Dust deposits were minimal with a relatively uniform residual ash layer over the candle elements. Throughout the 454 hours of testing, the filter operating pressure drop remained stable and cleaning cycles ranged around minutes. Segment 2 testing began in August 1997. An additional 587 hours of operation was accomplished completing the 1997 test programs.

During the period of the Karhula testing, inspections of the hot metal structures have been conducted. These periodic inspections and evaluations have confirmed the integrity of the base metal (minor oxidation and embrittlement) and structural welds. Based on the Karhula PCFB testing and follow-up cluster assembly inspections, the hot metal structures have performed as designed, with minor maintenance.

The Westinghouse 128-candle element cluster utilized at the Karhula PCFB facility was designed in 1991 and fabricated and installed into the Karhula facility in September 1992. Although candle elements have been changed, the basic hot metal structures have been utilized throughout the 3666 hours on coal operation 788 to 899°C (1450 to 1650°F) plus another 1600 hours of high temperature operation on heavy and light oil used during startup, shutdown and other operating periods. During this period, it is estimated that the filter has experienced over 300 thermal cycles (startup, shutdown, hot restart, load changes, etc.) under which metal damage accumulation would normally be expected. Although it is difficult to extrapolate this test experience to a commercial, base loaded power plant, this test experience has helped to establish the commercial viability of the hot metal structures.

FWDC/Livingston HGF Testing. Testing supporting the development of the Topping-PFBC has taken place at the Foster Wheeler Development Corporation (FWDC) pilot plant facility located at the John Blizzard Research Center in Livingston, New Jersey. As part of this program, separate carbonizer filter and combustor filter testing was conducted, followed by integrated operation of the test facility.

Recently the operation of the 22-element Carbonizer/Filter has been continued as part of the Foster Wheeler/DOE HIPPs program. The Foster Wheeler Development Corporation (FWDC) is a participant in the DOE HIPPS Program for advanced pulverized coal-fired electric utility plants. In the concept, an air-fluidized sand-bed pyrolyzer, with injected pulverized coal and limestone, generates a low-Btu fuel gas, and a char-sorbent mixture. The fuel gas and most of the char-sorbent mixture flows directly into a hot gas filter. The cleaned fuel gas is then fired in a combustion turbine, and the char-sorbent mixture is burned in a conventional PC-furnace.

FWDC is testing the fluidized bed pyrolyzer pilot unit with a hot gas filter supplied by Westinghouse. The filter pressure vessel contains 22 filter elements, 11 on each of two side-by-side plenum chambers. The filter elements are $1\frac{1}{2}$ m long ceramic elements, 2 supplied by Coors and 10 each by Schumacher and Pall. Filter test results have been compiled in one shakedown test (HSD-2, March 1997), and in the first test run (TR-1, April 1997). Six set points were established during the TR-1 campaign. The test conditions and performance results are summarized in Table 8.

The hot gas filter commercial temperature is about 537°C (1000°F), and the FWDC testing has operated at filter temperatures up to 760°C (1400°F). No cyclone is used in the plant, and the ash loading to the filter is very high. The filter internals were inspected by boroscope following the testing and found to have no damaged candles and to be free of bridging and deposits. No significant difficulties with ash drainage from the vessel were observed during the testing. The FWDC pyrolyzer filter testing has shown that the Westinghouse hot gas filter can operate well even with inlet dust loadings greater than 100,000 ppmw. The high dust loading of coarse particles, 30–50 μm in mass-mean diameter, may minimize problems with bridging and vessel drainage. The filter cake permeability is comparable to previous measurements made during carbonizer filter testing in the Topping-PFBC program. FWDC will continue pyrolyzer testing at higher pressures (up to 200 psig) during the second test run (TR-2), scheduled for end-1997.

Power Systems Development Facility (PSDF). Westinghouse designed and supplied two particle control devices (PCD-

Table 6 Summary of Karhula filter testing using alternative sorbents (segment 3)

Sorbent Feed	Operating Hours	Inspection
Original Linwood	142	Clear evidence of initiation of ash bridging, similar to that seen in Test Segments 1 and 2.
Iowa	266	Dramatic change in ash characteristics, no indication of further ash bridging or ash accumulation.
Resized Linwood	218	Inconclusive, some evidence of the initiation of ash accumulation that would lead to bridging.

Table 7 Summary of Karhula filter operation (April '97–continuing)

Parameter	Segment 1
Coal	E. Kentucky (Beech Fork)
Sorbent	Gregg Limestone
No. of Active Elements	128
Operating Hours (Coal)	454
Filter Temperature, °C	847 - 853
Filter Pressure, bara	11.3
Inlet Dust Loading, ppmw	9400
Pulse Interval, min.	20 - 30
Pressure Drop After Cleaning, mbar	60 - 95

Table 8 FWDC HIPPS pyrolyzer filter test conditions and performance

Test Period	HSD-2	TR-1
Filter pressure, bara (psig)	3.8-5.7 (40-60)	5.7-11.3 (60-120)
Filter temperature, °C (°F)	649 (1200)	760 (1400)
Face velocity, cm/s (ft/min)	1.27 (2.5)	1.38 (2.7)
Inlet dust loading, ppmw	40,000-120,000	40,000-180,000
Baseline DP, mbar (in-wg)	25-62 (10-25)	100-150 (40-60)
Pulse interval (min.)	10-12	9-10
Continuous test time (hr)	62	80

301 and PCD-352) for installation and operation at the Southern Companies Service, PSDF located in Wilsonville Alabama. The PCD-301 unit has been installed into the MWK Transport Reactor (TR) test loop. The TR is designed to operate in either a gasification or combustion mode. Testing to date has been in the combustion mode.

PCD-301 hot gas filter system is a two-plenum, single cluster unit containing 91 candle elements. The filter installation, and pressure and pulse-skid check-outs were completed in July 1996. The first operation on coal occurred Aug. 14–21, 1996 during which period the TR operated on coal for 80 hours. Up to the end of May 1997, the PCD has been subjected to more than 1000 hours in combustion with about 737 hours on coal feed with temperatures up to 754°C (1390°F) and pressures to 12.7 bara (170 psig). The on-coal run conditions through May 27, 1997 are summarized in Table 9.

The PCD-301 system in general has performed very well under a variety of particle loading conditions. Typical loading has been 4,000 to 20,000 ppm. Occasionally, upsets during commissioning of the TR have produced transient loading to the filter as high as 100,000 ppm. The high loading has been mitigated to some extent by the large average particle size distributions coming over from the TR. Pulsing has been regular and effective, requiring a tank pressure of 400–450 psig with a pulse frequency of one every 30 to 45 minutes. Pressure drop increases prior to pulsing have generally been relatively low, 25–150 mbar (10–60 iwg) being typical. Limited particulate sampling made at the PCD outlet has confirmed overall PCD collection efficiencies to be >99.9 percent.

During shakedown operations, and startup and commissioning activities, there were two candle failure events which were caused by TR upsets. In the first event which occurred in August 1996 (Run CCT1C), 77 of 91 filter elements were broken when the filter vessel was filled with ash almost up to the gas inlet pipe. During this event the fail-safe devices located at the outlet of each candle element operated exactly as designed and prevented the ash from flowing downstream. The second event occurred in early April 1997 (Run CCT4C, not included in summary table), in which during startup coal fines were inadvertently fed into the PCD. The temperature was high enough to cause ignition of fines on the filter elements. The resulting thermal stress produced by the event was sufficient to damage almost all of the 91 filter elements. All the other Test Runs shown on Table 9 were completed without incident.

Future Activities

Ceramic barrier filter systems designed and supplied for test and demonstration by Westinghouse have been found to function reliably, with high efficiency so long as significant ash bridging conditions and process upset conditions are avoided. Operating with relatively coarse inlet particle sizes, and high inlet particle loading tends to result in reliable filter operation and benefits the total power plant application economically. Ceramic barrier filter testing in continuing for IGCC and PFBC applications.

FWDC/Karhula Circulating-Bed PFBC Filter Testing. Test operations continue at the FWDC, 10 MWt circulating-Bed PFBC facility at Karhula Finland that utilize the Westinghouse hot gas filter candle unit containing up to 128 elements. Testing is focused on evaluating alternative candle materials to temperatures above 830°C. Following the completion of testing, currently planned for end-1997, the filter elements, gaskets, metal support structure, and other internal components will be evaluated.

Power Systems Development Facility. Operation of the Kellogg transport reactor and PCD-301 filter system is continuing under the combustion mode. Plans for operation in the gasification mode are being developed. The PCD-352 filter unit has been completely fabricated and delivered to site. This unit will serve as the hot gas filter for the Combustion Leg of the Topping-PFBC test loop. Installation is ongoing, with operation expected in 1998. The PCD-352 filter unit is a 3-Cluster, 2-Plenum unit that can hold up to 273 candle elements. Clusters from the PCD-301 filter unit are interchangeable with clusters from the PCD-352 filter unit. Candles for the PCD-352 filter unit have not been selected.

Sierra, Pinon Pine 95 Mwe IGCC. Plant start-up on coal is expected in early 1998. The Westinghouse hot gas filter unit is installed and ready for operation following checkout and cold testing. A substantial test program will proceed at the facility. A small, slip-stream filter unit is being installed at the site to subject

Table 9 Run conditions at the PSDF transport combustor filter test through April 27, 1997

Run. No.	Hours on Coal	Coal/Sorbent	TR Bed Materials	Max. Filter Temp. °C (°F)	Filter Pressure bara (psig)
CCTIC	80	AL Bituminous Dolomite	Alumina	371 (700)	11.4 (150)
CCT2C	146	AL Bituminous Dolonite	Sand	316 (600)	12.0 (160)
CCT4A/B	58	AL Bituminous Dolomite	Sand	499 (930)	12.0 (160)
CCT4D	173	AL Bitum. / Dolomite	Sand	538 (1000)	12.0 (160)
CCT5A	181	AL Bitum. / Dolomite	Sand	746 (1375)	12.0 (160)
CCT5B	99	AL Bitum. / Dolomite	Sanad	760 (1400)	12.0 (160)

advanced filter elements to the fuel gas environment for durability evaluation.

References

Alvin, M. A., et al., 1997, "Filter Component Assessment," paper presented at the Advanced Coal Based Power and Environmental Systems '97 Contractor's Review Meeting, Pittsburgh, PA, July 22–24, DOE/FETC, Pittsburgh, PA.

Breton, D., and Stultz, J., 1996, "Initial Operating Experiences at the Wabash River Coal Gasification Repowering Project," presented at the 1996 Gasification Technologies Conf., San Francisco, CA, October, EPRI, Palo Alto, CA.

Hoffman, J. D., et al, 1995, "Tidd Hot Gas Cleanup Program—Final Report," U.S. DOE Contract DE-FC21-89MC26042. Prepared by the American Electric Power Service Corporation, Columbus, OH, October 1995.

Lau, F. S., et al, 1993, "Development of the IGT RENUGAS® Process," Proceedings, Strategic Benefits of Biomass and Waste Fuels Conference, Electric Power Research Institute, Palo Alto, CA.

Lippert, T. E., et al, 1995, "Westinghouse Advanced Particle Filter System," Proceedings, Advanced Coal-Fired Power Systems '95 Review Meeting, DOE/METC-95/1018.

Lippert, T. E., Alvin, M. A., Smeltzer, E. E., Bachovchin, D. M., and Meyer, J. H., 1993, "Subpilot Scale Gasifier Evaluation of Ceramic Cross Flow Filter—Final Report," DOE/METC Contract no. DE-AC21-88MC24021.

Robertson, A., et al., 1989, "Second-Generation Pressurized Fluidized Bed Combustion Plant: Research and Development Needs," Foster Wheeler Development Corporation, Livingston, NJ. Phase 1, Task 2 Report FWC/FWDC-TR-89/06 to the U.S. DOE under contract DE-AC21-86MC21023.

Wiant, B. C., et al, 1993, "Biomass Gasification Hot Gas Cleanup for Power Generation," Proceedings, First Biomass Conference of the Americas, Burlington, VT, NREL, Golden, CO.

Zon, G. D., 1996, "Present Status and Operation Experiences IGCC Buggenum," presented at the 1996 Gasification Technologies Conf., San Francisco, CA, October, EPRI, Palo Alto, CA.

S. V. Sankar

K. E. Maher

D. M. Robart

W. D. Bachalo

Aerometrics Inc.,
755 North Mary Avenue,
Sunnyvale, CA 94086

Rapid Characterization of Fuel Atomizers Using an Optical Patternator

Planar laser scattering (PLS) and planar laser-induced fluorescence (PLIF) techniques are currently being used for rapid characterization of fuel sprays associated with gas turbine atomizers, diesel injectors, and automotive fuel injectors. These techniques can be used for qualitative, quantitative, and rapid measurement of fuel mass, spray geometry, and Sauter mean diameters in various sprays. The spatial distribution of the fuel mass can be inferred directly from the PLIF image, and the Sauter mean diameter can be measured by simultaneously recording the PLIF and PLS images and then ratioing the two. A spray characterization system incorporating the PLS and/or PLIF techniques has been loosely termed an optical patternator, and in this study, it has been used to characterize both steady and pulsed sprays. The results obtained with the optical patternator have been directly validated using a phase Doppler particle analyzer (PDPA).

Introduction

The performance and emissions of various engines and power plants, such as Diesel engines, automotive engines, gas turbines, and industrial furnaces, are dependent upon the global spray characteristics. Over the years, various diagnostic techniques have been developed for detailed experimental spray characterization. These measurement techniques can be broadly classified as either point measurement techniques or planar measurement techniques. Point measurement techniques generally use a focused laser beam to define a small measurement probe volume in the flow field. The dimensions of the measurement probe volume is typically about 1000 μm × 200 μm. Among the point measurement techniques developed for spray characterization, the most widely used is the phase Doppler interferometer that is capable of measuring the size and velocity of individual droplets in a spray [1]. More recently, the Rainbow Refractometer has been developed for droplet refractive index measurement, and, furthermore, this technique has been integrated with a phase Doppler interferometer for the simultaneous measurement of droplet size, velocity, and temperature in spray flames [2].

Planar measurement techniques that have been used for spray applications include particle image velocimetry (PIV) [3], exciplex vapor/liquid imaging [4], exciplex thermometry [5], and "Mie" imaging. More recently, planar laser-induced fluorescence imaging [6] has been used to measure the liquid mass distribution in sprays. With regard to planar droplet sizing in sprays, few different techniques have been investigated. Hodges et al. have used an ensemble scattering polarization ratioing technique for the planar measurement of mean droplet diameters in a spray [7]. Also, Herpfer and Jeng [8] have developed an extended PIV system, called the streaked particle imaging velocimeter and sizer, for particle size measurement in sprays. This technique basically measures the size of individual particles in the image field based upon the scattered light intensity.

We have been developing and testing an optical patternator, which can be used for the rapid evaluation of gas turbine nozzles, Diesel injector, and automotive fuel injector performance. It can be used to study the temporal and spatial (both planar and global) atomization and spray characteristics of different atomizers both qualitatively and quantitatively. In general, the Optical Patternator incorporates a planar fluorescence imaging technique to rapidly extract information on the fuel mass distribution in the spray. Various geometrical properties of the spray, such as spray angle and spray symmetry, can also be measured. Unlike mechanical patternators, injection phase resolved measurement is possible with the optical patternator. The optical patternator can also simultaneously record fluorescence and elastic-scattered light from the spray droplets for directly measuring the Sauter mean diameter [9, 10]. Using suitable validation or acceptance criteria, the optical patternator can evaluate the quality of the spray pattern. For quality assurance purposes, the optical patternator can be used to make a rapid decision with regard to the acceptance or rejection of the fuel injectors.

In this study we have applied the optical patternator to a steady-state spray created by a pressure atomizer and have compared the results to those obtained with a PDPA. The newly developed technique is also sufficiently robust to provide time dependent SMD information for transient spray processes such as in automotive fuel injectors and diesel sprays. Preliminary measurements have also been performed in a fuel injector spray.

Optical Patternator

The optical patternator employs both elastic light scattering and fluorescence scattering characteristics from an ensemble of spherical droplets to compute both the fuel mass and SMD. When a droplet (containing fluorescence excitable molecules) is illuminated by a laser light source, a portion of the incident light energy is absorbed by the excitable molecules that is then radiated as fluorescence (frequency shifted from the incident light wave). The remaining portion of the incident light basically experiences elastic light scattering (elastic scattering implies that the radiated light has the same frequency as the incident light). The fluorescent signal is used to infer the fuel mass, and the information contained in both the fluorescing and nonfluorescing scattered light is used to directly measure the Sauter mean diameter everywhere on a single plane of the spray.

Elastic Light Scattering Theory. A mathematical solution for describing the complex elastic-light scattering characteristics by spherical particles is provided by the Lorenz-Mie theory [11]. The Lorenz-Mie theory can be used to compute the magnitude of the scattered light intensity at any point in space. The solution is a complex function of the droplet diameter, the scat-

---

Contributed by the International Gas Turbine Institute and presented at the ASME Asia '97 Congress and Exhibition, September 30–October 2, 1997. Manuscript received by the ASME Headquarters June 19, 1997. Paper No. 97-AA-1. Associate Technical Editor: H. A. Kidd.

tering angle, the refractive index of the droplet, the incident beam polarization, and the wavelength of the incident laser beam. Figure 1 shows the predicted variation of the scattered light intensity as a function of droplet diameter when an f/5 lens is used to collect the scattered light at 45 deg and 145 deg scattering angles. The solid line shown in the figure is a second-order fit to the theoretically computed data. The scattered light intensity can be definitely observed to vary in proportion to the square of the droplet diameter. Similarly, Fig. 2 shows the computed intensity variation for a scattering angle of 90 deg. This angle corresponds to orthogonal viewing. At this viewing angle, not only is the magnitude of the scattered intensity lower than for the forward and backscattered angles, but also some oscillations can be seen in the scattered intensity versus diameter plot. The data presented in Figs. 1 and 2 were computed assuming the droplet refractive index to be $m = 1.334$. The imaginary component of the refractive index was assumed to be zero, implying that the droplets do not absorb the incident energy. However, if laser induced fluorescence is to be excited from the droplets, then they must absorb a portion of the incident energy. This implies that the fluorescing droplets must have a nonzero imaginary component for the refractive index. Figure 3 shows the results of the Lorenz-Mie calculations assuming the droplets to have a refractive index of $m = 1.334-0.001i$. The data show that a little absorption by the droplets helps to eliminate the oscillations in the intensity versus diameter curve, again yielding a D^2-relationship for the scattered light intensity.

The Lorenz-Mie theory clearly shows that for absorbing droplets the scattered light intensity is proportional to the square of the droplet diameter, especially for droplets greater than about 1 μm in diameter. Therefore, the dependence of the scattered light intensity on the particle diameter can be well approximated by the following equation:

$$I_s = kD^2, \tag{1}$$

where I_s is the scattered light intensity, k is a constant (which can either be theoretically computed or experimentally determined), and D is the droplet diameter.

Fluorescence Scattering. It is also known that the fluorescence signal is proportional to the concentration of fluorescing molecules, which, in turn, is proportional to the liquid volume or its mass [6]. This implies that the fluorescent intensity from a droplet is proportional to the cube of its diameter. Therefore, the dependence of the fluorescence light intensity on the particle diameter can be expressed as

$$I_f = \phi D^3, \tag{2}$$

where I_f is the fluorescent intensity, ϕ is a constant (which can either be theoretically computed or experimentally determined), and D is the droplet diameter.

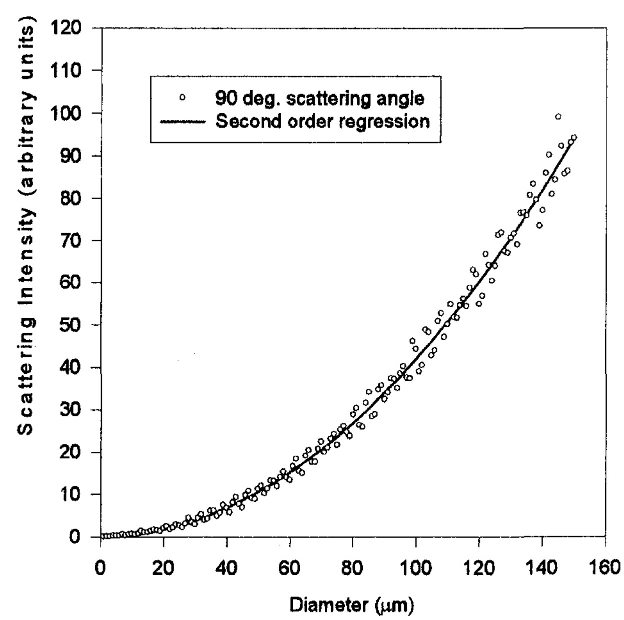

Fig. 2 Computed variation of scattered light intensity with droplet diameter. The calculations were performed using the Lorenz-Mie theory. The droplet refractive index was assumed to be $m = 1.334$.

Measurement Principle. As discussed earlier, the basic principle behind this measurement technique is to simultaneously excite both fluorescence and elastic-light scattering from an ensemble of spray droplets lying in a plane defined by a

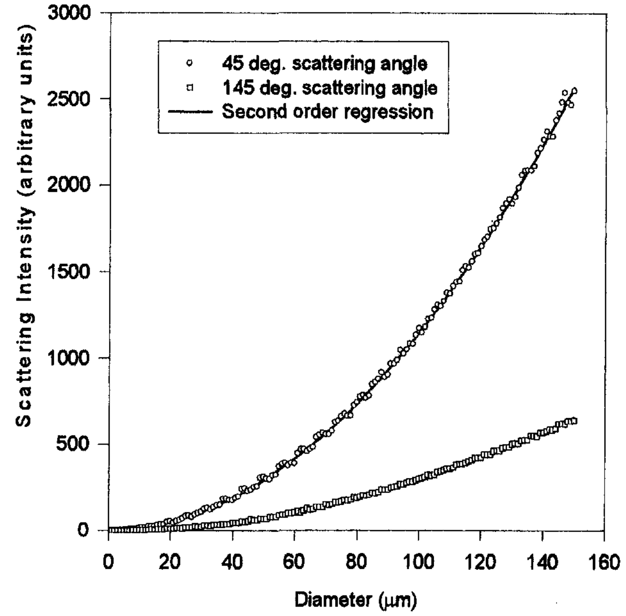

Fig. 1 Computed variation of scattered light intensity with droplet diameter. The calculations were performed using the Lorenz-Mie theory. The droplet refractive index was assumed to be $m = 1.334$.

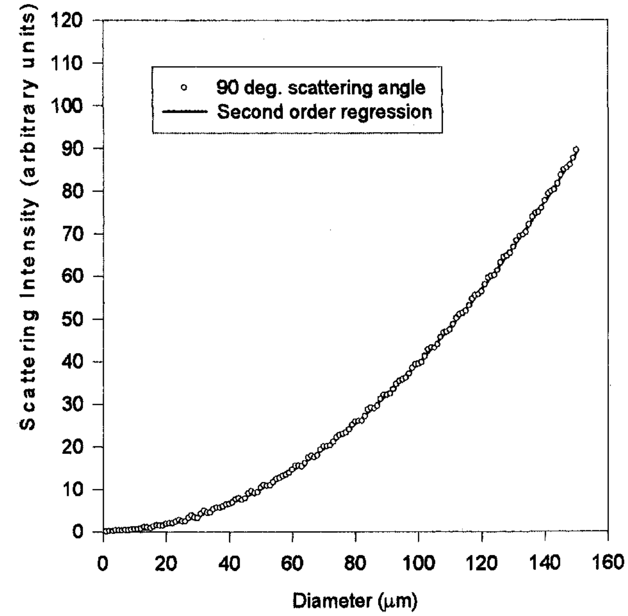

Fig. 3 Computed variation of scattered light intensity with droplet diameter. The calculations were performed using the Lorenz-Mie theory. The droplet refractive index was assumed to be $m = 1.334-0.001i$.

laser light sheet. The illuminated plane containing the ensemble of droplets is then imaged on to a photo-detector such as a two-dimensional CCD array camera, or maybe even a photographic film. Because fluorescence and elastic-light scattering occur at different optical frequencies, the two can be separated out before imaging with the help of appropriate optical line filters that are used in conjunction with other optical components. Therefore, two images (one fluorescence and one elastic-light scattering) can be obtained simultaneously. Each of these images can be recorded by two separate camera systems, or by a single camera fitted with appropriate image-splitting optics. In steady-state applications, where we have reasonable confidence that the flow or spray characteristics does not change with time, it is also possible to use a single camera to record the fluorescence and elastic-light scattering images in sequence.

Because the droplets have to absorb a portion of the incident laser light in order for the fluorescence to occur, the refractive index of the droplets will consist of both a real part and an imaginary part. Therefore, the unabsorbed portion of the incident light that undergoes elastic-light scattering can be suitably described using Eq. (1). That portion of the incident light that is absorbed and is re-emitted as fluorescence can be described using Eq. (2).

Typically, the imaging system will be set up in such a fashion that the magnification ratio is much less than 1. Each pixel will therefore map an area in the interrogation region that is several times greater than the area of the pixel. Therefore, the amount of light that will fall on each pixel (picture element) of the CCD camera will correspond to the combined fluorescent/scattered light from an ensemble of droplets that lie within the pixel's mapping area. Furthermore, because of the random placement of the droplets within this mapping area, the scattered/fluorescent light will lack coherence and will not interfere. For such a situation, the intensity of the fluorescent signal falling on a CCD pixel, defined by the coordinates (x, y), from a collection of randomly distributed droplets can be expressed as

$$I_f(x,y) = I_i(x,y)\phi \sum N_i(x,y)D_i^3(x,y), \tag{3}$$

and the intensity of the elastic light scattering can be expressed as

$$I_s(x,y) = I_i(x,y)k \sum N_i(x,y)D_i^2(x,y), \tag{4}$$

where $I_i(x, y)$ is the intensity of the incident light source, $I_f(x, y)$ is the fluorescent intensity, $I_s(x, y)$ is the elastic light scattering (Mie scattering) intensity, N_i is the number of particles of size class D_i, and ϕ and k are constants that were described earlier.

Taking the ratio of Eqs. (3) and (4) we get,

$$\frac{I_f(x,y)}{I_s(x,y)} = \frac{\phi}{k}\left[\frac{\Sigma N_i(x,y)D_i^3(x,y)}{\Sigma N_i(x,y)D_i^2(x,y)}\right]. \tag{5}$$

Equation (5) can be re-written in terms of the measured Sauter mean diameter (SMD) as follows:

$$\frac{I_f(x,y)}{I_s(x,y)} = KD_{32}(x,y), \tag{6}$$

where K is a calibration constant, and $D_{32}(x, y)$ is the spatial Sauter mean diameter representing the droplet region in a planar region that has been mapped into the CCD pixel identified by the coordinates (x, y). Equation (6) can be rewritten as follows:

$$D_{32}(x,y) = \frac{1}{K}\left(\frac{I_f(x,y)}{I_s(x,y)}\right). \tag{7}$$

Equation (7) shows that the measured fluorescent intensity and the scattered intensity can be directly used to compute the SMD. Since, a two-dimensional representation of the fluorescent and the elastic light scattering images have been recorded, Eq. (7) directly yields the spatial variation of the SMD in the spray.

Optical Patternator System Components

Typical components of the optical patternator are shown in Fig. 4. Basically, it consists of a laser, a light sheet projector, camera, frame grabber, timing controller, computer, and data acquisition, analysis, and visualization software. The light sheet projector is used to illuminate a two-dimensional plane within the spray field of interest. In dense spray fields such as that associated with rocket injectors and gas turbine atomizers, significant attenuation of the incident light sheet can occur. To overcome this effect a sequential double-pass light sheet system and suitable processing algorithm are needed [12]. The fuel droplets lying within the measurement plane scatter the incident light, and a two-dimensional array camera is used to image the illuminated plane. An image splitter is placed in front of the camera to split the image into two before being imaged by the camera. Appropriate optical filters placed in front of the camera will allow for simultaneously recording of both the elastic light scattering pattern as well the laser induced fluorescence pattern. The image is digitized by a frame grabber and processed by the computer to yield the spatial variation of the fuel mass as well as the Sauter mean diameter.

The type of laser that is needed depends upon the application at hand. For example, a continuous-wave (cw) laser, such as an argon-ion laser, can be used if the fuel (or simulant) can be doped with an appropriate dye that can fluoresce when excited by the argon-ion laser wavelengths. For example, water doped with fluorescein-di-sodium salt fluoresces at about 530 nm when excited by an argon-ion laser. On the other hand, for many production related applications, such as quality assurance, it is not feasible to dope the calibration fluid. In this case, appropriate lasers have to be chosen to excite fluorescence from the fluid. For example, different grades of Stoddard Solvent are generally used as automotive and gas turbine calibration fluids. Fluorescence at UV wavelengths can be excited from these fuel simulants by using a pulsed Nd:YAG laser fitted with a fourth harmonic generator.

Similarly, the type of camera (high resolution or low resolution, 8-bit or 16-bit, digital or RS170 compatible analog, gated intensified or not) depends upon the application at hand. For quality assurance purposes, where processing speed is important, a RS170 gated-intensified camera may be appropriate.

Complete control of the injector, camera, and laser is achieved via the software. The software displays the single-shot images as they are being acquired. Ensemble averaging provides

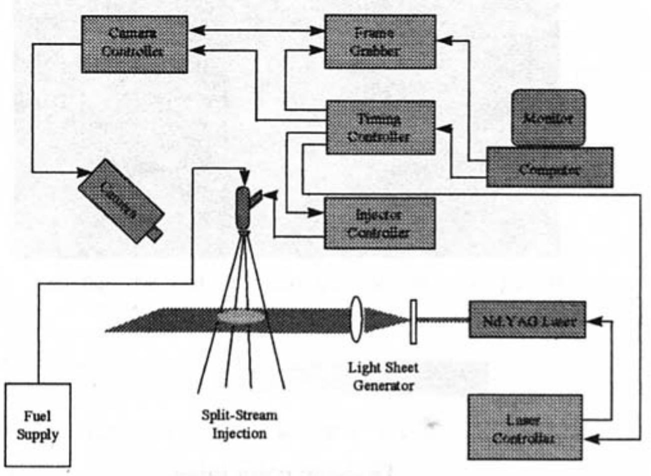

Fig. 4 Schematic of the optical patternator developed for fuel injector spray characterization

a means for smoothing out the images. Further smoothing is achieved by built-in digital filters. Because the camera and the laser light sheet is set up to have an oblique viewing angle, the acquired images have to be corrected for perspective distortion. The system software incorporates fast algorithms for perspective correction. After smoothing and correcting the ensemble averaged image, user selectable masks of various shapes and size can be applied to compute the spatial distribution of the liquid mass from the laser induced fluorescence image. Additional logic is applied, and the fluorescence image is divided by the elastic scattering image to yield the Sauter mean diameter distribution.

Results

Measurements in Pressure Atomizer Spray. The spray created by a Delavan pressure atomizer was chosen for this study. Water was chosen as the test liquid. Since water does not fluoresce when excited by the argon-ion laser source, a small amount of fluorescein-di-sodium salt was added to the water. The 488.0 nm wavelength from an argon-ion laser was used to create the light sheet. The fluorescein (in the water solution) absorbs the argon-ion light source and fluoresces at about 530 nm. At the same time, elastic-light scattering at the incident laser wavelengths can also be observed. Because the spray created by the pressure atomizer is a steady-state process, the fluorescence and scattered light images were recorded in sequence using a single camera. To record fluorescence, a 530 nm high pass optical filter was placed in front of the camera. To record light scattering, a 488.0 nm line filter was placed in front of the camera. For these studies, the camera was located to have an orthogonal viewing angle with respect to the illuminating light sheet.

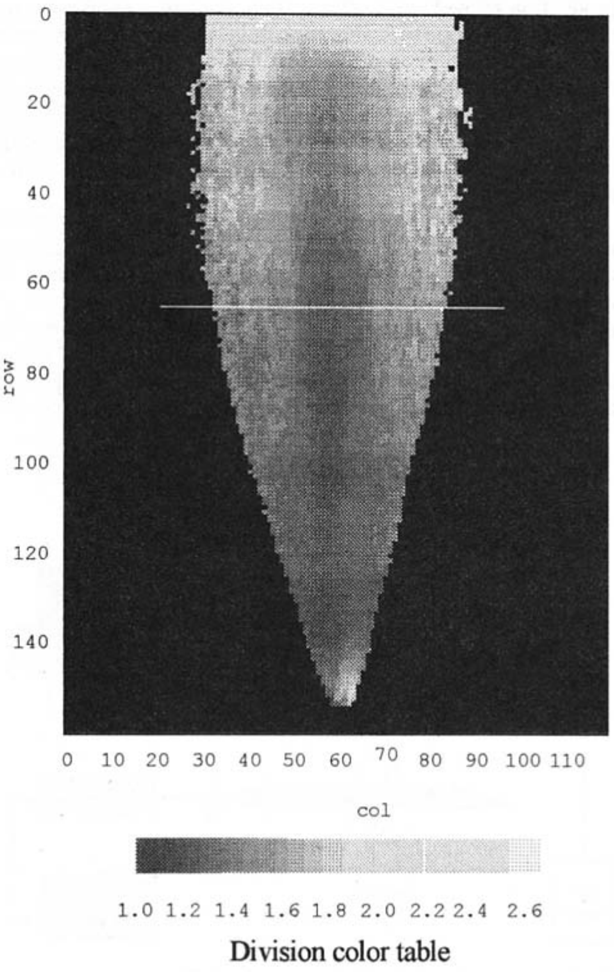

Fig. 5 Qualitative representation of the planar SMD variation in the spray

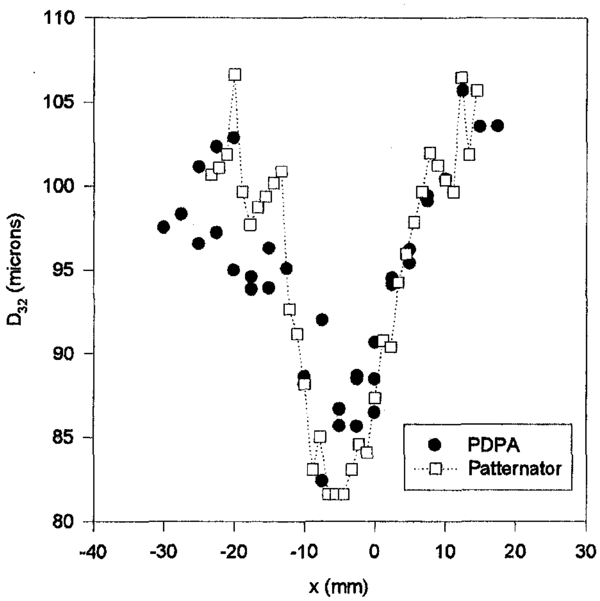

Fig. 6 Radial variation of the SMD at an axial location Z = 100 mm. Comparison of PDS and PDPA measurements.

Several (about 32) fluorescence and light scattering images were recorded and saved in the system computer. The first step in the processing algorithm involved performing a separate ensemble average of the acquired fluorescence and light scattering images. The fluorescence image was then divided by the scattering image to give rise to a qualitative image of the SMD. Appropriate logic was included in the system software to ensure that division by zero does not occur. Figure 5 presents a typical pseudo-color representation of the planar variation of the SMD within the spray.

The qualitative SMD image shown in Fig. 5 was transformed into a quantitative SMD image by calibrating the PDS results with that obtained with a PDPA. In other words, the D32 measured by the PDPA at a single point in the spray was used to calculate the calibration constant K in Eq. (7). Figure 6 shows the comparison of the SMD values obtained with the PDS (after calibration) and the PDPA. These measurements represent the radial variation of the SMD at a distance of about 100 mm from the injector (the location is depicted by the white horizontal line in Fig. 5). The pressure atomizer was operated at 50 psi. Similarly, Fig. 7 shows a comparison of the PDS and PDPA measurements at an axial distance of 75 mm from the nozzle.

In Figs. 6 and 7, the optical patternator measured D32 values are in excellent agreement with those obtained using the well-established PDPA, especially at the center of the spray. Toward the outer edges of the spray, the optical patternator and PDPA data begin to disagree. The reason for this is attributed to the low density of particles at these locations. The optical patternator measurements were obtained with a constant exposure time for the camera. This means that irrespective of the radial location within the spray, the sampling time remains fixed. Therefore, the optical patternator system does not see enough particles at the outer edges of the spray, and the ones that are recorded are the larger drops because of the available dynamic range of the camera. On the other hand, the PDPA was allowed to sample as long as was required to acquire 5000 samples.

Figure 8 shows the PDPA measured data rate at an axial location of z = 100 mm. The pressure atomizer was operated at 80 psi. It can be observed that the data rate is maximum at the center of the spray and drops toward the outer edges of the

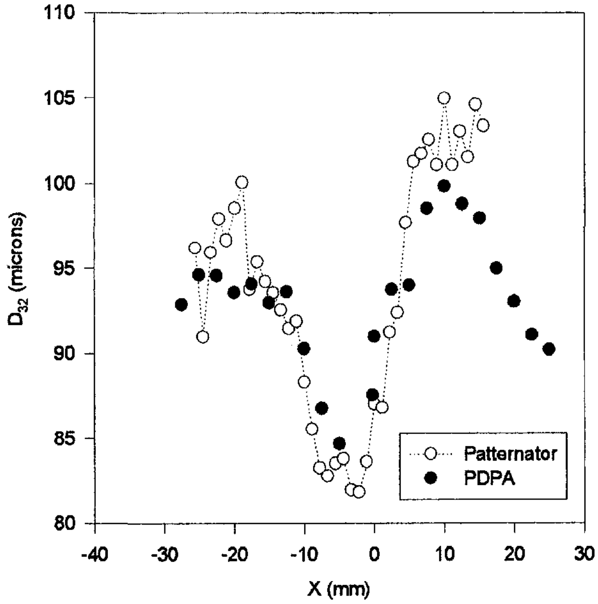

Fig. 7 Radial variation of the SMD at an axial location $Z = 75$ mm. Comparison of PDS and PDPA measurements.

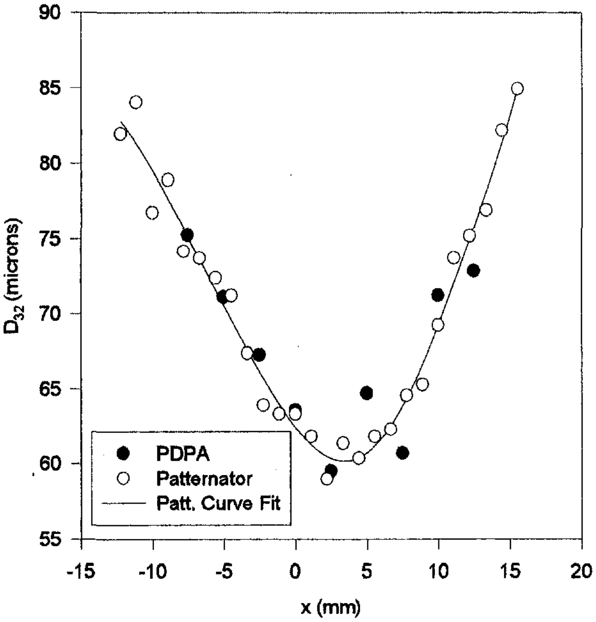

Fig. 9 Comparison of PDPA and PDS results at those radial locations where the data rate is greater than 400/sec

spray. If we were to arbitrarily set the minimum acceptable data rate as 400/sec then Fig. 9 shows that the comparison between the optical patternator measurement and PDPA measurements are excellent. This demonstrates that the Optical Patternator technique will yield good results provided the sampling time is long enough to record a large number of samples. This requirement makes the system ideal for dense spray application where the PDPA generally has difficulties.

Measurements in Fuel Injector Spray. Preliminary measurements have also been performed in a split-stream fuel injector spray with Stoddard solvent as the liquid. The injector and the Stoddard were supplied by Siemens' Automotive. The Stoddard solvent can be made to fluoresce at about 300 nm by exciting it at 266 nm. Therefore, a quadrupled Nd:YAG laser was used for these studies. Appropriate filters were placed before the camera to filter out the scattered light at 266 nm and the fluorescent light at 300 nm. The injector was operated at 60 Hz in synchronization with the camera frame rate. The laser was operated at 10 Hz, again in synchronization with a particular phase of the fuel injection cycle. This implies that an image was recorded for every six pulses of the injector. The laser pulse is only 5 ns wide, and, therefore, the individual droplets are basically "frozen." An ensemble average performed over 128 images helps to smooth out the statistical variation in the individual images. Another digital filter is applied to further smooth out the image. These measurements were performed with the light sheet being orthogonal to the spray direction and the camera was mounted at an oblique angle of about 30 deg, as shown in Fig. 1. The processed image was then corrected for perspective distortion.

Figures 10 and 11 show the spatial distribution of the fluorescent intensity at two different phases of the injection cycle;

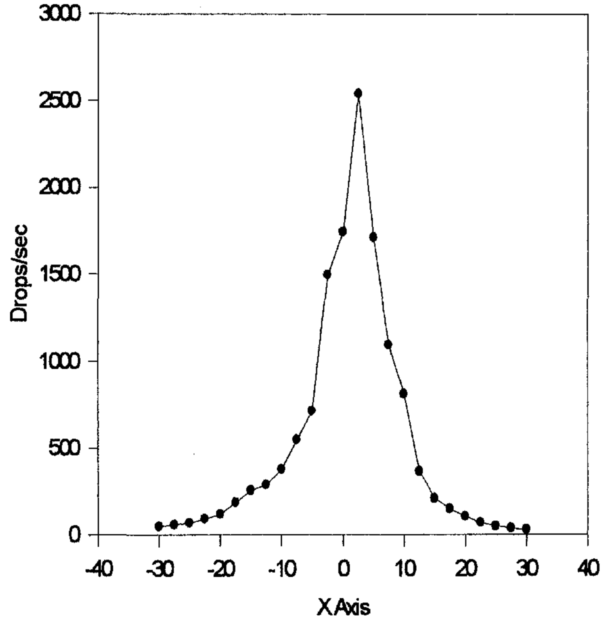

Fig. 8 PDPA measured data rate at $Z = 100$ mm

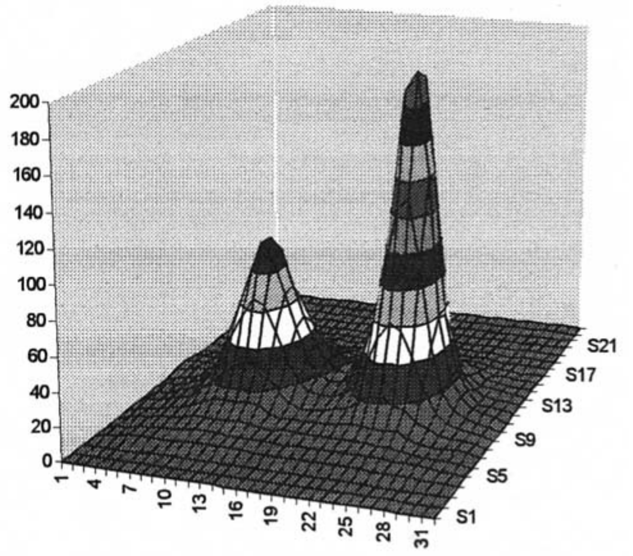

Fig. 10 Spatial distribution of fuel mass (fluorescence intensity) for a split-stream fuel injector 6 ms after onset of injection. The pulse duration was set for 20 ms. The fluorescence from Stoddard solvent was excited by a frequency quadrupled Nd:YAG laser.

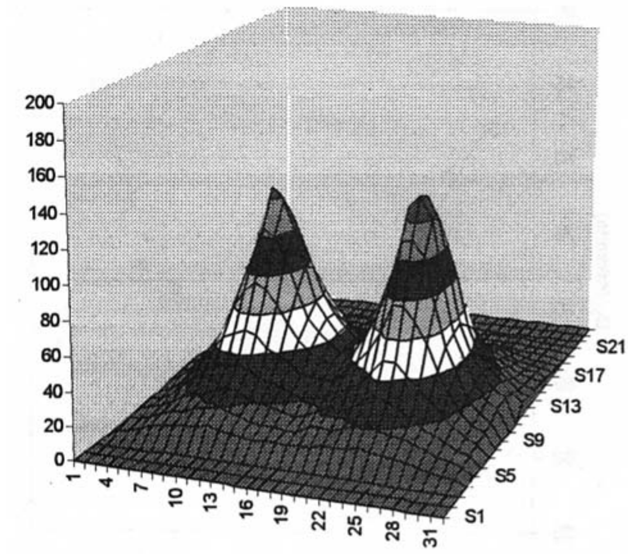

Fig. 11 Spatial distribution of fuel mass (fluorescence intensity) for a split-stream fuel injector 11 ms after onset of injection. The pulse duration was set for 20 ms. The fluorescence from Stoddard solvent was excited by a frequency quadrupled Nd:YAG laser.

namely, 6 ms and 11 ms after the start of injection. The measurements were made at an axial location of $Z = 100$ mm and the injection pulse width was set to 20 ms.

Conclusions

An instrument has been developed for rapid characterization of sprays. The validity of the optical patternator measurements has been verified in a pressure atomizer spray by comparing with PDPA measurements. Preliminary measurements have also been undertaken in fuel injector spray. The optical patternator shows tremendous potential for real-time measurement of the SMD in sprays. By traversing the atomizer, or by rapidly scanning the light sheet, a global characterization of the spray can be achieved in a relatively short time. This instrument is an ideal complement to the PDPA which is a single particle counter possessing excellent temporal and spatial resolution capabilities. Furthermore, the optical patternator is ideal for dense spray applications where the reliability of the PDPA becomes questionable.

References

1 Bachalo, W. D., and Houser, M. J., 1984, ''Phase Doppler Spray Analyzer for Simultaneous Measurements of Drop Size and Velocity Distributions,'' *Optical Engineering,* Vol. 23, pp. 583–590.

2 Sankar, S. V., Ibrahim, K. M., Buermann, D. H., Fidrich, M. J., and Bachalo, W. D., 1993, ''An Integrated Phase Doppler/Rainbow Refractometer System for Simultaneous Measurement of Droplet Size, Velocity, and Refractive Index,'' presented at the 3rd International Congress on Optical Particle Sizing, Yokohama, Japan, August 23–26.

3 Smallwood, G. J., 1992, ''A Technique for Two-Colour Particle Image Velocimetry,'' Ph.D. thesis, University of Ottawa, Ottawa, Canada.

4 Melton, L. A., and Verdieck, J. F., 1984, ''Vapor/Liquid Visualization in Fuel Sprays,'' *20th Symp. (International) on Combustion,* The Combustion Institute, p. 1283.

5 Yoshizaki, T., Funahashi, T., Nishida, K., and Hiroyasu, H., 1995, ''2-D Measurements of the Liquid Phase Temperature in Fuel Sprays,'' Paper No. 950461, SAE International Congress and Exposition, Feb. 27–March 3.

6 Talley, D. G., McDonnell, V. G., Lee, S., and Samuelsen, G. S., 1995, ''Accounting for Laser Sheet Extinction in Applying PLLIF to Sprays,'' presented at the 8th Annual Conference on Liquid Atomization and Spray Systems, Troy, Michigan, May 21–24.

7 Hodges, J. T., Baritaud, T. A., and Heinze, T. A., 1991, ''Planar Liquid and Gas Fuel and Droplet Size Visualization in a DI Diesel Engine,'' Paper No. 910726, presented at the SAE International Congress and Exposition, Detroit, Michigan, February 25–March 1.

8 Herpfer, D. C., and Jeng, S. M., 1995, ''Streaked Particle Imaging Velocimetry and Sizing in Burning and Non-Burning Sprays,'' AIAA No. 95-0141, presented at the 33rd Aerospace Sciences Meeting and Exhibit, Reno, Nevada, January 9–12.

9 Yeh, C.-N., Kosaka, H., and Kamimoto, T., 1996, ''Measurement of Drop Sizes in Unsteady Dense Sprays,'' *Recent Advances in Spray Combustion: Spray Atomization and Drop Burning Phenomena,* Vol. 1, K. K. Kuo, ed.,

10 Sankar, S. V., Robart, D. M., and Bachalo, W. D., 1996, ''A Planar Droplet Sizing Technique for Spray Characterization,'' presented at the 9th Annual Conference on Liquid Atomization and Spray Systems, San Francisco, May 19–22.

11 van de Hulst, 1957, *Light Scattering by Small Particles,* Dover Publications, Inc., New York.

12 Talley, D. G., Verdieck, J. F., Lee, S. W., McDonell, V. G., and Samuelsen, G. S., 1996, ''Accounting for Laser Sheet Extinction in Applying PLLIF to Sprays,'' AIAA-96-0469, presented at the 34th Aerospace Sciences Meeting and Exhibit, Reno, Nevada.

Nonlinear Heat-Release/ Acoustic Model for Thermoacoustic Instability in Lean Premixed Combustors

A. A. Peracchio

W. M. Proscia

United Technologies Research Center,
Combustion Technology,
411 Silver Lane, MS 129-19,
East Hartford, CT 06108

Lean premixed combustors, such as those used in industrial gas turbines to achieve low emissions, are often susceptible to thermoacoustic combustion instabilities, which manifest themselves as pressure and heat release oscillations in the combustor. These oscillations can result in increased noise and decreased durability due to vibration and flame motion. A physically based nonlinear parametric model has been developed that captures this instability. It describes the coupling of combustor acoustics with the rate of heat release. The model represents this coupling by accounting for the effect of acoustic pressure fluctuations on the varying fuel/air ratio being delivered to the flame, causing a fluctuating heat release due to both fuel air ratio variations and flame front oscillations. If the phasing of the fluctuating heat release and pressure are proper, an instability results that grows into a limit cycle. The nonlinear nature of the model predicts the onset of the instability and additionally captures the resulting limit cycle. Tests of a lean premixed nozzle run at engine scale and engine operating conditions in the UTRC single nozzle rig, conducted under DARPA contract, exhibited instabilities. Parameters from the model were adjusted so that analytical results were consistent with relevant experimental data from this test. The parametric model captures the limit cycle behavior over a range of mean fuel air ratios, showing the instability amplitude (pressure and heat release) to increase and limit cycle frequency to decrease as mean fuel air ratio is reduced.

Introduction

Lean premixed combustion systems are desirable from the standpoint of minimizing NOx emissions for industrial gas turbine applications. However, these systems are often susceptible to thermoacoustic combustion instabilities, which manifest themselves as pressure and heat release oscillations in the combustor. These oscillations can result in increased noise and decreased durability due to vibration and flame motion. Generally, the unstable behavior arises because of coupling between the combustion process and acoustic motions within the combustor. The chamber acoustics, a stable open-loop system, is made unstable by a positive feedback loop, the gain being associated with the combustion process. Elimination or reduction of these instabilities can be accomplished by passive means (design) or by active control. Increased understanding of the instability via models can be used to assess corrective design modifications and test control methodologies. It is also possible to include such models as an integral part of the adaptive control. The main focus of this effort, however, is to develop a model that can be used to suggest and assess control strategies with validation of the strategy depending on control experiments on rigs and engines.

Modeling of combustion oscillations was initially motivated by instabilities in rockets, ramjets and augmentors, with models developed using acoustic representations of the pressure oscillations, and delineating the coupling of the acoustics with the unsteady heat release (Culick, 1971, 1989). Instability models have also been developed that delineate the coupling between the heat release and an acoustic field, using stirred reactor (Janus and Richards, 1996; Janus et al., 1997) and flame front representations (Fleifil et al., 1996; Wang and Yang, 1997). Combustion instabilities result when acoustic and unsteady heat release models are coupled (see the above references and Mohanraj et al., 1997).

Combustion instabilities observed in engine tests have been reproduced in sub-scale rig tests, providing a means to study the characteristics of the instability in more depth. UTRC has been conducting such tests as part of corporate R&D and DARPA funded programs to study and control combustion instabilities in lean premixed burners. Extensive data on the behavior of the instability as a function of inlet operating condition and fuel/air ratio have been obtained in a single nozzle test rig (SNR) operating at engine pressures, temperatures, and scale. Results of these tests and suppression of the instability through active control are reported in a companion paper (Cohen et al., 1998). Data from these and other tests suggest that for premixed systems, instabilities give rise to velocity fluctuations that can cause variations in the flame front location/shape and the fuel/air ratio of the flow leaving the premixed nozzle and entering the flame front. In the low Mach number conditions of typical gas turbine combustors, the magnitude of acoustic velocity fluctuations are large relative to pressure fluctuations, with the result that unsteadiness in the heat release rate is primarily driven by velocity fluctuations rather than pressure fluctuations. These observations, coupled with the above mentioned need for instability models, lead to the formulation of a reduced order heat release model that accounts for flame surface area dynamics and varying fuel/air ratio, and whose free parameters are determined from the SNR data.

Model Development

The essential features required in a reduced order model for combustion instability are models for both the system acoustics and unsteady heat release and a description of the coupling between them. The acoustics part of the problem can be represented

---

Contributed by the International Gas Turbine Institute (IGTI) of THE AMERICAN SOCIETY OF MECHANICAL ENGINEERS for publication in the ASME JOURNAL OF ENGINEERING FOR GAS TURBINES AND POWER. Paper presented at the International Gas Turbine and Aeroengine Congress and Exhibition, Stockholm, Sweden, June 2–5, 1998; ASME Paper 98-GT-269.

Manuscript received by IGTI March 8, 1998; final revision received by the ASME Headquarters March 23, 1999. Associate Technical Editor: R. Kielb.

with an approximate analysis developed by Culick (1971, 1989). A nonlinear model which exhibits limit cycle behavior is desirable because it (1) provides a framework for predicting pressure fluctuation amplitudes, and (2) permits application of modern dynamical systems theory to the problem. The approach taken in this work is to couple linear acoustics with a nonlinear heat release model. This is in contrast to previous work by Culick (1994) and Jahnke and Culick (1994), which emphasized nonlinear acoustics. Culick (1995) has also investigated nonlinear heat release models for solid rocket combustion, but the physics—that of erosive burning—are not applicable here. Dowling (1996) introduced a nonlinear form for the heat release which saturated at high velocity fluctuation amplitudes. However, the data obtained in our experiments exhibits the opposite behavior—the heat release rate decreases with increasing amplitude of velocity fluctuations.

Acoustics. The formulation developed by Culick has been adopted for the following reasons: (1) satisfies requirement for low order model—two states per retained acoustic mode; (2) well documented in the literature; (3) successfully applied to solid and liquid propellant rocket motor instabilities; (4) used as the basis for dynamical systems analysis of nonlinear acoustic behavior; and (5) formulation developed for two-phase flow, and is, therefore, suitable for eventual application to aeroengine combustion instabilities.

The acoustic pressure field is expressed as a series of normal modes and the formulation yields a set of ODEs describing the temporal evolution of each acoustic mode,

$$p' = \bar{p} \sum \eta_i(t)\psi_i(x) \tag{1}$$

$$\ddot{\eta}_i + 2\alpha_i\dot{\eta}_i + \omega_i^2\eta_i = F_i^{\text{COMB}} + F_i^{\text{NLA}} + F_i^{\text{EXT}}, \tag{2}$$

where, F_i^{NLA} and F_i^{EXT} are defined in the list of symbols, and for longitudinal acoustic modes,

$$F_i^{\text{COMB}} = \frac{\gamma - 1}{\bar{p}E_i^2} \int \frac{\partial q'_v(x, t)}{\partial t} \psi_i(x)dv, \tag{3}$$

q'_v is the fluctuating component of the volumetric heat release rate, and

$$E_i^2 = \int \psi_i^2(x)dv \tag{4}$$

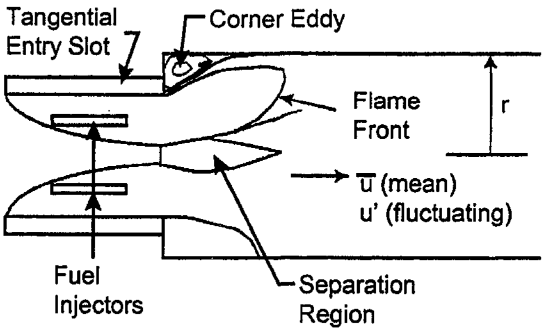

Fig. 1 Schematic of SNR/model

is a normalizing factor. Each acoustic mode is a one-degree-of-freedom oscillator with damping coefficient α_i, natural frequency ω_i, and "forcing" due to unsteady heat release, nonlinear acoustics, and external forces. Note that external forces acting on the flow in the combustion chamber are included here because they can be used to represent the effect of actuators used for active control. The second term on the LHS of Eq. (2) accounts for linear acoustic damping, the nonlinear acoustics term on the RHS is set to zero for the present analysis, and the combustion term on the RHS accounts for all linear and nonlinear processes associated with combustion. If the energy gain due to unsteady heat release is greater than acoustic damping, then instability of the particular mode results.

Heat Release. A schematic of the nozzle/burner used for the SNR testing, and around which the model is based, is shown in Fig. 1. Air is introduced through tangential entry slots at the outer diameter and directed axially to the nozzle exit. Liquid fuel is introduced through spoke injectors and mixed with the swirling air before leaving the nozzle exit. Details of the fuel and air premixing nozzle are described by Snyder et al. (1994a and 1994b). The flame is stabilized by recirculation zones (RZ), created by the sudden expansion geometry and by the highly swirling flow. The reverse flow of the recirculation zones backmix hot combustion products with the incoming reactant mixture and ignite it. The reactant mixture from the nozzle is channeled between the outer and central RZ towards the flame front. The flame is assumed to be anchored at the central RZ and possibly at the outer RZ, as shown.

Nomenclature

A = constant, defined in Eq. (11)
A_f = flame area
b_1 = SuGo/R
E = modal normalizing factor, Eq. (4)
F^{COMB} = external forcing due to combustion
F^{EXT} = external forcing due to actuation
F^{NLA} = external forcing due to non-linear terms
$f/a|_S$ = fuel to air ratio at stoichiometric conditions
Go = constant ≈2 (Fleifil et al., 1996)
HHV = higher heating value
$\hat{H}$ = $\Delta Hm/\text{HHV}{*}f/a|_s$
h_1 = magnitude of slope, Eq. (14)
h_0 = intercept, Eq. (14)
k_1 = empirical constant, Eq. (10)
k'_2 = $-(P/2)/(1 - \phi_{LB})$
k_{cr} = critical gain
$\dot{m}$ = mass flow rate of mixture subtended by flame front
$\tilde{m}$ = $\dot{m}'/\bar{\dot{m}}$
N_1 = $\beta(\gamma - 1)\psi(x_f)/(\bar{p}E_i^2)$
N_2 = $\bar{\dot{m}}$ HHV $f/a|_s{*}N_1$
N_3 = N_2Y
P = empirical constant, Eq. (11)
p = pressure
q = total heat release rate
q'_v = fluctuating volumetric heat release rate
R = combustor radius
s = Laplace variable
Su = turbulent flame speed (empirical)
t = time
u = velocity
$\tilde{u}$ = $u'/\bar{u}$
W_a = instantaneous airflow in nozzle, Eq. (9)
x = axial distance along burner
x_f = flame front location
Y = acoustic admittance, Eq. (13)
α = acoustic damping coefficient
β = empirical constant, Eq. (12)
γ = ratio of specific heats
ΔH_m = heat release per unit mass of mixture
ΔH_s = HHV* $f/a|_S$
η = coefficient giving modal time dependence, Eq. (1)
ρ_m = density of mixture
τ = time delay from nozzle to flame front heat release
ϕ = instantaneous equivalence ratio
$\bar{\phi}$ = mean equivalence ratio
ϕ_{LB} = equivalence ratio at lean blow out
ψ = modal spatial shape, Eq. (1)
ω, ω_a = acoustic mode natural frequency

Subscripts

i = mode number
o = denotes nozzle exit

Superscripts

$'$ = unsteady
$^-$ = Mean

An acoustic wave in the burner gives rise to variation of the axial velocity field in the burner and nozzle. This has the effect of causing the flame front to move in response to the acoustic wave and for the air flow in the nozzle to vary. For the experiments carried out in the SNR, fuel flow fluctuations were small, and will be neglected in the formulation of the model, although they could be easily included if desired. The varying nozzle velocity gives rise to a varying fuel air ratio of the mixture as it leaves the nozzle and approaches the flame front. Both the flame front response and equivalence ratio fluctuation mechanisms affect the heat released by the burning process. In general, other mechanisms, such as entropy and vorticity waves exist, but were not included since non-linear heat release and feed flow instability were found to be the dominant mechanisms for the system studied here.

In order to develop a simple model of the heat release, an "actuator disk" is assumed in which all heat is released into the fluid at a point, denoted x_f. This approximation is suggested by the frequency of the instability (about 200 Hz.), which indicates either a bulk mode or first axial mode. In either case, the variation of the acoustic mode (pressure) is negligible over the spatial extent of the flame region. This reduces Eq. (3) to the form

$$F_i^{\text{COMB}} = \frac{\gamma - 1}{\bar{p}E_i^2}\,\psi_i(x_f)\,\frac{dq(t)}{dt}, \tag{5}$$

where $q(t)$ is the total heat release rate, i.e., the volumetric heat release rate integrated over the combustor volume. The heat release rate can be written as

$$q(t) = \bar{q} + q' = \dot{m}(t)\Delta H_m(x_f, t), \tag{6}$$

where

$$\dot{m}(t) = \bar{\dot{m}} + \dot{m}' = \rho_m S_u A_f(t) \tag{7}$$

is the instantaneous mass flow rate of unburned mixture subtended by the motion of the flame front and $\Delta H_m(t)$ is the instantaneous mixture strength, or heat release per unit mass of mixture, reaching the flame front at time t. The mixture strength at time t is a function of the combustor inlet equivalence ratio at a time τ seconds earlier, the time it takes the mixture to convect from the nozzle to the flame front. Hence, $\Delta H_m(x_f, t) = \Delta H_m(x_o, t - \tau)$. In reality, the convective delay time is a function of the streamline location, but to allow for a simple model, it is approximated by a mean value obtained empirically.

Flame Surface Area Dynamics. The flame dynamics model of Fleifil et al. (1996) is used to describe the response of the flame front to acoustic velocity perturbations. In the Reference, the steady flow field was modeled as a Poiseuille flow and the flame dynamics were studied by linearizing around the mean flame shape. Solution of the resulting linearized equation gave the temporal and spatial behavior of the flame front displacement from the mean when subjected to an acoustic wave of a given frequency. These solutions were then converted to a flame front area change to relate it to the fluctuating heat release rate. The results from their analysis were shown to be reasonably represented by a first order lag equation, where, for laminar flames, the parameters are determined directly from fundamental quantities—flame speed and flameholder geometry. The assumptions used in formulating the model are not strictly applicable to turbulent flames; however, this model form can be used by fitting parameters to data. The first order formulation does have the desirable property that the flame response—magnitude and phase lag—is a function of frequency.

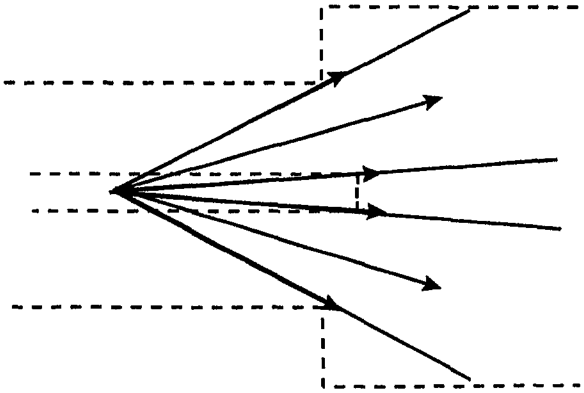

a) Conical Source

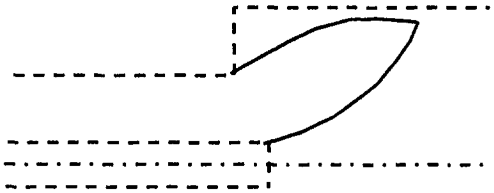

b) Steady Flame Front

Fig. 2 Approximation of flow field as conical source and resulting steady flame shape

In the nozzle of Fig. 1, the flow is axisymmetric, swirling, and has more of a source flow character since the streamlines are directed radially outward as well as axially. CFD flow solutions and flame images for the actual geometry with swirl are used to define the outer and inner recirculation zones and the conical flow region between the streamlines that bound the recirculation zones. This bounded conical flow region (which has swirl) can be approximated as a section of a source flow with swirl, see Fig. 2(*a*). Additionally, all the fuel is essentially evaporated and uniformly mixed with the air when it leaves the nozzle exit, see Snyder et al. (1994a and 1994b). The equations describing the steady flame shape for the premixed source flow with swirl approximation are then developed and solved explicitly to give the flame shape. The resulting solution is shown in Fig. 2(*b*).

The behavior of the fluctuating component of flame area is given by a modified version of Eq. (53) from Fleifil et al., and is shown as Eq. (8), where the term on the RHS is a constant times the acoustic velocity.

$$\frac{d}{dt}(\tilde{\dot{m}}) + b_1(\tilde{\dot{m}}) = b_1\tilde{u}, \tag{8}$$

where $\tilde{\dot{m}} = \dot{m}'/\bar{\dot{m}}$, $\tilde{u} = u'/\bar{u}$, $b_1 = SuGo/R$, $(Su \cong 3 m/s)$.

Mixture Strength. An expression for $\Delta H_m(t)$, the mixture strength (heat release rate per unit mass), is developed next. First, the behavior of the mixture fuel air ratio (or equivalence ratio) as a function of velocity is derived. As discussed earlier, the presence of acoustic waves in the chamber gives rise to velocity fluctuations in the chamber and the nozzle. For cases where the wavelength of the sound is long compared to the distance it takes the flow and acoustic waves to adjust to the area change between the nozzle and chamber (the present case), the steady continuity equation is approximately valid over this distance, even for unsteady flow. Applying continuity across this region results in Eq. (9), which gives the ratio of instantaneous to mean airflow in the nozzle in terms of the mean and acoustic velocities in the chamber.

$$\frac{W_a'}{\bar{W}_a} = \frac{(\bar{u} + u')}{\bar{u}}. \tag{9}$$

Taking fuel flow to be constant, Eq. (10) for the variation in phi of the mixture leaving the nozzle exit in terms of chamber acoustic and mean velocity results. The constant k_1, which is near one,

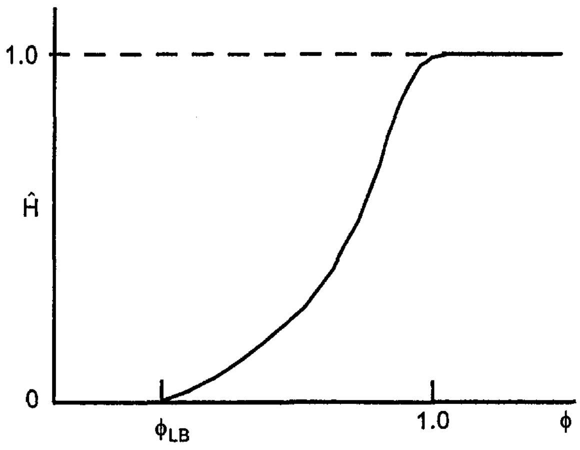

Fig. 3 Schematic depiction of heat release versus ϕ

accounts for deviations from simple one-dimensional steady flow assumed in obtaining Eq. (10).

$$\phi = \frac{\bar{\phi}}{1 + k_1 \dfrac{u'}{\bar{u}}} \tag{10}$$

The mixture strength (heat release) dependence on phi is modeled by Eq. (11), which is depicted schematically in Fig. 3.

$$\frac{\Delta H_m}{\Delta H_s} = A(\phi - \phi_{LB})^P \exp(-(1 - \phi + k_2')^2), \tag{11}$$

where

$$A = \exp(k_2'^2)/(1 - \phi_{LB})^P \quad \text{and} \quad k_2' = -(P/2)/(1 - \phi_{LB}).$$

Beyond a phi of unity, the mixture strength is assumed to saturate. There are two free parameters in the expression, ϕ_{LB}, accounting for lean blowout at low phi, and P, which controls the shape of the curve. These parameters are selected to give a best fit with the data. Combining Eqs. (10) and (11) leads to the desired final result for the dependence of mixture strength on acoustic velocity. The behavior of the model is seen to compare favorably with the data derived from the SNR rig, as shown in Fig. 4.

Coupling of Heat Release and Acoustic Models. The combustor pressure oscillation is modeled as being dominated by a single mode, which can be either a bulk (Helmholtz) mode or a longitudinal mode. The acoustics, represented by Eqs. (2) and (5), are coupled to the heat release rate, given by Eqs. (6), (7), (8), (10), and (11), resulting in

$$\ddot{\eta} + 2\alpha\dot{\eta} + \omega_a^2\eta = N_1 \frac{dq}{dt} = N_2 \frac{d}{dt}[(1 + \tilde{m})\hat{H}|_{(t-\tau)}], \tag{12}$$

where $\hat{H} = \Delta H_m/\Delta H_s$, $N_1 = \beta(\gamma - 1)\psi(x_f)/(\bar{p}E_i^2)$, and $N_2 = \bar{\dot{m}}\Delta H_s N_1$.

Note that a scaling factor, β, has been added to the definition of N_1 to allow for adjustment of the overall gain in the heat release model. (The analysis can be extended to include more than one mode, but for the data modeled here, one mode dominates). For an axial mode, η is the acoustic pressure normalized by the mean at the axial location of the flame. For the bulk mode, it is simply the pressure in the combustor normalized by the mean pressure. The parameters on the LHS, α and ω_a correspond to the acoustic system damping and mode natural frequency, respectively. The relation between acoustic pressure and acoustic velocity is approximated as

$$\tilde{u} = u'/\bar{u} = Y\dot{\eta}, \tag{13}$$

where Y is related to the acoustic admittance at the combustor inlet and can be inferred as described below, measured experimentally or obtained from CFD analyses. The complete model is comprised of Eqs. (12), (6), (8), (10), (11), and (13). Note that Eqs. (6), (8), (10), and (11) comprise a heat release model that has a nonlinear dependence on acoustic velocity. This feature allows the model, with appropriate parameter values, to be unstable to infinitesimal perturbations, but to limit growth so that a finite amplitude instability (limit cycle) results.

Application of the Model

The equations that comprise the model were solved in the time domain by formulating them into a Matlab SIMULINK block diagram, initially triggered with a small amplitude pulse of short duration. If the parameter set was such that the system was unstable, the disturbance would grow and then stabilize in a limit cycle. If the parameter set was such that the system was stable, then the disturbance would decay exponentially towards zero. Data from SNR tests for a power setting of 80 percent were used to calibrate the model. The data, discussed in Cohen et al. (1998), shows that a limit cycle exists whose amplitude varies with the mean value of phi, over a range of phi's from 0.45 to 0.56. The pressure and heat release amplitudes increase as phi decreases.

The parameters of the model that are available for selection are summarized as follows:

acoustic model:	α, ω_a, and Y
flame surface area dynamics model:	b_1
mixture strength model:	k_1, ϕ_{LB}, and P
heat release model:	τ and N_2 (or β)

These parameters were selected as follows:

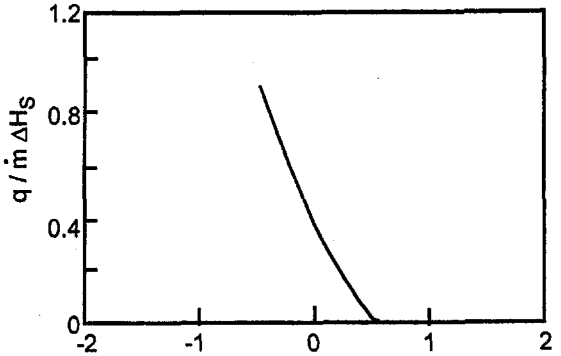

a) Heat release model

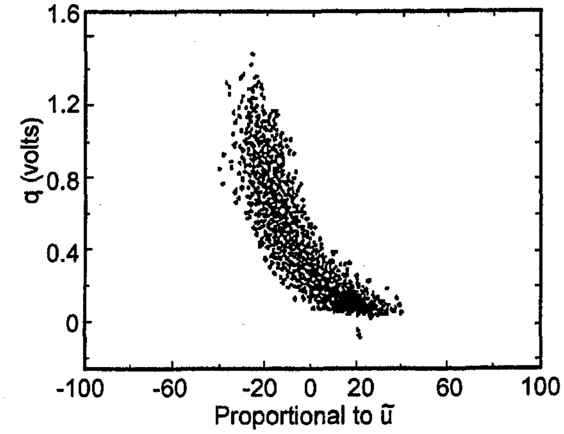

b) Experimental

Fig. 4 Model and experimental heat release transfer functions in qualitative agreement

Table 1 Model parameters

Name	α	ω_a	Y	b_1	k_1	ϕ_{LB}	P	τ	N_2	β
Units	1/s	rad/s	-	1/s	-	-	-	s	1/s	-
Value	150	1257	0.008135	80	0.85	0.35	1.4	Fig. 6	43.45	0.204

Acoustic Model. α and ω_a were selected based on analysis of data from the SNR and one-dimensional Euler simulations of the SNR acoustics (Wake et al., 1996), and Y was selected to give pressure values in the range of the data.

Flame Model. b_1 was obtained by applying the equation for b_1 from Fleifil et al. to the SNR configuration, using turbulent flame speed for Su.

Mixture Strength Model. k_1, ϕ_{LB}, and P were selected to give a best fit to the heat release versus acoustic velocity data (Fig. 4).

Heat Release Model. N_2 (or β) was selected such that acoustic velocity excursions were less than the mean flow velocity.

All of the above parameters, once selected, were frozen for a given power setting, and did not vary with phi within the power setting. Only τ was allowed to vary as a function of phi. This was done to accommodate the expectation that the delay time would increase somewhat as phi decreased to account for not only convection delay, but also a chemical kinetic delay expected to be negligible at high phi, but to increase as phi decreased and approached lean blow out values. The numerical values of the parameters are listed in Table 1.

Discussion. The model with these parameter values was able to reasonably capture the behavior of the data. Figure 5 shows the pressure amplitude and heat release amplitude versus phi, model predictions compared to data. Recall that the parameters were selected to fit only the pressure data, with the rest of the variables falling out at what ever value the model gives. The heat release predictions follow the data reasonably well. Figure 6 compares the time delays used in the model to those estimated directly from the data. The levels are in good agreement, suggesting the simplified actuator disk representation is capturing the first order effects, supporting the trade off of simplicity in favor of detail in developing a reduced order model. The agreement in the trends could perhaps be improved by further fine tuning of the model parameters, and will be investigated in the future. Finally the limit cycle frequency predicted by the model and measured from the data (Fig. 7) are shown to have the same qualitative behavior with the model predicting about 20 percent higher values. It should be noted that the limit cycle frequency does not equal the resonance frequency of the acoustic mode. The reason for this will be discussed in a later section. All the parameter values selected for the 80 percent power case were scaled to the 100 percent power case by adjusting the parameters to the pressure, temperature, etc., of the 100 percent power case, e.g., N_1 was scaled by pressure, ω_a by the square root of temperature, N_2 by $\dot{m}$. All other parameter values were retained. The resulting scaled parameter set was then used to predict the limit cycle pressure amplitudes for that case. Again, reasonable agreement was obtained with the data.

In the solution discussed above the parameter selection was such that the portion of the heat release attributed to the flame front oscillations was small compared to that due to the fuel air ratio variation coming from the nozzle. Examination of unsteady CFD solutions of similar problems and observation of flame fronts from other rigs suggests that the flame surface area fluctuations may be larger than predicted with the parameters used here. The simplified equations developed by Fleifil et al. (1996), see Eq. (8), can easily be adapted to predict larger flame front area variations, by selecting the parameter b_1 to be larger. This has the effect of changing the flame shape from highly wrinkled to much more of a bulk motion, more in keeping with the CFD solutions and observations of flame fronts. The methodology for extracting improved estimates for b_1 from two-dimensional unsteady CFD calculations is currently being developed and will be used to help further assess the importance of flame front dynamics. Additionally, inclusion of control actuation will allow the model to be used for the assessment of control strategies.

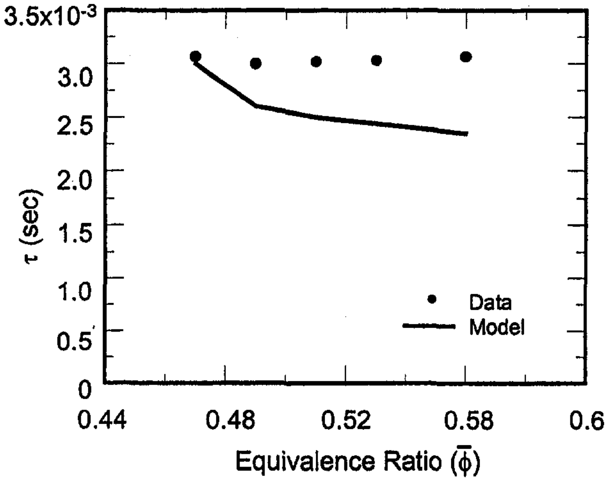

Fig. 6 Model and data comparisons; time delay τ

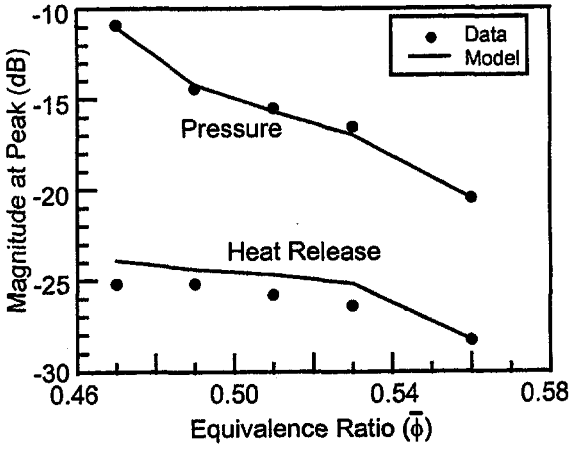

Fig. 5 Model and data comparisons; pressure and heat release amplitudes

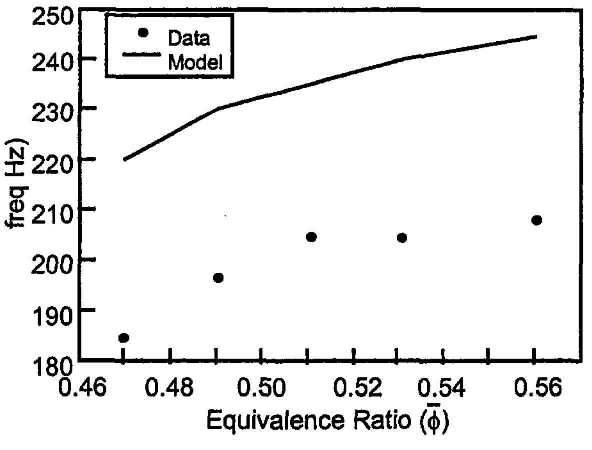

Fig. 7 Model and data comparisons; limit cycle frequency

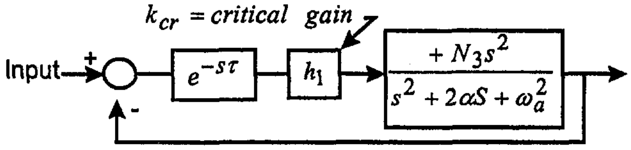

Fig. 8 Block diagram for linearized model

Linear Stability and Limit Cycle Analysis

In this section, a stability analysis of the model is performed by linearizing the equations. Then, an analytic procedure for determining limit cycle amplitudes by accounting for the dependence of the effective gain of the heat release model on the amplitude is described.

Model Simplifications. The above noted small contribution of the flame dynamics to the heat release provided a simplification to the model that allowed it to be formulated in a way that provided more insight into its behavior than could be obtained by running simulations for a variety of parameter values. The simplified model allows the system stability to be assessed and if unstable, then provides approximate values of the limit cycle amplitude and frequency, and more importantly, shows how the model parameters influence stability and limit cycle behavior. In the simplified model, $\dot{m}'$ in Eq. (6), Eq. (7), and Eq. (8) is set to zero. Additionally, Eqs. (10) and (11) are replaced by Eq. (14) below,

$$\hat{H} = \frac{\Delta H_m}{\Delta H_s} = -h_1\left(\frac{u'}{\bar{u}}\right) + h_0, \qquad (14)$$

which relates the mixture strength linearly to velocity, and where $-h_1$ is the slope of the curve. Combining Eqs. (12), (13), and (14) leads to Eq. (15), a linearized version of the model combining acoustics and heat release.

$$\ddot{\eta} + 2\alpha\dot{\eta} + \omega_a^2\eta = -h_1 N_3 \ddot{\eta}|_{(t-\tau)}, \qquad (15)$$

where $N_3 = N_2 Y$. Taking the Laplace transform of Eq. (15) and rearranging leads to Eq. (16),

$$\hat{\eta}(s) = \frac{-h_1 N_3 s^2 e^{-s\tau}}{(s^2 + 2\alpha s + \omega_a^2)}\hat{\eta}(s) \qquad (16)$$

Linear Stability Analysis. Equation (16) can be put in block diagram form, as shown in Fig. 8. By linearizing the heat release portion of the model (Eq. (14)), the stability characteristics can be defined by analysis of the Fig. 8 block diagram. The parameter, h_1, of the heat release equation can be looked at as a variable gain in the context of Fig. 8. By performing a Bode analysis on the open loop transfer function, the critical value of this gain for stability, k_{cr}, can be obtained, as can values of the critical frequency. For values of h_1 less than k_{cr}, the system is stable. For values of h_1 greater than k_{cr}, the system is unstable. From the block diagram, it can be seen that k_{cr} depends on τ, α, ω_a, and N_3, which depends on parameters of the model previously discussed, and is defined in Eq. (15). In Fig. 9, k_{cr} and critical frequency are plotted versus τ for a given value of ω_a and N_3, with α as a parameter. The range of τ selected spans the time delay range expected for the SNR rig. From Fig. 9 the behavior of the system can be inferred. Low k_{cr} implies more susceptibility to instability, so higher values are desired. These occur for higher damping and time delays that are short or long. The delay that corresponds to the minimum in the curve is believed to represent the time delay that puts the heat release and pressure in phase, as required by the Rayleigh criteria to maximize the destabilizing effect of the heat release. The resulting minimum value of k_{cr} represents the gain required to just overcome the acoustic damping in the system. Time delays on either side of this put the pressure and heat release more out of phase, reducing the Rayleigh criteria and enhancing the system stability.

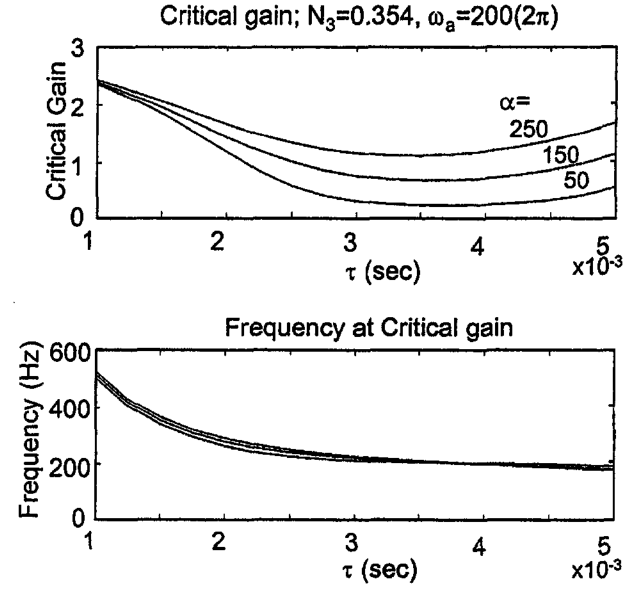

Fig. 9 Critical gain and frequency versus τ from linearized model

In order to determine if the system is stable, values of the slope magnitude, h_1, of the heat release versus velocity curve at zero perturbation velocity must be obtained from the full nonlinear version of the heat release model. This slope can be obtained from Eq. (6), (with $m' = 0$), Eq. (10), and Eq. (11), and is plotted in Fig. 10 for the values of P, ϕ_{LB}, and k_1 given in Table 1. Figures 9 and 10 can be used together to define system stability. For example, for a given set of τ, α, ω_a, and N_3, a value of k_{cr} is defined from Fig. 9. This value of k_{cr} is then compared to the value of slope, h_1, from Fig. 10, If $h_1 > k_{cr}$ then the system is unstable because the heat release model is giving a slope that is greater than that required for stability. Conversely, if $h_1 < k_{cr}$, then the system is stable.

Limit Cycle Analysis. Figure 9 can also be used to infer the limit cycle amplitude and frequency for an unstable system. The analysis is based on the discussion in Franklin et al. (1994), in section 5.7.2 on nonlinear systems, and is also similar to describing function analysis (Dowling, 1996; Murray et al., 1998). Consider the case of an unstable system, where the above analysis for stability is taken to define the response to an infinitesimal velocity perturbation. Since the system is unstable, the perturbation will grow, and to a first approximation, the

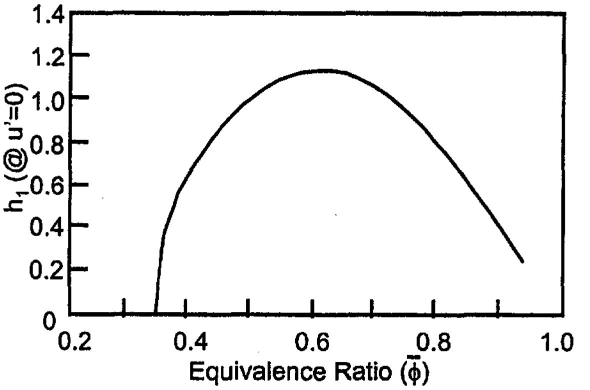

Fig. 10 Slope at zero velocity versus $\bar{\phi}$ from nonlinear heat release model

corresponding growth in heat release rate can be traced from the nonlinear heat release versus velocity curve shown in Fig. 11, (for the set of parameters given in Table 1 and a $\bar{\phi} = 0.51$). As the velocity grows, centered at $u' = 0$, to a value shown on the plot, the corresponding heat release fluctuation can be defined. The slope of the indicated secant line can then be obtained. This slope magnitude can then be plotted as a function of the perturbation velocity, see Fig. 12. The system will now continue to grow until (and if) the slope of the secant line equals the critical gain. At this point, the system is statically stable (in terms of root locus analysis, the gain is such that the system poles sit on the imaginary axis, and the corresponding frequency of the limit cycle is the frequency of that pole) and could operate in a limit cycle whose amplitude is given by the velocity from Fig. 12 and whose frequency is given from Fig. 9. Note that the limit cycle frequency is not equal to the acoustic resonance frequency. The limit cycle must be checked for its own stability to perturbations. If it is stable, than the system will operate in the limit cycle. If not, the methodology described above can be used to determine its character, but due to space limitations, this will not be discussed. (See also Murray et al. (1998) for a more detailed analytical stability analysis—both linear and nonlinear—of this model.) Note that it is not necessary to have saturation to have a limit cycle. The curvature of the heat release versus velocity curve is such that a limit cycle can exist, for example for the case shown in Fig. 11, if the slope of the secant line equals the critical gain.

Discussion. The simple model described above can be used as a preliminary design tool to define the effects on combustion instability of changing geometry or operating condition. It can also be used as the basis for initial parameter selection when trying to fit the model to a new set of data. The methodology is being extended to the case where the flame front variations are included, in order to help assess the importance of flame front bulk motion.

Summary and Conclusions

A reduced order model comprising linear acoustics and a nonlinear heat release model has been developed. The model extends previously published flame dynamic and acoustic analyses to include the effects of varying fuel air ratio induced by the acoustic field. Model parameters were selected that allowed replication of the instability observed in single nozzle rig tests of a lean premixed system run at engine scale and operating conditions. The model can be used as a preliminary design tool and a basis for evaluating control algorithms, with the addition of control system actuation. Additionally, a simplified model has also been developed that predicts stability and limit cycle behavior, and shows in a more graphic fashion how the parameters of the problem affect the stability and limit cycle behavior. This simple model can be used as a preliminary design tool and to determine parameter values required to have the model fit a particular set of data.

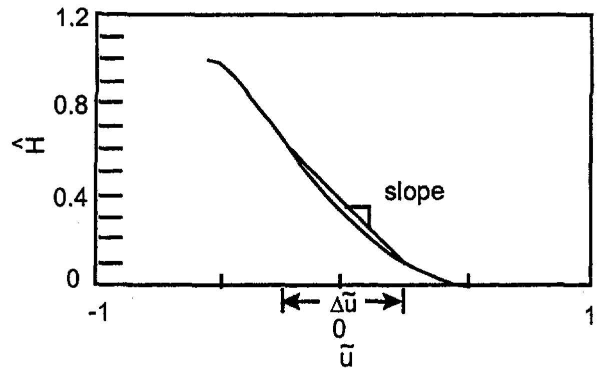

Fig. 11 Definition of slope of secant line

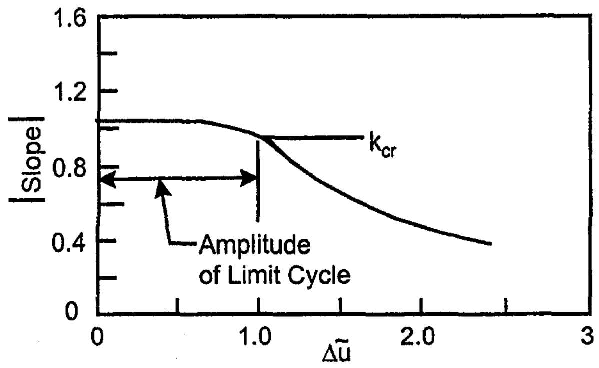

Fig. 12 Determination of limit cycle amplitude

Acknowledgments

The authors would like to acknowledge Dr. William Scheuren (DARPA program manager) and DARPA for providing the motivation and the data used in the model development and the application of the model to the selection of parameters that fit the model data. Additionally, we would like to acknowledge UTRC IR&D funding for the development of the model. We would also like to thank Drs. John McVey (consultant to UTRC) and Tom Rosfjord for guidance and consultation, Dr. Richard Murray (of Cal Tech and consultant to UTRC) for data analysis defining system heat release versus velocity characteristics and Ludwig Haber (of VPI and summer intern at UTRC) for application of the model to the 100 percent power case.

References

Cohen, J. M., et al., 1999, "Active Control of Combustion Instability in a Liquid-Fueled Low-NO_x Combustor," ASME JOURNAL OF ENGINEERING FOR GAS TURBINES AND POWER, Vol. 121, pp. 281–284.

Culick, F. E. C., 1971, "Non-Linear Growth and Limiting Amplitude of Acoustic Oscillations in Combustion Chambers," *Combust. Sci. and Tech.*, Vol. 3, No. 1, pp. 1–16.

Culick, F. E. C., 1989, "Combustion Instabilities in Liquid-Fueled Propulsion Systems—An Overview," AGARD CP-450.

Culick, F. E. C., 1994, "Some Recent Results for Nonlinear Acoustics in Combustion Chambers," *AIAA J.*, Vol. 32, No. 1, p. 146.

Culick, F. E. C., Burnley, V., and Swenson, G., 1995, "Pulsed Instabilities in Solid-Propellant Rockets," *J. Propulsion and Power*, Vol. 11, No. 4, p. 657.

Dowling, A. P., 1996, "Nonlinear Acoustically-Coupled Combustion Oscillations," AIAA Paper 96-1749.

Fleifil, M., Annaswamy, A. M., Ghoniem, Z. A., and Ghoniem, A. F., 1996, "Response of a Laminar Premixed Flame to Flow Oscillations: A Kinematic Model and Thermoacoustic Instability Results," *Combust. and Flame*, Vol. 106, pp. 487–510.

Franklin, F. F., Powell, J. D., and Emani-Naeini, A., 1994, "Feedback Control of Dynamic Systems," Third Ed., Addison-Wesley Publishing Company, Reading, MA.

Jahnke, C. C., and Culick, F. E. C., 1994, "Application of Dynamical Systems Theory to Nonlinear Combustion Instabilities," *J. Propulsion and Power*, Vol. 10, No. 4, p. 508.

Janus, M. C., and Richards, G. A., 1996, "Model for Premixed Combustion Oscillations," DOE/METC-961026 (DEE96004366) National Technical Information Service, Springfield, VA.

Janus, M. C. et al., 1997, "Effects of Ambient Conditions and Fuel Composition on Combustion Stability," ASME Paper 97-GT-266.

Mohanraj, R., Neumeir, Y., and Zinn, B. T., 1997, "A Combustor Model for Control Oriented Simulation of Combustion Instabilities," AIAA 97-0466.

Murray, R. M. et al., 1998, "System Identification For Limit Cycling Systems: A Case Study for Combustion Instabilities," 1998 American Control Conference Proceedings.

Richards, G. A., and Janus, M. C., 1997, "Characterization of Oscillations During Premixed Gas Turbine Combustion," ASME Paper 97-GT-244.

Snyder, T. S. et al., 1994, "Emission and Performance of a Lean-Premixed Gas Fuel Injection System for Aeroderivative Gas Turbine Engines," ASME Paper 94-GT-234.

Snyder, T. S. et al., 1994, "Comparison of Liquid Fuel/Air Mixing and NOx Emissions for a Tangential Entry Nozzle," ASME 94-GT-283.

Wake, B. E., Choi, D., and Hendricks, G., 1996, "Numerical Investigation of Pre-Mixed Step-Combustor Instabilities," AIAA Paper 96-0816.

Wang, T., and Yang, V., 1997, "Combustion Response of a Pre-Mixed Swirl Injector to Longitudinal Acoustic Oscillations," AIAA Paper 97-0694.

Y. Ozawa

Y. Tochihara

N. Mori

I. Yuri

Central Research Institute of Electric
Power Industry, 2-6-1 Nagasaka,
Yokosuka, Kanagawa 240-0196, Japan

T. Kanazawa

K. Sagimori

The Kansai Electric Power Company, Inc.
Amagasaki, Hyogo 661-0974, Japan

High Pressure Test Results of a Catalytically Assisted Ceramic Combustor for a Gas Turbine

A catalytically assisted ceramic combustor for a gas turbine was designed to achieve low NOx emission under 5 ppm at a combustor outlet temperature over 1300°C. This combustor is composed of a burner system and a ceramic liner behind the burner system. The burner system consists of 6 catalytic combustor segments and 6 premixing nozzles, which are arranged in parallel and alternately. The ceramic liner is made up of the layer of outer metal wall, ceramic fiber, and inner ceramic tiles. Fuel flow rates for the catalysts and the premixing nozzles are controlled independently. Catalytic combustion temperature is controlled under 1000°C, premixed gas is injected from the premixing nozzles to the catalytic combustion gas and lean premixed combustion over 1300°C is carried out in the ceramic liner. This system was designed to avoid catalytic deactivation at high temperature and thermal and mechanical shock fracture of the honeycomb monolith of the catalyst. A combustor for a 10 MW class, multican type gas turbine was tested under high pressure conditions using LNG fuel. Measurements of emission, temperature, etc. were made to evaluate combustor performance under various combustion temperatures and pressures. This paper presents the design features and the test results of this combustor.

Introduction

Recently, combined cycle power plants and cogeneration systems have been gradually introduced because of high thermal efficiency. However, since nitrogen oxides (NOx) are generated in a high-temperature gas turbine combustor that is at the heart of these systems and since it is necessary to meet stringent NOx regulations, NOx control is important for these systems. Although low NOx, lean premixed combustors are currently commercialized, a selective catalytic reduction system (SCR), which requires considerable capital, operating and maintenance costs, must be equipped in many cases.

In the 1970s, research was initiated on the application of catalytic combustion to gas turbine combustors as an ultra-low NOx technology (Pfefferle et al., 1975). In this method, a lean and homogeneous premixture is supplied to the catalyst, and combustion is approximately completed by the catalytic and thermal reaction within the catalyst bed. In the case of lean premixed combustion of clean fuel as in this method, NOx is mainly formed by the extended zeldovich mechanism, which is highly temperature dependent (Miller et al., 1989). Because there is no local high temperature region in this method, remarkably low NOx combustion can be realized. On the other hand, as the catalyst temperature rises over the combustor outlet gas temperature, it is difficult to apply the recent gas turbine for high temperature. Aimed at the realization of a low NOx combustor applied catalytic combustion technology for the high temperature gas turbine, a joint R&D project by CRIEPI (Central Research Institute of Electric Power Industry) and KEPCO (The Kansai Electric Power Co., Inc.) was started in 1988. In this work, to avoid the thermal degradation of the catalyst at high temperature, a catalytically assisted ceramic combustor was designed and an atmospheric pressure combustion test was completed in 1993 (Ozawa et al., 1994). Secondly, a metal liner combustor was tested under high pressure conditions in 1995 (Fujii et al., 1996). After that, a combustor with a ceramic liner was designed and tested under high pressure conditions aimed at NOx emission under 5 ppm (converted at 16 percent O_2) at a combustor exit temperature over 1300°C. The targeted goals are shown in Table 1.

Design of the Combustor

In the case of applying catalytic combustion to the high temperature gas turbine, if combustion is completed within the catalyst bed, the following difficulties exist: (1) thermal degradation of the catalyst, (2) thermal shock fracture of the ceramic monolith of the catalyst; and (3) necessity of a uniform fuel/air mixture. In order to overcome these difficulties, the catalytically assisted, premixed combustor shown in Fig. 1 was designed.

The scale is equivalent to one combustor of a 10 MW class, multican type gas turbine. The combustor is composed of a burner section and a premixed combustion section. The burner section (the front view is shown in Fig. 2 and the back view is shown in Fig. 3) consists of an annular preburner, 6 catalytic combustor segments, and 6 premixing nozzles. The preburner is an annular and reverse flow type, and it is placed on the periphery of the burner section to shorten the total length of the combustor. Diffusive combustion type is selected to meet a wider load range. Between the preburner and the inlet of the catalytic combustor segments and the premixing nozzles, a baffle is equipped to promote mixing air and hot gas. Each catalytic combustor segment is composed of three fuel nozzles, three venturi mixers and a catalyst holder. One fuel nozzle is inserted in the center of each venturi. A set of reliable, small catalysts is mounted in the holder with ceramic wool. Three fuel nozzles are inserted in each premixing nozzle. There are six holes for the injection of premixed gas into the catalytic combustion gas at both sides of the premixing nozzle exit. The catalyst segments and the premixing nozzles are arranged alternately to form a circle for adequate mixing. Premixed combustion is made in a ceramic liner, shown in Fig. 4, that is composed of an outer metal wall, a ceramic fiber layer and inner ceramic tiles (Yuri et al., 1997). The ceramic tiles hold the ceramic fiber layer to the metal wall. A ceramic transition piece used in the

---

Contributed by the International Gas Turbine Institute (IGTI) of THE AMERICAN SOCIETY OF MECHANICAL ENGINEERS for publication in the ASME JOURNAL OF ENGINEERING FOR GAS TURBINES AND POWER. Paper presented at the International Gas Turbine and Aeroengine Congress and Exhibition, Stockholm, Sweden, June 2–5, 1998; ASME Paper 98-GT-381.

Manuscript received by IGTI March 23, 1998; final revision received by the ASME Headquarters March 23, 1999. Associate Technical Editor: R. Kielb.

Table 1 Targets for combustor performance

Combustor exit gas temperature (Tg)	>1300°C
NOx emission	<5ppm (16%O_2)
Combustion efficiency (η)	>99.9%
Total pressure loss (ΔP)	<5%
Pattern factor (P.F.)	<15%

combustion test of a ceramic combustor at 1500°C for about 30 h (Yuri et al., 1997) is used in this test again. In the premixed combustion section, an igniter is temporarily inserted to assist the smooth ignition of the premixed gas.

Air is heated by the preburner to the temperature that will enable the catalyst to maintain stable activity and is distributed to the catalyst segments and premixing nozzles. Fuel is fed to the catalyst and catalytic combustion is conducted below 1000°C. Fuel is also fed to the premixing nozzles and the premixed gas is injected into the catalytic combustion gas at right angles. Recirculating flow then occurs behind the end face of the premixing nozzles. As a result, stabilized by both the catalytic combustion gas and the recirculating flow, lean premixed combustion over 1300°C is carried out. In this combustor system, fuel flow split can be controlled according to the changes in fuel conversion ratio in the catalyst bed under the various operating conditions. When inlet temperature of the catalyst grows lower or the inlet pressure or the velocity grows higher, fuel conversion in the catalyst bed becomes lower and inadequate to stabilize premixed combustion in the downstream of the catalyst. But in this combustor system, because fuel split to the catalyst can be controlled, stable combustion is realized under a wider range of combustor operating conditions.

In order to stabilize the premixed combustion at as low a catalyst temperature as possible, the cross sectional area of the catalyst and air distribution were increased as much as possible, and fuel concentration was limited by the peak temperature of the catalyst bed. Fuel and air distribution to the premixing nozzle was determined from the standpoint of combustion stability and the targeted NOx limitation of 5 ppm (at 16 percent O_2). The liner cooling air was minimized by applying a ceramic liner to lower the NOx emission. The typical airflow split in this combustor is 65 percent for the catalysts, 30 percent for the premixing nozzles, and 5 percent for cooling and leaking.

In order to avoid backfire into the premixing nozzle, gas velocity in the nozzle was maximized within the pressure loss limitations. This combustor was designed under the assumption that an air bypass valve (Aoyama et al., 1984) or another control method of combustion air was applied to keep adequate fuel/air ratio in the combustion area over a wide range of load.

As described above, the strong points of this combustor system are as follows:

- because small catalysts can be applied to the combustor, the structural reliability of the ceramic monolith of the catalyst will be maintained
- premixed combustion in the downstream of the catalyst is stabilized with lower temperature of catalytic combustion
- keeping the catalyst temperature low will prevent deterioration of the catalysts caused by heat, and permit a certain degree of lack of uniformity in the fuel/air mixture
- because fuel split can be controlled, stable combustion will be realized under a wider range of combustor operating conditions

Catalyst

In the case of this combustor, NOx emission is mainly caused by the preburner, but the remainder is caused by the premixed gas from the premixing nozzles. This gas has a higher fuel/air ratio than that of the catalytic combustor segments. For this reason, it is necessary to make the fuel/air ratio for the catalytic combustor segments as high as possible to reduce the fuel/air ratio in the premixing nozzles while keeping the catalyst temperature under 1000°C. Another way to reduce NOx emission is to reduce the ignition temperature of the catalyst to diminish the load of the preburner.

From these standpoints, catalyst improvement was studied, and the Pd/Pt/Rh catalyst was selected (Ozawa et al., 1996). The properties are shown in Table 2. Its major active ingredient is Pd, which is supported on a stabilized alumina washcoat on a honeycomb type monolith made of cordierite. Pt and Rh are added to Pd to promote the reaction activity and stability. In the case of catalytic combustion of methane with the Pd catalyst, self-oscillation phenomena occur, which cause the oscillation of the catalyst bed temperature. By adding Rh to the Pd/Pt catalyst, 30 percent of the temperature amplitude of the catalytic combustion was reduced (Ozawa et al., 1997). The ignition temperature was 360°C and this temperature was also needed to keep stable catalytic combustion.

Test Facility and Conditions

Figure 5 shows a schematic diagram of the test facility for a gas turbine combustor. Air from a compressor is heated with an indirectly fired heat exchanger and fed through a flow control valve to a vessel in which the combustor was included. A small amount of the air is used to cool the liner metal wall and the remaining air is introduced into the burner section. Air to the burner section is distributed to catalytic combustion segments and

Nomenclature

CO = carbon monoxide emission, ppm
cpi = cells per square inch
Hlco = lower heating value of CO, J/kg
Hlf = lower heating value of fuel, J/kg
Hl_{UHC} = lower heating value of UHC, J/kg
Mf = molecular weight of fuel, kg/k-mole
Mco = molecular weight of CO, kg/k-mole
M_{UHC} = molecular weight of UHC, kg/k-mole
NOx = nitrogen oxides emission, ppm
P.F. = pattern factor, % = ((peak Tg − mean Tg)/(peak Tg − mean Tbi)) × 100
Pi = inlet air pressure, MPa
Pg = combustor exit pressure, MPa
Tbi = combustor inlet temperature, °C
Tc = catalyst bed temperature, °C
Tci = catalyst inlet gas temperature, °C
Tg = combustor exit gas temperature, °C
Tth = adiabatic combustion temperature, °C
UHC = unburned hydrocarbon emission, ppm
Wa = air flow rate, kg/s
Wfd = fuel flow rate for preburner, kg/s
Wfc = fuel flow rate for catalyst, kg/s
Wfp = fuel flow rate for premixing nozzle, kg/s
Wft = total fuel flow rate, kg/s
ΔP = combustor pressure loss, % = ((Pi − Pg)/Pi) × 100
η = combustion efficiency, % = $100 - ((Wa + Wf)/(Wf \cdot Mf \cdot Hlf)) \times (CO \cdot Mco \cdot Hlco + UHC \cdot M_{UHC} \cdot Hl_{UHC}) \times 10^{-4}$
λ = excess air ratio

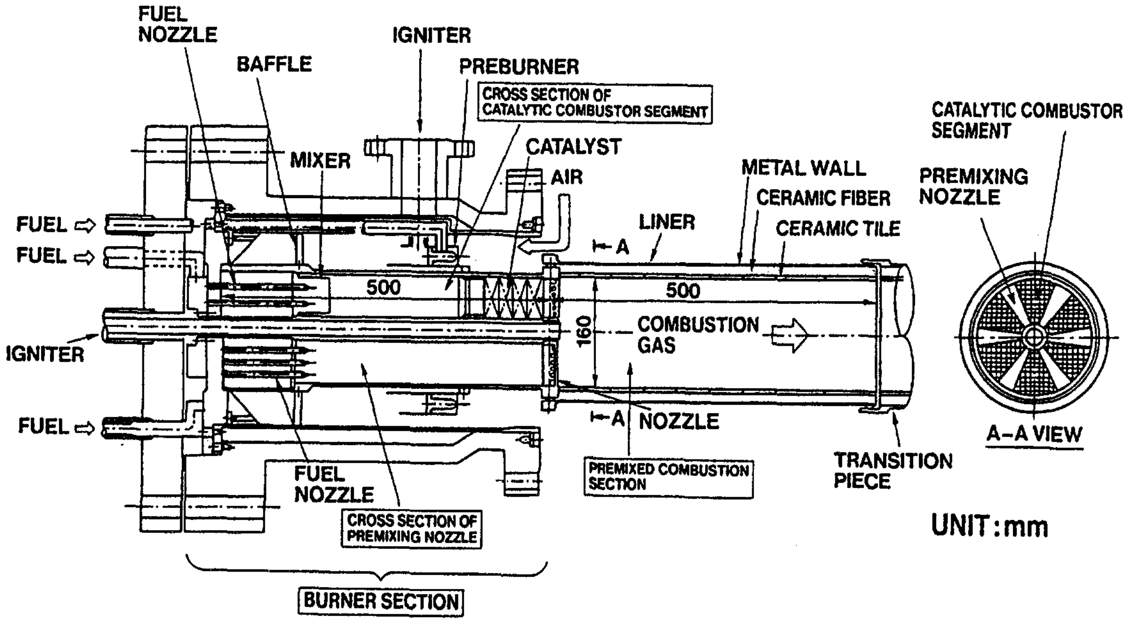

Fig. 1 Schematic of the combustor

premixing nozzles. Fuel is introduced to the preburner, the catalyst and the premixing nozzles, and controlled individually. In the measurement duct, which is behind the combustor exit, the combustion gas temperature is measured by 24 thermocouples of R-type and emission is sampled by two averaging sampling probes made of stainless steel and cooled by water. Emission is analyzed by the methods shown in Table 3, and combustion efficiencies are calculated. The catalyst bed temperatures are measured at the point of 5 mm inside the bed outlet by 18 thermocouples of K-type that are inserted and cemented in the catalyst cells. Each experimental data is measured continuously and averaged for one minute. Table 4 shows the fuel properties, which are sampled from the fuel line during the combustion test and analyzed by TCD gas chromatography.

Table 5 shows the test conditions at a base load. At this condi-

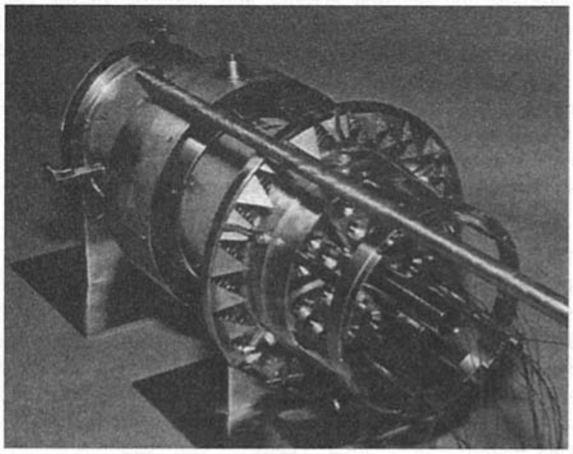

Fig. 2 Front view of the burner section

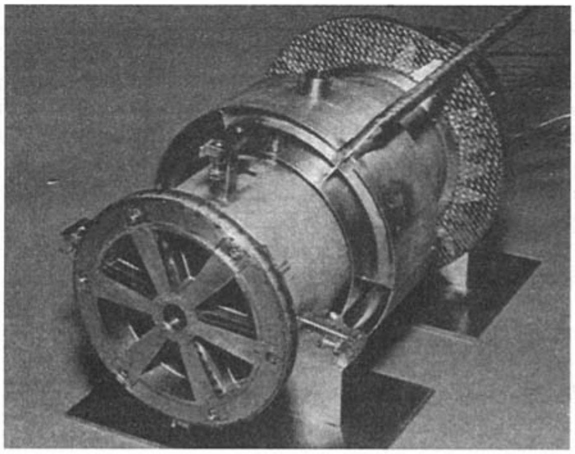

Fig. 3 Back view of the burner section

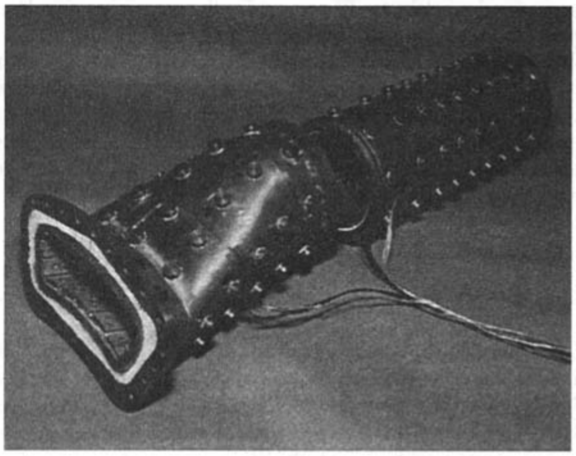

Fig. 4 View of the ceramic liner and transition piece

Table 2 Pd/Pt/Rh catalyst properties

Substrate	Cordierite honeycomb monolith
Washcoat	Stabilized $Al_2O_3$80g/l + $ZrO_2$20g/l
Catalyst	Pd20g/l + Pt5g/l + Rh2g/l
Ignition Temperature	320°C (Fresh catalyst)
	360°C (Aged catalyst)

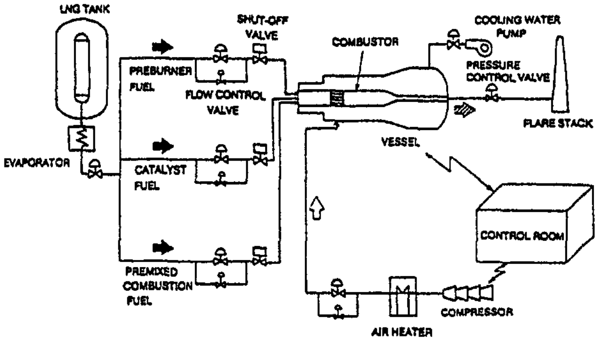

Fig. 5 Diagram of the test facility

Table 3 Analyzing method

Composition	Analyzing method
NOx	Chemi-luminescence
CO	Non-dispersive infrared
CO_2	Non-dispersive infrared
O_2	Paramagnetic
UHC	Flame ionization

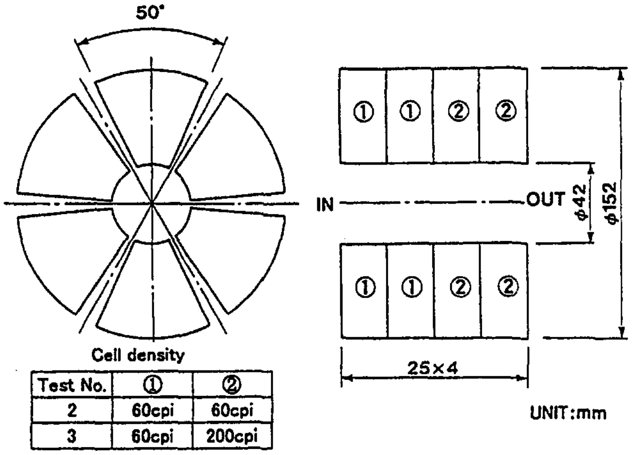

Test No.	①	②
2	60cpi	60cpi
3	60cpi	200cpi

Fig. 6 Catalyst segments

tion, catalyst inlet velocity is 25 m/s. Catalytic combustion and premixed combustion were initiated under the conditions of 0.35 MPa, then air and fuel are increased in proportion to the increasing pressure to investigate the effect of pressure under the constant residence time.

The following five kinds of combustion tests were made:

No. 1 a preburner test
No. 2*a* a combustor test using a set of 60 cpi catalysts
No. 2*b* a repeatability test
No. 3*a* a combustor test using a set of different cell density catalysts
No. 3*b* a repeatability test

At first, the preburner was tested to estimate NOx emission and temperature uniformity at the catalyst bed, then the combustor tests were held. A schematic of the catalyst segments is shown in Fig. 6. Combustion efficiency of the catalyst set for the No. 3 test is about 1.2 times higher than that for No. 2. Venturi mixers of wider internal diameter were installed at the inlet of the catalytic combustor segments for No. 3 test to offset the larger pressure loss of the catalyst set. The purpose of these changes is to estimate the effect of catalyst temperature on premixed combustion stability.

Test Results

Combustion Characteristics of the Preburner. In the test No. 1, the fuel was fed only to the preburner and temperature distribution in the catalyst bed and emission at the combustor exit were measured under various pressure conditions. Figure 7 shows the temperature distribution in the catalyst bed under the base load condition. The difference between the highest and lowest temperature measured 18 thermocouples is 30°C. From the standpoint of the necessary minimum temperature at the catalyst inlet, the mean temperature of 400°C at the catalyst inlet is estimated to be sufficient.

Figure 8 shows the NOx emission under various pressures and fuel/air ratios, keeping the combustor inlet temperature and the ratio of air flow rate to inlet air pressure constant (370°C and 1.95 kg/(MPa · s), respectively). NOx emission increases with increasing pressure up to 0.54 MPa, but, from 0.54 to 1.33 MPa, is hardly affected by pressure. At the base load condition, fuel/air ratio (Wfd/Wa) is 0.001 and NOx emission is 5 ppm (at actual O_2). On

Table 4 Typical composition of fuel

CH_4	80.38vol.%
C_2H_6	9.60vol.%
C_3H_8	6.62vol.%
i-C_4H_{10}	1.46vol.%
n-C_4H_{10}	1.90vol.%
i-C_5H_{12}	0.00vol.%
n-C_5H_{12}	0.00vol.%
N_2	0.04vol.%

Table 5 Base load conditions

Inlet air pressure (Pi)	1.33MPa
Air flow rate (Wa)	2.60kg/s
Fuel flow rate (Wft)	0.0690kg/s
Combustor inlet temp. (Tbi)	370°C
Catalyst temp. (Tc)	<1000°C
Combustor outlet gas temp. (Tg)	1350°C

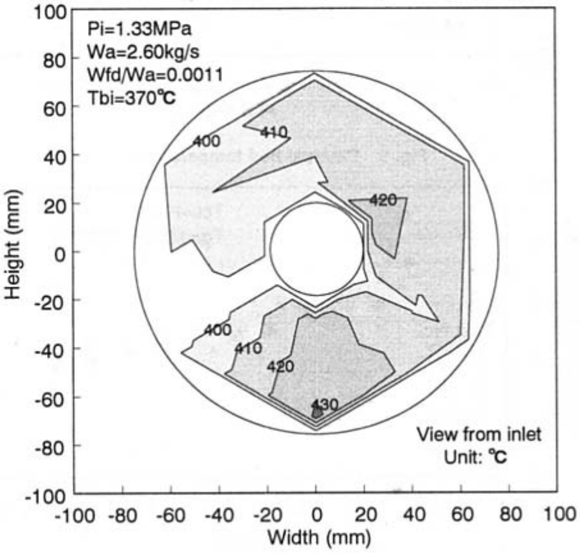

Fig. 7 Temperature distribution in catalyst bed

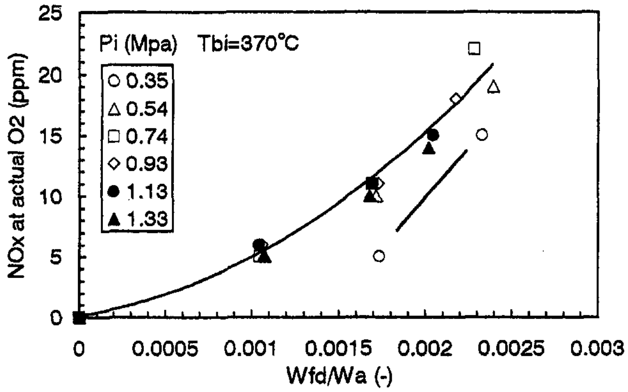

Fig. 8 Preburner NOx emission at combustor exit

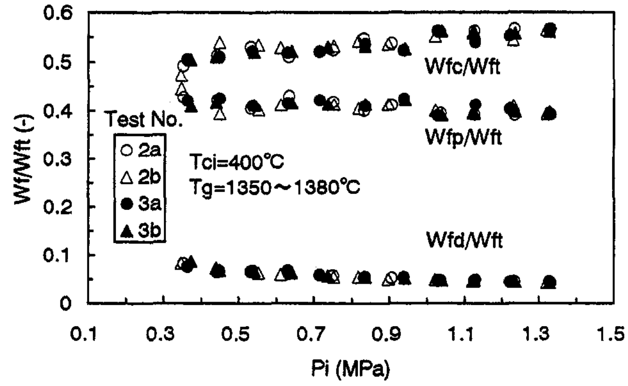

Fig. 11 Fuel distribution

the other hand, at all the test points, the combustion efficiency was over 99 percent.

Effect of Pressure. The effect of pressure on the combustion characteristics was examined in tests No. 2 and 3. Like the preburner test, inlet pressure was increased while keeping the ratio of the air flow rate to inlet pressure, catalyst inlet temperature and combustor exit gas temperature constant. Figure 9 shows the catalyst bed temperature. The peak of the oscillating temperature of the catalyst bed was controlled under 1000°C, but the mean temperature was increased with the increasing cell density of the catalyst, to around 700°C and 780°C in test No. 2 and 3, respectively.

Figure 10 shows the NOx emission. NOx emission decreases with increasing pressure. In these tests, owing to the capacity of the test facility, combustor inlet temperature was increased from 330°C to 370°C with increasing pressure, then the fuel/air ratio of preburner was decreased with increasing pressure to control the catalyst inlet gas temperature at 400°C. Changes in fuel distributions with pressure are shown in Fig. 11. Fuel distribution to the preburner is decreased with increasing pressure. From the data of this figure and Fig. 8, it is estimated that NOx emission from the preburner had a large tendency to decrease with increasing pressure in this test. This reveals that the NOx emissions from the preburner mainly affect the decrease of the total NOx emissions with increasing pressure. Though Fig. 11 shows a small decrease of fuel distribution to the premixing nozzle, this effect on total NOx emission is much less than the preburner, and NOx production in the premixed combustion section is estimated to be less than 2 ppm (at 16 percent O_2) over the tested pressure.

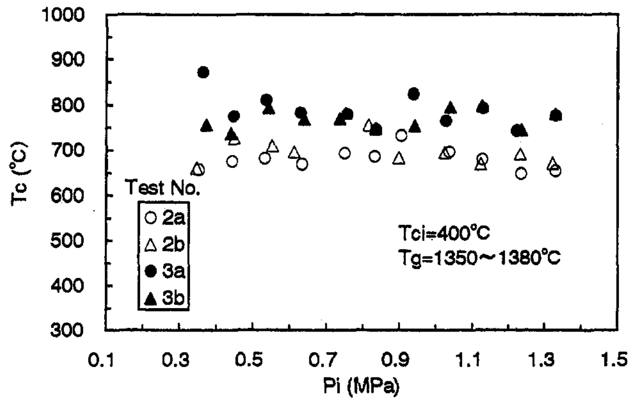

Fig. 9 Catalyst bed temperature

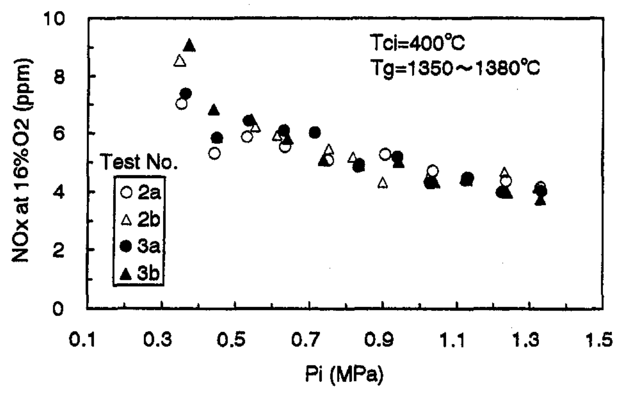

Fig. 10 NOx emission

CO and UHC emission is shown in Fig. 12. UHC emission in test No. 2 is higher than that in No. 3, but CO emission is at a similar level and stable combustion is kept in all the tests. From these results, combustion efficiency is calculated to be over 99.98 percent. Figure 13 shows the pattern factor of the combustor exit gas. It is an extremely low level and is less than 4 percent. Figure 14 shows an example of temperature distribution at the combustor exit. It is supposed that a significantly uniform lean premixed combustion is made in the combustor. On the other hand, combustor pressure loss decreased with increasing pressure. Five percent of the loss was achieved over 0.44 MPa and at the base load condition it was less than 4 percent. The difference of combustor performances between test No. *a* and *b* were negligible and repeatability was confirmed.

Effect of Excess Air Ratio under Full Pressure Condition. At the base load condition, the excess air ratio was changed a little to estimate the emission characteristics and combustion stability. Figure 15 shows NOx emission. The differences of NOx emission between test No. 2 and 3 were small and the effect of the excess air ratio was also small. NOx emission was kept less than 4.5 ppm

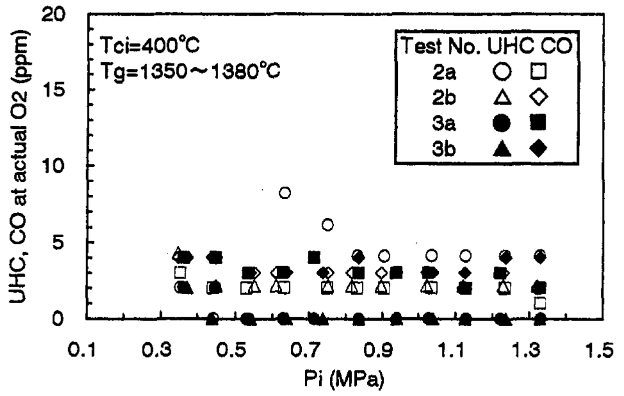

Fig. 12 UHC & CO emission

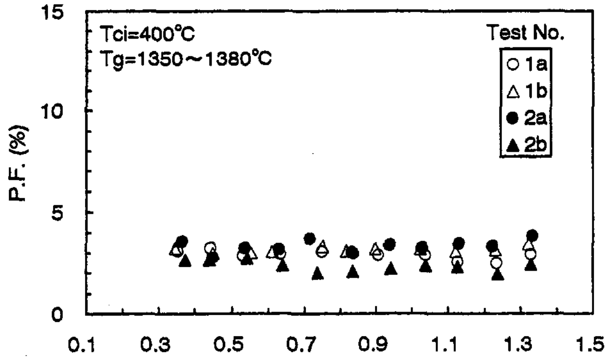

Fig. 13 Pattern factor

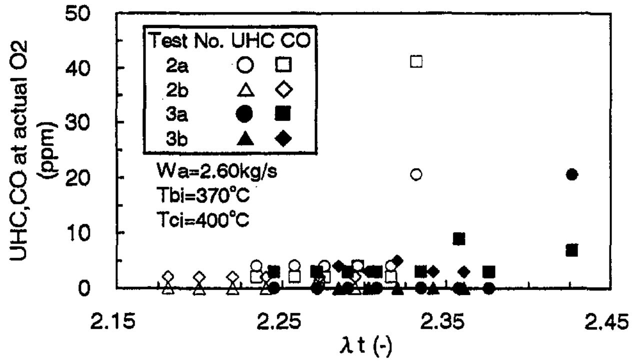

Fig. 16 Relation between λ and UHC, CO emission

(at 16 percent O_2) in the excess air ratio range from 2.18 to 2.43, which are equivalent to 1390°C and 1300°C of adiabatic combustion temperature, respectively. The differences of combustion stability between No. 2 and 3 clearly appeared in CO and UHC emission shown in Fig. 16. A small increase in CO and UHC emission began at 2.33 of the excess air ratio in test No. 2 while this was extended to 2.43 in test No. 3. This test result shows the effect of the higher temperature of catalytic combustion gas in promoting the stability of lean premixed combustion. On the other hand, except for these increase points, CO and UHC emission was less than 9 ppm (at actual O_2) and combustion efficiency was over 99.99 percent. As the stable combustion range was limited, the combustion air control method is thought to be important for this combustor and the increase of the mean temperature of catalytic combustion was effective.

Pattern factor was less than 4 percent and pressure loss was less than 4 percent. The test results are listed in Table 6, and all the targeted performance levels were cleared.

Effect of Oscillation of Catalytic Reaction. An oscillating behavior of the catalyst bed temperature was observed under all tested conditions. The mean period of oscillation was 35 s and the mean amplitude was 60°C. On the other hand, the gas temperature and emission at the combustor exit, both of which were continuously measured, were stable and little oscillating behavior was observed. Though combustor acoustic measurements were not made, the fluctuations of differential pressure (ΔP) through the combustor were measured. The mean period of oscillation was 35 s and the mean amplitude under the base load conditions was 0.8 kPa, which was affected by the oscillation of catalytic reaction, and the level was thought to be allowable. It is thought that this level of an oscillating behavior of the catalytic reaction has only an effect on the post-premixed combustion characteristics under unstable leaner condition.

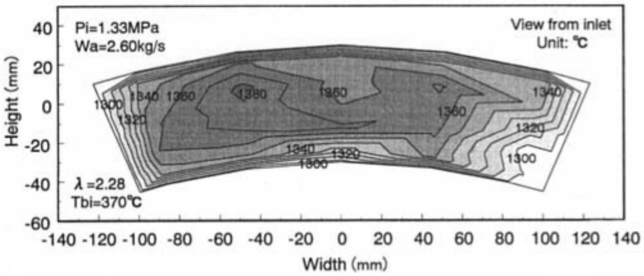

Fig. 14 Temperature distribution at combustor exit

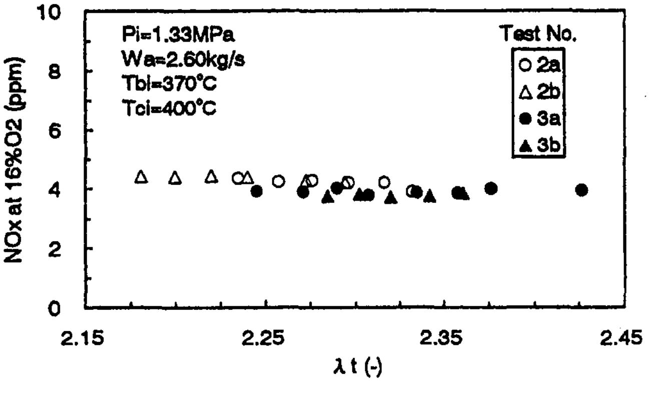

Fig. 15 Relation between λ and NOx emission

Soundness of Combustor and Catalyst. Combustion time over 1300°C in each test was about 4 h and total combustion time over 1300°C was 16 h, and especially, that of the transition piece was about 40 h including a previous ceramic combustor test at 1500°C. The ceramic tile temperature of the ceramic liner rose over 1000°C from point 280 mm from the exit of the burner section and the peak temperature was 1050°C at point 460 mm. On the other hand, the metal wall temperature of the ceramic liner was kept at the same temperature as that of the combustion air. Two stages of the catalyst set of 60 cpi were continuously used in tests No. 1, 2*a*, and 2*b*, the other two stages of 60 cpi were from tests No. 2*a* to 3*b*, and the other two stages of 200 cpi were in tests No. 3*a* and 3*b*. The total reaction times of these catalyst sets over 650°C were 20 h, 20 h, and 9 h, respectively. As shown in Fig. 11, test No. *b* was conducted under the same operating conditions as test No. *a*, and the catalyst bed temperature showed the same level as that of test No. *a* as shown in Fig. 9. This indicates no deactivation of the catalyst. After the tests, visual inspections of the combustor components; the burner section, the ceramic liner, the transition piece and the catalyst were conducted and no damage was detected.

In the previous combustor test using a metal liner and a catalyst set with a total length of 50 mm and a sell pitch of 200 cpi, the following results were obtained (Ozawa et al., 1996):

- NOx emission was 10 ppm (at 16 percent O_2) at a combustor exit gas temperature of 1300°C (Pi = 1.33 MPa)
- a small increase in CO emission began at a combustor exit gas temperature of 1250°C (Pi = 1.33 MPa)
- a catalyst bed temperature of 650°C was needed to maintain stable premixed combustion

Table 6 Test results

Item	Test No.			
	2a	2b	3a	3b
Adiabatic combustion temperature (°C)	1380	1390	1370	1350
NOx emission (16%O_2) (ppm)	4.3	4.4	3.9	3.7
Combustion efficiency (%)	99.99	>99.99	>99.99	>99.99
Total pressure loss (%)	3.6	3.5	4.0	3.8
Pattern factor (%)	2.8	2.7	3.7	2.4

Compared with these results, the following can be derived: by applying a ceramic liner, liner cooling air was reduced to one-third, while the fuel/air ratio in the catalytic combustor segments was a similar level; so the fuel/air ratio of the premixed gas injected additionally to the catalytic combustion gas became leaner. As a result, lower NOx emission was realized. At the same time, stability of premixed combustion was lowered and a higher temperature of catalyst bed was needed to stabilize premixed combustion, which can be realized by increasing the total catalyst length, that is, by decreasing the space velocity (S.V.) of the catalyst.

Conclusion

A catalytic combustor combined with premixed combustion was designed and tested at high pressures. As a result, NOx emission was below 5 ppm (at 16 percent O_2) at an adiabatic combustion temperature of 1390°C. Low NOx combustion was realized due to the assistance of catalytic combustion that stabilized lean premixed combustion and due to the ceramic liner that needed less cooling air. In the future, it will be necessary to estimate the long-term performance of the catalyst and combustor and to establish the control method.

Acknowledgments

Our deepest gratitude goes to S. Kikumoto, T. Yamanaka and J. Hirano of KEPCO and T. Abe, T. Hisamatsu, T. Fujii, and T. Nakayama of CRIEPI, who helped us in promoting this research project, and T. Inui of Kyoto Univ. and H. Fukuzawa, who helped us in the development of the catalyst.

References

Aoyama, K., and Mandai, S., 1984, "Development of a Dry Low NOx Combustor for a 120-MW Gas Turbine," ASME JOURNAL OF ENGINEERING FOR GAS TURBINES AND POWER, Vol. 106, pp. 795–800.

Fujii, T., Ozawa, Y., and Kikumoto, S., Yuasa, Y., and Inoue, H., 1996, "High Pressure Test Results of a Catalytic Combustor for Gas Turbine," ASME Paper 96-GT-382.

Miller, J. A., and Bowman, C. T., 1989, "Mechanism and Modeling of Nitrogen Chemistry in Combustion," *Progress in Energy and Combust. Sci.*, Vol. 15, No. 4, pp. 287–338.

Ozawa, Y., Fujii, T., Sato, M., Kanazawa, T., and Inoue, H., 1996, "Development of a Catalytically Assisted Combustor for a Gas Turbine," presented at the Third International Workshop on Catalytic Combustion, Amsterdam, The Netherlands, 23–25 September 1996; submitted for publication in Catalysis Today.

Ozawa, Y., Fujii, T., Tochihara, Y., Kanazawa, T., and Sagimori, K., 1987, "Test Results of a Catalytic Combustor for a Gas Turbine," Proceedings, Third Japan-EU Joint Workshop on the Frontiers of Catalytic Science & Technology for Energy, Environment and Risks Prevention, Tsukuba, Japan, 25–28 November 1997, pp. 421.

Ozawa, Y., Hirano, J., Sato, M., Saiga, M., and Watanabe, S., 1994, "Test Results of Low NOx Catalytic Combustors of Gas Turbines," ASME JOURNAL OF ENGINEERING FOR GAS TURBINES AND POWER, Vol. 116, pp. 511–516.

Pfefferle, W. C., Carrubba, R. V., et al., 1975, "Cata Thermal Combustion: A New Process for Low-Emissions Fuel Conversion," ASME Paper 75-WA/FU-1.

Yuri, I., Hisamatsu, T., Watanabe, K., and Etori, Y., 1997, "Structural Design and High-pressure Test of a Ceramic Combustor for 1500°C Class Industrial Gas Turbine," ASME JOURNAL OF ENGINEERING FOR GAS TURBINES AND POWER, Vol. 119, pp. 506–511.

D. W. Kendrick

T. J. Anderson

W. A. Sowa

United Technologies Research Center,
Aeromechanical, Chemical, and Fluid Systems,
411 Silver Lane, MS 129-16,
East Hartford, CT 06108

T. S. Snyder

Pratt & Whitney,
400 Main St., MS 163-16,
East Hartford, CT 06108

Acoustic Sensitivities of Lean-Premixed Fuel Injectors in a Single Nozzle Rig

An experimental and numerical investigation into the attenuation of combustion induced pressure oscillations in a single nozzle rig was undertaken at the United Technologies Research Center. Results from these investigations indicated a high combustor exit Mach number, similar to that used in a gas turbine engine, was required to correctly simulate the combustor dynamics and evaluate acoustic characteristics of lean premixed fuel injectors. Comparisons made between aerodynamically stabilized and bluff-body stabilized nozzles and the use of premixed and diffusion pilots showed that small levels of diffusion piloting behind a bluff-body yielded the best acoustic/emission performance. Their success is due to increased flame stabilization (superior anchoring ability), which reduced flame motion and thermal/acoustic coupling. For cases where diffusion piloting was not present, both designs exhibited similar dynamical behavior. Increases in the combustor exit Mach number and reductions in the inlet air temperature were shown to degrade acoustic performance of both nozzle designs. The bluff-body configuration with small levels of diffusion piloting, however, was found to be less sensitive to these changes when compared to its aerodynamic counterpart.

Introduction

The achievement of low NO_x emissions while maintaining acoustic stability over all power levels is essential to the viability and durability of any gas turbine to be used for large-scale industrial applications such as electrical power generation. Continued reductions in governmental emissions regulations and the desire to operate in low emissions mode over the entire engine operating range continue to drive lean-premixed combustion systems toward their lean stability limits.

In an effort to control emissions over the entire operating range, lean-premixed combustion systems are designed to maintain constant flame temperature as the engine changes power levels. Operation over the power range has been described in previous studies (Leonard and Stegmaier, 1993; Strand, 1996; McLeroy et al., 1995; Rocha et al., 1995). In all cases, stability of the lean-premixed combustion system relies upon the ability of the premixing fuel injector to maintain stable combustion while it is subjected to changes in nozzle equivalence ratio, inlet air temperature and inlet air pressure. The sensitivity of the premixer to these changes forms the basis of this study.

This paper examines the ability of two fuel-air mixing swirler designs (an aerodynamic and bluff-body flame stabilization design) to minimizing combustion induced pressure oscillations. These configurations which were based on earlier tangential entry (TE) nozzles (Snyder et al., 1994) were evaluated as part of a larger study of fuel-air mixing swirlers being considered for application in an industrial FT8 gas turbine engine. Parameters that were investigated included the use of a premixed and diffusion flame pilots, aerodynamic versus bluff-body stabilization, equivalence ratio, combustor exit Mach number, and inlet pressure and temperature. Because the designs with appropriate piloting levels had contrasting flame stabilization mechanisms, they exhibited contrasting acoustic signatures. Identification of the optimal fuel-air swirler design for the combustion system was the focus of the present work.

Experimental Set-Up

The introduction of acoustically quiet fuel nozzle designs into the lean combustion system was planned in three parts: (1) single nozzle rig tests to screen designs for acoustic performance while maintaining low emissions operation similar to or better than prior art; (2) sector rig tests to confirm acoustic and emissions performance demonstrated in the single nozzle rig and to map part power operation; and (3) engine tests to develop and optimize combustor performance. This paper describes the acoustic results obtained during the first phase. Designs which showed the best acoustic performance in phase (1) also demonstrated the best performance in phases (2) and (3).

Fuel Nozzle Designs. Figure 1(*a*) details an earlier aerodynamic nozzle design whose center-body was modified for the present series of tests (see Fig. 1(*b*)). A diffusion pilot was added to the tip of the center-body for configuration 1 (upper sketch, Fig. 1(*b*)) to evaluate the acoustic sensitivity to small levels of piloting. The addition of a diffusion pilot will negatively impact NO_x emissions performance. In order to evaluate the tradeoffs between a diffusion pilot and a premixing pilot, a second design modification was made (lower sketch). For this second configuration, 13 percent of the nozzle airflow (or 7 percent total airflow) and fuel were taken from the two inlet scrolls and premixed inside the center-body using a swirler having the same swirl direction as the main flow. The end of the center-body was also recessed to enhance mixing between the scroll and center-body flows while the end cap was extended into the scroll inlets to maintain similar interior velocities and main fuel penetration characteristics of configuration 1.

The diffusion and premixed pilot designs provided contrasting boundary conditions to the central recirculation zone located downstream. The diffusion pilot design relied upon a bluff-body for flame stability while the premixed pilot had an aerodynamically stabilized flame (open end, interior swirler). For these reasons, the diffusion pilot and premixed pilot designs will be referred to as a bluff-body nozzle and aerodynamic nozzle, respectively.

Contributed by the International Gas Turbine Institute (IGTI) of THE AMERICAN SOCIETY OF MECHANICAL ENGINEERS for publication in the ASME JOURNAL OF ENGINEERING FOR GAS TURBINES AND POWER. Paper presented at the International Gas Turbine and Aeroengine Congress and Exhibition, Stockholm, Sweden, June 2–5, 1998; ASME Paper 98-GT-382.

Manuscript received by IGTI March 23, 1998; final revision received by the ASME Headquarters March 23, 1999. Associate Technical Editor: R. Kielb.

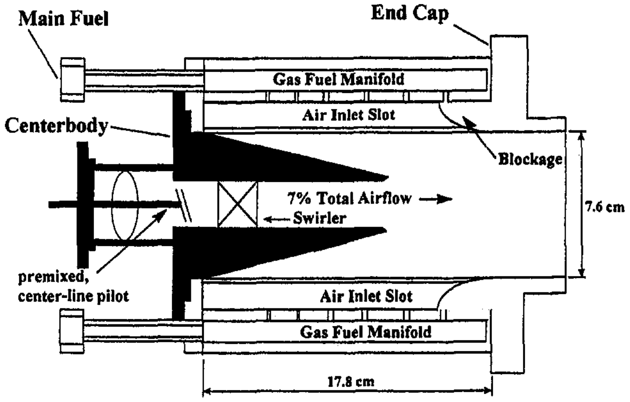

Fig. 1(*a*) Schematic of an earlier aerodynamic nozzle

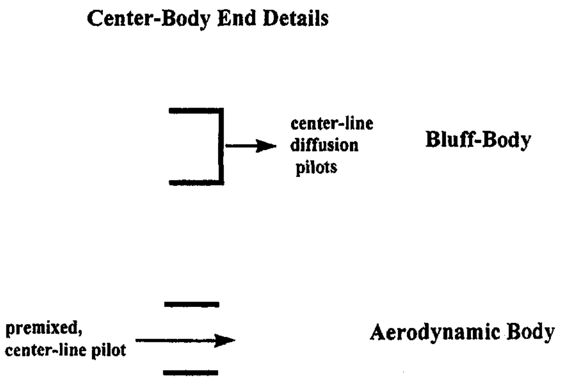

Fig. 1(*b*) Schematic of the center-body end details

Both have an effective nozzle flow area of approximately 26.2 cm^2 and similar center-body contouring.

Single Nozzle Rig. The single nozzle rig (SNR) shown in Fig. 2, allowed independent control of the air and gas fuel flows and inlet temperature and pressure supplied to the premixing fuel nozzle. Natural gas was used for all tests in this study. Airflow was metered using a choked venturi and heated using a non-vitiated, indirect gas fired heater. A perforated plate located upstream of the fuel nozzle, provided a uniform feed of air to the nozzle to simulate the air supply volume of the engine. The fuel nozzle was mounted on a bulkhead which allowed approximately 55 percent of the total airflow to pass through the nozzle and the remainder to act as bypass air. This bypass air, in turn, fed small diameter cooling holes (42 percent) and four dilution holes (58 percent) on the combustor liner. The axi-symmetric liner simulated the engine combustor volume and aspect ratio and incorporated a side wall, diffusion pilot. Dynamic pressure measurements were made inside the plenum (P_3) and combustor (P_4) using infinite tube probes (ITP). The exit Mach number was controlled through changes in the orifice plate diameter. Emission measurements were also made using an array of water-cooled probes inserted into another plate. A T-section downstream of this plate diverted the flow to allow for optical access (PMT and video camera). Combustor pressures were controlled using a back-pressure valve downstream of the T-section. To assess the nozzles over a wide operating range, the conditions detailed in Table 1 were examined. The equivalence ratio ("front end equivalence ratio" or ϕ_{fe} on the plots) is calculated by dividing all the fuel by the nozzle airflow. Therefore, the overall equivalence ratio is simply 0.55 (flow split) times ϕ_{fe}. Piloting levels are percentages of the total fuel flow rate and two ranges are shown depending on the type of piloting used.

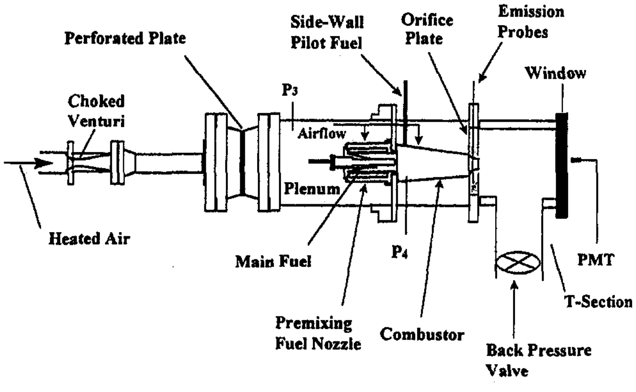

Fig. 2 Schematic of the single nozzle rig

Table 1 Operating conditions

Operating Pressure (P_3)	10.2-19.0 atm.
Inlet Temperature (T_3)	620-706 K
Equivalence Ratio (ϕ_{fe})	0.57-0.77
Side-Wall Pilots (%SW)	5%
Diffusion Center-Line Pilots (%CL)	0-5%
Premixed Center-Line Pilots (%CL)	11-20%

The above range of equivalence ratios defined operating conditions whereby the observed pressure oscillations were controlled purely by the excitation of system acoustic modes. Lean blowout limits for both designs were found below front end equivalence ratios of 0.4.

Theoretical Development: Rayleigh's Criterion

A thorough investigation of pulsed combustion cannot be achieved without addressing the chemical-acoustic interactions that inevitably occur. As shown by others (Keller and Barr, 1996; Raun et al., 1993; Samaniego et al., 1993; Sterling, 1991), it is this interaction between the pressure and the heat-release which typically sustains the instabilities. Quantification of this coupling is achieved through use of the Rayleigh Index which can be represented mathematically as

$$R = \frac{\gamma - 1}{\gamma \bar{p}} \int_V dV \int_t^{t+\tau} p'(\vec{x}, t) q'(\vec{x}, t) dt, \qquad (1)$$

where p' and q' are the fluctuating components of pressure and heat release, respectively, and γ, $\bar{p}$, and V are the ratio of specific heats, mean pressure and volume.

The above index can be broken down into temporally or spatially varying indices by dropping the integration in either time or space, respectively. Therefore, integration over both variables yields a Global Rayleigh Index which characterizes the level of overall acoustic coupling or driving. This index will be shown to be an important tool in characterizing the success of a prospective nozzle.

Results

Exit Boundary Condition Effects. Combustor acoustics are highly sensitive to boundary conditions as they effect the transmission and reflection of incident acoustic waves (Kinsler et al., 1982). To accurately characterize the flowfield entering the turbine blades on a typical gas turbine engine, the combustor exhaust gas must travel at near sonic conditions. The following section compares the two nozzles' performance under a series of tests conducted at two exit Mach numbers: 0.22 and 0.75. The tests were to

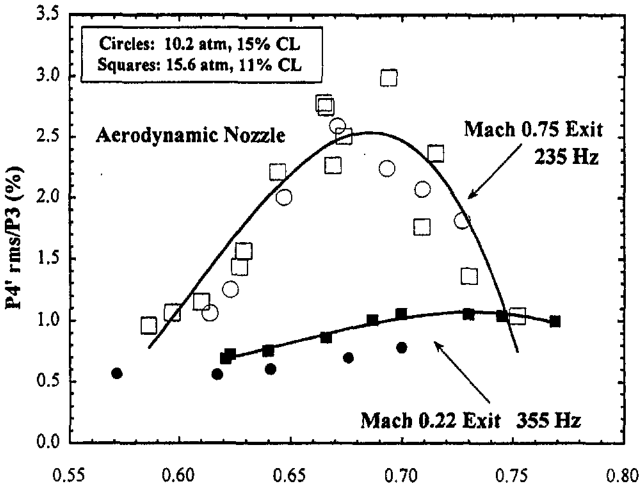

Fig. 3 Acoustic sensitivity of the aerodynamic nozzle to changes in the exit Mach number

assess the sensitivity of both nozzle families to varying exit conditions with one condition approximating a design engine exit flow state.

The high Mach number exit condition was achieved through insertion of a 5.6 cm diameter orifice plate at the exit of the liner while the low Mach number case used a straight, 10.8 cm diameter section. Figures 3 and 4 below depict the Root Mean Square (rms) dynamic combustor pressure levels nondimensionalized by operating pressure, P_3, as a function of front end equivalence ratio, ϕ_{fe}, for both configurations. Data are for a pressure of 10.2 and 15.6 atm. (aerodynamic nozzle) and 15.6 atm. (bluff-body nozzle). Side-wall piloting was held at 5 percent for all runs though center-line piloting varied between design as shown. It should be noted that since the objective was to maintain a constant operating pressure between the high and low Mach number conditions, a 17 percent reduction in air flow rate was incurred in transitioning from Mach 0.22 to 0.75. Numerical work detailed in the next section indicated that this reduction did not significantly affect the acoustic response of the system.

On examination of the figures, both nozzles revealed acoustic augmentation and greater stoichiometric sensitivity as the exit Mach number was increased from 0.22 to 0.75. For the aerodynamic configuration, for instance, nondimensional pressure levels increased from approximately 0.7 percent to 2.5 percent while for the bluff-body configuration, they increased from 0.5 percent to 1.5 percent. The peaked nature of the aerodynamic plot is also evident with the low Mach number configuration but in a more attenuated form (compare the 15.6 atm. data). Acoustic trends, it appears, are accentuated with choking of the exit flow. Perhaps more important, however, is the shift in instability frequency itself.

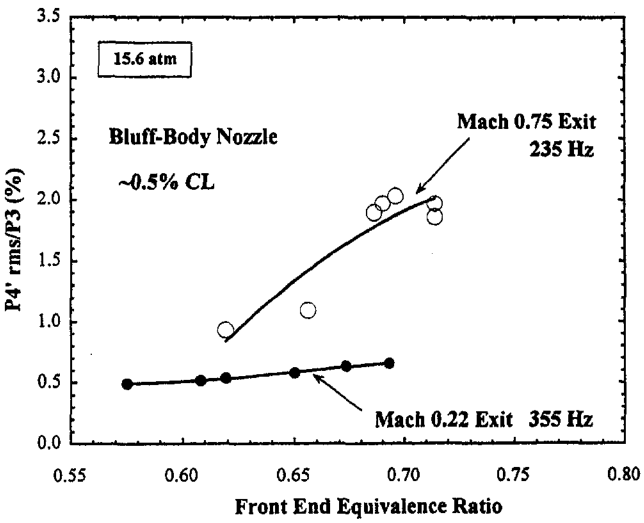

Fig. 4 Acoustic sensitivity of the bluff-body nozzle to changes in the exit Mach number

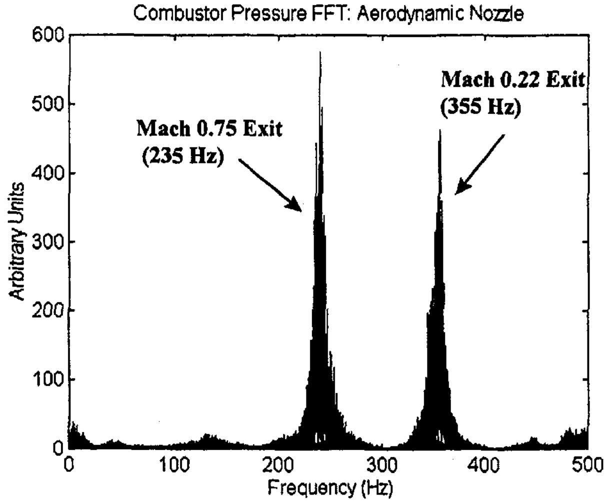

Fig. 5 Fast Fourier Transform of combustor pressure for the aerodynamic nozzle

Figure 5 depicts the corresponding Fast Fourier Transforms (FFTs) of the combustor's dynamic pressure trace at both exit conditions (15.6 atm.). As seen in the figure, a strong 355 Hz mode dominated the combustor's pressure spectrum when operating at the low exit Mach number condition while a 235 Hz mode dominated the high Mach number exit condition. (Sound speed changes through fuel/air ratio adjustments will affect these exact values.) Analysis have shown that the observed mode emanates from a Helmholtz or bulk mode instability and is not associated with longitudinal modes present in the system (Proscia, 1996). These extraneous modes do appear with changes in the local equivalence ratio and geometry but are typically weaker.

To understand this acoustic augmentation and frequency shift, a bulk mode model which captures only bulk or Helmholtz mode instabilities was implemented (Proscia, 1996). The model characterizes the system as a series of interconnected volumes (combustion chamber, diffuser volume, etc.) and necks (nozzle, orifice plate, etc.) and disregards any spatial variation as is typical in bulk mode analyses. The model takes the linearized conservation equations of mass and momentum and forms a state space representation in standard matrix form after assuming periodic solutions of the form $e^{i\omega t}$ as done elsewhere (Zsak, 1993; Bloxsidge et al., 1988):

$$\dot{\vec{X}} = A\vec{X}, \qquad (2)$$

where ω is the oscillation frequency, A is a matrix, and $\vec{X}$ is a column vector containing the fluctuating components of pressures and velocities throughout the system. The natural frequencies and damping ratio of the coupled system are easily determined from the complex eigenvalues of the system matrix A. Detailed models for the nozzle admittance and exit impedance functions were used where the admittance, η, and impedance, z, of the ith section are defined as

$$\eta_i = \rho c \frac{u'_i}{p'}$$

$$z_i = \frac{\rho c}{\eta_i}, \qquad (3)$$

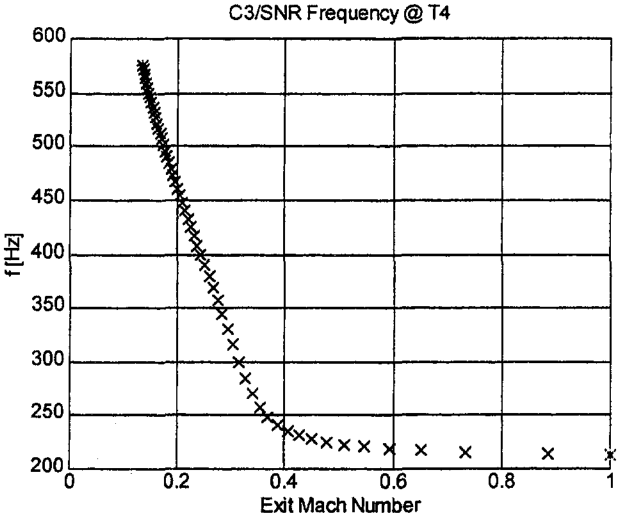

Fig. 6 Calculated bulk mode frequencies versus exit Mach number

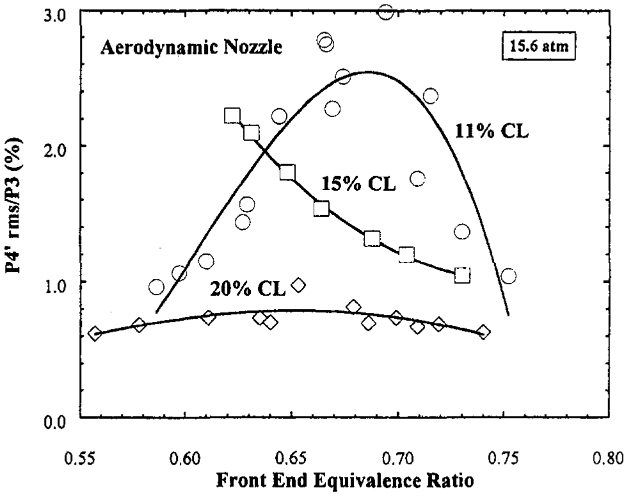

Fig. 8 Acoustic performance of the aerodynamic nozzle for various levels of center-line piloting

where u' and p' are the fluctuating components of velocity and pressure, respectively, and ρ and c are the density and sound speed. Figures 6 and 7 detail the calculated bulk mode frequencies and system damping, respectively, for a range of exit Mach numbers under hot (combustion) flow conditions and a pressure of 15.6 atm.

As shown in Fig. 6, the model accurately predicted the trend in bulk mode frequency in transitioning from Mach 0.75 to 0.22: lowering the exit Mach number caused an increase in the frequency of the acoustic mode. It did not, unfortunately, accurately predict the instability frequency at Mach 0.22: 355 Hz. This apparent discrepancy is most likely due to the model's extreme sensitivity to exit orifice length ("effective neck length") and inaccurate modeling of the liner cooling airflow. What is important, however, is how the system damping which is defined as the negative real part of the system eigenvalues divided by their magnitude responds with this Mach number shift. As detailed in Fig. 7, system damping is increased by approximately 50 percent in transitioning from Mach 0.75 to 0.22 so the observation of overall acoustic attenuation for both designs should seem consistent. (The damping ratio reaches a maximum and then falls since the bulk mode increases rapidly with lower exit Mach numbers.) Accounting for the approximate 17 percent increase in air flow rate for the low Mach configuration, this damping increase drops by only 5 percent to 45 percent. As shown more clearly by the aerodynamic configuration, this damping increase would also tend to reduce any stoichiometric sensitivity as evidence by the general flattening of the low Mach number curves. It should also be noted that with a 17 percent variation in air flow rate and different bulk mode frequencies characterizing the two cases, the relative phasing between the heat-release and acoustic cycles would most likely be different. Using the nozzle's exit annular width (2 cm) and velocity as the reference length and velocity scales, respectively, the change in convective time nondimensionalized by the acoustic period, for instance, would drop from 4.5 percent to 3.5 percent (low to high Mach transition). The combined effects of a more favourable heat release/acoustic interaction facilitated by changes in the convective time scales and acoustic periods and substantially less acoustic damping are undoubtively both contributing to the trends observed in Figs. 3 and 4.

Having established the sensitivity of both nozzles to boundary conditions and realizing the actual engine will operate at an elevated exit Mach number, testing was concentrated using the high Mach number exit.

Acoustic Comparison Between the Bluff-Body and Aerodynamic Nozzles. Figures 8 and 9 compare the combustor's nondimensional rms acoustic levels for a variety of center-line piloting percentages for the aerodynamic and bluff designs, respectively. Results were at a plenum pressure of 15.6 atm., 5 percent side-wall piloting, and high Mach number exit.

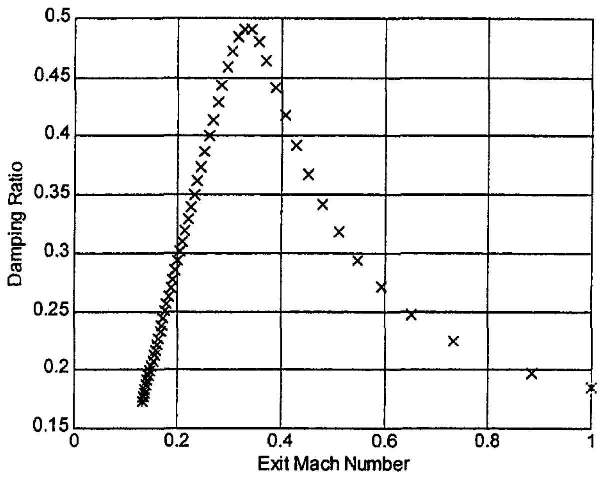

Fig. 7 System damping ratio versus exit Mach number

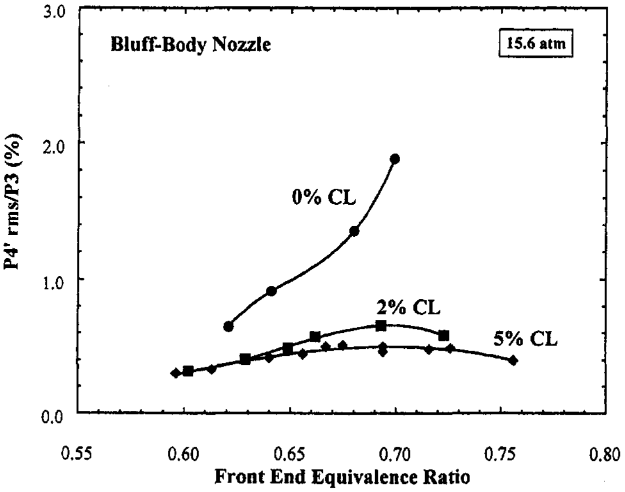

Fig. 9 Acoustic performance of the bluff-body nozzle for various levels of center-line piloting

Table 2 Nozzle to nozzle comparisons

Nozzle	Comparison 1	Comparison 2	Comparison 3
Bluff	0% CL	2% CL	5% CL
Aerodyn.	11% CL	15% CL	20% CL

A quick examination of the figures revealed that both nozzles behaved similarly with changes in center-line piloting (%CL): increasing %CL reduced acoustic/stoichiometric sensitivity and overall fluctuating combustor pressure levels. For the ranges of center-line piloting shown, a factor of 4 reduction was observed for both designs. A direct nozzle to nozzle comparison, however, is difficult due to the contrasting methods of piloting (diffusion versus premixed), which may obscure the separate effects of the levels of center-line piloting and roll of the bluff plate (bluff-body nozzle). This will, in turn, alter the overall level of premixing (fraction of premixed fuel issuing from the nozzle exit plane) and consequently emissions (NO_x and CO). A first order comparison can be made by comparing the nozzles based on identical NO_x-CO performance. This yields the three comparisons as detailed in Table 2.

Re-examining Figs. 8 and 9, all comparisons indicate the superiority of the bluff design. For comparisons 1, 2, and 3, the approximate reductions are, respectively, 0.8, 0.9, and 0.2 percent. A more accurate comparison can be made by simultaneously matching emission performance and level of premixing. Since the aerodynamic nozzle implements a 95 percent premixing level irrespective of %CL (5 percent diffusion side-wall pilot used throughout), the 0 percent CL bluff-body configuration should be compared with the 11 percent CL aerodynamic run (comparison 1). Again the superiority of the bluff design is evident. It is interesting to see how the performance of the aerodynamic design "approaches" that of its bluff counterpart at the expense of excessive piloting levels. The premixing pilot, it seems, is less effective in quelling acoustics since over 11 percent is needed to even approach the acoustic levels of the 0 percent CL bluff-body configuration. The following sections will compare the two designs with piloting levels chosen to delineate their contrasting dynamical behavior.

Inlet Air Temperature Effects. Variations in reactant enthalpy content through inlet air temperature changes alter the resulting adiabatic flame temperature and in turn the ignition delay (Grillo and Slack, 1976). System performance could possibly degrade as now there would be a temporal relocation in the heat pulse (Keller et al., 1989). Furthermore, the effectiveness of the recirculation zone could change which would also effect the stability of the system.

To assess the sensitivity of both nozzles to changes in inlet conditions, tests were conducted at various inlet air temperatures by adjusting the set point on the nonvitiated air heater. Figure 10 below depicts the findings for both the bluff-body (solid symbols) and aerodynamic nozzles (open symbols) at 15.6 atm. and 5 percent side-wall piloting. Center-line piloting was maintained at 5 percent for the bluff design and 15 percent for its aerodynamic counterpart.

For the bluff-body configuration, nondimensional rms pressure levels increased with front end equivalence ratio for a given T_3. More importantly, however, is the steepening in the curves with lowering T_3. A greater stoichiometric sensitivity, reminiscent of the aerodynamic design, was apparently achieved with lower inlet air temperatures. The above exercise was repeated for the aerodynamic design (dashed curves) and resulted in acoustic levels attaining such extreme values (>1.4 atm. peak to peak) that the main combustion zone would not remain lit for any T_3 below 675 K. Acoustic levels have also increased with lowering T_3 but in a more nonlinear form as is typical for this design. Note the dispersion of the data. As found elsewhere (Richards and Janus, 1997), inlet air temperatures are critical in shifting the stability boundaries for both nozzle designs through their effects on the total time delay (sum of the fluid dynamic and chemical time delays). Increasing inlet temperatures will increase reaction rates (lowering chemical time delay) and increase slightly nozzle exit velocities (lowering transport and mixing times). As such, the heat-release/acoustic phasing, critical in defining stability, will change. Apparently, increasing T_3 "de-tunes" this coupling and desensitizes stoichiometric effects.

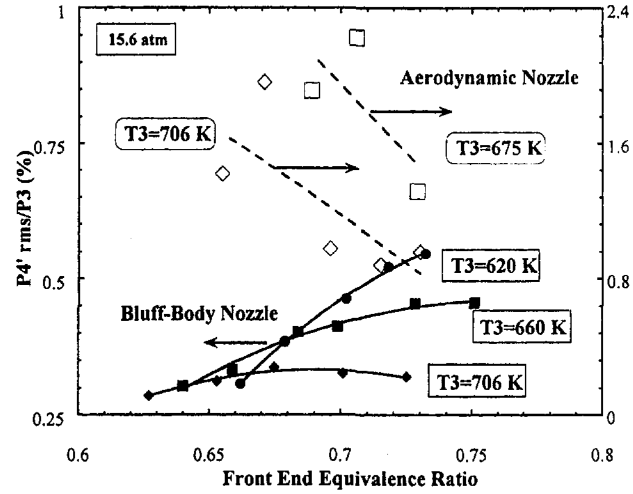

Fig. 10 Acoustic performance of both nozzles to changes in the inlet air temperature, T_3

In an attempt to condense the combined effects of inlet air temperature and equivalence ratio, the data was replotted versus the adiabatic flame temperature nondimensionalized by inlet air temperature. RMS acoustic values were substituted by their corresponding peak to peak values. Figure 11 details the findings for both nozzle families at three pressure levels: 10.2, 15.6, and 19.0 atm. The level of fuel piloting for the aerodynamic nozzle was 11 percent CL and 5 percent SW due to the increased database at these conditions. The corresponding 15 percent CL data were shown to exhibit near identical behavior. Due to previously mentioned stability issues, the aerodynamic configuration did not operate above a T_{ad}/T_3 of 3.1.

These results detail some interesting dissimilarities between the two nozzle families. Firstly, the acoustic superiority of the bluff-body nozzle is again apparent for all pressure levels by the upward displacement of all aerodynamic curves. Furthermore, the bluff-

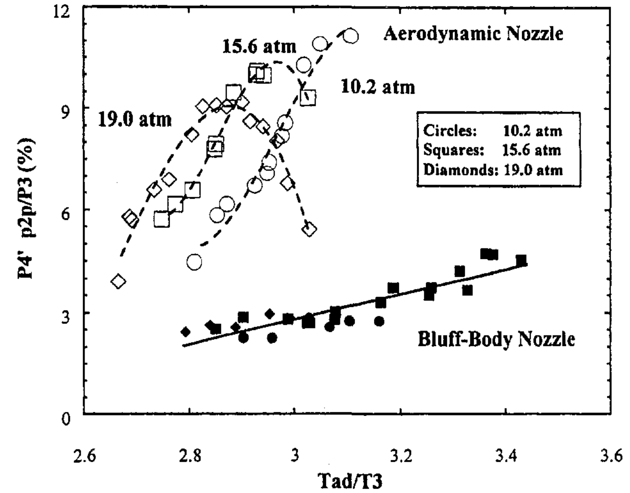

Fig. 11 Nondimensional acoustic scaling versus nondimensional adiabatic flame temperature

body's data collapsed onto a single curve which slopes upward with increasing T_{ad}/T_3; nondimensional peak to peak acoustic levels scale linear with operating pressure, P_3, and T_{ad}/T_3. These characteristics, however, are not shared by its aerodynamic counterpart. Peak to peak dynamic measurements are highly dependent on T_{ad}/T_3 and pressure sensitive. As shown, nondimensional peak to peak values are typically reduced with increasing plenum pressure. Instead of scaling linear with nondimensional adiabatic flame temperature as demonstrated by the bluff design, acoustic levels reveal an increasingly nonlinear behavior with increasing P_3. Acoustic sensitivity to pressure and equivalence ratio is apparent. Implementation of small diffusion piloting levels and a bluff plate, yielding superior recirculation zone strength, appears effective in quelling the effects of such flowfield changes. Remembering that the main combustion zone of the aerodynamic design is believed to be more susceptible to flowfield motion due to the absence of the bluff plate, it seems consistent that it should exhibit such nonuniformity.

Chemiluminescence Measurements. To better interpreted these two contrasting thermal-acoustic mechanisms, CCD imaging was done with the help of a fiber optic bundle inserted into the igniter port. A narrow band pass filter (10 nm FWHM) placed in front of the camera and centered at 430 nm selected radiation from excited CH radicals which are known to occupy the combustion zone (Samaniego et al., 1995; Dibble et al., 1986). Images were taken at 8 locations in the pressure cycle to yield an accurate representation of the periodic combustion process.

A complete cycle of images at a pressure of 15.6 atm. and front end equivalence ratio of 0.73 is shown in Fig. 12 for the bluff-body configuration. Both side-wall and center-line piloting were turned off to more accurately delineate the main combustion zone. Contour levels represent 20, 40, 60, 80, and 95 percent maximum intensity values and flow is from left to right. Examination of the images revealed that the upstream end of the reaction zone remained relatively fixed in space while the downstream end responded to the acoustic velocity fluctuations at the nozzle exit plane. The unsteady combustion process appears to be controlled by a periodically shed toroidal vortex structure. The subsequent combustion of these structures provides the necessary feedback mechanism to sustain the instability.

Figures 13(*a*) and 13(*b*) show the average combustion zone location at a pressure of 15.6 atm. for the bluff-body and aerodynamic configurations, respectively. Piloting levels were kept at standard levels for each design: 5 percent SW and 15 percent CL for the aerodynamic design and 5 percent SW and 5 percent CL for the bluff design. Each figure represents an average of over 896 images or 112 pressure cycles. Apparent is the axial lengthening of the combustion zone for the aerodynamic nozzle compared to its bluff-body counterpart. A closer examination of the instantaneous images revealed that this lengthening did not result from a spatial broadening in the reaction zone but rather from the axial movement of the combustion zone itself during the cycle. As anticipated, the absence of the bluff plate has rendered the flame highly susceptible to the influences of the external flowfield. It is liberated from the confines of a fixed recirculation zone and oscillates under the prevailing aerodynamic forces with an associated increase in combustion intensity. This can be contrasted to the bluff-body's image which depicts a more compact reaction zone; axial motion is reduced. Although not shown, excursions in center-line piloting for the bluff-body configuration revealed the influences of flame location on acoustic stability: by reducing center-line piloting from 5 percent to 0 percent, the main combustion zone detached from the bluff plate. Flame motion was seen to increase with a corresponding degradation in acoustic performance (consult 0 percent CL curve of Fig. 9). Nondimensional pressure fluctuations also became more sensitive to stoichiometric changes (Fig. 9) with this reduction in center-line piloting; the bluff-body nozzle now exhibits characteristics of its aerodynamic counterpart.

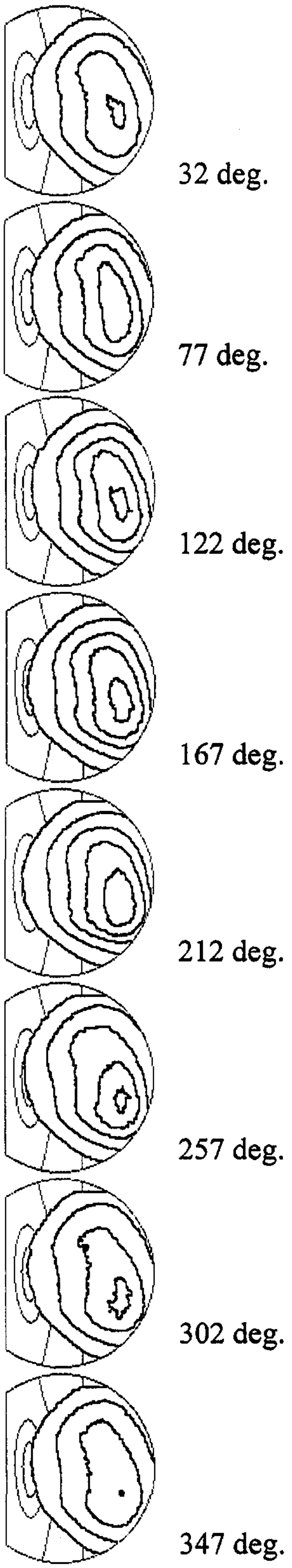

Fig. 12 Complete cycle of images for the bluff-body nozzle (0% SW, 0% CL, 15.6 atm.)

The acoustic stability and stoichiometric sensitivity of both designs, it appears, are highly coupled to the effectiveness of the recirculation zone, itself functions of lift off distance (bluff configuration only) and levels of center-line piloting. As the level of center-line piloting is increased, the effectiveness of the recirculation zone is most likely augmented.

Global Rayleigh Indices were calculated for both nozzles to

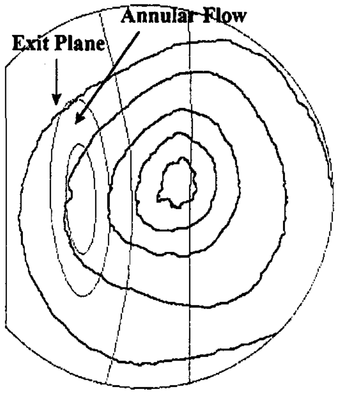

Fig. 13(*a*) Average combustion location for the bluff-body nozzle (5% SW, 5% CL, 15.6 atm.)

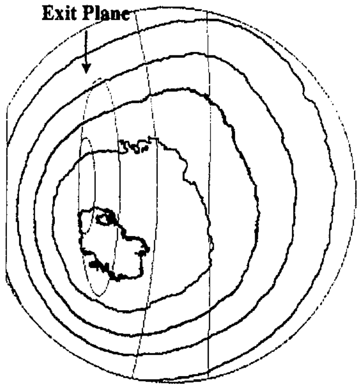

Fig. 13(*b*) Average combustion location for the aerodynamic nozzle (5% SW, 15% CL, 15.6 atm.)

quantify their acoustic/heat-release coupling. Two pressure levels were examined: 10.2 and 15.6 atm. A photomultiplier tube located at the end of the T-Section of the rig was used to determine the global heat release rate through the assumed linearity between chemiluminescence and burner output power for a fixed equivalence ratio (Hurle et al., 1968; Diederichsen and Gould, 1965). A filter to isolate excited CH radicals was placed in front of the PMT. The results are presented in Fig. 14. Fuel piloting for both nozzles was kept at standard values: 5 percent SW/5 percent CL for the bluff nozzle and 5 percent SW/15 percent CL for the aerodynamic configuration.

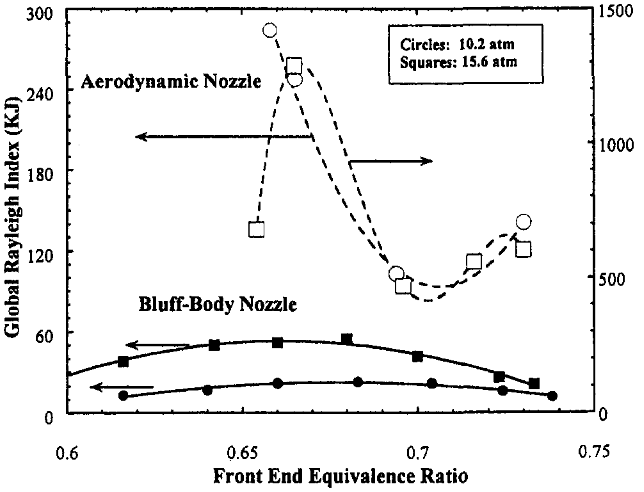

Fig. 14 Comparison of the Global Rayleigh Indices for both nozzle families

As anticipated, the bluff-body nozzle is characterized by much lower Rayleigh Indices: for the low pressure case (10.2 atm.), a factor of six reduction over the aerodynamic nozzle was seen. Even more impressive is the variation at 15.6 atm. Here one sees almost a one and a half order of magnitude reduction. The bluff design's insensitivity to stoichiometry is also evident and is reminiscent of earlier acoustic plots with similar piloting levels (Fig. 9). As expected, the different stabilization mechanisms have yielded sizeable disparities in acoustic driving.

Conclusions

Examination of the acoustics for two contrasting fuel/air swirler designs has demonstrated the superiority of the bluff-body configuration with small levels of center-line piloting. Improved acoustic stability was achieved through increased use of the recirculation zone which anchored the main combustion region and reduced the influences of the external flowfield. Excursions in center-line piloting have demonstrated how flame lift-off contributes to inferior acoustic performance by shifting the reaction zone further downstream where it can more easily be disturbed by the surrounding flowfield. The inferior performance of the aerodynamic design (<15 percent CL) or equivalently bluff configuration (0 percent CL) with low piloting levels can be now interpreted. By liberating the combustion zone from the confines of the recirculation zone, a more favourable acoustic/heat-release coupling is invoked, thereby reinforcing acoustic driving (increased Rayleigh Indices) and finally augmenting oscillatory pressure levels. Changes in combustor exit Mach number and inlet air temperatures had similar effects on both nozzle designs: increasing the exit Mach number and lowering the inlet air temperature both degraded acoustic performance.

Acknowledgments

The authors wish to thank the services of many individuals who aided in the completion of this paper including Miss Luu Vu, Mr. Paul Hamel, Mr. Jason Wegge, and Mr. William Proscia.

References

Bloxsidge, G. J., Dowling, A. P., and Langhorne, P. J., 1988, "Reheat Buzz: An Acoustically Coupled Combustion Instability: Part 2—Theory," *J. Fluid Mech.*, Vol. 193, pp. 445–473.

Dibble, R. W., Long, M. B., and Masri, A., 1986, "Two-Dimensional Imaging of C_2 in Turbulent Nonpremixed Jet Flames," Dynamics of Reactive Systems: Part II—Modeling and Heterogenous Combustion, *Progress in Aeronautics and Astronautics,* AIAA, Vol. 105, pp. 99–109.

Diederichsen, J., and Gould, R., 1965, "Combustion Instability: Radiation from Premixed Flames of Variable Burning Velocity," *Combustion and Flame,* Vol. 9, pp. 25–31.

Grillo, A., and Slack, M., 1976, "Shock Tube Study of Ignition Delay Times in Methane-Oxygen-Nitrogen-Argon Mixtures," *Combustion and Flame,* Vol. 27, pp. 377–381.

Hurle, I., Price, R., Sugden, T., and Thomas, A., 1968, "Sound From Open Turbulent Premixed Flames," *Proc. Roy. Soc.,* Vol. 303, pp. 409–427.

Keller, J. O., and Barr, P. K., 1996, "Premixed Combustion in a Periodic Flow Field," *Unsteady Combustion,* F. Culick, M. N. Heitor, and J. H. Whitelaw, eds., Kluwer Academic, Dordrecht.

Keller, J., Barr, P., Bramlette, T., Evans, L., and Marchant, R., 1989, "Pulse Combustion: Demonstration of the Characteristic Mixing Time in a Commercial Burner," *Combustion Science and Technology,* Vol. 66, pp. 127–137.

Kinsler, L. E., Frey, A. R., Coppens, A. B., and Sanders, J. V., 1982, *Fundamental Acoustics,* John Wiley & Sons, New York.

Leonard, G., and Stegmaier, J., 1994, "Development of an Aeroderivative Gas Turbine Dry Low Emissions Combustion System," ASME JOURNAL OF ENGINEERING FOR GAS TURBINES AND POWER, Vol. 116, pp. 542–546.

McLeroy, J., Smith, D., and Razdan, M., 1995, "Development and Engine Testing of a Dry Low Emissions Combustor for Allison 501-K Industrial Gas Turbine Engines," ASME Paper 95-GT-335.

Proscia, W., 1996, interdepartmental report on bulk mode instabilities, United Technologies Research Center, E. Hartford, CT.

Raun, R. L., Beckstead, M. W., Finlinson, J. C., and Brooks, K. P., 1993, "A Review of Rijke Burners and Related Devices," *Prog. Energy Combust. Sci.,* Vol. 19, pp. 313–364.

Richards, G. A., and Janus, M. C., 1997, "Characterizations of Oscillations During Premix Gas Turbine Combustion," ASME Paper 97-GT-244.

Rocha, G., Saadatmand, M., and Bolander, G., 1995, "Development of the Taurus 70 Industrial Gas Turbine," ASME Paper 95-GT-411.

Samaniego, J. M., Egolfopoulos, F. N., and Bowman, C. T., 1995, "CO2* Chemiluminescence in Premixed Flames," *Combustion Science and Technology,* Vol. 109, pp. 183–203.

Samaniego, J. M., Yip, B., Poinsot, T., and Candel, S., 1993, "Low-Frequency Combustion Instability Mechanism in a Side-Dump Combustor," *Combustion and Flame,* Vol. 94, pp. 163–180.

Snyder, T., Rosfjord, T., McVey, J., Hu, A., and Schlein, B., 1994, "Emission and Performance of a Lean-Premixed Gas Fuel Injection System for Aeroderivative Gas Turbine Engines," ASME Paper 94-GT-234.

Sterling, J., 1991, "Characterization and Modeling of Aperiodic Pressure Oscillations in Combustion Chambers," AIAA 91-2082.

Strand, T., 1996, "Dry Low NOx Combustion Systems Development and Operating Experience," ASME Paper 96-GT-274.

Zsak, T. W., 1993, "An Investigation of the Reacting Vortex Structures Associated with Pulse Combustion," Ph.D. thesis, California Institute of Technology, Pasadena, CA.

Active Control of Combustion for Optimal Performance

M. D. Jackson

A. K. Agrawal
Assoc. Mem. ASME

Gas Turbine Systems Laboratory,
School of Aerospace and
Mechanical Engineering,
University of Oklahoma,
Norman, OK 73019

Combustion-zone stoichiometry and fuel-air premixing were actively controlled to optimize the combustor performance over a range of operating conditions. The objective was to maximize the combustion temperature, while maintaining NO_x within a specified limit. The combustion system consisted of a premixer located coaxially near the inlet of a water-cooled shroud. The equivalence ratio was controlled by a variable-speed suction fan located downstream. The split between the premixing air and diffusion air was governed by the distance between the premixer and shroud. The combustor performance was characterized by a cost function evaluated from time-averaged measurements of NO_x and oxygen concentrations in products. The cost function was minimized by the downhill simplex algorithm employing closed-loop feedback. Experiments were conducted at different fuel flow rates to demonstrate that the controller optimized the performance without prior knowledge of the combustor behavior.

Introduction

With increasing concerns for air quality improvement, the combustion systems are undergoing major design changes to reduce the harmful by-products. In particular, emphasis has been placed on reducing emissions of nitrogen oxides (NO_x) coincident with high combustion efficiency to decrease carbon monoxide (CO), unburnt hydrocarbons (UHC), and soot etc. Techniques to reduce NO_x formed by the thermal mechanism usually involve lowering the combustion temperature, for example, by lean-premixed combustion. Although low-emission combustion systems are designed to operate efficiently at specified conditions, a particular challenge lies in achieving optimal performance at off-design operations. The operating conditions differ from the design point because of the part-load operation or changes in the inlet conditions due to ambient, fuel composition etc. Furthermore, a combustor design will not be optimal as new emission standards are introduced. Active control provides the means to adapt the combustor design to changes in the operating conditions.

The most common application of active techniques in combustion has been the control of pressure oscillations by continuously perturbing certain parameters in response to filtered outputs from sensors placed in the combustor (McManus et al., 1993; Wilson et al., 1995; Kemal and Bowman, 1996; Neumeier and Zinn, 1996). An application to improve the gas turbine combustor performance by actively controlling the fuel atomizing airflow rate was demonstrated by Brouwer et al. (1990). Although a single input was controlled, the combustor performance in practice is affected by several parameters requiring trade-off to achieve an optimal design.

Padmanabhan et al. (1995) implemented an active optimal control strategy to simultaneously control the volumetric heat release and pressure fluctuations in a laboratory-scale combustor. Measurements of pressure oscillations and heat release were used to quantify the performance in terms of a cost function, which was minimized by seeking the optimal combination of input parameters; periodic forcing of the boundary layer at the inlet, and crossflow jets upstream of the inlet. Recently, Davis and Samuelsen (1996) evaluated a similar approach to optimize performance of a model gas turbine combustor over a range of load conditions (or duty cycle) by articulating the geometry. The split between the dome airflow and primary jet airflow was controlled using variable area flow restrictors. The cost was evaluated from a weighted sum of the measured combustion efficiency and NO_x emissions.

In this paper, we introduce active control to optimize the combustor performance at different operating conditions by articulating the fuel-air premixing and combustion-zone stoichiometry. Recent combustor designs have involved manipulation of these parameters to achieve low emissions (Maughan et al., 1997; Puri et al., 1997; Yamada et al., 1997). Our combustion system is a burner used in residential furnaces. However, it represents some of the essential features of lean-premixed combustors used in advanced gas turbines. We employ the concept of control presented by Padmanabhan et al. (1995) although its implementation on the combustor, sensors, and actuators are different. In the following sections, we provide the experimental details, show results to demonstrate the controller, and summarize our findings.

Experimental Setup

The experimental setup consisted of the combustion system, instrumentation, and control system as discussed below.

Combustion System. The combustor chosen for this study is a burner used in residential furnaces (Kolluri et al., 1996). A schematic of the combustion system is shown in Fig. 1. The ambient air is entrained by the fuel ejected from a nozzle and subsequently, a fuel-air mixture is formed in the converging-diverging tube (or the premixer). The entrained air is denoted as the premixing air or primary air. The fuel-air mixture emerges from 12 equally spaced holes at the premixer exit, where the flame is stabilized. The premixer is located coaxially near the inlet of a tube or the combustor shroud. The ambient air is entrained from the space between the premixer and combustor shroud. This air is denoted as the diffusion air or secondary air. The overall airflow rate and hence, the equivalence ratio is controlled by a variable speed suction fan located downstream of the combustor shroud. At a given fan speed, the split between the premixing air and diffusion air is determined by the distance (x) between the premixer and combustor shroud. The fuel nozzle and premixer were mounted rigidly on a traversing table with a stepper motor to vary this distance. In residential furnaces, the conditioning air is forced through the combustor shroud to extract thermal energy from the hot gases. In experiments, the ordinary tap water was circulated in a jacket around the combustor shroud to remove the thermal energy.

Contributed by the International Gas Turbine Institute (IGTI) of The American Society of Mechanical Engineers for publication in the ASME Journal of Engineering for Gas Turbines and Power. Paper presented at the International Gas Turbine and Aeroengine Congress and Exhibition, Stockholm, Sweden, June 2–5, 1998; ASME Paper 98-GT-576.

Manuscript received by IGTI March 31, 1998; final revision received by the ASME Headquarters March 23, 1999. Associate Technical Editor: R. Kielb.

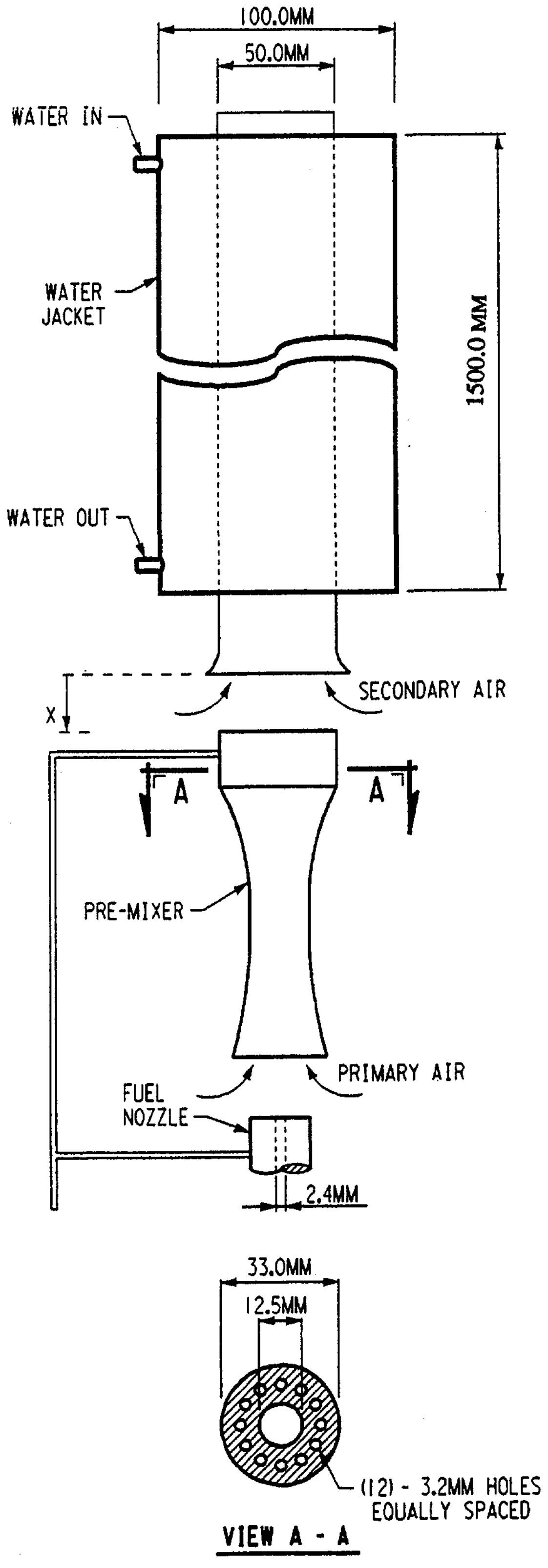

Fig. 1 A schematic of the combustion system

Propane gas supplied from a pressurized tank was used as the fuel. The fuel flow rate was regulated by a needle valve, and measured by a calibrated rotameter. The fuel ejected from a 2.4 mm ID circular nozzle at a velocity of 5.2 to 7.2 m/s, and a Reynolds number of 2800 to 3900. The power rating of the burner varied between 2.0 and 2.8 kW. The fuel and air were at typical ambient conditions of 25 C and 1 atm pressure. The distance between the fuel nozzle and premixer was 12 mm. The ID at the premixer inlet and exit was, respectively, 30 mm and 33 mm. The distance x varied from zero to 25 mm, and the maximum fan speed was 1600 rpm. The combustion process was fuel-lean at all operating points, with the overall equivalence ratio varying between 0.13 and 0.76. The split between the premixing air and diffusion air was not measured in this study. The flame was unstable at fan speeds close to 1600 rpm because the mixture exiting the premixer was highly fuel-lean. The flame blew-off at high fan speeds if the premixer was close to the combustor shroud (i.e., $x = 0$). The water flow rate was kept constant at 0.22 kg/s. The water flow rate was kept constant at 0.22 kg/s. The water temperature increased by 2 to 3 C depending upon the heat removed, which varied approximately from 60 to 80 percent of the energy released. Note that even though the combustion system used in this study is functionally different from gas turbine combustors, the concept to actively control the fuel-air premixing and overall equivalence ratio is applicable to lean-premixed combustors used in gas turbines.

Instrumentation. The combustor performance was monitored by a sampling probe and a thermocouple. The time-averaged measurements were taken at approximately 1.5 m downstream of the flame, allowing for one spatial data point to represent the average mixture value. The gas sample was drawn through a 6.4 mm diameter stainless steel probe with a 3.6 m long hose to cool the sample by ambient air before it reached a series of water traps and filters. The concentrations of O_2, CO, and NO_x (as NO) were measured by a Nova Analytical Systems Model 362. The full-scale of these electrochemical fuel-cell type sensors was, respectively, 25 percent, 2000 and 250 ppm. The sensors were accurate to ±0.1 percent, ±20 ppm and ±2 ppm. The CO emissions were monitored during experiments although they were inconsistent in the present setup. The product gas temperature was measured by a type-K thermocouple. Analog signals from the analyzer and thermocouple were digitized using a PC based data acquisition board by Strawberry Tree. Previous experiments (Padmanabhan et al., 1995; Davis and Samuelsen, 1996) have shown that repeatable measurements are necessary for controller to function properly. Therefore, we conducted several tests to determine the time required for such measurements. Based on these tests, the time-averaged value was obtained from data taken at 1 Hz for 1 min. Measurements at a new operating point were initiated after a waiting period of 1 min to reach steady state.

Control System. The control system performed three sequential tasks. First, it evaluated a cost function using outputs from performance sensors. Next, it executed a cost minimization algorithm to determine the premixer location and suction fan speed. Finally, the controller generated signals for actuators, which affected the primary and secondary airflow rates. A schematic of the control system is depicted in Fig. 2.

The cost function may take various forms depending upon the desired outcome. The objective of the present combustion system is to maximize heat transfer to the coolant, which normally coincides with a high combustion temperature. The high temperature however increases the NO_x emissions, which must be limited. Accordingly, the combustor must operate fuel-lean (to ensure high combustion efficiency) and at the highest possible combustion temperature (i.e. with the least amount of the excess air) while satisfying the NO_x emission standard. Note that the oxygen concentration in products indicates the combustion temperature and overall equivalence ratio. Assuming complete combustion, the equivalence ratio (ER) is found from the equation

$$\mathrm{ER} = 5(4.76X_{O_2} - 1)/(2X_{O_2} - 5), \qquad (1)$$

where X_{O_2} is the oxygen mole fraction in products. Figure 3 plots the equivalence ratio and combustion temperature versus the percentage volume of oxygen ($100X_{O_2}$) in products. The combustion temperature is the adiabatic flame temperature assuming complete combustion.

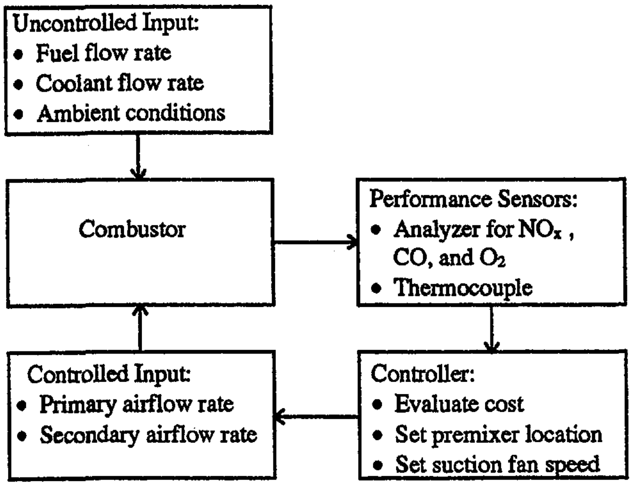

Fig. 2 A schematic of the control process

The contradictory requirements discussed above were considered in the design of the cost function evaluated as

$$J = J_{O_2} + J_{NO_x}, \tag{2}$$

where J_{O_2} is the percentage volume of oxygen in products normalized by its range of 5.5 to 18.5 percent. J_{NO_x} is the NO_x penalty given as

$$J_{NO_x} = 0.0 \quad \text{if } NO_x \leq 10 \text{ ppm}$$

$$= 1.0 \quad \text{if } NO_x > 10 \text{ ppm}. \tag{3}$$

Note that the combustor performance is affected by emissions of CO, UHC, and soot etc., which were not accounted for explicitly in the cost function. The step function in Eq. (3) imposed a high cost if the NO_x concentration exceeded 10 ppm. This is consistent with emission standards, which usually specify a limiting value. In Eq. (2), the cost function for oxygen varies linearly in the interval 0 to 1. Minimizing J in Eq. (2) optimizes the combustor performance. The present design of the cost function avoids the unstable combustion region (i.e., highly lean conditions), coinciding with the poor combustor performance (i.e., high volume of oxygen in products).

The cost function was minimized using the downhill simplex algorithm developed by Nelder and Mead (1965), and employed by Padmanabhan et al. (1995) for combustion control. Figure 4 shows a flow chart of the algorithm as implemented in this study. In a two-dimensional system with two control parameters, the algorithm begins by evaluating cost at three guess coordinate locations, which form a triangle or simplex. The algorithm searches through the domain to shrink the size of the simplex in successive iterations. At each iteration, the high cost vertex of the simplex is moved to a new location by reflecting, expanding, or contracting it with respect to the remaining vertices. The algorithm converges when the difference between the high and low costs of the simplex reduces to a specified tolerance.

The control parameters were the premixer distance (X) and suction fan speed (S) normalized by the maximum values of 25 mm and 1600 rpm, respectively. The physical constraints dictated that X and S vary between 0.0 and 1.0. The premixer will be damaged if it entered the combustor shroud, and the suction fan must not exceed the maximum rated speed. These constraints were imposed in the simplex algorithm by relocating at the boundary a vertex moving outside the boundary. However, this prompted the algorithm to get "stuck" when all 3 vertices were located at a boundary because the simplex reduced to a line. The problem was alleviated by adding a large penalty (1.0) to the cost function when the simplex attempted to move outside the physical boundaries. With this modification, the algorithm performed properly because the search beyond boundaries was costly and hence, it was rejected.

Each trial of the control algorithm produced new X and S values. The controller generated digital signals to drive the stepper motor to traverse the premixer to the new location X. An analog voltage signal was generated to change the fan speed to the desired value S. The control algorithm was coded in C (Press et al., 1992) and the control outputs were generated using PC based hardware from Strawberry Tree.

Results and Discussion

Experiments to demonstrate the controller were conducted at different fuel flow rates. A summary of the test conditions is shown in Table 1. For all test cases, the initial simplex was an equilateral triangle with vertex coordinates (X, S) located at (0.00, 0.00), (0.50, 0.00), and (0.00, 0.50). For each test case, we present the following results during the optimization: (1) the size and location of the simplex, (2) costs at the three vertices of the simplex, and (3) the sensor outputs at the high cost vertex of the simplex.

Figure 5(*a*) shows how the size and location of the simplex varied during optimization for case 1. Each iteration narrowed the search space, which shifted towards a higher fan speed and smaller premixer distance. The algorithm converged after 12 iteration when the specified tolerance of 0.03 was satisfied at (0.06, 0.41), (0.05, 0.43), and (0.05, 0.43). Figure 5(*b*) shows the high, mid, and low costs at vertices of the simplex during iterations. The high and mid costs increased initially and decreased subsequently, as the simplex reached the optimal location with cost values of 0.67, 0.70, and 0.70. Cost higher than 1.0 indicates NO_x greater than 10 ppm. Evidently, the low cost did not change noticeably because one of the initial vertices (0.00, 0.50) was near the optimal location. Figure 5(*c*) shows the NO_x concentration, percentage volume of oxygen, and product temperature at the high cost point during iterations. Results at this point are most revealing because the control algorithm optimizes by relocating the high cost point. Initially, the NO_x decreased from 26 ppm to 6 ppm as the volume percentage of oxygen increased from 6.7 to 15.4. Subsequently, the NO_x increased gradually to the 10 ppm limit as the percentage volume of oxygen decreased marginally to 14.5 percent. The product temperature had a trend opposite to that of the percentage volume of oxygen. The optimal point with minimum cost corresponded to 10 ppm NO_x, 14.2 percent volume of oxygen, and product temperature of 340 C. The optimal equivalence ratio and combustion temperature evaluated from Fig. 3 were 0.34 and 910 C, respectively. These results demonstrate that the controller maximized the combustion temperature while limiting NO_x to within 10 ppm. The CO emissions ranged from 35 to 540 ppm, with a value of 40 ppm in the optimal regime.

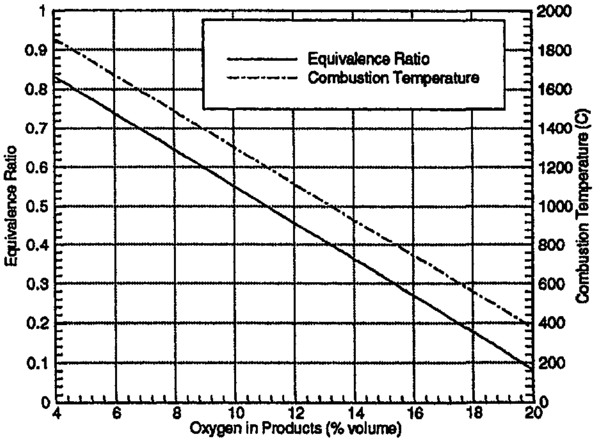

Fig. 3 Equivalence ratio and combustion temperature versus oxygen in products

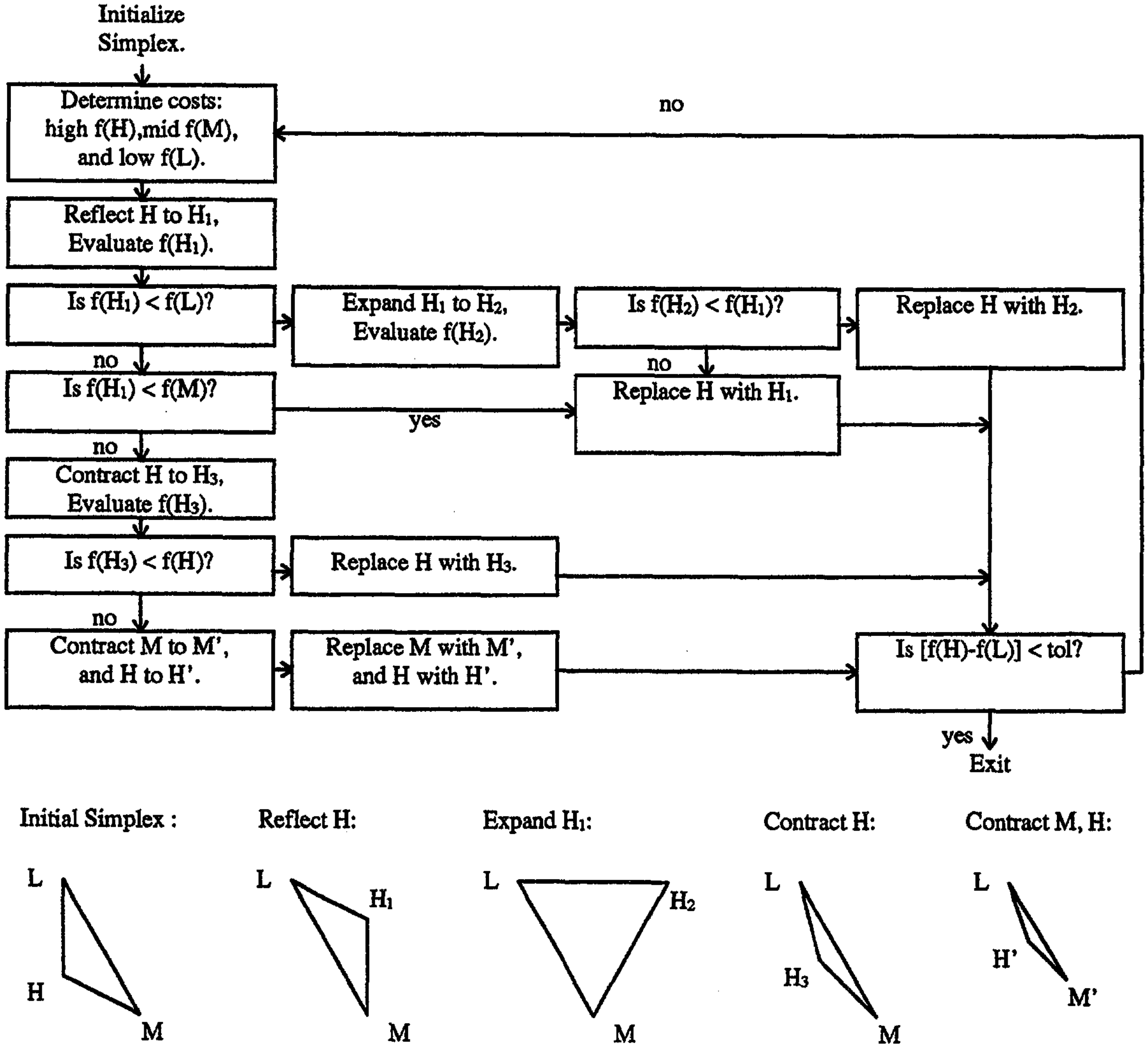

Fig. 4 Flow chart of the downhill simplex algorithm

The test results at a lower fuel flow rate (case 2) are shown in Figs. 6(*a*)–(*c*). The movement of the simplex during the optimization is tracked in Fig. 6(*a*), which reveals that the algorithm searched regions outside the initial simplex but it reverted back. The algorithm converged after 8 iterations when the simplex was located at (0.22, 0.22), (0.17, 0.23), and (0.25, 0.25). A lower fan speed, and, hence, a lower airflow rate, and larger premixer distance were required to achieve the optimal performance at a lower fuel flow rate. A larger size of the final simplex indicates that the cost function in the optimal region was less sensitive to the control parameters. Figure 6(*b*) shows the high, mid and low costs of the simplex during iterations. The cost decreased at all points to final low, mid and high values of, respectively, 0.55, 0.57, and 0.58. The NO_x concentration in Fig. 6(*c*) decreased from a high of 15 ppm to a low of 1 ppm after 3 iterations. Subsequently, the algorithm responded by increasing NO_x to the 10 ppm limit as the percentage volume of oxygen decreased. In agreement with case 1, the product temperature had a trend opposite to that of the percentage volume of oxygen. The optimal point with the lowest cost resulted in 10 ppm NO_x, 13.0 percent oxygen by volume, and product temperature of 260 C. The optimal equivalence ratio and combustion temperature were 0.40 and 1035 C, respectively. Note that the optimal combustion temperature was higher at the lower fuel flow rate. The CO emissions in the optimal regime varied from 50 to 80 ppm, with the overall range of 45 and 165 ppm.

Table 1 Summary of the test conditions

	Case 1	Case 2	Case 3
Fuel Flow Rate, kg/s*10^5	5.25	4.26	5.88
Fuel Jet Reynolds Number	3470	2815	3885
Air Flow Rate, kg/s*10^3	1.12 to 2.70	1.22 to 3.26	1.18 to 3.62
Equivalence Ratio	0.30 to 0.73	0.21 to 0.55	0.26 to 0.78
Power Input, kW	2.44	1.98	2.73

Fuel and Air Temperature	25 C
Operating Pressure	1 atm

As a final check, the fuel flow rate was increased in case 3. Figure 7(*a*) shows that the optimization required 5 iterations to converge the simplex at (0.00, 0.50), (0.06, 0.50), and (0.01, 0.53), which is near one of the initial guess points. A higher airflow rate and smaller premixer distance were required to optimize the combustor performance at a higher fuel flow rate. According to Fig. 7(*b*), costs at the final simplex were 0.72, 0.72, and 0.75. As shown

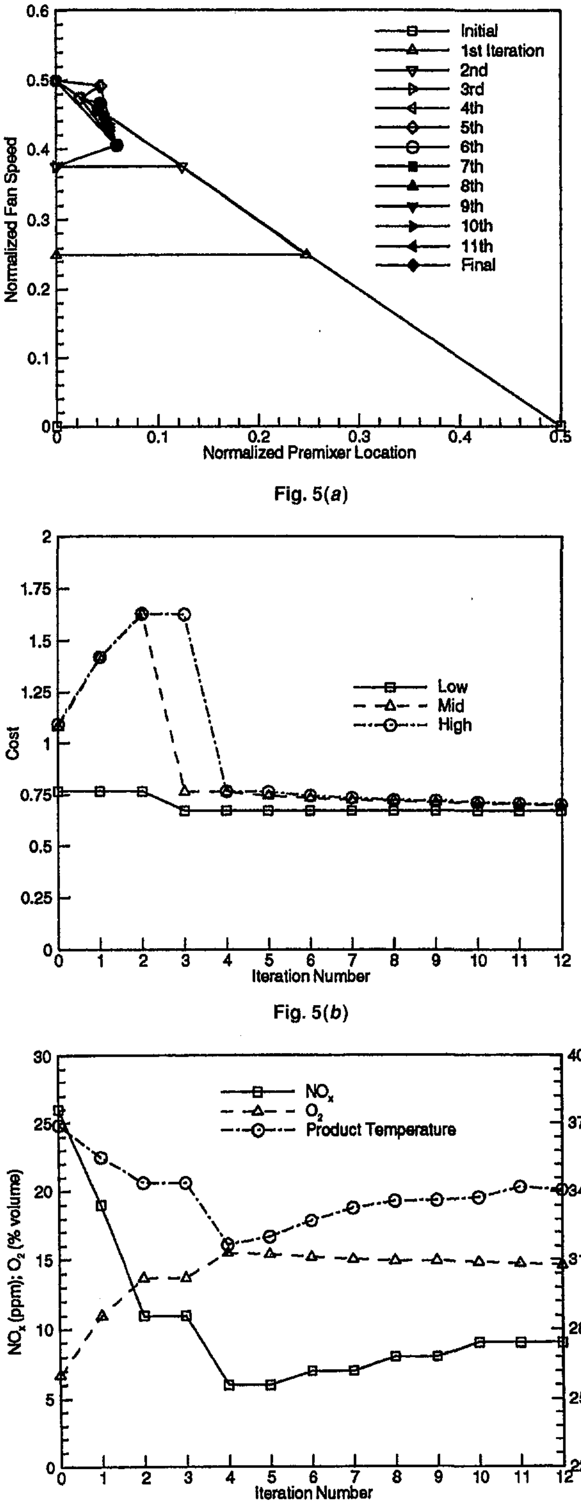

Fig. 5(*a*)

Fig. 5(*b*)

Fig. 5(*c*)

Fig. 5 (*a*) Simplex location during optimization (case 1); (*b*) high, mid, and low costs of simplex (case 1); and (*c*) sensor output at the high cost point of simplex (case 1)

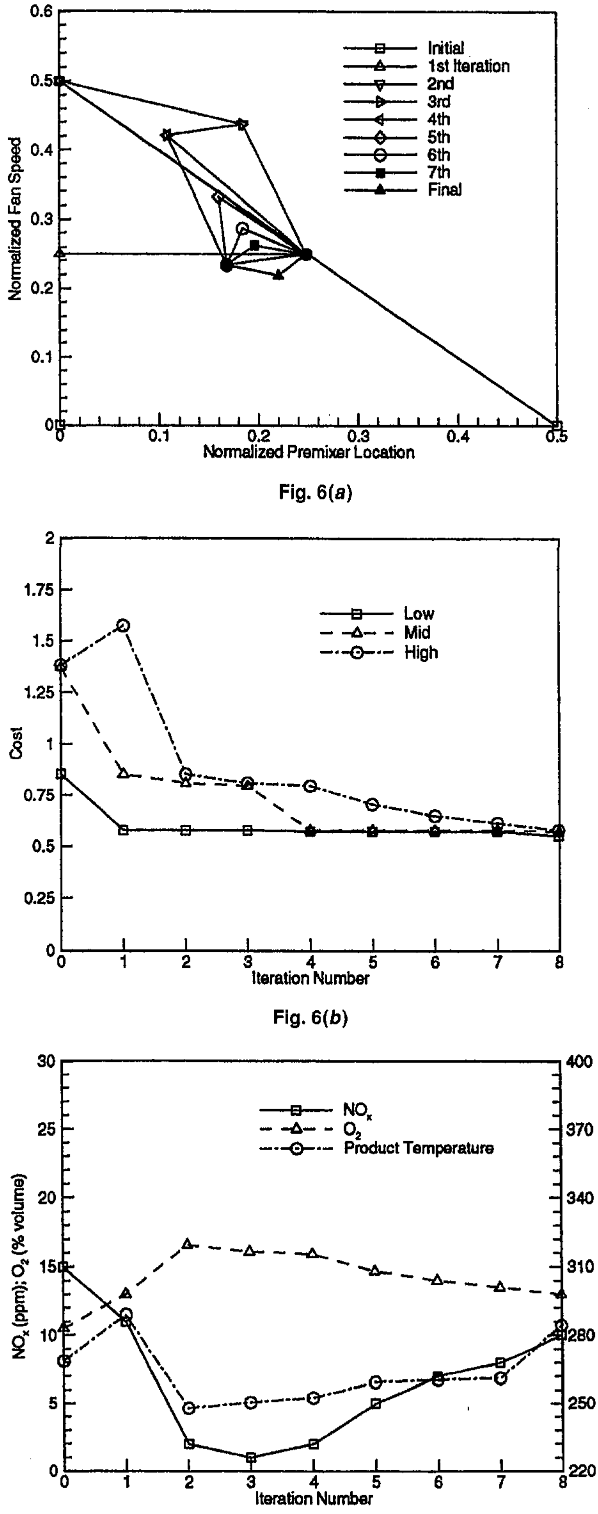

Fig. 6(*a*)

Fig. 6(*b*)

Fig. 6(*c*)

Fig. 6 (*a*) Simplex location during optimization (case 2); (*b*) high, mid, and low costs of simplex (case 2); and (*c*) sensor output at the high cost point of simplex (case 2)

in Fig. 7(*c*), the NO_x concentration at the high cost point decreased from 30 ppm to 7 ppm. The optimal point with the lowest cost corresponded to 10 ppm NO_x, 14.9 percent volume of oxygen, product temperature of 328 C, equivalence ratio of 0.30, and combustion temperature of 820 C. The CO emissions in the optimal regime varied from 50 and 110 ppm, with the overall range of 50 and 850 ppm. A summary of results at the optimal point is shown in Table 2 for all test cases. Evidently, the optimal equivalence ratio and combustion temperature increased as the fuel flow rate was decreased.

Conclusions

We have introduced active control to optimize combustor performance by articulating fuel-air premixing and combustion-

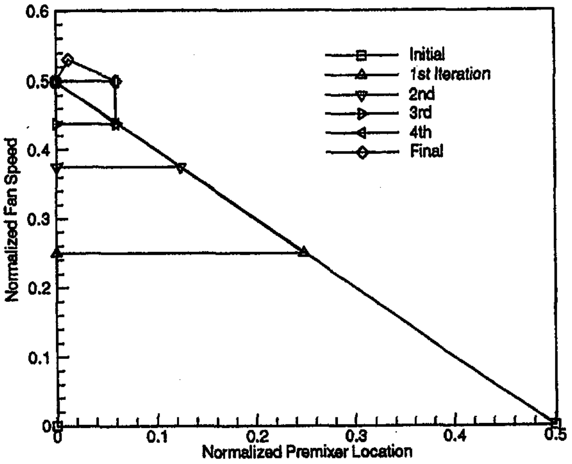

Fig. 7(*a*)

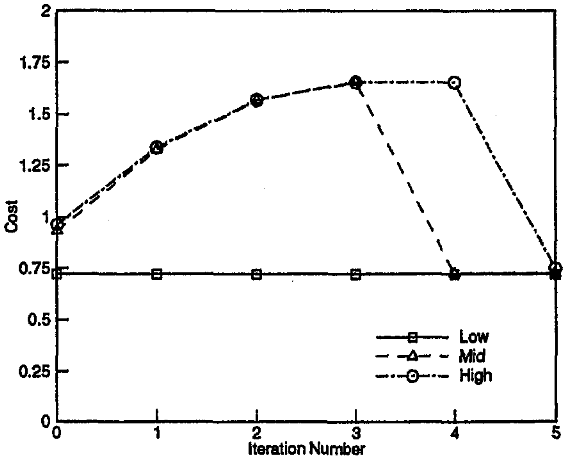

Fig. 7(*b*)

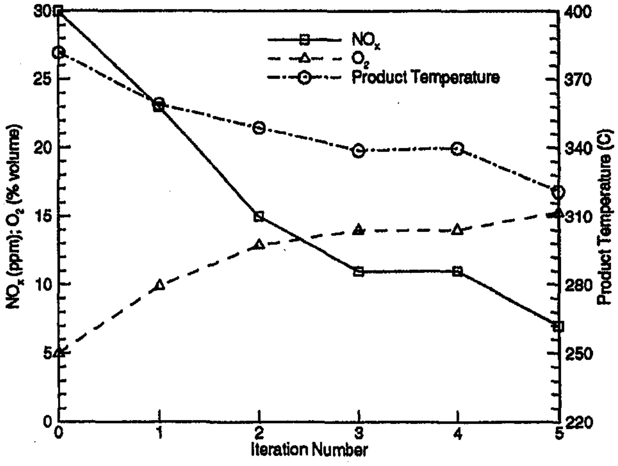

Fig. 7(*c*)

Fig. 7 (*a*) Simplex location during optimization (case 3); (*b*) high, mid, and low costs of simplex (case 3); and (*c*) sensor output at the high cost point of simplex (case 3)

Table 2 A summary of test results at the optimal point

	Case 1	Case 2	Case 3
Normalized Premixer Location	0.05	0.21	0.06
Normalized Fan Speed	0.42	0.23	0.51
% Volume of Oxygen	14.2	13.0	14.9
Equivalence Ratio	0.34	0.40	0.30
Combustion Temperature, C	910	1035	820
Product Temperature, C	340	260	328

zone stoichiometry. This flow articulation scheme is applicable to low-NO_x lean-premixed combustors used in advanced gas turbines. The concept was used in a burner for residential furnaces. The control scheme located the design point for optimal performance at different fuel flow rates without prior knowledge of the system behavior. Following is a summary of the important observations.

—The cost function design is crucial to achieve the desired outcome. The cost function in this study represents a practical scenario; maximize the combustion temperature, and comply with the NO_x emission standard. A limit of 10 ppm was arbitrarily chosen to demonstrate the controller. This limit will change to conform to a new regulation.

—The search algorithm avoided regions of poor combustion stability coinciding with a high volume of oxygen in products, which increased the cost. The controller rejected low fan speeds (or low airflow rates) producing high NO_x and CO emissions.

—The controller searched regions outside the initial simplex. The search space was constrained by structural features of the combustor. The controller was prevented from moving outside the known physical boundaries. A cost function penalty was devised to prevent the controller from getting "stuck" at the boundary.

—The effect of the premixer location on the combustor performance was less significant except at low fan speeds. A smaller premixer distance decreased the total airflow rate, and increased the NO_x production. Experiments providing independent measurements of the premixing airflow rate at different operating conditions are necessary to delineate the detailed mechanisms involved.

—The speed of the optimization was dictated by the time required to obtain repeatable measurements. This is not an issue in applications where the operating conditions change gradually and/or occasionally. Improving optimization speed using faster measurements requires optical techniques because sampling probes have inherently poor temporal response.

References

Brouwer, J., Ault, B. A., Bobrow, J. E., and Samuelsen, G. S., 1990, "Active Control for Gas Turbine Combustors," Proceedings, Twenty-third Symposium (International) on Combustion, The Combustion Institute, Pittsburgh, PA, pp. 1087–1092.

Davis, N. T., and Samuelsen, G. S., 1996, "Optimization of Gas Turbine Combustor Performance Throughout the Duty Cycle," Proceedings, Twenty-sixth Symposium (International) on Combustion, The Combustion Institute, Pittsburgh, PA, pp. 2819–2825.

Kolluri, P., Kamal, A., and Gollahalli, S. R., 1996, "Application of Noncircular Primary-Air Inlet Geometries in the Inshot Burners of Residential Gas Furnaces," *ASME Journal of Energy Resources Technology,* Vol. 118, pp. 58–64.

Maughan, J. R., Elward, K. M., DePietro, S. M., and Bautista, P. J., 1997, "Field Test Results of a Dry Low NO_x Combustion System for the MS3002J Regenerative Gas Turbine," ASME JOURNAL OF ENGINEERING FOR GAS TURBINES AND POWER, Vol. 119, pp. 50–57.

McManus, K. R., Poinsot, T., and Candel, S. M., 1993, "A Review of Active Control of Combustion Instabilities," *Progress in Energy and Combustion Science,* Vol. 19, pp. 1–29.

Nelder, J. A., and Mead, R., 1965, "A Simplex Method for Function Minimization," *The Computer Journal,* Vol. 7, pp. 308–313.

Neumeier, Y., and Zinn, B. T., 1996, "Experimental Demonstration of Active Control of Combustion Instabilities Using Real-Time Modes Observation and Secondary Fuel Injection," Proceedings, Twenty-sixth Symposium (International) on Combustion, The Combustion Institute, Pittsburgh, PA, pp. 2811–2818.

Padmanabhan, K. T., Bowman, C. T., and Powell, J. D., 1995, "An Adaptive Optimal Combustion Control Strategy," *Combustion and Flame,* Vol. 100, pp. 101–110.

Press, H. W., Saul, A. T., Vetterling, W. T., and Flannery, B. P., 1992, *Numerical Recipes in C, The Art of Scientific Computing,* Cambridge University Press, Cambridge.

Puri, R., Stansei, D. M., Smith, D. A., and Razdan, M. K., 1997, "Dry Ultralow NO_x Green Thumb Combustor for Allison's 501-K Series Industrial Engines," ASME JOURNAL OF ENGINEERING FOR GAS TURBINES AND POWER, Vol. 119, pp. 93–101.

Yamada, H., Shimodaira, K., and Hayashi, S., 1997, "On-Engine Evaluation of Emissions Characteristics of a Variable Geometry Lean-Premixed Combustor," ASME JOURNAL OF ENGINEERING FOR GAS TURBINES AND POWER, Vol. 119, pp. 66–69.

Wilson, K. J., Gutmark, E., Schadow, K. C., and Smith, R. A., 1995, "Feedback Control of a Dump Combustor with Fuel Modulation," *AIAA Journal of Propulsion and Power,* Vol. 11, pp. 268–274.

A. K. Agrawal
Assoc. Mem. ASME

A. Tinneti

S. R. Gollahalli
Fellow ASME

Gas Turbine Systems Laboratory,
School of Aerospace and
Mechanical Engineering,
University of Oklahoma, Norman, OK 73019

Flow Measurements in a Curved-Wall Annular Contraction

Flow development in an annular contraction is of fundamental and practical importance in various applications including the gas turbine systems. This paper describes an experimental study of flow characteristics in a curved wall annular contraction. The results are presented in terms of the velocity vectors, surface pressure coefficients, static and stagnation pressure distributions, and profiles of mean velocities, turbulence intensity, and Reynolds shear stress. The flow conditions at the entrance were varied to evaluate how they affected the flow development in the passage. Results show that the contraction produced uniform static pressure and axial velocity profiles at the exit plane. Higher inlet turbulence affected the Reynolds shear stress in the contraction although the change in the static and total pressure fields was insignificant. The overall stagnation pressure loss was only 2 to 3 percent of the dynamic head at the contraction exit plane. Results showing only typical data are included in this paper. More extensive data sets to validate computer codes are available from the authors.

Introduction

Gas turbine engines employ a duct to supply the ambient air to the compressor. In gas turbines used for propulsion, the duct behaves as a diffuser to decelerate the incoming flow. On the contrary, in power generating gas turbines, the inlet duct is an annular contraction to accelerate the stagnant ambient air to the operating inlet velocity of the compressor. This duct must provide uniform flow at the compressor inlet plane to avoid engine stall or surge. In addition, the stagnation pressure loss in the duct must be minimized to achieve a high overall engine efficiency. The ducts for jet engine have been studied extensively (e.g., Jenkins and Loeffler, 1991; Wellborn et al., 1994; Senseney et al., 1996) and a comprehensive, practical treatise is given by Seddon and Goldsmith (1985). The present paper focuses on the annular duct or contraction used in power generating gas turbines. Multiple annular contractions are necessary in gas turbines with cycle modifications such as intercooling (Shepard et al., 1995; Davidson et al., 1996; Agrawal et al., 1995). Engine modifications may introduce nonuniformities and high levels of turbulence in the flow entering the contraction. Therefore, the annular contraction must be designed to minimize these adverse effects of cycle modifications to achieve a high overall engine performance. In addition, the mechanical and structural requirements place limits on the length of the passage. These concerns provided the motivation for the present study on flow development in a compact annular contraction subjected to different flow conditions at the entrance. Besides gas turbine systems, annular contractions are also of fundamental and practical interest for various other applications.

Flow in annular passages has been the subject of several studies, in particular, those dealing with diffusers. A comprehensive review of the existing literature on annular diffusers and combustor-diffusers is given by Klein (1995). Flow in annular "S" shaped passages to connect multispool compressors or multistage turbines is a topic of considerable interest in recent years. In case of compressors, a constant area curved duct with its radius decreasing in the flow direction is used. Brichford et al. (1994), Bailey et al. (1997), and Sonoda et al. (1997) have performed experiments to determine flow characteristics of these passages, and to evaluate effects of inlet and exit flow conditions. Flow development in an interstage turbine passage was investigated by Dominy et al. (1996). In this "S" shaped annular diffuser of area ratio 1.5, the passage radius increased in the flow direction. Another configuration includes a contoured wall annular intercooler-diffuser investigated by Agrawal et al. (1998).

From the literature review, it is evident that the information on S-shaped or contoured annular passages in general, and that on contoured annular contractions in particular, is severely limited. This paper addresses that issue. Experimental data are necessary to develop the design guidelines, and to validate analytical techniques, e.g., those involving inverse design and/or optimization (Gao, 1997; Zangeneh, 1997). The flow field in this study is described by the velocity vectors, surface pressure coefficients, static and stagnation pressure distributions, and profiles of mean velocities, turbulence intensity, and Reynolds shear stress. The inlet flow conditions are varied to assess their effects on flow development in the contraction. The present emphasis is to obtain baseline test data, and, therefore, flow nonuniformities in the circumferential direction are not simulated.

Experimental Approach

The experimental facility consisted of a test model, a suction type wind-tunnel, and instrumentation and data acquisition systems. The collected data were processed to obtain detailed descriptions of the flow field.

Test Model. Geometric details and operational parameters of the contraction are given in Table 1. Annulus height at the contraction exit (h), contraction length (L/h), and contraction area ratio were, respectively, 0.0524 m, 8.7, and 5.4. The annular contraction test section and flow system are shown schematically in Fig. 1. The overall test section was an annular one-fourth scale model of the intercooler flow path in industrial gas turbines comprising of a diffuser, a heat exchanger simulator, and a contraction. The heat exchanger simulator functioned as an axisymmetric annulus. The casing and hub were made of, respectively, clear plexiglass and hard mahogany wood with precisely machined surfaces exposed to the flow. Approximately 75 static pressure taps were located at four circumferential locations along the hub and casing. Access ports to traverse probes in the radial direction were provided on the casing at 6 axial locations, identified as planes C1

Contributed by the Gas Turbine Division of THE AMERICAN SOCIETY OF MECHANICAL ENGINEERS for publication in the ASME JOURNAL OF ENGINEERING FOR GAS TURBINES AND POWER.

Manuscript received by the Gas Turbine Division April 1, 1998; final revision received by the ASME Headquarters March 17, 1999. Technical Editor: H. Nelson.

Table 1 Geometric and Operating Parameters of the Test Section

Hub diameter at the entrance	0.494 m
Casing diameter at the entrance	0.838 m
Hub diameter at the exit	0.352 m
Casing diameter at the exit	0.457 m
Contraction length	0.457 m
Contraction area ratio	5.4
Dynamic head at the contraction exit	890 Pascal
Reynolds number (based on hydraulic diameter at the contraction exit plane)	261,000
Mach number (based on average velocity at the contraction exit plane)	0.11

to C6 in Fig. 2, wherein the contraction hub and casing profiles are also shown.

Flow System. Airflow through the test section was provided by an open loop wind-tunnel shown schematically in Fig. 1. The room air entering the wind-tunnel passed through a honeycomb, a set of screens, a 9:1 area ratio circular contraction, a 2 m long annular flow conditioning section, and the test model. The airflow exiting the contraction passed through a 0.46 m long annular flow monitoring section, a 5.84 m long conical diffuser, fan inlet guide vanes to regulate the airflow rate, a constant speed centrifugal fan driven by a 30 kW electric motor, and an exhaust duct to discharge air to the outside of the laboratory.

Instrumentation and Data Acquisition. Flow measurements were obtained by wall pressure taps, and radial traverses of a cross-film anemometer probe and a 1.5 mm diameter five-hole pressure probe. Calibrated pressure transducers and a scanivalve system were used to scan inputs from wall pressure taps. Each pressure tap measurement required 10 s; 8 s of waiting time to reach steady state and 2 s for data collection at 20 Hz. The mean flow and turbulence characteristics were obtained by an anemometer system (TSI IFA-300) with cross-film sensors. During experiments the probe was traversed radially in increments of 2.5 mm with film sensors oriented normal and parallel to the test-section axis. The sensors were calibrated in these orientations to obtain curves relating (i) the effective velocity and voltage output, and (ii) the yaw coefficient and velocity parallel to the sensor. The measurements at each point were taken at 2000 Hz for a period of 2 s. The five-hole pressure probe was calibrated in a fixed position or non-nulling mode as explained by Treaser and Yocum (1979). A set of five pressure transducers was used to measure the probe outputs. Measurements at each location required 10 s; 9 s of waiting time to reach steady state and 1 s for data collection at 10 Hz. The voltage signals from pressure sensors and hot-film sensors were digitized using low- and high-speed data acquisition boards and accompanying software.

Data Reduction and Experimental Errors. The instantaneous axial (u) and radial (v) velocity components were determined from the cross-film probe measurements. The normalized turbulence intensity (T_i) and normalized Reynolds shear stress (τ_{uv}) are defined as

$$T_i = 100*\frac{\sqrt{(u_t^2 + v_t^2)}}{\bar{U}_e}; \quad \tau_{uv} = \frac{1}{\bar{U}_e^2}\sum_{i=1}^{n}\frac{[uv - UV]}{n}. \tag{1}$$

Here u_t and v_t are, respectively, the local axial and radial turbulent velocities, and $\bar{U}_e$ is the mass-averaged axial velocity at the contraction exit plane. The change in surface pressure between an axial location j and the inlet plane i was expressed by the surface pressure coefficient

$$Cp_{ij} = [p_j - \bar{p}_i]/[q_e], \tag{2}$$

where $\bar{p}_i$ is the mass-averaged static pressure at the inlet plane, and q_e is the dynamic head at the contraction exit plane. The pressure measurements were repeatable to within +/−14 Pascal, a variation of less than +/−1.6 percent of the dynamic head at the contraction exit plane. Trial experiments indicated that the hot-film measurements were minimally affected by sampling rates higher than 2000 Hz.

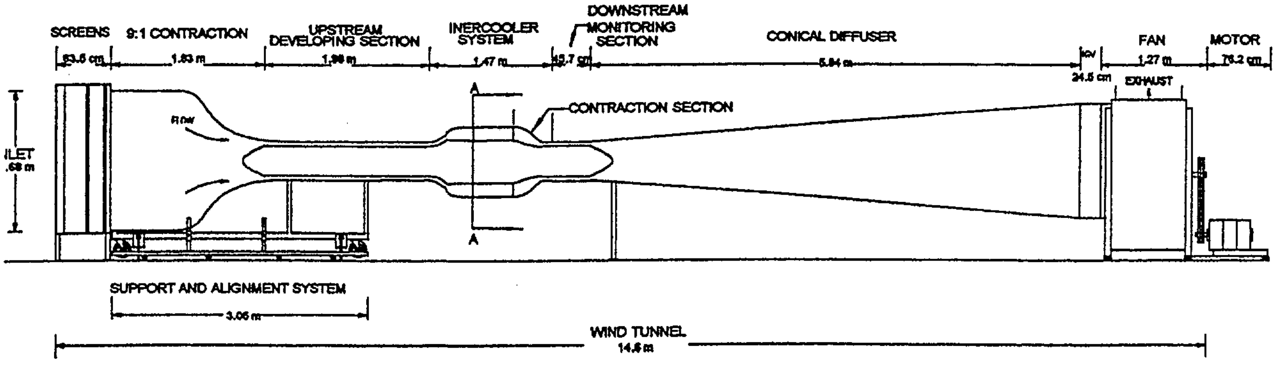

Fig. 1 Schematic of the Flow System

Nomenclature

C = designation of measurement locations
Cp = surface pressure coefficient
h = annulus height at the contraction exit
L = contraction length
n = number of instantaneous measurements
p = static pressure
q = dynamic head
T_i = turbulence intensity
U = mean axial velocity
u = instantaneous axial velocity
V = mean radial velocity
v = instantaneous radial velocity
x = axial coordinate
y = radial distance from the hub
τ_{uv} = Reynolds shear stress

Subscripts and Superscripts

$-$ = mass-averaged
e = exit plane
i = inlet plane
n = normal
t = turbulent

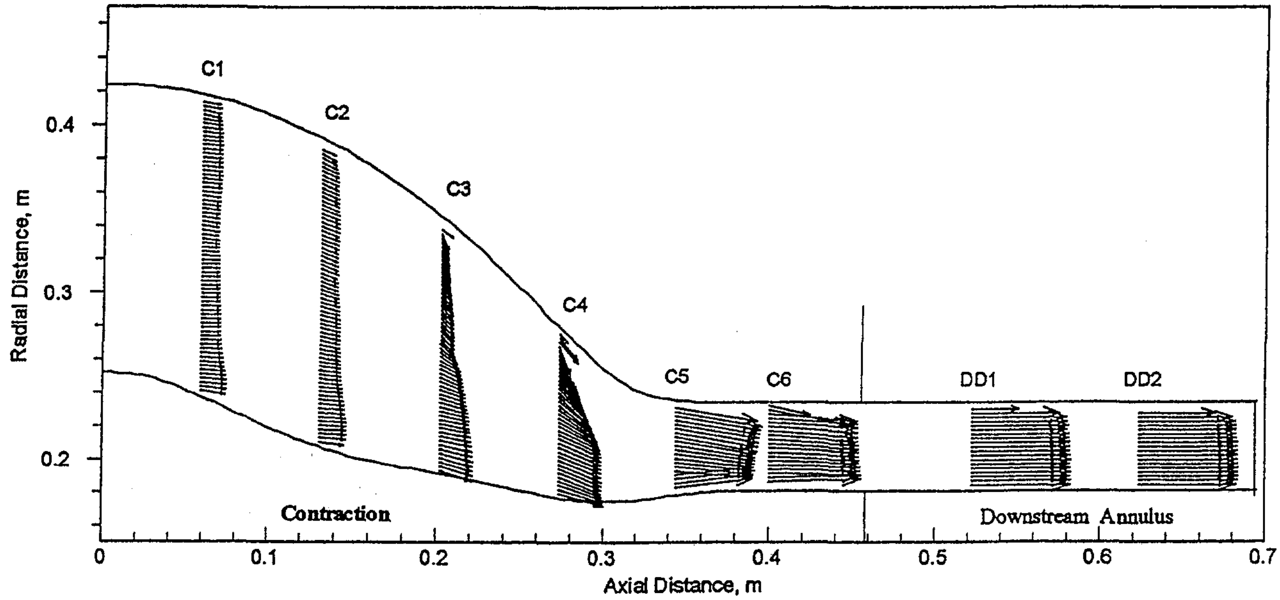

Fig. 2 Velocity Vectors in the Contraction

Results and Discussions

Detailed flow measurements were obtained for two different operating conditions at the contraction inlet. In case 1, the ambient air entered at plane "AA" in Fig. 1 because the diffuser section of the test model and wind-tunnel components upstream of it were removed. Instead, a filter element was placed at the inlet plane of the heat exchanger annulus to reduce the turbulence. This case simulated the flow entering a typical power generating gas turbine. In case 2, the ambient air passed through the diffuser and wind-tunnel sections upstream of it. This case simulated the baseline flow entering the contraction in gas turbines with cycle modification such as intercooling. Flow experiments were conducted for air mass flow rate from 2.8 to 3.1 kg/s, providing average axial 35 to 39 m/s at the contraction exit plane. The flow is incompressible because the Mach number is about 0.11. The flow is turbulent with a Reynolds number of approximately 261,000. At such high Reynolds numbers, the Reynolds number effect on flow behavior is considered second order in nature.

Overall Performance. The overall performance of the contraction is described by the velocity vectors, surface pressure distributions, and static and stagnation pressure profiles.

Velocity Vectors. The flow field in the contraction and downstream annular section is depicted in Fig. 2 by velocity vectors deduced from hot-film probe measurements. Close to the inlet, at plane C1 ($x/h = 1.32$), the flow was mainly in the axial direction and the velocity profile was uniform, except for a distinct peak near the hub. A similar profile (not shown) was also measured in the heat exchanger annulus upstream of the contraction. At plane C2 ($x/h = 2.69$), the flow accelerated marginally in the inner half of the passage, while that in the outer half turned radially towards the axis. The radial flow turning was caused by the curvature of the casing. The flow acceleration in the inner half and radial flow turning in the outer half of the passage were significant at planes C3 ($x/h = 4.05$) and C4 ($x/h = 5.40$). Velocity vectors at plane C4 indicate a highly nonuniform flow with velocity peaking near the hub. A significant change occurred between planes C4 and C5 ($x/h = 6.76$) as the flow accelerated. At plane C5, the flow was remarkably uniform with only a minor peak next to the casing. The velocity profile adjusted between planes C5 and C6 ($x/h = 7.83$), and a nearly uniform axially directed flow was achieved at plane C6 near the contraction exit. Figure 2 indicates negligible radial flow at planes DD1 ($x/h = 10.16$) and DD2 ($x/h = 12.08$) in the annulus downstream of the test model. These results imply that the contraction provided uniform exit flow even though the incoming flow was nonuniform. A similar conclusion was reached from measurements for case 2, which are presented later to highlight differences between the two cases.

Surface Pressure Coefficients. Pressure coefficient distributions along the hub and casing of the contraction are shown in Fig. 3 for case 1. Different symbols correspond to data at different circumferential locations (90 deg apart) of the pressure taps. The casing pressure was nearly constant at planes C1, C2, and C3. The pressure decreased slightly between planes C3 and C4 but significantly between planes C4 and C5 as the dynamic head increased because of the flow acceleration. Subsequently, the casing pressure decreased slightly as the flow profile adjusted between planes C5 and C6. Figure 3 shows that the hub pressure was constant between planes C1 and C2, decreased marginally between planes C2 to C4, substantially between planes C4 and C5, and slightly between

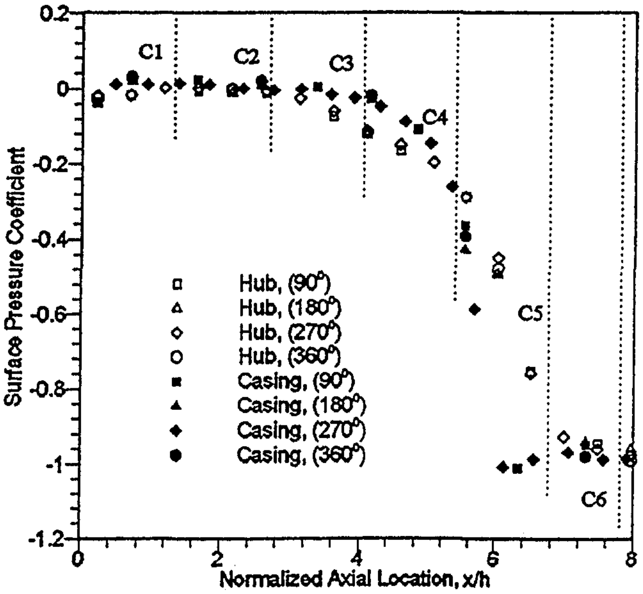

Fig. 3 Wall Pressure Coefficients

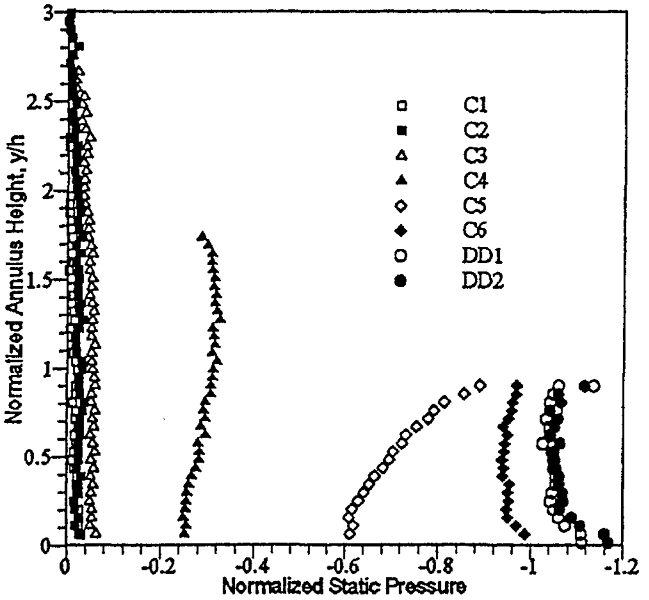

Fig. 4 Normalized Static Pressure Profiles for Case 1

planes C5 and C6. The overall trend was similar at the casing and hub, except that the pressure changed more gradually along the hub. In Fig. 3, the casing pressure was higher than the hub pressure between planes C1 and C4; necessary to radially turn the flow towards the axis. This situation was reversed between planes C4 to C6 as the flow adjacent to the hub accelerated and turned radially outward. The casing and hub pressures downstream of plane C6 were nearly the same because the contraction exit flow was axially directed. The surface pressure coefficient at plane C6 was about -1.0 indicating that the change in static pressure was caused by the flow acceleration and not by the stagnation pressure loss. Note that the measurements in Fig. 3 depict an excellent flow symmetry in the circumferential direction. The surface pressure distributions for case 2 were indistinguishable from those for case 1, and, hence, they are not shown.

Static and Stagnation Pressure Profiles. The radial profiles of normalized static pressure for case 1, deduced from five-hole pressure probe measurements, are shown in Fig. 4. The radial distance from the hub (y) was normalized by the annulus height at the contraction exit (h). The static pressure was referenced by its mass-averaged value at the inlet plane, and normalized by the dynamic head at the contraction exit. The static pressure decreased slightly between planes C1 and C3, which corroborates the small change in velocity between these planes observed in Fig. 2. A nearly constant static pressure at these axial planes suggests insignificant cross-stream flow. The static pressure decreased substantially as the flow accelerated, and the dynamic head increased between planes C3 and C4. The dynamic head at plane C4 was about one-fourth of that at the exit plane suggesting that the average velocity at this plane was about half of that at the contraction exit. Large cross-stream pressure gradients are observed at plane C5, where the hub pressure is higher than the casing pressure. The pressure nonuniformity is attributed to the sharp passage curvature between planes C4 and C5, which caused the flow to turn radially outward. The flow turning adjusted the static pressure profile, which became uniform near the contraction exit at plane C6 as desired. The normalized static pressure profiles for case 2 overlapped with those for case 1 and hence, they are not reported here.

Radial profiles of the normalized stagnation pressure for case 1 are shown in Fig. 5 to evaluate losses in the passage. As expected the stagnation pressure decreased in the flow direction although the change was small. The stagnation pressure loss between consecutive axial planes was not resolved accurately because of the measurement uncertainties. The overall stagnation pressure loss was approximately 2 to 3 percent of the dynamic head at the contraction exit plane. This result substantiates the previous observation, i.e., the static pressure decreased mainly because of the flow acceleration in the contraction. The overall stagnation pressure for case 2 was not resolved, in part, because of the high turbulence which increases uncertainties of pressure probe measurements (Christiansen and Bradshaw, 1981).

The results presented so far indicate that the contraction performed as desired; a distorted inlet flow was accelerated to an uniform axially directed exit flow with negligible cross-stream pressure gradients. The flow accelerated with only a minor loss of the stagnation pressure. An increase in turbulence at the entrance did not have a noticeable effect on pressure distribution in the passage.

Flow Development. In this section, we present profiles of normalized axial velocity ($U/\bar{U}_e$), normalized radial velocity ($V/\bar{U}_e$), normalized turbulence intensity, and normalized Reynolds shear stress at selected axial planes to help explain the observed performance. The measured data are presented for cases 1 and 2 to allow a direct comparison between them. Note that the contraction between planes C1 to C3 presented concave curvature both at the hub and casing. However, the casing curvature changed to a convex shape in the latter half of the contraction between planes C4 and C6. The discussion below is grouped according to these geometric features of the passage.

Planes C1 to C3. The normalized axial velocity profiles at planes C1 and C3 are shown in Fig. 6(*a*). Near the inlet at plane C1, the axial velocity profile for case 1 peaked next to the hub, while it was essentially uniform for case 2. The maximum axial velocity in the hub region for case 1 was about 50 percent higher than that for case 2. The two profiles were similar in the midregion of the annulus. Next to the casing, the axial velocity for case 1 was slightly higher than that for case 2. Between planes C1 and C3, the axial velocity increased in the hub region and decreased in the casing region. Although the increase was of similar magnitude for the two cases, the decrease was significant for case 1. The flow development between these planes is explained further by the normalized radial velocity profiles shown in Fig. 6(*b*). The radial velocity at plane C1 was negligible for case 1, while it was comparable to the axial velocity for case 2. Between planes C1 and

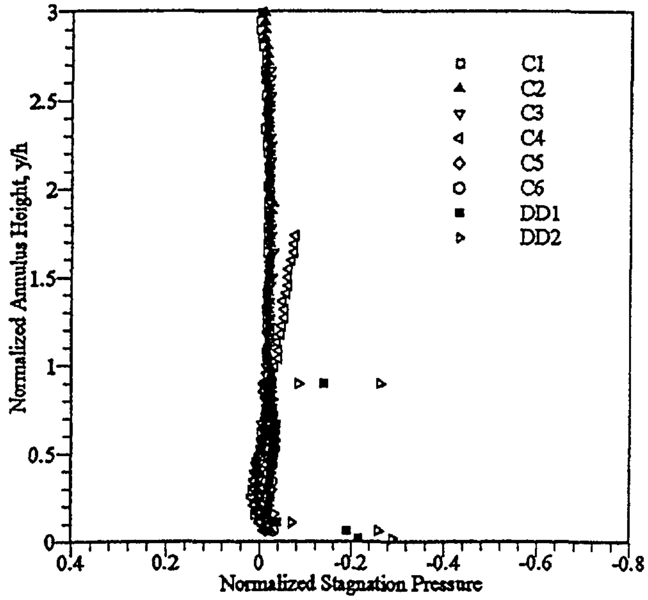

Fig. 5 Normalized Stagnation Pressure Profiles for Case 2

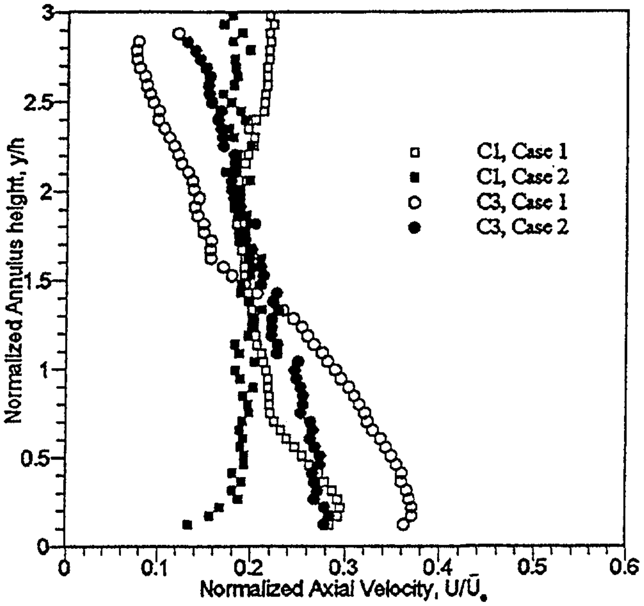

Fig. 6(*a*) Normalized Axial Velocity Profiles at Planes C1 and C3

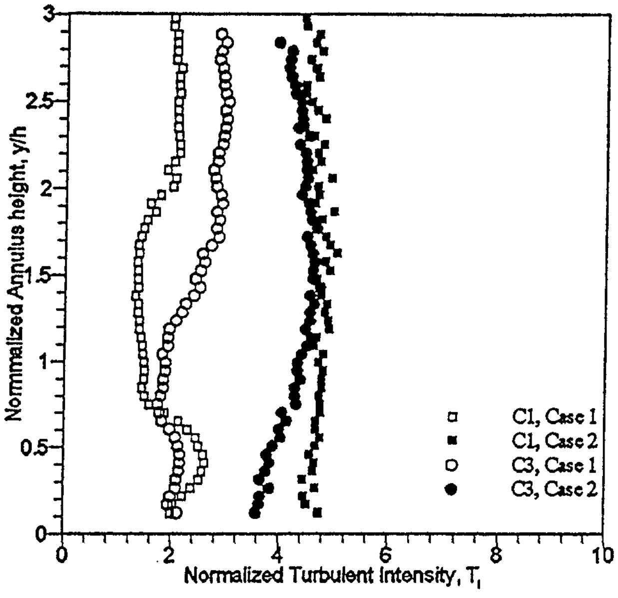

Fig. 6(*c*) Normalized Turbulence Intensity Profiles at Planes C1 and C3

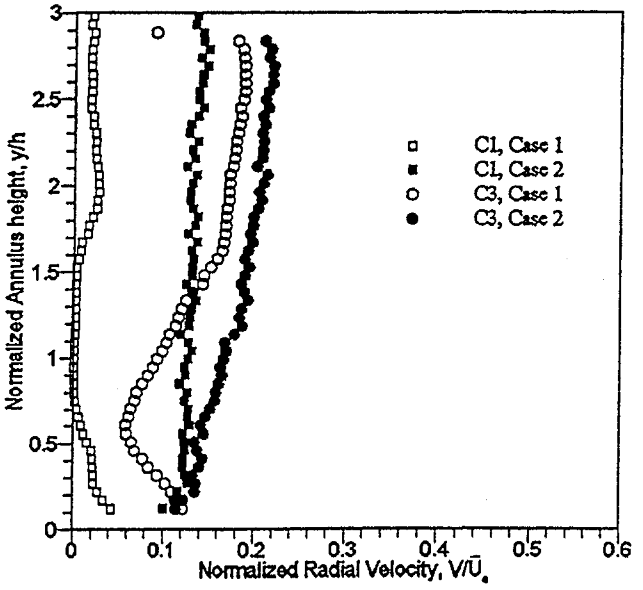

Fig. 6(*b*) Normalized Radial Velocity Profiles at Planes C1 and C3

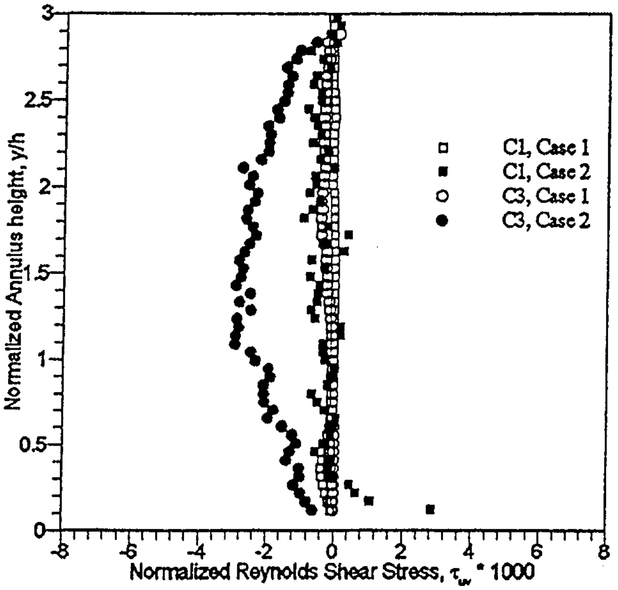

Fig. 6(*d*) Normalized Reynolds Stress Profiles at Planes C1 and C3

C3, the radial velocity increased at all locations implying radial turning of the flow caused by the passage curvature. The increase was greater in the outer half of the casing region. The radial flow turning was substantial for case 1 compared to that for case 2.

The turbulence intensity profiles in Fig. 6(*c*) show that the flow in case 2 was far more turbulent than that in case 1. The turbulence intensity between planes C1 and C3 increased for Case 1 but it decreased slightly for case 2. However, the ratio of turbulent to mean kinetic energy (not shown) decreased in the flow direction because the mean velocity increased more rapidly. Such behavior is typical of a contraction as discussed by Libby (1996). The turbulent structure in the passage affected the Reynolds shear stress as shown by profiles in Fig. 6(*d*). In case 1, the Reynolds shear stress was practically negligible because of the low turbulence. In case 2, the Reynolds shear stress was higher, with the maximum occurring at about mid-height of the passage.

Planes C4 to C6. As discussed above, the flow changed dramatically in the latter half of the contraction between planes C4 and C6. In Fig. 7(*a*), the axial velocity profiles for the two cases are similar at plane C4 even though they differed substantially near the inlet at plane C1 (see Fig. 6(*a*)). The profiles for the two cases were almost identical near the contraction exit at plane C6. Note that the hub peaked profile at plane C4 changed to the casing peaked profile at plane C5. Figure 7(*b*) shows that the radial velocity profiles for the two cases were also similar at plane C4. The flow turning was greater in the casing region compared to that in the hub region. The radial velocity for both cases decreased in the flow direction although the decrease was smaller for case 2. Figure 7(*c*) shows that the normalized turbulence intensity increased in the flow direction for both cases. Higher turbulence in case 2 persisted throughout the passage. In case 1, the normalized turbulence intensity at plane C6 was 3.6 percent, which is approximately twice that at the inlet plane C1. The corresponding value in case 2 was 4.6 percent, which is about the same as that at the inlet plane. In comparison, the average axial velocity between these planes increased almost by a factor of 5. Figure 7(*d*) shows that the Reynolds shear stress for case 1 was negligible as compared to that for case 2.

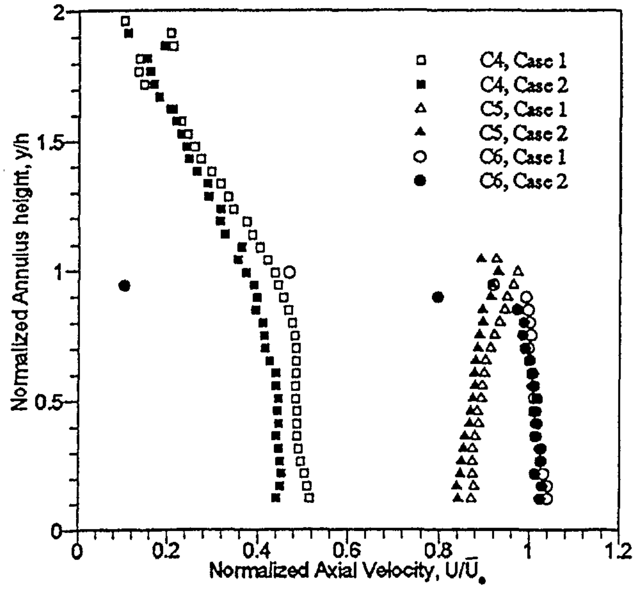

Fig. 7(*a*) Normalized Axial Velocity Profiles at Planes C4, C5, and C6

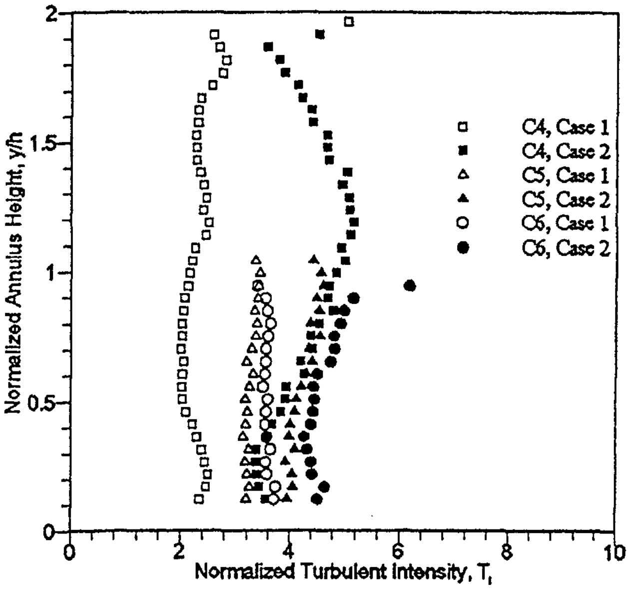

Fig. 7(*c*) Normalized Turbulence Intensity Profiles at Planes C4, C5 and C6

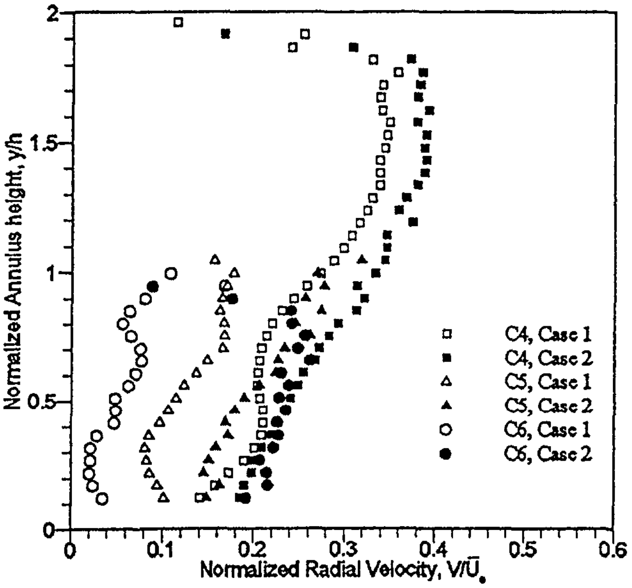

Fig. 7(*b*) Normalized Radial Velocity Profiles at Planes C4, C5 and C6

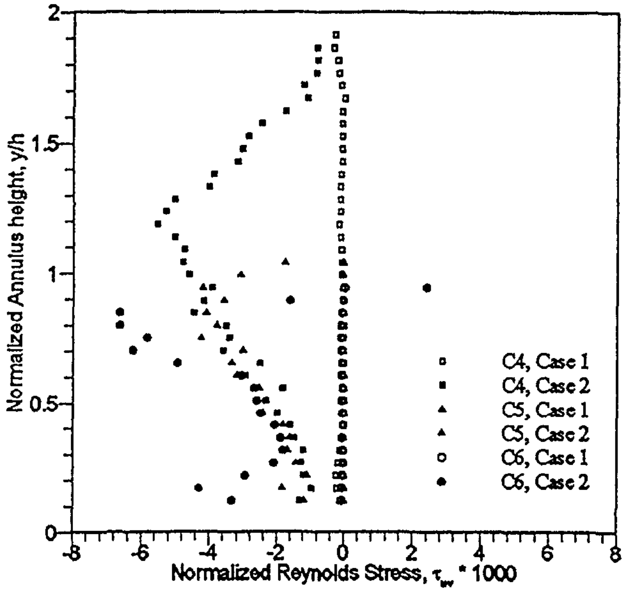

Fig. 7(*d*) Normalized Reynolds Stress Profiles at Planes C4, C5 and C6

Conclusions

Flow development in an annular contraction of area ratio 5.4 and a length of 8.7 times the annulus height at the exit was investigated. Experiments were conducted at a Reynolds number of 261,000 for two different inlet flow conditions. The inlet velocity and turbulence intensity profiles for these two cases differed substantially from each other. Results show that the contraction provided uniform static pressure and axial velocity profiles at the exit plane, regardless of the inlet flow conditions. The Reynolds shear stress was negligible when the inlet turbulence was low. Higher inlet turbulence did not have a noticeable effect on the static and stagnation pressure fields in the contraction. The overall stagnation pressure loss was minor; only 2–3 percent of the dynamic head at the contraction exit.

Acknowledgments

This research was sponsored by the U.S. Department of Energy's Federal Energy Technology Center under contract DE-FC21-92MC29061 with the Clemson University, subcontract 94-01-SR029 with the University of Oklahoma for the period from July 1994 to June 1997. The METC Contracting Officer's Representative was Dr. Norm Holcombe. Dr. Dan Fant was the program manager of the Advanced Gas Turbine Systems Research at Clemson University. We wish to thank Frank Carter, John Allen, and Mathew Jackson for their dedication in building the test facility for this research.

References

Agrawal, A. K., Gollahalli, S. R., Carter, F. L., and Allen, J. E., 1995, "Intercooler Flow Path for Gas Turbines: CFD Design and Experiments," DOE/METC-96/1023, Vol. 2, pp. 529–538.

Agrawal, A. K., Tinneti, A., and Gollahalli, S. R., 1998, "Flow Characteristics of an Annular Intercooler-Diffuser for Gas Turbines," ASME Paper 98-GT-283.

Bailey, D. W., Brichford, K. M., Carrotte, J. F., and Stevens, S. J., 1997, "Performance Assessment of an Annular S-shaped Duct," *ASME Journal of Turbomachinery*, Vol. 119, pp. 149–156.

Britchford, K. M., Carrotte, J. F., Stevens, S. J., and McGuirk, J. J., 1994, "The Development of the Mean Flow and Turbulence Structure in an Annular S-shaped Duct," ASME Paper 94-GT-457.

Christiansen, T., and Bradshaw, P., 1981, "Effect of Turbulence on Pressure Probes," *Journal of Physics E: Scientific Instruments,* Vol. 14, pp. 992–997.

Davidson, B., Whitney, D., Laursen, N., Cohn, A., and Hay III, G. A., 1996, "Collaborative Advanced Gas Turbine (CAGT) Program Status: An International Initiative to Catalyze an Intercooled Aeroderivative (ICAD) Gas Turbine Launch Order," ASME Paper 96-GT-292.

Dominy, R. G., Kirkham, D. A., and Smith, A. D., 1996, "Flow Development through Inter-Turbine Diffusers," ASME Paper 96-GT-139.

Gao, Y., 1997, "Aerodynamic Design and Optimization of Axisymmetric Annular Flow Passages," M.S. Thesis, School of Aerospace and Mechanical Engineering, University of Oklahoma, Norman, OK.

Jenkins, R. C., and Loeffler Jr., A. L., 1991, "Modeling of Subsonic Flow Through a Compact Offset Inlet Diffuser," AIAA Journal, Vol. 29, pp. 401–408.

Klein, A., 1995, "Characteristics of Combustor Diffusers," *Progress in Aerospace Sciences*, Vol. 31, pp. 171–271.

Libby, P. A., 1996, *Introduction to Turbulence,* Taylor and Francis, Washington, D.C.

Seddon, J., and Goldsmith, E. L., 1985, *Intake Aerodynamics,* AIAA, New York.

Senseney, M. B., Buter, T. A., and Bowersox, R. D. W., 1996, "Performance Characterization of a Highly Offset Diffuser With Vortex Generator Jets," *AIAA Journal of Propulsion and Power,* Vol. 12, pp. 237–244.

Shepard, S. B., Bowen, T. L., and Chiprich, J. M., 1995, "Design and Development of the WR-21 Intercooled Recuperated (ICR) Marine Gas Turbine," ASME JOURNAL OF ENGINEERING FOR GAS TURBINES AND POWER, Vol. 117, pp. 557–562.

Sonoda, T., Arima, T., and Oana, M., 1997, "The Influence of Downstream Passage on the Flow Within an Annular S-shaped Duct," ASME Paper 97-GT-83.

Treaser, A. L., and Yocum, A. M., 1979, "The Calibration and Application of Five-hole Probes," *ISA Transactions,* Vol. 18, pp. 23–34.

Wellborn, S. R., Reichert, B. A., and Okiishi, T. H., 1994, "Study of the Compressible Flow in a Diffusing S-Duct," *AIAA Journal of Propulsion and Power,* Vol. 10, pp. 668–675.

Zangeneh, M., 1997, "On the Inverse Design of Inter-Stage Ducts, Diffuser Walls and Meridional Geometry of Turbomachines," ASME Paper 97-GT-208.

Testing and Modeling Gas Turbines Using Multisine Signals and Frequency-Domain Techniques

C. Evans
dcevans@glam.ac.uk

A. Borrell

D. Rees

University of Glamorgan,
School of Electronics,
Pontypridd,
CF37 1DL,
Wales, United Kingdom

The frequency-domain identification of gas turbine dynamics is discussed. Models are directly estimated from engine data and used to validate linearized thermodynamic models derived from the engine physics. This work is motivated by the problems previously encountered when using time-domain methods. A brief overview of frequency-domain techniques is presented and the design of appropriate multisine test signals is discussed. Practical results are presented for the modelling of the fuel feed to shaft speed dynamics of a twin-spool engine. The gathered data are analyzed and the frequency response functions of the engine are estimated. The identification of parametric s*-domain models is discussed in detail and a comparison made between the identified models and the linearized thermodynamic models. The influence of engine nonlinearities on the linear models is also examined.*

1 Introduction

This paper describes the practical application of multisine test signals and frequency-domain system identification techniques to the problem of gas turbine modeling.

Engine models are required both in the development and operational stages of the life of a gas turbine. Thermodynamic models are derived during the development stage, based on knowledge of the engine physics, and provide important insights into the engine behavior. Such models are both complex and nonlinear, making them unsuitable for use in the design of engine control systems.

Therefore, it is common practice to linearize the thermodynamic models around a series of operating points and then carry out a model-order reduction, in order to arrive at models which are suitable for control system design. Since these models are based on a priori assumptions about the engine physics it is then important to validate their performance against real engine data.

Early work by Lawrence and Powell (1957) and Fitchie et al. (1959) studied the testing and modeling of single and twin-shaft turbojets using single sine and step inputs. More recently, Cottington and Pease (1979) employed multifrequency binary signals to measure the frequency responses of a range of engines. They stressed the importance of excluding the dynamics of the fuel feed system from the estimated model by using the measured fuel flow as the input signal. Further results using binary signals to test a Spey Mk 502 engine were reported by Onions and Foss (1982).

The development of increased computing power, along with advances in system identification techniques, now make it possible to apply a systematic approach to fitting parametric models to engine data. Recent work by Hill (1994) examined the application of a range of time-domain methods to estimating discrete engine models, with the aim of reducing engine test times while improving the accuracy of the estimated models and quantifying the model uncertainty. Particular importance was placed on the identification of the second-order effects, since they had not been adequately dealt with in past work.

This work showed that discrete models with good input-output properties could be estimated, making them suitable for engine simulation and control system design. However, some problems with the application of time-domain techniques were reported by Hill in a recent paper (1997). Under certain circumstances, discrete z-domain models can be estimated whose continuous s-domain equivalent cannot be realized by a physical system. This is due to the presence of a single real negative pole, which maps to a single complex pole in the s-domain. Such models clearly cannot be used to validate the linearized thermodynamic models. Evans (1998) has shown that this effect can be caused by using a measured, band-limited, input signal in time-domain estimation, or by the presence of a pure time delay which is not an integer multiple of the sampling period.

The work described in this paper was motivated by the need to find an alternative approach which overcome this problem. Frequency-domain techniques are employed, since they allow s-domain models to be directly estimated and the pure time delay to be included as a parameter for estimation. The influence of system nonlinearities can also be easily assessed. This paper thus complements that written by Hill (1997), and the results are based on testing the same engine, which allows a direct comparison to be made. A complete account of the work conducted can be found in Evans (1998).

Multisine signals are used to test the gas turbine, which are simply an arbitrary sum of harmonically related cosines. The use of broad-band multisines allows a large number of frequency points to be measured in one test, which is much faster than measuring frequency-by-frequency using single sines. Their advantage over binary signals is that all the signal power can be concentrated within the frequency range of interest. The use of multisine signals thus allows a significant reduction in engine test times and in the fuel burnt during testing, making systematic engine testing a more cost-effective option.

The aims of this investigation can thus be summarized as follows:

- —application of wide-band, low crest factor multisine signals to the testing of gas turbines
- —direct estimation of s-domain models from test data using frequency-domain techniques, which can then be used to

---

Contributed by the International Gas Turbine Institute (IGTI) of THE AMERICAN SOCIETY OF MECHANICAL ENGINEERS for publication in the ASME JOURNAL OF ENGINEERING FOR GAS TURBINES AND POWER. Paper presented at the International Gas Turbine and Aeroengine Congress and Exhibition, Stockholm, Sweden, June 2–5, 1998; ASME Paper 98-GT-98.

Manuscript received by IGTI March 2, 1998; final revision received by the ASME Headquarters March 23, 1999. Associate Technical Editor: R. Kielb.

validate the linearized thermodynamic engine models
- —assessment of the influence of system noise and nonlinearities on the estimated linear models
- —estimation of the engine pure time delay as part of the s-domain models

2 Thermodynamic Engine Models

The engine tested in this work was a Rolls Royce Spey Mk 202, which is a typical military twin-shaft turbofan, with a low bypass ratio and a variable reheat nozzle. Although no longer in service, it has the same basic architecture, for control purposes, as that of more modern engines such as the EJ200, which is used to power the Eurofighter (Dadd et al., 1996). The work concentrated on the dynamic relationship between the measured input fuel flow and the high pressure (HP) and low pressure (LP) shaft speeds, denoted *NH* and *NL*.

The derivation of thermodynamic engine models has been extensively discussed in the literature. One of the earliest approaches was described by Saravanamuttoo and Fawke (1970), who developed a nonlinear thermodynamic model for use in the analogue and digital simulation of an Olympus engine. This model was derived from the engine physics and was able to predict the change in engine dynamics due to changing operating conditions, over the complete running range of the engine.

In work conducted for Rolls Royce plc, Jackson (1988) showed that, for a given stationary operating point, the higher-order nonlinear thermodynamic models derived from the engine physics could be reduced to linear models with the same order as the number of engine shafts. The models were first linearized using small perturbations and then a model reduction procedure was employed. The model reduction is possible because the thermodynamic processes in the gas stream, associated with rates of change of pressure, have time constants in the order of 10 ms, while the shaft time constants are in the order of 0.2–2.5 s.

The linearized models were expressed in a state space form and the shaft speeds selected as the states, which is convenient since they can be directly measured. A complete library of models was generated for the Spey engine, across a range of operating points, by staff at section APD5 of the Defence Research Agency at Pyestock (1993). These linearized, reduced-order thermodynamic models will be referred to simply as the thermodynamic models for the remainder of this paper.

Evaluating the transfer function matrices of these state space models allows the HP and LP shaft dynamics to be expressed in transfer function form, with common poles but different zeros. The variation of these poles and zeros with the HP shaft speed is shown in Fig. 1. It can be seen that the HP shaft model is effectively first-order, with a cancelling pole-zero pair for much of the operating range. The poles and zeros of the LP shaft model are more distinct.

3 Frequency-Domain Identification

Under steady-state conditions, the basic input-output relationship in the frequency domain is given by

$$Y(j\omega) = H(j\omega)U(j\omega), \qquad (1)$$

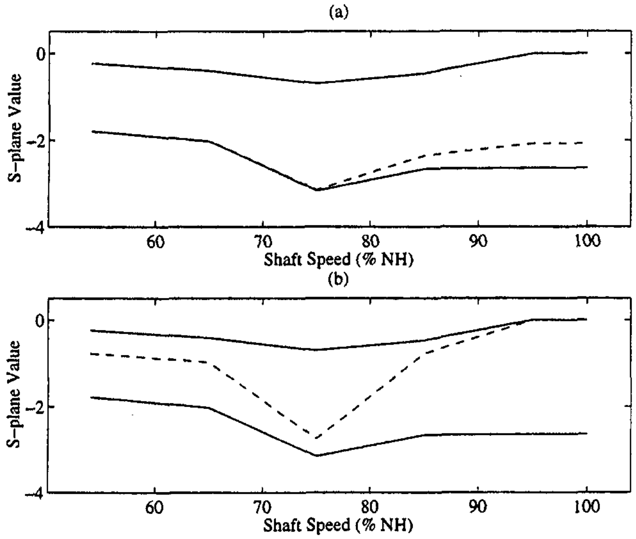

Fig. 1 Poles and zeros of thermodynamic Spey engine models for (*a*) HP shaft and (*b*) LP shaft. Poles (solid) and zero (dashed).

where $U(j\omega)$ and $Y(j\omega)$ are the Fourier transforms of the input and output signals and $H(j\omega)$ is a complex valued function of frequency, termed the frequency response function (FRF) of the system. If periodic signals are used to excite the system then the FRF can be estimated as the ratio of the mean values of the output and input Fourier coefficients, at the discrete test frequencies ω_K

$$\hat{H}_{EV}(j\omega_K) = \frac{\frac{1}{N}\sum_{m=1}^{N} Y_m(j\omega_K)}{\frac{1}{N}\sum_{m=1}^{N} U_m(j\omega_K)} = \frac{\bar{Y}(j\omega_K)}{\bar{U}(j\omega_K)}, \qquad (2)$$

where $U_m(j\omega_K)$ and $Y_m(j\omega_K)$ are the input and output spectra, measured across N periods of the input and output signals. This was termed the error-in-variables (EV) estimator by Guillaume (1992), who showed that it is both asymptotically unbiased and efficient.

Parametric frequency-domain identification involves selecting the parameters of an s-domain model

$$\begin{aligned} H(s) &= \frac{b_0 + b_1 s + \ldots b_{nb} s^{nb}}{a_0 + a_1 s + \ldots a_{na} s^{na}} \exp(-sT_D) \\ &= \frac{N(s)}{D(s)} \exp(-sT_D), \end{aligned} \qquad (3)$$

where nb is the number of zeros, na is the number of poles, and T_D is the pure time delay. Under the assumption of noise on both the input and output signals, Schoukens et al. (1988) derived an estimator of $H(s)$, which was subsequently developed by Pintelon et al. (1992), to arrive at a cost function

Nomenclature

CF = crest factor
F = number of estimation frequencies
FRF = frequency response function
NH = high pressure (HP) shaft speed
NL = low pressure (LP) shaft speed
T_D = pure time delay
$U(j\omega)$ = input Fourier coefficients
$V(\mathbf{p})$ = estimator cost function
V_{MIN} = expected value of cost function
W_F = demanded fuel flow to burners
$Y(j\omega)$ = output Fourier coefficients
$\mathbf{i}$ = harmonic vector
np = number of estimation parameters
$u(t)$ = input signal
σ_P = standard deviation of estimated poles
σ_Z = standard deviation of estimated zeros
ω_K = angular frequency of the Kth harmonic

$$V(\mathbf{p}) = \frac{1}{2}\sum_{K=1}^{F} \frac{|\exp(-j\omega_K T_D) N(j\omega_K, \mathbf{p}) \bar{U}(j\omega_K) - D(j\omega_K, \mathbf{p}) \bar{Y}(j\omega_K)|^2}{\sigma_U^2(\omega_K, \mathbf{p}) + \sigma_Y^2(\omega_K, \mathbf{p}) - \sigma_{UY}(\omega_K, \mathbf{p})}, \tag{4}$$

where the terms $\sigma_U^2(\omega_K, \mathbf{p})$ and $\sigma_Y^2(\omega_K, \mathbf{p})$ are proportional to the variances of the input and and output noises and the term $\sigma_{UY}(\omega_K, \mathbf{p})$ is proportional to their covariance. The summation is across the number of frequency points F and $\mathbf{p}$ is a vector of the model parameters. The covariance term accounts for any correlation between the input and output noise, which in the case of the gas turbine is caused by the turbulence in the fuel flow, which has a stochastic effect on the measured fuel flow and also influences the output.

This somewhat daunting cost function can be interpreted as a least squares formulation, with each frequency point weighted by a noise variance term. Large noise variances at a given frequency will reduce its relative influence on the cost function. The estimator has maximum likelihood properties in the presence of normally distributed noise on the real and imaginary parts of the input and output Fourier coefficients.

Under this assumption, double the value of the cost function is the sum of $2F$ squared Gaussian variables and is hence χ^2 distributed with $2F\text{-}np$ degrees of freedom, where np is the number of estimated parameters. Consequently, if there are no modeling errors, the expected value of the cost function will be

$$V_{\text{MIN}} = F - \frac{np}{2}. \tag{5}$$

The pure time delay T_D can be included as a free parameter for estimation, which is an attractive feature of the frequency-domain approach, since its value is not fixed to multiples of the sampling interval. Numerical techniques developed for nonlinear least squares problems, such as Gauss-Newton, Levenberg Marquard or singular value decomposition, can be used to find the parameters which minimize the cost function.

The frequency response of the estimated model can then be compared to the estimated FRF to see how well the system dynamics have been modeled. The presence of systematic modeling errors may be due to under-modeling, in which case the model order should be increased, or due to nonlinear effects, which cannot be eliminated by fitting higher-order linear models.

4 Test Signal Design

Periodic test signals are a requirement for frequency-domain identification, if systematic leakage errors are to be avoided when transforming the signals to the frequency domain using the fast Fourier transform. The signals must also be sampled across complete periods, using a sampling frequency which is an integer multiple of the signal fundamental.

The periodic signals chosen for application in this work were multisines, which are an arbitrary ensemble of harmonically related cosines

$$u(t) = \sum_{K=1}^{F} a_K \cos(i_K 2\pi f_0 t + \Phi_K), \tag{6}$$

with $\mathbf{a}$ a vector of amplitudes, $\mathbf{i}$ a vector of harmonic numbers, f_0 the signal fundamental frequency, and Φ a vector of phases. The number of harmonics in the signal F must be larger than the number of model parameters to be estimated (np), in order to ensure persistence of excitation. In practice, F should be many times larger than np in order to allow the detection of modeling errors.

The relative phases of the harmonics must be carefully selected to minimize the crest factor (CF) of the signal, which is the ratio of the maximum absolute value of a signal to its root mean square (rms) value.

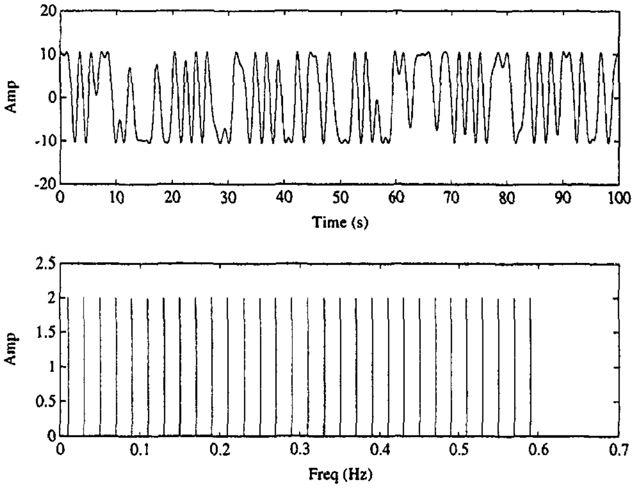

Fig. 2 30 odd-harmonic, low CF multisine

$$\text{CF} = \frac{\max\{|u(t)|\}}{\text{rms}\{u(t)\}} \tag{7}$$

This is a measure of the time-domain compression of a signal and it is desirable that the CF of a multisine signal approaches that of a single sine, which is always $\sqrt{2}$. The problem of CF minimization has been addressed by many authors and, while no analytical solution has yet been found, a number of approaches yield significantly improved values. The technique proposed by Guillaume et al. (1991) produces the lowest CF achieved to date and was the method employed in this work.

The signals employed for these tests were designed using a priori information, gleaned from previous engine tests. The previous tests suggested second-order shaft speed models, with poles at 0.07 Hz and 0.14 Hz for the HP shaft and at 0.08 Hz and 0.27 Hz for the LP shaft. The low-frequency modes detected in these data were of particular interest, since they are not predicted by the thermodynamic models.

A signal composed of 30 odd-harmonics was thus designed, with a fundamental frequency of 0.01 Hz, the harmonic vector of which is given in Eq. (8). This choice of fundamental frequency and number of harmonics ensures that the power of the test signal is concentrated in the frequency range suggested by the previous data.

$$\text{Odd Multisine} \quad \mathbf{i} = [1\ 3\ 5\ 7\ 9\ 11 \ldots 59] \tag{8}$$

A signal such as this, composed of only odd-harmonics, is immune to even-order nonlinear effects and remains amenable to CF minimization (see Evans et al., 1995). The CF was minimized using the Guillaume approach and the resulting signal is shown in the time and frequency domains in Fig. 2. This signal was injected at ±2 percent, ±5 percent, and ±10 percent of the demanded steady-state fuel flow (W_F), in order to investigate any nonlinear effects.

The results obtained with the 30 odd-harmonic signal were cross-validated using a 15 odd-harmonic signal with the same bandwidth but with its power concentrated at low frequencies. This will be termed a quasi-log multisine since it has a spectrum which is similar in appearance to that of a log-tone signal. The harmonic vector of the signal is given in Eq. (9) and the design allows more power to be injected at low frequency, for a given maximum time-domain amplitude, as shown in Fig. 3.

$$\text{Quasi-log Multisine} \quad \mathbf{i} = [1\ 3\ 5\ 7 \ldots 37\ 43\ 51\ 59] \tag{9}$$

5 Engine Testing and Data Analysis

The engine tests were conducted at the Glen sea-level test facility of the Defence Evaluation and Research Agency at Pye-

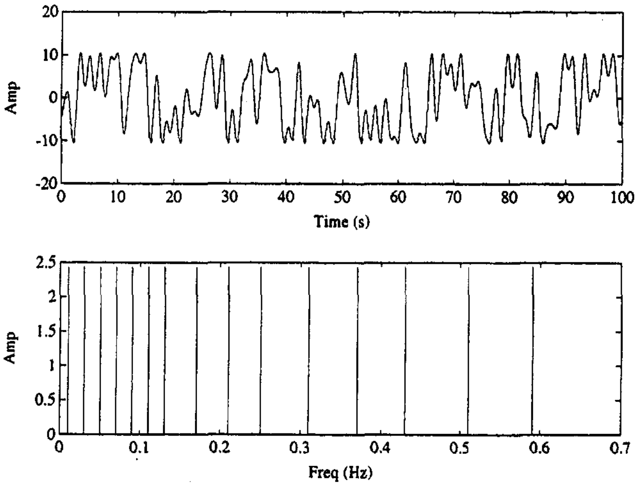

Fig. 3 15 quasi-log harmonic, low CF multisine

stock. The initial tests were conducted at an operating point of 75 percent of the maximum *NH* (henceforth, 75 percent *NH*). The results of these tests will now be described in some detail. Further tests were then conducted at a series of different operating points, which will be discussed in Section 8.

The engine is controlled by five primary inputs, these being: the fuel flow, the angle of the inlet guide vanes, the reheat nozzle area, the reheat fuel flow, and the HP compressor bleed valve position. The reheat system was inoperative during the tests and the compressor bleed valve was closed. The angle of the inlet guide vanes and the reheat nozzle area were fixed to their low speed positions for the duration of the tests.

Once the engine had stabilized at 75 percent *NH*, the speed control was operated in open loop and a perturbed fuel demand signal fed to the fuel feed system, which regulated the fuel flow to the engine by means of a stepper valve. Since the fuel feed valve has both linear and nonlinear dynamics, the actual fuel flow was measured downstream of the valve using a turbine flow meter.

Six signal periods were measured during each test, in order to allow signal averaging. The signal-to-noise ratios were found to be very good, with raw values of around 25 dB at the input and 30 dB at the outputs, for input amplitudes of ±10 percent W_F. These were improved by over-sampling and excluding the noise lines from the data and also by averaging over the six periods, to arrive at values of 40 dB at the input and 42 dB at the outputs.

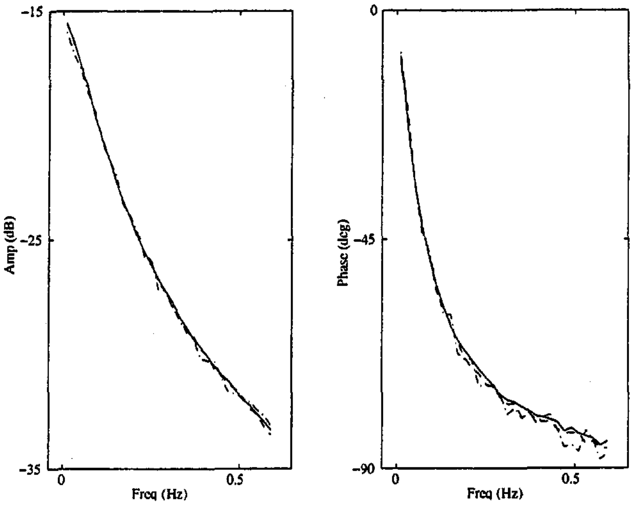

Fig. 4 Estimated FRF's of HP shaft at ±10 percent W_F (solid), ±5 percent W_F (dashed) and ±2 percent W_F (dash-dot)

Table 1 Cost function for HP shaft models

Order	Cost Function - $V(\mathbf{p})$	V_{MIN}
0/1	280	28.5
1/2	34	27.5
2/3	32	26.5
3/4	28	25.5

The influence of nonlinearities was examined using techniques described in detail by Evans et al. (1995). Lack of space prevents a full discussion of these methods in this paper but they revealed the presence of a weak even-order nonlinear effect in the engine, for an input amplitude of ±10 percent W_F. This nonlinearity did not have any influence on the test signals used, since they were composed of only odd-harmonics and hence all even-order nonlinear contributions fell at even output harmonics. Using the odd multisine data for linear estimation will thus give high quality estimates of the engine dynamics, unaffected by nonlinearities.

6 Identification of Gas Turbine Models

The FRF's of the HP and LP shafts were estimated for each of the tests, using the H_{EV} estimator defined in Eq. (2). The FRF's of the HP shaft, calculated with the 30 odd-harmonic data at each of the three input amplitudes, are plotted in Fig. 4. It can be seen that the bandwidth of the test signals was well chosen, since they cover a drop of 17 dB in the amplitude and a phase shift of −10 to −80 deg.

The plots are very similar, with the only real difference being the increased scatter in the FRF estimated with the data gathered at an amplitude of ±2 percent W_F, which can be attributed to the increased influence of noise. This suggests that the FRF is not dependant on the amplitude of the input signal and that the influence of nonlinearities is indeed very small.

The estimation of s-domain transfer function models will now be considered for each shaft in turn. Only the data gathered at an amplitude of ±10 percent W_F will be considered, since the noise effect is reduced at the higher amplitude and the nonlinear effects are seen to be minimal.

6.1 High Pressure Shaft. The variation of the estimator cost function with model order is shown in Table 1 for the 30 odd-harmonic signal. The value of V_{MIN} was calculated using Eq. (5), with the number of estimation frequencies fixed at 30 and the number of estimated parameters varying from three to nine. The major drop in the cost function occurs with the one zero, two pole (1/2) model, suggesting that this is the best structure. Table 2 shows the pole and zero positions of the first three of these models, with their standard deviations expressed as a percentage of their magnitudes.

The 1/2 model has a pole-zero pair close to the origin, whose 2σ

Table 2 Estimation results for HP shaft

Order	Delay (ms)	Zeros	σ_Z (%)	Poles	σ_P (%)
0/1	8.5	—	—	-0.5015	0.2
1/2	13.2	-0.3405	9.2	-0.2749 -0.6017	7.3 2.4
2/3	12.5	-0.3606 -19.640	11 64	-0.2860 -0.6145 16.336	8.1 3.6 39

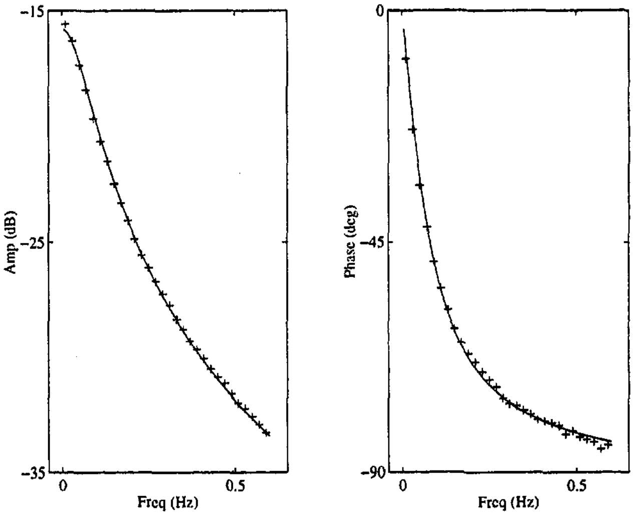

Fig. 5 Frequency response of model (solid) and FRF (crosses), for 0/1 model, HP shaft

Table 3 Cost function for LP shaft models

Order	Cost Function - $V(\mathbf{p})$	V_{MIN}
0/1	4609	28.5
1/2	69	27.5
2/3	39.55	26.5
3/4	39.54	25.5

regions of uncertainty do, however, overlap. Adding another pole and zero gives an unstable pole, which is not a credible model. The frequency responses of the 0/1 and 1/2 models are shown in Figs. 5 and 6, where the additional pole and zero are seen to be modeling a localized low-frequency effect.

These models were cross-validated using the 15 quasi-log harmonic data and the results showed the same pattern as those for the 30 odd-harmonic signal, with the major drop in the cost function occurring with the 1/2 model. This model has a dominant pole at $s = -0.5$ and a close pole-zero pair near the origin, with overlapping 2σ uncertainty regions.

It could be argued that the close pole-zero pairs in the 1/2 models estimated with each data set are simply an indication of over-modeling. However, they are seen to model a real feature of the data in each case, this being the slight shift in the FRF at low frequency, which cannot be fitted by a first-order model. The drop in the estimator cost function is also very significant.

This indicates the presence of a localized low-frequency dynamic, though the difference between the models suggests that there is some uncertainty about the exact location of the pole and zero. The low-frequency pole is at 0.04 Hz in the model estimated with the 30 odd-harmonics and at 0.02 Hz in the model estimated with the 15 quasi-log harmonics. Since the fundamental frequency of the signals is only 0.01 Hz, the pole-zero pairs are clearly on the limits of modeling with these data.

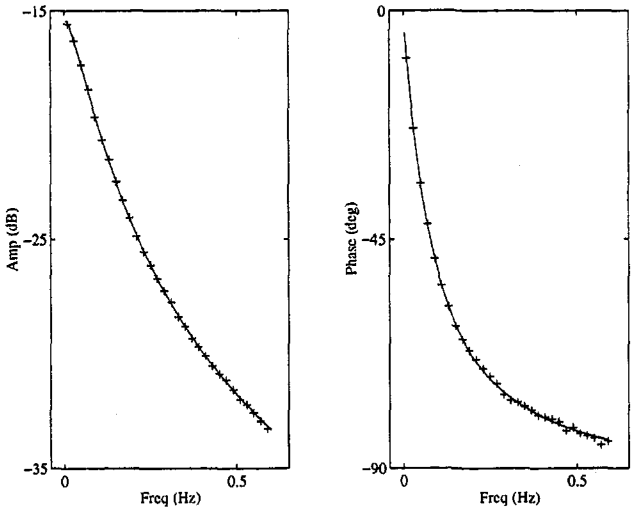

Fig. 6 Frequency response of model (solid) and FRF (crosses), for 1/2 model, HP shaft

6.2 Low Pressure Shaft. The variation of the cost function for the LP shaft models, estimated using the 30 odd-harmonic data, is presented in Table 3. The large drop in the cost function between the 0/1 and 1/2 models shows that the dynamics are at least second-order. There is even a case for selecting a 2/3 model, though the drop in the cost function is not as significant as that for the 1/2 model.

Table 4 shows that the 2/3 model has a very close pole-zero pair near the origin, the uncertainty regions of which do overlap. This close pole-zero pair is once again modeling a low-frequency effect in a similar way to the pole-zero pair in the 1/2 model of the HP shaft. The difference between the frequency response of the 1/2 and 2/3 models is however so small as to be almost indistinguishable in Fig. 7.

Once again, cross-validation was performed using the 15 quasi-log harmonics and the results were found to be very similar. The low-frequency pole-zero pairs are once again on the limits of modeling but there is a case for selecting the 2/3 model.

6.3 Pure Time Delay. Another advantage of parametric frequency-domain estimation is that the delay can be included as a parameter for estimation. Values of between 13 and 21 ms were obtained for the selected models of each shaft, which match the values of combustion delay proposed by Thomson (1974), of around 15–20 ms for a typical engine. This small delay presents a problem in the time-domain estimation of discrete models, since faster sampling is required in order to correctly specify the delay. This can introduce problems of numerical conditioning if the sampling interval T_s is greatly reduced. The poles and zeros of the discrete model will tend to cluster around the point $z = 1$, since $z = \exp(sT_s)$.

7 Comparison With Thermodynamic Models

Models of the HP and LP shafts have been estimated with a high degree of confidence from the test data and it is now possible to

Table 4 Estimation results for LP shaft

Order	Delay (ms)	Zeros	σ_Z (%)	Poles	σ_P (%)
0/1	-32	—	—	-0.7939	0.2
1/2	14.7	-0.9064	2.2	-0.4199 -1.8250	1.2 1.7
2/3	17.2	-0.1127 -1.0496	31 3.9	-0.1042 -0.4754 -1.9783	30 3.3 2.6
3/4	17.3	-0.1156 -1.0533 1.5033	31 4.1 28	-0.1068 -0.4768 1.5026 -1.9831	30 3.4 28 2.7

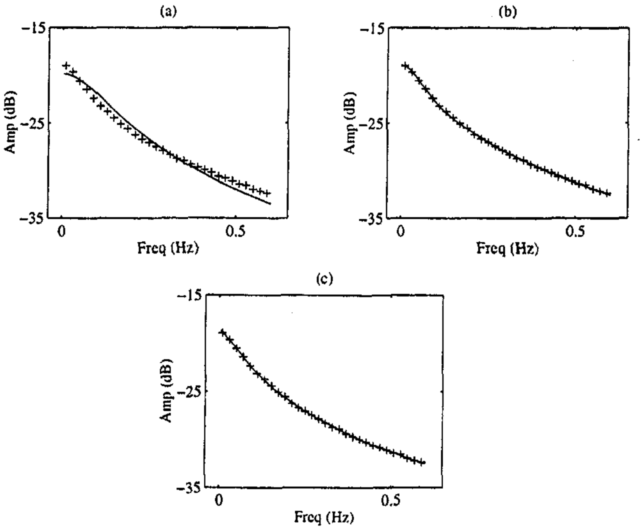

Fig. 7 Amplitude response of LP shaft models (solid) and FRF (crosses), for model orders (*a*) 0/1, (*b*) 1/2, and (*c*) 2/3

compare these with the thermodynamic models derived from the engine physics. In Table 5, the estimated 1/2 HP shaft model, previously listed in Table 2, is compared with the thermodynamic model at 75 percent NH.

Each of the models has a dominant pole close to the same point (around 0.1 Hz) and an additional close pole-zero pair, which indicates that the HP shaft dynamics are predominantly first order. The major difference is that the pole-zero pair of the frequency-domain model is much closer to the origin. This has been shown to model a real feature of the data but it is clearly modeling a different effect to that modeled by the higher frequency pole-zero pair in the thermodynamic model.

For the LP shaft, the estimated 2/3 model is compared with the 1/2 thermodynamic model in Table 6. The separation of the zero and poles of the thermodynamic model is greater than that in the HP shaft model, suggesting that the dynamics are at least second order.

Neglecting for a moment the close pole-zero pair in the frequency-domain model, a direct comparison can be made between the two models. The dominant pole of the frequency-domain model is at a lower frequency than that of the thermodynamic model, with a time constant of 2.1 sec. compared to 1.4 sec. The zero and second pole are also at a lower frequency. This suggests that the LP shaft response is actually slower than that predicted by the thermodynamic model at 75 percent *NH*.

Comparing the frequency-domain results for the HP and LP shafts it is seen that they share a close, but not identical, dominant mode at a frequency of around 0.09 Hz. The results suggest that the HP shaft dynamics are first order and the LP shaft dynamics are second order. The additional pole-zero pairs in the estimated models are too slow to be associated with these shaft dynamics and are probably modeling a heat soakage effect.

Such effects become prominent during large transient manoeuvres of an engine and while the tests were carried out around a fixed operating point there may have been sufficient variation of the engine operation during the tests to excite some heat transfer dynamics. It is possible that the low-frequency modes are modeling one of the faster heat soakage effects, such as blade expansion. Blade expansion time constants of 5 sec. were quoted by Hennecke and Trappman (1982) and blade and casing time constants of 2 sec. and 10 sec. respectively, by Pilidis and Maccallum (1982). The estimated low-frequency modes have time constants of between 3 and 10 sec.

Table 5 Comparison of models, HP shaft

	S-plane Zeros	*S*-plane Poles	Time Constants
Frequency-domain Model	-0.34	-0.27	3.6
		-0.60	1.7
Thermodynamic		-0.70	1.4
Model	-3.14	-3.16	0.3

Table 6 Comparison of models, LP shaft

	S-plane Zeros	*S*-plane Poles	Time Constants
Frequency-domain	-0.11	-0.10	9.6
Model		-0.48	2.1
	-1.05	-1.98	0.5
Thermodynamic		-0.70	1.4
Model	-2.75	-3.16	0.3

8 Variation With Operating Point

In addition to a detailed study at 75 percent *NH*, tests were conducted at a range of other operating points and parametric models estimated. The poles and zeros of these models will now be compared to those of the thermodynamic models, which were previously plotted in Fig. 1. This comparison will focus on the shaft dynamics and the low-frequency pole-zero pairs discussed in the last section will not be included.

The poles and zeros of the estimated HP and LP shaft models are plotted in Fig. 8, along with those of the thermodynamic models. It can be seen that the estimated HP shaft pole matches the lower frequency pole of the thermodynamic model quite well, up to an operating point of 80 percent *NH*. There is a clear discrepancy between the models at higher operating points.

For the LP shaft, the estimated 1/2 models have a pole at low frequency, a second pole at a higher frequency and a zero which migrates between them as the shaft speed increases. This suggests that the low-frequency pole is dominant at lower operating points,

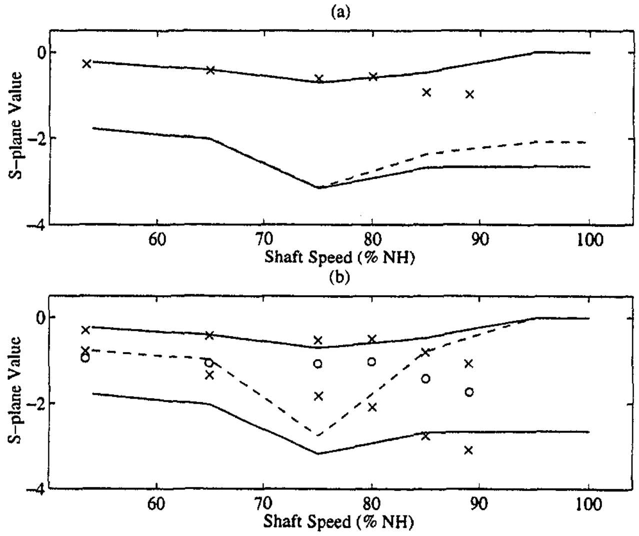

Fig. 8 Variation of engine models for (*a*) HP shaft and (*b*) LP shaft. Estimated models shown as poles (x) and zeros (o) and thermodynamic models as poles (solid) and zeros (dashed).

while the dynamics of the higher frequency pole are more significant at higher shaft speeds.

Comparing the estimated LP models with the thermodynamic models, there is once again quite good agreement between the low-frequency poles, up to an operating point of 80 percent *NH*. However, the second pole of the estimated models is at a lower frequency for most of the operating range and the variation of the zero with shaft speed is very different to that of the thermodynamic models. Both the estimated and thermodynamic models suggest that the influence of the low frequency pole is reduced at higher shaft speeds.

It is clear from these results that the thermodynamic models are not adequately representing the dynamics of either shaft at higher operating points and that the second-order dynamics of the LP shaft are also badly represented. These second-order dynamics are of particular interest since they model the interaction between the shafts.

9 Conclusions

The frequency-domain identification of the fuel flow to shaft speed dynamics of a twin-shaft gas turbine has been studied, with the aim of validating the thermodynamic engine models. Frequency-domain methods are better suited to the aims of this investigation and to the measurement setup employed. The s-domain models required for validating the thermodynamic models can be directly estimated and the use of a measured, noise corrupted, input signal is assumed as part of the estimator model.

The results presented in this paper show the potential of employing broad-band multisines as test signals. Such signals can be designed to concentrate their whole power within the system bandwidth. The flexibility of multisine signals has been illustrated by the different signal designs applied to the gas turbine. Application of multisine signals significantly reduces the time taken to test an engine.

High quality models of each shaft were estimated using the 30 odd-harmonic data and their fit to the frequency data was illustrated. The results were cross validated on a data set of 15 quasi-log harmonics and the estimated models found to be broadly similar. The pure time delay was included as a parameter for estimation and the results were close to those obtained in previous studies for a typical gas turbine.

The estimated models show the HP shaft dynamics to be first order and the LP shaft dynamics second order. The models thus match the linearized thermodynamic models in terms of overall structure. A comparison of the models showed that the first-order shaft dynamics are well represented by the thermodynamic models, up to an operating point of 80 percent *NH*. There is a clear discrepancy above this point. In addition, the variation of the second-order dynamics of the LP shaft is very different to that predicted by the thermodynamic models. This suggests that the derivation of the thermodynamic models needs to be re-examined.

Additional low-frequency effects were detected on both shafts which could be modeled by the addition of a close pole-zero pair. The time constants of the additional pole-zero pairs are too slow to be associated with the shaft dynamics and suggest that they are modeling thermal effects, which are not incorporated in the thermodynamic models. Further work is currently being conducted to verify the presence of these modes, using test signals with a lower fundamental frequency.

The presence of a weak even-power engine nonlinearity was detected during the data analysis, which did not influence the test frequencies due to the use of odd-harmonic signals. It was thus possible to use frequency-domain techniques to estimate linear engine models which were free from the influence of any significant nonlinear effects. It can be stated with some confidence that the small signal dynamics of the shafts have been accurately identified, which is shown clearly by the quality of the model fits to the frequency data.

The use of frequency-domain techniques thus overcomes the problem associated with the more commonly applied time-domain methods, where discrete models are estimated which include a single real negative pole. Such a pole has no continuous counterpart and cannot be compared to the poles of the s-domain thermodynamic models.

This work has produced a large body of results and illustrates the potential of frequency-domain techniques for modeling industrial systems where a physical interpretation of the model parameters is to be made. This is particularly true if the system contains a pure time delay, which can be freely estimated in the frequency domain, or if the input signal has to be measured in order to eliminate the input actuator dynamics.

Acknowledgments

This work was conducted with the support of Rolls Royce plc and the UK Defence Evaluation and Research Agency at Pyestock. The authors would like to thank all the staff involved.

References

Cottington, R. V., and Pease, C. B., 1979, "Dynamic Response Testing of Gas Turbines," ASME *Journal of Engineering for Power*, Vol. 101, pp. 95–100.

Dadd, G. J., Sutton, A. E., and Greig, A. W. M., 1996, "Multivariable Control of Military Engines," AGARD Conference Proceedings No. 572, *Advanced Aero-Engine Concepts and Controls*, Paper No. 28, pp. 1–12.

Evans, C., Rees, D., and Jones, L., 1995, "Identifying Linear Models of Systems Suffering Nonlinear Distortions, With a Gas Turbine Application," IEE Proceedings, *Control Theory and Applications*, Vol. 142, No. 3, pp. 229–240.

Evans, C., 1998, "Identification of Linear and Nonlinear Systems Using Multisine Signals, With a Gas Turbine Application," PhD thesis, University of Glamorgan, School of Electronics, Wales, UK.

Fitchie, J. W., White, S. W., Cronshaw, R. H., and Willcocks, H. J., 1959, "An Experimental and Theoretical Study of the Response of a Two Shaft Turbojet Subjected to Small Disturbances," National Gas Turbine Establishment (UK), Note NT 420.

Guillaume, P., Schoukens, J., Pintelon, R., and Kollár, I., 1991, "Crest Factor Minimisation Using Nonlinear Chebyshev Approximation Methods," *IEEE Trans. Instrumentation and Measurement*, Vol. 40, No. 6, pp. 982–989.

Guillaume, P., 1992, "Identification of Multi-Input Multi-Output Systems Using Frequency-Domain Methods," Ph.D. thesis, Vrije Universiteit Brussel, Department ELEC, Belgium.

Hennecke, D. K., and Trappmann, K., 1982, "Turbine Tip Clearance Control in Gas Turbine Engines," AGARD Conference Proceedings No. 324, *Engine Handling*, Paper No. 16, pp. 1–12.

Hill, D. C., 1994, "System Identification of Gas Turbine Engines," PhD. thesis, University of Birmingham, School of Electronic and Electrical Engineering, UK.

Hill, D. C., 1997, "Identification of Gas Turbine Dynamics: Time-Domain Estimation Problems," *ASME Gas Turbine Conference*, Paper No. 97-GT-31.

Jackson, D., 1988, "Investigation of State Space Architectures for Engine Models," Report TDR 9331, Rolls Royce plc.

Lawrence, J. O. N., and Powell, R. D., 1957, "The Application of Servo-Mechanism Analysis to Fuel Control Problems," Proceedings of the Institute of Mechanical Engineers, Vol. 172, pp. 439–469.

Onions, R. A., and Foss, A. M., 1982, "Improvements in the Dynamic Simulation of Gas Turbines," AGARD Conference Proceedings No. 324, *Engine Handling*, Paper No. 27, pp. 1–16.

Pilidis, P., and Maccallum, N. R. L., 1982, "Models for Predicting Tip Clearance Changes in Gas Turbines," AGARD Conference Proceedings No. 324, *Engine Handling*, Paper No. 17, pp. 1–10.

Pintelon, R., Guillaume, P., Rolain, Y., and Verbeyst, F., 1992, "Identification of Linear Systems Captured in a Feedback Loop," *IEEE Trans. Instrumentation and Measurement*, Vol. 41, No. 6, pp. 747–754.

Saravanamuttoo, H. I. H., and Fawke, A. J., 1970, "Simulation of Gas Turbine Dynamic Performance," *ASME Gas Turbine Conference*, Paper No. 70-GT-23.

Schoukens, J., Pintelon, R., and Renneboog, J., 1988, "A Maximum Likelihood Estimator for Linear and Nonlinear Systems—A Practical Application of Estimation Techniques in Measurement Problems," *IEEE Trans. Instrumentation and Measurement*, Vol. 37, pp. 10–17.

Staff at Section APD5, 1993, "Thermodynamic Model of the Spey Engine. Linearised for Rolls Royce by Stirling Dynamics Ltd," DRA Pyestock.

Thomson, B., 1974, "Basic Transient Effects of Aero Gas Turbines," AGARD Conference Proceedings No. 151, *Power Plant Controls for Aero-Gas Turbine Engines*, Paper No. 2, pp. 1–16.

A. Agazzani

A. F. Massardo
Mem. ASME

University of Genova,
Istituto di Macchine e Sistemi Energetici
Via Montallegro 1,
Genova, Italy

T. Korakianitis
Washington University,
St. Louis, MO 63130

An Assessment of the Performance of Closed Cycles With and Without Heat Rejection at Cryogenic Temperatures

This paper presents optimized cycle performance that can be obtained with systems including a closed cycle gas turbine (CCGT). The influence of maximum temperature, minimum temperature, and recuperator effectiveness on cycle performance is illustrated. Several power-plant arrangements are analyzed and compared based on thermodynamic performance (thermal efficiency and specific work); enabling technologies (available at present); and developing technologies (available in the near term or future). The work includes the effects of utilization of high temperature ceramic heat exchangers and of coupling of CCGT systems with plants vaporizing liquid hydrogen (LH_2) or liquefied natural gas (LNG). Given the versatility of energy addition and rejection sources that can be utilized in closed gas-cycle systems, the thermodynamic performance of power plants shown in this paper indicate the remarkable capabilities and possibilities for closed gas-cycle systems.

Introduction

Even though practical applications of closed cycle gas turbine (CCGT) systems were realized during the Second World War (Keller, 1945), at present they suffer a developmental standstill. This is related to the constant improvements in open cycle gas turbine (OCGT) performance (Stambler, 1994), and to the low cost of natural gas (which makes other energy sources economically uncompetitive). At present, maximum temperatures of OCGT have approached 1750 K (*Turbomachinery International,* 1995), whereas with present enabling technology it is impossible to reach this value in "heavy-duty" CCGT systems. The maximum temperature constraint of CCGT systems is governed by the maximum operating temperature of the heat exchanger adding energy to the closed cycle. Therefore, it is impossible to utilize the blade-cooling technology developed for OCGT systems in CCGT systems.

Past studies of CCGT systems concentrated on matching closed cycle systems with gas-cooled reactors for nuclear applications (McDonald, 1977, 1994a, b; Yan and Lidsky, 1993) and on space or underwater systems (Korakianitis et al., 1993, 1994; Massardo, 1993; Harper et al., 1990; Harper and Jansen, 1990; Massardo and Arnulfi, 1992). Beyond these applications, where CCGT are indispensable, two other terrestrial CCGT applications are presently dominant.

The first application is driven by the interest of the international scientific community in external combustion for OCGT plants (Huang and Wang, 1987; Klara, 1994; Klara et al., 1995; Consonni and Farina, 1995). These systems present the following analogies with CCGT systems: the possibility of exploitation of different energy sources; the need for a recuperating heat exchanger, and the particularly need to operate with energy-addition heat exchangers working at high temperature (in excess of 1500 K in order to achieve good performance). Using the results of research in external combustion systems, and utilizing other experience developed in ceramic materials (Nakakado et al., 1995; Tatsuzawa et al., 1995), it is possible to consider the use of such technologies for closed cycle systems. Therefore, the constraint of maximum allowable material temperature can be overstepped.

The second application involves coupling closed cycle systems with low (cryogenic) temperature heat-rejection sources. This is possible because in closed cycles the working fluid can be chosen for the operating requirements of the plant (Lee et al., 1981) and the availability of systems in which the liquefied natural gas (LNG) must be vaporized from 112 K to environmental temperature. In the future, closed cycle gas systems may be coupled to systems for the vaporization of liquid hydrogen (LH_2) from 20 K to environmental temperature (Bisio et al., 1995). This kind of coupling would permit the partial exploitation of the exergy available during liquefaction of natural gas or hydrogen (Krey, 1979; Griepentrog and Sackarendt, 1976). It also allows the minimum temperature of closed cycle plants to be substantially reduced from the environmental temperature, and results in very high CCGT performance (thermal efficiency and specific work).

Sample component arrangements of simple or combined plants using technology mentioned above are shown in Fig. 1, and analyzed in the remainder of this paper. Beginning from "standard" conditions (those feasible at present), and using technological limits for compressor pressure ratio and recuperator effectiveness, the performance of more-advanced cycles (with maximum temperatures up to 1700 K and minimum temperatures down to 50 K) are evaluated. Cycle performance has been evaluated using an automatic calculation method coupled with a nonlinear constrained minimization algorithm (Massardo et al., 1990). The results of this paper identify near-term development areas of CCGT plants.

Calculation Model

The calculation method used to generate the results has been specifically developed to predict the optimum performance of closed cycle gas turbine systems. The structure and the capabilities of the model have been described in previous papers (Massardo, 1993).

The system (plant) whose performance is to be evaluated is defined as an ensemble of interconnected components. This

---

Contributed by the International Gas Turbine Institute and presented at the 41st International Gas Turbine and Aeroengine Congress and Exhibition, Birmingham, United Kingdom, June 10–13, 1996. Manuscript received by the ASME Headquarters March 3, 1996. Paper No. 96-GT-344. Associate Technical Editor: J. N. Shinn.

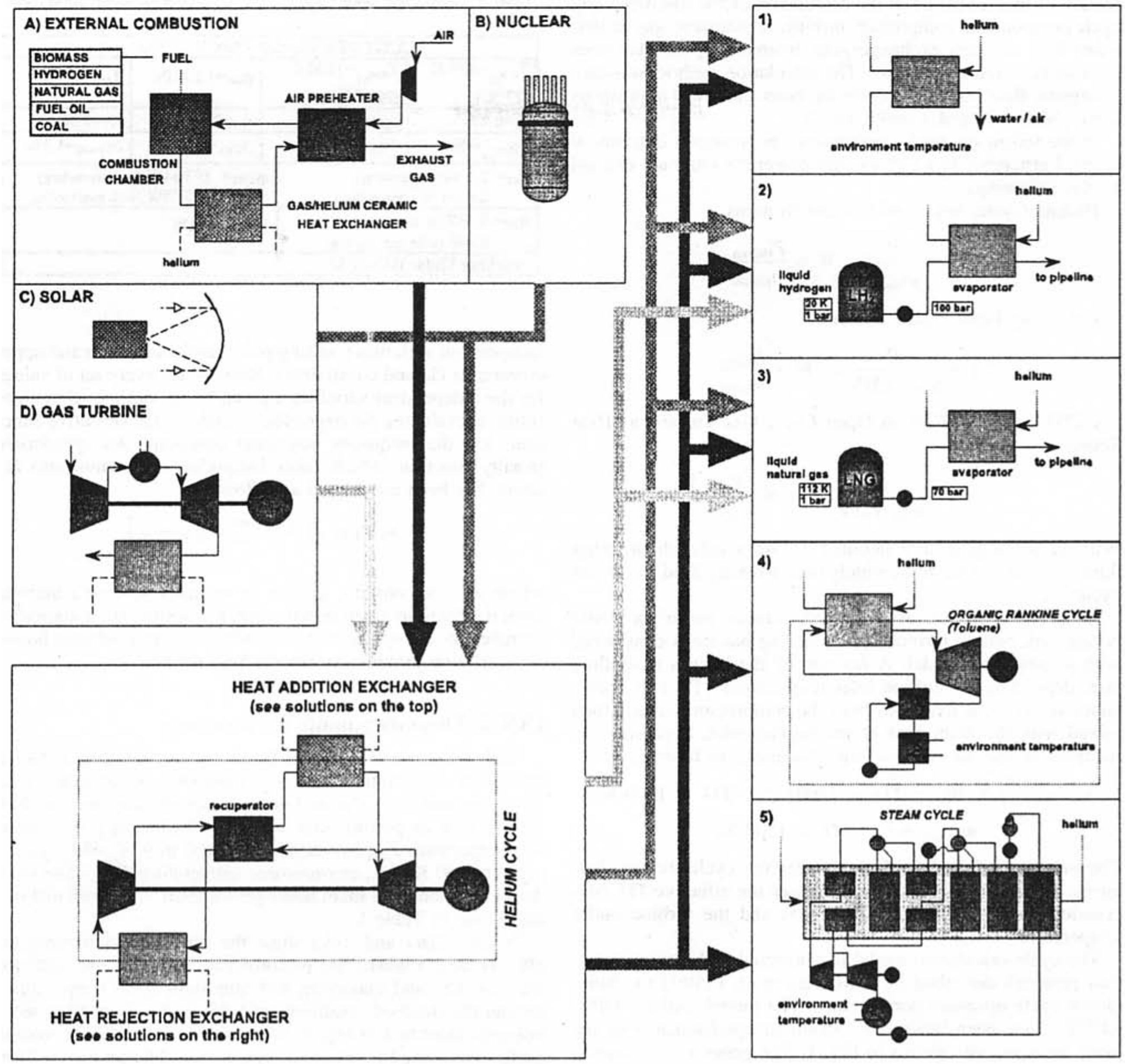

Fig. 1 Power system arrangements including closed cycle gas turbine (CCGT)

allows a modular component structure to be used. Operating characteristics and mass/energy balances of each component are calculated sequentially until the thermodynamic conditions (pressure, temperature, mass flow, etc.) at all component interconnections converge towards a stable value. Aside from the algorithm handling the component network, the most distinctive

Nomenclature

CCGT = closed cycle gas turbine
EC = external combustion
F = objective function
g = set of inequality constraints
LHV = fuel low heating value (kJ/kg)
h = set of equality constraints
m = mass flow rate (kg/s)
OCGT = open cycle gas turbine
ORC = organic rankine cycle
p = pressure (bar)
P = net power (kW)
T = temperature (K)
W = specific work (kW/kg/s)
x = set of independent decision variables for optimization
y = set of dependent variables
β = pressure ratio
ϵ = recuperator effectiveness
η = thermal efficiency
φ = heat flow rate (kW)
φ_1 = rate of CCGT heat addition (kW)

Subscripts

c = compressor
cold = cold side
el = electrical
env = environment
g.c. = gas cooler
hot = hot side
max = maximum
min = minimum
rec = recuperator
ST = standard
t = turbine
TT = total to total

feature of this model lie in the calculation of the following key cycle components: compressor, turbine, regenerator, gas cooler, waste heat recovery exchanger, etc. Intercooling has also been considered in the calculations. The calculation method for steam or organic-fluid bottoming cycle has been addressed in previous work (Massardo and Arnulfi, 1992).

In the following, cycle performance is presented in terms of thermal efficiency (η) and specific power (W) that are defined by the following:

Helium Cycle, Solar and Nuclear Systems.

$$\eta = \frac{P}{\varphi_{t_{\mathrm{Helium}}}}, \quad W = \frac{P_{\mathrm{Helium}}}{m_{\mathrm{Helium}}}$$

Externally Fired CCGT Systems.

$$\eta = \frac{P}{m_{\mathrm{fuel}} \cdot \mathrm{LHV}}, \quad W = \frac{P_{\mathrm{Helium}}}{m_{\mathrm{Helium}}}$$

CCGT Systems With an Open Cycle Gas Turbine as Heat Source.

$$\eta = \frac{P}{m_{\mathrm{fuel}} \cdot \mathrm{LHV}}, \quad W = \frac{P}{m_{\mathrm{Air}}}$$

Without loss of generality, helium (He) was used as the working fluid because it is the most widely used working fluid for closed cycles.

Even though it was assumed that ceramic materials would be utilized, helium-turbine blade cooling has been considered with a simplified model. A fraction of the helium mass flow rate, depending on turbine inlet temperature (TIT) in accordance with (1), is extracted from the compressor exit and then mixed with the main flow at the turbine inlet, bypassing the recuperator and the ceramic heat exchanger, as follows:

$$m_{\mathrm{cooling}} = 1.5 \cdot 10^{-6} \cdot (\mathrm{TIT} - 1500)^{1.75}, \quad \mathrm{TIT} \geq 1500 \text{ K}$$
$$m_{\mathrm{cooling}} = 0, \quad \mathrm{TIT} < 1500 \text{ K}. \tag{1}$$

The presence of cooling flow changes the cycle thermal balances. The blade cooling flow decreases the effective TIT (decreasing the available enthalpy drop) and the turbine outlet temperature.

The cycle-calculation model is connected with the optimization program described by Massardo et al. (1990) to obtain closed cycle optimum performance. The model, called "OPT-CCGT", has been utilized to obtain the performance of the plant arrangements shown in Fig. 1. The general optimization problem is stated by the objective function

$$\min F = F(x, y)$$

where

$$F = 1 - \eta$$

subject to the constraints

$$h_i(x, y) = 0$$
$$g_j(x, y) \leq 0.$$

The equality constraints h_i are developed by proper analysis of the system. The inequality constraints g_j, defined negative (i.e., g_j must be negative if they are verified), are imposed by the operability of the system, safety considerations, etc.. Therefore, these last are needed since a direct restriction of every single design decision variable doesn't assure that, in a particular combination of them, some dependent variables (thermodynamic or mechanical) may exceed their usual limits.

The computer program for the numerical solution of the optimization problem consists of the following parts: the main program and the optimization algorithm. The main program reads the values of the fixed parameters—the initial values of the independent variables (starting point) and their lower and upper constraints (lateral constraints). Besides, for every set of values for the independent variables x given by the optimization algorithm, it evaluates the dependent variables, the objective function, and the inequality constraint functions. An appropriate penalty function, which takes inequality constraints into account, has been considered as follows:

$$F = F(x, y) + A \cdot \sum_j (|g_j| + g_j),$$

where A is a constant, greater in comparison to F. Starting from the feasible given initial point, the optimization algorithm searches for the optimum. Essentially it solves nonlinear bound minimization problem by the gradient method.

Table 1 CCGT standard conditions and calculation main conditions

CCGT STANDARD CONDITIONS			
$T_{\mathrm{min}_{ST}}$=300 K (27 °C)	$T_{\mathrm{max}_{ST}}$=1100 K (827 °C)	p_{min}=1.2 MPa	T_{env}=25 °C
η_c=0.87	η_t=0.95	η_{el}=0.98	ε_{ST}=0.96
$\Delta p_{\mathrm{rec}_{\mathrm{hot}}}$=4%	$\Delta p_{\mathrm{rec}_{\mathrm{cold}}}$=1.5%	$\Delta p_{\mathrm{g.c.}}$=4%	$\Delta p_{\mathrm{heater}}$=1.3%
β_{ST}= 2.1 (no intercooling) 2.64 (with intercooling)		φ_{recST}= 193 MW (no intercooling) 150 MW (with intercooling)	
η_{ST}= 0.437 (no intercooling) 0.448 (with intercooling)		P=50000 kW	
Working Fluid: HELIUM			

CCGT Thermodynamic Performance

With reference to a closed Brayton cycle working between maximum temperature T_{max} and minimum temperature T_{min}, with pressure ratio β_{TT} and recuperator effectiveness ϵ, Fig. 2(*a*) shows its performance in terms of efficiency η_{TT} versus the temperature T_{max} by varying ϵ from 0 to 0.96, while T_{min} is equal to 300 K (i.e., environment temperature T_{env}). The standard conditions and main assumptions used in the calculations are shown in Table 1.

Figures 2(*a*) and 2(*b*) show the influence of recuperator effectiveness (substantial performance increases are obtained for $\epsilon > 0.8$) and maximum and minimum cycle temperatures around the standard conditions of table 1, using enabling technologies identified in Fig. 1. With $\epsilon = 0.96$, the CCGT system performance reaches efficiency values near 0.45 for $T_{\mathrm{max}} = 1100$ K and 0.6 for $T_{\mathrm{max}} = 1700$ K. It is advantageous to consider intercooling, which allows the performance of the plant to be substantially increased for higher values of ϵ.

Figure 3 shows the variations of maximized efficiency, specific work, pressure ratio, and recuperator heat flow of an optimized CCGT plant versus the variations of T_{max} and T_{min}, with reference to the starting standard (ST) plant values identified in table 1 (η_{ST}, β_{ST}, W_{ST}, $\varphi_{\mathrm{rec}_{ST}}$, $T_{\mathrm{max}_{ST}}$, $T_{\mathrm{min}_{ST}}$). Reducing T_{min} has a much greater effect on thermal efficiency (Figs. 2(*b*) and 3(*a*)) than increasing T_{max}. An efficiency increase of about 30 percent can be achieved by increasing T_{max} by about 60 percent (from 1100 K to 1700 K), while thermal efficiency is almost doubled by decreasing T_{min} by about 80 percent (from 300 K to 50 K).

Figure 3(*b*) shows the specific work variation with T_{min} and T_{max}. In this case, the effect of T_{max} variation is more significant (because of the increase in turbine work), and the effect of T_{min} variations is not so evident (with T_{max} increase of 60 percent the specific work increase is about 150 percent; with T_{min} increase of 60 percent the specific work increase is about 120 percent). With lower T_{min} values (50 K) the specific work increase exceeds 200 percent. This result is important because it is directly connected with the size (and cost) of a CCGT plant.

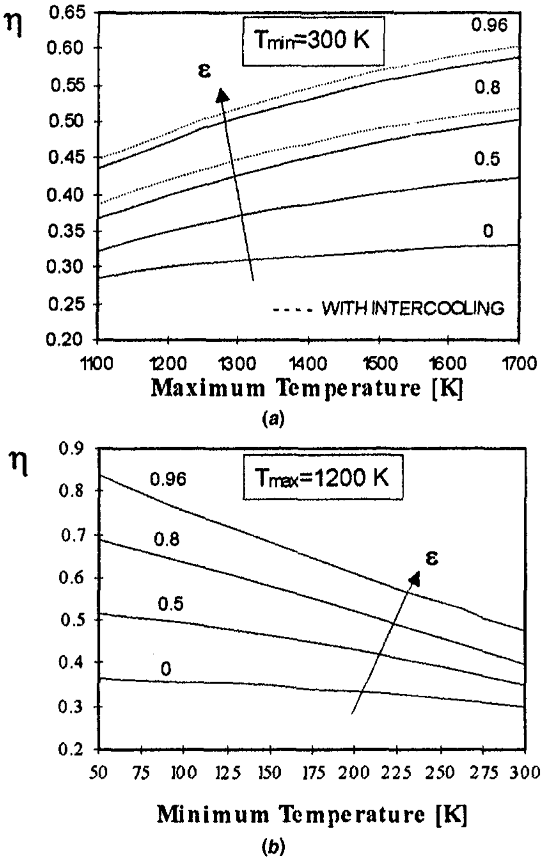

Fig. 2 Influence of T_{max} (*a*) and T_{min} (*b*) on the CCGT efficiency

Increasing the difference between T_{max} and T_{min} implies an increase of recuperator specific heat transfer, easily seen in a temperature versus specific entropy diagram of the cycle. Because of this increase it might be erroneously assumed that the heat flow exchanged by the recuperator also increases considerably. However, for a fixed power plant output, the curves in Fig. 3(*d*) (variation of recuperator heat flow compared to standard values) indicate a significant reduction of mass flow rate. The combination of these two effects results in reduced heat flow through the recuperator, and, therefore, a smaller recuperator. This recuperator reduction is particularly evident when T_{min} is very low. With T_{min} = 100 K, the heat flow decrease is about 60 percent in comparison with the standard value. Similarly, with increases of T_{max} by 60 percent heat flow reductions of around 25–30 percent can be achieved. This result is important because the recuperator size, taking into account the high values of ϵ, affects economics significantly.

Figure 3(*c*) shows the variation of optimal pressure ratio (i.e., the pressure ratio which maximize the thermal efficiency) versus T_{max} and T_{min} percentage variations. This analysis has been carried out to estimate if such variations require optimal pressure ratio values greater than 4. This pressure ratio has been considered an upper constraint for helium (low molecular weight) because it is necessary to limit the maximum number of stages of compressors and turbines (McDonald, 1995). Figure 3(*c*) indicates that T_{min} reduction permits an increase in β. With T_{min} values near 100 K, the maximum value $\beta = 4$ must be selected instead of the higher optimized value obtained without the constraint. The influence of T_{max} is very low.

Figure 3 shows the performance variations obtainable with new technologies in CCGT systems. However, it is instructive to show the performance of CCGT plants in thermal efficiency versus specific work diagrams (η-W). Figure 4 shows the optimized performance (in each case the optimum pressure ratio for maximum thermal efficiency has been specified) of CCGT with and without intercooling by varying T_{max} from 1100 K to

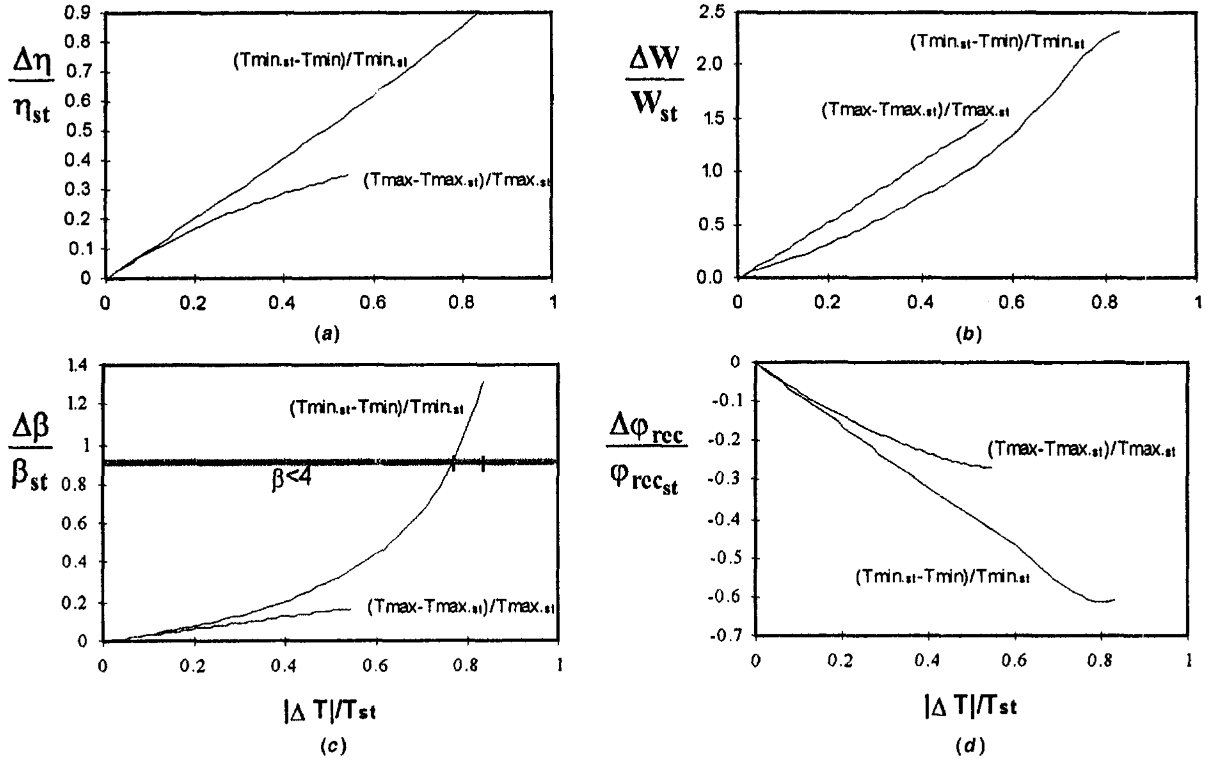

Fig. 3 Variation of CCGT performances compared to standard conditions (Table 1): (*a*) efficiency; (*b*) specific work; (*c*) pressure ratio; and (*d*) recuperator heat flow rate

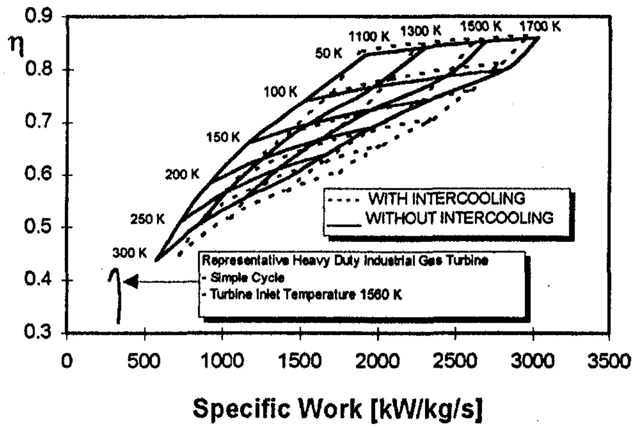

Fig. 4 CCGT efficiency versus specific work

1700 K and $T_{\min}$ from 300 K to 50 K. The curve of a standard open cycle gas turbine with $T_{\max} = 1560$ K and $T_{\min} = 288$ K for various pressure ratios is also shown in the same figure for comparison. Clearly, the specific work and thermal efficiency values of a CCGT are higher than those of a simple OCGT system. The main contributor in these performance increases is the decrease of $T_{\min}$. For $T_{\min} = 50$ K, the efficiency is always greater than 0.8 and the specific work reaches values higher than 2000 kW/kg/s (with helium as working fluid). If intercooling is considered, these values become slightly higher. For $T_{\min} = T_{\text{env}} = 300$ K, the influence of $T_{\max}$ is more evident and provides efficiencies in excess of 60 percent, with a specific work equal to 1500 kW/kg/s, about four times higher than the open cycle gas turbine. The technological implications of the high performance obtained for high $T_{\max}$ and low $T_{\min}$ (for $T_{\max} = 1700$ K and $T_{\min} = 50$ K the thermal efficiency and specific work are higher than 0.85 and 3000 kW/kg/s, respectively) are discussed below.

Enabling and Developing Technologies

CCGT systems development depends on the following: enabling technology; transfer of enabling technology from the combustion gas turbine industry; ceramic developments; and heat rejection at cryogenic temperatures.

Enabling Technology for CCGT Systems. This is based on the following two main aspects: operating experience from the Oberhausen II gas turbine plant and experience from Helium cooled reactor plants. The largest of the European closed cycle gas turbines was the 50 MW Oberhausen II helium turbine that operated in Germany (Zenker, 1988). The selection of a relatively low system pressure for this plant yields a larger volumetric flow of the working fluid, and, accordingly, the actual equipment is comparable in size to a plant rated close to 300 MW. Valuable experience from operation of this plant is in the areas of plant control, component characteristics, acoustic data, transient data, helium leak tightness, and reliability. Experience gained from the operation of Helium circulators in the AVR (Arbeigtsgemeinschaft Versuch Reaktor), THTR (Thorium High Temperature Reactor), and FSV (Fort St. Vrain reactor) nuclear plants provides another valuable data source for CCGT systems. Particularly valuable expertise associated with helium operation includes sealing techniques (which are difficult with a low molecular weight gas) and coatings (to avoid galling and self-welding in mating oxide-free surfaces).

Another source of enabling technology for CCGT plants is the small closed cycle turbine for space power generation. Over the last 30 years, extensive design and development has been undertaken in the USA by Allied-Signal and others on small-size CCGT (up to 100 kW). Most of the units were designed to operate on a mixture of helium/xenon gas, and were designed for operation with a variety of heat-addition sources. While these units were small, much of the experience gained with their operation using an inert gas is applicable to large size CCGT turbo-compressors, particularly in the areas of seals, materials, rotor-dynamic stability, high effectiveness plate-fin recuperators, and system control. The reliability of these CCGT systems was convincingly demonstrated in tests done at NASA-Lewis laboratory (Harper et al., 1990).

Transfer of Enabling Technology From the Combustion Gas Turbine Industry. The key to near term deployment of CCGT plants is the transfer of enabling technologies from the combustion gas turbine industry (Massardo and McDonald, 1995). Technology transfer is required in the areas of analytic and design methodologies, compressor and turbine aerodynamics, high-effectiveness compact heat exchangers, materials technology, fabrication methods, instrumentation and diagnostics, and testing approaches.

One important transfer area for CCGT performance improvements is turbomachinery design. Well-developed, air-breathing engine analytic and design methodologies are applicable to CCGT systems. Computer codes can be validated and component and system design can be verified based on operational CCGT hardware. Another important transfer area is the utilization of compact recuperators. Significant advancements in heat exchangers have been made in the last decade, with technologies applicable to both clean working fluids (McDonald, 1994b) and air breathing systems. Compact plate fin recuperators combine high effectiveness (0.95) with low pressure loss (2 percent) and small volume. Operating with a clean fluid in a closed circuit (eg., helium), very small hydraulic diameter passages can be used with resultant surface compactness values of the order of three times that of OCGT recuperators. Operating in the laminar flow regime, but with highly offset surfaces, very high heat transfer coefficients can be realized by virtue of the surface geometry, high system pressure, and high thermal conductivity of the working clean fluid (helium). This results in a very high value of thermal density. More details on this aspect of CCGT can be found in McDonald (1994b).

The use of large recuperators in heavy-duty OCGT provides operational experience and materials and fabrication techniques. Experience from aircraft and aerospace applications in the areas of high performance and use of very compact plate-fin geometries is extremely valuable.

High Temperature Ceramic Components (for the Energy-Addition Heat Exchanger). For future power conversion systems (in particular future CCGT), emphasis will be placed on maximizing efficiency. In many cases, this can be achieved only with significant increases in operating temperatures. For future CCGT, high temperatures will necessitate the utilization of ceramic heat exchangers for thermal primary energy recovery. The technology (design, materials, testing) of high temperature ceramic heat exchangers is developed in the field of externally fired OCGT (La Haye and Bary, 1994; Klara 1994; Klara et al. 1995). Heat up, shut downs, quick thermal transients found in gas turbine operations, and fouling are key problems for large heat exchangers and ceramic components. Current development activities in the field of ceramic heat exchangers operating at 1600 K to 1800 K in the presence of corrosive abrasive hot gas are emerging (Gentile, 1995), but it is projected that the encouraging results from these programs will stimulate a broader interest in high temperature waste heat energy recovery. Another important aspect is the considerable effort expended in Japan and the United States to apply ceramic materials to OCGT in order to raise the efficiency of thermal power generation. For example, structural and design results of a hybrid ceramic stator vanes for 1600 K gas turbine are already presented by Nakakado et al. (1995), while studies on turbine vanes and blades for 1800 K are being conducted.

Structural ceramic materials offer excellent characteristics (compared with super alloys) in terms of heat, corrosion and wear resistance at high temperature. The clean working fluid in CCGT plants permits improvements in ceramic materials performance. Ceramic components are also studied and developed for a 300 kW ceramic gas turbine engine (Tsatsusawa et al., 1995).

Development of ceramic heat exchangers for CCGT plants operating at $T_{\max}$ under 1400 K is a near term technology, while for higher temperatures (around 1700 K) it is expected in the near future. For CCGT the heat transfer coefficient of Helium is an important advantage.

Heat Rejection at Cryogenic Temperature (LNG, LH_2). Natural gas is often found in remote locations far from industrial areas, and the gas is transported by pipeline to the end user. Currently, where the gas source and the user are separated by oceans and continents, the only viable way to transport the gas is to convert it to liquid natural gas (LNG), and convey it using insulated LNG tankers at a temperature of approximately 112 K. The LNG is transported to a receiving terminal where it is off-loaded into storage tanks. The LNG is then pumped from storage at the required pressure and vaporized for final transmission to the consumer. A cheap and convenient method of vaporizing the LNG is by using sea water.

The construction of LNG terminals and the need to vaporize LNG offers a cooling source at much lower temperature than that of the environment or sea water. By using the cold sink and by adapting the waste heat available from a cycle plant, it is possible to recover power from the vaporization of LNG. Wong (1994) affirmed that "it is impossible to find a single fluid that will operate within the full range created by the maximum practical temperature and the temperature of LNG." On the contrary, we believe that by utilizing a CCGT system with helium or nitrogen as working fluid, it is possible to operate in these conditions as presented by Krey (1979), Griepentrog and Sackarendt (1976), and Lee (1981).

Snamprogetti and BBC (now ABB) developed an interesting study on LNG regasification plants utilizing nitrogen as the working fluid, including economical evaluation (SP/BBC, 1980). Compared to other inert gases, helium and nitrogen offer the additional advantage of real-gas behavior in the lower temperature range (the power input required for compressor work is less than that for ideal gas).

The output pressure required from LNG vaporizing terminals varies according to the end user (e.g., steam power stations 0.6 MPa; combined cycle station 2.5 MPa; local distribution 3 MPa; and long distance transmission 7 MPa). Therefore, it is possible to include in the plant a turbine for the power recovery from natural gas expansion, thus improving system efficiency.

Bisio et al. (1995) discussed the possibility of coupling CCGT with LH_2 plants to use the physical exergy of LH_2. In this case, due to the very low temperature of LH_2 (20 K) the only utilizable working fluid is helium. While LNG systems are already available, for LH_2 plants we can consider this technology for future or near term applications.

Performance of Power Systems Including CCGT and Utilizing Enabling and Future Technologies

The performance of complex systems including a simple CCGT plant is shown as thermal efficiency (η) versus specific work (W) in Fig. 5. The source for energy addition is nuclear, solar, or external combustion (Fig. 1). The plant solution symbols are based on Table 2.

All points are obtained with the optimization procedure for maximum thermal efficiency. The constraint of helium pressure ratio less than 4 ($\beta < 4$) has been imposed on all systems. The performance has been calculated at four helium $T_{\max}$: 1100 K, 1300 K, 1500 K, and 1700 K (in case A5, a CCGT plant with a steam bottoming plant, performance has been evaluated starting from helium $T_{\max}$ about 1300 K). The following design decision variables have been selected: CCGT pressure ratio and CCGT recuperator effectiveness for all solutions; inlet CCGT compressor temperature for solutions 2, 3, 4, and 5; ORC recuperator effectiveness for solutions 4; and steam pressures for solutions 5. The following inequality constraints have been considered: stack temperature for solutions A; outlet turbine quality for solutions 4 and 5; and heat rejection exchanger pinch point for solutions 2, 3, and 4.

The symbols marked with one or two stars indicate plants in which vaporized LH_2 or LNG is expanded to produce further useful power, as described by Bisio et al. (1995), until a pressure of 25 bar for natural gas (marked with *) or a pressure of 5 bar for hydrogen and natural gas (marked with * and **, respectively).

The efficiency of a CCGT system coupled with a nuclear reactor has been estimated equal to that of the helium cycle (i.e., ratio of net helium cycle power to rate of nuclear heat addition). The intercooled cycle directly coupled to a reactor ("direct cycle," Yan and Lidsky, 1993) is analyzed using $T_{\min} = 300$ K (T_{env}) and $T_{\max}$ from 1100 K to 1300 K ($T_{\max} = 1300$ K is the maximum temperature at which a helium nuclear plant could operate in the near future). The performance of nuclear power plants is plotted in Fig. 5 using symbols B1 (Table 2). As mentioned by McDonald (1977, 1994a, 1994b, 1995), Fig. 5 indicates that it is possible to achieve thermal efficiencies near 50 percent, remarkably greater than those of nuclear plants with water cooled reactors or liquid metal cooled reactors (MHTGR Plant, 1993).

Matching a steam bottoming cycle or an organic rankine cycle (ORC) with nuclear source of energy addition is not considered because of obvious economic reasons, and the low gas temperature at the low pressure side recuperator exit (i.e., heat rejection exchanger inlet). Coupling cooling systems operating at cryogenic temperatures (combinations B2 and B3, table 2) with nuclear energy appears antithetical to utilization of hydrogen and natural gas. Such possibilities are not absolutely discarded (Bisio and Cerullo, 1993), and, therefore, their performance has been evaluated and shown in Fig. 5 (see curves B2-B2, B2*-B2*, B3-B3, B3*-B3*, B3**-B3**).

Solar energy addition with ceramic materials would permit high $T_{\max}$ values (1700 K), and the efficiency of the solar system has been modeled using space application analyses by Harper et al. (1990) and Massardo (1993). The analyses of solar systems should take into account the availability of solar energy over time (it has been assumed here that the collectors are big enough for continuous operation), and the thermal stresses to which the solar receiver is subjected (constraint on $T_{\max}$). It is possible to match solar energy addition with heat rejection to LNG or LH_2 liquefaction. The corresponding curves of actual and future performance are marked C1 ($T_{\min} = 300$ K), C2, ($T_{\min} = 140$ K) and C3 ($T_{\min} = 45$ K). In the first case (C1), efficiency values up to 0.6 with specific work around 1500 kW/kg/s are achieved. In the case C3, matching with a LNG vaporization terminal, it is possible to attain efficiency values from 0.66 (available technology) to 0.75 (future technology) with specific work from 1200 to 2400 kW/kg/s. The last alternative (C2), coupling with a LH_2 vaporization terminal, shows the highest performance (efficiency between 0.78 and 0.83, specific work between 1800 and 3000 kW/kg/s). The performance of C2 and C3 can be higher if a turbine expansion is used after the vaporization of LNG or LH_2 (curves C2*, C3*, and C3**).

The thermal efficiency of systems using external combustion for heat addition (using natural gas, oil fuel, hydrogen, biomass, coal, etc.) is low because part of fuel energy is lost through the stack exhaust gas. Natural gas provides the easiest emissions treatment at the exhaust. The exhaust temperature should be over 373 K to avoid condensation at atmospheric pressure. Actually, fuels containing sulfur or vanadium combine with water

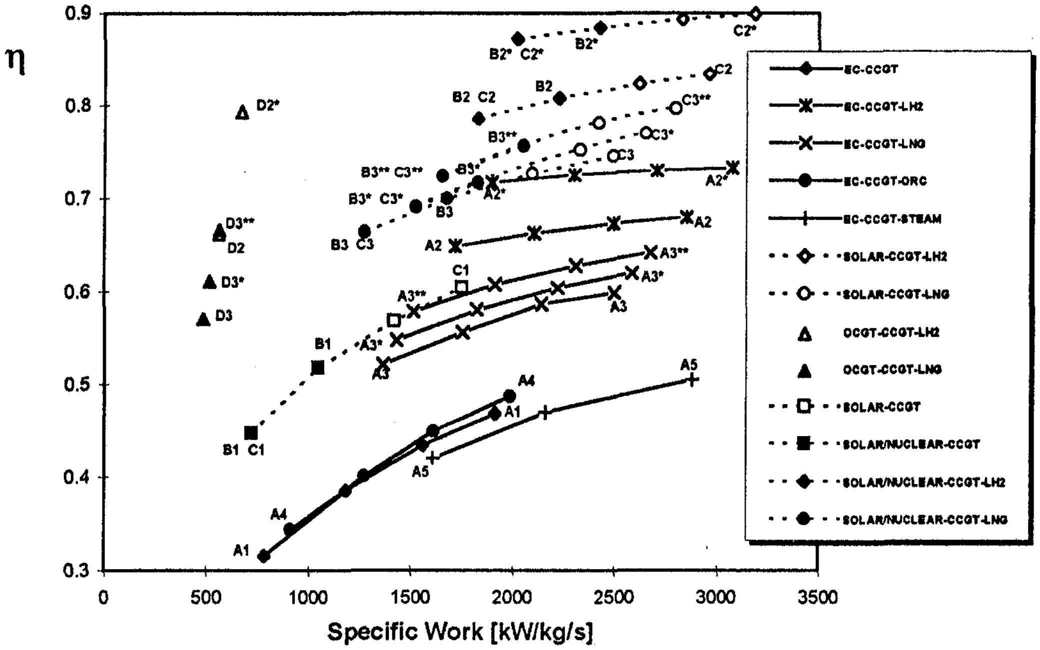

Fig. 5 Performance of power plants including CCGT systems

and free oxygen to form sulfurous and sulfuric acid, and vanadium pentoxide at the stack; thus, restricting stack temperatures even higher to avoid condensation of these substances). Even if heat recovery with air preheating is used (see Fig. 1, alternative A) the efficiency is still low.

The performance improvement with a simple intercooled CCGT heated by an external combustion (case A1) and working with a minimum temperature equal to 300 K (T_{env}) is rather low ($\eta = 0.32$ and $W = 750$ kW/kg/s with $T_{max} = 1100$ K; $\eta = 0.47$ and W near to 2000 kW/kg/s with $T_{max} = 1700$ K). The improvement obtained by adding an ORC bottoming cycle to a simple externally fired CCGT system using toluene as the working fluid (solution A4) or a steam bottoming cycle (solution A5), both working with $T_{min} = 300$ K (condenser temperature) and a higher compressor inlet temperature, is slightly higher than the other externally fired solutions in terms of efficiency. In terms of specific work, only solution A5 (with the steam cycle) presents values in the range of 1500–3000 kW/kg/s by varying the maximum temperature from 1300 K to 1700 K. However, the small increases in performance are not justified by the required plant complexity.

Solutions A3 and A2 (externally fired CCGT cycle with LH_2 or LNG cooling systems) provide specific work similar to those of the solar systems discussed above. Their efficiencies reach 0.52–0.60. These can be increased using a turbine expansion after the vaporization of the cryogenic fluid. In the first case (A3) increased to 0.65–0.68; in the second case (A2), increased to 0.72–0.73.

Table 2 Possible power plant solutions including CCGT (see Fig. 1)

HEAT SOURCE	HEAT REJECTION SYSTEM T env. 1	LH₂ 2	LNG 3	ORC 4	STEAM 5
A - EXTERNAL COMBUSTION	YES	YES	YES	YES	YES
B - NUCLEAR	YES	YES	YES	NO	NO
C - SOLAR	YES	YES	YES	NO	NO
D - OCGT	NO	YES	YES	NO	NO

Combined plants using a stationary heavy-duty or aero-derivative gas turbine (OCGT) and a bottoming CCGT cycle with cooling using vaporization of LNG or LH_2 are marked as solutions D2 and D3. The specific work has been defined as the ratio between system net power and mass flow rate of air at the inlet of the OCGT, because the OCGT is considered the main part of the combined plant. The helium maximum temperature is now reduced (to around 700 K). In this case, the gas/helium heat exchanger does not present any of the higher temperature considerations. The corresponding performance in Fig. 5 indicates efficiencies of 0.57 and 0.66 for LNG and LH_2 cooling, respectively. Higher values can be achieved if the expansion of LNG or LH_2 is utilized in a turbine (0.67 and 0.79, respectively).

Conclusions

The performance of power systems using closed cycle gas turbine (CCGT) plants have been evaluated. The different plants were analyzed and compared using thermal efficiency, specific power, and available and near future technologies. The following conclusions are drawn:

1 CCGT systems coupled with gas cooled reactor have a thermal efficiency increase of 10 percent or more in comparison with traditional nuclear systems.

2 Matching CCGT using ceramic materials with solar systems working between high maximum temperatures (1700 K) and minimum temperatures near environmental temperature (T_{env}) provide efficiencies around 0.60, with negligible environmental impact or pollution.

3 Employing different fuels in externally fired systems makes CCGT plants interesting if coal or biomass are selected. In these cases, the thermal efficiency is still high (around 0.50 with a minimum temperature near T_{env}).

4 Providing cycle cooling with fluids working at cryogenic temperatures, such as LNG and in the future LH_2, is easily adaptable to the working fluids of CCGT (helium, nitrogen, etc). It allows very high performance to be obtained (efficiency in excess of 0.70 and specific work in excess of 2500 kW/kg/s). Such systems save part of the energy that would otherwise be required for the liquefaction of LNG or LH_2.

5 If ceramic heat exchangers working at high temperatures are not desirable, then it is possible to select solution *D* of Fig. 1 (a Gas Turbine as topping cycle). This, coupled to an LNG/LH_2 cooling system, still gives very high performance, even if the helium-cycle pressure ratio is kept below 4.

6 Most plants combined with CCGT attain high specific work (see Fig. 5) resulting in compact and economic plants.

7 CCGT systems combined with ORC or steam bottoming cycles result in small performance increases that do not justify the plant complexity, reduced reliability, and increased cost.

8 For each individual plant studied here, it is possible to carry out a detailed thermoeconomic analysis. (Agazzani and Massardo, 1997).

Acknowledgment

This work has been partially supported by the Italian Ministry of University and Research (60 percent). We thank Colin McDonald for his valuable comments in the fields of Helium Turbomachinery and Heat Exchangers.

References

Agazzani, A., and Massardo, A., 1995, "Advanced Solar Dynamic Space Power System—Part I and Part II," *ASME Journal of Solar Energy Engineering*, Vol. 117, pp. 265–281.

Agazzani, A., Massardo, A., 1997, "A Tool for Thermoeconomic Analysis and Optimization of Gas, Steam, and Combined Plants," ASME JOURNAL OF ENGINEERING FOR GAS TURBINES AND POWER, Vol. 119, pp. 885–892.

Bisio, G., and Cerullo, N., 1992, "Thermodynamic Analysis of Combined Plants Utilizing Helium Turbine with Nuclear Heating and Liquid Hydrogen Refrigerating," IECEC Paper 929410.

Bisio, G., Massardo, A. F., and Agazzani, A., 1995, "Combined Helium and Combustion Gas Turbine Plant Exploiting Liquid Hydrogen (LH_2) Physical Exergy," ASME Paper 95-GT-298.

Consonni, S., and Farina, F., 1995, "L'utilizzo del carbone in impianti non convenzionali a ciclo combinato con combustione esterna," *Technologies and Complex Energy Systems Conference*, Bologna, Italy, June, SGE ed., pp. 31–48.

Gentile, G., 1995, private communication, Ansaldo Ricerche, Genova, Italy.

Griepentrog, H., and Sackarendt, P., 1976, "Vaporization of LNG with Closed Cycle Gas Turbine," ASME Paper 76-GT-38.

Harper, A., and Jansen, J., 1990, "Closed Brayton Cycle Engine Application to Emerging Unmanned Underwater Vehicle Missions," ASME Paper 90-GT-307.

Harper, W., Boyle, R., and Kudjia, C., 1990, "Solar Dynamic CBC Power for Space Station Freedom," ASME Paper 90-GT-70.

Huang, F. F., and Wang, L., 1987, "Thermodynamic Study of an Indirect Fired Air Turbine Cogeneration System with Reheat," ASME JOURNAL OF ENGINEERING FOR GAS TURBINES AND POWER, Vol. 109, pp. 16–21.

Keller, C., 1945, "The Escher Wyss-AK Closed Cycle Turbine: Its Actual Development and Future Prospects," ASME Paper, ASME, NY, November, 1945.

Klara, J. M., 1994, "High Performance Power Systems for the Near-Term and Beyond," ASME Paper 94-GT-315.

Klara, J. M., Izsak, M. S., and Wherley, M. R., 1995, "Advanced Power Generation: the Potential of Indirectly-Fired Combined Cycles," ASME Paper 95-GT-261.

Korakianiitis, T., Hochstein, J. I., and Ziou D., 1993, "Prediction of the Transient Thermodynamic Response of a Closed-Cycle Regenerative Gas Turbine," ASME Paper 94-GT-483.

Korakianitis, T., Vlachopoulos, N. E., and Zou, D., 1994, "Models for Prediction of Transients in Closed Regenerative Gas Turbine Cycles with Centrifugal Impellers," ASME Paper 94-GT-342.

Krey, G., 1979, "Utilization of the Cold by LNG Vaporization with Closed-Cycle Gas Turbine," ASME Paper 79-GT-84.

La Haye, P. G., and Bary, M. R., 1994, "Externally Fired Combustion Cycle (EFCC), A DOE Clean Coal V Project: Effective Means of Rejuvenation for Older Coal-Fired Stations," ASME Paper 94-GT-483.

Lee, J. C., Campbell, Jr., J., and Wright, D. E., 1981, "Closed Cycle Gas Turbine Working Fluids," ASME JOURNAL OF ENGINEERING FOR GAS TURBINES AND POWER, Vol. 103, pp. 220–228.

Massardo, A., 1993, "Design and Performance Evaluation of a CBC Solar Space Power System: the Influence of Orbital and Solar Conditions," ASME Paper 93-GT-180, presented at the International Gas Turbine and Aeroengine Congress and Exposition, Cincinnati, OH, May 24–27.

Massardo A., and Arnulfi G., 1992, "Combined Closed Cycle (C^3) Systems for Underwater Power Generation," ASME Paper 92-GT-97.

Massardo, A., and McDonald, C. F., 1995, "Closed Cycle Gas Turbine Perspective: Enabling Technologies from Combustion Turbines—the Key Factor for Future Deployment," Technologies and Complex Energy Systems Conference, Bologna, June, SGE ed., pp. 503–518.

Massardo, A., Satta, A., and Marini M., 1990, "Axial Flow Compressor Design Optimization—Part I and Part II," *ASME Journal of Turbomachinery*, Vol. 112, pp. 399–410.

McDonald, C. F., 1977, "Heat Exchanger Design Consideration for Gas Turbine HTGR Power Plant," ASME JOURNAL OF ENGINEERING FOR GAS TURBINES AND POWER, Vol. 99, pp. 237–245.

McDonald, C. F., 1994a, "Enabling Technologies for Nuclear Gas Turbine (GT-MHR) Power Conversion Systems," ASME Paper 94-GT-415.

McDonald, C. F., 1994b, "The Key Role of Heat Exchanger in Advanced Gas-Cooled Reactor Plants," Heat Recovery Systems CHP, Vol. 14, No. 1, Pergamon Press, NY, pp. 7–28.

McDonald, C. F., 1995, private communication, General Atomic, September.

MHTGR Plant, 1993, General Atomic, San Diego, CA.

Nakakado, K., et al., 1995, "Strength Design and Reliability Evaluation of a Hybrid Ceramic Stator Vane for Industrial Gas Turbines," ASME JOURNAL OF ENGINEERING FOR GAS TURBINES AND POWER, Vol. 117, pp. 245–250.

Snamprogetti-Brown Boveri Company, 1980, *LNG Regasification Plants*.

Stambler, I., 1994, "Utilities Are Looking to ICADS for Unrivaled Economy and Flexibility," *Gas Turbine World*, Nov./Dec.

Tatsuzawa, M., Taoka, T., Sakida, T., and Tanaka, S., 1995, "Development of 300 kW-Class Ceramic Gas Turbine (CGT 301) Engine System," ASME 95-GT-201.

Turbomachinery International Handbook, 1995, Vol. 36, No. 5, Turbomachinery International Publications, Norwalk, CT.

Wong, W., 1994, "LNG Power Recovery," *Proceedings of the Institution of Mechanical Engineers*, Vol. 208, No. A1, Mechanical Engineering Publications Limited, London and Birmingham, AL, pp. 3, 12.

Yan, X. L., and Lidsky, L. M., 1993, "Design of Closed Cycle Helium Turbine Nuclear Power Plants," ASME Paper 93-GT-196.

Zenker, P., 1988, "10 Years of Operating Experience with the Oberhausen Helium Turbogenerator Plant," VGB Krafftnerkstechnik, No. 7, pp. 616–621.

Minimization of the Local Rates of Entropy Production in the Design of Air-Cooled Gas Turbine Blades

G. Natalini

E. Sciubba

Dipartimento di Meccanica e Aeronautica,
Universita' di Roma 1, "La Sapienza,"
Rome, 00184,
Italy

The paper presents the results of a numerical configuration study made on a two-dimensional model of an internally cooled gas turbine vane. The analysis applies to a two-dimensional cascade at medium Reynolds number, subsonic Mach number, and steady state. The full Navier-Stokes equations of motion for turbulent viscous flow, together with the appropriate energy equation, are solved via a standard finite-element code with a k-ϵ *closure, to obtain complete velocity and temperature fields. These fields are then used to compute the entropy generation rates corresponding to the viscous* (s_v) *and thermal* (s_t) *dissipation. The thermo-fluid dynamic efficiency of different versions of the same base configuration is assessed comparing the global (or integral) entropy generation rate in the passage. The procedure is general, can be extended to different configurations and different operational conditions, and provides the designer with a rational and effective tool to assess the actual losses in the fixed and rotating turbomachinery cascades.*

1 Introduction

Component efficiency is certainly the single most important performance parameter for gas turbines, in the sense that a slight change in the efficiency of one of the main components (e.g., the compressor) produces, in percentage points, a much larger change in the plant net power output and consequently in its overall conversion efficiency.

Over the years, enormous technological efforts have been devoted to the improvement of the performance of components of gas turbine plants, and the result has been a remarkable increase of their conversion efficiency, from the roughly 25 percent of the 1960 models to the over 38 percent of some 1997 models.

From a theoretical point of view, the simplest way to improve cycle efficiency is to raise both the pressure ratio and the combustion temperature. Unfortunately, higher gas temperatures pose enormous design and technological problems, and, therefore, the increase in turbine entry temperature has been steady but not dramatic in the last two decades or so. However, it is not uncommon today to observe a 25:1 pressure ratio together with an 1800°K gas turbine temperature at the turbine inlet, at least in advanced, high-performance jet engines. Even heavy-duty gas turbines have inlet temperatures well above 1400°K.

For such temperatures, efficient blade cooling is mandatory: first-row nozzles and blades (and sometimes, second-row nozzles) are usually cooled by routing compressor air (dry or in some instances humidified by water or steam injection) into the vane root, and letting it expand along radial holes internal to the vane (Fig. 1), before being discharged into the main stream through a series of "slots" or "holes" properly placed on the vane external surface. This discrete hole film cooling method is very effective in keeping the blade surface temperature noticeably below the (bulk) mainstream gas temperature, and it does so by exploiting three physical mechanisms: conduction cooling through the blade walls, driven by the low inner wall temperature; convection cooling on the inner side of the blade and along the ejecting holes; and film cooling, by a layer ("film") of "cold" air which isolates to a certain extent the vane external surface from the high temperature mainstream gas, thereby reducing the thermal stresses on the material.

Film cooling on the stator vanes is influenced mainly by nozzle geometry and by location and number of the cooling holes; on the rotating blade, rotation and unsteadiness effects come also into play. To correctly assess the mechanism of the cooling effectiveness, it is customary to perform numerical simulations of the flow in the entire stage (nozzle + rotor), to be able to choose the most appropriate design, i.e., the combination of number, type, and location of cooling holes which produces the lowest thermal stresses compatible with the type of materials and operation. But there is another important design aspect: any film cooling configuration will produce losses in the system, which will decrease its performance. These losses have different causes:

—The reduced mass flow in the compressor, which requires a portion of the expander's shaft work to be used to pressurize air which then bypasses combustion.

—Pressure losses in the cooling circuit, which reduce the effectiveness of the convective cooling.

—Mixing losses at the ejection points (holes), which disturb the boundary layer/mainstream interface and modify the endwall/wake interaction (thereby also reducing the cooling effectiveness).

A novel approach to the design problem would be to consider the most appropriate configuration as the one that produces the minimal amount of losses, for a certain value of the blade maximum allowable temperature and thermal stress, under the constraints of a fixed upstream stagnation enthalpy and stage work output.

The most complete and rational way of taking into account qualitatively as well as quantitatively all these different types of losses is that of separately considering the entropy generation rates produced by each loss. Then it becomes possible to devise design changes that address one type of loss (i.e., pressure loss in cooling passages) and have possibly little effect on the others. Local and global entropy values are not difficult to compute, but their correct calculation requires very accurate velocity and temperature fields,

---

Contributed by the Advanced Energy Systems Division of THE AMERICAN SOCIETY OF MECHANICAL ENGINEERS for publication in the ASME JOURNAL OF ENGINEERING FOR GAS TURBINES AND POWER.

Manuscript received by the Advanced Energy Systems Division December 10, 1997; final revision received by the ASME Headquarters February 17, 1999. Technical Editor: H. Nelson.

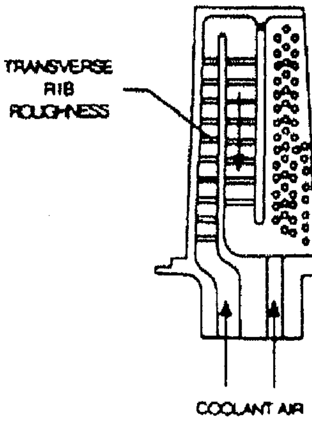

Fig. 1 Typical film cooling arrangement for a gas turbine blade [9]

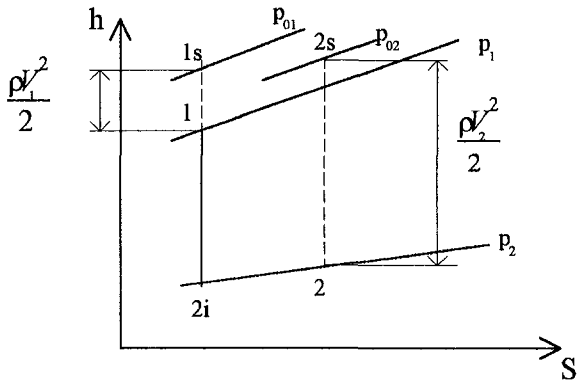

Fig. 2 Enthalpy-entropy representation of the expansion in the first stage of a gas turbine

so that, with some notable exceptions [3, 6, 9, 12] losses are not usually associated with their corresponding entropy generation rates.

Here, we present the results of an application of this "minimization of entropy generation" approach to a configuration study of a representative geometry of an internally cooled gas turbine stator blade.

The analysis takes into consideration a two-dimensional cascade at a Reynolds number of 86000, entry Mach number of 0.14 (so that compressibility effects can be neglected), and steady state. The full Navier-Stokes equations of motion for a turbulent viscous flow, together with the appropriate energy equation, are solved via a standard finite elements code with a k-ϵ closure, so that complete velocity and temperature fields are obtained (including boundary-layer effects, via proper wall functions). These fields are ten used to compute the entropy generation rates corresponding to the viscous (s_v) and thermal (s_t) dissipation.

Four configurations have been numerically tested, the reference one being the vane with no film cooling: the other three configurations include cooling holes placed on the leading edge, at $\frac{3}{4}$ chord on the pressure side, and at both locations. The influence of a variation in the flow coefficient φ has been examined as well.

The thermo-fluid dynamic performance of each configuration can be assessed at the following two levels:

1 At a local level, by examining the local entropy generation rates at each point of the computational domain: where these rates are high, the design can be modified to reduce local losses.

2 At a global level, by considering the integral value (over the whole of the domain) of the entropy generation rates, vz. of their ratio s_v/s_t, which can be expressed in terms of a dimensionless dissipation number [3, 16], named after Bejan who first gave a comprehensive treatment of a similar problem [2].

2 Viscous and Thermal Entropy Generation in a Cascade

Consider the expansion in the first stage of a gas turbine (Fig. 2). For a fixed expansion ratio (i.e., for a fixed p_2), the temperature of the gas at the stage exit, T_2, will be higher than the corresponding isentropic value T_{2i}: the difference is due to a series of dissipative effects, which result in an effective loss of "work" (in a more precise sense, a destruction of exergy [16]), and in a degradation of the thermodynamic quality of the fluid. Both of these effects are expressed by the "lost work" theorem of Guy-Stodola:

$$w_{\text{lost}} = T_0 \Delta s^1 \qquad (1)$$

Standard engineering practice recommends the use of loss coefficients to take into account the various mechanisms that repre-

Nomenclature

A = area
α = angle of attack
β = coolant ejection angle
Be = $s_t/s_t + s_v$ = Bejan number [16]
c_p = specific heat at constant pressure
ΔT = $T_{\text{gas}} - T_{\text{air}}$ = reference temperature difference
d_h = cooling hole diameter
h = enthalpy
h_s = stagnation enthalpy
k = turbulent kinetic energy
k_{air} = air thermal conductivity
ϵ = turbulent dissipation
η_s = stage efficiency
L_c = chord length
M_{cool} = $m_{\text{air}}/m_{\text{gas}}$ = cooling mass ratio coefficient
m = mass flowrate
μ = air dynamic viscosity
μ_t = turbulent eddy viscosity
ν = air kinetic viscosity
p = pressure
p_s = stagnation pressure
φ = flow coefficient (= V_m/U_g)
Φ = viscous dissipation function
r_r = numerical residual error
R = gas constant
$\|R\|$ = numerical residual
Re = Reynolds number
s_v = viscous entropy generation rate
s_t = thermal entropy generation rate
S_{0v}, S_{0t} = scaling factors for s_v and s_t (Eqs. A.9 and A.10)
T_0 = ambient reference temperature
T_c = cooling air temperature
T_g = inlet gas temperature
U = rotor blade reference speed
U_c = cooling air outlet velocity (from the hole)
V_g = inlet gas velocity
V_m = meridional component of the absolute velocity
V = control volume
w = work
y^+ = dimensionless wall distance
Y = stagnation loss coefficient
ζ = entropy loss coefficient

---

[1] The practical application of the Gouy-Stodola theorem is invariably afflicted by a debate over the value to be assigned to T_0. It is important to remark that for the purpose of the optimisation procedure discussed in this paper, it is irrelevant whether T_0 is taken to be the exhaust gas temperature, or the "standard air" temperature, or any other temperature in between: as long as we compare the relative irreversible entropy generation rates, the "optimal" design is insensitive to the numerical value of T_0. In all cases, though, where component efficiency is employed in a more general context of "cycle" or "process" efficiency, we maintain that the proper value for T_0 is the ambient temperature, conventionally defined as the static temperature of standard air at compressor inlet.

sent departures from the ideal case (profile loss, secondary losses, tip-leakage losses). These coefficients are predicted by semi-empirical correlations [6]. Once w_{lost} has been computed by means of these correlations, the corresponding entropy increase Δs can be derived from Eq. 1 and the expansion line can be traced.

The most popular among these coefficients is the stagnation pressure loss coefficient, Y, defined as

$$Y = \frac{p_{1s} - p_{2s}}{p_{2s} - p_2}, \tag{2}$$

which is easily measured in cascade tests. Another widely used coefficient is the enthalpy loss coefficient, ΔH:

$$\Delta H = \frac{h_2 - h_{2i}}{h_{2s} - h_2}. \tag{3}$$

As pointed out in [6] though, the only definition which of interest in turbomachinery design and applications is the so-called stage isentropic efficiency, defined as the ratio of the actual to the isentropic work:

$$\eta_s = \frac{h_1 - h_2}{hh_1 - h_{2i}}. \tag{4}$$

The global measure of the performance deterioration, i.e., of the reason why the actual work is lower than the work that would be expected if the expansion was isentropic, is of course the Guy-Stodola lost work and, in end effect, the entropy generation in the process. So, it appears that entropy generation is the only consistent measure of the lost work due to irreversibilities. Recently, the entropy generation concept has been employed as a measure of the irreversible losses in gas turbine components, and the results are very promising [8, 9, 13, 14, 17, 18]. In particular, the use of entropy generation rates as a quantitative measure of the work lost in irreversibilities has the following advantages over "loss coefficients" methods: specific entropy generation rates

—do not depend on the frame of reference (rotating or fixed);

—do not depend on mass or volume flowrate (i.e., they scale in dynamic similitude);

—can be easily split into their viscous and thermal contributions;

—enjoy the additive property, and, thus, can be computed separately for each single stage and then summed up to obtain the overall machine irreversibility; furthermore, they can be computed for one blade passage and in the assumption of flow periodicity multiplied by the number of passages in the cascade to obtain the total stage loss;

—are implicitly dependent on the temperature level at which irreversibilities take place, i.e., they give a second-law weighted loss assessment.

—can be used, as proposed in [6], to define a more rational measure of performance, the irreversibility coefficient[2]:

$$\zeta = \frac{T_0 \Delta s}{h_{1s} - h_{2i}}. \tag{5}$$

The value of the specific entropy generation rate can be computed from a global point of view, using the perfect gas approximation

$$s_2 - s_1 = c_p \ln\left(\frac{T_2}{T_1}\right) - R \ln\left(\frac{p_2}{p_1}\right) \tag{6}$$

and

$$s_{1-2} = m(s_2 - s_1), \tag{7}$$

or can be computed in a local perspective, considering the thermal and viscous contributions to the overall dissipation [2]:

$$s_{1-2} = \int_V \left(\frac{\mu\Phi}{T} + \frac{k(\nabla T)^2}{T^2}\right) dV. \tag{8}$$

In the right side of Eq. 8, the first term in the integrand represents the irreversible entropy production rate due to local shear (Φ being the so-called dissipation function), while the second term represents the irreversible entropy production due to local thermal imbalances. In this paper, these two contributions are handled separately, and indicated by s_v (viscous entropy generation rate) and s_t (thermal entropy generation rate), respectively.

The procedure proposed in this work can be now described and justified on the basis of the above remarks. For a given cascade configuration, if a complete quantitative description of the velocity and temperature fields is available, one can compute s_v and s_t locally, i.e., in every point of the flowfield. The integral of the sum of both entropy generation rates over the entire flow domain (Eq. 8) gives then a value which is numerically identical to the s_{1-2} obtained by Eq. 7, and is therefore a measure of the work lost in viscous and thermal irreversibilities in the flow. It has to be remarked, however, that the two contributions in Eq. 8 can be computed separately, while this would not be possible if one used Eq. 7. Now, if the cascade operational configuration is modified, for instance by adding a row of cooling holes on the leading edge of the vanes, the same calculation can be repeated, and the new values of s_v and s_t, as well as their integral over the entire flow domain, will allow a direct comparison of the relative performance of the modified configuration with respect to the original one, and, what is perhaps even more important, will show the map of the viscous and thermal irreversibility distribution in the flow domain. The information thus gathered is of significance to the designer who can use it to choose the configuration which produces the lower total irreversibility (lower entropy generation rate, Eq. 8), and to determine by inspection where design changes might be desirable to reduce irreversible losses under the applicable design constraints.

But the application of the procedure proposed in this paper goes well beyond this simple example: suppose an alternative, cheaper material is being suggested for the manufacturing of the blades, and that the adoption of this material would require a drastic lowering of the $T_{\mathrm{max,blade}}$. For equal coolant inlet temperature, better cooling can only be achieved by an increased coolant mass flow rate. The additional irreversible entropy generation rates due to this increased mass flow could be translated into an efficiency penalty and consequently assigned a monetary value, to be algebraically added to the unit savings generated by the new material: the objective function thus obtained would provide a "thermo-economically optimal" solution to the problem.

The following Sections describe an application of this procedure to a first-stage air-cooled nozzle of a gas turbine. No cost factor has been included in the objective function: the optimization is performed solely with respect to the global entropy generation rate.

3 An Air-Cooled, Two-Dimensional Stator Blade: Configuration Study

Consider a two-dimensional section of a gas turbine first-row stator blade (Fig. 3). For the purpose of the present study, the profile can be taken as being representative of the section at mid-span of a generic gas turbine nozzle. The vane is internally cooled by a radial flow of air (perpendicular to the plane of the drawing in Fig. 3) through three separate internal channels. The difference between the configurations analyzed in this study consists in the presence (or absence) and location of one or more rows of cooling holes (represented in this two-dimensional schematization by their longitudinal midsection). In the configuration without cooling holes ("A" in Fig. 4) the cooling air is assumed to be discharged from the vane tip.

---

[2] Denton [6] considers the difference $h_{2s} - h_2$ in the denominator, but the definition used in Eq. 5 seems more appropriate here.

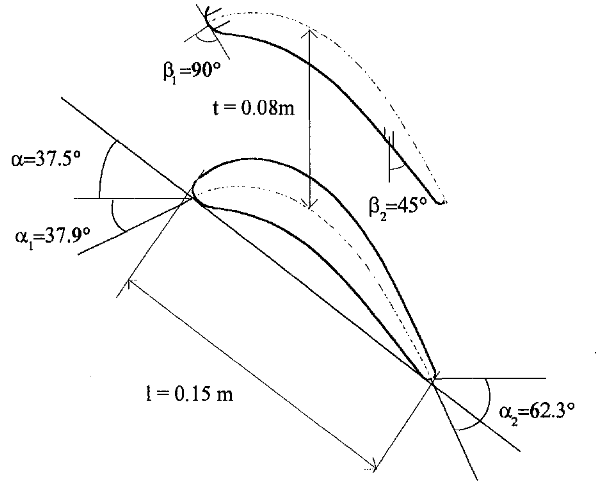

Fig. 3 Radial mid-section of a representative first-stage gas turbine stator vane

Table 1 Synoptic table of the four vane configurations under analysis

	A (reference case)	B	C	D
- chord lenght, L_c [m]	0.15	0.15	0.15	0.15
- inlet gas velocity, U_{ref} [m/s]	103	103	103	103
- inlet gas temperature, T_{gas} [°K]	1400	1400	1400	1400
- ambient reference temperature, T [°K]	300	300	300	300
- cooling hole diameter, d_h [m]	n/a	0.002	0.002	0.002
- cooling mass ratio, $M_{cool} = \frac{\rho_c V_c}{\rho_{gas} V_{gas}}$	0	0.6	0.6	0.6
- cooling jet velocity, V_c [m/s]	0	28.8	28.8	14.4
- cooling air temperature, T_c [°K]	n/a	760	760	760
- cooling jet ejection angle β_1 [°]	n/a	90°	n/a	90
- cooling jet ejection angle β_2 [°]	n/a	n/a	35	45
- number of rows of cooling holes & locat	0	1/fore	1/aft	2/fore & aft

3.1 Description of the Analyzed Configurations. Four geometric configurations (described in detail in Fig. 4) have been analyzed, without and with cooling holes. The relevant geometric parameters, together with the flow characteristics, are (see also Table 1)

— configuration with no cooling holes ("A" in Fig. 4)

— configuration with one row of cooling holes on the leading edge ("B" in Fig. 4)

— configuration with one row of cooling holes at $\frac{3}{4}$ of chord ("C" in Fig. 4)

— configuration with two rows of cooling holes, one on the leading edge and one at $\frac{3}{4}$ of chord ("D" in Fig. 4)

The values assumed for the air and material properties, as well as the dimensionless characteristic flow parameters, are shown in Tables 2 and 3.

It should be noted that the cooling air average velocity has been assigned the same value in configurations C and D, while it is known that the ejected mass flow rate depends on the cooling hole location on the profile. This assumption was made so that different configurations could be compared on the same basis. In a more detailed simulation, the cooling air velocity ought to be computed as a part of the solution.

A similar remark applies to the cooling jet velocity: the plug profile chosen here is clearly a simplification. Realistically developed profiles would give a different cooling performance and would thus affect both the thermal and the viscous entropy generation rates.

As an additional exercise, configuration D has been tested under different angles of attack, ranging from −8.5° to +7.5°.

3.2 Boundary Conditions. The boundary conditions were the same for all four configurations, the only difference being, of course, the flow injection into the mainstream in cases B, C, and D:

— inlet velocity: fully turbulent profile, with V_g = 103 m/s. Design angle of attack $\alpha = -5.5°$. Cases $D_{(i)}$ had α varying between −8.5 and +7.5°.

— inlet temperature: plug profile, with T_g = 1300 K

— inlet turbulent quantities: $k_g = 0.01\ V_g^2$; $\epsilon_g = 0.006\ V_g^2$

— blade inner wall temperature: T_{inside} = 1118°K

— air velocity at cooling hole inlet: U_c = 28.8 m/s for cases B and C, 14.4 m/s for case D

— air temperature at cooling hole inlet: T_c = 760°K

— outflow conditions: $\partial T/\partial n = \partial V/\partial n = \partial k/\partial n = \partial \epsilon/\partial n = 0$

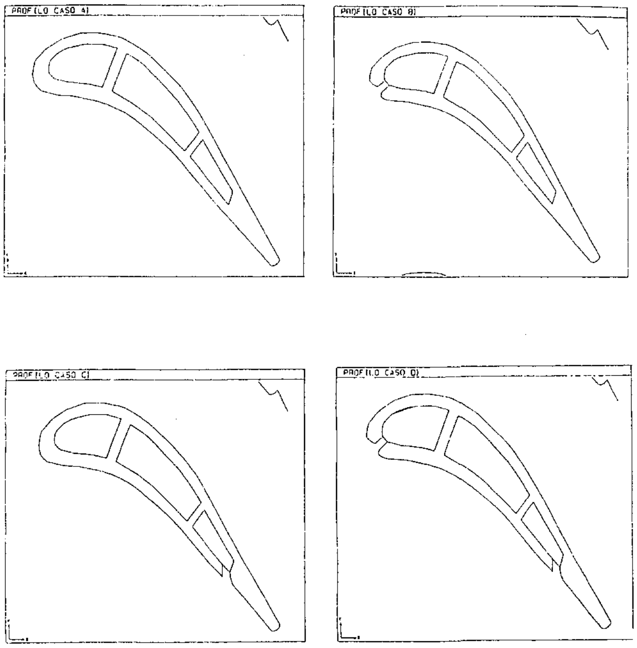

Fig. 4 The four air-cooled blade configurations considered in this study

Table 2 Air and material properties

Air density (kg/m^3)	ρ = 0.2716 ρ = 0.4707	T=1300K T= 760K
Air dynamic viscosity (kg/m s)	$\mu = 4.88 \cdot 10^{-5}$ $\mu = 3.5 \cdot 10^{-5}$	T=1300K T= 760K
Air conductivity (W/m K)	k = 0.0797 k = 0.0541	T=1300K T= 760K
Air constant-pressure specific heat (kJ/kg K)	c_p = 1.189 c_p = 1.087	T=1300K T= 760K
Steel conductivity (W/m K)	k_s = 26	

Table 3 Scaling quantities and dimensionless flow parameters

l_{ref} = 0.15 m U_{ref} = 103 m/s T_{ref} = 300 K $\text{Re} = \frac{U_{ref} l_{ref}}{\nu_{1300}} = 86000$ Pe = Re Pr = 60200 ΔT_{ref} = 1000 K	$S_{v,\text{ref}} = \frac{\mu U^2}{\Delta T \ell_{ref}}$ $S_{t,\text{ref}} = \frac{k}{\ell_{ref}}$ $Pr = \frac{\nu_{1300} c_{p,1300}}{k_{1300}}$ $Br = \frac{k \Delta T}{\mu U^2}$

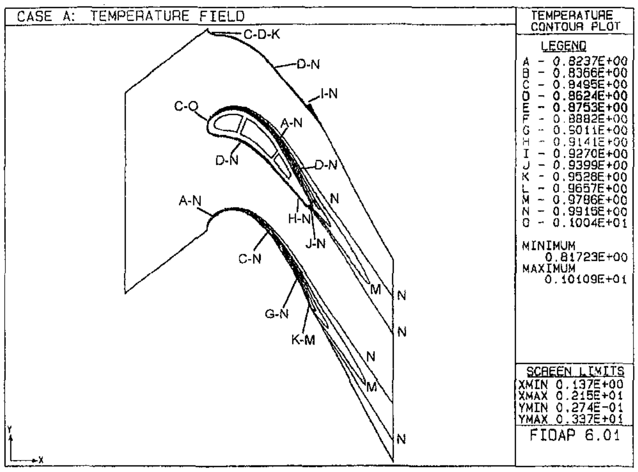

Fig. 5 Blade temperature contours

Periodicity is enforced between the upper and lower portions of the channel (but not on the blade profile).

3.3 The Numerical Procedure. Since circumferential periodicity is assumed, only a portion of the two-dimensional cascade (a "cell" containing one blade) is actually computed. The mesh consists of 16718 gridpoints, arranged on 16384 isoparametric quadrilateral four-node elements: the final mesh is the same as that used in previous studies [13, 14].

The full Navier-Stokes equations with the addition of the temperature transport equation were solved. The entire procedure was made dimensionless to achieve larger generality, and the scaling quantities are listed in Table 3.

Turbulence has been modeled with a two-equations k-ϵ model, which requires wall functions to represent the law-of-the-wall profiles for velocity and temperature. The turbulent kinetic energy k and the turbulent dissipation ϵ are approximated by scaling laws in the wall layer, and their values are then matched to the free-stream calculations.

The code used for the numerical simulation is FIDAP,[3] a commercial finite elements package, here supplemented with all the additional numerics required for the calculation of the entropy generation rates. FIDAP provides several solution strategies for two-dimensional and three-dimensional viscous problems: we chose the so-called "segregated" approach, in which each variable (u, v, T, k, ϵ) is solved for independently, its solution at the ith iteration is substituted in the remaining equations at the $(i + 1)$th iteration and under-relaxation is employed to stabilize the solution. The pressure is solved for by means of a separate Poisson-like equation. The specific dimensionless form of the equations and details on the solution procedure are reported in Appendix 1.

Convergence was measured by two parameters, namely, the relative error and the residual error, respectively defined (for a generic variable f) as

$$e_r = \frac{f_i - f_{i-1}}{f_i} \tag{9}$$

$$r_r = \frac{\|R_i\| - \|R_{i-1}\|}{\|R_i\|} . \tag{10}$$

A solution was considered to have converged when $e_r \leq 1$ percent and either $r_r \leq 1$ percent or $(r_{r_i} - r_{r_{i-1}}) \leq 5$ percent. The *initial flow conditions were taken in all cases from a laminar* converged solution (Re = 400): typically, full convergence was achieved in less than 500 iterations.

The flow field resulting from a converged solution was then used to compute the values of the entropy generation rates, which in the two-dimensional formulation adopted here are given by the following expressions:

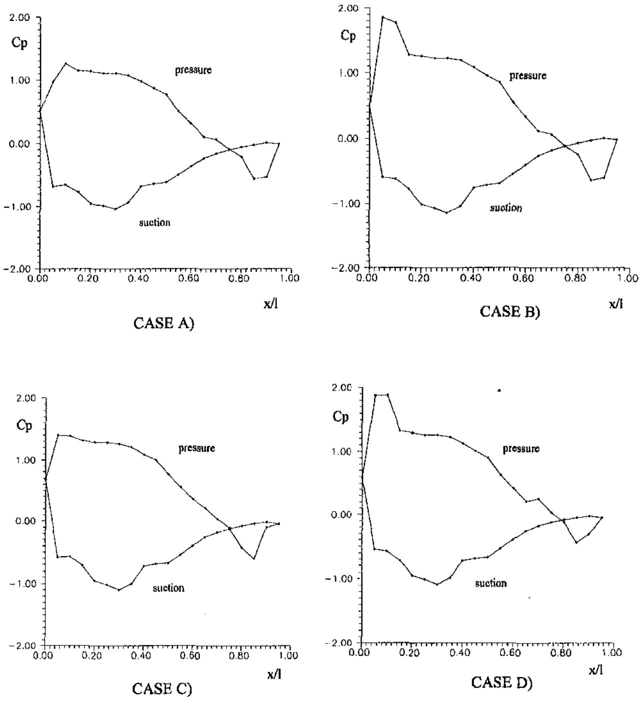

CASE A)

CASE B)

CASE C)

CASE D)

Fig. 6 Computed pressure coefficients for the four configurations

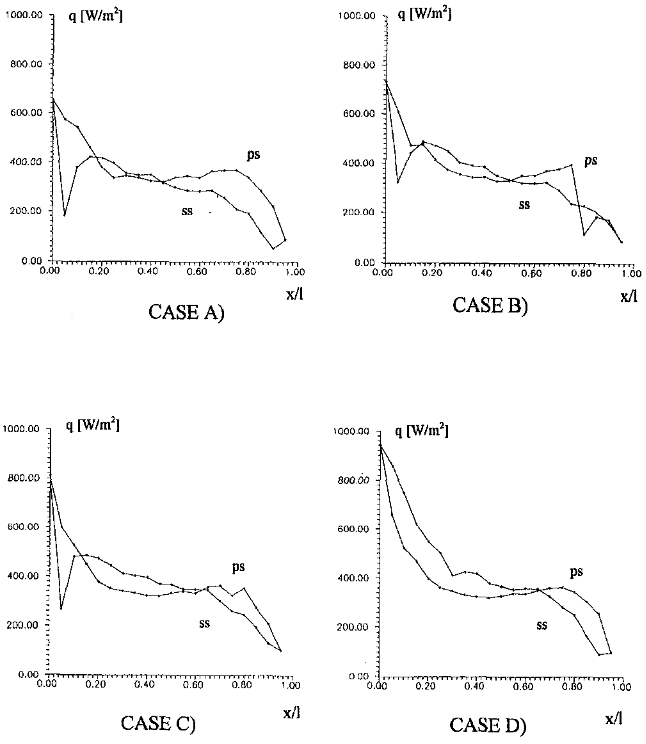

CASE A)

CASE B)

CASE C)

CASE D)

Fig. 7 Computed blade surface heat flux for the four configurations *ps* = pressure side; *ss* = suction side

---

[3] Presently owned by FLUENT Inc.

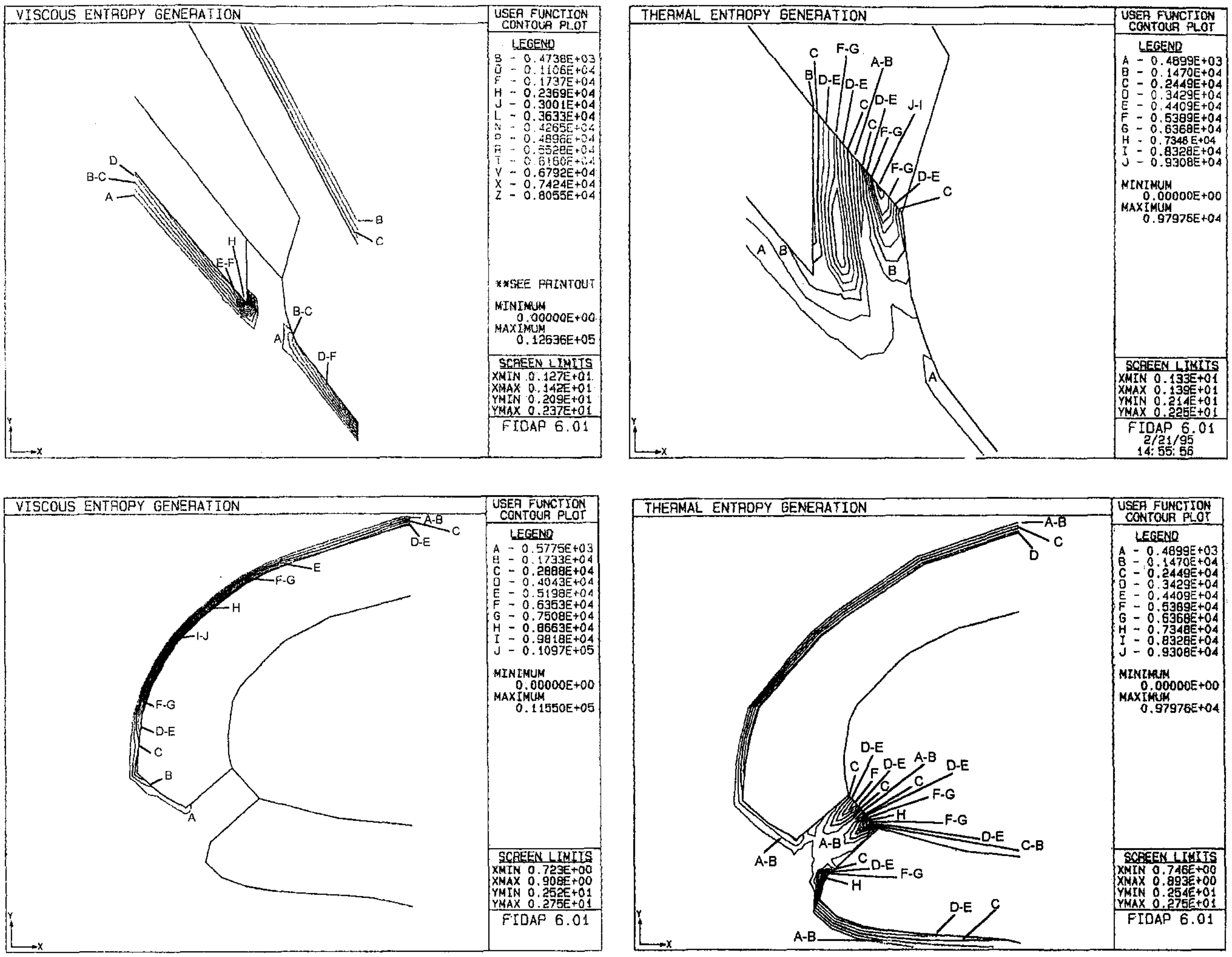

Fig. 8 Computed viscous and thermal entropy generation rates for configuration "*d*"

$$s_v = \frac{2\mu}{T}\left\{\left(\frac{\partial u}{\partial x}\right)^2 + \left(\frac{\partial v}{\partial y}\right)^2 + \frac{1}{2}\left(\frac{\partial u}{\partial y} + \frac{\partial v}{\partial x}\right)^2\right\} \quad (11a)$$

$$s_t = \frac{k_{\text{air}}}{T^2}\left\{\left(\frac{\partial T}{\partial x}\right)^2 + \left(\frac{\partial T}{\partial y}\right)^2\right\}. \quad (11b)$$

The procedure used for numerically computing the elemental values of s_v and s_t is also described in detail in Appendix 1.

The values thus obtained for s_v and s_t are treated as passive scalars, in the sense that their values are considered to be element averages, and are ideally assigned to the centroid of each element of the flow domain, thus obtaining a map of the entropy generation rates over the flow domain, represented by two discrete functions $S_V(x, y)$ and $S_T(x, y)$.

Then, the total entropy generation rates over the entire flow domain can be obtained by numerically integrating these functions, and this can be easily done by weighing the nodal values by the proper element "volumes" (in two-dimensional, areas) and summing over all fluid elements.

4 Results and Discussion

Not all details of the numerical solution are shown here: the general features of the flow fields are the same for all four cases, and the differences are detectable only by inspecting the velocity and temperature fields, as well as the entropy generation rate maps, in some detail [13, 14]. The velocity and temperature profiles are in general agreement with the flow patterns that one would expect in such a cascade. Notice that, since no experimental data are available (at such a low Ma) for a direct comparison, the only conclusion that can be drawn from these flowfields is that the simulation reproduces the general features of the flow as expected. For the purpose of comparing this qualitative agreement with that of "similar" blade profiles, two of the cascade performance parameters of importance for the designer, namely the pressure coefficient and the heat flux from the blade are shown in Figs. 6 and 7. The cooling holes appear to introduce limited disturbances in the flowfield: the cooling jet exiting from the vane at stagnation point is deflected towards the suction side, and maintains its identity (shown by the temperature profiles, reported in [13]) for about $\frac{1}{6}$ of chord length. The jet exiting at $\frac{3}{4}$ chord on the pressure side is very effective in cooling the blade trailing edge, since it is squeezed by the mainstream towards the vane wall, and leaves a thermal signature which extends beyond the trailing edge (Fig. 9). Notice that the maximum blade temperature is not the same for all examined configurations: this is due to the combined effects of the constraints of equal total enthalpy drop across the blade and of fixed coolant temperature and of the different cooling effectiveness of the four designs. Since thermal stress is not an issue here ($T_{\text{max,blade}}$ varies between 1151 and 1268°K), we chose to discount these differences: in critical cases, where thermal fatigue considerations make $T_{\text{max,blade}}$ a relevant parameter, it would be convenient for the designer to release the constraint of equal total enthalpy drop, and tune the simulation so that all configurations display the same $T_{\text{max,blade}}$. All other considerations remain the same, and the

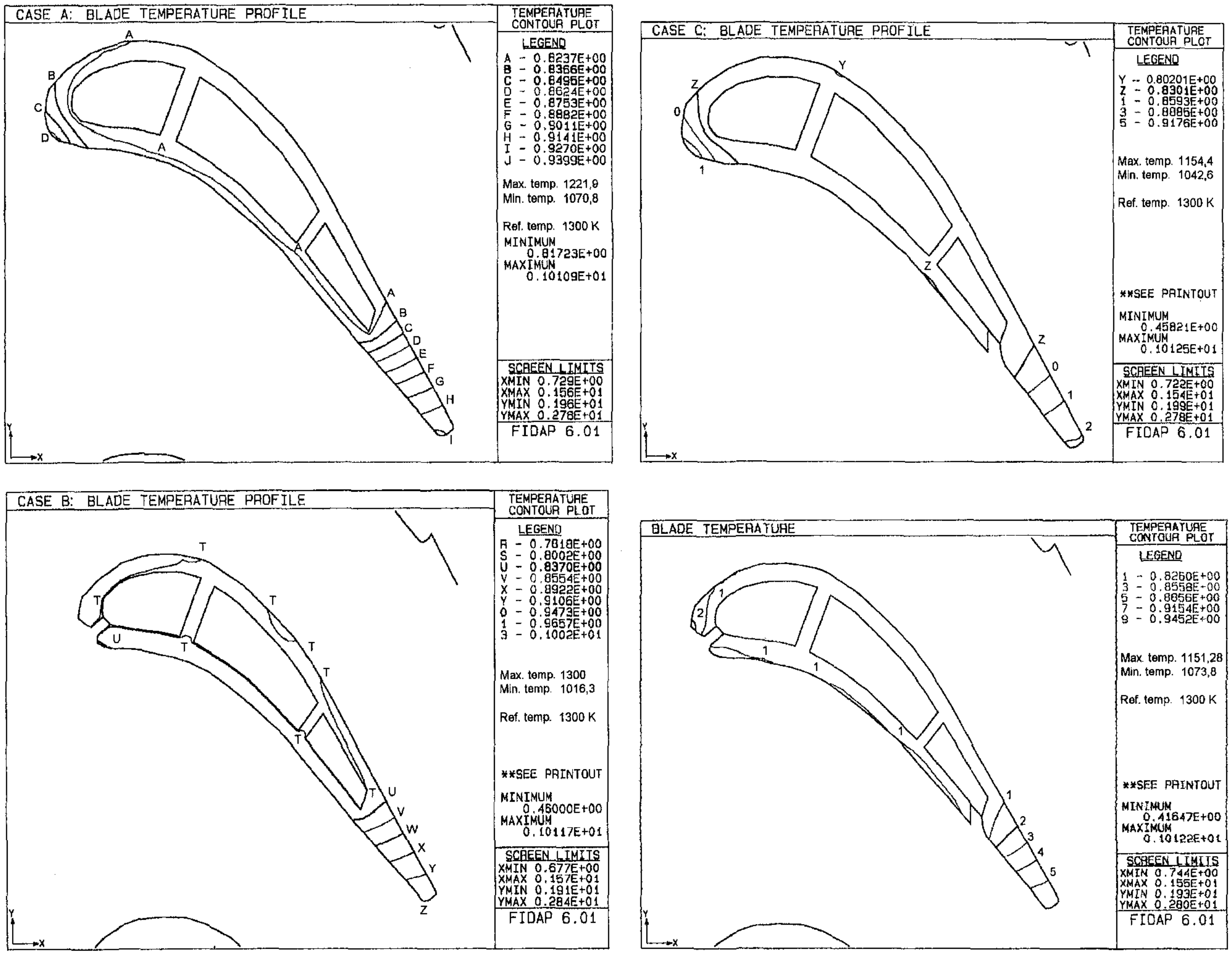

Fig. 9 Computed blade thermal maps

method proposed here maintains its validity. This said, let us recall that what is of importance here is to examine in detail the entropy production rates and their distribution, to assess the merit of the proposed procedure, which (see sections 1 and 2 above) predicts the possibility of relating the performance of a cascade, under the given constraints, to its total entropy production.

From the maps of the viscous and thermal entropy generation rates for the four general configurations studied here, the following conclusions can be drawn:

1 Both s_v and s_t are almost entirely produced in the boundary layer around the blade, due to the high local gradients at the wall (see Figs. 8, 11(*a*) and (*b*). While a "better" blade design could reduce s_v by reducing the wake and eliminating the strong viscous mixing which produces irreversibility, this would only decrease the total viscous entropy generation rate by a non substantial amount. The thermal entropy production, on the other hand, can be substantially reduced by avoiding strong local gradients: this is shown by the lower values of s_t displayed by the film cooled configurations (Table 4). From this point of view, transpiration cooling (i.e., continuous ejection of the cooling air through permeable vane walls) would be the best solution (but has not been simulated here).

2 All three film cooled configurations display a lower value of s_t than that of the internally cooled blade, and this was expected, because the thermal gradients at the wall are, on the average, higher for the nonfilm-cooled design. The unexpected result is that the viscous entropy production can be lower in the film cooled configurations as well (Table 4). A possible physical explanation is that the velocity gradients along the vane wall are significantly reduced, on a large portion of both the pressure- and suction sides, by the thin layer of cooling air, which is squeezed towards the wall and acts as a sort of a "transition layer" between the viscous sublayer and the mainstream flow. Adopting this point of view, transpiration cooling would increase the cascade performance, by decreasing the irreversible viscous losses.

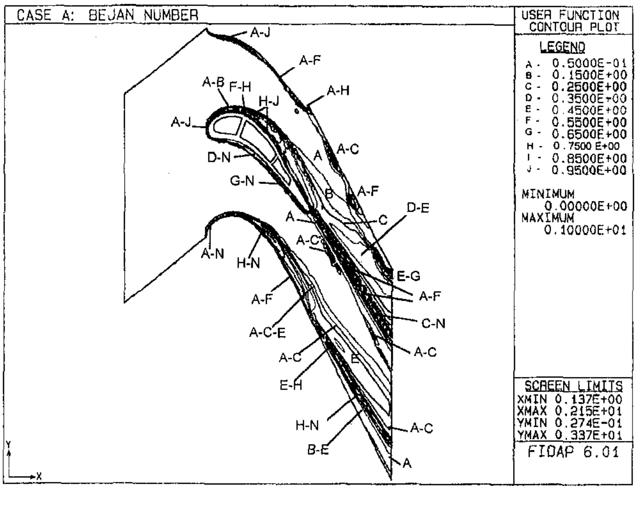

Fig. 10 Computed Bejan number contours

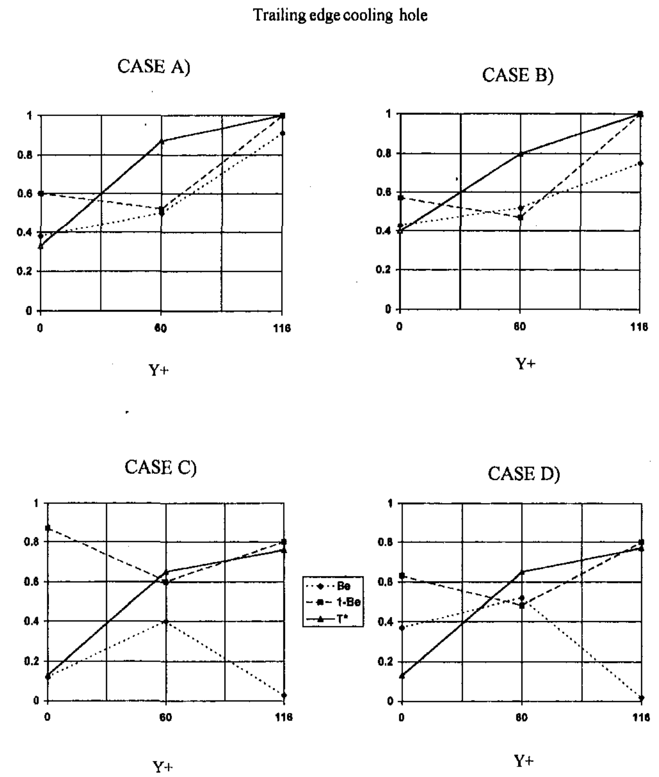

Fig. 11(*a*) Dimensionless thermal (Be) and viscous (1 − Be) entropy generation rates in the wall region. T^* is the dimensionless fluid temperature: $T^* = T/T_{\mathrm{ref}}$

3 The Bejan number, $\mathrm{Be} = s_t/(s_v + s_t)$, which gives an indication of the relative importance of the two causes of flow irreversibility, attains (Fig. 10: again, only the Be for case A is shown, because it is also representative of the general features of the remaining maps) a value of about 0.5 in the vicinity of the wall, where the two contributions s_v and s_t are of the same order of magnitude, reaches a peak value of about .95 in the so-called "inviscid" flow region, where s_v is negligible and s_t is produced by turbulent convective mixing, and it is almost zero (≈ 0.05) upstream of the vane and in the "isothermal core" that constitutes the central portion of the interblade space. Around the cooling holes, Be is about 0.4 to 0.6, (see also Fig. 10), and shows that the two irreversibilities are of the same magnitude.

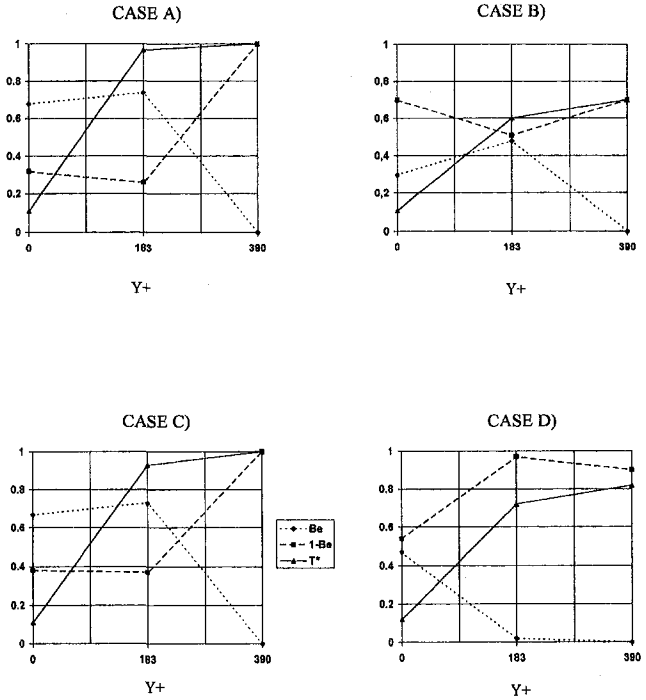

Fig. 11(*b*) Dimensionless thermal (Be) and viscous (1 − Be) entropy generation rates in the wall region. T^* is the dimensionless fluid temperature: $T^* = T/T_{\mathrm{ref}}$

Table 4 Entropy generation rate, enthalpy, drop efficiencies, and Bejan number for the four configurations

configuration	s_t	s_v	s_{tot}	ζ	η	Δh_i	Δh_r	$\overline{\mathrm{Be}}$
design ("a")	76	84.6	160.6	0.318	0.871	70.8	61.7	0.47
"b"	59.3	76.3	135.7	0.26	0.849	72.7	61.7	0.44
"c"	65.5	77.3	152.8	0.288	0.888	69.5	61.7	0.46
"d"	64.5	73.7	148.3	0.27	0.860	71.7	61.7	0.47

(Note: entropy generation rates in W/K, $T_0 = 300$ K, Δh in J/kg)

$$\Delta h_i = h_{1s} - h_{2i}$$
$$\Delta h_r = h_{2s} - h_2$$

$$\zeta = \frac{T_0\, s_{tot}}{m_{blade}\, \Delta h_i} = \text{irreversibility coefficient}$$

Since for a fixed maximum blade temperature the enthalpic efficiency of the blade, given by Eq. 4, depends on the cooling arrangements, it can happen that the same blade profile, with a different number and/or location of cooling holes, produces a different enthalpy drop: this makes the analysis of the relative importance of the losses more difficult, and detracts from the generality of the procedure. Therefore, it was decided to maintain *the total enthalpy drop across the blade constant: this can only be* achieved by slightly modifying the inlet gas temperature. Numerically, the efficiency was computed by integrating the ΔH_{tot} between the inlet (T_g, V_g, m_1) and the outlet (T_2, V_2, $m_1 + m_{\mathrm{cool}}$) sections: in the assumption that T_1 is constant and V_1 has a known profile:

$$H_1 = m_1 h_{1,\mathrm{tot}} = \left[c_p(T_1)T_1 + \tfrac{1}{2}\int_0^{l_1} V_1^2(y)dy \right]$$

$$H_1 \cong m_1 \left[c_p(T_1)T_1 + \frac{1}{2Y}\sum_{n=1}^{n=N_1} \Delta y_n V_n^2 \right], \tag{12}$$

while at the outflow, both T and V vary with y:

$$H_2 = m_2 h_{2,\mathrm{tot}} =$$

$$= (m_1 + m_{\mathrm{cool}}) \left\{ \int_0^{l_1} \left[c_p(T_2)T_2(y) + \frac{V_2^2(y)}{2} \right] dy \right\} =$$

$$= m_1 + m_{\mathrm{cool}} \cdot$$

$$\cdot \left\{ \sum_{n=1}^{n=N_1} \left(\frac{\Delta m_n}{m_1 + m_{\mathrm{cool}}} \right) \left(c_p(T_n)T_n + \frac{V_{2n}^2}{2} \right) \right\}.$$

Taking into account the cooling flow, Eq. 4 now reads

$$\eta_s = \frac{H_1 - H_2}{H_1 - H_2 + H_{\mathrm{cool}}} =$$

$$= \frac{m_1 h_1 - (m_1 + m_{\mathrm{cool}})h_2}{m_1(h_1 - h_{2i}) + m_{\mathrm{cool}}(h_{\mathrm{cool}} - h_{2i})}.$$

Values for η_s and Δh_s are shown in Table 4.

Since it is apparent that the flow topology at the leading edge of

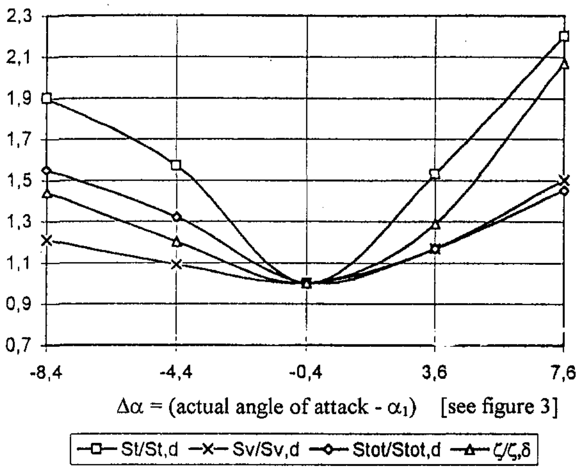

Fig. 12 Influence of the flow coefficient on the entropic losses

the blade has a large influence on the outcome of the calculations, five different sub-cases have been additionally considered, in which the flow coefficient φ has been varied, thus affecting the angle of attack α. It was found (Fig. 12) that the entropic losses show a quadratic dependence on α, which is a result already known, both from conventional loss analyses and from experimental tests. The obvious implication here is that entropic analysis provides the designer with a very strong suggestion, namely that of adopting a value of α in the vicinity of -0.4, and this suggestion is entirely compatible with the conventional one provided by the usual loss correlations: $\alpha = -0.4$ deg was in fact the design value for the blade under consideration.

While the procedure per se is correct both from a theoretical and from a numerical point of view, there are four objections that can be raised about the details of its implementation: first, all simulations being at steady state, the details of the flow have obviously only the validity of "statistical averages". Second, the turbulence has been modeled by a k-ϵ closure, and the behavior of the turbulent quantities in the vicinity of the wall might be only a crude approximation of the actual local flow conditions: therefore, since most s_v is produced in the sub (which was in fact the design value for the blade under consideration) and inner layers, this could invalidate the results. Third, the procedure used to compute s_v and s_t inside of the boundary layer (see Appendix 1) might have introduced numerical errors which would again affect the results. Fourth, the two-dimensional model used here neglects the jet-in-cross stream character of the cooling jet/main flow interaction, and substitutes a turbulent diffusion process for it.

The first two objections can be addressed only by simulating a transpiration cooled vane in unsteady flow conditions and using a different turbulence modeling, and we plan to do so in the future. For what the third objection is concerned, we have found that substantial grid refinements in the inner and viscous sublayer do not cause any significant difference in the trends of s_v and s_t reported in Table 4. The fourth objection cannot be resolved but with more expensive three-dimensional calculations: preliminary results independently obtained on a different stage geometry [9] are entirely compatible with those presented here.

5 Conclusions

A new procedure to assess the losses in a cascade is described in this paper. As a "performance parameter", the total entropy generation rate is proposed.

The total entropy generation rate has the following advantages:

1 It can be computed numerically from known flowfields (where local values for both velocity and temperature are available).

2 It can be readily linked to the real efficiency of the machine of which the cascade is a component through, for example, the "entropy loss" coefficient [6] (called irreversibility coefficient here) or the dimensionless Bejan number [16], or the Guy-Stodola lost work.

3 It can be conveniently split into its viscous and thermal contributions, thus allowing better insight in the flow phenomena.

4 It contains information at two physical levels: at a local level, it shows how and where irreversibilities are present, and to what extent they can be removed by design changes; at a global or integral level, it gives a measure of the "degree of irreversibility" of the flow process in the cascade, which enables a designer to assess the relative performance of different configurations.

The procedure has been applied to a two-dimensional model of a first-row stator of a gas turbine, and four possible configurations have been studied, which differ for the number and locations of the cooling holes. Furthermore, the influence of the flow coefficient φ on the entropy generation rates has been studied for one of the configurations.

The results show that it is indeed possible to differentiate between more and less "irreversible" configurations, and that the increase of irreversible losses is numerically reflected by a corresponding decrease in the blade efficiency. Furthermore, since the two effects (viscous and thermal) can be easily separated, it becomes easier for the designer to assess the merits of the proposed design changes. This is just an introductory study, but the conclusions already show that

—The procedure is indeed feasible and shows potential for being applied to real industrial (three-dimensional) configuration studies.

—There are areas which require further investigation. In particular, the turbulence model (especially the wall functions) is likely to affect the absolute numerical value of the computed entropy generation rates; further, unsteady effects can change the picture: endwall and wake losses, tip leakage effects, and interactions with upstream flow disturbances can change the relative importance of the two effects s_v and s_t; one should keep in mind, of course, that the procedure is as good as the underlying numerical data.

—The method can be employed in field tests as well: if experimental data about the flowfields are known, the calculation of s_v and s_t is straightforward.

As a final note, let us remark that, though not explicitly implemented in this study, a configuration optimization appears feasible, and it appears entirely feasible to develop a design procedure in which the choice of an "almost optimal" blade configuration is heuristically obtained by successive small modifications to a given profile, using an objective function based on the entropy generation in the fluid caused by the local characteristics of the flow.[4]

References

1 Arnone, A., Benvenuti, E., Corradini, U., and Stecco, S. S., 1992, "Theoretical and Experimental Investigation of Temperature Distribution in a Gas Turbine First Stage Nozzle," ASME-IGTI, Vol. 7., pp. 557–562.

2 Bejan, A., 1982, *Entropy Generation Through Heat and Fluid Flow,* John Wiley & Sons, Inc., New York.

3 Benedetti, P. L., and Sciubba, E., 1993, "Numerical Calculation of the Local Rate of Entropy Generation in the Flow Around a Heated Finned Tube," ASME AES-3, ASME, New York.

4 Boyle, R. J., 1991, "Navier-Stokes Analysis of Turbine Blade Heat Transfer," *ASME Journal of Turbomachinery,* Vol. 113, No. 3, pp. 392–403.

5 Camci, C., and Arts, T., 1990, "An Experimental Convective Heat Transfer Investigation Around a Film-Cooled Gas Turbine Blade," *ASME Journal of Turbomachinery,* Vol. 112, No. 3, pp. 497–503.

---

[4] Such a design is "optimal" only inasmuch it produces the least entropy generation under the given operational constraints: if different parameters (in particular, cost) are brought into the picture, the irreversibly generated entropy is only one of the facets of the problem. This is an extremely important point, and the Authors are indebted to D. Sama for stressing it.

6 Denton, J. D., 1993, "Loss Mechanisms in Turbomachines," *ASME Journal of Turbomachinery*, Vol. 115, No. 4, pp. 621–656.

7 Dorney, D. J., and Davis, R. L., 1992, "Navier-Stokes Analysis of Turbine Blade Heat Transfer and Performance," *ASME Journal of Turbomachinery*, Vol. 114, No. 4.

8 Farina, F., and Donatini, F., 1993, "Second Law Approach to the Analysis of Blade Cooling Effects on Gas Turbine Performance," ASME Paper 93-JPGC-GT-7.

9 Holzwart, A., 1997, Private Communication.

10 Mayle, R. E., 1991, "Pressure Loss and Heat Transfer in Channels Roughened on Two Opposite Walls," *ASME Journal of Turbomachinery*, Vol. 113, No. 1.

11 Mayle, R. E., and Andersen, A., 1991, "Velocity and Temperature Profiles for Stagnation Film Cooling," *ASME Journal of Turbomachinery*, 113, No. 3.

12 Moore, J., and Moore, J. G., 1983, "Entropy Production Rates From Viscous Flow Calculations: Part I—A Turbulent Boundary Layer," ASME Paper 83-GT-70.

13 Natalini, G., and Sciubba, E., 1994, "Entropy Generation Rates in Air-Cooled Gas Turbine Nozzles: A Numerical Configuration Study," Proceedings, IGTI-COGEN-TURBO, ASME, New York.

14 Natalini, G., and Sciubba, E., 1994, "A New Criterion for Configuration Optimization of Air-Cooled Gas Turbine Blades, Based on the Minimization of the Local Entropy Production," ASME-AES-33, ASME, New York.

15 Sangiovanni, L., and Gusso, R., 1990, "Recent Trends in the Development of Gas Turbines for Combined Cycles and Cogeneration," Proceedings, ASME-FLOWERS '90, ASME, New York.

16 Sciubba, E., 1990, "Numerical Calculation of Local Irreversibilities in Compact Heat Exchangers," Proceedings, NATO-TIBTD Workshop on 2nd Law, Erciyes University, Kayseri, Turkey.

17 Sciubba, E., 1998, "Optimisation of Turbomachinery Components by Constrained Minimisation of the Local Entropy Production Rate," Proceedings, NATO-ASI Workshop on Thermodynamics and the Optimisation of Complex Energy Systems, Neptun, Romania, Kluwer, pp. 267–295.

18 Sullivan, T. J., 1995, "Novel Aerodynamic Loss Analysis Tecnique Based on CFD Predictions of Entropy Production," SAE Paper 951430.

19 Takeishi, K., Aoki, S., Sato, T., and Tsukagoshi, K., 1992, "Film Cooling on a Gas Turbine Rotor Blade," *ASME Journal of Turbomachinery*, Vol. 114, No. 4, pp. 828–834.

APPENDIX

The Governing Equations and the Numerical Solution Procedure

The governing equations are the Navier-Stokes equations in their cartesian formulation, the continuity- and the energy equation; the problem is two-dimensional, steady, incompressible and with constant fluid properties. The dimensionless form of the equations read as follows (summation convention applies):

$$u_j \frac{\partial u_i}{\partial x_j} = \frac{\partial p}{\partial x_i} + \frac{1}{\mathrm{Re}} \left(\frac{\partial^2 u_i}{\partial x_i \partial x_i} \right) + \mathrm{SGS}_V \tag{A.1}$$

$$\frac{\partial u_i}{\partial x_i} = 0 \tag{A.2}$$

$$u_j \frac{\partial T}{\partial x_j} = \frac{1}{\mathrm{Re}\,\mathrm{Pr}} \left(\frac{\partial^2 T}{\partial x_i \partial x_i} \right) + \mathrm{SGS}_T, \tag{A.3}$$

where SGS represents the effects of the turbulent stresses (simulated here via the k-ϵ model).

The code used for the simulation (FIDAP, presently trademark of FLUENT Inc.) has several built-in turbulence models: the so-called high Reynolds number k-ϵ model has been employed here, and the equations are of the form

$$u_j \frac{\partial k}{\partial x_j} = \frac{1}{\mu_t \,\mathrm{Re}} \frac{\partial^2 k}{\partial x_i \partial x_j} + f_1(k, \epsilon, \mu_t) \tag{A.4}$$

$$u_j \frac{\partial \epsilon}{\partial x_j} = \frac{1}{\mu_t \,\mathrm{Re}} \frac{\partial^2 \epsilon}{\partial x_i \partial x_j} + f_2(k, \epsilon, \mu_t) \tag{A.5}$$

$$\mu_t = f_3(k, \epsilon) \tag{A.6}$$

$$\mathrm{SGS}_V = \frac{\mu_t}{\mathrm{Re}} \frac{\partial u_i}{\partial x_j} \tag{A.7}$$

$$\mathrm{SGS}_T = \frac{\mu_t}{\mathrm{Pr}\,\mathrm{Re}} \frac{\partial T}{\partial x_i}. \tag{A.8}$$

The equations are discretized with a standard finite elements procedure, and the solution is obtained by an iterative "segregated" method, which solves for each variable (u, v, T, k, ϵ) separately, using the values of the other variables known from the previous iteration. The pressure is solved for via a Chorin-like procedure, which originates a Poisson equation.

As an initial flowfield, both a laminar (Re = 400) and an inviscid (Re $\cong \infty$) flowfield have been employed. No direct effect of the initial flowfield on the converged solution has been observed. The entire process has been repeated for each configuration.

The entropy generation rates (also in dimensionless form) have been computed from the converged flowfield via the following equations (in which indicial notation has been substituted by explicit two-dimensional notation for the sake of clarity):

$$\dot{s}_V = \frac{1}{T} \left[\left(\frac{\partial u}{\partial x} \right)^2 + \left(\frac{\partial v}{\partial y} \right)^2 + \frac{1}{2} \left(\frac{\partial u}{\partial y} + \frac{\partial v}{\partial x} \right)^2 \right] \tag{A.9}$$

$$\dot{s}_V = \frac{1}{T^2} \left[\left(\frac{\partial T}{\partial x} \right)^2 + \left(\frac{\partial T}{\partial y} \right)^2 \right]. \tag{A.10}$$

To compute the dimensional specific entropy generation rates, one must multiply s_v and s_t respectively by

$$S_{0v} = \frac{\mu U^2}{L^2 \Delta T} \tag{A.11}$$

$$S_{0T} = \frac{k_{\mathrm{gas}}}{L^2}. \tag{A.12}$$

These entropy generation rates are treated as elemental variables, i.e., they are assigned to the centroid of the element for which they have been computed.

For the wall elements, which have special wall functions to better fit the turbulent logarithmic law of the wall, the following ad hoc procedure had to be employed:

1 The nodal values at the "top" of the wall element ($y^+ \approx 100$) are taken from the flowfield; values from the wall (where $u = v = 0$) upwards are calculated on n intermediate points (here, $n = 10$, but in a three-dimensional calculation this might be too time consuming) using the special wall functions, i.e., these intermediate values can be regarded as "exact" (They are as good as the wall function!)

2 The derivatives are then calculated at each intermediate point by forward differencing, starting from the point on the wall.

3 The entropy generation rates are computed in each of the $2n$ points (n for each side of the quadrilateral perpendicular to the wall).

4 The elemental value of the entropy generation rates is then obtained by numerically integrating the $2n$ intermediate nodal values computed in step 3).

Reaction Diffusion Behaviors for Interface Between Ni-Based Super Alloys and Vacuum Plasma Sprayed MCrAlY Coatings

Y. Itoh

M. Tamura

Power and Industrial Systems
R&D Center,
Toshiba Corporation,
2-1 Ukishima-cho, Kawasaki-ku,
Kawasaki, Kanagawa, 210-0862

The object of this study is overlay coatings of MCrAlY alloy sprayed by a vacuum plasma spray (VPS) process for the protection against high-temperature corrosion and oxidation in the field of gas turbine components. Reaction diffusion behaviors at the interface between the MCrAlY coatings and the substrate, which have an important effect on coating degradation, have not always been clarified. Three kinds of substrate, equiaxis IN738LC, directional solidified CM247LC and single-crystal CMSX-2, and the four kinds of vacuum plasma sprayed MCrAlY coating have been selected for these experiments.

The experimental results showed that the reaction diffusion layers consisted of aluminum compound layer and aluminum depleted layer, excepting that the aluminum depleted layer could not be observed in the case of CoNiCrAlY and NiCoCrAlY coatings. It also indicated that the diffusion thickness could be observed to follow a parabolic time dependence.. The order of reaction diffusion rate was NiCrAlY > CoCrAlY > CoNiCrAlY > NiCoCrAlY independent of the substrates. A convenient computer-aided system was developed for analyzing the reaction diffusion behaviors at the interface between coating and substrate. It was also clear that the estimated results of long time diffusion behaviors by simulation analysis was in good agreement with experiments.

Introduction

For gas turbines, the working environment is extremely severe. The hot-section components must endure various stresses and severe environment at operating temperature. Recently, coating technologies became indispensable to protect against the combustion environment at high-temperature. High-temperature protective coatings used in gas turbine components must withstand extremely severe environmental conditions (Bettridge and Ubank, 1986; Mevrel, 1989). There are two basic coating systems which are currently being used in gas turbines to provide improved corrosion and oxidation resistance, and thereby extend the component life. These are called diffusion coatings and overlay coatings (Nicolls and Stephenson, 1991). The diffusion coatings provide a surface enrichment of aluminum, chromium, and/or silicon element. On the other hand, the overlay coatings are specifically designed corrosion and oxidation resistant alloys which are deposited onto the gas turbine components. In recent years, the MCrAlY alloys where M is iron, nickel, and/or cobalt, have been widely used, and a vacuum plasma spraying (VPS) system has been used to apply the coatings to hot parts, such as blades and duct segments, which are exposed to aggressive gases at high-temperature. In case of the MCrAlY overlay coatings, it was recognized that the interaction of MCrAlY coatings with the substrate was generally negligible during thermal spraying in comparison with the application of diffusion coatings (Wood, 1985). Thermal barrier coatings, which consisted of a air-plasma sprayed Y2O2 partial-stabilized ZrO2 layer applied directly over a air-plasma sprayed MCrAlY bond coat layer, provide to improve the thermal resistivity for air-cooled gas turbine combustors. Nowadays, as operating temperature of gas turbines are increased, thermal barrier coatings, which consisted of a vacuum plasma sprayed MCrAlY bond coat layer, are developed for air-cooled gas turbine blades and vanes (Duvall et al., 1982; Miller, 1987). In addition to extending the components life, the coating technologies, such as high-temperature protective coatings and thermal barrier coatings, can increase turbine operating temperature. However, thermal stability of sprayed coatings tends to decrease with increasing gas turbine operating temperature. The thermal stability of sprayed coatings is one of the important factors for maintaining the protective quality against extremely severe environmental conditions. The thermal sprayed coatings degrade not only by loss of scale forming elements such as aluminum and chromium from the coating surface, but also by interdiffusion loss between the sprayed coating and the substrate (Mazars et al., 1987; Nicholls and Stephensen, 1991). The interdiffusion degradation tends to be important as the temperature increases (Sugita et al., 1995; Srinivasan et al., 1995). The mechanical interactions between coatings and superalloy substrates were investigated (Wood, 1989; Ishiwata et al., 1995). However, the interdiffusion behaviors at the interface between the MCrAlY coatings and Ni-based superalloy substrates have not been fully clarified. On the other hand, computer simulations of polyphase diffusion begin to develop for its importance (Engstrom et al., 1997).

In the present paper, a convenient polyphase diffusion model based on the theory of reaction diffusion was investigated for analyzing the growth behavior of interdiffusion layer. Three typical kinds of Ni-based superalloys, and four kinds of vacuum plasma sprayed MCrAlY coatings were selected for diffusion experiments because of their industrial importance. The reaction diffusion behaviors among these materials combination were made clear. Moreover, the thicknesses of reaction diffusion layers at the interface between the MCrAlY coatings and Ni-based superalloys were estimated for some cases.

Contributed by the Gas Turbine Division of The American Society of Mechanical Engineers for publication in the ASME Journal of Engineering for Gas Turbines and Power.

Manuscript received by the Gas Turbine Division December 1, 1998; final revision received by the ASME Headquarters March 3, 1999. Technical Editor: H. Nelson.

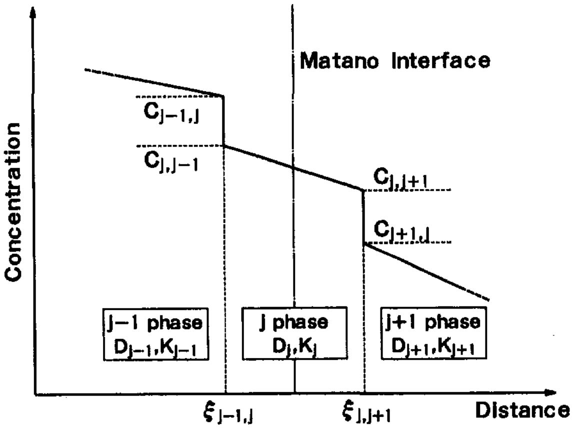

Fig. 1 Concentration-distance curve in reaction diffusion layers

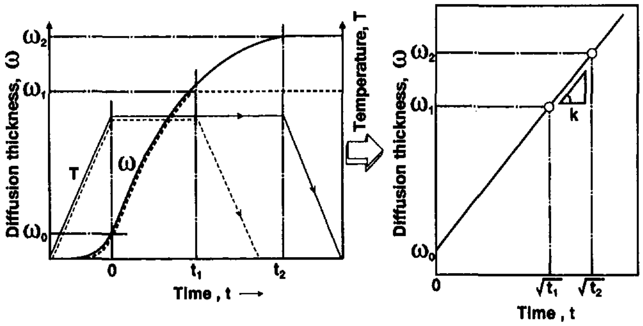

Fig. 2 Determination method of diffusion rate constant from diffusion thickness versus time curve based on a parabolic time law

Reaction Diffusion Model

The application of Fick's first law to polyphase diffusion in binary systems leads to a simple physical interpretation of various possible types of behavior in the growth of diffusion layers (Heumann, 1952; Wagner, 1959). On the other hand, numerous experimental observations of the isothermal growth of the intermediate phase layers in binary systems have been reported, and it has generally been found that the position of the phase interfaces and the thickness of the reaction diffusion layers formed to follow a simple parabolic time law (Takahashi et al., 1992). Figure 1 schematically illustrates the concentration-distance curve in the reaction diffusion layers which show the formation of polyphases due to mutual diffusion in the binary system. The rate equation for reaction diffusion in the jth layer in n-phase system (as shown in Fig. 1) has been given as Eq. (1) (Kidson, 1961).

$$\omega_j\ (=\xi_{j,j+1}-\xi_{j-1,1})=k_j\cdot t^{1/2},\tag{1}$$

where

$$k_j=2\{[((DK)_{j+1,j}-(DK)_{j,j+1})/(C_{j,j+1}-C_{j+1,j})]\\-[((DK)_{j,j-1}-(DK)_{j-1,j})/(C_{j-1,j}-C_{j,j-1})]\},$$

where ω_j is the thickness of the jth layer.

k_j is called rate constant for reaction diffusion layer growth of the jth phase. Where D is the diffusion coefficient, K is the material constant, and C is the concentration. This equation indicates that the each diffusion thickness formed by the reaction diffusion can be observed to follow the parabolic time dependence. This equation shows theoretical basis of this study and the appropriateness of regarding the rate constant, k_j, as a material constant.

Recently, it is pointed out that the diffusion rate is controlled by the activity gradient and not the concentration gradient. Namely, the concentration gradient is an approximation of the activity gradient in case of polyphase diffusion. As described later, it is necessary to confirm that experimental information reveals the parabolic behavior in the polyphase diffusion.

By the way, the reaction diffusion growth during heating and cooling in experiments is not negligible under the case of analyzing the experimental datum as shown in Fig. 2. This is especially so during the heating process, because each of the reaction diffusion layers begin to grow. Namely, the reaction diffusion thicknesses, ω_0 and ω' can't be ignored in comparison with the total diffusion thickness, such as ω_1 and ω_2. The ω_0 is the reaction diffusion thickness during the heating process, and the ω' is the one during the way to cooling process as shown in Fig. 2. Then, the total diffusion thickness, ω_1 and ω_2 can be indicated as follows, respectively:

$$\omega_1=\omega_0+\omega'+k\cdot t_1^{1/2}\tag{2}$$

$$\omega_2=\omega_0+\omega'+k\cdot t_2^{1/2},\tag{3}$$

where k is the rate constant of this diffusion phase under the condition that the rate of heating and cooling is always constant.

The rate constant, k is given by

$$k=(\omega_1-\omega_2)/(t_1^{1/2}-t_2^{1/2}).\tag{4}$$

It is clear that Eq. (4) doesn't include the ω_0 and ω'. Therefore, the both ω_0 and ω' are considered negligible in calculating the rate constant, k from experimental datum in case that the rate of heating and cooling is constant in experiments. Figure 2 shows the experimental technique to determine the rate constant, k. Actually, three datum points for holding time were used to determine it.

Experimental Procedures

This investigation used three kinds of substrates, such as equiaxed IN738LC, directionally solidified CM247LC and single-crystal CMSX-2, which were typical Ni-based superalloys for gas turbine blades. Four kinds of commercial spraying powders, CoCrAlY, CoNiCrAlY, NiCrAlY, and NiCoCrAlY, were selected. The CoCrAlY is a well known powder for corrosion protective coatings at medium-temperature (1000–1200 K). The NiCrAlY is generally used for oxidation and high-temperature protective coatings (>1200 K) and as a bond coat layer of thermal barrier coatings. The CoNiCrAlY and NiCoCrAlY are advanced coating powders that are more stable in interdiffusion than the CoCrAlY and NiCrAlY. The chemical compositions of these materials are given in Table 1. In the middle of Table 1, the normal heat-treatment conditions for each Ni-based superalloys are shown.

Table 1 Chemical composition of materials used

Substrates	Chemical composition (mass %)									
	Ni	Cr	W	Mo	Co	Aℓ	Ti	Nb	Ta	Hf
IN738LC*1	Bal.	15.8	2.46	1.78	8.11	3.45	3.60	0.92	1.92	–
CM247LC*2	Bal.	8.04	9.38	0.51	9.31	5.63	0.72	0.01	3.27	1.56
CMSX-2*3	Bal.	7.73	7.89	0.59	4.56	5.66	1.03	<0.01	6.07	<75ppm

Heat treatment ; *1 1393K×2h Ar gas cooled, 1116K×24h Ar gas cooled
*2 1503K×2h Ar gas cooled, 1353K×4h Ar gas cooled, 1143K×20h Ar gas cooled
*3 1588K×3h Ar gas cooled, 1353K×4h Ar gas cooled, 1143K×20h Ar gas cooled

Coating powders	Chemical composition (mass %)					Powder size
	Co	Ni	Cr	Aℓ	Y	
CoCrAℓY	Bal.	–	28.20	6.25	0.35	-400 mesh
CoNiCrAℓY	Bal.	31.27	20.33	8.20	0.51	-400 mesh
NiCrAℓY	–	Bal.	31.45	11.55	0.83	-400 mesh
NiCoCrAℓY	23.23	Bal.	16.94	12.47	0.49	-325 mesh

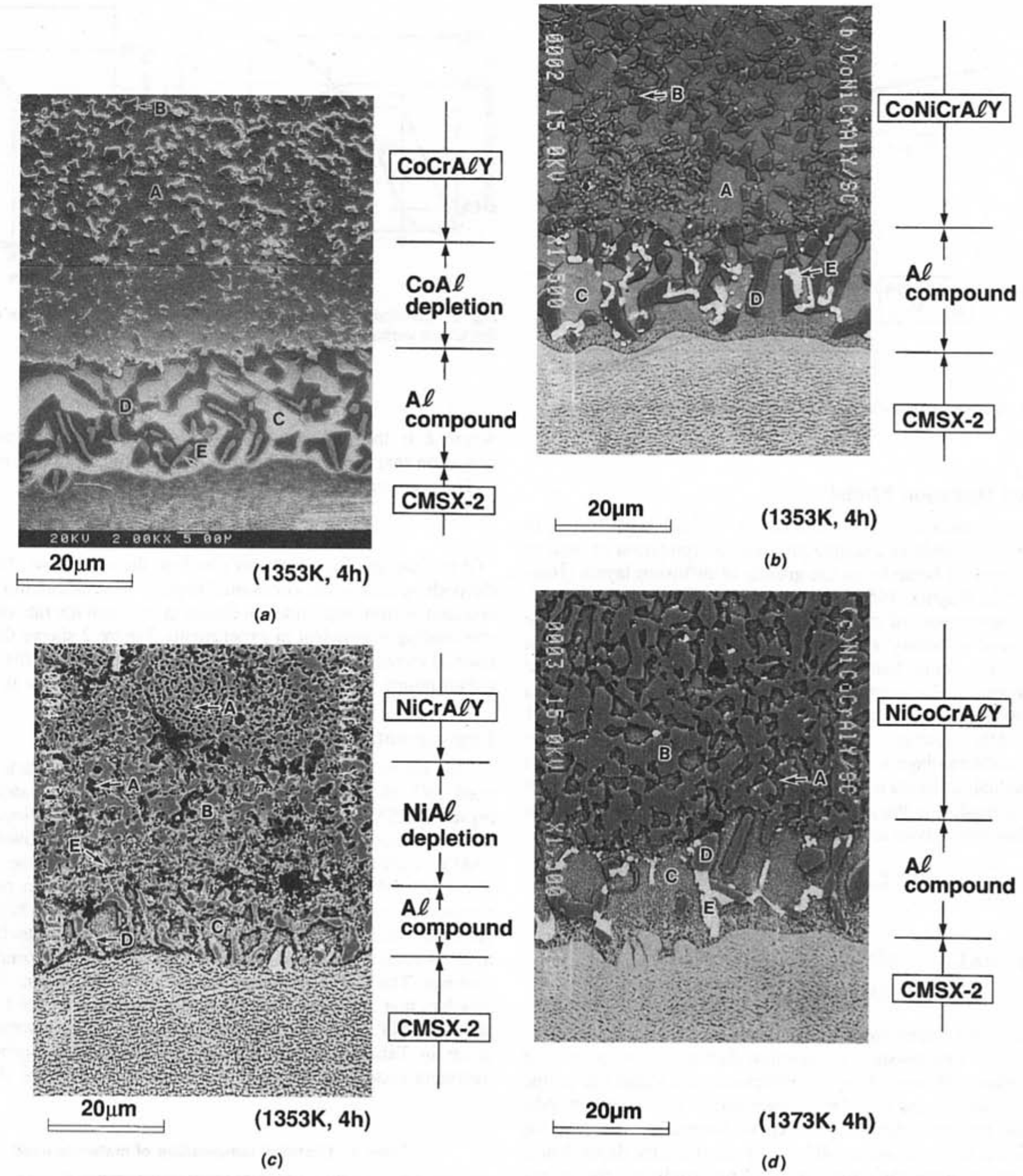

Fig. 3 Microstructure of diffusion layers formed between plasma sprayed MCrAlY and single-crystal CMSX-2: (*a*) CoCrAlY/CMSX-2 interface; (*b*) CoNiCrAlY/CMSX-2 interface; (*c*) NiCrAlY/CMSX-2 interface; and (*d*) NiCoCrAlY/CMSX-2 interface.

The VPS coatings were carried out with A-2000V VPS system (Plasma Technik), under the following conditions: preheating temperature 823 K during transferred arc treatment, voltage 66 V, current 750 A, spraying distance 275 mm, and argon gas atmosphere 6.5 kPa. Single face of all substrates which were 5 mm in thickness was sprayed MCrAlY coatings with 0.3 mm in thickness after the pretreatment of blasting and transferred arcing. In case of directionally solidified and single-crystal substrates, the MCrAlY coating side of substrate is parallel to the (1 0 0) crystal face of CMSX-2 and CM247LC, which shows the excellent high-temperature strength. The as-sprayed specimens (20 × 10 × 5 mm) for investigating the reaction diffusion behaviors were machined out, and the MCrAlY sprayed specimens were placed in a furnace set at 1323–1413 K in argon atmosphere 101.3 kPa and exposed for 2.0, 4.0, and 10.0 h in order to make clear the reaction diffusion behaviors between MCrAlY coatings and substrates. The heating rate was 540 K/h (=constant), and the cooling rate was 2900 K/h (=constant) until 400 K and furnace cooled after that.

After the heat-treatment, the cross-section of test specimens was observed and reaction diffusion thickness measured using an optical microscope. Metallic compounds precipitated in the coating layer and the reaction diffusion layer were observed by a scanning electron micrography (SEM) and a electron probe microanalyzer (EPMA).

Reaction Diffusion Behaviors

A typical microstructure of diffusion layer formed at the interface between VPS CoCrAlY coating and single-crystal CMSX-2 after heat-treatment at 1353 K for 4 h is shown in Fig. 3(*a*). The micrographs of Fig. 3 are reflection electron images for only polished surfaces. It is clearly found that the VPS CoCrAlY coating is composed of two phases, which are CoAl metallic compounds (particle "B" in Fig. 3(*a*)) and CoCr solid solution matrix (part "A"). Two reaction diffusion layers can be observed, consisting of a CoAl depleted layer and an Al compound precipitate layer. It is considered that the CoAl depleted layer is formed by Co diffusion from the VPS CoCrAlY coating to the single-crystal substrate (Mazars et al., 1987). Also, Ni diffusion occurs from the CMSX-2 substrate to the VPS CoCrAlY coating, and fine NiAl precipitates can be newly observed in the CoAl depleted layer by EDX analysis. On the other hand, it is confirmed by EDX and EPMA analyses that the black Al compound precipitate (part "D") in NiCoCr matrix (part "C") is coarse (Ni, Co)Al. Fine precipitated particles are formed along the lower boundary of Al compound layer. The white precipitations ("E" part) appeared to precipitate inside the (Ni, Co)Al precipitates, and *W* and Ta elements are clearly detected and *C* element cannot be clearly detected. Also, by EDX analysis Ta and Ti elements are detected from fine precipitates formed at the interface between the CoAl depleted layer and the (Ni, Co)Al precipitate layer.

Also, a typical microstructure of diffusion layer is shown in Fig. 3(*b*) in case of VPS CoNiCrAlY coating and single-crystal substrate CMSX-2 after the same heat-treatment at 1353 K for 4 h. One reaction diffusion layer of nearly 22 μm in thickness can be observed. The diffusion of Co, Cr, and Al elements is recognized from the VPS CoNiCrAlY to the single-crystal CMSX-2 and conversely the diffusion of Ni and Ti elements is recognized from the single-crystal CMSX-2 to the VPS CoNiCrAlY. Though the reaction diffusion layer cannot be clearly observed on the CoNiCrAlY coating side, it is observed in CoNiCr matrix (part "A") that precipitated (Ni, Co)Al compounds (part "B") become fine particles as the Al compound layer is approached. It seems that the (Ni, Co)Al compounds begin to dissolve into the CoNiCr matrix as the result of decreased the Al concentration, which is caused by the diffusion of Al element from the coating layer to the substrate and the diffusion of Ni element from the substrate to the coating layer. On the other hand, black slender precipitates ("D") and neighboring white precipitates ("E") are clearly observed in the CoNiCr matrix in the reaction diffusion layer on the substrate side. Using EPMA and EDX analyses, the precipitate of "D" is thought to be coarse (Ni, Co)Al, and Ti, *W*, and Ta elements are detected from the precipitate of "E" and *C* element cannot be clearly detected. Fine precipitated particles are formed along the lower boundary of Al compound layer.

A microstructure of the diffusion layer formed at the interface between VPS NiCrAlY coating and single-crystal substrate CMSX-2 after heat-treatment at 1353 K for 4 h is shown in Fig. 3(*c*). Two layered reaction diffusion can be clearly observed. It seems that these reaction diffusion layers are formed by the diffusion of Cr and Al elements from the NiCrAlY coating layer to the substrate (Mazars et al., 1987), and the diffusion of Ni and Ti elements from the substrate to the NiCrAlY coating. The reaction diffusion layer of nearly 20 μm in thickness can be observed. The NiCrAlY coating layer is formed by the NiCr matrix (part "B") and a lot of precipitated NiAl compounds (part "A"). However, the precipitated NiAl particles are diminished and condensed. This phenomenon can be explained by the disappearance and reprecipitation of NiAl compound phase by the Al diffusion from the NiCrAlY coating to the substrate and the Ni diffusion from the substrate to the NiCrAlY coating. On the other hand, the reaction diffusion layer of nearly 20 μm in thickness can be observed on the side of CMSX-2 substrate. In this reaction diffusion layer formed on the substrate side, the featureless matrix (part "C") and the slender precipitates (part "D") are observed. The CMSX-2 is the Ni-based superalloy with Ni_3 (Al, Ti) precipitates, but the precipitates (part "D") are NiAl from EPMA and EDX analyses. This is caused by the Al diffusion from the NiCrAlY coating to the substrate and the Ni diffusion from the substrate to the NiCrAlY coating. By EPMA analysis, a lot of Cr element which diffused from the NiCrAlY coating layer to the CMSX-2 substrate was detected at part "C", and it seems that the featureless part "C" is NiCr solid-solution. Moreover, Ti element is detected here and there at the initial interface (part "E") and/or the NiCrAlY coating layer. In case of the equiaxed IN738LC and directionally solidified CM247LC substrates, chromium carbides can be clearly detected in each Al compound layers.

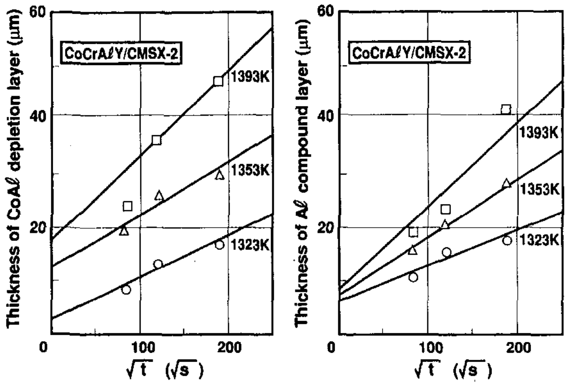

Fig. 4 Growth behaviors of reaction diffusion layer at interface between vacuum plasma sprayed CoCrAlY and single-crystal CMSX-2

Figure 3(*d*) shows a typical microstructure of diffusion layer that is formed at the interface between VPS NiCoCrAlY coating and single-crystal substrate CMSX-2 after heat-treatment at 1373 K for 4 h. It is clear that only one reaction diffusion layer can be observed. The same behavior of reaction diffusion as interface of CoNiCrAlY/CMSX-2 is observed. Namely, the reaction diffusion layer cannot be observed on the side of NiCoCrAlY coating layer. And there is not a change of the precipitate state of (Ni, Co)Al compound phase (part "B") in the NiCoCr matrix (part "A"). This causes many (Ni, Co)Al precipitates in the NiCoCrAlY coating layer and small difference of chemical compositions between the NiCoCrAlY coating and the CMSX-2 substrate. The reaction diffusion change in quality of NiCoCr matrix is small in comparison with any other MCrAlY coating. On the other hand, the reaction diffusion layer of nearly 20 μm in thickness can be observed on the side of CMSX-2 substrate. The featureless NiCoCr matrix (part "C"), the black slender precipitates (part "D") and the neighboring white precipitates (part "E") are observed. It seems that the precipitates (part "D") are (Ni, Co)Al by EPMA and EDX analyses, and Ti, *W*, and Ta elements are detected in part "D" by EDX analysis. But, *C* element cannot be clearly detected in part "D".

Rate Constants for Reaction Diffusion Analysis

It was found that any sprayed MCrAlY coatings were composed of the precipitate Al compound phase in the Ni and/or Co matrix as shown in Fig. 3. Also, it was observed that the reaction diffusion layers between the MCrAlY coating and the substrate were basically formed with the newly precipitate Al compound layer and the Al compound depleted layer. In the case of equiaxed IN738LC and directionally solidified CM247LC, basically the same behavior of reaction diffusion could be observed except the thickness of diffusion.

The representative growth behaviors of two reaction diffusion layers formed at the interface of CoCrAlY/CMSX-2 are shown in Fig. 4. The experimental data of reaction diffusion thickness follows approximately a simple parabolic time law. There is a tendency for the reaction diffusion thickness to increase with increasing the heating temperature and the holding time. In any other combination between the coatings and the substrates, the parabolic time law was confirmed to apply in the same manner.

The temperature dependence of rate constants that were obtained from the slope of straight lines in Fig. 4 was shown in Fig. 5(*a*). It is clear that the Arrhenius type temperature dependence in both CoAl depleted layer thickness and (Ni, Co)Al precipitate

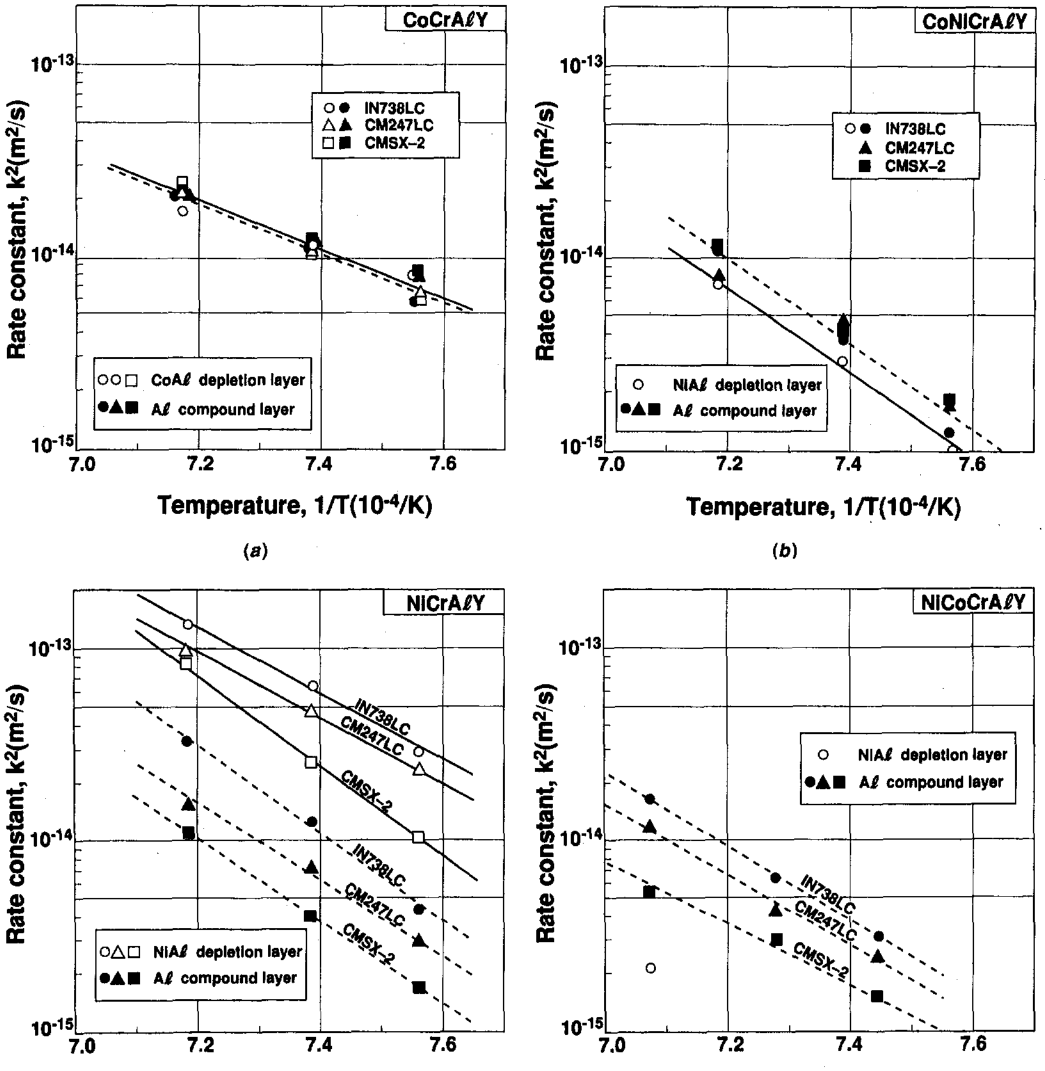

(*a*) (*b*) (*c*) (*d*)

Fig. 5 Temperature dependency of diffusion rate constants between vacuum plasma sprayed MCrAlY coating and Ni based superalloy on a parabolic time law: (*a*) CoCrAlY coating; (*b*) CoNiCrAlY coating; (*c*) NiCrAlY coating; and (*d*) NiCoCrAlY coating.

layer thickness applies. And all rate constants are in fairly good agreement within this experimental range. The effect of substrate on the rate constants was not significant in this case. The rapid formation of reaction diffusion layers at the CoCrAlY/Ni-based superalloys interface is caused by the concentration slope of Ni element from the substrate to the coating layer, which does not contain Ni element. Namely, it was because the Co concentration in the coating matrix decreased due to the Co diffusion from the coating layer to the substrate, and the precipitate CoAl in the coating layer was dissolved and depleted. It was also considered that the Ni concentration in the substrate matrix decreased due to the Ni diffusion from the substrate to the coating layer and the Ni_3 (Al, Ti) precipitate in the coating layer was dissolved and depleted, and (Ni, Co)Al compounds were precipitated.

In Fig. 5(*b*), the temperature dependence of rate constants for two reaction diffusion layers formed at the CoNiCrAlY/Ni-based superalloys interface is shown. The Arrhenius type temperature dependence for NiAl depleted layer, which formed in case of only CoNiCrAlY/IN738LC, was observed. There is a tendency for the rate constants of CoNiCrAlY to be smaller than the rate constants of CoCrAlY as shown in Fig. 5(*a*). It seems that the rate constants of NiAl depleted layer were smaller than the rate constants of (Ni, Co)Al precipitate layer. The effect of substrate on the rate constants of (Ni, Co)Al precipitate layer is not remarkable. It is considered that the reaction diffusion layers at the interface of CoNiCrAlY/Ni-based superalloys are formed by the difference of Ni and Co concentration between the coating layer and the substrate. However, the difference of Ni and Co concentration is small in comparison with the CoCrAlY/Ni-based superalloy systems. Namely, by the Ni diffusion from the substrate to the coating layer, the Ni concentration in the substrate matrix decreases and the Ni_3 (Al, Ti) precipitates in the substrate is dissolved and depleted and (Ni, Co)Al compounds are newly precipitated. The CoCr concentration in the coating matrix does not remarkably change despite the Co diffusion from the coating matrix to the substrate, and the formation of a NiAl depleted layer is not clearly observed.

The temperature dependence of rate constants in case of the NiCrAlY/Ni-based superalloys is shown in Fig. 5(*c*). In the case of both the NiAl depleted layer and the (Ni, Co)Al precipitate layer, the Arrhenius type temperature dependence is observed. The rate constants of the NiAl depleted layer are larger than the rate constants of (Ni, Co)Al precipitate layer. The effect of substrate on the rate constants is remarkable, and the order of rate constants is IN738LC > CM247LC > CMSX-2. Especially, the rate constants of the NiAl depleted layer show higher values in comparison with the interface of CoCrAlY/Ni-based superalloys. This is caused by the Co and Ni diffusion from the substrate to the coating matrix, and it seems that the NiAl precipitates are decreased relatively. It is considered that the Ni concentration in the substrate matrix decreases and the Ni_3 (Al, Ti) precipitates in the substrate is dissolved and depleted and (Ni, Co)Al compounds are newly precipitated.

Finally, Fig. 5(*d*) shows the temperature dependence of rate constants in case of the NiCoCrAlY/Ni-based superalloys. The NiAl depleted layer can be observed only in case of the IN738LC substrate heat-treated at 1413 K using a scanning electron micrography. Also, the Arrhenius type temperature dependence for rate constants of (Ni, Co)Al precipitate layer is confirmed as shown. The effect of substrate on the rate constants of (Ni, Co)Al precipitate layer is remarkable, and the order of rate constants is IN738LC > CM247LC > CMSX-2. However, the rate constants of reaction diffusion layer are as small as the rate constants for CoNiCrAlY/Ni-based superalloys. Especially, it is clear that the rate constants for the interface of NiCoCrAlY/CMSX-2 are extremely small.

As mentioned above, it is very important to match the coating compositions, such as Ni and Co elements in order to suppress the reaction diffusion at the interface between the coating layer and the substrate. As a matter of course, the substrate compositions are important in controlling the reaction diffusion. However, it seems that crystal morphologies don't affect the reaction diffusion behaviors. Within this experimental range, it is possible to suppress the reaction diffusion at the interface between the MCrAlY coating layer and Ni-based superalloy. The apparent activation energies for the growth of reaction diffusion layer, which were calculated from the Arrhenius plot of total diffusion thickness, were between 220 and 280 kJ/mol, and the remarkable differences for the MCrAlY coatings and Ni-based superalloys were not observed. These values are nearly agreement with the activation energies of the diffusion of Ni (269 kJ/mol) in Co or Co (282 kJ/mol) in Ni. It is considered that the apparent activation energy for the growth of reaction diffusion layer is related to the activation energy of the diffusion element inside the coating layer. From the consideration of activation energies for the growth of reaction diffusion layers, it may be deduced that the growth of reaction diffusion layers is controlled by the diffusion of Ni and Co elements through the reaction layer.

Estimation for Reaction Diffusion Behaviors

The rate equation for the reaction diffusion in the binary system has been already reported as described Eq. (1) (Kidson, 1961). According to Eq. (1), the estimation method of reaction diffusion thickness during various heating histories is described below.

Namely, from the differential of Eq. (1).

$$d\omega_j/dt = k_j^2/(2\omega_j). \tag{5}$$

Thus, Eq. (5) may be written as

$$\omega_j = \sum_{t=0}^{t} [k_j^2/(2\omega_j)]dt. \tag{6}$$

Using the rate constants, k_j^2 that are obtained by the experiments as shown in Fig. 5(*a*)–(*d*), it is possible to estimate the growth of reaction diffusion thickness ω_j of each phases by Eq. (6). When heating temperature changes with heating time, the reaction diffusion thickness of each phases can be estimated to grow subject to Eq. (6). The developed system flow for the reaction diffusion analysis is shown in Fig. 6. In this system, the reaction diffusion analysis can be conducted by the input of initial datum and temperature history on the condition that n equals to 0.5.

By the way, in case of the high-temperature protective MCrAlY coatings for gas turbines, the diffusion heat treatment as described in Table 1 is conducted after vacuum plasma spraying to improve the adhesion of coating, removing the porosity and recovering the substrate damage caused by VPS heating. The quantitative estimation of reaction diffusion thickness is important to control the coating degradation.

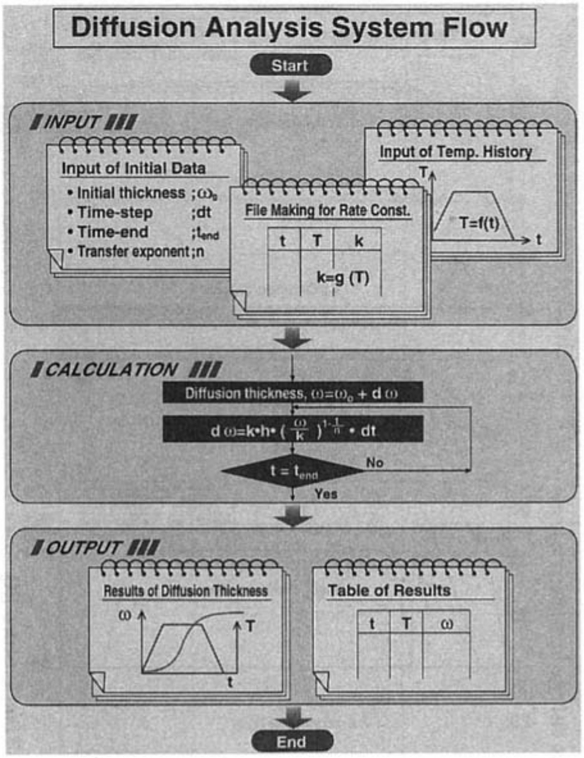

Fig. 6 System flow of reaction diffusion analysis

In Fig. 7(*a*), (*b*), and (*c*), the reaction diffusion behaviors at the interface between the VPS MCrAlY coating and the CMSX-2 substrate are shown during the diffusion heat-treatment. The temperature history for the diffusion heat-treatment is also shown in figures. In any cases the reaction diffusion thickness is almost completely formed during the first heat-treatment at higher temperature and is far greater than the diffusion thickness growth during the second heat treatment at lower temperature. It is clear that the growth of reaction diffusion thickness during heating process cannot be ignored in comparison with the total reaction diffusion thickness. The reaction diffusion thickness of CoAl depleted layer is almost equal to the thickness of (Ni, Co)Al compound layer in the case of CoCrAlY coating (Fig. 7(*a*)). The reaction diffusion thickness of NiAl depleted layer is about four times as thick as the thickness of NiAl compound layer in the case of NiCrAlY coating (Fig. 7(*b*)). As shown in Fig. 7(*a*), (*b*), and (*c*), it is possible to reduce the total reaction diffusion thickness during the diffusion heat-treatment to $\frac{1}{7}$–$\frac{1}{8}$ using the NiCoCrAlY and CoNiCrAlY coatings. The same analyses were conducted for the combinations of CoCrAlY/IN738LC and CoCrAlY/CM247LC. The obtained results for each divided temperature step (A–H) are shown in Fig. 8. It is a natural result that the reaction diffusion layer grows thick in the temperature range of region D. However, the reaction diffusion thickness during heating process (A–C) cannot be ignored, and the reaction diffusion thickness during cooling process (*E*, *H*) is fairly thin layer. These tendencies are not remarkably affected by the substrate, such as IN738LC, CM247LC and CMSX-2.

The degradation due to the interdiffusion during long term thermal exposure is an important problem in practical use of high-temperature components (Srinivasan et al. 1995). In Fig. 9, the long time estimation results of reaction diffusion thickness are shown in case of heating temperature 1273 K. It is clear that both

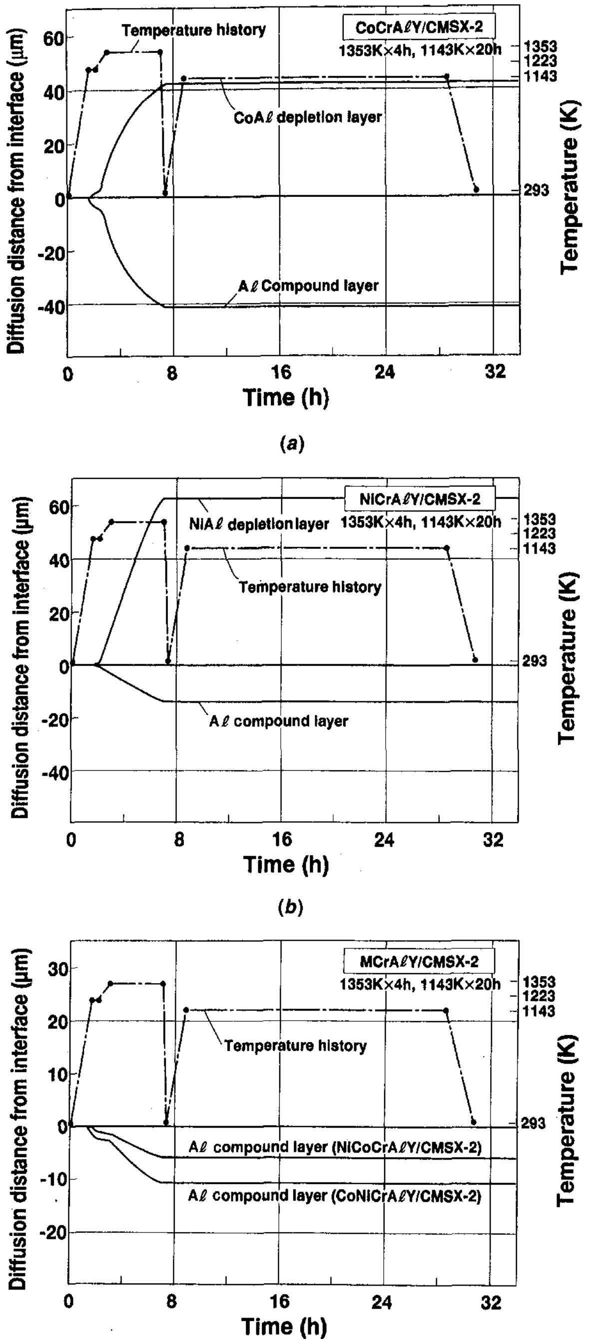

(*a*)

(*b*)

(*c*)

Fig. 7 Analysis results of reaction diffusion behavior between vacuum plasma sprayed MCrAlY coatings and single-crystal CMSX-2 during aging heat-treatment: (*a*) CoCrAlY coating; (*b*) NiCrAlY coating; and (*c*) CoNiCrAlY and NiCoCrAlY coatings.

the CoAl depleted layer and (Ni, Co)Al compound layer grow gradually with increasing the heating time. The dashed line is the result of (Ni, Co)Al compound layer in the case of the interface of CoNiCrAlY/CMSX-2. Though the heating temperature 1273 K is higher than the operating temperature of CMSX-2, this test temperature is setup to compare the experimental datum as shown in the figure. Though the rate constants used for estimation are the experimental datum as shown in Fig. 5, it is also clear that comparison with the experiments shows that the estimation of long time diffusion behaviors is effective. The microphotographs are shown in Fig. 10(*a*) and (*b*). The interface between the VPS CoCrAlY coating and the CMSX-2 substrate is shown in Fig. 10(*a*) at 1273 K for 1000 h. And the interface between the VPS CoNiCrAlY coating and the CMSX-2 substrate is shown in Fig. 10(*b*) at 1273 K for 1000 h. Though each reaction diffusion layer is thick, the microstructure is in good agreement with the thin reaction diffusion layer at 1353 K for 4 h as shown in Fig. 3. However, the (Ni, Co)Al compounds grow longer in the direction of coating thickness, and the white precipitates such as *W* and Ta increase in quantity as shown in Fig. 10(*a*). The CoNiCrAlY coating on CMSX-2 substrate is effective in suppressing the coating degradation at high temperature in comparison with the CoCrAlY coating.

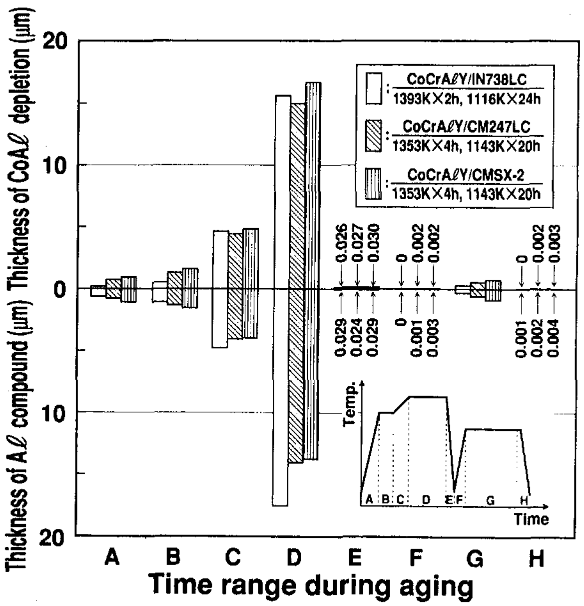

Fig. 8 Effect of temperature change during aging heat-treatment on growth of reaction diffusion layer

Conclusion

The experimental results showed that the reaction diffusion layers formed between MCrAlY coatings and Ni-based superalloys, consisted of Al compound layer and Al compound depleted layer. However, the Al compound depleted layer could not be observed clearly in the case of CoNiCrAlY and NiCoCrAlY coatings except for IN738LC substrates. The thickness of reaction diffusion layer formed between MCrAlY coatings and Ni-based superalloys increased with increasing the heating temperature and

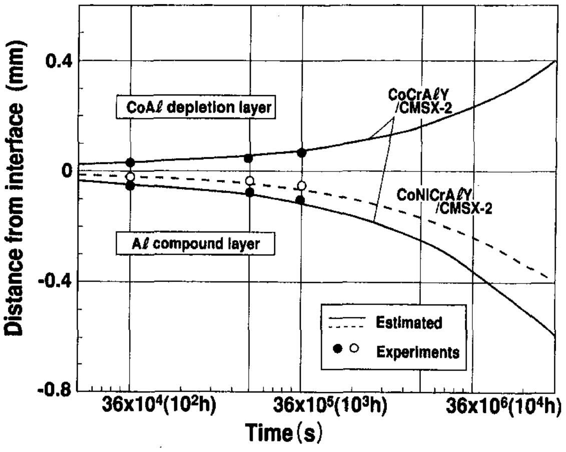

Fig. 9 Long time estimation of growth of reaction diffusion layer for MCrAlY/CMSX-2 interface

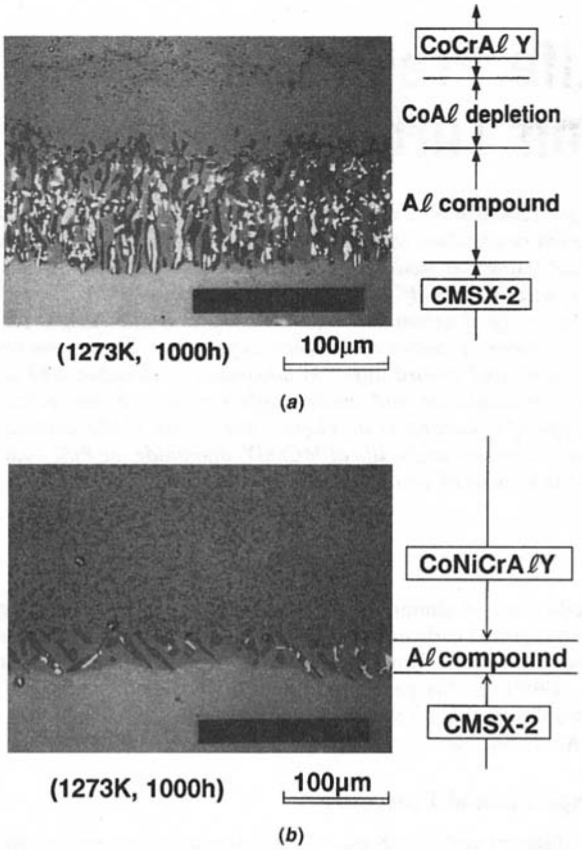

Fig. 10 Microstructure of reaction diffusion layers formed at interface between vacuum plasma sprayed MCrAlY and single-crystal CMSX-2: (*a*) CoCrAlY/CMSX-2 interface; and (*b*) CoNiCrAlY/CMSX-2 interface.

heating time. It was demonstrated that the growth of reaction diffusion layer could be expressed by the parabolic law with time exponent $\frac{1}{2}$. And the order of reaction diffusion rate was NiCrAlY > CoCrAlY > CoNiCrAlY > NiCoCrAlY with independent of the substrate type, such as IN738LC, CM247LC, and CMSX-2. From the consideration of activation energy for the growth of reaction diffusion layers, it may be deduced that the growth of reaction diffusion layers are controlled by mutual diffusion of Ni and Co elements through the reaction layer.

The convenient computer-aided interactive system was developed for analyzing the reaction diffusion behaviors at the interface of bonded materials. The reaction diffusion thickness formed at the interface between the MCrAlY coatings and CMSX-2 substrate was estimated during diffusion heat treatment. It was clear that the growth of reaction diffusion thickness during heating process could not be ignored in comparison with the total reaction diffusion thickness. It was also clear that the estimation of long time diffusion behaviors at the interface between the MCrAlY coatings and CMSX-2 substrate was possible by comparison with experiments.

References

Bettridge, D. F., and Ubank, R. G., 1986, "Quality Control of High-Temperature Protective Coatings," *Materials Science and Technology*, Vol. 2, pp. 232–242.

Duvall, D. S., and Ruckle, D. L., 1982, "Ceramic Thermal Barrier Coatings for Turbine Engine Components," ASME Paper 82-GT-322.

Engstrom, A., Morral, J. E., and Agren, J., 1997, "Computer Simulations of Ni-Cr-Al Multiphase Diffusion Couples," *Acta Mater.*, Vol. 45-3, pp. 1189–1199.

Heumann, T., 1952, "Zur Berechnung von Diffusions koeffizienten bei Ein- und Mehrphasiger Diffusion in Festen Legierungen," *Zeit. Physik. Chem.*, Vol. 201, pp. 168–189.

Ishiwata, Y., Saitoh, M., and Itoh, Y., 1995, "Coating Design and Evaluation of High-Temperature Strength," Proceedings, of 1995 Yokohama International Gas Turbine Congress, 95-Yokohama-IGCT-71, pp. 199–106.

Kidson, G. V., 1961, "Some Aspects of the Growth of Diffusion Layers in Binary Systems," *J. of Nuclear Materials*, Vol. 3-1, pp. 21–29.

Mazars, P., Manesse, D., and Lopvet, C., 1987, "Degradation of MCrAlY Coatings by Interdiffusion," ASME Paper 87-GT-58.

Mevrel, R., 1989, "State of the Art on High-Temperature Corrosion-Resistant Coatings," *Material Science and Engineering*, Vol. A120, pp. 13–24.

Miller, A. M., 1987, "Current States of Thermal Barrier Coatings—An Overview," *Surface and Coating Technology*, Vol. 30, pp. 1–11.

Nicholls, J. R., and Stephenson, D. J., 1991, "High Temperature Coatings for Gas Turbine," *Surface Engineering*, pp. 156–163.

Srinivasan, V., Cheruvu, N. S., Cari, T. J., and O'Brien, C. M., 1995, "Degradation of MCrAlY Coating and Substrate Superalloy During Long Term Thermal Exposure," *Materials and Manufacturing Processes*, Vol. 10-5, pp. 955–969.

Sugita, Y., Ito, M., Isobe, N., Sakurai, S., Gold, C. R., Bloomer, T. E., and Kameda, J., 1995, "High-Temperature Degradation of Coating and Substrate in Gas Turbine Blade," ASME Paper 95-GT-358.

Takahashi, Y., Nakamura, T., and Nishiguchi, K., 1992, "Dissolution Process of Surface Oxide Film During Diffusion Bonding of Metals," *J. of Material Science*, Vol. 27, pp. 485–498.

Takahashi, M., Itoh, Y., and Miyazaki, M., 1995, "Thermal Barrier Coatings Design for Gas Turbine," Proceedings, Thermal Spraying (ITSC'95), High-temperature Society of Japan, pp. 83–88.

Wagner, C., 1956, "Reaktionstypen bei der Oxydation von Legierungen," *Zeitschrift fur Elektrochemie*, Vol. 63-7, pp. 772–782.

Wood, M. I., 1989, "Mechanical Interactions between Coatings and Superalloys Under Conditions of Fatigue," *Surface and Coating Technology*, Vol. 39/40, pp. 29–42.

Wood, J. H., Schilke, P. W., and Collins, M. F., 1985, "Vacuum Plasma Spray Turbine Bucket Coating Development," ASME Paper 85-GT-9.

K. S. Chan
Mem. ASME

N. S. Cheruvu

G. R. Leverant

EPRI Materials Center for
Combustion Turbines,
Southwest Research Institute,
Mechanical and Materials Engineering Division,
P. O. Drawer 28510,
San Antonio, TX 78228

Coating Life Prediction for Combustion Turbine Blades

A life prediction method for combustion turbine blade coatings has been developed by modeling coating degradation mechanisms including oxidation, spallation, and aluminum loss due to inward diffusion. Using this model, the influence of cycle time on coating life is predicted for GTD-111 coated with an MCrAlY, PtAl, or aluminide coating. The results are used to construct a coating life diagram that depicts failure and safe regions for the coating in a log-log plot of number of startup cycles versus cycle time. The regime where failure by oxidation, spallation, and inward diffusion dominates is identified and delineated from that dominated by oxidation and inward diffusion only. A procedure for predicting the remaining life of a coating is developed. The utility of the coating life diagram for predicting the failure and useful life of MCrAlY, aluminide, or PtAl coatings on the GTD-111 substrate is illustrated and compared against experimental data.

Introduction

Land-based combustion turbine blades are generally coated with overlay or diffusion coatings to improve oxidation and corrosion resistance. The effectiveness of these coatings diminishes with time after exposure to high temperatures and repeated heat-up and cool-down cycles. These coatings usually fail when a continuous protective oxide layer, e.g., alumina, cannot be formed on the coating surface due to the depletion of Al. The loss of Al from the coating can take place by the following three means: (1) oxidation; (2) spallation; and (3) inward diffusion. All three degradation mechanisms, which reduce the amount of Al available for forming a protective oxide layer, are detrimental to the useful life of the coatings; consequently, they must be taken into account in any coating life model.

Several investigators (Nesbitt and Heckel, 1984; Lee et al., 1987; Nesbitt, 1989a, 1989b; Nesbitt and Barrett, 1993) have developed life prediction methods for coatings based on consideration of cyclic oxidation, spallation, and diffusion of oxide forming elements. These earlier life prediction approaches were based on an empirical spallation model that contains temperature-dependent material constants (Probst and Lowell, 1988; Lowell et al., 1991). Applications of these models at low temperatures can be difficult because of the lack of spallation data for obtaining the model constants. For life estimation, the following two criteria were proposed for defining the onset of coating failure: (1) a critical Al content (Nesbitt and Barrett, 1993) and (2) the volume fraction of the β phase in the aluminide coatings (Lee et al., 1987).

A new coating life model was recently proposed for predicting the useful life of combustion turbine coatings such as MCrAlY, aluminide, and PtAl (Chan et al., 1997). The model, named COATLIFE, includes treatment of oxidation, spallation, and inward diffusion of Al. The mechanism-based model differs from previous models in the treatment of oxide spallation by adapting a fracture mechanics approach that results in explicit relationships between weight of oxide spalled and relevant physical and mechanical properties of the oxide (Chan, 1997). As a consequence, possible temperature dependence of material parameters is easily defined and any extrapolation of model constants with temperature, if necessary, can be justified and done with confidence. Applications of the model to the oxidation, spallation, and lifetime predictions of aluminide and platinum aluminide coatings have been reported earlier for cases without the effect of inward diffusion of the oxide forming element, Al, into the substrate (Chan et al., 1997). In this paper, the effect of oxidation, spallation, and inward diffusion on the coating lives of MCrAlY, aluminide, and PtAl coatings are considered.

Experimental Procedure

Material and Coatings. Cyclic oxidation data were generated for GTD-111 test specimens coated with MCrAlY, aluminide, and PtAl coatings. These experimental data were used for obtaining the material constants in the coating life model and for verifying the predictive capability and accuracy of the model. The MCrAlY coating was processed by an EB-PVD process while the aluminide and PtAl coatings were processed via a pack cementation process. The MCrAlY coating is a CoCrAlY with a microstructure of approximately equal volume percent of β phase and γ solid solution. Both the aluminide and PtAl coatings show a microstructure of equiaxed β grains in the as-processed condition. The nominal coating thicknesses were 33.8, 65, and 253 μm for aluminide, platinum aluminide, and MCrAlY coatings, respectively. The GTD-111 material was heat-treated to a microstructure containing a bimodal distribution of primary (cuboidal) and secondary (spherical) gamma prime particles.

Cyclic Oxidation Testing. The cyclic oxidation tests were performed in the cyclic oxidation testing facility at SwRI. During cyclic oxidation tests, the specimens were inserted in a furnace maintained at a constant peak temperature, which was 1066°C (1950°F) or 954°C (1750°F). They were held in the furnace for 30 or 55 min and then moved to the cooling system and cooled by forced air for 5 min. The specimens took approximately four minutes to reach the peak temperature and one minute to cool from the peak temperature to room temperature. They were then returned to the furnace and the thermal cycle repeated. The cyclic oxidation test was interrupted at specified intervals to weigh the specimens. After a selected number of thermal cycles, microsections were prepared from some coated specimens for metallographic evaluation. The microstructure and coating composition were determined using optical and scanning electron microscopy and energy dispersive spectroscopy (EDS). Details of the experimental procedure are described elsewhere (Chan et al., 1997; Cheruvu et al., 1998).

Coating Life Model

The coating life model used in this investigation is COATLIFE, which is a computer program that simulates cyclic oxidation on a

---

Contributed by the International Gas Turbine Institute (IGTI) of THE AMERICAN SOCIETY OF MECHANICAL ENGINEERS for publication in the ASME JOURNAL OF ENGINEERING FOR GAS TURBINES AND POWER. Paper presented at the International Gas Turbine and Aeroengine Congress and Exhibition, Stockholm, Sweden, June 2–5, 1998; ASME Paper 98-GT-478.

Manuscript received by IGTI March 25, 1998; final revision received by the ASME Headquarters March 23, 1999. Associate Technical Editor: R. Kielb.

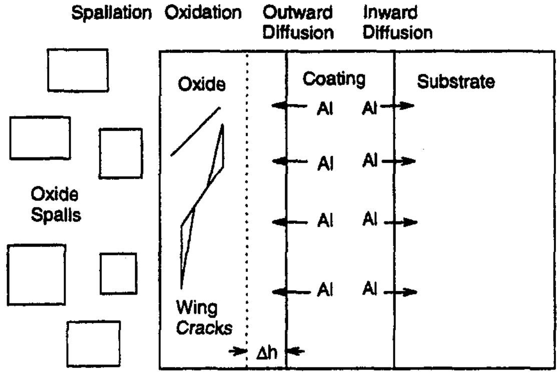

Fig. 1 Schematics of degradation mechanisms treated in the COATLIFE model

cycle-by-cycle basis and predicts the useful life of a coating based on a critical Al criterion. The development of the cyclic oxidation model is described in a paper by Chan (1997), while an extension of the model for predicting the usable life of coatings under cyclic oxidation without the effect of inward diffusion is presented in Chan et al. (1997). In this paper, the influence of inward diffusion on coating life is modeled. The result is then used to develop a coating life diagram for predicting the remaining life of combustion turbine coatings.

Figure 1 shows a schematic of the cyclic oxidation model and the proposed methodology for predicting the usable life of a coating. The important features in the coating life model: (1) oxidation kinetics; (2) oxide fracture and spallation; (3) inward diffusion; (4) overall kinetics of cyclic oxidation and depletion of the oxide-forming element, Al, due to oxidation, spallation, and inward diffusion; and (5) a life predicting scheme based on a critical concentration of Al for the formation of a protective oxide layer. A brief description of these essential features of the coating life model is presented in the next five sections.

1 Oxidation Kinetics

The weight of oxide, W_{ox}, formed during a thermal cycle is modeled using a parabolic growth law that relates the weight of oxide formed to the weight of oxygen gained by the coating, as given by

$$W_{ox} = Z\sqrt{k_p t}, \tag{1}$$

where k_p is the oxidation kinetic constant, t is time of oxidation, and Z is the ratio of the molecular weight of the oxide to the atomic weight of oxygen in the oxide. After spallation occurs at the end of a thermal cycle, the thickness of the oxide is reduced, leading to an increase in the oxidation rate. This increase in the oxidation rate after spallation is modeled by using the concept of an equivalent time introduced by Probst and Lowell (1988). The equivalent time, t_e, for cyclic oxidation corresponds to the time required to form an oxide layer of identical thickness under isothermal conditions. The equivalent time, t_e, is calculated at each cycle based on the cycle time and the current thickness of oxide layer on the coating surface.

2 Spallation

The spallation law proposed by Chan (1997) was used in COATLIFE. As described earlier, the spallation model treats both bulk and interface spallation. In the current model, the weight of oxide spalled, W_s, during an arbitrary thermal cycle is given by

$$W_s = q_c(\Delta T - \Delta T_c)^2 H(\Delta T - \Delta T_c) \times \left[1 + p\left(\frac{W_o}{W_{ox}}\right)^m\right]\left[\frac{W_{ox}}{W_o}\right]^{1+m}, \tag{2}$$

where p and q_c are the interface and bulk spallation constants, respectively; m is the spallation exponent; $H()$ is the Heaviside function; ΔT is the temperature drop; and ΔT_c is the critical temperature drop below which spallation does not occur. The parameter q_c incorporates material parameters concerning the length (l_o), angle (ψ), and density (ζ_o) of microcracks, the Young's modulus (E_{ox}), fracture toughness (K_{ox}), and the difference in the CTE, $\Delta\alpha$, between the oxide and the coating. The parameter p relates interface defect length and fracture toughness to their counterparts for the bulk. The referenced weight, W_o, is arbitrary and can be taken as 1 mg/cm^2 or any other convenient value. In general, only the constants p, q_c, ΔT_c, and m need to be evaluated from experimental data if one adopts a phenomenological approach. In the present paper, the values for these model constants were evaluated from the experimental weight change data.

3 Inward Diffusion

The current version of COATLIFE includes a treatment of inward diffusion of Al from the coating to the substrate. The diffusion of aluminum into the substrate requires a multicomponent analysis since most engineering alloys and coatings contain several elements in their compositions. In an n-component system the diffusivity $[D]$ is an $(n - 1) \times (n - 1)$ property matrix, and the corresponding Fick's second law, given by (Kirkaldy, 1970), is

$$\frac{\partial[C]}{\partial t} = \frac{\partial}{\partial x}[D]\frac{\partial[C]}{\partial x}, \tag{3}$$

where $[C]$ is concentration, x is distance, and t is time. A simple but approximate solution to Eq. (3) was developed and used in COATLIFE. The validity of this simplified diffusion was verified using the a finite-difference diffusion code, COSIM, developed at NASA-Lewis (Nesbitt, 1984). The input to the simplified diffusion model is coefficients of diffusion of Al and Cr in the diffusion matrix. In many cases, the coefficients of diffusion are not known for the coating of interests and must be evaluated by calibrating the coating life model to pertinent experimental data.

4 Overall Kinetics of Cyclic Oxidation

The overall kinetics of cyclic oxidation has been modeled as a process that involves the formation and spallation of oxides during thermal cycling. The weight of oxide remained, W_r, on the coating surface after a thermal cycle can be expressed as (Probst and Lowell, 1988; Lowell et al., 1991)

$$W_r = W_{ox} - W_s, \tag{4}$$

where W_{ox} and W_s are given by Eqs. (1) and (2), respectively. Expressions for the cumulative weight change, total weight of oxide spalled, and the weight of aluminum loss have been formulated as a function of number of thermal cycles. The expression for the cumulative weight change per unit area, W_c, after n thermal cycles is (Probst and Lowell, 1988; Lowell et al., 1991)

$$W_c(n) = (1/Z)W_r(n) - (1 - 1/Z)\left(\sum_1^n W_s(n)\right), \tag{5}$$

while the cumulative metal loss, W_m, of the oxide-forming element from the coating due to oxidation and spallation is given by (Probst and Lowell, 1988; Lowell et al., 1991)

$$W_m(n) = (1 - 1/Z)\left[W_r(n) + \sum_1^n W_s(n)\right] \tag{6}$$

for the n^{th} cycle. The parameters of W_{ox}, W_r, W_s, W_c, W_m, t_e, and weight gain, W_g, are calculated for each of the thermal cycles. The loss of Al due to inward diffusion is then subtracted from Eq. (6).

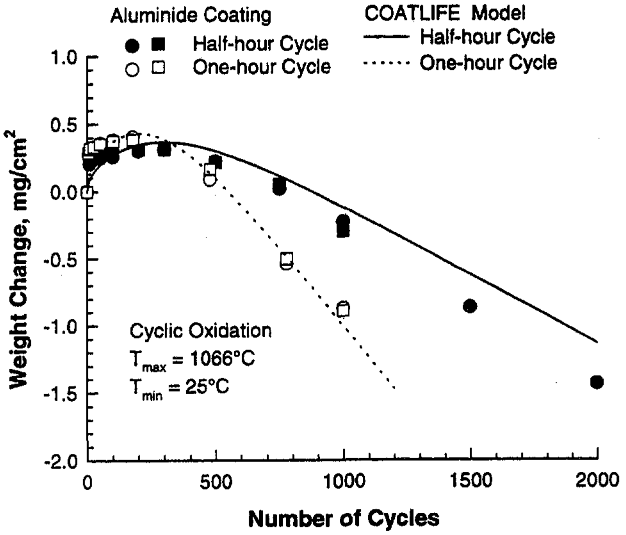

Fig. 2 Experimental weight change data compared against model calculation for aluminide coated GTD-111

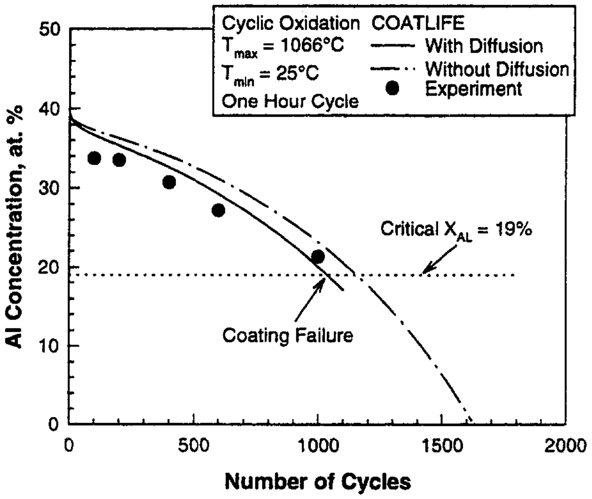

Fig. 3 Comparison of calculated and observed Al content as a function of thermal cycles for aluminide-coated GTD-111

5 Life Prediction Methodology

The volume fraction of the β phase, $V_\beta(n)$, in the coating at the n^{th} cycle is calculated using the lever rule and is given by

$$V_\beta = 1 \quad \text{for} \quad X_{\text{Al}} \geq X^{\beta}_{\text{Al}} \tag{7}$$

and

$$V_\beta(n) = \frac{X_{\text{Al}}(n) - X^{*}_{\text{Al}}}{X^{\beta}_{\text{Al}} - X^{*}_{\text{Al}}} \quad \text{for} \quad X^{\beta}_{\text{Al}} \geq X_{\text{Al}}(n) \geq X^{*}_{\text{Al}}, \tag{8}$$

where X^{β}_{Al} is the aluminum content in the β phase and X^{*}_{Al} is the aluminum content in the γ' or γ phase at the appropriate phase boundary in equilibrium with the β phase.

The remaining life, RL, is defined based on the assumption that the useful life of the coating is zero when the volume fraction of the β phase is zero, leading to

$$RL = \frac{X_{\text{Al}}(n) - X^{*}_{\text{Al}}}{X_{\text{Al}}(0) - X^{*}_{\text{Al}}} \quad \text{for} \quad X_{\text{Al}}(0) \geq X_{\text{Al}}(n) \geq X^{*}_{\text{Al}}, \tag{9}$$

which gives a remaining life of unity when $X_{\text{Al}}(n) = X_{\text{Al}}(0)$ but a zero remaining life when $X_{\text{Al}}(n) \leq X^{*}_{\text{Al}}$.

Comparison of Model Prediction and Experimental Data

The COATLIFE model was applied to predict the useful life of coatings on laboratory specimens subjected to cyclic oxidation. The experimental data were those generated on GTD-111 specimens coated with an aluminide, PtAl, or MCrAlY coating. They were thermally cycled between room temperature and a peak temperature of either 954°C (1750°F) or 1066°C (1950°F). Experimental weight change curves were obtained and used to determine the material constants in the coating life model. Once the model constants have been determined, COATLIFE was used to compute the aluminum content, volume fraction of β, and the remaining life of the coating as a function of thermal cycles.

Figure 2 shows a comparison of the calculated and measured weight change curves for thermal cycling between 25°C and a peak temperature of 1066°C in one-hour and half-hour cycles. The calculated and measured Al content in the coating as a function of thermal cycling between 25°C and 1066°C is shown in Fig. 3. The experimental values of Al content were calculated based on experimental values of the volume fraction and aluminum content of β and γ' in the coating. Model calculations with and without diffusion are presented in Fig. 3. The dash-dotted line shows that the model prediction without diffusion slightly overpredicts the Al content in the coating during thermal cycling. The COATLIFE model calculation with diffusion is shown as the solid curve in Fig. 3. This result was obtained by matching the calculation with diffusion to the experimental values of the Al content in order to establish the effective diffusion coefficient. Once the effective diffusion is calibrated at one temperature, the model can be used to predict the coating life at any other temperatures.

Comparison of the calculated and measured weight change curves for PtAl coating at two cycle times is shown in Fig. 4. The volume fraction of β in the platinum aluminide coating is compared against model calculations as a function of thermal cycle in Fig. 5 for the case of a maximum cycling temperature of 1066°C. Model calculations with and without inward diffusion are presented in Fig. 5, which shows the model overpredicted the volume fraction of the β phase when inward diffusion was ignored. Agreement between model calculations and experimental data was improved when inward diffusion was included in the model, Fig. 5. This result indicates that inward diffusion was important and affected the life of the PtAl coating significantly.

A comparison of the calculated and measured weight change curves for MCrAlY coatings at 954° and 1066°C is presented in

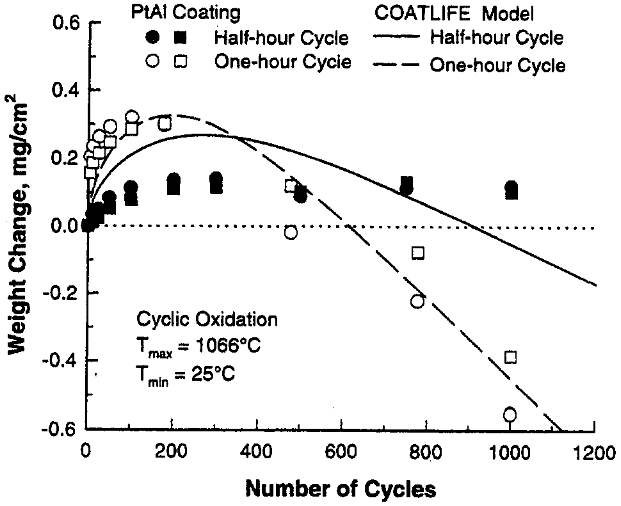

Fig. 4 Experimental weight change data compared against model calculation for platinum aluminide-coated GTD-111

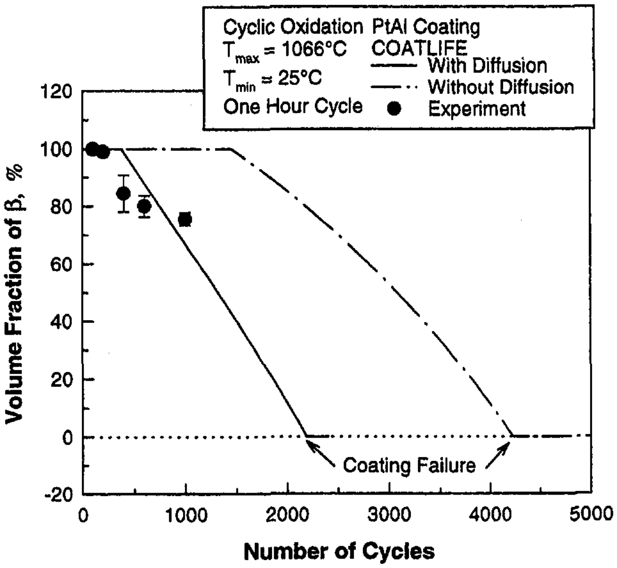

Fig. 5 Calculated and measured values of the volume fraction of β as a function of thermal cycles for PtAl-coated GTD-111

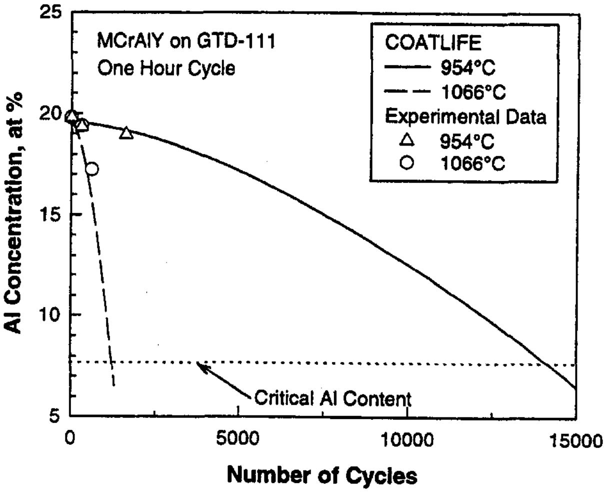

Fig. 7 Computed and measured values of the Al content in MCrAlY-coated GTD-111

Fig. 6. Both experimental data were used to obtain the material constants in the oxidation kinetics and spallation equations. The Al content and volume fraction of the β phase have been calculated; the result for the Al content is compared against experimental data in Fig. 7, which shows good agreement between model and experiment.

Coating Life Diagram

Once a set of model constants has been obtained for a coating, COATLIFE can be used to calculate the time to failure of the coating by varying the cycle time. The calculated values of the times-to-failure are then divided by the cycle time to obtain the number of startup cycles to coating failure. A coating life diagram is then obtained by plotting the number of startups as a function of cycle time in a log-log plot. As an illustration, a coating life diagram calculated for MCrAlY coatings subjected to cycling between 25° and 1066°C is presented in Fig. 8. The solid line, calculated via COATLIFE, represents the failure boundary for the coating under the imposed temperature. The coating is protective when the number of startup cycles at a given cycle time, e.g., point *P*, is less than that of the failure boundary. Conversely, the coating has failed if the number of startup cycles exceeds the coating failure boundary, as illustrated by point *F* in Fig. 8. The coating life diagram thus provides a simple and rigorous means for forecasting the remaining life of a coating after it has been in service. The controlling failure mechanism along the coating failure boundary varies with cycle time and temperature. In general, oxidation and spallation dominate at short cycle times while oxidation and inward diffusion dominate at long cycle times. At intermediate cycle times, coating failure involves oxidation, spallation, and inward diffusion, as shown in Fig. 8.

For illustration, Fig. 9 shows the coating life diagram calculated for PtAl coating on IN738 and compared against field data. The actual operating temperatures of the blades were not known but were estimated to be in the range of 870°C to 927°C. The coating life boundaries were computed for 870°C and 927°C and the results are shown as the solid and dotted lines, respectively. COATLIFE predicted that the coatings in these five blade are still functional and protective. EDS measurements indicated the Al content in the coatings ranged from 24 percent to 39 percent, which are in accord with model calculations. The remaining life of these coatings are represented by the difference in the number of startup cycles from their current positions to the failure boundary at a given cycle time.

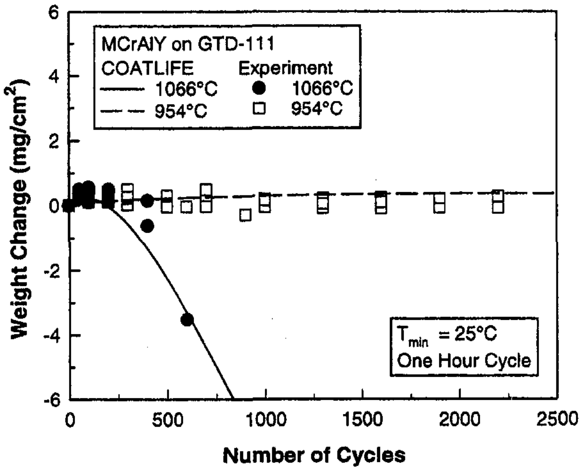

Fig. 6 Experimental weight change data compared against model calculation for MCrAlY-coated GTD-111

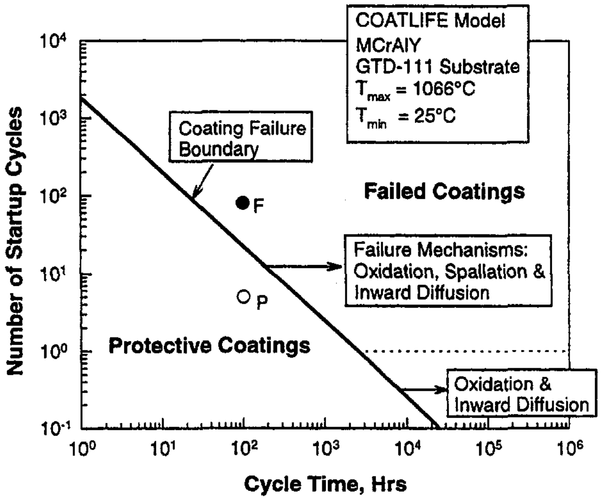

Fig. 8 Coating life diagram calculated via COATLIFE shows the protective and failed regimes of MCrAlY-coated GTD-111

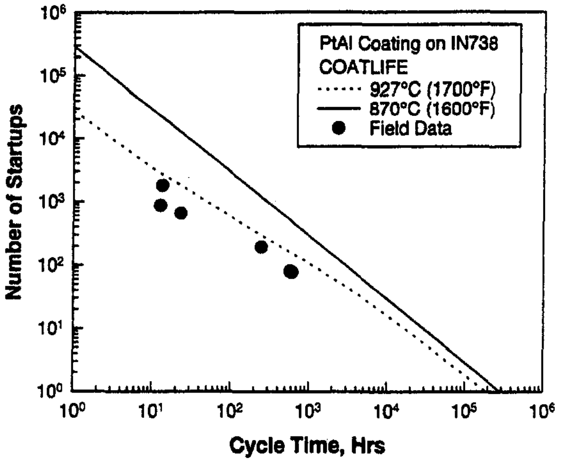

Fig. 9 Calculated coating life diagram for PtAl-coated IN738 compared against field data

Conclusions

A recent coating life model, COATLIFE, has been extended to treat the effect of inward diffusion on coating life. Applications of the model for GTD-111 with MCrAlY, PtAl, and aluminide coatings are demonstrated using laboratory specimens. A life prediction methodology based on COATLIFE and a coating life diagram is introduced. The utility of the coating life diagram is explained and evaluated with a comparison of model calculations against field data for PtAl-coated IN738 blades. The result indicates that COATLIFE shows promise as a predictive tool for forecasting the useful life of combustion turbine coatings in service.

Acknowledgments

This work was supported by the Electric Power Research Institute's Materials Center for Combustion Turbines at Southwest Research Institute (SwRI) through Contract No. RP3643-01, Mr. Robert Frischmuth, Program Manager. Discussion of this work with Dr. James Nesbitt, NASA-Lewis Research Center is acknowledged. The technical assistance of Ms. Fawn Cobia and the clerical assistance of Ms. Patty Soriano and Lori Salas, SwRI, are appreciated.

References

Chan, K. S., 1997, "A Mechanics-Based Treatment of Cyclic Oxidation," *Met. Mat. Transactions A,* Vol. 28A, pp. 411–422.

Chan, K. S., Cheruvu, N. S., and Leverant, G. R., 1997, "Coating Life Prediction Under Cyclic Oxidation Conditions," ASME Paper No. 97-GT-389.

Cheruvu, N. S., Chan, K. S., and Leverant, G. R., 1998, "Cyclic Oxidation Behavior of Aluminide, Platinum Modified Aluminide, and MCrAlY Coatings on GTD-111," presented at the 1998 ASME TURBO EXPO, June 2–5, 1998, Stockholm, Sweden.

Kirkaldy, J. S., 1970, "Isothermal Diffusion in Multi Component Systems," *Adv. In Mat. Research,* H. Herman, ed., Vol. 4, Interscience, New York, pp. 55–100.

Lee, E. Y., Charter, D. M., Biederman, R. R., and Sisson, Jr., R. D., 1987, "Modeling the Microstructural Evolution and Degradation of M-Cr-Al-Y Coatings During High Temperature Oxidation," *Surface and Coatings Technology,* Vol. 32, pp. 19–39.

Lowell, C. E., Barrett, C. A., Palmer, R. W., Auping, J. V., and Probst, H. B., 1991, "COSP: A Computer Model of Cyclic Oxidation," *Oxidation of Metals,* Vol. 36, No. 1/2, pp. 81–112.

Nesbitt, J. A., 1984, "Overlay Coating Degradation by Simultaneous Oxidation and Coating/Substrate Interdiffusion," NASA TM 83738, NASA-Lewis Research Center, Cleveland, OH.

Nesbitt, J. A., 1989, "Diffusional Aspects of the High-Temperature Oxidation of Protective Coatings," *Diffusion Analysis & Applications,* A. D. Romig, Jr., and M. A. Dayananda, eds., TMS, Warrendale, PA, pp. 307–324.

Nesbitt, J. A., 1989, "Predicting Minimum Aluminum Concentrations for Protective Scale Formation on Ni-base Alloys," *Journal of Electrochemical Society,* Vol. 136, pp. 1518–1527.

Nesbitt, J. A., and Barrett, C. A., 1993, "Predicting the Oxidation-Limited Lifetime of β NiAl," *Structural Intermetallics,* R. Darolia, J. J. Lewandowski, C. T. Liu, P. L. Martin, D. B. Miracle, and M. V. Nathal, eds., TMS, Warrendale, PA, pp. 601–609.

Nesbitt, J. A., and Heckel, R. W., 1984, "Modeling Degradation and Failure of Ni-Cr-Al Overlay Coatings," *Thin Solid Films,* Vol. 119, pp. 281–290.

Probst, H. B., and Lowell, C. E., 1988, "Computer Simulation of Cyclic Oxidation," *Journal of Metals,* Vol. 40, No. 10, pp. 18–21.

Diffusion Bonding of CMSX-4 to UDIMET 720 Using PVD-Coated Interfaces and HIP

R. Larker
Division of Engineering Materials,
Lulea University of Technology,
S-971 87 Lulea,
Sweden

J. Ockborn

B. Selling

Materials Technology,
Volvo Aero Corporation,
S-461 81 Trollhattan,
Sweden

There is an increasing interest in development of manufacturing methods for Dual Property BLISKs, consisting of creep resistant airfoils and fatigue resistant disks bonded together by a durable joint. Optimum heat treatments are, however, very different for creep resistant single crystal CMSX-4 and fatigue resistant polycrystalline Udimet 720 selected in this study, but fortunately the first aging treatment for CMSX-4 (1140°C, 2–6 h, AC) is similar to the partial solution treatment of U 720 HS2 (1115°C, 4 h, OQ). Based on this, diffusion bonding was performed by HIP at 1120°C and 200 MPa argon pressure for 4 h, followed by cooling to 400°C. Subsequently, a shortened Udimet 720 HS2 two-step aging treatment was adopted by heating to 650°C for 6 h followed by cooling to 400°C, heating to 760°C for 2 h, and finally cooling to R.T. under remaining HIP pressure. Plasma etching followed by thin (80 nm) PVD coating with either nickel or titanium were used to clean and protect the polished surfaces before joining. The selection of coatings was governed by the possibility to reduce oxidized nickel by flushing with hydrogen at 330°C during evacuation of the HIP capsules, and by the large solubility of oxygen in titanium. Hot tensile testing was performed at 750°C on both joined and reference materials subjected to the modified heat treatment. Initially solution treated Udimet 720 and CMSX-4 comprised the reference materials. The testing showed that joints with Ni-PVD coatings were almost as strong as Udimet 720 (although with very limited elongation), while the joints with Ti-PVD coatings were weaker.

Introduction

Present gas turbine materials are in principal optimized to sustain either creep under high stresses and very high temperatures in the airfoils, or fatigue under higher stresses and intermediate temperatures in the disk. This makes it necessary to manufacture the different parts from different superalloys, and subsequently to join them efficiently together. Today the preferred method is mechanical interlocking using a firtree geometry, but the need to further reduce weight and cost has spurred efforts to develop direct joining methods for BLISK's (BLaded dISK's). However, conventional fusion welding methods (TIG, EB) are generally not usable due to their inherent weld cracking sensitivity. Alternative joining methods include diffusion bonding, shear bonding, friction welding (rotational or linear) or brazing.

For the fabrication of BLISK's, one promising method is diffusion (solid state) bonding by HIP. This method has been certified for use in production GTCP331 APU's (Hoppin and Danesi, 1986). Due to its isostatic nature, the applied pressure can be allowed to be very high (100–200 MPa) to promote joint formation at the interface through plastic deformation and creep on the microscopical level, without any macroscopic distortion of the parts to be joined, as would be the result of uniaxial pressing even at much lower pressures. Therefore, the joining temperature can be relatively low, resulting in a thin and well-controlled reaction zone (Larker and Larker, 1996).

The two major challenges associated with diffusion bonding of two different superalloys are as follows:

— the joining process must be as compatible as possible with optimum heat treatments for each of the two superalloys (Larker et al., 1992)

— the large amounts of strong oxide formers (Al, Cr, Ti, etc.) present in the superalloys, together with their low solubility of oxygen, make it crucial to maintain the surfaces to be joined in the solid state as clean and free of oxide layers as possible

This paper describes methods to overcome challenges associated with diffusion bonding of creep resistant single-crystalline CMSX-4 to fatigue resistant polycrystalline Udimet 720 by HIP.

Materials

Composition and Phases. The composition of the single-crystalline CMSX-4 and the polycrystalline Udimet 720 materials are shown in Table 1.

CMSX-4 contains about 70 vol% of cubic (0.5 μm) γ' precipitates (Ni, Co, Cr)$_3$ (Al, Ti, Ta, W), in a solution strengthened γ matrix (Ni, Cr, Co, Ta, Re, W), and with clusters of Re ($\approx$1.0 nm) to reduce γ' coarsening kinetics.

The Udimet 720 has a γ matrix (Ni, Co, Cr) that contains both γ' (Ni, Co)$_3$ (Ti, Al) and carbide/boride precipitates such as M C (rich in Ti, W, Mo), M$_{23}$ (C, B)$_6$ (rich in Cr), M$_3$ B$_2$ (rich in Cr, Mo and some W, Ti), and M B$_2$ (rich in Cr and some W, Mo).

Heat Treatments. The recommended heat treatments for single-crystalline CMSX-4 and polycrystalline Udimet 720 HS2 (fine grained for maximum fatigue strength) are shown in Table 2.

The solution and the aging heat treatments take place at unusually high temperatures for the single-crystalline alloy (Sengupta et al., 1994). Fortunately the first aging treatment for CMSX-4 (1140°C <6 h, AC) is similar to the partial solution treatment for Udimet 720 HS2 (1115°C 4 h, Oil Quenching), and therefore, a common heat treatment could be conducted.

The main remaining obstacle is the high cooling rate required for the HS2 (and HS1) solution treatment of Udimet 720 to produce an optimum γ' distribution after aging (Sczerzenie et al.,

---

Contributed by the International Gas Turbine Institute (IGTI) of The American Society of Mechanical Engineers for publication in the ASME Journal of Engineering for Gas Turbines and Power. Paper presented at the International Gas Turbine and Aeroengine Congress and Exhibition, Stockholm, Sweden, June 2–5, 1998; ASME Paper 98-GT-589.

Manuscript received by IGTI March 31, 1998; final revision received by the ASME Headquarters March 23, 1999. Associate Technical Editor: R. Kielb.

Table 1 Alloy composition

Alloy composition [wt%]	Ni	Co	Cr	Ti	Al	W	Mo	Ta	Re	Hf
CMSX-4 (average for joined bars)	bal.	9.36	6.20	0.99	5.58	6.40	0.55	6.40	2.90	0.09
Udimet 720 (HS1 used in joints)	bal.	14.35	16.37	5.20	2.53	1.18	2.98	–	–	–

1988). Common laboratory HIP units can only reach cooling rates of about 25°C/min. However, large commercial HIP units designed today for the densification of metal powders are equipped with forced convection cooling giving cooling rates up to 500°C/min, which is similar to oil quenching.

However, there is also a CR (Creep Resistant) heat treatment for Udimet 720, producing a coarse-grained microstructure at a higher solution temperature (1170°C, 4 h) and allowing slower cooling in air, preceeding an aging also conducted at higher temperatures (1080°C, 4 h, AC + 845°C, 24 h, AC + 760°C, 16 h, AC) (Sczerzenie et al., 1988).

Cleaning and Protection of Surfaces to be Joined. It is imperative that the metal surfaces to be joined in the solid state are as clean and free of oxide layers as possible. The large amounts of strong oxide formers (Al, Cr, Ti, etc.) present in the superalloys, together with their low solubility of oxygen, make this extremely difficult. However, it is possible to remove these oxide layers by plasma etching in a vacuum chamber, but the clean surfaces must then be protected by a suitable PVD coating before exposure to air during encapsulation and evacuation of the HIP capsules.

The coatings were selected for the following reasons:

— by using pure nickel, the coating would oxidize slightly, but the oxide could be reduced by alternating between addition of pure hydrogen and vacuum pumping during capsule evacuation at 330°C

— by using pure titanium, the coating would also oxidize, but since the solubility of oxygen is very high in titanium (35 percent below and 8 percent above 882°C, while <0.05 percent in pure Ni), the oxide might dissolve if diffusion was rapid enough and the Ti coating was sufficiently thick compared to the oxide layer.

Experimental

Available materials for joining trials were six short bars of solution treated CMSX-4, and a larger bar (ØD = 24 mm) of U 720 HS1 (with the aging treatment at 760°C preceeding the one at 650°C, compared to HS2, see Table 2). For reference tests, solution treated CMSX-4 and solution treated U 720 were used. The final aim was to perform hot tensile testing of joints and reference materials.

Preparation of Superalloy Bars and HIP Capsules. Three Ni tubes were available for HIP encapsulation and were internally threaded (M14) in one end. The superalloys were machined as follows (see Fig. 1):

— CMSX-4 bars were turned, followed by wire-EDM and pol-

Table 2 Heat treatments

CMSX-4 (Cannon Muskegon Single Crystal alloy 4)	**Udimet 720 HS2 (Special Metals)**
1277°C stepwise to 1321°C 2 h GFQ; solution treatment (>18 h) of ≤99.9% of γ/γ' remnant eutectic while avoiding incipient melting.	1115°C 4 h OQ; partial solution treatment of lower solvus γ'; (very coarse γ' remain to avoid grain growth).
1140°C <6 h AC + 870°C 20 h AC; aging to precipitate 70 vol% of γ' (0.5 μm size).	650°C 24 h AC + 760°C 8 h AC; aging to precipitate fine γ' as well as $M_{23}(C,B)_6$ and MB_2.

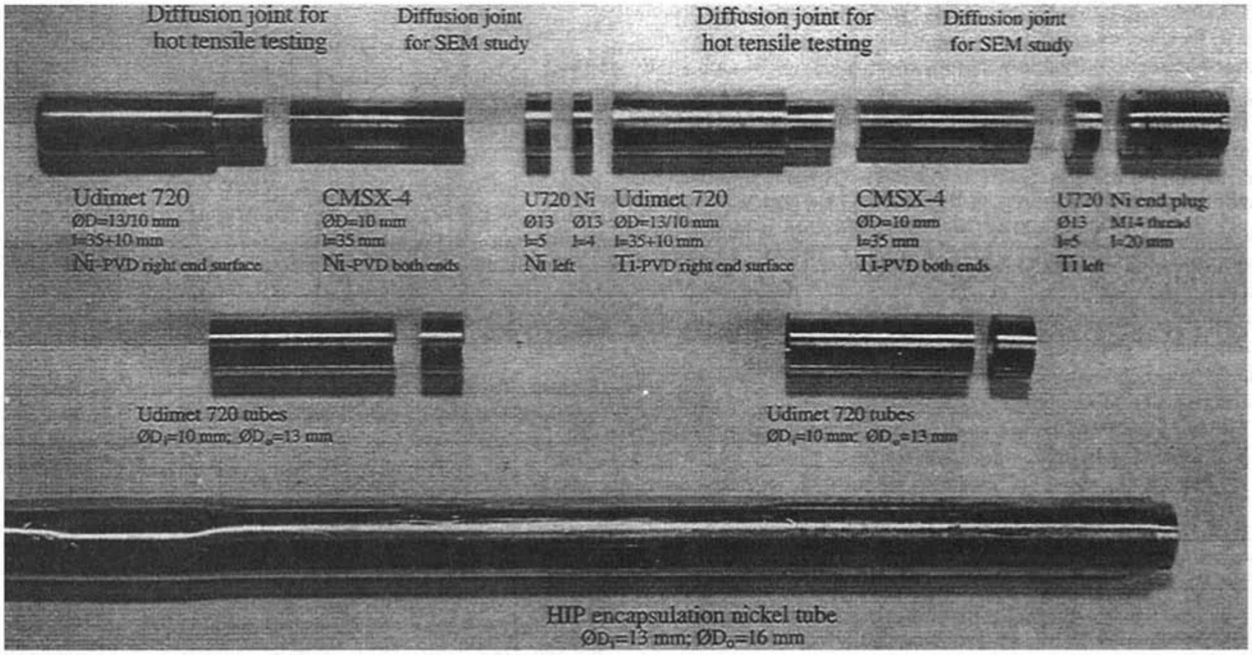

Fig. 1 Design of superalloy bars and HIP encapsulation

ishing (see next section) on the butt-ends perpendicular to the creep resistant ⟨100⟩-direction to a final length of 35 mm.

- U 720 HS1 was turned into six bars having two diameters (see Fig. 1), followed by polishing (see next section) on the butt-ends to be joined (with the smaller diameter).
- Tubes were made from coarse-grained U 720 CR, to be slid around the single-crystalline and the U 720 HS1-bars. This arrangement was designed to give initial stability at the joint position inside the soft nickel encapsulation tubes during HIP.
- To enable a later SEM study of diffusion bonding reactions taking place in the capsules, 5 mm thick spacers were turned, followed by polishing (see next section) on the butt-ends to be joined against the other end of the single-crystalline bars.

Surface Preparation. To enable a rational procedure for grinding and polishing of the 24 surfaces to be joined, perpendicular to their axial bar directions, a dedicated fixture was fabricated for the Buehler ECOMET 4 semi-automatic polishing machine.

The surfaces were treated according to Buehler DIALOG® Method #5.01, first by a slight planar grinding on 240 grit SiC paper before diamond polishing (9 μm and 6 μm). Final polishing was then conducted using Masterpolish (colloidal silica).

To clean the polished surfaces before plasma etching, the specimens were degreased in UPON 5800 (1–5 percent KOH, pH 11) at 60°C, rinsed in deionized water, and finally in ethanol. After drying, half of the bars were placed into the coating chamber in each batch (Ni or Ti PVD) before evacuation to 1×10^{-6} mbar. Adsorbed gases from the surfaces were removed by heating to 450°C for 40 min under an Ar partial pressure of 2×10^{-3} mbar.

Plasma etching was conducted for 15 min under an Ar partial pressure of 1.5×10^{-3} mbar. Immediately afterwards, the PVD coating was applied for 16 min (for Ni) and 4 min (for Ti), to produce a final coating thickness of 80 nm in both cases.

Assembly and Evacuation of the HIP Capsules. Two sets of PVD coated bars (one with Ni-PVD coatings and one with Ti-PVD) were assembled in each Ni capsule, together with the Ni spacers and threaded end plug.

By a slight prior flattening of the tubes ahead of the position for the first U 720 HS1-bars (see Fig. 1), the complete packages could be axially prestressed at the surfaces to be joined by turning the threaded end plugs as much as possible, before sealing these ends by TIG welding. Finally a piece of Zr-foil (total area 10 cm^2) was slid through the open end of the three capsules up to a short distance from the slightly flattened part of the tubes, in order to later act as an oxygen getter during final evacuation immediately before sealing these ends of the HIP capsules.

The capsules were positioned in a computer-controlled furnace at R.T. and connected to a diffusion pump stack. Initially the capsules were evacuated down to 2.3×10^{-2} mbar, measured close to the capsules (8×10^{-5} mbar at the pump stack). The capsules were then heated up to 330°C for 100 min, during which the pressure levels were almost unaffected. The capsules were switched to a timer-controlled valve system allowing inlet of pure hydrogen for 1 min up to 0.08 MPa to reduce nickel oxides, followed by rotary pump evacuation for 9 min down to initially 1.3×10^{-1} mbar (4.5×10^{-2} mbar). This cycle was repeated ten times (with a final pressure of 1.5×10^{-1} mbar (4.5×10^{-2} mbar)), before switching back to diffusion pumping down to 2.5×10^{-2} mbar (3×10^{-4} mbar).

The capsules were then heated by 250°C/h up to 500°C, followed by a hold time for 15 min, resulting in a final pressure of 2.4×10^{-2} mbar (8.5×10^{-5} mbar). The furnace was shut off and cooled down to 280°C.

Then one capsule after another was heated by an oxyacetylene torch to red heat between the slightly flattened part of the tube and the Zr-foil (causing an improvement of the vacuum reading by at least one order of magnitude). This was followed by a total flattening using a hydraulic jaw, and with hard wires (positioned perpendicular to the tube) put in between on one side, to give efficient local plasticizing and sealing. Finally the flat end of the tube was cut off and sealed by TIG welding.

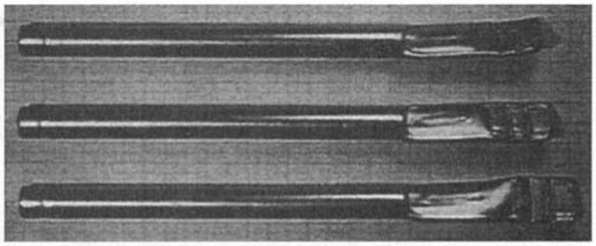

Fig. 2 HIP capsules after diffusion bonding

HIP Treatment. Three capsules were, together with reference materials of solution treated CMSX-4 and solution treated U 720 (intended for HS2), subjected to the following HIP cycle:

- evacuation of the HIP chamber, followed by Ar pressure increase to 66 MPa
- heating to 1120°C with associated pressure increase to 200 MPa, hold time 4 h, followed by cooling to 400°C
- heating to 650°C; hold time 6 h (a shortened U 720 HS2 aging treatment), followed by cooling to 400°C
- heating to 720°C; hold time 2 h; (a shortened U 720 HS2 aging treatment), followed by cooling to R.T.

The total time for the HIP cycle was 14 h.

By observing the further flattening of the empty evacuation ends of the capsules, together with waistlines formed at discontinuities inside, it could be concluded that all capsules were leak-free and the HIP cycle successful, see Fig. 2.

Manufacturing of Tensile Test Bars. Tensile testing was performed using cylindrical test specimens with a diameter of 6.25 mm, except in the case of CMSX-4 reference bars where the diameter was reduced to 4.1 mm to prevent grip failure. Their parallel lengths were 40 mm, except for one of the joined test bars having a parallel length of 38 mm, see Fig. 3. The test bars were machined from the centre of the HIP capsules and reference materials by turning and cylindrical grinding, followed by axial polishing along the gauge section. The bond line was placed in the middle of each test bar.

No indications of scratches from cylindrical grinding, defects or lack of bonding could be found using optical microscope and SEM, see Fig. 4. The vertical scratches are from the final longitudinal polishing along the tensile test bars.

Hot Tensile Testing. The twelve bars were hot tensile tested at 750°C. CMSX-4 reference specimens were tested in accordance with ASTM E21. The other specimens were also tested in accor-

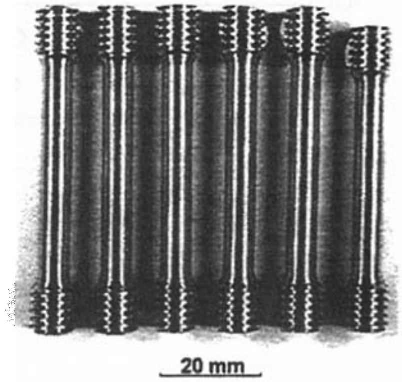

Fig. 3 Overview of cylindrical tensile testbars machined from CMSX-4/U 720 diffusion joints

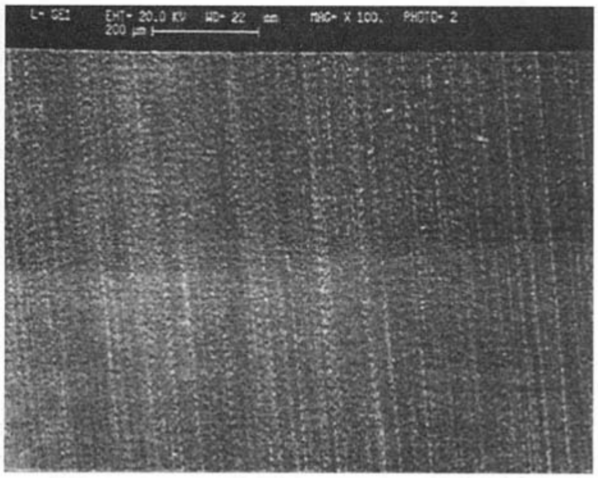

Fig. 4 SEM micrograph from the bond area with CMSX-4 on top of Udimet 720

dance with ASTM E21, but with a displacement control of 0.2 mm/min, (strain rate 0.5 percent/min over the entire parallel length). The resulting yield strengths, tensile strengths and elongations are, together with literature data (Sengupta et al., 1994; Sczerzenie et al., 1988), shown in Fig. 5.

The three joints made with Ni-PVD coatings (J1301, C1300, and H1301) showed the best results with an average UTS of 872 MPa. This is almost equal to the yield and ultimate tensile strength of the tested U 720 reference bars (in average 837 MPa and 880 MPa, respectively).

The Udimet 720 reference bars showed, however, about 150–250 MPa lower strengths (and about 20 percent larger elongation A_4) compared to U 720 HS2 literature data, probably due to less precipitation strengthening caused by the slow cooling in the laboratory HIP. Vickers measurement on HIPed U 720 (413 HV 100) also indicated hardness levels lower than for HS (509 HV 100) and similar to the level for CR treatment (419 HV 100).

For the tested CMSX-4 reference bars, however, the yield strengths were similar compared to CMSX-4 literature data, (where condition A and B indicate the first aging temperature of 1080°C for 4 h and 1140°C for 6 h, resp.) (Sczerzenie et al., 1988), and the UTS about 75–150 MPa higher, showing shear fractures typical for single crystals in planes at 55 deg to the principal stress direction ⟨100⟩, while elongations were halved compared to literature data.

Elongation and area contraction were small for all joints compared to the reference materials. To monitor plastic deformation close to the fracture, measurements of area contraction were performed using a Roundness Tester CEJ 8525. Plastic deformation was detected up to 25 mm axially from the fracture surface level. Area contraction at each of the twelve fracture surfaces from the six joints was determined by comparing the measured projected area at fracture and at 3 mm axial distance, see Table 3.

The crystallographic directions of CMSX-4 in the joint plane (perpendicular to the axial ⟨100⟩ direction) could be indirectly determined by the periodic deviations from roundness, found at high radial magnification (5000×) at locations with slightly larger diameter close to the threaded bar ends (where plastic deformation

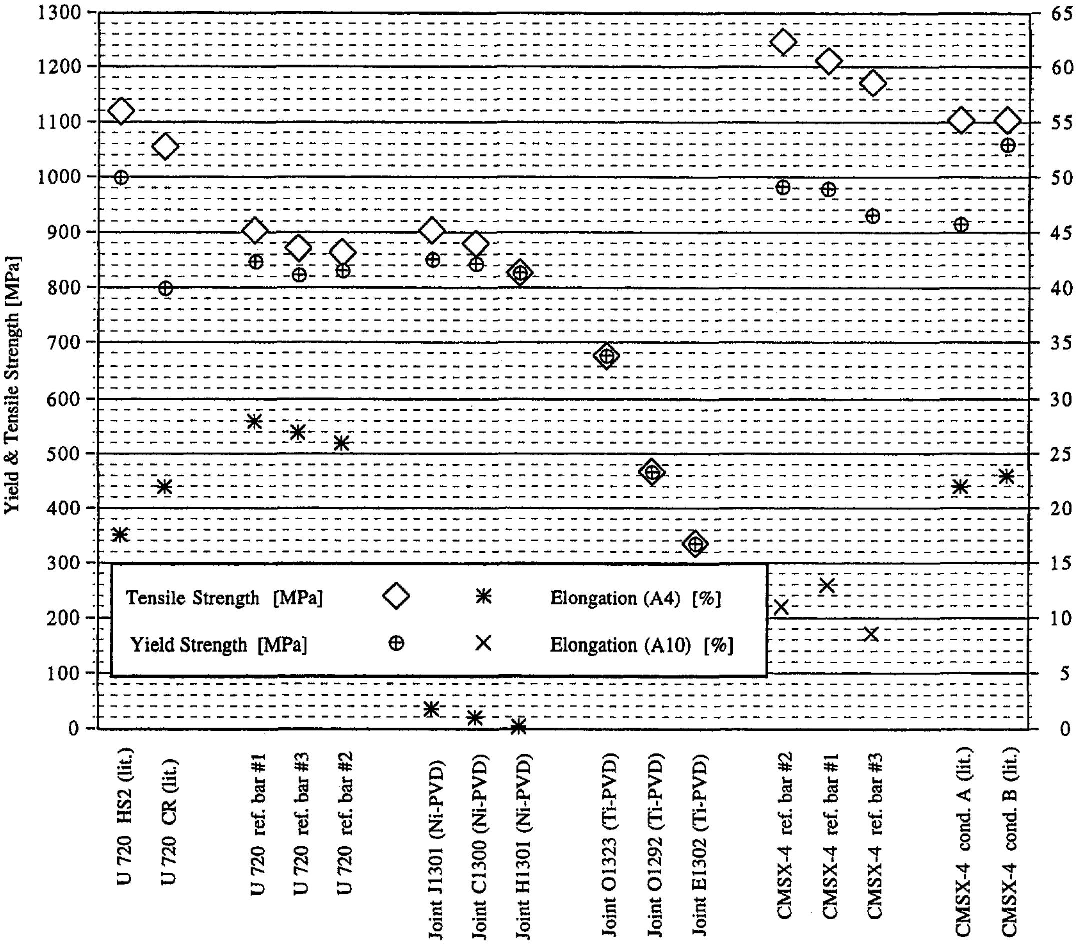

Fig. 5 Results from hot tensile testing at 750°C in comparison with reference data (Sengupta et al., 1994; Sczerzenie et al., 1988)

Table 3 Area contraction

Joined bar	J1301	H1301	C1300	E1302	O1292	O1323
Coating	Ni-PVD			Ti-PVD		
$Z_{\text{CMSX-4}}$ [%]	0.9	0.3	0.3	0.2	0.02	0.2
$Z_{\text{U 720}}$ [%]	0.7	0.6	0.2	0.05	0.04	0.2
$Z_{\text{CMSX-4}}$ ref. bar [%]	18					
$Z_{\text{U 720}}$ ref. bar [%]	39					

was negligible). The magnified shape was a square with rounded corners and radial amplitudes in the range 1.4–2.7 μm. This was probably caused by different contact pressures and thus material removal against the grinding wheel during preparation of the test bars, due to large elastic anisotropy in the $\langle 100\rangle$ and $\langle 110\rangle$ directions, see Table 4 below.

The direction of largest plastic deformation in the joint plane in CMSX-4 was for all of the four strongest joints found to be at an angle of 15 deg relative to the $\langle 110\rangle$ direction (and thus 30 deg relative to $\langle 100\rangle$).

Discussion

The strength levels for the Ni-coated joints suggest that plasma etching was able to remove detrimental oxide layers from the polished superalloy surfaces, and that any nickel oxide formed on the PVD coating during exposure to air could be reduced by hydrogen at 330°C during capsule evacuation. However, further work by AEM to examine the resulting diffusion profiles and phases formed at the interface will be conducted to confirm this.

The lower strengths and larger scatter for Ti-coated joints might be due to the coating layer being too thin (80 nm) to dissolve necessary amounts of oxygen during joining, and/or that the resulting solid solution of oxygen in titanium was too brittle.

An important contribution to the stress field at the joint is the large elastic anisotropy of the single crystal alloy, as shown in Table 4.

Contrary to the E value, Poisson's ratio ν is considerably larger (0.36) in the $\langle 100\rangle$ direction compared to the isotropic ν (0.31). At 750°C, $E_{\langle 100\rangle} = 92$ GPa while $E_{\text{isotropic}} = 160$ GPa (Sengupta et al., 1994; Sczerzenie et al., 1988).

Table 4 Elastic constants for the superalloys (Sengupta et al., 1994; Sczerzenie et al., 1988)

Crystallogr. direction	<100>	<110>	<111>	isotropic
$E_{\text{CMSX-4}}$ [GPa] at R.T.	137	233	303	-
$E_{\text{U 720}}$ [GPa] at R.T.				205

The properties of the reference bars subjected to the combined diffusion bonding, solution and aging treatment during HIP show that their optimized properties were (as anticipated) not fully reached. However, the main difference (the lower strength relative to Udimet 720 HS2) is probably due to the slow cooling (25°C/min) from 1120°C, but this disadvantage would disappear in real BLISK joining using larger HIP units with forced convection cooling (500°C/min).

Further development of suitable joint orientation and partial encapsulation techniques are needed to make the method feasible for the combined joining and heat treatment of BLISK's.

Conclusions

— Single crystal CMSX-4 and polycrystalline Udimet 720 can be diffusion bonded to each other by HIP, using plasma etching followed by Ni-PVD and reduction of nickel oxides by hydrogen during capsule evacuation

— The strength level at 750°C of joints made with Ni-PVD coatings were comparable with the U 720 base material, although with much reduced ductility, probably due to the anisotropic stress field at the joint

— Joints made with Ti-PVD coatings were less successful, producing lower strengths and zero ductility

— The properties of the two superalloys were relatively well retained after the joining heat treatment

Acknowledgments

Funding from the Swedish Aeronautical Research Programme (NFFP) is gratefully acknowledged. Dr. Mats Larsson, Department of Materials Science, Uppsala University, is thanked for conducting plasma etching and PVD coating of the surfaces before joining.

References

Hoppin, G. S., III, and Danesi, W. P., 1986, "Manufacturing Processes for Long-Life Gas Turbines," *Journal of Metals*, pp. 20–23.

Larker, H. T., and Larker, R., 1996, "Hot Isostatic Pressing," Chap. 16 in Vol. 17B of *Materials Science and Technology—A Comprehensive Treatment*, R. W. Cahn, P. Haasen, and E. J. Kramer, eds., VCH Verlagsgesellschaft mbH, Weinheim, pp. 145–175.

Larker, R., Anevik, K., Kristiansson, S., and Loberg, B., 1992, "Heat Treatments of Low-Expansion Superalloy Incoloy 909 for Application in Ceramic/Metal Joints and in Metal Matrix Composites," *Materials and Design*, Vol. 13, No. 1, pp. 11–15.

Sczerzenie, F. E., Mancuso, S. O., Keefe, P. W., Maurer, G. E., and Boesch, W. J., 1988, "UDIMET® ALLOY 720," Class I—unrestricted report, Action # TR-88-002, Special Metals Corporation, 4317 Middle Settlement Road, New Hartford, NY, 13413-5392.

Sengupta, A., Putatunda, S. K., Bartosiewich, L., Hangas, J., Hailos, P. J., Peputapeck, M., and Alberts, F. E., 1994, "Tensile Behavior of a New Single Crystal Nickel-Based Superalloy (CMSX-4) at Room and Elevated Temperatures," *Journal of Materials Engineering and Performance*, Vol. 3, No. 5, pp. 664–672.

T. N. Shiau
Institute of Mechanical Engineering,
National Chung Cheng University,
Chia-Yi, 621, Taiwan

J. S. Rao
Indian Institute of Technology,
New Delhi, India

J. R. Chang

S.-T. Choi

National Cheng Kung University,
Tainan, Taiwan

Dynamic Behavior of Geared Rotors

This paper is concerned with the dynamic behavior of geared rotor systems supported by squeeze film dampers, wherein coupled bending torsion vibrations occur. Considering the imbalance forces and gravity, it is shown that geared rotors exhibit chaotic behavior due to nonlinearity of damper forces. The route to chaos in such systems is established. In geared rotor systems, it is shown that torsional excitation can induce lateral vibrations. It is shown that squeeze film dampers can suppress large amplitudes of whirl arising out of torsional excitation.

Introduction

Determination of lateral and torsional frequencies of rotor systems is an important factor in the design of high speed rotor systems. Considerable amount of work has been reported in this direction, and reference may be made to Rao (1996).

When the drive system incorporates gear transmission units, the lateral and torsional modes get coupled. Lund (1978) considered such coupling in the torsional-lateral vibrations in a geared system of rotors. Shiau et al. (1994) used a hybrid method to study the dynamic characteristics of geared rotor systems. Rao et al. (1995) developed a general finite element model to determine the coupled bending-torsion natural frequencies and mode shapes of geared rotors including the effect of pressure angle.

Squeeze film dampers are now commonly employed to suppress the lateral vibrations arising out of rotor imbalance. Mohan and Hahn (1974) considered the design of squeeze film damper supports for rigid rotors. Cookson and Kossa (1980) studied the effectiveness of squeeze film dampers for flexible rotors without a centralizing spring.

Hwang and Shiau (1991) applied Generalized Polynomial Expansion method to study the nonlinear effects of squeeze film forces on flexible rotors. They used the harmonic balance method, which is associated with time collocation method. Chen et al. (1993) considered the application of squeeze film dampers to control lateral vibrations of a gear pair system. They reported one result with Poincare section from direct integration method which indicated irregular, aperiodic long-time response near the frequency dominated by lateral mode or torsional mode.

In geared rotor systems subjected to torsional excitation, the usual practice is to determine the torsional response and ignore the coupling of bending torsion vibrations, Rao et al. (1980). This forms an important part of the geared rotors, particularly in the presence of short circuit excitation from the generator, see Rao (1996). Most important disturbances that create abnormal pulsating torques in a turbo-alternator system are a short circuit at the generator terminals, faulty synchronizing, a short circuit clearing, and line switching. Of these, a sudden short circuit at generator terminals is considered to be the most unfavorable condition that sets up large torques in the rotor and induces severe stresses of the order of four to five times the normal values. Concordia (1956) gives details of these different electrical phenomena. Using a torsional analysis of a typical turbogenerator system, Rao (1992) has shown that the gear transmission unit can fail under high cycle fatigue due to an electrical short circuit torque.

In this paper, a simple gear pair system is first considered to obtain the coupled lateral-torsional response due to imbalance and gravity. Using FFT spectra as well as Poincare maps, the route to chaos is established. A geared rotor system is considered, with short circuit excitation to determine the lateral response.

Equations of Motion

A typical geared rotor is shown in Fig. 1. Equations of motion of different elements are given below, see Rao et al. (1995).

Rigid Disk. The equations of motion of a rigid disk can be shown to be

$$[M^d]\{\ddot{q}^d\} + \Omega[G^d]\{\dot{q}^d\} = \{F_s^d\}, \tag{1}$$

where

$$\{q^d\}^T = \{V^d \quad W^d \quad B^d \quad \Gamma^d \quad a^d\}.$$

For the elements of the above matrices, see Rao et al. (1995).

Shaft Element. The equations of motion of the shaft element can be shown as

$$[M^s]\{\ddot{q}^s\} + \Omega[G^s]\{\dot{q}^s\} + [K^s]\{q^s\} = \{F_s^s\}, \tag{2}$$

where

$$\{q^s\}^T = \{V_1^s \quad W_1^s \quad B_1^s \quad \Gamma_1^s \quad a_1^s \quad V_2^s \quad W_2^s \quad B_2^s \quad \Gamma_2^s \quad a_2^s\}$$

and

$$\begin{aligned}
[M^s] &= [M_T^s] + [M_R^s] + [M_\theta^s] \\
[M_T^s] &= [M_T^s]_0 + \Phi[M_T^s]_1 + \Phi^2[M_T^s]_2 \\
[M_R^s] &= [M_R^s]_0 + \Phi[M_R^s]_1 + \Phi^2[M_R^s]_2 \\
[G^s] &= [G^s]_0 + \Phi[G^s]_1 + \Phi^2[G^s]_2 \\
[K^s] &= [K^s]_0 + \Phi[K^s]_1 + [K_\theta^s].
\end{aligned}$$

For the elements of the above matrices, see Rao et al. (1995).

Axial Torque (Incremental Stiffness Matrix). The effect of axial torque is considered by Zorzi and Nelson (1980), which gives rise to an incremental stiffness matrix. Rao, Chang, and

---

Contributed by the International Gas Turbine Institute and presented at the International Gas Turbine and Aeroengine Congress and Exhibition, Orlando, FL, June 2–5, 1997. Manuscript received by the ASME Headquarters March 7, 1997. Paper No. 97-GT-187. Associate Technical Editor: H. A. Kidd.

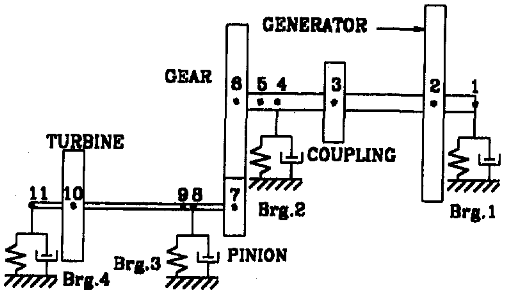

Fig. 1 Geared turbo Generator set

Shiau derived this incremental stiffness matrix for a Timoshenko shaft element.

Gear Pair. For the gear pair, we can obtain

$$\begin{bmatrix} [M_1^g] & \\ & [M_2^g] \end{bmatrix} \{\ddot{q}^g\} + \Omega_1 \begin{bmatrix} [G_1^g] & \\ & \frac{\Omega_2}{\Omega_1}[G_2^g] \end{bmatrix} \{\dot{q}^g\} - k_h \begin{bmatrix} [S_1] \\ [S_2] \end{bmatrix} \{q^g\} = \{F_s^g\}, \quad (3)$$

where

$$[M_1^g] = [M_1^d] \text{ and } [G_1^g] = [G_1^d]$$

$$\{q^g\}^T = \{V_1^g \quad W_1^g \quad B_1^g \quad \Gamma_1^g \quad a_1^g \quad V_2^g \quad W_2^g \quad B_2^g \quad \Gamma_2^g \quad a_2^g\},$$

and the elements of the remaining matrices can be taken from Rao et al. (1995).

Hydrodynamic Bearing. For a hydrodynamic bearing we have

$$\begin{bmatrix} c_{yy} & c_{yz} \\ c_{zy} & c_{zz} \end{bmatrix} \begin{Bmatrix} \dot{V}^b \\ \dot{W}^b \end{Bmatrix} + \begin{bmatrix} k_{yy} & k_{yz} \\ k_{zy} & k_{zz} \end{bmatrix} \begin{Bmatrix} V^b \\ W^b \end{Bmatrix} = \{F_s^b\}. \quad (4)$$

Squeeze Film Damper Element. The damper forces are considered to be nonlinear. Neglecting fluid inertia and air entrainment effects, the radial and tangential components of the film forces using short bearing theory from the Reynolds equation are as follows (see Mohan and Hahn, 1974):

$$F_r = -\frac{\mu R L^3}{c_r^2}(\epsilon\dot{\phi}A^{11} + \dot{\epsilon}A^{02})$$

$$F_\phi = -\frac{\mu R L^3}{c_r^2}(\epsilon\dot{\phi}A^{20} + \dot{\epsilon}A^{11})$$

$$A^{ij} = \int_{\phi_g+\pi}^{\phi_g+2\pi} \frac{\sin^i\theta\cos^j\theta}{(1-\epsilon\cos\theta)^3}\,d\theta;\ \phi_g = \tan^{-1}\frac{\dot{\epsilon}}{-\epsilon\dot{\phi}}. \quad (5)$$

The horizontal and vertical components of these forces are

$$F_V = (F_r V - F_\phi W) \div \sqrt{V^2 + W^2}$$

and

$$F_W = (F_r W + F_\phi V) \div \sqrt{V^2 + W^2}. \quad (6)$$

System Equations

The system equations can be written as

$$[M]\{\ddot{q}\} + [\Omega_1[G] + [C]]\{\dot{q}\} + ([K] - [K_T])\{q\} = \{F\}, \quad (7)$$

where the force vector consists of imbalance forces, gravity, short circuit torque, and squeeze film damper forces. The following two specific examples are considered: (1) a gear pair on squeeze film damper supports; and (2) a geared turbo generator set.

Gear Pair on Squeeze Film Damper Supports

A simple gear pair mounted on squeeze film damper supports is considered here. The equations of motion can be shown to be

$$[M]\{\ddot{q}\} + (c_h[S_h] + [C_c])\{\dot{q}\} + (k_h[S_h] + [K_c])\{q\} = \{Q\}, \quad (8)$$

where

$$\{q\} = \{V_1 \quad W_1 \quad a_1 \quad V_2 \quad W_2 \quad a_2\}^T$$

$$[S_h] = \begin{bmatrix} S^2 & SC & r_1S & -S^2 & -SC & r_2S \\ SC & C^2 & r_1C & -SC & -C^2 & r_2C \\ r_1S & r_1C & r_1^2 & -r_1S & -r_1C & r_1r_2 \\ -S^2 & -SC & -r_1S & S^2 & SC & -r_2S \\ -SC & -C^2 & -r_1C & SC & C^2 & -r_2C \\ -r_2S & r_2C & r_1r_2 & -r_2S & r_2C & r_2^2 \end{bmatrix}$$

Nomenclature

C_1, C_2 = centralizing spring damping coefficients
C, S = $\cos\phi_p$, $\sin\phi_p$
c_h = gear mesh damping coefficient
c_r = radial clearance
c_{yy}, c_{zz} = direct damping coefficients
c_{yz}, c_{zy} = cross-coupled damping coefficients
e = eccentricity
F, f = SFD force, nondimensional SFD force
I_P = polar mass moment of inertia
K = centralizing spring stiffness
k_h = gear mesh stiffness
k_{yy}, k_{zz} = direct stiffness coefficients
k_{yz}, k_{zy} = cross-coupled stiffness coefficients
L = length of squeeze film damper
M = mass
R = journal radius
r = gear base circle radius
$[S_1], [S_2]$ = gear mesh stiffness matrices
$S_D = \mu RL^3 \div (M_1 c_r^3 \omega_1)$
$[S_h]$ = gear mesh stiffness matrix
$U, W_g = e \div c_r,\ g \div (c_r\omega_1^2)$
V, W = lateral displacements in Y, Z-directions
$v, w = V \div c_r,\ W \div c_r$
a = torsional displacement about X-direction
a, β = saliency constants
B, Γ = angles of rotation about Y, Z-directions
$\epsilon = \sqrt{v^2 + w^2} \div c_r$
ϕ = angular velocity of journal
ϕ_p = pressure angle
$\eta_C, \eta_K, \eta_M = C_2 \div C_1,\ K_2 \div K_1,\ M_2 \div M_1$
$\eta_I, \eta_r = I_{P2} \div I_{P1},\ r_2 \div r_1$
$\xi_c, \xi_I, \xi_K = c_r \div r_1,\ M_1 r_1^2 \div I_{P1},\ k_h \div K_1$
$\zeta, \zeta_h = C_1 \div (2M_1\omega_1),\ C_h \div (2M_1\omega_1)$
μ = viscosity of lubricant
$\omega_1 = \sqrt{K_1/M_1}$
Ω = rotational (spin) speed
$\Omega_r = \Omega_1/\omega_1$
$\tau = \Omega_1 t$
$'$ = denotes differentiation with τ

$$\{Q\} = \begin{Bmatrix} F_{V1} + M_1 e_1 \Omega_1^2 \cos(\Omega_1 t + \psi_1) \\ F_{W1} + M_1 e_1 \Omega_1^2 \sin(\Omega_1 t + \psi_1) - M_1 g \\ 0 \\ F_{V2} + M_2 e_2 \Omega_2^2 \cos(\Omega_2 t + \psi_2) \\ F_{W2} + M_2 e_2 \Omega_2^2 \sin(\Omega_2 t + \psi_2) - M_2 g \\ 0 \end{Bmatrix},$$

and nonzero elements of $[M]$, $[C_c]$, and $[K_c]$ are

$$M_{11} = M_{22} = M_1,\ M_{44} = M_{55} = M_2,\ M_{33} = I_{p1} \text{ and } M_{66} = I_{p2}$$

$$C_{c11} = C_{c22} = C_1,\ C_{c44} = C_{c55} = C_2,$$

$$K_{c11} = K_{c22} = K_1,\ K_{c44} = K_{c55} = K_2.$$

In the above system of equations (8), the first two are divided by $M_1 c_r \Omega_1^2$, the third one is divided by $I_{P1}\Omega_1^2$, the fourth and fifth by $M_2 c_r \Omega_1^2$, and the sixth one by $I_{P2}\Omega_1^2$ to obtain the nondimensional form as

$$[I]\{\bar{q}''\} + \left(\frac{2\zeta_h}{\Omega_r}[\bar{S}_h] + \frac{2\zeta}{\Omega_r}[\bar{C}_c]\right)\{\bar{q}'\} + \left(\frac{\xi_K}{\Omega_r^2}[\bar{S}_h] + \frac{1}{\Omega_r^2}[\bar{K}_c]\right)\{\bar{q}\} = \{\bar{Q}\} \quad (9)$$

where

$$\{\bar{q}\} = \{v_1 \quad w_1 \quad a_1 \quad v_2 \quad w_2 \quad a_2\}^T$$

$$\{\bar{Q}\} = \begin{Bmatrix} \dfrac{S_D}{\Omega_r} f_{v1} + U_1 \cos(\tau + \psi_1) \\ \dfrac{S_D}{\Omega_r} f_{w1} + U_1 \sin(\tau + \psi_1) - \dfrac{W_g}{\Omega_r^2} \\ 0 \\ \dfrac{S_D}{\eta_M \Omega_r} f_{v2} + \dfrac{U_2}{\eta_r^2} \cos\left(-\dfrac{\tau}{\eta_r} + \psi_2\right) \\ \dfrac{S_D}{\eta_M \Omega_r} f_{w2} + \dfrac{U_2}{\eta_r^2} \sin\left(-\dfrac{\tau}{\eta_r} + \psi_2\right) - \dfrac{W_g}{\Omega_r^2} \\ 0 \end{Bmatrix}$$

$$f_v = (f_r v - f_\phi w) \div \sqrt{v^2 + w^2} \quad f_w = (f_r w + f_\phi v) \div \sqrt{v^2 + w^2}$$

$$f_r = -(\epsilon\phi' A^{11} + \epsilon' A^{02}) \quad f_\phi = -(\epsilon\phi' A^{20} + \epsilon' A^{11})$$

$$\bar{C}_{c11} = \bar{C}_{c22} = 1,\ \bar{C}_{c44} = \bar{C}_{c55} = \frac{\eta_C}{\eta_M} \text{ rest } \bar{C} = 0$$

$$\bar{K}_{c11} = \bar{K}_{c22} = 1,\ \bar{K}_{c44} = \bar{K}_{c55} = \frac{\eta_K}{\eta_M} \text{ rest } \bar{K} = 0$$

$$[\bar{S}_h] = \begin{bmatrix} S^2 & SC & \dfrac{S}{\xi_c} & -S^2 & -SC & \dfrac{\eta_r S}{\xi_c} \\ SC & C^2 & \dfrac{C}{\xi_c} & -SC & -C^2 & \dfrac{\eta_r C}{\xi_c} \\ \xi_I \xi_c S & \xi_I \xi_c C & \xi_I & -\xi_I \xi_c S & -\xi_I \xi_c C & \xi_I \eta_r \\ \dfrac{-S^2}{\eta_M} & \dfrac{-SC}{\eta_M} & \dfrac{-S}{\eta_M \xi_c} & \dfrac{S^2}{\eta_M} & \dfrac{SC}{\eta_M} & \dfrac{-\eta_r S}{\eta_M \xi_c} \\ \dfrac{-SC}{\eta_M} & \dfrac{-C^2}{\eta_M} & \dfrac{-C}{\eta_M \xi_c} & \dfrac{SC}{\eta_M} & \dfrac{C^2}{\eta_M} & \dfrac{-\eta_r C}{\eta_M \xi_c} \\ \dfrac{\xi_I \xi_c \eta_r S}{\eta_I} & \dfrac{\xi_I \xi_c \eta_r C}{\eta_I} & \dfrac{\xi_I \eta_r}{\eta_I} & \dfrac{-\xi_I \xi_c \eta_r S}{\eta_I} & \dfrac{-\xi_I \xi_c \eta_r C}{\eta_I} & \dfrac{\xi_I \eta_r^2}{\eta_I} \end{bmatrix}.$$

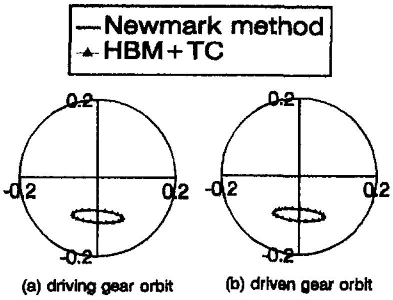

(a) driving gear orbit (b) driven gear orbit

Fig. 2 Comparison of results

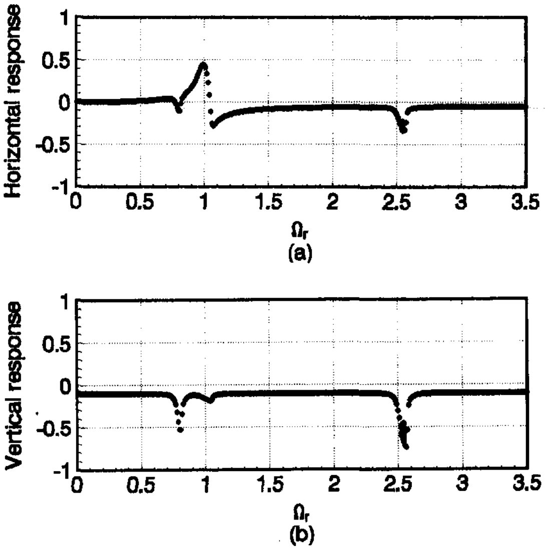

Fig. 3 Bifurication maps of driving gear response for $U_1 = U_2 = 0.045$

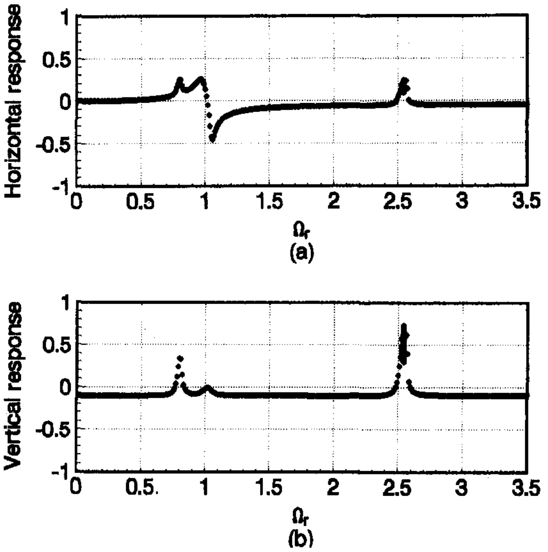

Fig. 4 Bifurcation maps of driving gear response for $U_1 = U_2 = 0.045$

A computer program using Newmark's (1959) method is developed to determine the response of the above system of equations (9). Harmonic balance method associated with time collocation is used for a typical case, only to verify the results obtained from Newmark's procedure. The gear pair chosen has the following data: $\xi_I = 2$, $\xi_c = 10^{-5}$, η_M, η_C, η_K, η_r, η_I, $\xi_K = 1$, $\phi_p = 22.5°$, $\zeta_h = \zeta = 0.0005$, $S_D = 0.03$, $W_g = 0.1$, and $\psi_1 = \psi_2 = 0$.

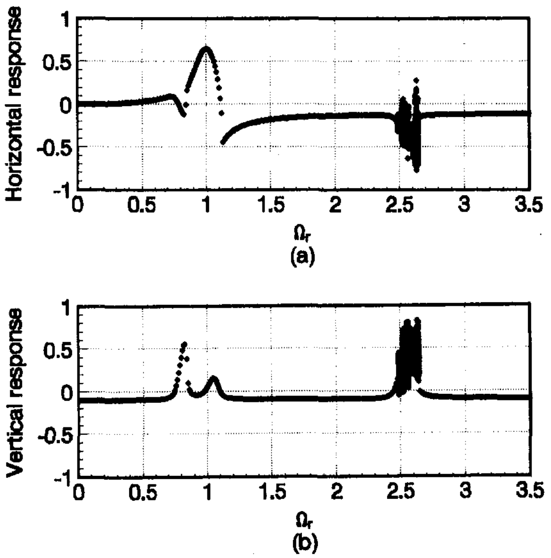

Fig. 5 Bifurcation maps of driving gear response for $U_1 = U_2 = 0.1$

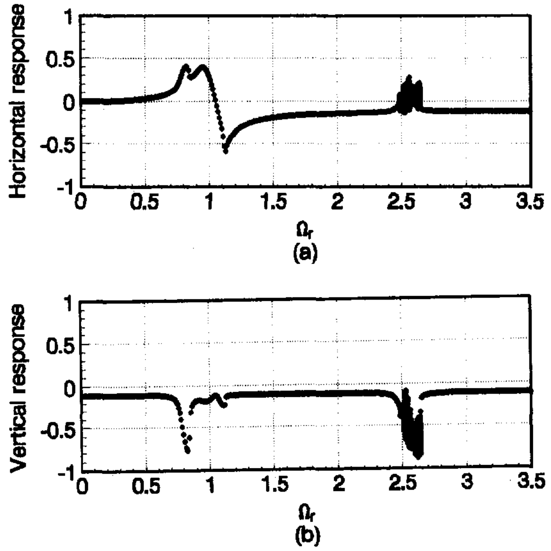

Fig. 6 Bifurcation maps of driving gear response for $U_1 = U_2 = 0.1$

The critical speeds due to synchronous excitation occur at Ω_r equal to 0 (rigid body torsional), 0.79 (coupled), 1.0, 1.0, 1.0 (lateral), and 2.52 (coupled). For an imbalance $U_1 = U_2 = 0.045$, $\Omega_r = 1.89$ with periodic solutions, results from both Newmark and harmonic balance methods are given in Fig. 2, which show good agreement. RK-5 solution is also tried, which gave similar results, however, it consumed considerably larger computer time and therefore has been dropped in favor of Newmark's method.

Effect of Imbalance. For the gear pair under consideration, the response obtained by Newmark's method is reported here. In all the cases, the initial conditions are kept the same, i.e., zero for both the response and velocities. After reaching the steady-state regime in time domain, 100 consecutive one-per-rotation speed marks, which appear on the response, are recorded. For periodic response, all these marks appear at a constant position for any number of rotations. For a steady-synchronous response, there will be only one mark. If the response is half synchronous, there will be two marks, etc. If the response is chaotic, multiple marks result from these consecutive one hundred positions; also, see Goldman and Muszynska (1994) and Ehrich (1995). These positions for both the vertical and horizontal response of the system are given as bifurcation maps in Figs. 3 and 4 for an imbalance of $U_1 = U_2 = 0.045$, Figs. 5 and 6 for $U_1 = U_2 = 0.1$, and Figs. 7 and 8 for $U_1 = U_2 = 0.45$.

It can be seen from Figs. 3 and 4 that the response is almost periodic except for a very narrow region near the second coupled mode $\Omega_r = 2.52$. In Figs. 5 and 6 the chaotic region is still around the second coupled mode but a little wider than in Figs. 3 and 4. With a further larger imbalance, $U_1 = U_2 = 0.45$, the influence on the chaotic range becomes significant, as shown in Figs. 7 and 8. Here, the chaotic region is divided into two wider parts on both sides of the second coupled mode region. The response is periodic for $\Omega_r < 1.75$. Beyond this region, the response becomes chaotic with intermittent zones of periodic solutions. It is also clear from these figures that the response is periodic around all the critical speeds, 0.79 (coupled), 1.0, 1.0, 1.0 (lateral), and 2.52 (coupled).

Typical responses obtained by Newmark's direct integration method for $\Omega_r = 1.83$, 1.85, 1.867, and 1.8 are given in Figs. 9 to 12, respectively, where (*a*) shows the orbital response of the driving gear, (*b*) that of the driven gear, (*c*) the spectra of the semi-major axis of the driving gear, and (*d*) the Poincare map for response of the driving gear in horizontal direction. It can be seen from Fig. 9 that the response has no subharmonic for $\Omega_r = 1.83$, however, there are superharmonics possible.

Just by increasing Ω_r from 1.83 to 1.85, the result in Fig. 10 shows that the response becomes quasi-periodic, see Thomson and Stewart (1986). The quasi-periodic solutions result in closed orbits on Poincare map as shown in Fig. 10(*d*). It can also be seen from Fig. 10(*c*), the frequency spectrum contains two fundamental components $p_1 = \Omega_1$ and $p_2 = 0.627\Omega_1$. These incommensurate frequencies are related by an irrational factor. The remaining are combinations of the fundamental components, given by

$$0.119\Omega_1 = 2p_1 - 3p_2, \quad 0.254\Omega_1 = 2p_2 - p_1,$$

$$0.373\Omega_1 = p_1 - p_2, \quad 0.492\Omega_1 = 3p_1 - 4p_2,$$

$$0.508\Omega_1 = 4p_2 - 2p_1, \quad 0.746\Omega_1 = 2p_1 - 2p_2,$$

$$0.881\Omega_1 = 3p_2 - 2p_1, \quad \text{etc.}$$

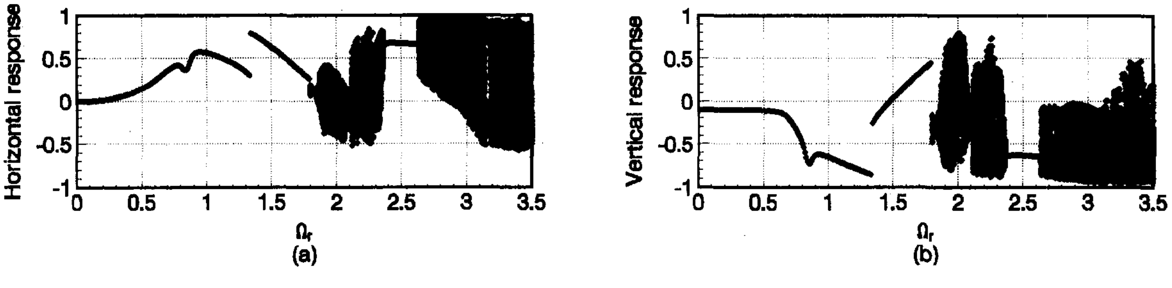

Fig. 7 Bifurcation maps of driving gear response for $U_1 = U_2 = 0.45$

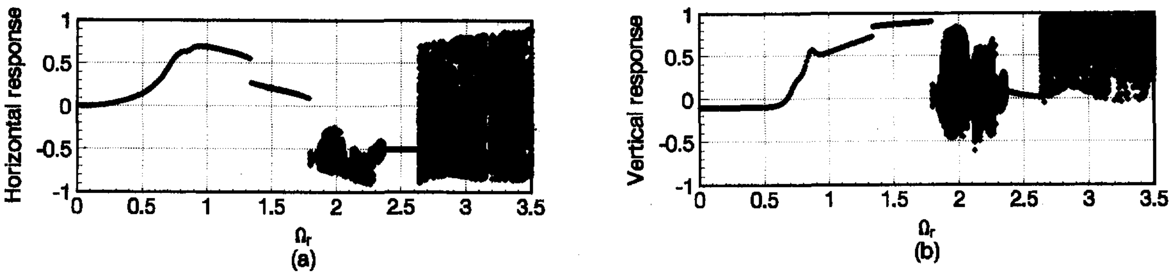

Fig. 8 Bifurcation maps of driving gear response for $U_1 = U_2 = 0.45$

Since there are two fundamental components and that it is difficult to guess both of them, e.g., $p_2 = 0.627\Omega_1$ in this case, it can be clearly observed that the harmonic balance method is not applicable to determine the system response. The factor 0.627 is different for different spin speeds, e.g., for $\Omega_r = 1.86$, it is 0.631.

By increasing the frequency ratio further to $\Omega_r = 1.867$, the quasi-periodic motion of Fig. 10 tends to become chaotic as shown in Fig. 11. This is typically the transition observed from quasi-periodic motion to chaotic motion as reported by Singh et al. (1992). For $\Omega_r = 1.89$, the system experiences a clear chaos as can be seen in Fig. 12.

In addition, the jump phenomena is also found in Figs. 7 and 8 in two regions at $\Omega_r = 1.33 - 1.34$ and $1.79 - 1.80$. The orbital response at $\Omega_r = 1.3338$ and 1.3339 is shown in Fig. 13. It shows that the driving gear orbits at these two close spin speed ratios are quite different though the driven gear orbits are very close.

Effect of Gravity. For the gear pair data chosen earlier, the bifurcation maps obtained with $W_g = 0.0$, are found to be similar to those of Figs. 7 and 8 with 0.45 imbalance. However, the larger the gravity say, $W_g = 1$, at $\Omega_r = 1.89$, the larger the offset of both gear centers as shown in Fig. 14. Comparing Figs. 12(c) and 14(c), we find that the broad band spectrum with $W_g = 0.1$ now has many discrete peaks at zero frequency and multiples of spin speed. Further, the Poincare map containing many points in Fig. 12(d) now contains only one mark as shown in Fig. 14(d). Therefore, gravity has a tendency to remove chaos in the system.

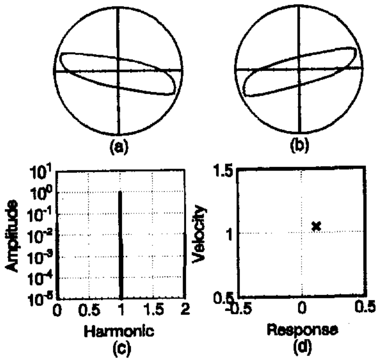

Fig. 9 Response for $\Omega_r = 1.83$

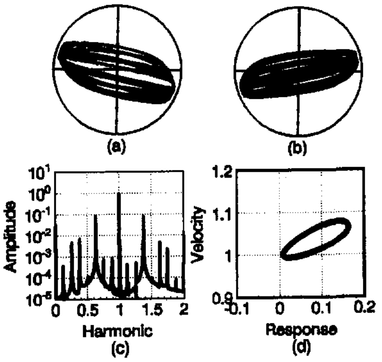

Fig. 10 Response for $\Omega_r = 1.85$

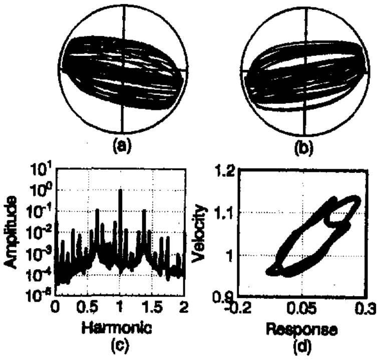

Fig. 11 Response for $\Omega_r = 1.867$

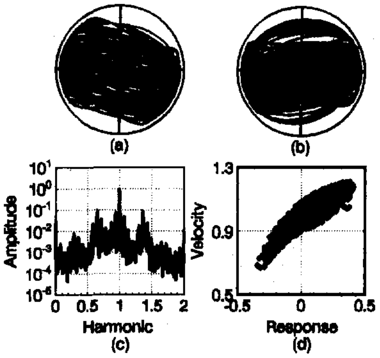

Fig. 12 Response for $\Omega_r = 1.89$

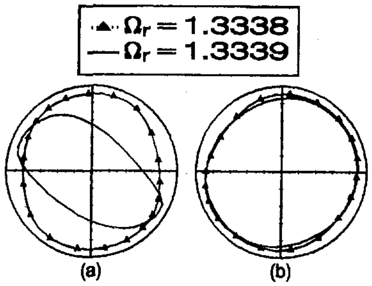

Fig. 13 Orbital responses for $\Omega_r = 1.3338$ and 1.3339

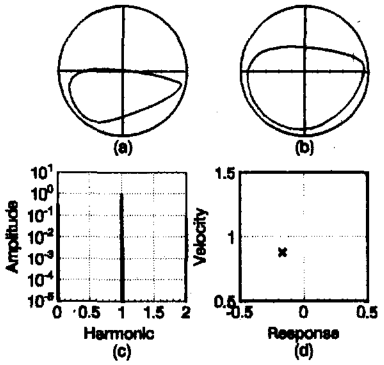

Fig. 14 Response for $W_g = 1$

Effect of Squeeze Film Damper. For $S_D = 0.1$, Figs. 15 and 16 give the bifurcation maps that show that the response is periodic for $\Omega_r < 2.13$ and that the chaotic regime has intermittent zones of periodic response. Comparing these figures with Figs. 7 and 8, we find that major range of chaos for $S_D = 0.03$ is 1.8 to 2.38 and above 2.64 and for $S_D = 0.1$, it is 2.13 to 2.3 and above 2.5.

At $\Omega_r = 1.89$, the orbital responses of both gears, the associated spectra and Poincare maps are given in Figs. 17 and 18 for $S_D = 0.05$ and 0.1, respectively. We find the chaos of Fig. 12 becomes quasi-periodic in Fig. 17 and as damping becomes larger the spectrum in Fig. 18 shows periodic-one solution.

For the system under consideration, the resonant response at $\Omega_r = 1$ obtained without the squeeze film dampers, $S_D = 0$, is given in Fig. 19. The response is 470 times that of the clearance. To control these large whirl amplitudes, we can use a squeeze film damper in the supports. For a value of $S_D = 0.03$ of the squeeze film damper, the response is predominantly suppressed and contained within the clearance as shown in Fig. 20.

Effect of Mesh Stiffness. Keeping all the parameters as considered above, when the mesh stiffness is changed, the natural frequencies change, e.g., when $\xi_K = 0.1$, the critical speeds are $\Omega_r = 0$, 0.55 (coupled), 1.0, 1.0, 1.0 (lateral), and 1.13 (coupled). Chaotic response is also found in this case around the second coupled mode, as in the previous cases with intermittent zones of periodic responses.

Effect of Imbalance Phase Angle. Keeping $\psi_1 = 0$, increasing ψ_2 makes the chaos disappear, e.g., when $\psi_2 = 45$ deg quasi-periodic response was observed with two or more incommensurate frequencies. For $\psi_2 = 90$ deg, seven-fold loop motions are observed, as shown in Figs. 21(*a*) and 21(*b*), though the loops shown are very close in Fig. 21(*b*). The FFT spectrum has peaks at zero frequency and the integer multiples of 1/7 subharmonic frequency, as shown in Fig. 21(*c*). Seven points are found on the Poincare map of Fig. 21(*d*). It shows that the steady-state solution for this case is periodic and classified to be period seven. When $\psi_2 = 180$ deg, the results are shown in Fig. 22. It is interesting to see that sevenfold loop orbits occur again, though the orbit of the driving gear is almost like a circle.

Geared Turbo Generator Set

Referring to Fig. 1, the following data is chosen: $M_{10} = 7.45$, $M_2 = 525.7$, $M_3 = 116.04$, $M_7 = 5.0$, and $M_6 = 726.4$ kg; $I_{T10} = 0.0745$, $I_{T2} = 16.1$, $I_{T3} = 3.115$, $I_{T7} = 0.002$, and $I_{T6} = 56.95$ kgm^2; $I_{P10} = 0.149$, $I_{P2} = 32.2$, $I_{P3} = 6.23$, $I_{P7} = 0.004$, and $I_{P6} = 113.9$ kgm^2.

The pinion has 23 teeth with $r_7 = 0.03567$ m, while the gear has 328 teeth with $r_6 = 0.5086$ m, $k_h = 10^8$ N/m, and $\phi_p = 22.5$ deg. Shaft lengths between nodes are taken as $l_{12} = 0.1$, $l_{23} = 4.24$, $l_{34} = 1.16$, $l_{45} = l_{56} = 0.15$, $l_{78} = 0.3$, $l_{89} = 0.05$, $l_{9,10} = 4.95$, and $l_{10,11} = 0.1$ m, radius between nodes 1 and 3 = 0.15 m, between nodes 3 and 6 = 0.11 m, and for turbine shaft = 0.075 m. Young's modulus = 207 GPa, shear modulus = 79.5 GPa, and density = 7800 Kg/m^3.

Bearings 1 and 2 have $k_{yy} = 1.839 \times 10^8$, $k_{zz} = 2.004 \times 10^8$, respectively, and bearings 3 and 4 have $k_{yy} = 1.010 \times 10^7$, $k_{zz} = 4.160 \times 10^7$ N/m, respectively. Damping in all bearings = 3000 Ns/m. Nominal torque, T_n, = 318.31 Nm. The short circuiting torque, see Rao (1992), is

$$T = T_n m_a e^{-at} \sin \omega t + T_n m_s e^{-\beta t} \sin 2\omega t, \qquad (10)$$

where $m_a = 12.353$, $m_s = 0.5$, $a = 33.97$, and $\beta = 5.45$.

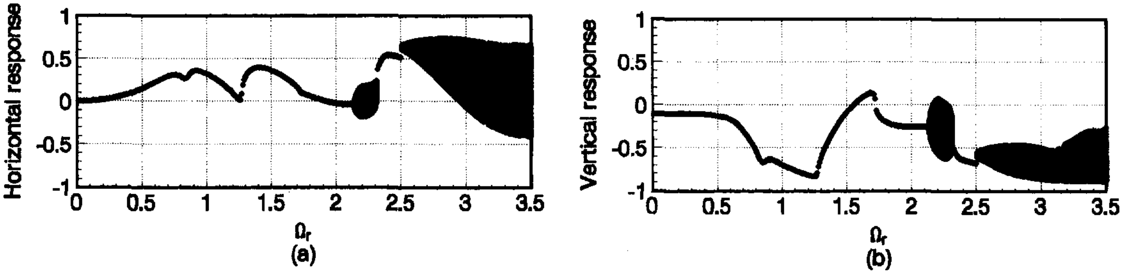

Fig. 15 Bifurcation maps of driving gear response for $S_D = 0.1$

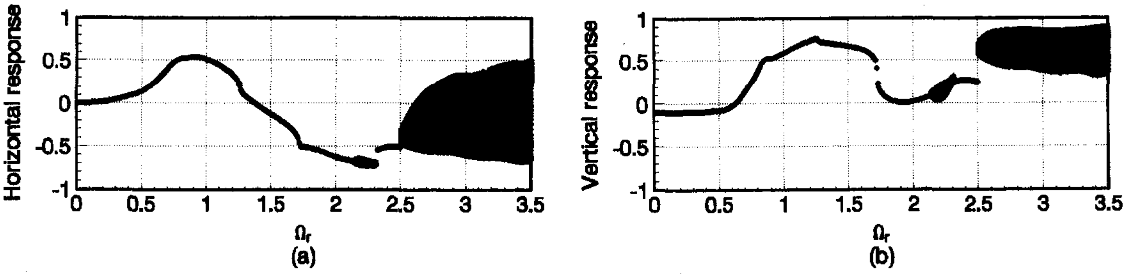

Fig. 16 Bifurcation maps of driving gear response for $S_D = 0.1$

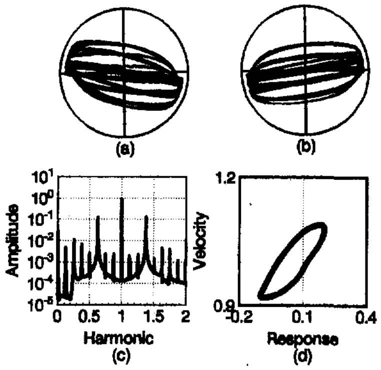

Fig. 17 Response for $S_D = 0.05$

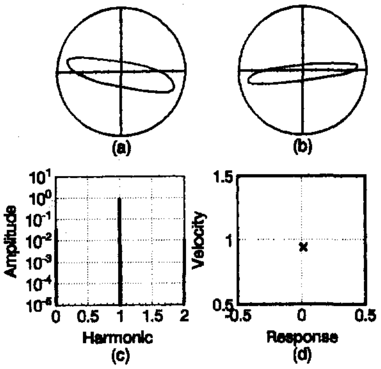

Fig. 18 Response for $S_D = 0.1$

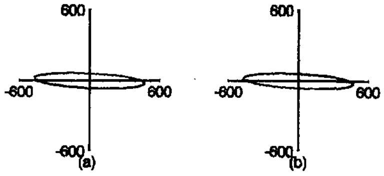

Fig. 19 Response without squeeze film damper $\Omega_r = 1$

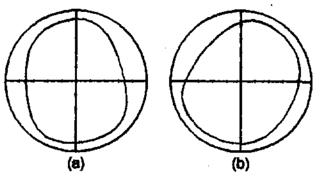

Fig. 20 Response with squeeze film damper $S_D = 0.03$, $\Omega_r = 1$

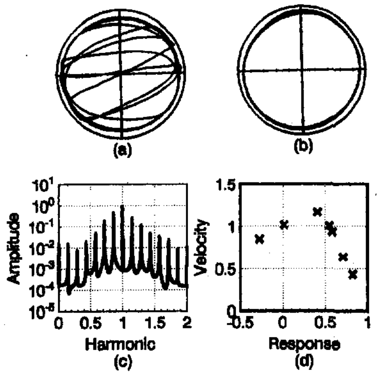

Fig. 21 Response for $\psi_1 = 0$ deg, $\psi_2 = 90$ deg

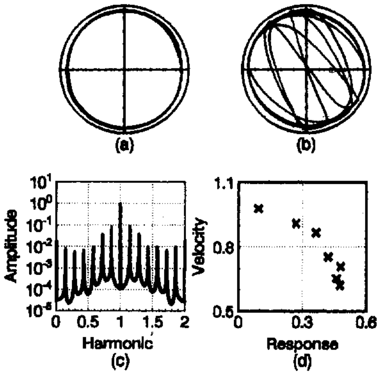

Fig. 22 Response for $\psi_1 = 0$ deg, $\psi_2 = 180$ deg

The coupled natural frequencies of the system for $\Omega_1 = 1500$ rpm (157.08 rad/s) are 73.1, 77.2, 108.5, 116.0, 150.5, 236.8, 313.5, 319.6, 353.5, 362.9, 371.9, 396.6, and 466.2 rad/s.

Since the rotational speed is close to the coupled natural frequency 150.5 rad/s, the predominant frequency components of the lateral and torsional response will occur at this mode shape. This mode shape is shown in Fig. 23.

An uncentralized spring configuration for the damper is chosen with $R = 50.8$ and $L = 25.4$ mm. The following three arrangements are chosen: (1) $\mu = 0.015016$ Ns/m^2, $c_r = 152.4$ microns; (2) $\mu = 0.015016$ Ns/m^2, $c_r = 304.8$ microns; and (3) $\mu = 0.030032$ Ns/m^2, $c_r = 152.4$ microns. The shaft torques without damper for sections 4–5 and 5–6 near the gear and 7–8 near the pinion are shown in Fig. 24(a). The corresponding torques for case I-5 (squeeze film damper I at location 5) are shown in Fig. 25(a). The torque value initially is larger than the undamped case, however, it decays faster because of squeeze film damper (the difference in torque values is very small as the amplitude at node 5 in Fig. 23 is very small). For case I-9, the corresponding values given in Fig. 26(a) show that the damper location 9 is far more effective in decreasing the torque values in a shorter time. This can be confirmed from Fig. 27(a) with two dampers I-5 + 9 (located at 5 and 9) since the torque response is almost same as in case I-9.

The lateral response of both the gear and pinion is given in Fig. 24(b) for the undamped case. The pinion response is nearly 8 times that of the gear. With I-5 arrangement, the response given in Fig. 25(b) shows that it has practically no effect on the response. However, with the damper located at station 9 (I-9), it has a significant influence in reducing the pinion response by nearly 2.5 times, as can be seen from Fig. 26(b). As in the case of shaft torques, the arrangement I-5 + 9 gives a response shown in Fig. 27(b), (same as in Fig. 26(b). Therefore, it can be deduced that the squeeze film damper should be located near the pinion experiencing maximum lateral response.

The undamped torsional response for both the pinion and gear is shown in Fig. 24(c). The corresponding response for the case I-5 is given in Fig. 25(c). The damper becomes effective when it is located at station 9, and, for clarity, only the pinion response is shown in Fig. 26(c). As in the previous cases the response, though initially larger decays rapidly. The

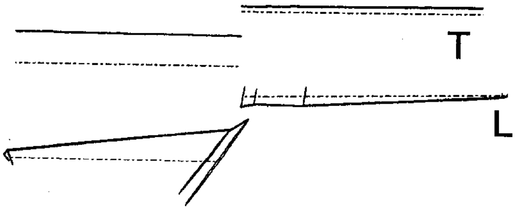

Fig. 23 Mode shape of natural frequency 150.5 rad/s at $\Omega_1 = 1500$ rpm

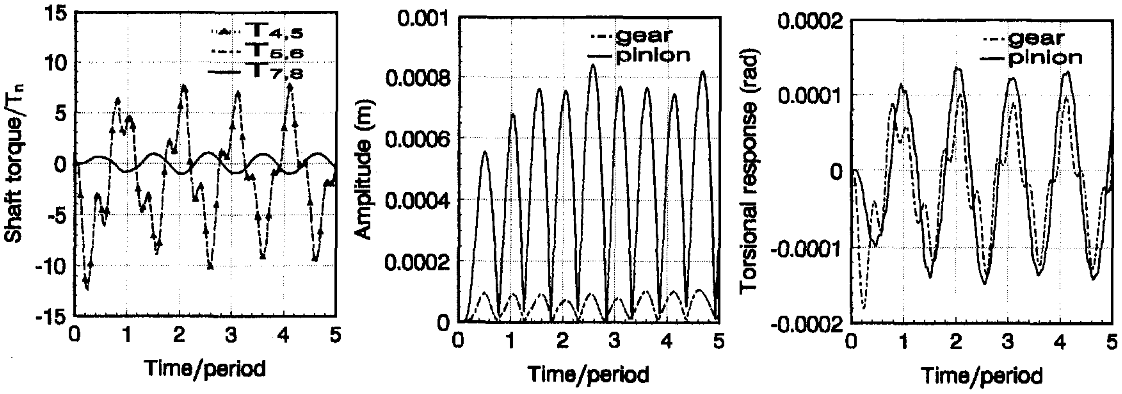

(a) (b) (c)

Fig. 24 (*a*) Shaft torques without SFD; (*b*) lateral response without SFD; (*c*) torsional response without SFD

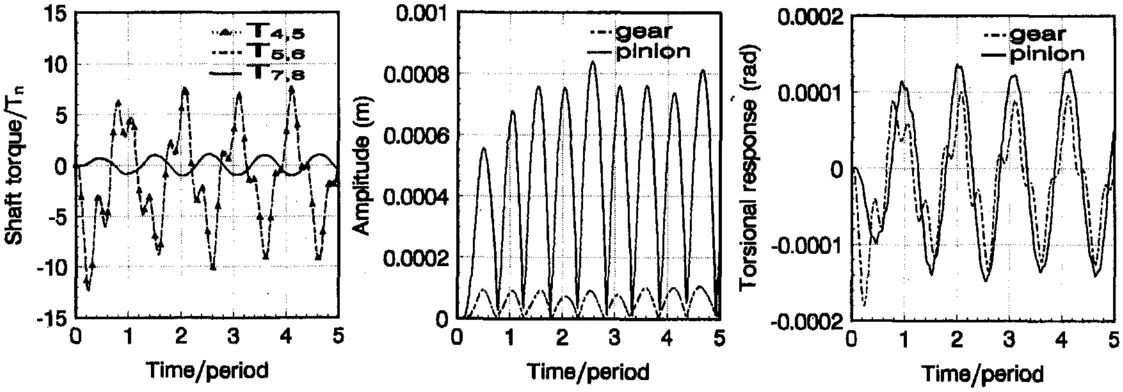

(a) (b) (c)

Fig. 25 (*a*) Shaft torques with SFD I-5; (*b*) lateral response with SFD I-5; (*c*) torsional response with SFD I-5

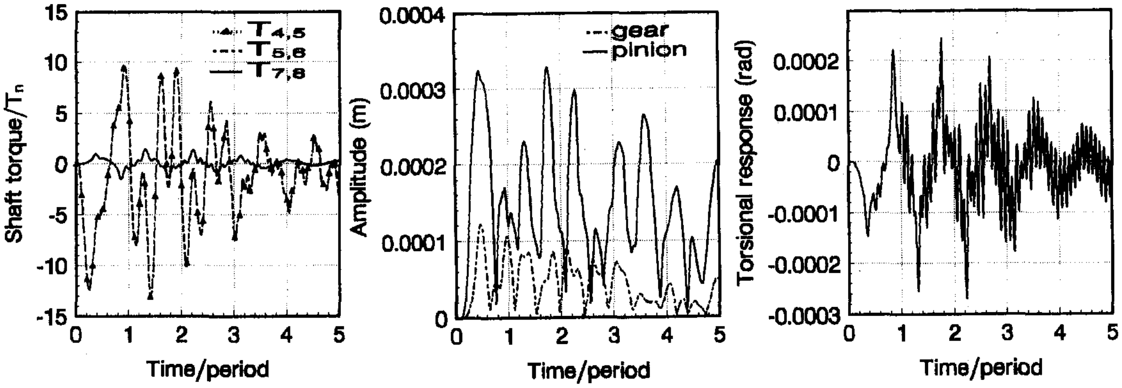

(a) (b) (c)

Fig. 26 (*a*) Shaft torques with SFD I-9; (*b*) lateral response with SFD I-9; (*c*) torsional response with SFD I-9

high frequency component is also clearly seen. Fig. 27(*c*) shows the response with I-5 + 9 arrangement.

The lateral response for case II-9 is shown in Fig. 28(*a*). Compared to Fig. 26(*b*) (I-9), the response here is nearly 1.6 times larger for the pinion and almost the same for the gear. With a larger clearance, damping force decreases, as can be seen from Eq. (5), and, therefore, the effect of squeeze film damper is also decreased. Fig. 28(*b*) shows the results for case III-9, which has double the viscosity compared to I-9. The peak amplitude is slightly lower in Fig. 28(*b*) and decreases faster than that in Fig. 26(*b*). Figure 29 shows the force transmitted by the damper at node 9 for case I-9. It can be seen that the transmitted force decreases rapidly because of the damping action.

Conclusions

Considering a simple gear pair system with nonlinear squeeze film damper supports, the response is shown to be periodic, quasi-periodic, and transitional in nature before becoming chaotic. Under quasi-periodic conditions, the response typically contains two fundamental components and several combinations of these components. Through bifurcation diagrams, the chaotic behavior of the system is discussed. It is shown that

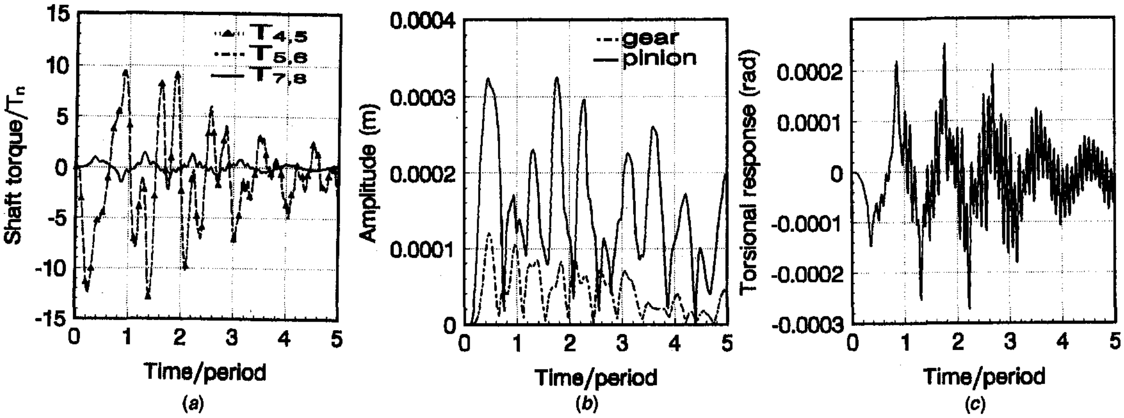

Fig. 27 (*a*) Shaft torques with SFD I-5 + 9; (*b*) lateral response with SFD I-5 + 9; (*c*) torsional response with SFD I-5 + 9

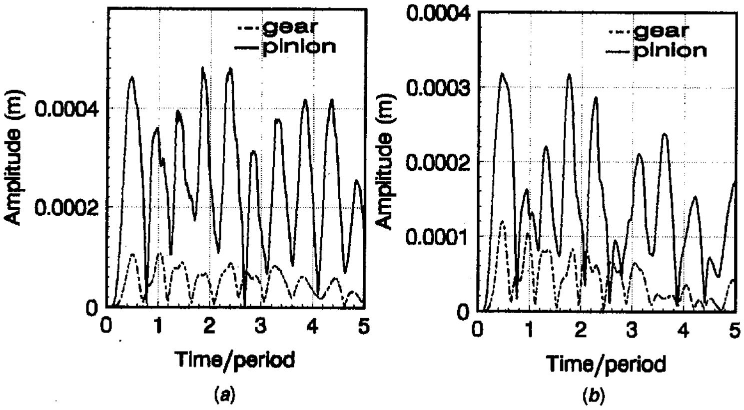

Fig. 28 (*a*) Shaft torques with SFD II-9; (*b*) lateral response with SFD III-9

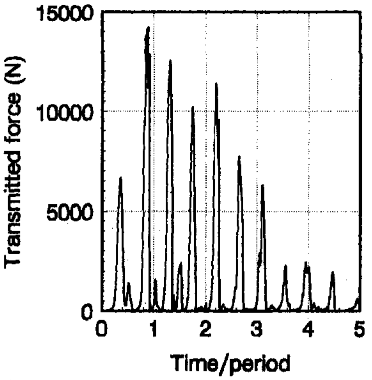

Fig. 29 Transmitted force at node 9 with SFD I-9

(1) the larger the imbalance, the wider the chaotic regime, (2) gravity suppresses chaos in the system, (3) increasing the damping coefficient can reduce the chaotic region, (4) irrespective of mesh stiffness values, chaos occurs around the second coupled mode, and (5) in-phase unbalances give rise to chaos. As the relative phase angle increases, the response becomes quasi-periodic, and with out-of-phase imbalances it is periodic. Coupled bending-torsion vibrations of a geared turbine are considered. The lateral response due to short circuit torque is determined and shown to be substantial. It is shown that squeeze film dampers can be used to suppress the lateral response arising from torsional excitation.

Acknowledgments

The authors are very thankful to the National Science Council of Taiwan for the grant NSC 84-2212-E-194-001 and to provide a research chair to Professor J S Rao during 1994–96.

References

Chen, C.-S. et al., 1993, "Coupled Lateral-Torsional Vibration of a Gear-Pair System Supported by a Squeeze Film Damper," *ASME Design Engineering Div.*, Vol. 54, p. 53.

Concordia, C., 1956, *Synchronous Machine Theory and Performance*, John Wiley & Sons, New York.

Cookson, R. A., and Kossa, S. S., 1980, "The Effectiveness of Squeeze Film Damper Bearings Supporting Flexible Rotors Without a Centralizing Spring," *Intl. J. Mech. Sci.*, Vol. 22, p. 313.

Ehrich, F., 1995, "Nonlinear Phenomena in Dynamic Response of Rotors in Anisotropic Mounting Systems," *ASME Special 50th Anniversary Design Issue*, Vol. 117, p. 154.

Goldman, P., and Muszynska, A., 1994, "Chaotic Behavior of Rotor/Stator Systems with Rubs," ASME JOURNAL OF ENGINEERING FOR GAS TURBINES AND POWER, Vol. 116, p. 692.

Hwang, J. L., and Shiau, T. N., 1991, "An Application of the Generalized Polynomial Expansion Method to Nonlinear Rotor Bearing Systems," ASME *Journal of Vibration and Acoustics*, Vol. 113, p. 299.

Lund, J., 1978, "Critical Speed, Stability and Response of a Geared Train of Rotors," ASME *Journal of Mechanical Design*, Vol. 100, p. 535.

Mohan, S., and Hahn, E. J., 1974, "Design of Squeeze Film Damper Supports for Rigid Rotors," *ASME Journal of Engineering for Industry*, Vol. 96, No. 3, p. 976.

Newmark, N. M., 1959, "A Method of Computation for Structural Dynamics," *ASCE Journal of Engineering Mechanics*, Vol. 85, p. 67.

Rao, J. S., 1992, "Life Estimation of Gear Transmission Unit in a Turbine Generator Set Due to Short Circuits," *Mechanism and Machine Theory*, Vol. 27, No. 3, p. 283.

Rao, J. S., 1996, *Rotor Dynamics*, 3rd ed., New Age International, New Delhi, London.

Rao, J. S., Chang, J. R., and Shiau, T. N., 1995, "Coupled Bending-Torsion Vibration of Geared Rotors," *ASME Design Engng. Technical Confs.*, DE-Vol. 84-2, Vol. 3—Part B, p. 977.

Rao, J. S., Chang, J. R., and Shiau, T. N., "Lateral Response Due to Torsional Excitation of Geared Rotors," submitted to *Mechanism and Machine Theory.*

Rao, J. S., Rao, D. K., and Bhaskara Sarma, K. V., 1980, "The Transient Response of Turbo-Alternator Rotor Systems Under Short Circuiting Conditions," *Proc. Vibrations of Rotating Machinery Conf.*, Instn. of Mech. Engrs., Cambridge, England, p. 271.

Shiau, T. N., Chou, Y. W., Chang, J. R., and Nelson, H. D., 1994, "A Study on the Dynamic Characteristics of Geared Rotor-Bearing System With Hybrid Method," ASME paper no. 94-GT-355.

Singh, R., et al., 1990, Nonlinear Dynamic Analysis of Geared Systems, Contractor report no. 4338, NASA.

Thomson, J. M. T., and Stewart, H. B., 1986, *Nonlinear Dynamics and Chaos*, John Wiley & Sons, New York.

Zorzi, E. S., and Nelson, H. D., 1980, "The Dynamics of Rotor Bearing Systems With Axial Torque: A Finite Element Approach," *ASME Journal of Mechanical Design*, Vol. 102, pp. 158.

E. H. Maslen

C. K. Sortore

G. T. Gillies

Department of Mechanical, Aerospace, and
Nuclear Engineering,
University of Virginia,
Thornton Hall, McCormick Road,
Charlottesville, VA 22903

R. D. Williams

S. J. Fedigan

Department of Electrical Engineering,
University of Virginia,
Charlottesville, VA 22903

R. J. Aimone
Mobile Technology Company,
Paulsboro, NJ 08066

Fault Tolerant Magnetic Bearings

A fault tolerant magnetic bearing system was developed and demonstrated on a large flexible-rotor test rig. The bearing system comprises a high speed, fault tolerant digital controller, three high capacity radial magnetic bearings, one thrust bearing, conventional variable reluctance position sensors, and an array of commercial switching amplifiers. Controller fault tolerance is achieved through a very high speed voting mechanism which implements triple modular redundancy with a powered spare CPU, thereby permitting failure of up to three CPU modules without system failure. Amplifier/cabling/coil fault tolerance is achieved by using a separate power amplifier for each bearing coil and permitting amplifier reconfiguration by the controller upon detection of faults. This allows hot replacement of failed amplifiers without any system degradation and without providing any excess amplifier kVA capacity over the nominal system requirement. Implemented on a large (2440 mm in length) flexible rotor, the system shows excellent rejection of faults including the failure of three CPUs as well as failure of two adjacent amplifiers (or cabling) controlling an entire stator quadrant.

Introduction

Critical to the acceptance of magnetic bearing technology in process critical industrial applications is a very high level of reliability. This reliability will be achieved through a combination of fundamental component level reliability improvements in concert with operating schemes which are inherently tolerant of component level failures. This paper explores two mechanisms for tolerating component level failures directed at those components which seem most likely to fail: the digital controller CPU/memory subsystem and the actuator coil/amplifier/connector strings.

Conventional radial magnetic bearings employ a magnetic stator with a multiplicity of radial legs surrounding a magnetically permeable rotor. Electromagnet coils are wound on some or all of the stator legs and forces are exerted on the rotor by passing currents through these coils. By suitably controlling the coil currents, a radial force of a prescribed magnitude and orientation can be applied to the rotor. The current command is determined in response to measured rotor motion in order to achieve stable rotor support with appropriate dynamic properties [5]. As such, the magnetic bearing is a feedback device consisting of a rotor motion sensor, a controller which determines the appropriate coil commands in response to the sensed motion and an amplifier/actuator set which will produce the required force. Conventionally, failure of any element of any of these components produces failure of the entire bearing system, with concomitant damage to the machine.

Accurate statistics concerning failure mechanisms in commercial magnetic bearing systems are not yet available. However, anecdotal field accounts indicate that amplifier, coil, and power cabling failures are of significant concern. Any of these three failures produces essentially the same result: loss of current in a particular coil circuit. Industrial experience with digital controllers in other applications suggests that fault tolerance in the digital controller will emerge as equally critical to the overall system reliability.

The fault tolerance schemes described here have been demonstrated on a test rig built at the University of Virginia Rotating Machinery and Controls Laboratory. Figure 1 is a photograph of the test rig. The rotor consists of a shaft, approximately 2440 mm (8 ft) in length and 57 mm (2.25 in) in diameter fitted with three radial magnetic bearing journals and one magnetic thrust disk. The radial bearings each have a design load capacity of 5780 N (1300 lbf). The rotor is controlled axially by a magnetic thrust bearing whose design load capacity is 3330 N (750 lbf). The rotor is driven by a variable speed motor through a flexible-disk/splined coupling. The first two free-free bending modes of the rotor are computed to occur at 32 Hz and 107 Hz. The rotor has been operated up to 87 Hz (5200 rpm); above three system critical speeds. The electronics control rack consists of the University of Virginia Fourth Generation Digital Controller, sensor demodulation and signal conditioning electronics, and an array of transconductance current amplifiers (Copley Controls) including a 50 VDC power supply. Position sensing is achieved with Bently Nevada eddy current proximitors.

Fault tolerance for the position sensing system is not presented in this paper. There are two avenues to pursue in obtaining position sensor fault tolerance. The most obvious approach is to deploy redundant sensors and use an analog voting mechanism based on the two sensors for each axis whose outputs most nearly agree. Aside from some issues of noise introduced by voter hunting between the two closest matches, this approach is easy to implement and doesn't appear to merit close investigation. An alternative approach is based on self-sensing in which the actuator electrodynamics are interrogated to determine the rotor position [11, 10]. If such a scheme can be adapted to a fault tolerant actuator, then the sensor fault tolerance problem is essentially subsumed into the actuator fault tolerance, which is presented here. In the opinion of the authors, the latter

---

Contributed by the International Gas Turbine Institute (IGTI) of THE AMERICAN SOCIETY OF MECHANICAL ENGINEERS for publication in the ASME JOURNAL OF ENGINEERING FOR GAS TURBINES AND POWER. Paper presented at the International Gas Turbine and Aeroengine Congress and Exhibition, Stockholm, Sweden, June 2–5, 1998; ASME Paper 98-GT-377.

Manuscript received by IGTI March 12, 1998; final revision received by the ASME Headquarters March 23, 1999. Associate Technical Editor: R. Kielb.

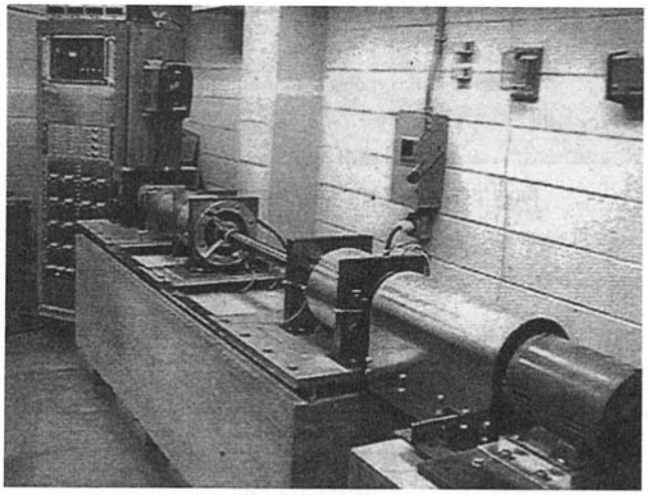

Fig. 1 Fault tolerant magnetic bearing test rig

approach is more likely to produce the levels of reliability required by process critical industrial or military applications.

Controller Hardware

The controller hardware architecture is a fault-tolerant design, consisting of four processor modules arranged in a triple modular redundant configuration with a hot spare[1] [2]. Figure 2 provides a schematic overview of the architecture.

A voting module provides active repair and reconfiguration in the event of data disagreements or "lost" processors. The processor modules are independent computers based on the Texas Instruments TMS320C40, a high speed 32-bit floating point digital signal processor, operating at 40 MHz, capable of executing 220 million operations per second. Reliability is further enhanced by a custom fault tolerant I/O bus, whose data and address buses are each augmented with a set of check bits for single-bit error correction. Like most DSPs, the TMS320C40 offers a single-cycle floating point multiply and accumulate, and a circular addressing mode, making it ideal for digital filtering applications and Discrete Fourier Transforms.

It is important to comment that triple modular redundancy (TMR) is widely implemented in commercial digital controllers: the concept is not a new one. What is significant in the present implementation is the speed of the controller. Typical throughput rate for commercial TMR controllers is on the order of 4 milliseconds [1]: these systems are designed for process control on processes with relatively slow dynamics. Digital controllers for magnetic bearings need much higher throughput: typically on the order of 100 microseconds, to meet the system's dynamic requirements. Consequently, software based voting implementations as are found on most commercial digital controllers (even very high performance systems such as the MAFT [6] and FTMP [4] controllers developed for aircraft control) are inappropriate here.

To satisfy the need for high performance and high reliability, the fourth generation digital controller realizes fault tolerance through hardware redundancy, and hardware-based information redundancy. Each of the four digital signal processing modules is a separate but identical printed-circuit board, which plugs directly into the motherboard. With this configuration, modules can be replaced easily if repairs become necessary, and maintenance and development of application software is greatly simplified. The control actions of each processor are sent out through a communications port to the voter subsystem. This voter compares the three commands for consistency: if one of the three processors disagrees with the other two, it is deemed to have failed. It is then disregarded and replaced with the output from the spare processor, if available. The bus controller performs the requested transfer between the processors and a specified I/O device across a fault tolerant synchronous bus.

In normal operating mode, all four modules execute the same control software and generate a series of control actions every sampling period. These actions are translated into bus operations, and are sent through each outbound communications port. Each element in this data stream passes onto the voter which performs a bitwise majority vote on the results arriving from the three processors T1, T2, and T3. To make sure that all processors move in lockstep despite variations in their local oscillators, data arriving from each communications channel is stored in an outbound data buffer until results from all four processors become available, as indicated by a buffer full signal. Once all of these signals have been asserted, the voter latches the results of the majority vote. This is done even for the hot standby processor, T4, to guarantee that it remains synchronized with the voting processors. In addition, synchronization is maintained at the beginning of each sampling period when the sensor data becomes available. The voter waits until each one of the inbound FIFOs asserts its buffer empty signal, and then loads all four in parallel. This assures that the sensor inputs arrive at each processor at the same time. Thus, the voter provides both fault masking through data voting, and data synchronization by updating the input and output FIFOs at the same time.

If T1, T2, or T3 fails during normal operation, its failure is detected if it sends out two consecutive words of bad data, or if its FIFO control signals disagree with the others for more than 8 ms. If T4 fails in one of these two ways, the event is noted but no action is taken until another processor fails and T4 becomes one of the voting processors. When a failure is indicated by T1, T2, or T3, the voter removes the offending processor from the voting process and replaces it with T4, the standby spare. In this reconfigured mode, the standby and the two remaining processors vote on the data coming from the outbound FIFOs. Bad data from one of these three does not cause further reconfiguration, because it is masked by the other two. However, if the control signals from one of the processors disagree for more than 8 ms, the voter switches to simplex mode (single processor, not fault tolerant), selecting the working processor with the lowest number. At this point, the controller would no longer be operating in a fault tolerant mode.

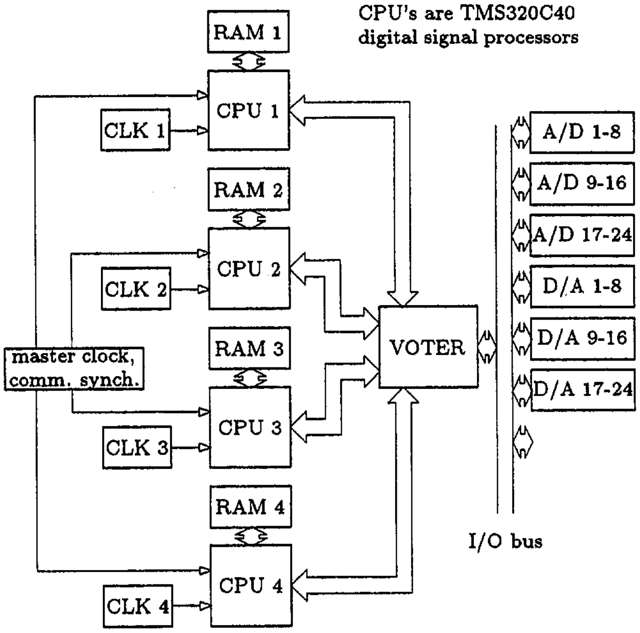

Fig. 2 Schematic of the hardware TMR architecture

---

[1] Hot spare means that the extra processor not participating in voting is powered up and executing the software.

Since the voter represents a single point of failure, it must be highly reliable. This issue has been addressed in both its design and implementation. From the design side, the voter's state machine is synchronous and only has three states which represent the three operating modes: normal, reconfigured, and failed. With a small number of states, the design can be verified easily by simulation and by testing in the lab, and the state machine can be designed by hand, without resorting automated synthesis tools, which can introduce logic hazards. Since the voter runs on the same clock as the bus controller, control lines which pass between them do not need to be synchronized and metastability problems are avoided completely. From the implementation end, the voter's logic is embedded in three PLDs with good reliability records. Data from the voter is sent on to the channel bus controller, which performs block read/write operations on I/O devices over a fault-tolerant bus.

The I/O bus can address up to 512 I/O channels. To guarantee the integrity of bus operations, the clock and control signals are triply redundant, and are voted on by the I/O devices. The data and address buses are each augmented with a set of check bits, which are used for single bit error correction. If one address bit is corrupted, the proper board and board channel will still be addressed. If a data bit is corrupted on the back-plane during a write, it will automatically be corrected before it is applied to its output channel. To prevent bit corruptions in the first place, the signals are passed along a controlled impedance backplane, which reduces transmission line effects, and control/clock lines are interlaced with grounds to prevent signal crosstalk.

The current system has four I/O devices: a D/A board, A/D board, a two-channel RS-232 link, and a JTAG interface. The 8 channel A/D board offers 14 bits of resolution and can support sampling rates in excess of 150 kHz. Differential inputs reject common mode noise and provide ground isolation between the controller and the sensors. Unlike many commercially available A/D boards which multiplex one converter across the board channels, this board has one sample-and-hold (S/H) device and one A/D converter for each channel. This permits all the channels to be sampled simultaneously and for all conversions to proceed in parallel. The 8 channel D/A board offers 14 bits of resolution, with differential outputs for common mode rejection and ground isolation. Low glitch converters help to reduce the transients which result from the conversion process. With 8 channels assigned to each board and 10 slots available on the backplane, the controller can support up to 80 channels of combined digital and analog I/O. A programmable DUART on the mother board provides a two channel RS-232 link for host-to-target communications. One channel can be used for inspecting/modifying control variables and another for streamback data that may be captured by a host terminal. A JTAG interface (10.0 MHz serial link) on the motherboard can be used with a commercially available emulator for inspecting machine registers, single-stepping through code, and source-level debugging.

Controller

Although the controller hardware is well suited to using high order MIMO control [3], the objectives of this project were adequately served using fairly simple, low order local feedback controllers. Each of the seven control axes (two radial axes at each of three planes plus the thrust direction) is uncoupled from the others. The controllers are simple PID control running at a sampling rate of 7.4 kHz. Table 1 summarizes the properties of the controllers. The sensor/actuator pair at rotor midspan is separated by a node of the second rotor free-free bending mode, leading to difficult control of this mode: stability is somewhat sensitive to friction in the drive coupling spline.

Table 1 PID controller parameters

Location	Parameter	Value
non–drive end $x-$ and $y-$	proportional gain	2.4
	derivative gain	0.005
	integrator gain	0.5
	first time constant	9.5e-5
	second time constant	3.5e-5
midspan $x-$ and $y-$	proportional gain	0.8
	derivative gain	0.002
	integrator gain	1.14
	first time constant	4.2e-4
	second time constant	3.5e-5
drive end $x-$ and $y-$	proportional gain	2.4
	derivative gain	0.005
	integrator gain	0.5
	first time constant	9.5e-5
	second time constant	3.5e-5
thrust ($z-$)	proportional gain	8.1
	derivative gain	0.096
	integrator gain	2.24
	first time constant	9.1e-4
	second time constant	9.8e-4

all sensor gains: 500 volts/inch
radial actuator gains: 80 lbf/amp
radial open loop stiffness: 11,690 lbf/inch
thrust actuator gain: 50 lbf/amp
thrust open loop stiffness: 5,200 lbf/inch

Amplifiers and Coils

Most commercial radial magnetic bearings have at least eight legs in the stator and at least four independent coils or coil sets. In order to obtain significant fault tolerance within this magnetic structure, we separate the coils associated with each leg and control each coil with an independent power amplifier. The resulting increase in the number of power amplifiers (from four to eight in the simplest and most common case,) doesn't actually increase the amplifier capacity requirement: each amplifier can have substantially less capacity than in the more conventional schemes so that the total kVA capacity stays fixed.

With this arrangement, the number of independent coils in the stator substantially exceeds the number of force components which are to be generated (usually two, F_x and F_y). The relationship between these coil currents and the resulting force components is fairly easily determined by analysis,

$$I_1, I_2, \ldots, I_n \Rightarrow F_x, F_y,$$

but the inverse relationship:

$$F_x, F_y \Rightarrow I_1, I_2, \ldots, I_n$$

is not only difficult to find but is not unique [8]: a property of the quadratic character of the mapping from currents to forces.

For the purposes of designing the feedback control, this latter relationship is crucial since the general dynamic problem relates the bearing forces to the rotor motion; ideally, the character of the magnetic device should not enter directly into the design of the controller. Meeker [8] demonstrates that, for most stator geometries, a basis for the currents can be chosen so that the various bearing force components are related linearly to a set of control force request terms and scaled by a biasing term. Such a mapping can be found not only for stators with a full complement of independently functioning coils, but also for stators with one or more nonfunctioning coils: the coil/amplifier fault condition. In this manner, the excess number of controlling coils provides an opportunity for fault tolerance. If one or even several of the coils fail, a new relationship (basis for the currents) can be implemented which will permit the controller to still provide the same bearing dynamic properties that were provided with a full complement of operating coils.

Conceptually, the key property permitting bearing operation with one or more coil circuits failed is that the coils in a typical magnetic bearing stator are strongly coupled: each coil affects the flux in all of the air gaps. This coupling permits other coils in the stator to assume the responsibilities of the failed coils. In this manner, the fault tolerance scheme presented here is based on resource reallocation rather than more conventional schemes of resource replacement as discussed by Lyons et al. [7].

Attractive magnetic bearings are linearized by imposing a biasing current in each coil which produces a magnetic stress but no net force at an equilibrium position. Although the current to force relationship is quadratic, bias and control currents are chosen so that all second-order control current terms are identically zero at the equilibrium point. When the bias current magnitudes are held constant, the relationship between control current and bearing force relationship is linear. A detailed description of the bias linearization principle can be found in [9]. It can be shown that the inverse current-to-force relationship that permits linear bearing force control is

$$\mathbf{I} = \frac{1}{c_o}\mathbf{W}\begin{Bmatrix} c_o^2 \\ F_x \\ F_y \end{Bmatrix} \tag{1}$$

in which the bias current is proportional to the parameter c_o.

The linearization matrix **W** is computed numerically and a different **W** exists for each different configuration of failed coils. Consider an 8-pole symmetric bearing, with each pole face having equal area, which is the type contained in the test rig. In the normal operating mode, coils on all 8 legs would be operational. This configuration allows for the linearizing current set

$$\mathbf{W} = \frac{g_o}{4N\sqrt{\mu_o A}}\begin{bmatrix} 2 & 2 & 0 \\ -2 & -\sqrt{2} & -\sqrt{2} \\ 2 & 0 & 2 \\ -2 & \sqrt{2} & -\sqrt{2} \\ 2 & -2 & 0 \\ -2 & \sqrt{2} & \sqrt{2} \\ 2 & 0 & -2 \\ -2 & -\sqrt{2} & \sqrt{2} \end{bmatrix} \tag{2}$$

in which N is the number of coil turns per coil (pole), A is the pole face area, g_0 is the nominal air gap length, and μ_0 is the relative permeability of a vacuum.

If only one coil circuit fails, there is no loss in load capacity. An alternate set of currents can be picked that yields the same flux densities as realized in the all-coils-active case. The only cost is in an increase in I^2R losses in the coils. For example, for the particular case where coil circuit 8 has failed the linearizing current set is

$$\mathbf{W} = \frac{g_o}{4N\sqrt{\mu_o A}}\begin{bmatrix} 4 & 2+\sqrt{2} & -\sqrt{2} \\ 0 & 0 & -2\sqrt{2} \\ 4 & \sqrt{2} & 2-\sqrt{2} \\ 0 & 2\sqrt{2} & -2\sqrt{2} \\ 4 & -2+\sqrt{2} & -\sqrt{2} \\ 0 & 2\sqrt{2} & 0 \\ 4 & \sqrt{2} & -2-\sqrt{2} \\ 0 & 0 & 0 \end{bmatrix}. \tag{3}$$

The I^2R loss associated with this coil mapping is readily shown to be twice that of the solution with all eight coils functioning, under zero load condition. This increase in power is a significant shortcoming to the method in that the bias current, responsible for most of the power loss, is carried only in the odd-numbered coils (1, 3, 5, and 7). That is, the power dissipation in these coils is four times as high under the coil failure condition than when the full complement of coils is active.

Now, consider the case in which coils 1, 2, and 3 have failed. Despite the massive asymmetry introduced by the failure of three adjacent coils, linearized control is still possible as shown by the fact that a new **W** matrix can be computed. Numerical studies have shown that in this configuration,

$$\mathbf{W} = \frac{g_o}{4N\sqrt{\mu_o A}}\begin{bmatrix} 0 & 0 & 0 \\ 0 & 0 & 0 \\ 0 & 0 & 0 \\ 5.09 & 0.359 & 3.32 \\ 0 & 3.68 & 3.68 \\ 0 & 3.68 & 3.68 \\ 0 & 3.68 & 3.68 \\ 5.09 & 3.32 & 0.359 \end{bmatrix} \tag{4}$$

is a good solution. Control is still linearized, but load capacity is substantially reduced because flux is no longer evenly distributed in the stator.

The most extensive failure that this type of stator can tolerate are the two configurations involving four failed coils where no two adjacent coils have failed. Obviously, it is not possible to support the rotor with four adjacent coils failed.

This scheme is clearly a mechanism for achieving fault tolerance to coil circuit failures. If one or more coils fail, a new coil current control scheme can be implemented which preserves the linear relationship between required forces and coil currents. This fault tolerance comes at some expense in load capacity because the necessary redistribution of magnetic flux in the stator, in order to achieve high forces along vectors passing through the poles of the failed coils, leads to premature saturation in the stator or journal.

What makes this solution so elegant is the actual implementation in the software running on the digital controller. The digital controller, of course, is performing the computation represented by (1). It is also continually monitoring the fault detection circuitry through a bitmap delivered to the controller. (Commercial current amplifiers used in magnetic bearing systems generally provide coil current sensing, making this kind of failure quite easy to detect.) Because of the required method of computing the current linearization matrices, **W**, all the matrices corresponding to all tolerable combinations of coil failures are computed off-line and stored in the memory of the controller, (i.e., these matrices cannot be computed as they are needed). Upon detection of a failed coil circuit, the control software simply changes a pointer to the appropriate new current linearization matrix, **W**.

Implementation of coil fault tolerance consists of only a few lines of code. There is essentially no computational overhead involved in the implementation. The only overhead lies in storing all the different 24 element (8 × 3) linearization matrices in the memory of the digital controller. Apparently, the number of different matrices is excessive. For an 8 pole stator there are 8 different linearization matrices for a single coil failure, 56 matrices for two failed coils and 168 matrices for the case of three failed coils: a total of 232 distinct matrices. Assuming standard C format storage using 4-byte data and 4-byte pointers, each matrix requires 132 bytes of memory. Thus, the total storage requirement is about 30 kB: reasonably modest. If it is only necessary to protect against single coil and double coil failures, then the storage requirement drops to slightly over 8 kB.

Tests

Testing of the fault tolerant capabilities of the controller hardware has been accomplished so far through the rather crude mechanism of simply physically extracting one or several of the CPU modules from the controller motherboard while the test rig is running at full speed: 5200 RPM. As might be expected from the structure of the controller, there is no detectable effect when one, two, or even three of the CPU's are extracted. Ideally, the testing would involve inducing either a software fault or a localized hardware fault on one or more individual CPU modules. However, there is no obvious mechanism for inducing software faults: once

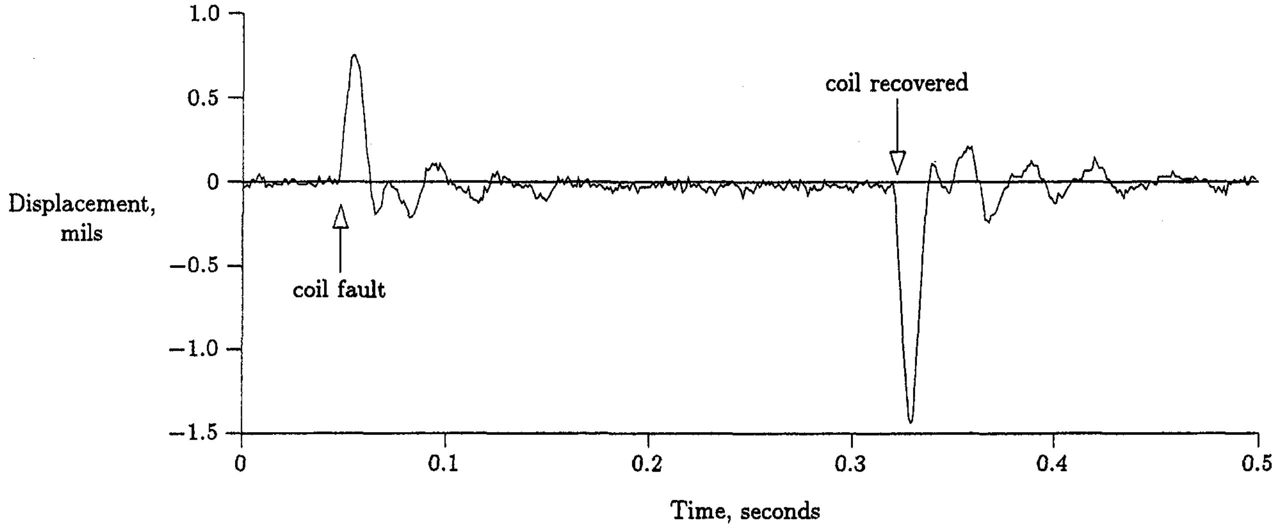

Fig. 3 Transient rotor response during a coil circuit failure

the CPUs are running, it is not possible to address an individual CPU; all messages are routed equally to all of the functioning CPUs. Further, the cost associated with the likely damage produced by inducing localized hardware faults on individual CPU modules (ie., short circuit one of the components) is prohibitive.

Testing of the actuator/amplifier/coil fault tolerance has been accomplished by hardware disabling individual power amplifiers or pairs of power amplifiers. In the present hardware, the fault correction scheme has been implemented on just one of the three radial bearings on the test rig with all the single coil failure matrices included but only a few two-coil and three-coil failure matrices included (enough for proof of concept). The rotor has operated at 5200 rpm with one coil circuit disabled and with two adjacent coil circuits disabled with no perceived performance degradation and very little transient response when the circuit(s) are disabled. Figure 3 shows a transient response of the rotor during an amplifier failure event. The amplifier was disabled at approximately .05 seconds and then re-enabled at approximately .32 seconds. To prevent noise from causing an unintended false failure detection, there is a 4 ms delay between the time that the failure is detected and when the new linearization matrix is implemented. Reducing this delay would reduce the transient reflected in Fig. 3.

Under the one failed coil case, there is no loss in load capacity but a significant increase in stator heating, as discussed above. With 2 adjacent coils (one quadrant) failed, the bearing does exhibit a loss in load capacity. This is due to uneven distributions of flux in the stator which cause premature saturation of the stator poles and back-iron.

Conclusions

For many years, for many potential users, the advantages of magnetic bearings have not outweighed the perceived risks. The risk of loosing the use of a particular machine due to bearing failure was (and still is) unacceptable, especially when a competing bearing system, such as a fluid film bearing, has extremely good reliability and performance records. Magnetic bearings will be excluded from a great many applications until their reliability can compete with that of competing technologies. The present work establishes efficient mechanisms for constructing fault tolerant magnetic bearings; a significant step toward this required level of reliability.

Probably the most useful extension of the present work is to find better alternative coil current distributions under the failed coil scenario which reduce the increment in coil thermal load. This problem is specifically addressed in the work of Meeker [8], but not developed to a physical realization.

Acknowledgments

This research was supported in part by the Center for Innovative Technology of the Commonwealth of Virginia, the NASA Lewis Research Center and by the Mobil Research and Development Corporation.

References

1 Cleaveland, P., 1995, "Triple Modular Redundant Controllers Meet Safety and Critical Control Needs," *I&CS*, Vol. 68, p. 118.

2 Fedigan, S. J., Williams, R. D., Shen, F., Ross, R. A., 1996, "Design and Implementation of a Fault Tolerant Magnetic Bearings Controller," Proceedings, Fifth International Symposium on Magnetic Bearings, pp. 307–312.

3 Fittro, R. L., Knospe, C. R., and Stephens, L. S., 1996, "Experimental Results of μ-Synthesis Applied to Point Compliance Minimization," Proceedings, Fifth International Symposium on Magnetic Bearings, pp. 203–208.

4 Hopkins, A. L., Smith, T. B., and Lala, J. H., 1978, "FTMP—A Highly Reliable Fault-Tolerant Multiprocessor for Aircraft," *Proceedings of the IEEE*, Vol. 66, No. 10, pp. 1221–1239.

5 Humphris, R. R., Kelm, R. D., Lewis, D. W., and Allaire, P. E., 1986, "Effect of Control Algorithms on Magnetic Journal Bearing Properties," ASME JOURNAL OF ENGINEERING FOR GAS TURBINES AND POWER, Vol. 108, No. 4, pp. 624–632.

6 Kieckhafer, R. M., Walter, C. J., Finn, A. M., and Thambidural, P. M., 1988, "The MAFT Architecture for Distributed Fault Tolerance," *IEEE Transactions on Computers*, Vol. 37, No. 4, pp. 398–405.

7 Lyons, J. P., Preston, M. A., Gurumoorthy, R., and Szczesny, P. M., 1994, "Design and Control of a Fault-Tolerant Active Magnetic Bearing System for Aircraft Engines," Proceedings, Fourth International Symposium on Magnetic,

8 Meeker, D. C., 1996, "Optimal Solutions to the Inverse Problem in Quadratic Magnetic Actuators," Ph.D. dissertation, University of Virginia, Ann Arbor, MI.

9 Meeker, D. C., and Maslen, E. H., 1995, "Fault Tolerance of Magnetic Bearings by Generalized Bias Current Linearization," *IEEE Transactions on Magnetics*, Vol. 31, pp. 2304–2314.

10 Mizuno, T., Namiki, H., and Araki, K., 1996, "Self-Sensing Operations of Frequency-Feedback Magnetic Bearings," Proceedings, Fifth International Symposium on Magnetic Bearings, pp. 119–123.

11 Noh, M. D., and Maslen, E. H., 1997, "Self Sensing Active Magnetic Bearings Based on Parameter Estimation," *IEEE Transactions on Instrumentation and Measurement*, Vol. 46, No. 1, pp. 45–50.

E. A. Memmott
Tubo Products Division,
Dresser-Rand Company,
P.O. Box 560,
Olean, NY 14760

Stability Analysis and Testing of a Train of Centrifugal Compressors for High Pressure Gas Injection

This paper describes the rotor dynamic stability analysis and the PTC-10 Class 1 test of a three body centrifugal compressor train for high pressure natural gas injection service. This train had a full load full pressure string test on hydrocarbon gasses to a final discharge pressure of 500 BAR (7250 PSIA). Each compressor is of the back to back configuration, and is equipped with tilting pad seals, damper bearings, and a honeycomb labyrinth at the division wall with shunt holes. The driver is a gas turbine.

1 Introduction

In 1995 a string of high pressure barrel compressors was given a full load full pressure hydrocarbon test at the manufacturer's facility. The final discharge pressure of the compressor train was very high, 500 BAR (7250 PSIA). Because of successes with a honeycomb seal with shunt holes at the division wall (e.g., Memmott, 1994), these were applied at the design stage to each of the three compressors.

The rotor dynamic analysis of the compressors with the honeycomb seals predicted that the compressors would be very well damped. This was confirmed by the testing, which showed no evidence of subsynchronous vibration, in fact the first natural frequency was so well damped that it could not be found during the full load test, for every compressor in the train.

The component rotor dynamic designs applied to these compressors consisted of four specific items, tilting pad seals, damper bearings, shunt holes at the division wall, and a honeycomb seal at the division wall. A significant amount of operating experience has been accumulated in high pressure applications, such as natural gas reinjection, with compressors using the first three items (Coletti and Crane, 1981; Shemeld, 1986; Memmott, 1987, 1990, 1992, 1994, 1996; Marshall et al., 1993). Honeycomb seals have been used for years and were applied recently for improved rotor dynamic characteristics (Kuzdzal et al., 1994; Sandberg et al., 1994; Memmott, 1994; Gelin et al., 1996).

The full load full pressure hydrocarbon test results will be shown, as well as the lateral rotor dynamic stability analysis of the high pressure compressor. A full analysis is made of all the labys, toothed and honeycomb, and their coefficients are included in the stability analysis. The large amount of damping in the honeycomb laby will be seen in the analysis and from the test results.

2 Description of Equipment

Each turbomachinery train consists of a gas turbine driving three centrifugal compressors through a speed increasing gear as shown in Fig. 1. The train is designed for natural gas injection service. The PTC-10 Class 1 full load full pressure performance testing on hydrocarbon gas was completed in 1995 and the compressors were shipped in late 1995 and early 1996. They were started up in 1997.

Each compressor is of the back-to-back configuration. The low pressure compressor, discharging at 179 BAR (2596 PSIA), has eight stages of compression. The medium pressure compressor, discharging at 308 BAR (4460 PSIA), has six stages of compression. The high pressure compressor, discharging at 500 BAR (7253 PSIA), has six stages of compression. There are four identical trains designed for natural gas injection service. A sketch of the train is shown in Fig. 1. The MW is 19.0, the maximum continuous speed is 11502 rpm, and the power at the normal speed is 17500 KW (23500 BHP) for the train.

This paper will focus on the high pressure compressor, a 191B3/3, with the cross section depicted in Fig. 2. The seal span is 1006 mm (39.62 in), the impeller bore is 114.3 mm (4.5 in), and the bearing diameter is 95.25 mm (3.75 in). The compressor power is 4280 KW (5750 BHP).

3 Component Description

The tilting pad seals, damper bearings, shunt holes at the division wall, and honeycomb seal at the division wall are described below.

3.1 Tilting Pad Seals. The tilting pad seal is shown in Fig. 3. The tilting pads are mounted concentrically with the outer oil ring and minimize any cross coupling coefficients created by the ring. The tilting pads also provide substantial load carrying capability. The tilting pad seals create a four bearing system, with beneficial spring and damping coefficients at the seal location.

The tilting pad seals effectively shorten the bearing span of the compressor. The first critical of the compressor is raised by a large amount, and thus the flexibility ratio, or ratio of the maximum continuous speed over the first critical speed, is lowered. This effect of the tilt pad seals has been discussed many times (Memmott, 1990, 1992, 1994, 1996; Marshall et al., 1993). A low flexibility ratio is seen as beneficial (Kirk and Donald, 1983; Fulton, 1984a, b; Memmott, 1990, 1992, 1994, 1996; Marshall et al., 1993; Bromham et al., 1996; Gelin et al., 1996).

Over 610 compressors with tilting pad seals have been installed around the world, in many different services. The design has been used at sealing pressures up to 21475 kpa (3100 PSIG), and for speeds up to 22800 rpm. The first installation was in 1972, and the consistent reliability of units using the design has led to it becoming the standard in many types of compressors. Damper bearings are installed in 37 percent of these compressors.

3.2 Damper Bearings. The specific damper bearing design uses the lubricating oil supply as the damping medium, and o-rings to both seal and center the damper. The damper, in series with the

---

Contributed by the International Gas Turbine Institute (IGTI) of THE AMERICAN SOCIETY OF MECHANICAL ENGINEERS for publication in the ASME JOURNAL OF ENGINEERING FOR GAS TURBINES AND POWER. Paper presented at the International Gas Turbine and Aeroengine Congress and Exhibition, Stockholm, Sweden, June 2–5, 1998; ASME Paper 98-GT-378.

Manuscript received by IGTI March 27, 1998; final revision received by the ASME Headquarters March 23, 1999. Associate Technical Editor: R. Kielb.

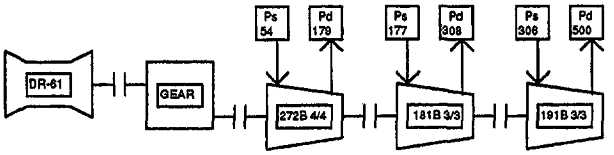

Fig. 1 Train sketch

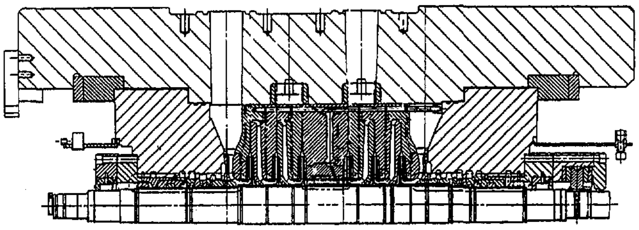

Fig. 2 Compressor cross section

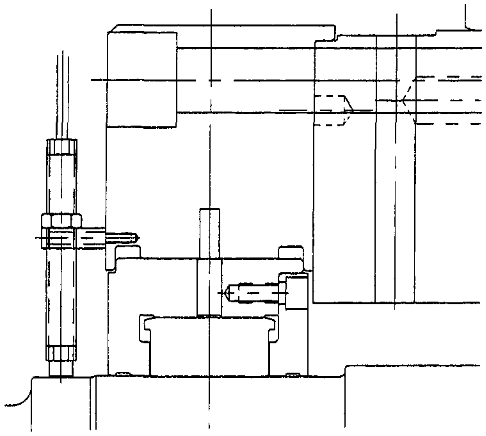

Fig. 4 Damper bearing

hydrodynamic bearing oil film, provides much improved stiffness and damping characteristics. A cross section of the damper bearing is shown in Fig. 4.

Dampers of this type have been used in over 460 compressors since their first field installation in 1973 to a 207 BAR (3000 PSIA) discharge syn gas compressor (Memmott, 1992). Their typical application has been in high pressure compressors to improve the resistance to subsynchronous vibration problems. The rotor-support system is tuned by softening the support to provide more optimum rotor dynamic characteristics.

The compressors discussed in this paper have tilting pad seals and damper bearings. Over 230 compressors with gas or laby seals have damper bearings. Applications of damper bearings to these compressors are discussed in (Memmott, 1987, 1990, 1992).

3.3 Shunt Holes. The application of shunt holes from the final stage diffuser to the division wall of this back-to-back compressor is shown in Fig. 5. The pressure of the gas in the diffuser is higher than that at the exit of the impeller, due to the static pressure rise in the diffuser. The gas supplied by the shunt holes to the labyrinth comes in radially to the laby. The shunt holes eliminate prerotation of the flow into the division wall labyrinth and provide radially outward flow along the back side of the last impeller. Minimizing prerotation into labyrinths decreases the cross coupled stiffness coefficients generated by the labyrinths (Childs, 1993). This in turn increases the stability of the rotor system.

The gas behind the last stage impeller should flow out radially and not inward. If it flows inward, as it would without shunt holes from the diffuser, an unstable flow field can be created in the region between the rotating disc and the stationary wall (Maroti et al., 1959). There is evidence that a shunt hole system from the discharge volute of a straight-though compressor is not the best application (Kuzdzal et al., 1994; Sandberg et al., 1994; Gelin et al., 1996).

Without the shunt hole from the last stage diffuser, a flow down the back of the impeller would fight the natural pumping action of the back side of the impeller. A tight gap between the back side of the impeller and the stationary wall increases the number of unsteady flow regions (Maroti et al., 1959). There is test experience which shows that the lack of shunt holes at the division wall honeycomb laby of a back-to-back compressor contributed to instability (Memmott, 1994). This could be due either to the action going on in the back of the impeller or due to the high pre-swirl coming into the honeycomb.

Shunt holes were first applied in 1974 to a 145 BAR (2100 PSIA) CO_2 compressor (Memmott, 1987), and over 410 compressors have been built with shunt holes to date. Most of these applications have been to back to back compressors at the division wall, where they have become a standard (Coletti and Crane, 1981; Shemeld, 1986; Memmott, 1990, 1992, 1994). Shunt holes have been applied to straight-through compressors at the balance piston. (Memmott, 1990, 1992, 1996; Marshall et al., 1993; Gelin et al., 1996). Their primary usage has been in high pressure compressors, since the cross coupled stiffness coefficients caused by labyrinths increase with increasing pressure differential.

3.4 Honeycomb Division Wall Laby. The honeycomb seal at the division wall with the shunt holes is shown in Fig. 5. Honeycomb seals supply large amounts of damping compared to the negligible amount available from toothed laby seals (Memmott, 1994; Kuzdzal et al., 1994; Sandberg et al., 1994; Gelin et al., 1996). This has been taken advantage of in assuring stable operation in several recent compressor applications. It is important to note that they do not decrease the cross-coupled stiffness over that of a comparable toothed laby, it is the large increase in direct damping that is crucial. Honeycomb seals also have a much larger direct stiffness than a toothed laby.

The damping available from the honeycomb seals is not so high

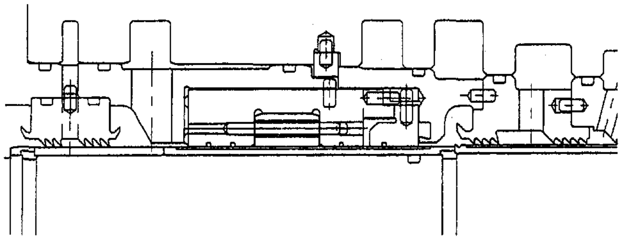

Fig. 3 Tilt pad seal

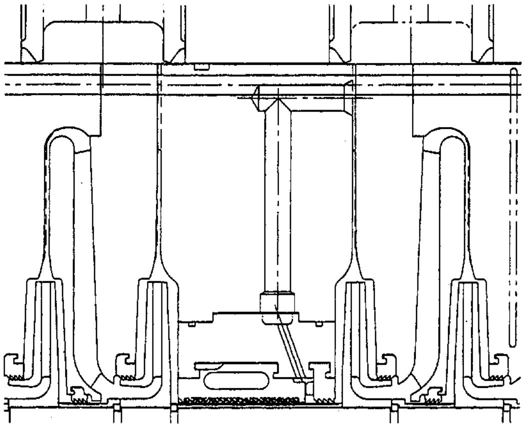

Fig. 5 Shunt holes and honeycomb seal at the division wall

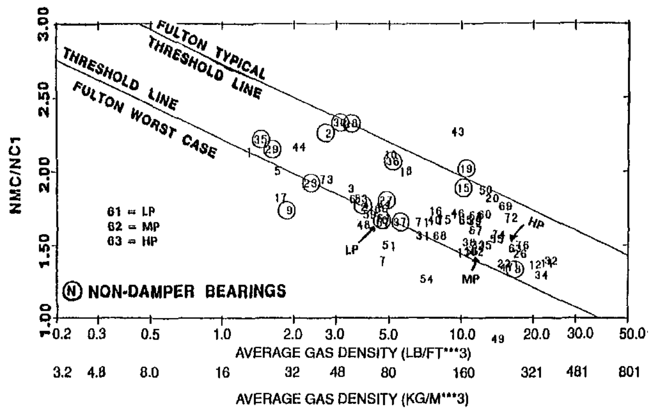

Fig. 6 Flexibility ratio with tilt pad seals versus average gas density

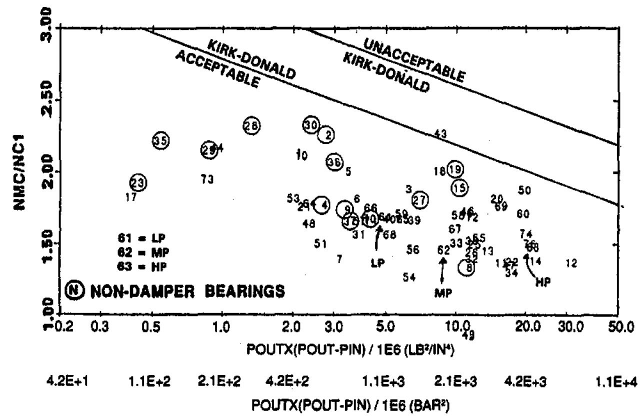

Fig. 7 Flexibility ratio with tilt pad seals versus discharge pressure *x* (discharge–inlet pressure)

that it can always control subsynchronous vibration without a shunt hole system from the diffuser. This was shown by the full load full pressure testing of the 400 BAR (5800 PSIA) compressor in 1994 (Memmott, 1994). This is also implied by (Gelin et al., 1996).

Honeycomb seals were initially used in centrifugal compressors for strength reasons, where differential pressures were in excess of what could be handled by conventional knife edge seals. They have been used since the late 1960s for that purpose, mainly in high pressure syn gas compressors. More recently they have been applied for the benefits of damping available from the honeycombs. This followed research in the 1980s (Childs, 1993, pp. 331–341) and the development of design codes for stiffness and damping calculations for honeycomb seals (Scharrer and Pelletti, 1994–5).

Over 110 compressors with honeycomb seals have recently been shipped, not counting the numerous previous applications to syn gas service. The honeycomb seal has been especially helpful in application to high pressure gas injection compressors. See Memmott (1994) for discussion of an application to a 400 BAR (5800 PSIA) natural gas injection compressor. See Gelin et al. (1996) for discussion of applications to a 205 BAR (2970 PSIA) reinjection compressor and a 141 BAR gas lift compressor.

4 Stability Experience Guidelines

Various experience guidelines have been used to evaluate the stability of high pressure compressors. These are used as a preliminary guide in deciding on the feasibility of building a compressor, to see that the compressor is within the range of experience with the components that are being used. The guidelines are not used for the detailed design of the components and analysis of the system, as sophisticated rotor dynamic codes have become available. Application of two of these guidelines to the compressors for this installation are shown below.

4.1 Flexibility Ratio Versus Average Gas Density. A widely used experience guideline is the plot of flexibility ratio, maximum continuous speed divided by the first critical speed, versus average gas density, commonly called the Fulton plot, as shown in (Fulton, 1984a, b; Memmott, 1992, 1994, 1996). A similar plot is where discharge, instead of average, gas density is used (Bromham et al., 1996). Tilting pad seals raise the first critical speed significantly and thus lower the flexibility ratio (Memmott, 1990, 1992).

The Fulton type plot is shown in Fig. 6, for a representative sample of compressors with tilting pad seals. The compressors discussed in this paper are marked. They are comfortably within the range of experience and well below Fulton's typical threshold line. Without the tilting pad seals, the flexibility ratio would put them above Fultons acceptable line, where he predicts instability is likely to occur.

If the gas is less dense and the first critical is higher then it is harder to excite the first critical speed.

4.2 Flexibility Ratio Versus Discharge Pressure *x* (Discharge Pressure—Inlet Pressure). Another experience guideline is the plot of flexibility ratio versus discharge pressure *x* (discharge pressure—inlet pressure) as shown in (Kirk and Donald, 1983; Fulton, 1984b). This is commonly called the Kirk–Donald plot.

The Kirk–Donald type plot is shown in Fig. 7, for a representative sample of compressors with tilting pad seals. The compressors discussed in this paper are marked. They are comfortably within the range of experience. Without the tilting pad seals, the flexibility ratio would put the low pressure compressor just above and the other compressors just below Kirk–Donalds acceptable line.

If the discharge pressure is lower, the differential pressure through the compressor is lower, and the first critical is higher then it is harder to excite the first critical speed.

5 Stability Analysis

Rotor dynamic stability analyses were made of the low, medium, and high pressure compressors. The analytical results are presented for the high pressure compressor.

The damped natural frequency program used to calculate the log dec after the input of the rotor model and bearing, oil-film seals, and toothed laby and honeycomb seal stiffness and damping coefficients was developed from the original paper by Lund (1974).

The stability program is used to produce a plot of the log dec of the first critical frequency versus aerodynamic excitation at the mid span. The use of this plot as a tool in stability analysis of compressors is shown in many papers (Memmott, 1987, 1990, 1992, 1994, 1996; Marshall et al., 1993; Kuzdzal et al., 1994; Sandberg et al., 1994; Gelin et al., 1996).

5.1 Oil Film Seal Analysis. The cross coupled stiffness coefficients of the outer seal ring with the tilt pads in the seal is shown in Table 1. The cross coupled stiffness coefficients are considerably smaller than they would be without the tilt pads (Memmott, 1990, 1992, 1994, 1996), and thus the compressor will be more stable.

Table 1 Outer oil ring cross coupled stiffness coefficient

CLEARANCE	KXY	KYX
	(N/M)	(N/M)
MINIMUM	2.26 E+6	-2.56 E+6
MAXIMUM	2.00 E+6	-3.10 E+6

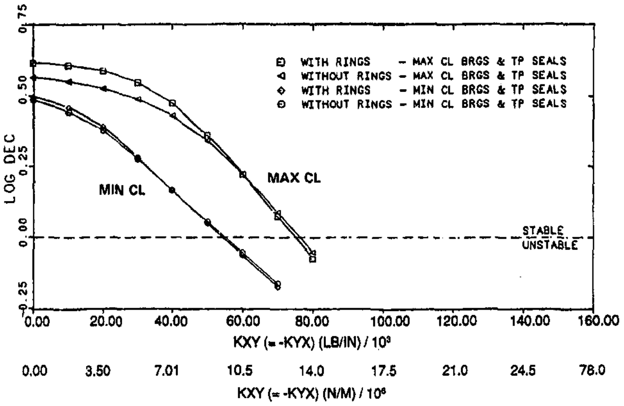

Fig. 8 Log dec versus aerodynamic excitation with and without outer ring seal—no labys

The majority of the load on a tilt pad seal ring is carried by the pads (Memmott, 1990, 1992, 1996). In this case the pads carry 90 to 95 percent of the load. The load carrying capacity of the tilt pads is such that the tilt pad seal assembly acts like a tilt pad bearing, and not like a sleeve bearing.

The log decrement of the first critical as it responds to aerodynamic excitation (cross-coupled stiffness) at the mid span is plotted in Fig. 8. A study is made of the sensitivity of the compressor to arbitrary added amounts of cross-coupling at the mid span. The speed of the rotor is the maximum continuous speed. In Fig. 8 the effects of the toothed labys and honeycomb seal are not included.

Figure 8 shows that the effect of the outer ring is negligible, due to the tilt pads, and it customarily may be ignored in the analysis. This is true for both minimum and maximum clearance bearings and seals. For the rest of the analyses the outer ring is included.

5.2 Toothed Laby and Honeycomb Seal Analysis. Toothed laby seals can provide significant stiffness and damping coefficients. They are more significant as pressures, differential pressures, and length of labys rises. The code (Kirk, 1990a) used to analyze the toothed laby seals is described in a series of papers (Kirk, 1985, 1990b).

The code used to calculate the coefficients of honeycomb seals was developed by Scharrer and Pelletti (1994–5). According to them, it matches the test data as taken at Texas A&M (Elrod et al., 1990).

Negative direct stiffness terms from the toothed labys are ignored. Compressor natural frequencies calculated using negative direct stiffness coefficients have not matched test data (Memmott, 1994; Gelin et al., 1996). A full pressure test done on a 400 BAR (5800 PSIA) discharge compressor yielded data which would say the direct stiffness coefficients are positive for toothed labys (Memmott, 1994).

The direct stiffness coefficients have been measured to be positive in a test rig of a division wall toothed laby for pressures in the range 8 to 19 bar, with the higher the pressure and the higher the pressure differential the more positive is the direct stiffness. (Private test for a contract.) More testing needs to be done to refine toothed laby codes. The direct damping terms from the toothed labys are small, but raise the log dec of the system much in relation to their size, as is noted in (Childs, 1994). It would be conservative to not use them for toothed labys.

The calculated stiffness and damping coefficients for the toothed labys and honeycomb division wall seal are shown in Table 2. It would be advantageous to deswirl the impeller eyes, but this was not done. Due to the large amount of direct damping available from the honeycomb laby it was used at the division wall and not a toothed laby. There is test data (Childs, 1994, p. 339) that shows that honeycomb labys have much higher direct damping than toothed labys.

The division wall seal was analyzed as deswirled because of the shunt holes. If the honeycomb seal at the division wall had not been deswirled the cross-coupled stiffness would be about double that shown, with not much change in the other coefficients.

Table 2 Labyrinth coefficients

	KXX (N/M)	KXY (N/M)	BXX (N-S/M)
IMP EYE *	7.29 E+4	2.57 E+6	2.45 E+3
EYE DESWIR *	-1.65 E+5	2.85 E+4	2.42 E+3
INTST SEAL *	-1.21 E+6	3.26 E+5	6.36 E+2
DW - TOOTH	-1.20 E+6	-9.26 E+5	5.31 E+2
DW - HONEY	1.60 E+7	2.03 E+7	9.02 E+4
2ND SEC IN	-5.13 E+6	-3.85 E+5	4.99 E+2

* AVERAGE

The four stability analyses made with the toothed labys and the honeycomb division wall seal and the one without the labys or honeycomb seal are shown in Table 3. The stability threshold is the amount of additional arbitrary cross-coupling needed at the mid-span to produce a zero log dec. The stability analysis with the inclusion of the toothed labys and toothed division wall laby, but without their small amount of calculated damping, shows instability without any added safety factors. This corresponds with the experience shown for a similar compressor (Memmott, 1994). If the damping from the toothed labys is included and the impeller eyes are not deswirled, stability is predicted with the toothed division wall laby, which does not correspond with recent experience. Deswirling the impeller eyes is a definite advantage, but the honeycomb division wall has so much damping that this is not necessary, which fits recent experience.

In Fig. 9, a plot of log dec versus arbitrary aero excitation at the midspan is made, comparing the system with a honeycomb division wall laby and no impeller eye deswirl to the system with a toothed division wall laby and impeller eye deswirl.

Since the shunt holes are included, the division wall is deswirled. No damping is assumed at the toothed labys. The log decs plotted versus the horizontal axis are due to extra additional cross-coupled stiffness at the midspan besides that of the labys or honeycomb seal. The large log dec and resistance to aerodynamic excitation by use of the honeycomb seal is evident.

6 Testing of the Compressor

Each compressor had an API-617 mechanical test with a ASME PTC 10 Class III performance test. There was a string test with full

Table 3 Log dec and stability threshold

For Minimum to Maximum Clearance Bearings and Oil Seals	LOG DEC.	STABILITY THRESHOLD (N/M)
Without Labys & W/O Honeycomb Seal	.50/.62	9.51 E+6/ 1.31 E+7
Tooth DW, No Laby Damp, No Eye Deswirl	-.16/-.03	
Tooth DW, Laby Damp, No Eye Deswirl	.51/.78	9.32 E+6/ 1.13 E+7
Tooth DW, No Laby Damp, Eye Deswirl	.50/.71	9.49 E+6/ 1.21 E+7
Honey DW, No Laby Damp, No Eye Deswirl	3.0/3.8	6.41 E+7/ 6.23 E+7

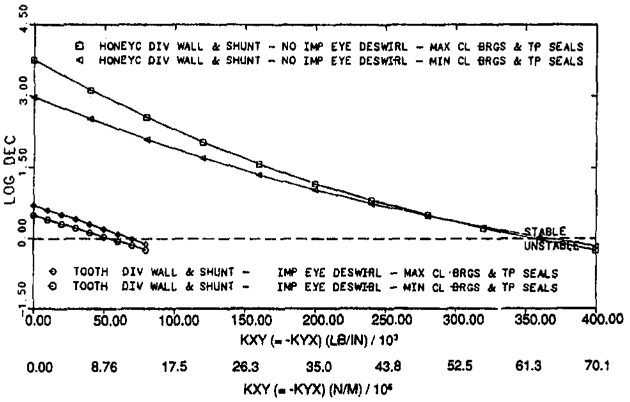

Fig. 9 Log dec versus aerodynamic excitation with laby honeycomb division wall laby and no impeller eye deswirl versus toothed division wall laby and impeller eye deswirl

load full pressure on hydrocarbon gas. This included the contract gas turbine. The full load, full pressure hydrocarbon test was completed in less than a week.

6.1 Mechanical and Performance Test. There were minor problems with the mechanical and performance tests. Post test inspection of the XX1Bs early on before the full load test showed evidence of rubbing of the honeycomb division wall laby at the tight end of the tapered bore. The clearance was increased slightly at the tight end (taper angle was changed) and no more rubs occurred. The XX1Bs performance tested slightly low in capacity. This was fixed by opening diffusers and return channel areas.

6.2 Full Load Full Pressure Hydrocarbon Test. No evidence of subsynchronous vibration is seen at the first critical frequency or any other kind of subsynchronous. The decell plots will show that the first critical is so well damped it did not show up as a peak in response. This was true for all three compressors. Figures 10–14 are from the four hour full load full pressure test. There are spectrum plots from near the end of the test for each compressor and a steady state plot for the four hours and a final decell plot for the high pressure compressor. The low and medium pressure compressors looked the same. The decell took 22 minutes, so the damped first critical is from the honeycomb seal.

7 Other High Pressure Compressors

There has been experience with the application of honeycomb division wall seals to other high pressure back to back compressors. These compressors also had shunt holes at the division wall, tilt pad seals, and damper bearings. They were of the same frame size and impeller bore, and all had longer seal spans, which is the important comparison with the tilt pad seals (Memmott, 1990, 1992). Besides the compressor described in Memmott (1994), are the following:

- In 1991 a ten stage back to back compressor with 285 BAR (4135 PSIA) discharge was shipped without full load full pressure testing. In the field there was subsynchronous at the first critical and the division wall was changed to honeycomb (still with shunt holes) in 1994 and the subsynchronous vibration disappeared.
- In 1995 six trains of back to back compressors were shipped without full load full pressure testing. Honeycomb seals with shunt holes at the division wall were part of the initial design. They have since started with discharge pressures from 243 to 312 BAR (3523 to 4524 PSIA), and all are free of subsynchronous vibration and performing well both aerodynamically and mechanically.
- In 1997 a train of back to back compressors was shipped after a full load full pressure test on hydrocarbon gas of the

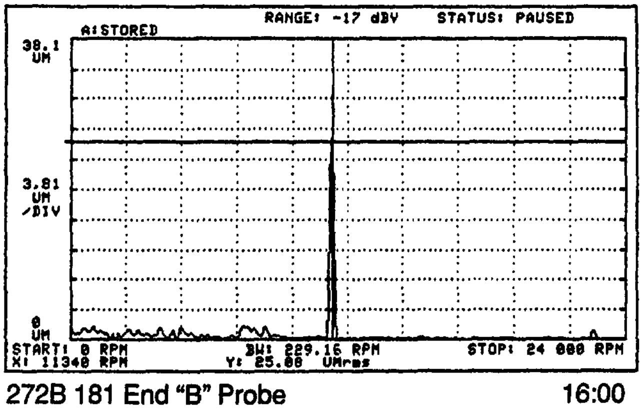

Fig. 10 Spectrum plot—272B4/4 compressor

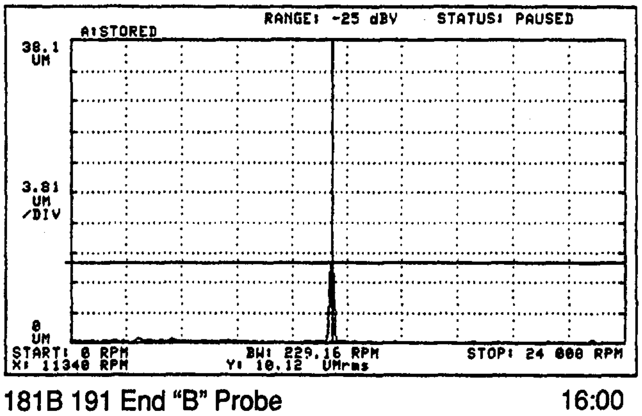

Fig. 11 Spectrum plot—181B3/3 compressor

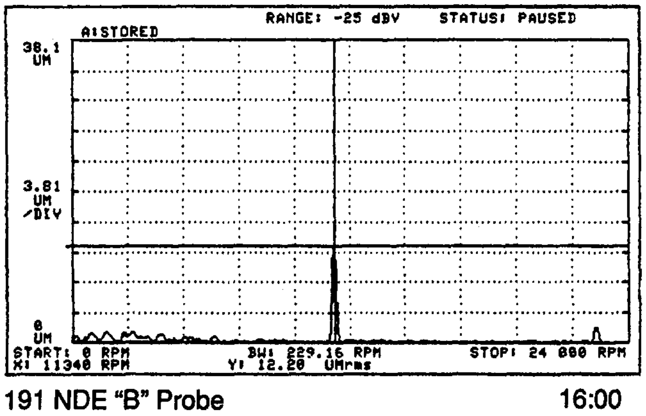

Fig. 12 Spectrum plot—191B3/3 compressor

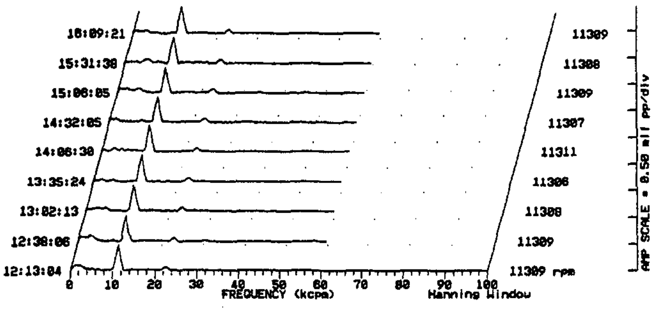

Fig. 13 Steady-state plot—191B3/3 compressor

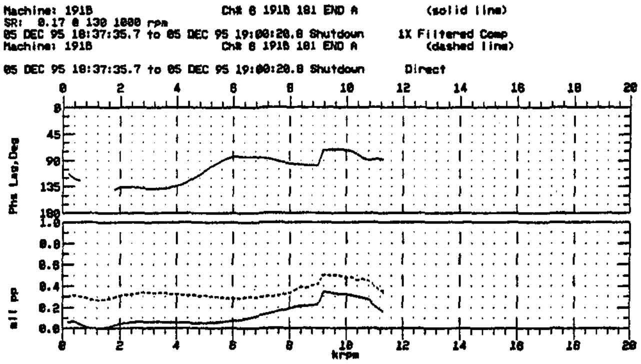

Fig. 14 Final decell—191B3/3 compressor

- high pressure compressor, with a discharge pressure of 381 BAR (5520 PSIA). There was no subsynchronous vibration.
- In 1997 a back to back compressor was shipped after a full load full pressure Class 1 Hydrocarbon test, with a discharge pressure of 405 BAR (5875 PSIA). Again, there was no subsynchronous vibration.

8 Conclusion

Full load full pressure hydrocarbon testing of the high pressure compressors discussed in this paper, along with the same testing and field experience for other high pressure compressors, confirms the rotor dynamic stability analyses that shows that a honeycomb seal at the division wall supplies sufficient damping to ensure stable operation. Thus another weapon has been added to the time proven tools of tilt pad seals, damper bearings, and shunt holes to insure satisfactory operation of high pressure compressors.

Acknowledgments

The author would like to thank K. Ramesh for modeling the laby seals and automating the calculations of the toothed and honeycomb seals, H. Dourlens for advice on laby seal modeling, D. N. Trask for modeling the rotor and making the original analysis, D. F. Marshall for editing the paper, and J. R. Shufelt for inserting the figures for publication.

10 References

Bromham, R. J., Lorenzen, and Aicher, W., 1996, "The Integration of Process and Compressor Design for a Difficult North Sea Gas Re-injection Duty," *IMechE*, C508/030/96.

Childs, D., 1993, *Turbomachinery Rotordynamics—Phenomena, Modeling, & Analysis*, John Wiley and Sons, Inc., New York, pp. 227–354.

Coletti, N. J., and Crane, M. E., Jr., 1981, "Centrifugal Compression on the Arun High Pressure Injection Project," Proceedings of the IMechE Conference on Fluid Machinery for the Oil, Petrochemical and Related Industries, The Hague, Netherlands, pp. 63–70.

Elrod, D., Nelson, C., and Childs, D., 1990, "An Entrance Region Friction Factor Model Applied to Annular Seal Analysis: Theory Versus Experiment for Smooth and Honeycomb Seals," *ASME Journal of Tribology*, Vol. 111, pp. 337–343.

Fulton, J. W., 1984a, "The Decision to Full Load Test a High Pressure Centrifugal Compressor in its Module Prior to Tow-Out," 2nd European Congress on Fluid Machinery for the Oil, Petrochemical and Related Industries, The Hague, The Netherlands, IMechE, pp. 133–138.

Fulton, J. W., 1984b, "Full Load Testing in the Platform Module Prior to Tow Out: A Case History of Subsynchronous Instability," Proceedings, Rotordynamic Instability Problems in High Performance Turbomachinery, NASA Conference Publication 2338, Texas A&M University, pp. 1–16.

Gelin, A., Pugnet, J.-M., Bolusset, D., and Friez, P., 1996, "Experience in Full Load Testing Natural Gas Centrifugal Compressors for Rotordynamics Improvements," IGT & A C&E, Birmingham, UK, ASME Paper 96-GT-378.

Kirk, R. G., and Donald, G. H., 1983, "Design Criteria for Improved Stability of Centrifugal Compressors," AMD Vol. 55, ASME, New York, pp. 59–71.

Kirk, R. G., 1985, "Evaluation of Aerodynamic Instability Mechanisms for Centrifugal Compressors," ASME Paper 85-DET-147, Design Engineering Vibration Conference, Cincinnati, Ohio, Sept. 10–13.

Kirk, R. G., 1990a, "Users Manual for the Program DYNPC28—A Program for the Analysis of Labyrinth Seals," Negavib Research & Consulting Group, Virginia Tech, Blacksburg, VA.

Kirk, R. G., 1990b, "A Method for Calculating Labyrinth Seal Inlet Swirl Inlet Velocity," *ASME Journal of Vibration and Acoustics*, Vol. 112; July, pp. 380–383.

Kuzdzal, M. J., Hustak, J. F., and Sorokes, J. M., 1994, "Identification and Resolution of Aerodynamically Induced Subsynchronous Vibration During Hydrocarbon Testing of a 34,000 HP Centrifugal Compressor," Proceedings, 4th International Conference on Rotordynamics, Chicago, Sept. 7–9, IFToMM, Vibration Institute, Willowbrook, IL.

Lund, J. W., 1974, "Stability and Damped Critical Speeds of a Flexible Rotor in Fluid-Film Bearings," *ASME Journal of Engineering for Industry*, pp. 509–517.

Maroti, L. A., Deak, G., and Kreith, F., 1959, "Flow Phenomena of Partially Enclosed Rotating Disks," ASME Paper 59-A-49.

Marshall, D. F., Hustak, J. F., and Memmott, E. A., 1993, "Elimination of Subsynchronous Vibration Problems in a Centrifugal Compressor by the Application of Damper Bearings, Tilting Pad Seals, and Shunt Holes," NJIT-ASME-HI-STLE, Rotating Machinery Conference and Exposition, Somerset, New Jersey, Nov. 10–12.

Memmott, E. A., 1987, "Damper Bearings and Stability of a CO_2 Compressor," presented at the Seventh Annual Rotating Machinery & Controls Industrial Research Conference, San Diego, June.

Memmott, E. A., 1990, "Tilt Pad Seal and Damper Bearing Applications to High Speed and High Density Centrifugal Compressors," Proceedings, 3rd International Conference on Rotordynamics, Lyon, IFToMM, pp. 585–590.

Memmott, E. A., 1992, "Stability of Centrifugal Compressors by Applications of Tilt Pad Seals, Damper Bearings, and Shunt Holes," Proceedings, 5th International Conference on Vibrations in Rotating Machinery, IMechE, pp. 99–106.

Memmott, E. A., 1994, "Stability of a High Pressure Centrifugal Compressor Through Application of Shunt Holes and a Honeycomb Labyrinth," Proceedings, 13th Machinery Dynamics Seminar, Toronto, CMVA, pp. 211–233.

Memmott, E. A., 1996, "Stability of an Offshore Natural Gas Centrifugal Compressor," Proceedings, 15th Machinery Dynamics Seminar, CMVA, pp. 11–20.

Sandberg, M. R., Sorokes, J. M., Kuzdzal, M. J., and Colby, G. M., 1994, "Recent Experiences in Full Load Full Pressure Shop Testing of a High Pressure Gas Injection Centrifugal Compressor," Proceedings, Twenty Third Turbomachinery Symposium, Turbomachinery Laboratory, Department of Mechanical Engineering, Texas A&M University, College Station, TX.

Scharrer, J. K., and Pelletti, J. M., 1994–1995, "DCELL™—A Computer Program for: Calculating Steady-State and Dynamic Characteristics of Honeycomb Annular Seals," Rotordynamics-Seal-Research, North Highlands, CA.

Shemeld, D. E., 1986, "A History of Development in Rotordynamics—A Manufacturer's Perspective," Rotordynamic Instability Problems in High Performance Turbomachinery, NASA Conference Publication 2443, Texas A&M University, pp. 1–18.

Reduced Order Modeling and Vibration Analysis of Mistuned Bladed Disk Assemblies With Shrouds

R. Bladh

M. P. Castanier

C. Pierre

Department of Mechanical Engineering and
Applied Mechanics,
The University of Michigan
Ann Arbor, MI 48109-2125

This paper presents important improvements and extensions to a computationally efficient reduced order modeling technique for the vibration analysis of mistuned bladed disks. In particular, this work shows how the existing modeling technique is readily extended to turbomachinery rotors with shrouded blades. The modeling technique employs a component mode synthesis approach to systematically generate a reduced order model (ROM) using component modes calculated from a finite element model (FEM) of the rotor. Based on the total number of degrees of freedom, the ROM is typically two or three orders of magnitude smaller than the FEM. This makes it feasible to predict the forced response statistics of mistuned bladed disks using Monte Carlo simulations. In this work, particular attention is devoted to the introduction of mistuning into the ROM of a shrouded assembly. Mistuning is modeled by projecting the mistuned natural frequencies of a single, cantilever blade with free shrouds onto the harmonic modes of the shrouded blade assembly. Thus, the necessary mistuning information may be measured by testing individual blades.

1 Introduction

Based on the nominal design, a bladed disk assembly is a rotationally periodic structure. If it is assumed that each sector is identical, then the theory of cyclic symmetry may be used to analyze the dynamics of the entire structure based on, say, a finite element model of one sector (Joseph, 1981; Elchuri et al., 1984; Hitchings and Singh, 1987). In practice, however, there are small differences among the structural properties of individual blades—due to manufacturing tolerances, material deviations, and non-uniform operational wear. These small, random discrepancies, commonly referred to as mistuning, are unavoidable. Furthermore, mistuning destroys the cyclic symmetry of the bladed disk assembly, and it can drastically affect the vibratory behavior of the structure. In particular, certain mode shapes may become spatially localized. As a result, a blade may experience forced response amplitudes and stresses that are substantially larger than those predicted by a tuned analysis.

The effects of mistuning on blade vibrations have been documented by experiments, as well as by analyses of representative lumped parameter models using numerical, statistical, and perturbation methods (Wagner, 1967; Dye and Henry, 1969; Ewins, 1969; Ewins, 1973; El-Bayoumy and Srinivasan, 1975; Griffin and Hoosac, 1984; Wei and Pierre, 1988a and 1988b; Lin and Mignolet, 1997). See Srinivasan (1997) for a survey of the literature. More recently, there have been efforts to use component mode synthesis (Irretier, 1983; Zheng and Wang, 1985; Castanier et al., 1997) and receptance techniques (Yang and Griffin, 1997) combined with finite element models in order to obtain more accurate models of mistuned bladed disks.

The studies by Castanier et al. (1997) and Yang and Griffin (1997) are notable because specially tailored techniques were employed to obtain, in a systematic fashion, highly reduced order models from parent finite element models of bladed disks. In particular, significant order reduction was achieved by reducing the number of degrees of freedom (DOF) needed to connect the disk and blade components. Yang and Griffin treated the disk-blade interface as having only rigid body motion, which reduced the necessary DOF to six for each blade. However, this approximation did cause some loss in accuracy in frequency regions that feature disk-blade interaction. In (Castanier et al., 1997), a novel component mode technique was developed to eliminate the so-called constraint modes.

The technique of Castanier et al. (1997) has been applied to the analysis of the forced response of mistuned bladed disks (Kruse and Pierre, 1996a), and it has been validated using a finite element model of an industrial rotor (Kruse and Pierre, 1996b). However, these investigations concentrated on unshrouded bladed disk assemblies. In this paper, the reduced order modeling technique is extended to turbomachinery rotors with shrouded blades. The tuned blade-shroud ring is modeled as a single, cyclic component structure. Thus, the limiting cases of full stick or full slip at the shroud interfaces may be treated. Mistuning is added by projecting the mistuned natural frequencies of a single blade onto the cyclic modes of the blade-shroud ring. For an example finite element model, using the case of full stick at the shroud connections, excellent correlation between finite element and ROM predictions of the free and forced response is demonstrated.

This paper is organized as follows. The reduced order modeling technique is presented in section 2, including updates to the ROM matrices, and specific formulations pertinent to shrouded assemblies are derived. A fairly detailed derivation of the proposed method to model mistuned shrouded assemblies is also included. In section 3, the technique is applied to the vibration analysis of a shrouded test case rotor. The results are validated by comparisons with finite element results. Concluding remarks are given in section 4.

2 Reduced Order Modeling Technique

2.1 General Formulation of Reduced Order Model. It may be assumed that the disk (d) and blade (b) degrees of freedom

---

Contributed by the International Gas Turbine Institute (IGTI) of THE AMERICAN SOCIETY OF MECHANICAL ENGINEERS for publication in the ASME JOURNAL OF ENGINEERING FOR GAS TURBINES AND POWER. Paper presented at the International Gas Turbine and Aeroengine Congress and Exhibition, Stockholm, Sweden, June 2–5, 1998; ASME Paper 98-GT-484.

Manuscript received by IGTI March 25, 1998; final revision received by the ASME Headquarters March 23, 1999. Associate Technical Editor: R. Kielb.

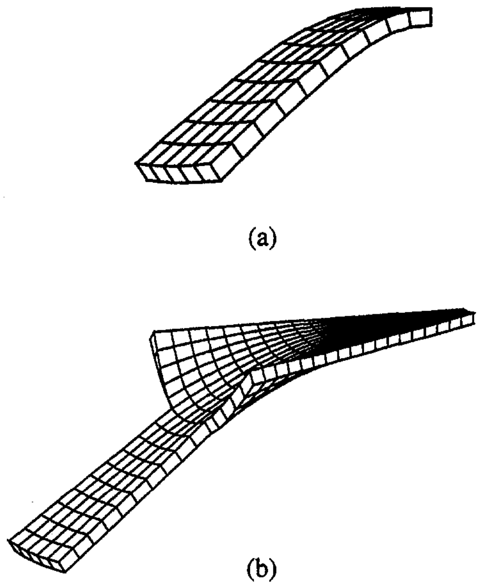
(a)

(b)

Fig. 1 Cantilever blade (*a*) and disk-induced (*b*) motions

are ordered in such a manner as to give the following partitioning of the assembled mass and stiffness matrices of the entire structure:

$$\mathbf{M} = \begin{bmatrix} \mathbf{M}_d & \mathbf{0} \\ \mathbf{0} & \mathbf{M}_b \end{bmatrix} \quad \mathbf{K} = \begin{bmatrix} \mathbf{K}_d & \mathbf{0} \\ \mathbf{0} & \mathbf{K}_b \end{bmatrix} \tag{1}$$

The location of the disk-to-blade interface can be chosen completely arbitrarily. In practice, though, this choice may affect the accuracy of the approximate solutions.

Each sector is here treated as an isolated substructure and since all sectors are assumed identical, the non-zero matrix blocks will be block-diagonal:

$$\mathbf{M}_d = \mathbf{I} \otimes \tilde{\mathbf{M}}_d \quad \mathbf{M}_b = \mathbf{I} \otimes \tilde{\mathbf{M}}_b$$

$$\mathbf{K}_d = \mathbf{I} \otimes \tilde{\mathbf{K}}_d \quad \mathbf{K}_b = \mathbf{I} \otimes \tilde{\mathbf{K}}_b, \tag{2}$$

where $\mathbf{I}$ is an identity matrix, and the symbol $\otimes$ denotes the Kronecker product, which is defined in appendix A. The "tilde" notation will be used throughout the following to indicate that a quantity refers to a single blade or disk sector. Note that this implies that all degrees of freedom associated with the boundaries between adjacent sectors will appear twice.

A key idea for this reduced order modeling technique (Castanier et al., 1997) is to describe the motion of the bladed disk assembly using two particular sets of component modes. Figure 1 depicts the two fundamental component mode types for a greatly simplified finite element model of a bladed disk sector. The first set is comprised of disk-induced modes, which are the cyclic modes of the entire assembly where the attached blades are massless. In this case, the blade motion is a rigid-body motion plus elastic deformation due to the boundary motion. The blade portion of the disk-induced modes, i.e., the part belonging to the blade degrees of freedom, will be denoted $\mathbf{U}^d$, and the disk portion $\mathbf{V}^d$. The second mode set consists of the modes of a cantilever blade alone, which is clamped at the chosen disk-blade interface location. Note that for unshrouded blades, the modal matrix $\mathbf{U}^b$ for all N identical blades is block-diagonal and is assembled as $\mathbf{I} \otimes \tilde{\mathbf{u}}^b$, where $\tilde{\mathbf{u}}^b$ is the cantilever mode shapes of a single blade. For shrouded blades, however, this set of modes is also cyclic in nature, due to the presence of direct blade-to-blade structural coupling, and thus, the cyclic assembly modes will yield a full matrix $\mathbf{U}^b$.

Through superposition of these two sets of component modes, and using the node ordering configuration in Eq. (1), the resulting nodal displacements of the entire assembly can be expanded as

$$\mathbf{x} = \begin{bmatrix} \mathbf{V}^d \\ \mathbf{U}^d \end{bmatrix} \mathbf{a} + \begin{bmatrix} \mathbf{0} \\ \mathbf{U}^b \end{bmatrix} \mathbf{b}, \tag{3}$$

where $\mathbf{a}$ and $\mathbf{b}$ are modal coordinates for the disk-induced and the cantilever blade modes, respectively. With above definitions, the strain and kinetic energies of the system, as well as the external virtual work done by a time-harmonic engine order excitation force, $\mathbf{Q}$, may be formulated in component modal-referred quantities.

Applying Hamilton's principle yields the governing equations of motion for the reduced order model. They are conveniently written in matrix form as

$$\mathcal{M}\ddot{\mathbf{z}} + \mathcal{C}\dot{\mathbf{z}} + (1 + Gj)\mathcal{K}\mathbf{z} = \mathcal{Q}, \tag{4}$$

where

$$\mathbf{z} = \begin{Bmatrix} \mathbf{a} \\ \mathbf{b} \end{Bmatrix} \quad \mathcal{C} = \begin{bmatrix} \mathbf{0} & \mathbf{0} \\ \mathbf{0} & \mathbf{C} \end{bmatrix} \quad \mathcal{Q} = \begin{Bmatrix} \mathcal{Q}_d \\ \mathcal{Q}_b \end{Bmatrix} = \begin{Bmatrix} \mathbf{U}^{d^T}\mathbf{Q} \\ \mathbf{U}^{b^T}\mathbf{Q} \end{Bmatrix}$$

$$\mathcal{M} = \begin{bmatrix} \mathbf{I}_d + \mathbf{U}^{d^T}\mathbf{M}_b\mathbf{U}^d & \mathbf{U}^{d^T}\mathbf{M}_b\mathbf{U}^b \\ \mathbf{U}^{b^T}\mathbf{M}_b\mathbf{U}^d & \mathbf{I}_b \end{bmatrix}$$

$$\mathcal{K} = \begin{bmatrix} \hat{\mathbf{K}}_d & \mathbf{U}^{d^T}\mathbf{K}_b\mathbf{U}^b \\ \mathbf{U}^{b^T}\mathbf{K}_b\mathbf{U}^d & \hat{\mathbf{K}}_b + \Delta\hat{\mathbf{K}}_b \end{bmatrix}.$$

$\hat{\mathbf{K}}_d$ and $\hat{\mathbf{K}}_b$ are diagonal matrices, and the elements on the diagonals are modal stiffnesses (eigenvalues) obtained from the disk-induced and cantilever blade finite element analyses, respectively. $\mathbf{I}_d$ and $\mathbf{I}_b$ are the corresponding modal mass matrices, which in view of the employed method of eigenvector normalization will be identity matrices. Recall that the blade is massless in the disk-induced analysis. Thus, the effect of blade mass on the disk is included as the second term in the upper-left quadrant of the mass matrix, but no such term is needed in the stiffness matrix.

Structural damping with damping coefficient G, as well as viscous modal damping of the cantilever blade modes, $\mathbf{C}$, have now been added to the reduced order model, in order to facilitate more realistic modeling of the structure's dynamic response. In addition, some general measure of mistuning, $\Delta\hat{\mathbf{K}}_b$, is added into the stiffness matrix $\mathcal{K}$. This measure of mistuning, although general at this point, implies the following three assumptions:

- —The mistuned characteristics of a blade are restricted to its stiffness (lower-right quadrant of $\mathcal{K}$). While stiffness mistuning is sufficient for the purposes of this study, it may be more accurate to model mistuning in other structural parameters as well; for instance, by using the mixed least squares—maximum likelihood method of Mignolet and Lin (1997).
- —The effects of stiffness mistuning on the other three quadrants of $\mathcal{K}$ are assumed negligible. This is to a large extent justified by considering the kind of rigid-body-like motion the blade undergoes in this set of component modes.
- —The mistuned cantilever modes of a blade may be realized by a linear combination of the tuned modes (i.e., they span approximately the same space).

Note that the resulting structural matrices are all symmetric. In general, this symmetry is destroyed if aerodynamic coupling between blades is introduced into the system. However, aerodynamic coupling will not be considered in this work.

At this point, the reduced order model formulation is completely general in that it is applicable to both unshrouded and shrouded assemblies. However, a closer examination of the various partitions of the structural matrices reveals significant differences between the two designs, leading to slightly different degrees of further simplifications. Further refinement of the formulation for unshrouded assemblies is detailed for the free response by Castanier et al. (1997), and extended for the forced response by Kruse and Pierre (1996a), and, therefore, will not be repeated here. A presentation of formulation details for the reduced order model of a shrouded assembly, including a novel method for modeling shrouded blade mistuning, will follow.

2.2 Formulation Refinement for Shrouded Designs. A modal matrix containing cyclic modes can be represented as

$$\mathbf{U}^{\mathrm{r}} = (\mathbf{F} \otimes \mathbf{I})\tilde{\mathbf{U}}^{\mathrm{r}}, \tag{5}$$

where $\mathbf{F}$ is defined in Eq. (B.3), and $\tilde{\mathbf{U}}^{\mathrm{r}}$, which contains the mode shapes of a fundamental sector in cyclic coordinates, has a pseudo-block-diagonal structure (see appendix B), as follows:

$$\tilde{\mathbf{U}}^{\mathrm{r}} = \underset{k=0,\ldots,P}{\tilde{\mathbf{B}}\mathbf{diag}} [\tilde{\mathbf{u}}_{\mathrm{k}}^{\mathrm{r}}], \tag{6}$$

where $\tilde{\mathbf{B}}\mathbf{diag}[\cdot]$ denotes a pseudo-block-diagonal matrix, with the argument being the k^{th} "block", and the range of k is shown. The mode type designation $\mathbf{r}$ could be either the disk-induced modes, $\mathbf{d}$, or the cantilever blade modes, $\mathbf{b}$, since the structure of both these modal matrices is cyclic. Combining Eqs. (5) and (6), one may write the internal structure of a cyclic modal matrix $\mathbf{U}^{\mathrm{r}}$ as

$$\mathbf{U}^{\mathrm{r}} = [\mathbf{f}_0 \otimes \tilde{\mathbf{u}}_0^{\mathrm{r}} \quad \mathbf{f}_{1,\mathrm{c}} \otimes \tilde{\mathbf{u}}_{1,\mathrm{c}}^{\mathrm{r}} + \mathbf{f}_{1,\mathrm{s}} \otimes \tilde{\mathbf{u}}_{1,\mathrm{s}}^{\mathrm{r}}, \ldots$$
$$\mathbf{f}_{\mathrm{k,c}} \otimes \tilde{\mathbf{u}}_{\mathrm{k,c}}^{\mathrm{r}} + \mathbf{f}_{\mathrm{k,s}} \otimes \tilde{\mathbf{u}}_{\mathrm{k,s}}^{\mathrm{r}}, \ldots \mathbf{f}_{\mathrm{N/2}} \otimes \tilde{\mathbf{u}}_{\mathrm{N/2}}^{\mathrm{r}}]. \tag{7}$$

Because of the cyclicity of both $\mathbf{U}^{\mathrm{d}}$ and $\mathbf{U}^{\mathrm{b}}$ and the block-diagonal structure of $\mathbf{M}$ and $\mathbf{K}$, all three projection products in $\mathcal{M}$ and $\mathcal{K}$ will become pseudo-block-diagonal, as follows:

$$\mathbf{U}^{\mathrm{d}^{\mathrm{T}}}\mathbf{M}_{\mathrm{b}}\mathbf{U}^{\mathrm{d}} = \underset{k=0,\ldots,P}{\tilde{\mathbf{B}}\mathbf{diag}} [\tilde{\mathbf{u}}_{\mathrm{k}}^{\mathrm{d}^{\mathrm{T}}}\tilde{\mathbf{M}}_{\mathrm{b}}\tilde{\mathbf{u}}_{\mathrm{k}}^{\mathrm{d}}]$$
$$\mathbf{U}^{\mathrm{d}^{\mathrm{T}}}\mathbf{M}_{\mathrm{b}}\mathbf{U}^{\mathrm{b}} = \underset{k=0,\ldots,P}{\tilde{\mathbf{B}}\mathbf{diag}} [\tilde{\mathbf{u}}_{\mathrm{k}}^{\mathrm{d}^{\mathrm{T}}}\tilde{\mathbf{M}}_{\mathrm{b}}\tilde{\mathbf{u}}_{\mathrm{k}}^{\mathrm{b}}]$$
$$\mathbf{U}^{\mathrm{d}^{\mathrm{T}}}\mathbf{K}_{\mathrm{b}}\mathbf{U}^{\mathrm{b}} = \underset{k=0,\ldots,P}{\tilde{\mathbf{B}}\mathbf{diag}} [\tilde{\mathbf{u}}_{\mathrm{k}}^{\mathrm{d}^{\mathrm{T}}}\tilde{\mathbf{K}}_{\mathrm{b}}\tilde{\mathbf{u}}_{\mathrm{k}}^{\mathrm{b}}]. \tag{8}$$

The external excitation force vector shown in Eq. (4), $\mathbf{Q}$, defines the forcing on all the blade degrees of freedom of the assembly. The restriction to blade degrees of freedom is not an absolute requirement, but leads to a more compact formulation, and it should also be sufficient from a practical perspective. Moreover, we assume an engine order excitation which is harmonic in time and differs only in phase from blade to blade. The phase at blade i, ϕ_i, is given by

$$\phi_i = \frac{2\pi C(i-1)}{N} \quad i = 1, \ldots, N, \tag{9}$$

where C is the engine order of the excitation. The external force vector can then be expressed as:

$$\mathbf{Q} = \begin{Bmatrix} \tilde{\mathbf{f}}e^{j\phi_1} \\ \tilde{\mathbf{f}}e^{j\phi_2} \\ \vdots \\ \tilde{\mathbf{f}}e^{j\phi_N} \end{Bmatrix}, \tag{10}$$

where $\tilde{\mathbf{f}}$ is the force vector on a single blade.

The expression for the modal force vector $\mathcal{Q}$ given in Eq. (4) can be simplified to a much more convenient form in terms of the disk-induced and cantilevered blade mode shapes of a single sector, $\tilde{\mathbf{u}}_{\mathrm{k}}^{\mathrm{d}}$ and $\tilde{\mathbf{u}}_{\mathrm{k}}^{\mathrm{b}}$, respectively. Using Eq. (10), and the modal matrix as written in Eq. (7), the corresponding modal force partition becomes:

$$\mathcal{Q}_{\mathrm{r}} = \mathbf{U}^{\mathrm{r}^{\mathrm{T}}}\mathbf{Q}$$
$$= \sqrt{N} \begin{Bmatrix} (\mathbf{f}_0 \otimes \tilde{\mathbf{u}}_0^{\mathrm{r}})^{\mathrm{T}}(\mathbf{e}_{\mathrm{C}} \otimes \tilde{\mathbf{f}}) \\ (\mathbf{f}_{1,\mathrm{c}} \otimes \tilde{\mathbf{u}}_{1,\mathrm{c}}^{\mathrm{r}} + \mathbf{f}_{1,\mathrm{s}} \otimes \tilde{\mathbf{u}}_{1,\mathrm{s}}^{\mathrm{r}})^{\mathrm{T}}(\mathbf{e}_{\mathrm{C}} \otimes \tilde{\mathbf{f}}) \\ \vdots \\ (\mathbf{f}_{\mathrm{k,c}} \otimes \tilde{\mathbf{u}}_{\mathrm{k,c}}^{\mathrm{r}} + \mathbf{f}_{\mathrm{k,s}} \otimes \tilde{\mathbf{u}}_{\mathrm{k,s}}^{\mathrm{r}})^{\mathrm{T}}(\mathbf{e}_{\mathrm{C}} \otimes \tilde{\mathbf{f}}) \\ \vdots \\ (\mathbf{f}_{\mathrm{N/2}} \otimes \tilde{\mathbf{u}}_{\mathrm{N/2}}^{\mathrm{r}})^{\mathrm{T}}(\mathbf{e}_{\mathrm{C}} \otimes \tilde{\mathbf{f}}) \end{Bmatrix}, \tag{11}$$

where $\mathbf{e}_{\mathrm{C}}$ is the $(C+1)^{\mathrm{th}}$ column of the complex Fourier matrix, $\mathbf{E}$, defined in Eq. (B.2). This expression can now be greatly simplified, first by using the general algebraic properties of the Kronecker product stated in Eqs. (A.2) and (A.4), and then by making use of the orthogonal properties of the transformation column vectors involved. The expansion of Eq. (11) will yield modal force partitions that are zero everywhere, except for the C^{th} harmonic disk-induced and cantilever blade modes. Thus, the engine order excitation, C, determines which modes of the assembly that are being excited. The resulting modal force vector is given in section 2.4.

The modal viscous damping matrix for the shrouded cantilever blade modes, $\mathbf{C}$, will be a diagonal matrix expressed as

$$\mathbf{C} = \underset{k=0,\ldots,P}{\tilde{\mathbf{B}}\mathbf{diag}} \left[\underset{n=1,\ldots,m_b/2m_b}{\mathbf{diag}} [2\zeta_n^k] \right] \sqrt{\hat{\mathbf{K}}_{\mathrm{b}}}, \tag{12}$$

where $\mathbf{diag}[\cdot]$ denotes a diagonal matrix (block), with the argument being the n^{th} diagonal element, and the range of n is shown. Also, ζ_n^k is the modal damping coefficient of the n^{th} cantilever blade mode of the k^{th} harmonic. Note that for shrouded blades, $\hat{\mathbf{K}}_{\mathrm{b}}$ is comprised of diagonal blocks associated with the various cyclic harmonics of the assembly of shrouded blades.

2.3 Mistuning of Shrouded Blades. Perhaps the most fundamental feature of this technique is its suitability for stiffness mistuning of the individual blades, since the modal stiffness of each individual cantilever blade mode is isolated in the diagonal matrix $\hat{\mathbf{K}}_{\mathrm{b}}$. Therefore, in the unshrouded case, the formulation lends itself to a very convenient and simple input of individual mistuning of each cantilever blade modal stiffness for each blade as

$$\Delta\hat{\mathbf{K}}_{\mathrm{b}} = \underset{n=1,\ldots,N}{\mathbf{Bdiag}} \left[\underset{k=1,\ldots,m_b}{\mathbf{diag}} [\delta_n^k] \right] \hat{\mathbf{K}}_{\mathrm{b}}, \tag{13}$$

where $\mathbf{Bdiag}[\cdot]$ denotes a block-diagonal (versus pseudo-block-diagonal) matrix. The mistuning parameter associated with the k^{th} cantilever blade mode of the n^{th} blade, δ_n^k, is defined as

$$\delta_n^k = \left(\frac{\bar{\omega}_n^k}{\omega^k}\right)^2 - 1, \tag{14}$$

where $\bar{\omega}_n^k$ represents the mistuned natural frequency of the k^{th} mode of blade n, and ω^k is the corresponding nominal, or tuned, natural frequency.

However, the manner in which the mistuning is put into the ROM stiffness matrix for unshrouded blades is not particularly well suited for shrouded assemblies, in that $\hat{\mathbf{K}}_{\mathrm{b}}$ is now represented in cyclic, or harmonic, modal coordinates. This implies that in order to obtain any relevant measures of mistuning, one would need to know the effects of individual blade mistuning on the whole shrouded blade assembly. In theory, it would be possible to obtain this information through frequency tests of the full blade-shroud assembly, but this approach is not practical.

In view of this, an alternative approach is to project mistuning measurements for a single blade onto the cyclic modes of the blade assembly. In this case, the test data would consist of the deviations in natural frequencies of each individual mode of each blade. This data could then be used to generate estimates of the mistuned stiffness matrices for all blades, which would be possible to achieve without very complicated and specialized testing procedures.

First, one must establish the manner in which the individual shrouded blade natural frequencies are measured. Here, it is assumed that the shrouded blades are tested while being clamped at the root, but are otherwise completely unconstrained, as indicated in Fig. 2. Thus, the tests give measurements of the natural frequencies of a cantilever blade with free shrouds, $\bar{\omega}_n^k$. Using the mistuning parameter δ_n^k defined in Eq. (14), a diagonal matrix containing the measured mistuned natural frequencies may be defined as

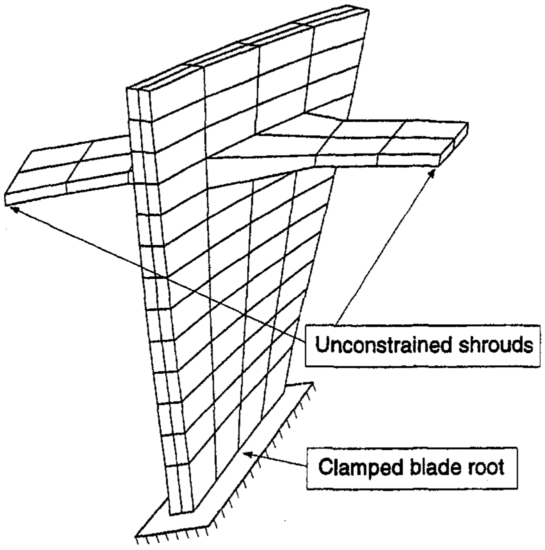

Fig. 2 Proposed configuration for measuring natural frequencies of shrouded blades individually

$$\underset{n=1,\ldots,N}{\mathbf{Bdiag}}\left[\underset{k=1,\ldots,p}{\mathbf{diag}}\,[1+\delta_n^k]\right]\hat{\mathbf{K}}_{\mathrm{b}}^{\mathrm{nom}} = (\mathbf{I}\otimes\bar{\mathbf{u}}^{\mathrm{b}})^{\mathrm{T}}\mathbf{K}_{\mathrm{b}}^{\mathrm{mt}}(\mathbf{I}\otimes\bar{\mathbf{u}}^{\mathrm{b}}), \quad (15)$$

where $\bar{\mathbf{u}}^{\mathrm{b}}$ is the nominal modal matrix, or the nominal mode shapes, for one cantilever blade; $\mathbf{K}_{\mathrm{b}}^{\mathrm{mt}}$ is a mistuned, block-diagonal stiffness matrix, where each block corresponds to the stiffness matrix of one of the N mistuned blades; and $\hat{\mathbf{K}}_{\mathrm{b}}^{nom}$ is a diagonal matrix of squared nominal natural frequencies for a tuned cantilever blade. The nominal natural frequencies may be taken either as some average values from tests, or directly from the finite element analysis needed to obtain the tuned cantilever blade mode shapes $\bar{\mathbf{u}}^{\mathrm{b}}$. Note that there is already an approximation made at this point, namely that the eigenvectors $\bar{\mathbf{u}}^{\mathrm{b}}$ of the mistuned blades are the same as the tuned ones (see discussion in section 2.1).

Returning to Eq. (15), the mistuned frequencies are grouped in blocks associated with each individual blade, where these blocks are diagonal in themselves. Moreover, the mistuned stiffness matrix will have the following block-diagonal configuration:

$$\mathbf{K}_{\mathrm{b}}^{\mathrm{mt}} = \underset{n=1,\ldots,N}{\mathbf{Bdiag}}\,[\bar{\mathbf{K}}_{\mathrm{b,n}}^{\mathrm{mt}}]. \quad (16)$$

Finally, the matrix of nominal modal stiffnesses will also be of a block-diagonal form, but where all the blocks are identical and diagonal. By denoting such a diagonal block $\hat{\hat{\mathbf{K}}}_{\mathrm{b}}^{\mathrm{nom}}$, the matrix of nominal modal stiffnesses can be expressed as

$$\hat{\mathbf{K}}_{\mathrm{b}}^{\mathrm{nom}} = \underset{n=1,\ldots,N}{\mathbf{Bdiag}}\,[\hat{\hat{\mathbf{K}}}_{\mathrm{b}}^{\mathrm{nom}}] = \mathbf{I}\otimes\hat{\hat{\mathbf{K}}}_{\mathrm{b}}^{\mathrm{nom}}. \quad (17)$$

Since $\hat{\hat{\mathbf{K}}}_{b}^{\mathrm{nom}}$ represents the nominal modal stiffnesses for one blade, Eq. (17) can be rewritten as

$$\hat{\mathbf{K}}_{\mathrm{b}}^{\mathrm{nom}} = \mathbf{I}\otimes\bar{\mathbf{u}}^{\mathrm{b}^{\mathrm{T}}}\tilde{\mathbf{K}}_{\mathrm{b}}\bar{\mathbf{u}}^{\mathrm{b}} = (\mathbf{I}\otimes\bar{\mathbf{u}}^{\mathrm{b}})^{\mathrm{T}}(\mathbf{I}\otimes\tilde{\mathbf{K}}_{\mathrm{b}})(\mathbf{I}\otimes\bar{\mathbf{u}}^{\mathrm{b}}). \quad (18)$$

From Eqs. (15) and (18), one obtains

$$\mathbf{K}_{\mathrm{b}}^{\mathrm{mt}} = (\mathbf{I}\otimes\bar{\mathbf{u}}^{\mathrm{b}})^{\mathrm{T}^{-1}}\,\underset{n=1,\ldots,N}{\mathbf{Bdiag}}\left[\underset{k=1,\ldots,p}{\mathbf{diag}}\,[1+\delta_n^k]\right](\mathbf{I}\otimes\bar{\mathbf{u}}^{\mathrm{b}^{\mathrm{T}}}\tilde{\mathbf{K}}_{\mathrm{b}}) \quad (19)$$

by virtue of the Kronecker product property given in Eq. (A.2).

Now, making use of the eigenvector normalization assumption, it is realized that

$$\mathbf{I} = \underset{n=1,\ldots,N}{\mathbf{Bdiag}}\,[\bar{\mathbf{u}}^{\mathrm{b}^{\mathrm{T}}}\tilde{\mathbf{M}}_{\mathrm{b}}\bar{\mathbf{u}}^{\mathrm{b}}] = (\mathbf{I}\otimes\bar{\mathbf{u}}^{\mathrm{b}})^{\mathrm{T}}(\mathbf{I}\otimes\tilde{\mathbf{M}}_{\mathrm{b}})(\mathbf{I}\otimes\bar{\mathbf{u}}^{\mathrm{b}})$$

$$\Rightarrow(\mathbf{I}\otimes\bar{\mathbf{u}}^{\mathrm{b}})^{\mathrm{T}^{-1}} = \mathbf{I}\otimes\tilde{\mathbf{M}}_{\mathrm{b}}\bar{\mathbf{u}}^{\mathrm{b}}. \quad (20)$$

By substituting Eq. (20) into Eq. (19), and by using the fact that $\tilde{\mathbf{M}}_{\mathrm{b}}$ is symmetric, one may express the mistuned blade stiffness matrix as

$$\mathbf{K}_{\mathrm{b}}^{\mathrm{mt}} = \mathbf{I}\otimes\tilde{\mathbf{K}}_{\mathrm{b}} + (\mathbf{I}\otimes\tilde{\mathbf{M}}_{\mathrm{b}}\bar{\mathbf{u}}^{\mathrm{b}})\,\underset{n=1,\ldots,N}{\mathbf{Bdiag}}\left[\underset{k=1,\ldots,p}{\mathbf{diag}}\,[\delta_n^k]\right] \times (\mathbf{I}\otimes\bar{\mathbf{u}}^{\mathrm{b}^{\mathrm{T}}}\tilde{\mathbf{K}}_{\mathrm{b}}). \quad (21)$$

For convenience, the quantity $\Delta\mathbf{K}_{\mathrm{b}}$ is introduced to denote the stiffness deviation matrix as

$$\Delta\mathbf{K}_{\mathrm{b}} = (\mathbf{I}\otimes\tilde{\mathbf{M}}_{\mathrm{b}}\bar{\mathbf{u}}^{\mathrm{b}})\,\underset{n=1,\ldots,N}{\mathbf{Bdiag}}\left[\underset{k=1,\ldots,p}{\mathbf{diag}}\,[\delta_n^k]\right](\mathbf{I}\otimes\bar{\mathbf{u}}^{\mathrm{b}^{\mathrm{T}}}\tilde{\mathbf{K}}_{\mathrm{b}}) \quad (22)$$

such that

$$\mathbf{K}_{\mathrm{b}}^{\mathrm{mt}} = \mathbf{I}\otimes\tilde{\mathbf{K}}_{\mathrm{b}} + \Delta\mathbf{K}_{\mathrm{b}} = \mathbf{K}_{\mathrm{b}} + \Delta\mathbf{K}_{\mathrm{b}}. \quad (23)$$

The expression for the stiffness deviation matrix, $\Delta\mathbf{K}_{\mathrm{b}}$, can be simplified to

$$\Delta\mathbf{K}_{\mathrm{b}} = \underset{n=1,\ldots,N}{\mathbf{Bdiag}}\left[\tilde{\mathbf{M}}_{\mathrm{b}}\bar{\mathbf{u}}^{\mathrm{b}}\,\underset{k=1,\ldots,p}{\mathbf{diag}}\,[\delta_n^k]\bar{\mathbf{u}}^{\mathrm{b}^{\mathrm{T}}}\tilde{\mathbf{K}}_{\mathrm{b}}\right]. \quad (24)$$

Finally, the complete blade stiffness matrix for the tuned case, $\mathbf{K}_{\mathrm{b}}$, is now simply replaced by $\mathbf{K}_{\mathrm{b}}^{\mathrm{mt}}$ in the reduced order model formulation. Thus, replacing $\mathbf{K}_{\mathrm{b}}$ by $\mathbf{K}_{\mathrm{b}}^{\mathrm{mt}}$ in Eq. (1), and ignoring any contributions of mistuning from the projection onto the disk-induced modes, as per discussion in section 2.1, yield the ROM stiffness matrix for a general mistuned shrouded bladed disk assembly

$$\mathcal{K} = \begin{bmatrix} \hat{\mathbf{K}}_{\mathrm{d}} & \underset{k=0,\ldots,P}{\tilde{\mathbf{B}}\mathbf{diag}}\,[\tilde{\mathbf{u}}_{\mathrm{k}}^{\mathrm{d}^{\mathrm{T}}}\tilde{\mathbf{K}}_{\mathrm{b}}\tilde{\mathbf{u}}_{\mathrm{k}}^{\mathrm{b}}] \\ \underset{k=0,\ldots,P}{\tilde{\mathbf{B}}\mathbf{diag}}\,[\tilde{\mathbf{u}}_{\mathrm{k}}^{\mathrm{b}^{\mathrm{T}}}\tilde{\mathbf{K}}_{\mathrm{b}}\tilde{\mathbf{u}}_{\mathrm{k}}^{\mathrm{d}}] & \hat{\mathbf{K}}_{\mathrm{b}} + \mathbf{U}^{\mathrm{b}^{\mathrm{T}}}\Delta\mathbf{K}_{\mathrm{b}}\mathbf{U}^{\mathrm{b}} \end{bmatrix}$$

$$\Delta\mathbf{K}_{\mathrm{b}} = \underset{n=1,\ldots,N}{\mathbf{Bdiag}}\left[\tilde{\mathbf{M}}_{\mathrm{b}}\bar{\mathbf{u}}^{\mathrm{b}}\,\underset{k=1,\ldots,p}{\mathbf{diag}}\,[\delta_n^k]\bar{\mathbf{u}}^{\mathrm{b}^{\mathrm{T}}}\tilde{\mathbf{K}}_{\mathrm{b}}\right]. \quad (25)$$

Thus, the stiffness mistuning $\Delta\mathbf{K}_{\mathrm{b}}$, which may be obtained from measuring natural frequencies of individual blades with clamped roots and unconstrained shrouds, is now projected onto the cyclic modes of the shrouded blade assembly, $\mathbf{U}^{\mathrm{b}}$. Note that the mistuning projection term $\mathbf{U}^{\mathrm{b}^{\mathrm{T}}}\Delta\mathbf{K}_{\mathrm{b}}\mathbf{U}^{\mathrm{b}}$ does not yield any particular matrix structure, since there are no special relations, such as orthogonality, between the modes of the cantilever blade with unconstrained shrouds, and the cyclic modes of the shrouded blade assembly. Thus, in general, the lower-right quadrant of the ROM stiffness matrix becomes fully populated when mistuning is introduced for shrouded bladed disk assemblies.

2.4 Final Formulation for Shrouded Designs. To conclude this section, the reduced order model structural matrices (in the absence of aerodynamic coupling), and modal force for shrouded bladed disks are stated in their final forms:

$$\mathcal{M} = \begin{bmatrix} \mathbf{I}_{\mathrm{d}} + \underset{k=0,\ldots,P}{\tilde{\mathbf{B}}\mathbf{diag}}\,[\tilde{\mathbf{u}}_{\mathrm{k}}^{\mathrm{d}^{\mathrm{T}}}\tilde{\mathbf{M}}_{\mathrm{b}}\tilde{\mathbf{u}}_{\mathrm{k}}^{\mathrm{d}}] & \underset{k=0,\ldots,P}{\tilde{\mathbf{B}}\mathbf{diag}}\,[\tilde{\mathbf{u}}_{\mathrm{k}}^{\mathrm{d}^{\mathrm{T}}}\tilde{\mathbf{M}}_{\mathrm{b}}\tilde{\mathbf{u}}_{\mathrm{k}}^{\mathrm{b}}] \\ \underset{k=0,\ldots,P}{\tilde{\mathbf{B}}\mathbf{diag}}\,[\tilde{\mathbf{u}}_{\mathrm{k}}^{\mathrm{b}^{\mathrm{T}}}\tilde{\mathbf{M}}_{\mathrm{b}}\tilde{\mathbf{u}}_{\mathrm{k}}^{\mathrm{d}}] & \mathbf{I}_{\mathrm{b}} \end{bmatrix}$$

$$\mathcal{C} = \begin{bmatrix} \mathbf{0} & \mathbf{0} \\ \mathbf{0} & \underset{k=1,\ldots,m_bN}{\mathbf{diag}}\,[2\zeta^k]\sqrt{\hat{\mathbf{K}}_{\mathrm{b}}} \end{bmatrix}$$

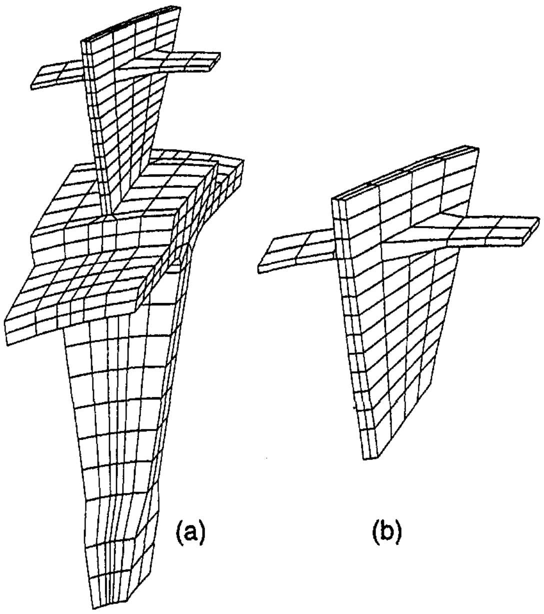

Fig. 3 (*a*) **Finite element mesh of a single disk-blade-shroud sector. (*b*) Finite element mesh of a single blade with shrouds.**

$$\mathcal{K} = \begin{bmatrix} \hat{\mathbf{K}}_{\mathrm{d}} & \underset{k=0,\ldots,P}{\tilde{\mathbf{B}}\mathbf{diag}} \, [\tilde{\mathbf{u}}_{\mathrm{k}}^{\mathrm{d}^{\mathrm{T}}} \tilde{\mathbf{K}}_{\mathrm{b}} \tilde{\mathbf{u}}_{\mathrm{k}}^{\mathrm{b}}] \\ \underset{k=0,\ldots,P}{\tilde{\mathbf{B}}\mathbf{diag}} \, [\tilde{\mathbf{u}}_{\mathrm{k}}^{\mathrm{b}^{\mathrm{T}}} \tilde{\mathbf{K}}_{\mathrm{b}} \tilde{\mathbf{u}}_{\mathrm{k}}^{\mathrm{d}}] & \hat{\mathbf{K}}_{\mathrm{b}} + \mathbf{U}^{\mathrm{b}^{\mathrm{T}}} \boldsymbol{\Delta}\mathbf{K}_{\mathrm{b}} \mathbf{U}^{\mathrm{b}} \end{bmatrix}$$

$$\boldsymbol{\Delta}\mathbf{K}_{\mathrm{b}} = \underset{n=1,\ldots,N}{\mathbf{Bdiag}} \left[\tilde{\mathbf{M}}_{\mathrm{b}} \bar{\mathbf{u}}^{\mathrm{b}} \underset{k=1,\ldots,p}{\mathbf{diag}} \, [\delta_n^k] \bar{\mathbf{u}}^{\mathrm{b}^{\mathrm{T}}} \tilde{\mathbf{K}}_{\mathrm{b}} \right]$$

$$\mathcal{Q} = \begin{Bmatrix} \mathcal{Q}_{\mathrm{d}} \\ \mathcal{Q}_{\mathrm{b}} \end{Bmatrix} = \begin{Bmatrix} \mathbf{0} \\ \vdots \\ \mathbf{0} \\ \sqrt{N}\{\mathbf{f}_{\mathrm{C,c}}^{\mathrm{T}} \mathbf{e}_{\mathrm{C}} \otimes \tilde{\mathbf{u}}_{\mathrm{C,c}}^{\mathrm{d}^{\mathrm{T}}} \tilde{\mathbf{f}} + \mathbf{f}_{\mathrm{C,s}}^{\mathrm{T}} \mathbf{e}_{\mathrm{C}} \otimes \tilde{\mathbf{u}}_{\mathrm{C,s}}^{\mathrm{d}^{\mathrm{T}}} \tilde{\mathbf{f}}\} \\ \mathbf{0} \\ \vdots \\ \mathbf{0} \\ \hline \mathbf{0} \\ \vdots \\ \mathbf{0} \\ \sqrt{N}\{\mathbf{f}_{\mathrm{C,c}}^{\mathrm{T}} \mathbf{e}_{\mathrm{C}} \otimes \tilde{\mathbf{u}}_{\mathrm{C,c}}^{\mathrm{b}^{\mathrm{T}}} \tilde{\mathbf{f}} + \mathbf{f}_{\mathrm{C,s}}^{\mathrm{T}} \mathbf{e}_{\mathrm{C}} \otimes \tilde{\mathbf{u}}_{\mathrm{C,s}}^{\mathrm{b}^{\mathrm{T}}} \tilde{\mathbf{f}}\} \\ \mathbf{0} \\ \vdots \\ \mathbf{0} \end{Bmatrix}.$$

3 Analysis of a Shrouded Test Case Rotor

3.1 Finite Element and Reduced Order Models. The finite element model of the test case rotor that is analyzed in this study is shown in Figs. 3 and 4. The rotor features 24 blades. Each blade has a base pitch of 30 deg (measured from the axial direction), and a uniform twist of an additional 30 deg over its length. The base radius is 212 mm, and the blade length is 68 mm. The rotor is fixed at the interfaces towards adjacent rotating blade stages. This is believed to provide a reasonable description of the dynamics of the bladed disk assembly. Moreover, the studied test case rotor features shrouds, which are arbitrarily positioned at 10/13 of the blade length.

The construction of the reduced order model of a shrouded assembly requires the following two finite element models:

—A complete sector subject to cyclic constraints at disk-to-disk and shroud-to-shroud interfaces. This model consists of 488 eight-noded brick elements and 2646 degrees of freedom before model reduction due to applied constraints. The finite element mesh of this model is shown in Fig. 3(*a*).

—A single cantilever blade. This model consists of 116 linear solid elements, and 738 degrees of freedom before model reduction. The finite element mesh of this model is shown in Fig. 3(*b*).

From these fundamental finite element models, the reduced order model (ROM) is derived using the component mode synthesis technique described in section 2. This analysis is based on a reduced order model that is created from five cantilever blade modes ($m_b = 5$) and five disk-induced modes ($m_d = 5$) per harmonic, leading to a total of 240 degrees of freedom.

In addition, five cantilever blade modes with unconstrained shrouds were used to generate the stiffness deviation matrix, $\boldsymbol{\Delta}\mathbf{K}_{\mathrm{b}}$ ($p = 5$). This, however, does not influence the size of the resulting reduced order model. It should be pointed out that, if the cantilever blade mode shapes from the cyclic symmetry analysis conform relatively closely with the cantilever blade mode shapes with unconstrained shrouds, very little improvement in accuracy is gained by including more than m_b modes for the stiffness deviation generation. In this case, the principal effects of the stiffness deviations are already captured by the m_b modes. However, using fewer than m_b modes yields poor accuracy. Thus, in general, the condition $p \geq m_b$ should always be satisfied in order to obtain a reduced order model with reasonable accuracy.

Finally, a finite element model of the full mistuned rotor was created to allow comparisons of mistuned mode shapes and forced responses for a single, random mistuning pattern. The mistuning pattern was sampled from a uniform distribution of mean zero and standard deviation 5 percent. Individual mode mistuning is not employed in this analysis. Therefore, the mistuning is readily introduced to the full finite element model by appropriately varying Young's modulus in the blade elements as

$$E_n = (1 + \delta_n)E_o \quad n = 1, \ldots, N. \tag{26}$$

The material properties for the finite element model were taken to be those of steel. The full finite element model consists of 11,712

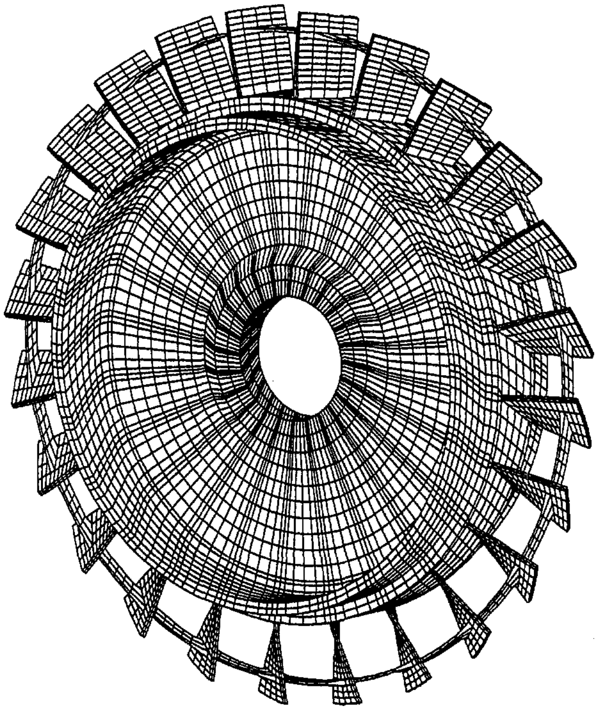

Fig. 4 Finite element mesh of full shrouded test case rotor

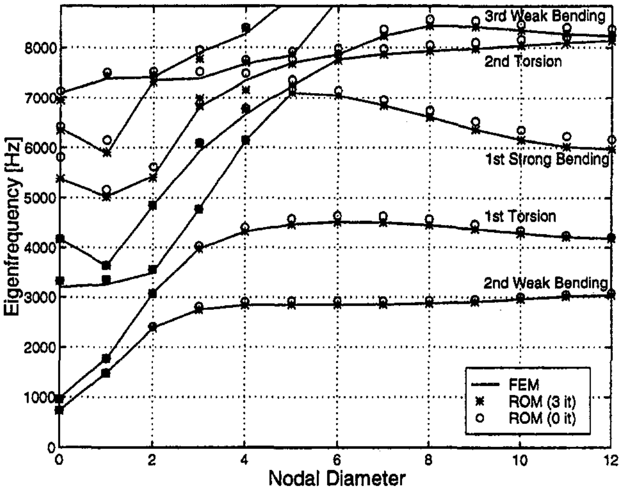

Fig. 5 Comparison of tuned eigenfrequencies from finite element model (FEM) and reduced order model (ROM) with and without eigenvalue adjustment iterations

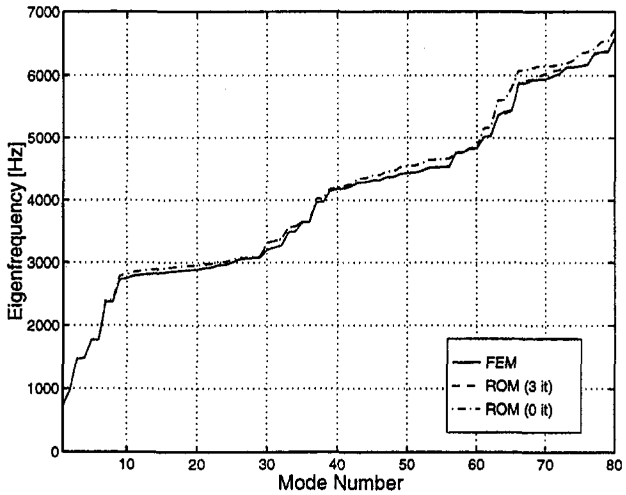

Fig. 6 Comparison of the 80 lowest mistuned eigenfrequencies from finite element model (FEM) and reduced order model (ROM) with and without eigenvalue adjustment iterations

linear solid elements and 56,376 degrees of freedom, and its finite element mesh is shown in Fig. 4.

It should be noted that the shroud-to-shroud connection is modeled as being continuous (full stick). Since no effort has been made to include friction at the shroud mating surfaces, the present modeling technique can be used for the limiting cases of full stick or full slip conditions. The incorporation of shroud interface models (Srinivasan et al., 1978; Menq et al., 1986; Valero and Bendiksen, 1986) into this type of reduced order model will be the subject of future work.

3.2 Free Vibration. Figure 5 displays the tuned natural frequencies versus the number of nodal diameters for the test case rotor in the lower frequency range, as obtained from finite element analysis and ROM analysis. MSC/NASTRAN^{TM} was used to calculate the natural frequencies and mode shapes of the finite element models, and to extract the blade mass and stiffness matrices ($\tilde{\mathbf{M}}_b$ and $\tilde{\mathbf{K}}_b$).

Clearly, as the number of nodal diameters increases, the disk becomes much more stiff. Thus, the slanted lines to the left in Fig. 5 correspond to disk-dominated modes. The lines which are approximately horizontal represent families of blade-dominated modes. The characteristic types of blade motion for the blade-dominated mode families are indicated in the plot. One can observe that, depending on the mode family, a slight stiffening or a slight softening occurs as the number of nodal diameters increase for the blade-dominated modes. This is somewhat different from the unshrouded case, where the frequencies associated with a certain family of blade-dominated modes are nearly constant over a certain range of nodal diameters.

Figure 5 also depicts the increase in ROM accuracy via eigenvalue adjustment. By directly adjusting the eigenvalues, or modal stiffnesses, associated with the blade modes (i.e., the diagonal elements of $\hat{\mathbf{K}}_b$), the ROM's representation of the blade-dominated modes is enhanced.

The adjustment procedure is a simple iterative process, where the cantilever blade eigenvalues are re-scaled based on the ratio between the tuned finite element eigenvalues from a cyclic symmetry analysis of a complete sector and the corresponding ROM eigenvalues. Once a sufficiently small residual is achieved, one may move on and introduce mistuning. As seen in Fig. 5, after three iterations of eigenvalue adjustments, the blade-mode frequencies for the ROM are nearly identical to those of the FEM. Naturally, the adjustments of the cantilever blade mode eigenvalues have a much smaller effect on the disk-dominated modes.

Figure 6 illustrates the correlation between finite element and ROM natural frequencies for the mistuned rotor. Since the nodal diameter description of the modes fails for certain mistuned modes due to localization, the natural frequencies are instead plotted versus the mode number in the mistuned case. Again, the results obtained from the reduced order model after eigenvalue adjustments compare very well with the finite element results.

Figure 7 illustrates the correlation between finite element and ROM mistuned mode shapes. The Euclidean norm displacement measure, $\bar{u}_i$, for each blade i, is defined as

$$\bar{u}_i = \left[\frac{\displaystyle\sum_{j=1}^{N_n} (u_{ij,r}^2 + u_{ij,\theta}^2 + u_{ij,z}^2)}{\displaystyle\sum_{i=1}^{N_b} \sum_{j=1}^{N_n} (u_{ij,r}^2 + u_{ij,\theta}^2 + u_{ij,z}^2)} \right]^{1/2}, \qquad (27)$$

where $u_{ij,x}$ is the displacement component in the x-direction, N_n is the number of nodes in one blade, and N_b is the total number of blades. The Euclidean norm is a scalar value, which may be interpreted as a measure of relative blade energy content.

Specifically, Fig. 7 shows the 17th mistuned mode at 2862 Hz, in which the vibration energy is largely confined to blades 17 and 19.

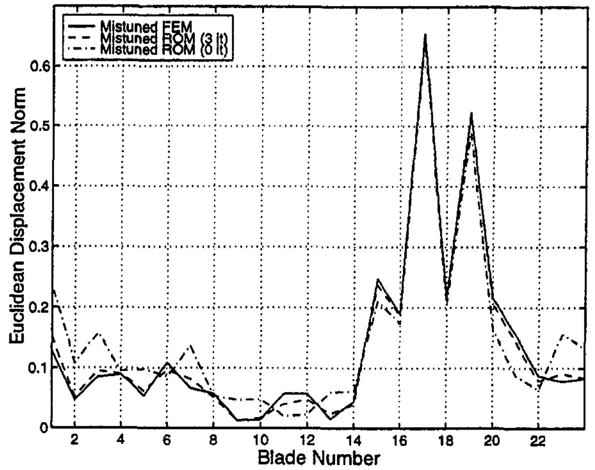

Fig. 7 Mistuned mode number 17 at 2861.7 Hz, as obtained by finite element model (FEM) and reduced order model (ROM) with and without eigenvalue adjustment iterations. This mode exhibits significant localization.

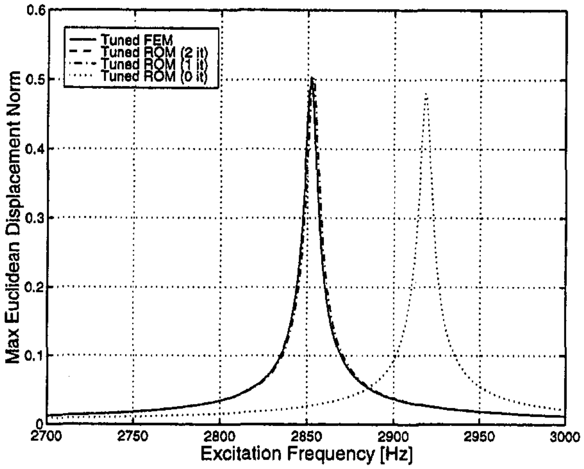

Fig. 8 Tuned forced response for engine order 7 excitation, as obtained by finite element model (FEM) and reduced order model (ROM) with and without eigenvalue adjustment iterations

The dramatic mode localization exhibited by this mode is due to the high modal density in this particular frequency region (Pierre, 1988). In fact, it is virtually impossible to find any traces of the corresponding smooth harmonic tuned shape from which it derives.

Note the excellent agreement between the FEM and the ROM mode shapes, especially after eigenvalue adjustment. Several important factors are extremely well captured, such as peak amplitude, position of localization, and rate of spatial decay away from the localized area.

3.3 Forced Response. Next, we consider the forced response of the blisk. The external excitation force consists of a unit nodal load applied on the tip of the blade's leading edge in the axial direction. This applied force was chosen arbitrarily, and it serves only to verify the accuracy of the reduced order model. Furthermore, the structure is excited according to engine order 7 excitation, which has a blade-to-blade forcing phase shift of 105 deg.

The tuned rotor's response to this external forcing is shown in Fig. 8. After only two iterations of eigenvalue adjustments, the FEM and ROM predictions of the tuned rotor's response are nearly identical. The difference between the resonant frequencies of the FEM and the ROM is reduced from 2.3 percent to 0.0007 percent after these two iterations. Also, the error in peak response amplitude decreases from −3.9 percent to 0.9 percent. This amplitude error did not improve during subsequent iterations.

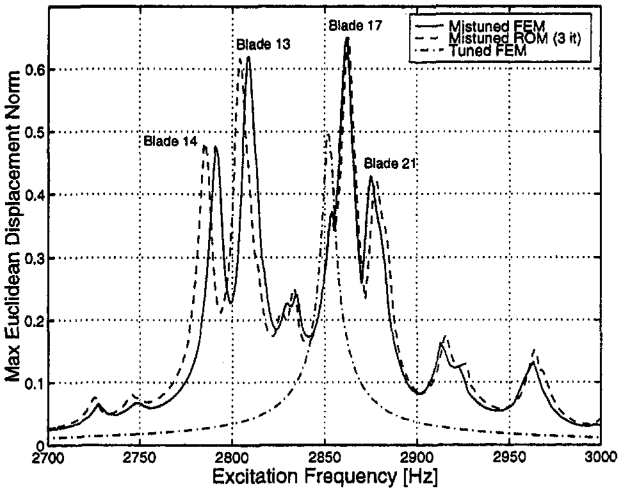

Fig. 9 Forced response for engine order 7 excitation, for both tuned and mistuned rotor, as obtained by finite element model (FEM) and reduced order model (ROM) with three eigenvalue adjustment iterations. The mistuned FEM has 56,376 degrees of freedom, while the ROM has only 240 degrees of freedom.

Figure 9 shows the response of the mistuned rotor for the same source of excitation. The mistuning and localization effects lead to a substantial increase in peak response amplitude and, in addition, a very significant widening of the resonant frequency bandwidth, compared to the corresponding response of a tuned rotor. In absolute normed displacement values, the maximum resonance amplitude predicted by the ROM is less than 0.2 percent lower than that predicted by the FEM (0.649 versus 0.650), which is an acceptable discrepancy, considering the huge difference in model sizes.

A notable effect of the order reduction is that the reduced order model here predicts a somewhat wider band of resonant frequencies, compared to the finite element analysis, due to residual errors in the ROM mistuned eigenfrequencies. The ROM mistuned eigenfrequency of the 12th mode is 0.16 percent lower than the corresponding FEM frequency, while the approximation of the 17th mode eigenfrequency is 0.04 percent higher. The conformity of the response characteristics predicted by the reduced order model is otherwise reasonably accurate.

4 Conclusions

This paper demonstrates how the vibratory behavior of a mistuned bladed disk of a general design may be analyzed by a systematic and computationally efficient reduced order modeling technique, based on a component mode approach. In particular, this work showed how the technique could be extended to designs with shrouded blades, and how a convenient measure of individual blade mistuning may be incorporated into the analysis with relative ease. Stiffness mistuning was included by projecting the mistuned natural frequencies of individual blades (with clamped roots and free shrouds) onto the cyclic modes of the shrouded blade assembly.

The reduced order modeling technique and the proposed method of mistuning for shrouded blade assemblies were validated using a finite element model (FEM) of a test case rotor. The total number of degrees of freedom for this FEM was 56,376, compared to only 240 for the reduced order model (ROM). The free and forced response results obtained for the ROM were in excellent agreement with those of the much larger FEM. Of special importance was the agreement of the forced response amplitudes for a rotor with mistuned blades. These results show that this reduced order modeling technique may provide a valuable tool for predicting the statistics of forced response for mistuned bladed disks.

Acknowledgments

This work is supported by the GUIde Consortium on blade durability at Carnegie Mellon University. The authors would like to acknowledge the beneficial discussions of mistuning and reduced order modeling that they have had with the Director of the GUIde Consortium, Prof. J. H. Griffin.

References

Castanier, M. P., Óttarsson, G., and Pierre, C., 1997, "A Reduced-Order Modeling Technique for Mistuned Bladed Disks," *Journal of Vibration and Acoustics,* Vol. 119, No. 3, pp. 439–447.

Davis, P. J., 1979, *Circulant Matrices,* Wiley-Interscience, New York.

Dye, R. C. F., and Henry, T. A., 1969, "Vibration Amplitudes of Compressor Blades Resulting From Scatter in Blade Natural Frequencies," *ASME Journal of Engineering for Power,* Vol. 91, No. 3, pp. 182–188.

El-Bayoumy, L. E., and Srinivasan, A. V., 1975, "Influence of Mistuning on Rotor-Blade Vibrations," *AIAA Journal,* Vol. 13, No. 4, pp. 460–464.

Elchuri, V., Smith, G. C. C., and Gallo, A. M., 1984, "NASTRAN Forced Vibration Analysis of Rotating Cyclic Structures," *ASME Journal of Vibration, Acoustics, Stress, and Reliability in Design,* Vol. 106, pp. 224–234.

Ewins, D. J., 1969, "The Effects of Detuning Upon the Forced Vibrations of Bladed Disks," *Journal of Sound and Vibration,* Vol. 9, No. 1, pp. 65–79.

Ewins, D. J., 1973, "Vibration Characteristics of Bladed Disc Assemblies," *Journal Mechanical Engineering Science,* Vol. 15, No. 3, pp. 165–186.

Griffin, J. H., and Hoosac, T. M., 1984, "Model Development and Statistical Investigation of Turbine Blade Mistuning," *ASME Journal of Vibration, Acoustics, Stress, and Reliability in Design,* Vol. 106, pp. 204–210.

Hitchings, D., and Singh, M., 1987, "Cyclic Symmetry Through Constraint Equations with Application to the Analysis of Steam Turbines," *Bladed Disk Assemblies,* Proceedings, ASME 11th Biennial Conference on Mechanical Vibration and Noise, Boston, Massachusetts, ASME, New York, pp. 113–119.

Irretier, H., 1983, "Spectral Analysis of Mistuned Bladed Disk Assemblies by Component Mode Synthesis," *Vibrations of Bladed Disk Assemblies,* Proceedings, ASME 9th Biennial Conference on Mechanical Vibration and Noise, Dearborn, Michigan, ASME, New York, pp. 115–125.

Joseph, J. A., 1981, "Cyclic Symmetry in MSC/NASTRAN," *MSC/NASTRAN Application Manual,* Chap. 3.2, The MacNeal-Schwendler Corporation, Los Angeles, CA, pp. 10–24.

Kruse, M. J., and Pierre, C., 1996a, "Forced Response of Mistuned Bladed Disks Using Reduced-Order Modeling," Proceedings, 37th AIAA/ASME Structures, Structural Dynamics, and Materials Conference, Salt Lake City, UT. AIAA, New York, Vol. 4, pp. 1938–1950.

Kruse, M. J., and Pierre, C., 1996b, "Dynamic Response of an Industrial Turbomachinery Rotor," AIAA Paper 96-2820.

Lin, C.-C., and Mignolet, M. P., 1997, "An Adaptive Perturbation Scheme for the Analysis of Mistuned Bladed Disks," ASME JOURNAL OF ENGINEERING FOR GAS TURBINES AND POWER, Vol. 119, No. 1, pp. 153–160.

Menq, C.-H., Griffin, J. H., and Bielak, J., 1986, "The Forced Response of Shrouded Fan Stages," *ASME Journal of Vibration, Acoustics, Stress, and Reliability in Design,* Vol. 108, pp. 50–55.

Mignolet, M. P., and Lin, C.-C., 1997, "Identification of Structural Parameters in Mistuned Bladed Disks," *ASME Journal of Vibration and Acoustics,* Vol. 119, No. 3, pp. 428–438.

Pierre, C., 1988, "Mode Localization and Eigenvalue Loci Veering Phenomena in Disordered Structures," *Journal of Sound and Vibration,* Vol. 126, No. 3, pp. 485–502.

Srinivasan, A. V., 1997, "Flutter and Resonant Vibration Characteristics of Engine Blades," ASME JOURNAL OF ENGINEERING FOR GAS TURBINES AND POWER, Vol. 119, No. 4, pp. 742–775.

Srinivasan, A. V., Lionberger, S. R., and Brown, K. W., 1978, "Dynamic Analysis of an Assembly of Shrouded Blades Using Component Modes," *ASME Journal of Mechanical Design,* Vol. 100, pp. 520–527.

Strang, G., 1988, *Linear Algebra and Its Applications,* 3rd ed., Saunders HBJ, Orlando, FL.

Thomas, D. L., 1979, "Dynamics of Rotationally Periodic Structures," *International Journal for Numerical Methods in Engineering,* Vol. 14, pp. 81–102.

Valero, N. A., and Bendiksen, O. O., 1986, "Vibration Characteristics of Mistuned Shrouded Blade Assemblies," ASME JOURNAL OF ENGINEERING FOR GAS TURBINES AND POWER, Vol. 108, pp. 293–299.

Wagner, J. T., 1967, "Coupling of Turbomachine Blade Vibrations Through the Rotor," *ASME Journal of Engineering for Power,* Vol. 89, No. 4, pp. 502–512.

Wei, S. T., and Pierre, C., 1988a, "Localization Phenomena in Mistuned Assemblies with Cyclic Symmetry: Part I—Free Vibrations," *ASME Journal of Vibration, Acoustics, Stress, and Reliability in Design,* Vol. 110, No. 4, pp. 429–438.

Wei, S. T., and Pierre, C., 1988b, "Localization Phenomena in Mistuned Assemblies with Cyclic Symmetry: Part II—Forced Vibrations," *ASME Journal of Vibration, Acoustics, Stress, and Reliability in Design,* Vol. 110, No. 4, pp. 439–449.

Yang, M.-T., and Griffin, J. H., 1997, "A Reduced Order Approach for the Vibration of Mistuned Bladed Disk Assemblies," ASME JOURNAL OF ENGINEERING FOR GAS TURBINES AND POWER, Vol. 119, pp. 161–167.

Zheng, Z.-C., and Wang, F.-R., 1985, "Dynamic Analysis of Blade Groups Using Component Mode Synthesis," *Vibrations of Blades and Bladed Disk Assemblies,* Proceedings, ASME 10th Biennial Conference on Mechanical Vibration and Noise Cincinnati, OH, ASME, New York, pp. 97–103.

APPENDIX A

The Kronecker Product

The Kronecker product of two matrices is defined as

$$\mathbf{A} \otimes \mathbf{B} = \begin{bmatrix} a_{11}\mathbf{B} & a_{12}\mathbf{B} & \cdots & a_{1N}\mathbf{B} \\ a_{21}\mathbf{B} & a_{22}\mathbf{B} & \cdots & a_{2N}\mathbf{B} \\ \vdots & \vdots & \ddots & \vdots \\ a_{N1}\mathbf{B} & a_{N2}\mathbf{B} & \cdots & a_{NN}\mathbf{B} \end{bmatrix}. \tag{A.1}$$

The following are selected useful properties of the Kronecker product:

$$(\mathbf{A} \otimes \mathbf{B})(\mathbf{C} \otimes \mathbf{D}) = (\mathbf{AC}) \otimes (\mathbf{BD}) \tag{A.2}$$

$$(\mathbf{A} \otimes \mathbf{B})^{-1} = \mathbf{A}^{-1} \otimes \mathbf{B}^{-1} \tag{A.3}$$

$$(\mathbf{A} \otimes \mathbf{B})^{\mathrm{T}} = \mathbf{A}^{\mathrm{T}} \otimes \mathbf{B}^{\mathrm{T}} \tag{A.4}$$

APPENDIX B

Circulant Matrices and Cyclic Symmetry

The reduced order model formulation outlined in this paper makes frequent use of the properties of circulant matrices and their eigenvectors, as applied to cyclic symmetry problems. The properties of circulant matrices are thoroughly examined in Davis (1979). Moreover, a detailed description of modes of vibration for cyclic structures is contained in the important work by Thomas (1979), although certain related mathematical aspects, such as the *fundamentals of circulant matrices, appear to have been unrealized* at the time.

The general form of a square circulant matrix is

$$\mathbf{C} = \mathbf{circ}\,(c_1, c_2, \ldots, c_N) = \begin{bmatrix} c_1 & c_2 & \cdots & c_N \\ c_N & c_1 & \cdots & c_{N-1} \\ \vdots & \vdots & \ddots & \vdots \\ c_2 & c_3 & \cdots & c_1 \end{bmatrix}. \tag{B.1}$$

All circulant matrices of order N possess N independent eigenvectors. In particular, they share the same set of eigenvectors that make up the complex Fourier matrix, $\mathbf{E}$:

$$\mathbf{E} = [e_{ki}]; \quad e_{ki} = \frac{1}{\sqrt{N}} e^{j\alpha(i-1)(k-1)} \quad k, i = 1, \ldots, N, \tag{B.2}$$

where $j = \sqrt{-1}$, and $\alpha = 2\pi/N$. In addition, there exists an "almost-equivalent" real-valued form of Eq. (B.2):

$$\mathbf{F} = [\mathbf{f}_0 \quad \mathbf{f}_{1,c} \quad \mathbf{f}_{1,s} \ \ldots \ \mathbf{f}_{n,c} \quad \mathbf{f}_{n,s} \ \ldots \ \mathbf{f}_{N/2}]$$
$$= \begin{bmatrix} \frac{1}{\sqrt{N}} & \sqrt{\frac{2}{N}} & 0 & \cdots & \frac{1}{\sqrt{N}} \\ \frac{1}{\sqrt{N}} & \sqrt{\frac{2}{N}}\cos\alpha & \sqrt{\frac{2}{N}}\sin\alpha & \cdots & -\frac{1}{\sqrt{N}} \\ \frac{1}{\sqrt{N}} & \sqrt{\frac{2}{N}}\cos 2\alpha & \sqrt{\frac{2}{N}}\sin 2\alpha & \cdots & \frac{1}{\sqrt{N}} \\ \vdots & \vdots & \vdots & & \vdots \\ \frac{1}{\sqrt{N}} & \sqrt{\frac{2}{N}}\cos(N-1)\alpha & \sqrt{\frac{2}{N}}\sin(N-1)\alpha & \cdots & \frac{(-1)^{N-1}}{\sqrt{N}} \end{bmatrix}, \tag{B.3}$$

where the last column only exists if N is even.

Note that both $\mathbf{E}$ and $\mathbf{F}$ are orthonormal, or unitary, such that $\mathbf{E}^*\mathbf{E} = \mathbf{F}^{\mathrm{T}}\mathbf{F} = \mathbf{I}$, where $\mathbf{I}$ is an identity matrix of size N, and * denotes the Hermitian adjoint (complex conjugate transpose). In addition, this implies that $\mathbf{E}^{-1} = \mathbf{E}^*$ and $\mathbf{F}^{-1} = \mathbf{F}^{\mathrm{T}}$, such that the *typical transformation products* $\mathbf{E}^*\mathbf{CE}$ *and* $\mathbf{F}^{\mathrm{T}}\mathbf{CF}$ *are similarity* transformations (Strang, 1988).

The reason behind calling $\mathbf{F}$ "almost-equivalent" to $\mathbf{E}$ is that the columns of $\mathbf{F}$ are not true eigenvectors of $\mathbf{C}$, and, hence, the similarity transformation $\mathbf{F}^{\mathrm{T}}\mathbf{CF}$ will not yield a diagonalized matrix. However, it will result in a matrix where all non-zero elements will be grouped into 2 × 2 blocks ("double" harmonics) on the diagonal, except for the (1,1) and, for N even, the (N,N) elements ("single" harmonics). This matrix type is referred to as pseudo-block-diagonal.

These properties are readily extended to the case of block-circulant matrices by expanding $\mathbf{E}$ and $\mathbf{F}$ as $\mathbf{E} \otimes \mathbf{I}$ and $\mathbf{F} \otimes \mathbf{I}$, respectively. The scalar c_i then represents a matrix block $\mathbf{C}_i$, where $\mathbf{C}_i$ and $\mathbf{I}$ are of the same size. The symbol ⊗ denotes the Kronecker product, which is defined in appendix A.

Prediction of Resonant Response of Shrouded Blades With Three-Dimensional Shroud Constraint

B. D. Yang

J. J. Chen

C. H. Menq

Department of Mechanical Engineering,
206 W. 18th Avenue,
The Ohio State University,
Columbus, OH 43210

In this paper, the three-dimensional shroud contact kinematics of a shrouded blade system is studied. The assumed blade motion has three components, namely axial, tangential, and radial components, which result in a three dimensional relative motion across the shroud interface. The resulting relative motion can be decomposed into two components. The first one is on the contact plane and can induce stick-slip friction. The other component is perpendicular to the contact plane and can cause variation of the contact normal load and, in extreme circumstances, separation of the two contacting surfaces. In order to estimate the equivalent stiffness and damping of the shroud contact an approach is proposed. In this approach, the in-plane slip motion is assumed to be elliptical and is decomposed into two linear motions along the principal major and minor axes of the ellipse. A variable normal load friction force model (Yang and Menq, 1996) is then applied separately to each individual linear motion, and the equivalent stiffness and damping of the shroud contact can be approximately estimated. With the estimated stiffness and damping, the developed shroud contact model is applied to the prediction of the resonant response of a shrouded blade system. The effects of two different shroud constraint conditions, namely two-dimensional constraint and three-dimensional constraint, on the resonant response of a shrouded blade system are compared and the results are discussed.

Introduction

In the turbine jet engine industry, shrouds are often employed in turbine design to attenuate blade vibration and at the same time to increase aeroelastic stability of the turbine. During the engine operation, the shrouded fan blades rotate through the fluid flow with severe fluctuation, and as a result, the blades vibrate and experience friction constraint at the shroud contact. During a cycle of motion, the shroud contact point experiences alternating stick-slip friction force that adds friction damping as well as additional spring force to the system (Cameron et al., 1990; Ferri, 1996; Griffin, 1980). Therefore, in order to analytically evaluate the performance of the shroud and to help the design, there is a need to consider this three-dimensional shroud constraint so that the resulting resonant frequencies and vibration magnitudes of the shrouded blades can be accurately estimated.

The protruding shrouds constrain the blade motions not only along the contact plane but also along the normal direction of the plane, resulting in complex contact kinematics, in which the relative motion has two components: in-plane tangential motion on the contact plane and normal component perpendicular to the contact. The in-plane tangential relative motion is two-dimensional, and it can induce stick-slip friction (Yang and Menq, 1996). On the other hand, the normal relative motion can cause variation of the contact normal load and, in extreme circumstances, separation of the two contacting surfaces, an effect which cannot be adequately modeled by a simple friction contact model having constant normal load (Griffin, 1980). In our prior study (Yang and Menq, 1996), a two-dimensional version of shroud contact kinematics was investigated, in which the interface retains the normal component of the relative motion that causes normal load variation, while the in-plane tangential component of the relative motion degenerates into linear motion. This simplification is the result of neglecting the radial component of the blade motion and can be regarded as the first step towards understanding the effect of shroud contact kinematics on the resonant response of a shrouded blade system. In other words, in this shroud contact model, the assumed blade motion has only two components, namely axial and tangential components. These two components results in a relative motion which has linear trajectory on the shroud contact plane and has the other component perpendicular to the shroud contact plane. Since shrouds protrude from the sides of the airfoils, the radial component of the relative motion of the shroud contact may become as important as the other two components. If this is the case, the actual relative motion on the shroud contact plane will have an elliptical trajectory rather than a linear one. Since the effective stiffness of the friction interface and the energy dissipated by friction are strongly effected by the relative motion between the two contact surfaces, the assumed trajectory of the relative motion becomes very important to the prediction of the resonant amplitude and frequency of the shrouded blade system. In other worlds, assuming a linear trajectory imposes a rather severe limitation on the predictive ability of the current approach.

In this paper, the three-dimensional shroud contact, including contact geometry and kinematics, of a shrouded blade system is studied. The assumed blade motion has three components, namely axial, tangential, and radial components. At the shroud contact, these three components result in a three dimensional relative motion which has a two dimensional trajectory on the shroud contact plane and the other component perpendicular to the contact plane. It is apparent that the two components of the in-plane two dimensional slip motion are coupled together when inducing stick-slip friction. However, the coupling effect of a two dimensional

---

Contributed by the International Gas Turbine Institute (IGTI) of THE AMERICAN SOCIETY OF MECHANICAL ENGINEERS for publication in the ASME JOURNAL OF ENGINEERING FOR GAS TURBINES AND POWER. Paper presented at the International Gas Turbine and Aeroengine Congress and Exhibition, Stockholm, Sweden, June 2–5, 1998; ASME Paper 98-GT-485.

Manuscript received by IGTI March 25, 1998; final revision received by the ASME Headquarters March 23, 1999. Associate Technical Editor: R. Kielb.

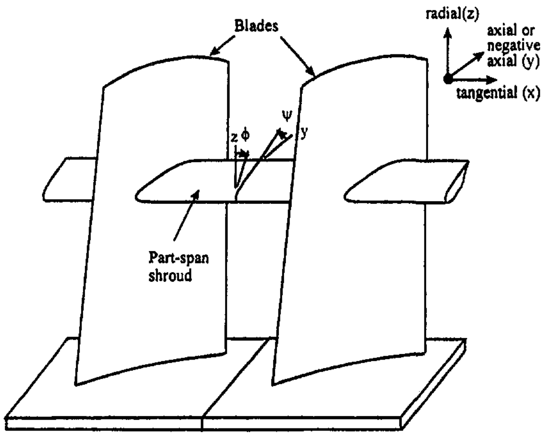

Fig. 1 Contact geometry of a shrouded blade system

relative motion having variable normal load on the stick-slip phenomenon is not well understood at this stage. To estimate the equivalent stiffness and damping of the shroud contact experiencing a two-dimensional slip motion and a variable normal load, the first attempt of this study is to use an approximate approach. In this approach, the in-plane slip motion is assumed to be elliptical and is decomposed into two linear motions along the principal major and minor axes of the ellipse. A variable normal load friction force model (Yang and Menq, 1996) is then applied separately to each individual linear motion, and the equivalent stiffness and damping of the shroud contact can be approximately estimated. With the estimated stiffness and damping, the developed shroud contact model can be applied to the prediction of the resonant response of a shrouded blade system. In this paper, the effects of two different shroud constraint conditions, namely two-dimensional constraint and three-dimensional constraint, on the resonant response of a shrouded blade system are compared and the results are discussed.

Three-Dimensional Shroud Contact

In the analysis of a shrouded bladed system, a great simplification can be obtained by assuming that the bladed system is tuned, namely each blade of the system has exactly the same dynamic characteristics. In addition, the excitation of interest is that induced by the blades rotating through circumferential variations in the flow field. It can be shown that in effect each blade is exposed to a periodic excitation having the same amplitude but differing in phase by an amount which is proportional to the blade's angular location on the disk. It is assumed that the resonant response of the bladed system is also periodic and has the same fundamental period as the excitation. Thus the external excitation and the motions of the blades as well as the nonlinear constrained forces can be represented by infinite Fourier series. By truncating these series after the fundamental terms, an approximate solution assuming that the resonant response is simply harmonic can be derived (Menq and Griffin, 1985; Menq et al., 1986; Yang and Menq, 1996). In this approach, each blade vibrates in the same manner but with an interblade phase difference (φ) from its adjacent blades. The interblade phase angle is defined as follows:

$$\varphi = \frac{2\pi E}{N}, \tag{1}$$

where N is the total number of the blades in the system, and E is the engine order of the excitation on the system.

Contact Geometry. Figure 1 shows two shrouded blades contact each other through their protruding shrouds and the xyz coordinate system is defined in accordance with the tangential (x), axial (y or $-y$), and radial (z) directions. The geometry of the three-dimensional shroud contact is defined by two angles ψ (called shroud angle) and ϕ (called inclination angle), whose detailed definitions are shown in Fig. 2. First, a shroud contact plane with its normal pointing towards the x-axis is shown in Fig. 2(a). By orienting the contact plane a ψ angle with respect to the z-axis, a new contact plane is obtained and shown in Fig. 2(b). The $x'y'z'$ coordinate system associates with this oriented plane, and its x'-axis is along the normal direction of the plane and the y' and z'-axes are on the plane. The final geometry of the three-dimensional shroud contact can be obtained by rotating the oriented plane again a ϕ angle with respect to the y'-axis, and the configuration is shown in Fig. 2(c). The $x''y''z''$ (or uvw) coordinate system associates with this oriented plane, and its x'' (v) axis is along the normal direction of the plane and the y'' (u) and z'' (w) axes are on the plane. In this paper, the global coordinate system is specified by three basis unit vector, namely $[\hat{\mathbf{x}}\ \ \hat{\mathbf{y}}\ \ \hat{\mathbf{z}}]$, and the local coordinate system is defined as $[\hat{\mathbf{v}}\ \ \hat{\mathbf{u}}\ \ \hat{\mathbf{w}}]$. These two coordinate systems can be related to each other as follows.

$$[\hat{\mathbf{v}}\ \ \hat{\mathbf{u}}\ \ \hat{\mathbf{w}}] = [\hat{\mathbf{x}}\ \ \hat{\mathbf{y}}\ \ \hat{\mathbf{z}}]\mathbf{T}_0, \tag{2}$$

where $\mathbf{T}_0$ is the coordinate transformation matrix.

$$\mathbf{T}_0 = \begin{bmatrix} \cos\psi\cos\phi & -\sin\psi & \cos\psi\sin\phi \\ \sin\psi\cos\phi & \cos\psi & \sin\psi\sin\phi \\ -\sin\phi & 0 & \cos\phi \end{bmatrix}. \tag{3}$$

In current design practice, the inclination angle ϕ is often set to be zero.

Contact Kinematics. Figure 3 depicts two neighboring blades of a shrouded blade system, whose protruding shrouds are brought into contact with their neighboring shrouds by the centrifugal force during the engine operation. A "substructure" can be used to represent the friction interface that contains the contact plane and small portions of the two neighboring shrouds. Compared to the otherwise massive structure, the substructure can be modeled as two massless elastic elements that are held together by a preload n_0. The points A and B, which are located almost at the ends of the

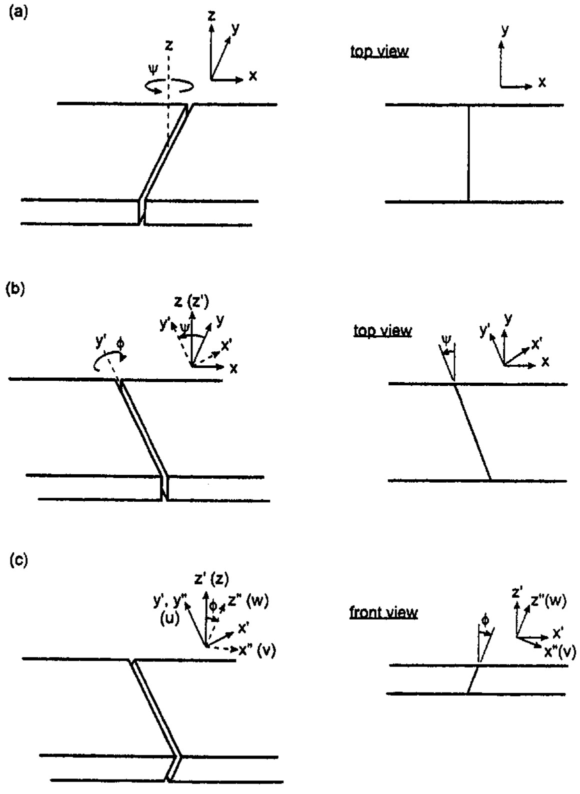

Fig. 2 Definition of shroud angle ψ and inclined angle ϕ

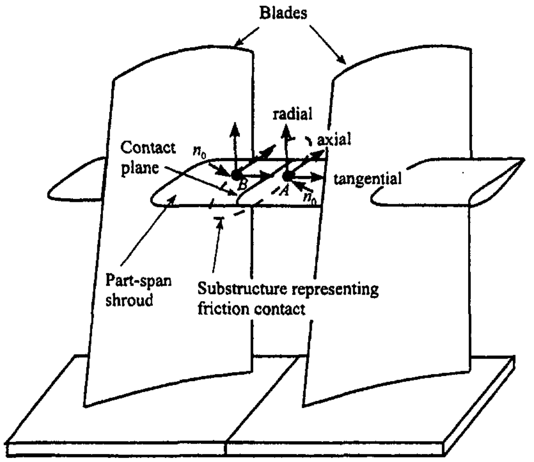

Fig. 3 Shroud contact of two neighboring shrouded blades

protruding shrouds, are the outermost points of these two elastic elements; the difference of their respective motions can describe the relative motion of the two neighboring shrouds. When the beam-like turbine blade is subjected to excitation during the engine operation, the twisting action of the blade can cause the points A and B to vibrate in the tangential and axial directions, while the bending action can cause the points A and B to vibrate in the radial direction. Therefore, the motion of the two points are three-dimensional.

In this paper, the three dimensional motion is limited to the one having an elliptical trajectory in the three-dimensional space and can be represented as a coordinate vector as follows:

$$\mathbf{x} = \begin{bmatrix} x \\ y \\ z \end{bmatrix} = \begin{bmatrix} A_x \sin(\omega t + \phi_x) \\ A_y \sin(\omega t + \phi_y) \\ A_z \sin(\omega t + \phi_z) \end{bmatrix}$$

$$= \begin{bmatrix} x_s & x_c \\ y_s & y_c \\ z_s & z_c \end{bmatrix} \begin{bmatrix} \sin \omega t \\ \cos \omega t \end{bmatrix}, \tag{4}$$

where ω and t are the oscillating frequency and time. For a shrouded blade, several pairs of shroud contact points can be defined. For each pair of shroud contact points, one is on the right and the other left and their motions are denoted as $[\mathbf{x}_r \quad \mathbf{x}_l]^T$.

Since the shrouded blade system is assumed to be tuned, the condition of cyclic symmetry can be applied when deriving the relative motion of a shroud contact. Take the relative motion between the point B of the right shroud and the point A of the left shroud in Figure 3 as an example. First, the motions of the two contact points of the first shrouded blade (left one) are defined and they are $[\mathbf{x}_r \quad \mathbf{x}_l]^T$. Therefore, the motion of point B is now $\mathbf{x}_r$ and the motion of point A differs from $\mathbf{x}_l$ with the interblade phase angle (φ). As a result, the relative motion of the two neighboring shrouds, $\mathbf{w}_r$, can be derived as

$$\mathbf{w}_r = \mathbf{T}_1[\mathbf{x}_r \quad \mathbf{x}_l]^T \tag{5}$$

where $\mathbf{T}_1$ is the interblade relative displacement transformation matrix.

$$\mathbf{T}_1 = [\mathbf{I}_{3\times 3} \quad -e^{-j\varphi}\mathbf{I}_{3\times 3}] \tag{6}$$

It is worthy noting that only the relative motion at the right shroud contact point is derived. Since the shrouded blade system is assumed to be tuned, the relative motion and the resulting constrained force of the left shroud contact point can be related to those of the right shroud contact point by using the condition of cyclic symmetry. Since both $\mathbf{x}_r$ and $\mathbf{x}_l$ are elliptical motions, the resulting relative motion $\mathbf{w}_r$ also has elliptical trajectory in the three-dimensional space.

The elliptical relative motion is often not parallel to the contact plane. In order to analyze the induced friction, the elliptical relative motion in the three-dimensional space can be decomposed into an in-plane elliptical motion on the contact plane and a sinusoidally varying component normal to the contact plane. The in-plane elliptical motion can induce stick-slip friction, and thus can attenuate the resonant response of the shrouded blades. On the other hand, the normal component tends to alter the normal load across the interface; and this effect, in extreme circumstances, may lead to a separation of the interface. This decomposition is shown in Figure 4 schematically. It should be noted that the variable normal load is taken as the sum of the initial contact pressure at equilibrium plus a term that is proportional to the sinusoidally varying normal component of the relative motion. Since this decomposition is to transfer the relative motion from the global coordinate system to the local coordinate system defined in equation (2), it can be carried out by performing a coordinate transformation on the three-dimensional relative motion.

$$\mathbf{u}_r = \mathbf{T}_0^T \mathbf{w}_r \tag{7}$$

Here the three-dimensional relative motion is described in the local coordinate system as follows:

$$\mathbf{u}_r = \begin{bmatrix} v \\ u \\ w \end{bmatrix} = \begin{bmatrix} v_s & v_c \\ u_s & u_c \\ w_s & w_c \end{bmatrix} \begin{bmatrix} \sin \omega t \\ \cos \omega t \end{bmatrix} \tag{8}$$

Constrained Force at Shroud Contact

After the decomposition, the u and w components of the relative motion follow an elliptical trajectory on the contact plane and can induce the stick-slip friction, while the v component can cause the normal load across the interface to vary dynamically. It is apparent that the u and w motions are coupled together when inducing stick-slip friction. However, the coupling effect of a two-dimensional relative motion having variable normal load on the stick-slip phenomenon is not well understood at this stage. To estimate the equivalent stiffness and damping of a shroud contact experiencing a two-dimensional slip motion and a variable normal load, the first attempt of this study is to use an approximate approach. In this approach, the in-plane elliptical motion is decomposed into two linear motions along the principal major and minor axes of the ellipse. Let u' and w' be the principal major and minor axes, respectively. The decoupled relative motion can be derived as follows:

$$\mathbf{u}'_r = \mathbf{T}_2 \mathbf{u}_r \tag{9}$$

and

$$\mathbf{T}_2 = \begin{bmatrix} 1 & 0 & 0 \\ 0 & \cos\alpha & \sin\alpha \\ 0 & -\sin\alpha & \cos\alpha \end{bmatrix}, \tag{10}$$

where $\mathbf{T}_2$ is the decoupling matrix, and α is the inclination of the principle major axis $\hat{u}'$ to the local coordinate axis $\hat{u}$, as shown in Fig. 5. Based on the coordinate vector of the relative motion defined in Eq. (8), the inclination can be established as follows.

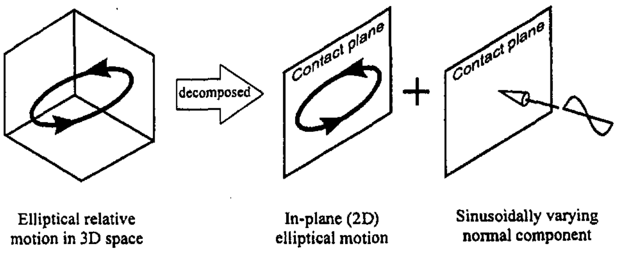

Fig. 4 Decomposition of three-dimensional elliptical relative motion

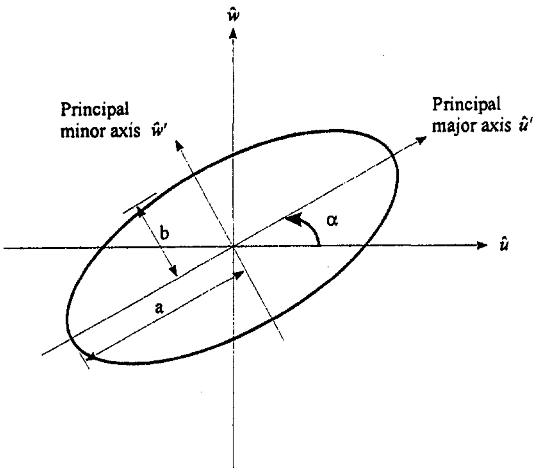

Fig. 5 An elliptical trajectory and its principal axes

$$\alpha = \frac{1}{2}\left\{\tan^{-1}\left[\frac{u_c + w_s}{u_s - w_c}\right] + \tan^{-1}\left[\frac{w_s - u_c}{u_s + w_c}\right]\right\}. \tag{11}$$

The concept of two decoupled linear motions is shown in Fig. 6. After the in-plane tangential motion is decoupled into two linear motions, a well developed variable normal load shroud contact model[1] (Yang and Menq, 1996) can be applied separately to each individual linear motions, and the equivalent stiffness and damping of the shroud contact can be approximately estimated, as shown in Fig. 7. Based on this approach, a simplified three-dimensional shroud contact model is developed.

Using the available variable normal load friction force model (Yang and Menq, 1996), the constrained force at the right shroud contact point can be determined. It is a nonlinear function of the decoupled relative motions and can be expressed as follows:

$$\mathbf{p}'_r = \begin{bmatrix} \mathbf{p}'_{rv} \\ \mathbf{p}'_{ru} \\ \mathbf{p}'_{rw} \end{bmatrix} = \begin{bmatrix} \mathbf{p}'_{rv}(v') \\ \mathbf{p}'_{ru}(v', u') \\ \mathbf{p}'_{rw}(v', w') \end{bmatrix}, \tag{12}$$

where the nonlinear functions, $\mathbf{p}'_{rv}(v')$, $\mathbf{p}'_{ru}(v', u')$, and $\mathbf{p}'_{rw}(v', w')$, were established in (Yang and Menq, 1996). The constrained force is now defined in the principal directions. It can be transferred to the local coordinate system using the transpose of the decoupling matrix.

$$\mathbf{p}_r = \mathbf{T}_2^T \mathbf{p}'_r \tag{13}$$

Then, the constrained force can be transferred to the global coordinate system as follows:

$$\mathbf{f}_r = \mathbf{T}_0 \mathbf{p}_r. \tag{14}$$

Furthermore, the constrained forces at a pair of shroud contact points can be related to the force at the right shroud contact point using the interblade relative displacement transformation matrix.

$$\begin{bmatrix} \mathbf{f}_r \\ \mathbf{f}_l \end{bmatrix} = \mathbf{T}_1^H \mathbf{f}_r, \tag{15}$$

where $\mathbf{T}_1^H$ is the complex conjugate transpose of $\mathbf{T}_1$.

Prediction of Resonant Response

The equation of motion of a shrouded blade under a harmonic excitation can be expressed as follows:

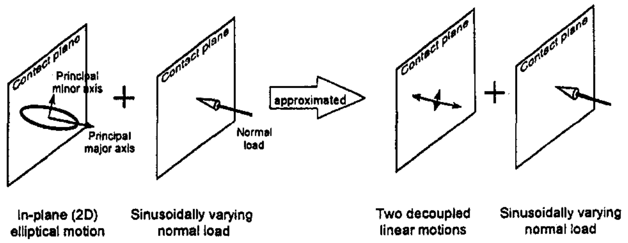

Fig. 6 Decoupled in-plane motion

$$\mathbf{m}\ddot{\mathbf{x}} + \mathbf{c}\dot{\mathbf{x}} + \mathbf{k}\mathbf{x} = \mathbf{f}_e - \mathbf{f}_N, \tag{16}$$

where $\mathbf{x}$ is the nodal displacement vector, $\mathbf{m}$ is the mass matrix, $\mathbf{c}$ is the damping matrix, $\mathbf{k}$ is the stiffness matrix, $\mathbf{f}_e$ is the external harmonic excitation, and $\mathbf{f}_N$ is the nonlinear constrained force which is a nonlinear function of the relative motion at the shroud contact. The finite element model can be three-dimensional and if the model contains n nodes, all the matrices will be $3n \times 3n$ matrices, and all the vectors will be $3n$-element vectors.

The external harmonic excitation can be expressed as follows:

$$\mathbf{f}_e(t) = \mathbf{f}_e e^{j\omega t}, \tag{17}$$

where ω is the excitation frequency and $\mathbf{f}_e$ is a complex vector representing the magnitude and phase of the excitation. It is worthy noting that except for the elements associated with those shroud contact points the other elements of $\mathbf{f}_N$ are zeros. It is clear that the nonlinear aspect of the dynamic problem is embedded in the nonlinear friction force $\mathbf{f}_N$. By using the modal analysis method, the mode shape matrix can be obtained and is denoted as Φ. Using the mode shape matrix and the associated modal information, the receptance of the blade can be derived.

$$\mathbf{r} = [r_{kl}] = \sum_{i=1}^{3n} (\Phi_i \Lambda_i \Phi_i^T) \tag{18}$$

and

$$\Lambda_i = [(\mathbf{k}_i - \omega^2 \mathbf{m}_i) + j(\omega \mathbf{c}_i)]^{-1}, \tag{19}$$

where r_{kl} is defined as the steady state response of the kth node due to unit harmonic excitation force at the lth node, Φ_i is the ith mode shape, $\mathbf{m}_i$ is the ith modal mass, $\mathbf{k}_i$ is the ith modal stiffness, and $\mathbf{c}_i$ is the ith modal damping.

When the blade is constrained by its neighboring blades through shroud contacts, the resulting constrained forces are characterized by the displacements of a pair of contact points, $[\mathbf{x}_r \quad \mathbf{x}_l]^T$, and they can be considered as feedback forces that influence the response of the blade. This feedback effect along with the contact

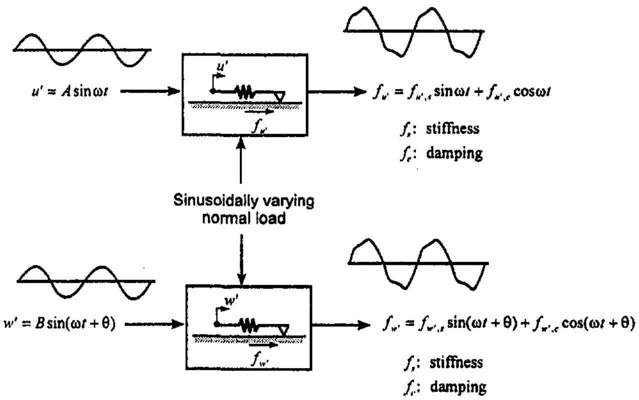

Fig. 7 Estimation of effective stiffness and damping

---

[1] This shroud contact model has been successfully used in the two-dimensional shroud contact analysis, in which the two-dimensional contact kinematics consists of a linear motion that induces friction and a sinusoidally varying normal component that causes the normal load to alter dynamically.

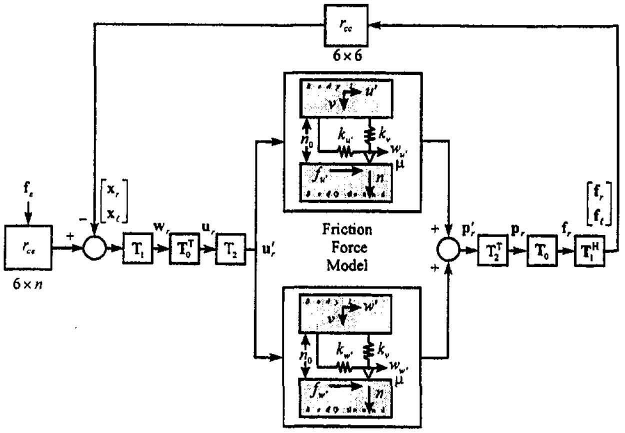

Fig. 8 Nonlinear feedback loop and calculation of nonlinear constrained force

kinematics is shown in Fig. 8. By using the harmonic balance method, the constrained forces can be approximated by harmonic functions having the same frequency as the external harmonic excitation, and their amplitude and phase are nonlinear functions of the displacements of the pair of contact points. From the nonlinear feedback loop shown in Fig. 8, it is evident that in the calculation of nonlinear forced response of a shrouded blade, all the linear degrees of freedom can be condensed to receptance and the modeling of friction contact can be separated from the complex structure model. This approach results in a set of nonlinear algebraic equations, which can be formulated as follows:

$$\begin{bmatrix}\mathbf{x}_r\\ \mathbf{x}_l\end{bmatrix} = \mathbf{r}_{ce}\mathbf{f}_e - \mathbf{r}_{cc}\begin{bmatrix}\mathbf{f}_r\\ \mathbf{f}_l\end{bmatrix}, \tag{20}$$

where $[\mathbf{x}_r \quad \mathbf{x}_l]^T$ is the nodal displacement vector of the right and left shroud contact points, $[\mathbf{f}_r \quad \mathbf{f}_l]^T$ is the resulting constrained force vector, $\mathbf{r}_{ce}$ is the receptance at the shroud contact points due to unit harmonic excitation force, and $\mathbf{r}_{cc}$ is the receptance at the shroud contact points due to unit constrained force.

Effect of Three-Dimensional Shroud Contact

A shrouded blade system is employed to demonstrate the effect of three-dimensional shroud constraint on the resonant response when compared to two-dimensional shroud constraint. The shrouded blade system is assumed tuned and 20 modes of a single blade are included in the prediction of the resonant response. Each mode shape consists of axial, tangential, and radial components.

The resonant response predicted by using three-dimensional shroud constraint is compared with that predicted by using two-dimensional shroud constraint (Yang and Menq, 1996). Figures 9, 10, and 11 show the prediction of the resonant response when the shroud contact is fully stuck. It is clear that the blade's resonant frequency changes significantly from the region where it is fully slipping, to the region where it is fully stuck. Since three-dimensional shroud constraint provides additional stiffness, the resulting resonant frequency is significantly higher than that predicted using two-dimensional shroud constraint. Figure 9 shows that in the axial direction, in addition to the frequency shift, the amplitude of the resonant response is attenuated to 26.2 percent, using three-dimensional shroud constraint, and 28.8 percent, using two-dimensional shroud constraint, when the shroud contact is fully stuck. However, as shown in Fig. 10, the amplitude attenuation in the tangential direction is much greater, e.g., attenuated to 0.22 percent, using three-dimensional constraint, and 0.39 percent, using two-dimensional constraint. It is evident that the additional stiffness provided by the shroud contact is more significant in the tangential direction than in the axial direction. Figure 11 shows the resonant response in the radial direction. It is clear that when the shroud contact is fully stuck three-dimensional constraint provides additional constraint in the radial direction, therefore, the resonant response is much significantly attenuated.

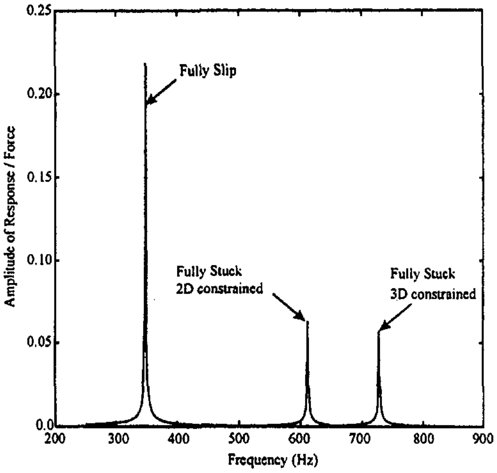

Fig. 9 Resonant frequency shift and magnitude attenuation (axial direction)

Figures 12, 13, and 14 show the effect of preload, n_0, on the resonant response in the axial, tangential, and radial directions

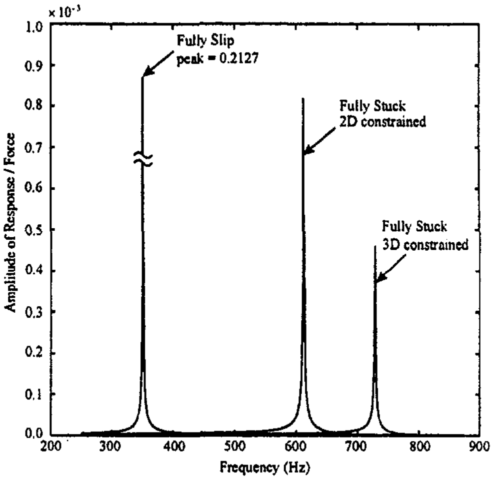

Fig. 10 Resonant frequency shift and magnitude attenuation (tangential direction)

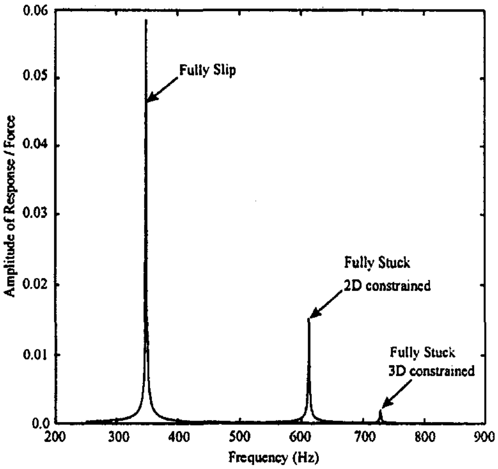

Fig. 11 Resonant frequency shift and magnitude attenuation (radial direction)

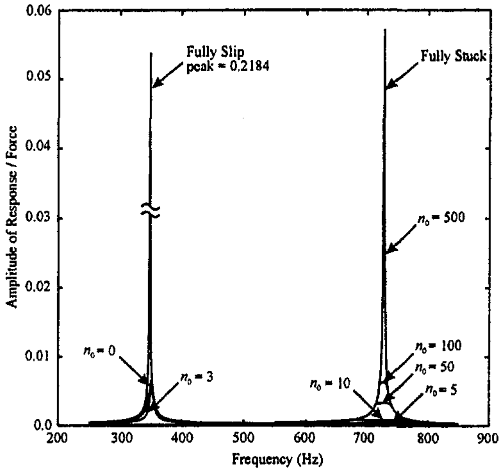

Fig. 12 Effect of preload on the resonant response (axial direction)

respectively. It can be seen that when the preload is small the shroud contacts provide mostly damping effect; therefore, the resonant response is attenuated. When increasing preload both damping and stiffness are in effect and the resonant frequency shifts to higher side. However, when the preload becomes too high, damping starts to diminish and the resonant response rises rapidly. In this simulation, $n_0 = 10$ can be considered as the optimal preload, which gives the minimum response.

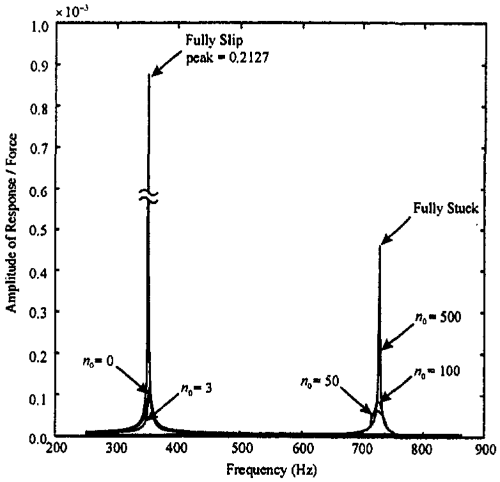

Fig. 13 Effect of preload on the resonant response (tangential direction)

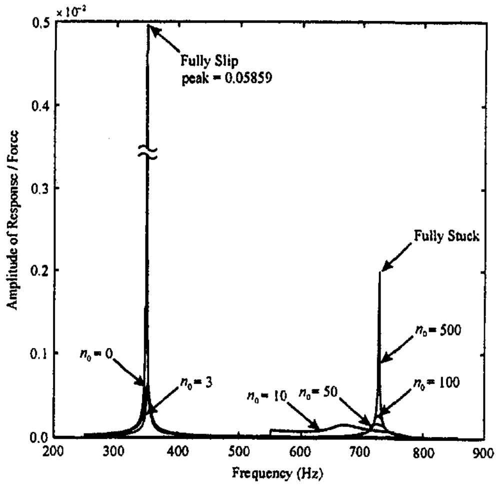

Fig. 14 Effect of preload on the resonant response (radial direction)

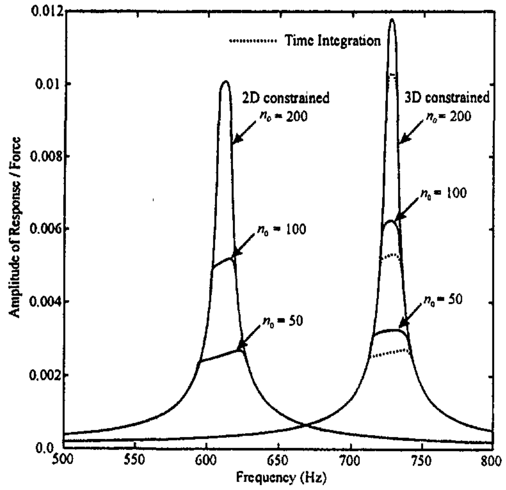

Fig. 15 Comparison of resonant responses with time-integration (axial direction)

Comparison With Time Integration Method

Since the proposed approach uses two steps of approximation, it is necessary to examine the accuracy of the predicted results. Figures 15 and 16 show the comparison of the predicted results with those of time integration. In these two figures, the predicted results using two-dimensional and three-dimensional constraint are also compared. Each figure shows three groups of tracking curves. These tracking curves are the predicted resonant response of the shrouded blade system for the cases in which contact preload is relatively high. High contact preload is usually desirable for shroud design. The first group of curves are the predicted results using time integration method and the second group are those of the proposed approach using three dimensional shroud constraint. It can be seen that the proposed approach predicts the frequency and amplitude of the resonant response reasonably well. The third group of curves are the predicted results when applying two dimensional shroud constraint. It is evident that the resonant frequency is underestimated. It can also be seen in Figure 16 that the resonant amplitude in the radial direction is much overestimated when using two dimensional shroud constraint.

Conclusion

In this paper, the three-dimensional shroud contact kinematics of a shrouded blade system is studied and a simplified three-

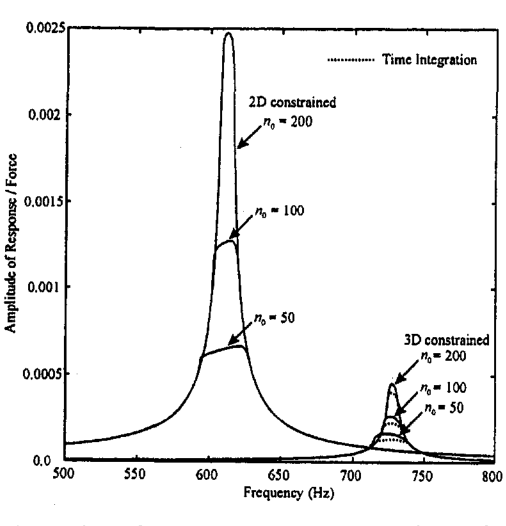

Fig. 16 Comparison of resonant responses with time-integration (radial direction)

dimensional shroud contact model is developed. In this study, the assumed blade motion has three components, namely axial, tangential, and radial components, which result in a three-dimensional relative motion at the shroud contact. The resulting relative motion has an in-plane component and the other component perpendicular to the contact plane. The in-plane tangential relative motion can have an elliptical trajectory, and it induces stick-slip friction. On the other hand, the normal relative motion can cause variation of the contact normal load and, in extreme circumstances, separation of the two contacting surfaces.

Using the developed shroud contact model, the equivalent stiffness and damping of the shroud contact can be approximately estimated. With the estimated stiffness and damping, the developed shroud contact model is applied to the prediction of the resonant response of a shrouded blade system. It is shown that since three-dimensional shroud constraint provides additional stiffness, when the shroud contact has high preload and it is near the region of fully stuck the resulting resonant frequency is significantly higher than that predicted using two-dimensional shroud constraint. It is also shown that when the shroud contact is fully stuck three-dimensional constraint provides additional constraint in the radial direction; therefore, the resonant response in the radial direction is much significantly attenuated.

The effect of preload, n_0, on the resonant response of a shrouded blade system is also studied. It shows that when the preload is small the shroud contacts provide mostly damping effect, therefore, the resonant response is attenuated. When increasing preload both damping and stiffness are in effect and the resonant frequency shifts to higher side. However, when the preload becomes too high, damping starts to diminish and the resonant response rises rapidly.

In order to examine the accuracy of the proposed approach, the predicted results are compared with those obtained using time integration method. It is shown that the proposed approach predicts the frequency and amplitude of the resonant response reasonably well.

Acknowledgment

This material is based on the work supported by the Naval Air Systems Command under Contract NO. N00421-96-C-5145 and by the GUIde Consortium under Contract No. 537934-52253. Any opinions, findings, and conclusions or recommendations expressed in this material are those of the authors and do not necessarily reflect the views of the Naval Air Systems Command or the GUIde Consortium.

References

Cameron, T. M., Griffin, J. H., Kielb, R. E., and Hoosac, T. M., 1990, "An Integrated Approach for Friction Damper Design," *ASME Journal of Vibration, Acoustics, Stress, and Reliability in Design,* Vol. 112, pp. 175–182.

Ferri, A. A., 1996, "Friction Damping and Isolation Systems," *ASME Journal of Vibration and Acoustics,* Vol. 117(B), pp. 196–206.

Griffin, J. H., 1980, "Friction Damping of Resonant Stresses in Gas Turbine Engine Airfoil," *ASME Journal of Engineering for Power,* Vol. 102, pp. 329–333.

Menq, C. H., and Griffin, J. H., 1985, "A Comparison of Transient and Steady State Finite Element Analysis of the Forced Responses of a Frictionally Damped Beam," *ASME Journal of Vibration, Acoustic, Stress, and Reliability in Design,* Vol. 107, pp. 19–25.

Menq, C. H., Griffin, J. H., and Bielak, J., 1986, "The Forced Responses of Shrouded Fan Stages," *ASME Journal of Vibration, Acoustic, Stress, and Reliability in Design,* Vol. 108, pp. 50–55.

Svinivasan, A. V., and Cutts, D. G., 1983, "Dry Friction Damping Mechanisms in Engine Blades," *ASME Journal of Engineering for Power,* Vol. 105, pp. 332–341.

Williams, E. J., and Earles, S. W., 1974, "Optimization of the Response of Frictionally Damped Beam Type Structures with Reference to Gas Turbine Compressor Blading," *ASME Journal of Engineering for Industry,* Vol. 96, pp. 471–476.

Yang, B. D., and Menq, C. H., 1996, "Modeling of Friction Contact and Its Application to the Design of Shroud Contact," ASME Paper 96-GT-472.

K. Rama Mohan
Assistant Professor.
VNR Vignana Jyothi
Institute of Engineering and Technology,
Batchpally, Hyderabad,
Andhra Pradesh,
India

C. M. Vara Parasad
Principal.
Sri Venkateswara
Engineering College, Suryapet,
Nalgonda (Dt.),
Andhra Pradesh,
India

M. V. S. Murali Krishna
Senior Lecturer.
Mechanical Engineering Department,
Chaitanya Bharati Institute of Technology,
Gandipet, Hyderabad,
Andhra Pradesh,
India

Performance of a Low Heat Rejection Diesel Engine With Air Gap Insulated Piston

A threaded air gap insulated piston provided effective insulation without causing sealing problems. The performance of the diesel engine with the air gap insulated piston was obtained with different piston crown materials, at differing magnitudes of air gap with varying injection timings. The engine using Nimonic for the piston crown with an air gap of 3 mm at an injection timing of 29.5° bTDC reduced the BSFC by 12 percent at part loads and 4 percent at full load. The performance in terms of P-θ and T-θ was predicted employing a zero dimensional multizone combustion model, and the model results have been validated with measured pressures and the exhaust gas temperatures. More appropriate piston surface temperatures were employed in Annand's equation to improve the computer predictions using finite element modeling of the piston. The measured temperatures of air in the air gap using an L-link mechanism provided excellent validation for the finite element prediction of isotherms in the piston.

Introduction

The second law requirement of Thermodynamics necessitates the inevitable heat loss to the coolant to realise work output. Any saving in this part of the energy distribution would either increase the energy lost through exhaust gases or increase the power output. Considerable efforts are under way to reduce heat loss to the coolant by various researchers. However, the results are a little confusing as to whether the insulation would improve or deteriorate thermal efficiency. The two approaches that are being pursued to decrease heat rejection are (1) ceramic coating and (2) air gap insulation. Both these methods are still having problems. Ceramic coatings are found to be peeling off over a period of operation. There are serious problems of leakage of gases in the case of air gap insulation.

Krishnan et al. (1980) and Wade et al. (1984) observed an improvement in thermal efficiency with ceramic coated components. While Woschni et al. (1987) and Cole et al. (1985) reported reduction in BSFC with an air gap insulated piston at part loads, Woschni found deterioration of engine performance and Cole observed no change in fuel economy at full load. However Cheng et al. (1989) reported that the BSFC increased when chamber walls were insulated with ceramic coatings and Alkidas et al. (1987) found deterioration of engine performance with air gap insulated piston. Though Cole et al. and Parker et al. (1987) observed effective insulation provided by an air gap, the bolted design employed by them could not provide complete sealing of air in the air gap. While Seigla et al. (1989) and Miyairi et al. (1988) found deterioration of engine performance with retarded injection timings, Dhinagar et al. (1989) claimed improved performance with retarded injection timing in low heat rejection (LHR) engines.

A two zone combustion model was used by Miyairi (1988) and a computer simulation model was used by Rafiqul Islam et al. (1991) for predicting the performance of the ceramic coated direct injection (DI) diesel engines.

A study of the existing literature on LHR engines thus reveals inconclusive results. There is not only a need to develop a satisfactory technique of joining the crown with the piston body, achieving complete and durable sealing of the air gap, but also to adjust the injection timing as the combustion phenomenon in LHR engines gets modified. No systematic study has been reported on the use of different crown materials with varying magnitudes of air gap for an air gap insulated piston. The performance of the engine with an air gap insulated piston employing different crown materials with varying magnitudes of the air gap is reported in this paper. The paper also attempts to develop a multizone model with more appropriate input for more precise prediction of performance of LHR engines.

Experimental Program

As an attempt to insulate the combustion chamber, a threaded design of air gap insulated piston was employed in a single cylinder direct injection diesel engine. The details of the air gap provided in the piston are shown in the Fig. 1.

This design could provide perfect sealing of air in the air gap. Figure 2 shows the experimental setup employed. The test engine (1) which is a constant speed engine has an aluminum alloy piston with a bore of 80 mm and a stroke of 110 mm. The rated output of the engine was 3.68 kW at the rated speed of 1500 rpm. The compression ratio 16:1 and the manufacturer's recommended injection timing and injection pressure are 27° bTDC and 195 bars, respectively. The fuel injector has 3 holes of size 0.25 mm. The combustion chamber consists of direct injection type with no special arrangement for swirling motion of air. The naturally aspirated engine was provided with water cooling system in which the outlet water temperature was maintained at 60°C by adjusting the water flow rate. The engine oil was provided with a pressure feed system and no temperature control was provided for measuring oil temperature. The engine is coupled to a hydraulic dynamometer (2). Air and fuel consumption were measured using air flow meter (3) and fuel measuring pipette (4). The outlet temperature of water and the exhaust gas temperatures were observed using a gas thermometer (5) and an iron-iron constantan thermocouple connected to temperature indicator (6). The mass flow rate of cooling water is measured using a measuring tank (7). The piston temperatures are noted using an iron-iron constantan ther-

---

Contributed by the Internal Combustion Engine Division (ICE) of The American Society of Mechanical Engineers for publication in the ASME Journal of Engineering for Gas Turbines and Power.

Manuscript received by the ICE February 10, 1997; final revision received by the ASME Headquarters March 3, 1999. Associate Technical Editor: D. Assanis.

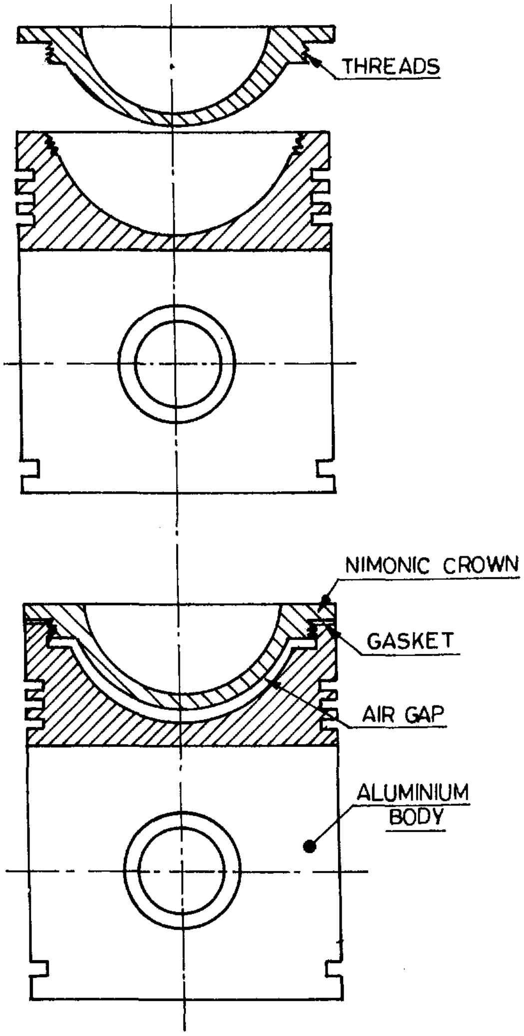

Fig. 1 Details of air gap insulated piston

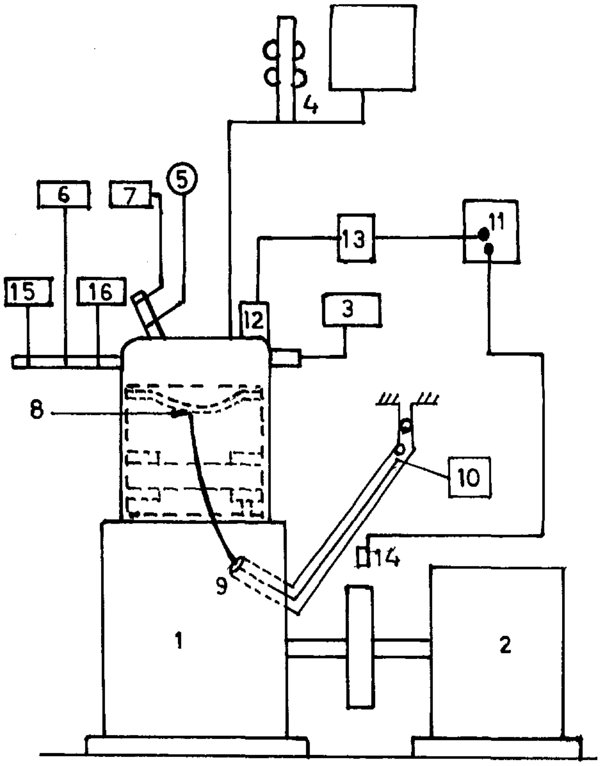

Fig. 2 Experimental set-up

mocouple (8) connected through an L-link mechanism (9) millivoltmeter (10). The pressure crank angle diagrams were obtained at full load operation of the engine with each piston configuration using a double beam oscilloscope (11), Kistler piezo electric pressure transducer (12), charge amplifier (13), and a magnetic pickup (14). The smoke levels of the engine were noted using a Nisalco smoke meter (15). Exhaust pollutants CO and NOx were measured using a sophisticated microprocessor based TMT-36 stack analyser (16). With each configuration of air gap insulated piston load tests were carried out from which performance data like brake specific fuel consumption (BSFC), exhaust gas temperature (EGT), coolant load and volumetric efficiency were calculated for different brake mean effective pressures (BMEP). Based on the pressure crank angle diagrams, combustion parameters like peak pressure (PP), time of occurrence of peak pressure (TOPP), maximum rate of pressure rise (MRPR), and average rate of pressure rise (ARPR) were evaluated.

Nomenclature

a, b, c = constants in Annand's equation
aTDC = after top dead center
A = area
bTDC = before top dead center
B = Spalding number
C_p, C_v = specific heat at constant pressure or volume
D = binary diffusion coefficient
D_1 = cylinder bore
D_{32} = Sauter mean diameter
F_w = validation constant
h = enthalpy
HSU = Hartridge smoke units
IT = injection timing
k = thermal conductivity
M = mass
N = number of droplets
phi = equivalence ratio
ppm = parts per million
P = pressure
Q = heat transfer
dQ = net Heat Release
r = radius
R = universal gas constant
Re = Reynolds number
t = time
T = temperature
v = velocity
V = volume
X = spray penetration length
Y = mass fraction of a chemical species
ρ = density
θ = crank angle
τ = ignition delay

Subscripts

a = air
ai = after injection
b = burnt
c = combustion
e = entrainment
f = fuel
inj = injection
i, j = indexes for the elements in axial and radial directions
s = surface of a droplet
NS = index for chemical species
n = net
st = stoichiometric
ae = air entrainment
l = liquid
v = vapour
w = wall
p = piston
h = cylinder head

Table 1 Thermo-physical properties of different crown materials employed

Property	Material			
	Al-Alloy	Nimonic	SS	MS
Tehrmal Conductivity (W/m-K)	175	12	36.3	53.6
Density (Kg/m^3)	2700	8000	77.53	78.33
Modulus of Elasticity (Pascal) x 10^{-11}	0.703	1.86	1.9	2.01
Specific heat (kJ/kg-K)	0.921	0.461	0.486	0.465
Poission's ratio	0.3	0.30	0.305	0.292

Different Configurations of Air Gap Insulated Piston

The experiments were carried out with various crown materials Nimonic, stainless steel (SS) (Austenitic) and mild steel (MS). With each crown material the magnitudes of different air gaps employed were 1, 2, 3, and 3.8 mm. The composition of the Nimonic material used is 3 percent Fe, 77.1 percent Ni, 0.3 percent Ti, 0.1 percent C and 19.5 percent Cr. The thermo-physical properties of the different crown materials employed are given in Table 1.

Experiments With Different Injection Timings

As the combustion system was modified for the low heat rejection concept, performance tests were also conducted with various advanced injection timings which included 25, 27, 28.5, 29, and 29.5° bTDC. The injection timing for the conventional engine was 27° bTDC. The injection timing was varied by employing suitable copper shims between the pump body and the engine frame.

Results and Discussions

(A) Performance Parameters. The performance tests were carried out on the diesel engine with a conventional piston and with different configurations of air gap insulated piston. Among various materials tested like Nimonic, mild steel, and stainless steel for the piston cap, Nimonic is found to provide better performance on the basis of lowest magnitude of BSFC. A 3 mm air gap is found to be optimum among various air gaps tested. Figure 3 shows the variation of BSFC with BMEP for the conventional piston at an injection timing of 27° bTDC and the piston with Nimonic crown with 3 mm air gap at 27 and 29.5° bTDC. The air gap insulated piston with Nimonic crown with an injection timing of 27° bTDC gave lower BSFC upto 80 percent of full load in comparison with the conventional piston. Beyond 80 percent of full load BSFC for the insulated piston increased over and above that of the conventional piston. The reason for the deterioration of the engine performance at higher loads might be due to the friction and increased diffusion combustion resulting from reduced ignition delay due to higher temperatures. Increased radaition heat losses might have also contributed to the deterioration. The draw back of higher BSFC at full load with air gap piston disappeared with advanced injection timing of 29.5° bTDC. As the injection timing was advanced BSFC reduced further at all the loads. This shows that a significant part of the retained heat is directly converted to piston work rather than being merely available in the exhaust stream, from which it would be recoverable giving much lower BSFC. The air gap insulated piston engine with Nimonic crown and 3 mm air gap at an injection timing of 29.5° bTDC decreased the BSFC by 4 percent at full load and 12 percent at part loads in comparison with the conventional engine operating with the manufacturer's recommended injection timing of 27° bTDC. It can be observed that the magnitudes of BSFC are a little high on all versions of the engine as the test engine was an old engine which has run for a large number of hours. However, in view of this, the comparison was not done on ISFC basis. It can also be noted that the magnitudes of BSFC can also be affected by the oil temperature variation. As the oil temperatures were not measured, this aspect is not taken into consideration while reporting BSFC values.

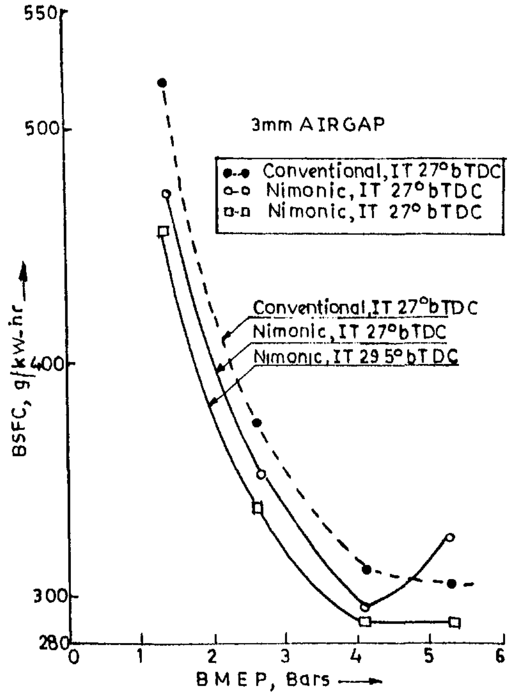

Fig. 3 Variation of BSFC with BMEP for conventional piston at 27° bTDC and insulated piston with Nimonic crow at 27° bTDC and 29.5° bTDC

Figure 4 shows the variation of BSFC with injection timing, which agreed with the trends reported by Miyairi (1989) and Seigla (1989).

Figures 5 and 6 present the variation of EGT and coolant load with BMEP for the conventional piston at 27° bTDC and insulated piston with Nimonic crown at 27° and 29.5° bTDC. EGT for the insulated piston at 27° bTDC increased throughout the load range. But when the injection timing was maintained at 29.5° bTDC, EGT for the insulated piston reduced in comparison to the operation at 27° bTDC on the same insulated piston confirming the conversion of retained heat to the piston work.

Coolant load for the insulated piston at 27° bTDC reduced up to a load of 80 percent of full load in comparison with that for conventional piston.

Beyond this load, the insulated piston with injection timing of 27° bTDC showed increase in coolant load in comparison with that

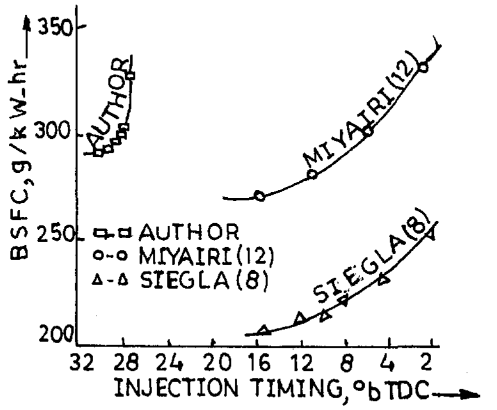

Fig. 4 Variation of BSFC with injection timings for the insulated piston engine

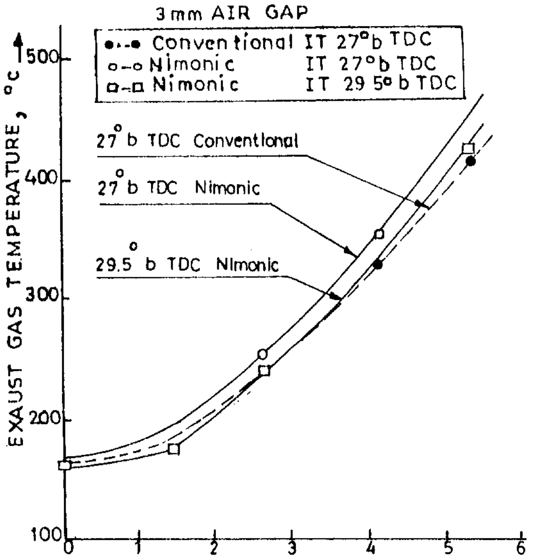

Fig. 5 Variation of EGT with BMEP for conventional piston at 27° bTDC and insulated piston with Nimonic crow at 27° bTDC and 29.5° bTDC

for conventional piston. This is because incylinder heat rejection at full load is primarily due to unburnt fuel concentration near the combustion chamber walls. This trend has also been reported by Wallace et al. (1984). The air fuel ratio got reduced to a reasonably low value at this load confirming the above trend. However, when the injection timing was maintained at 29.5° bTDC the coolant load for the same insulated piston decreased at all loads in comparison with conventional piston. This is because at advanced injection timing, the part of retained energy gets converted into useful work giving lower EGT values. This aspect is further confirmed in the observation of EGT and BSFC magnitudes. However, when heat rejection calculations of coolant load are made, the heat lost to lubricant should also be considered. As in the present investigation the lubricant heat loss is not considered, this aspect is not depicted in the coolant load calculations.

Figure 7 presents the variation of volumetric efficiency with BMEP for the conventional piston at 27° bTDC and the piston with Nimonic crown at 27° and 29.5° bTDC.

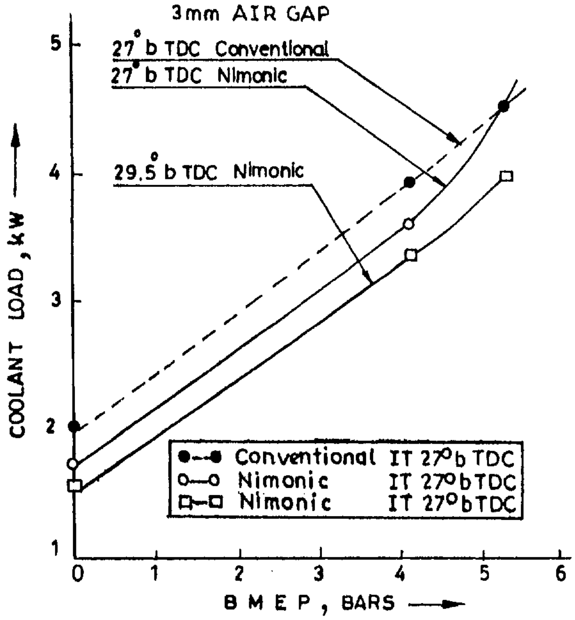

Fig. 6 Variation of coolant load with BMEP for conventional piston at 27° bTDC and insulated piston with Nimonic crow at 27° bTDC and 29.5° bTDC

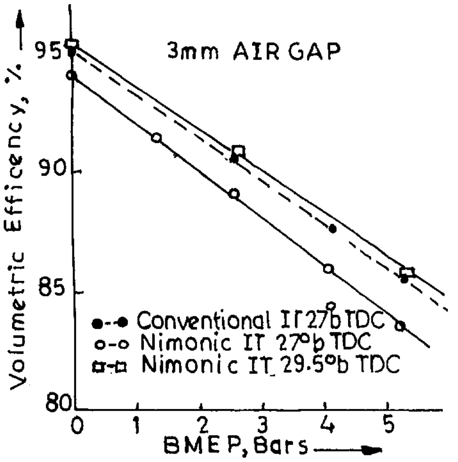

Fig. 7 Variation of volumetric efficiency with BMEP for conventional piston at 27° bTDC and insulated piston with Nimonic crow at 27° bTDC and 29.5° bTDC

While the volumetric efficiency for the insulated piston at 27° bTDC reduced in comparison to the conventional piston, it increased when the injection timing was maintained at 29.5° bTDC. With increase in insulation, the volumetric efficiency naturally decreases because of heating effect of incoming air. However, with advanced injection timing the gas temperature gets reduced leading to an increase in volumetric efficiency.

(B) Pollution Parameters. Figure 8 presents the variation of smoke density with BMEP for the conventional piston at 27° bTDC and insulated piston with Nimonic crown at 27 and 29.5° bTDC. Though smoke densities were lower up to a load of 80 percent of full load, at loads higher than this, the smoke density increased over and above that of conventional piston. This increase is due to decrease in volumetric efficiency and air fuel ratio. This is also due to fuel cracking at higher temperatures leading to increased smoke density.

With the injection timing of 29.5° bTDC for the insulated piston the smoke density reduced at all loads.

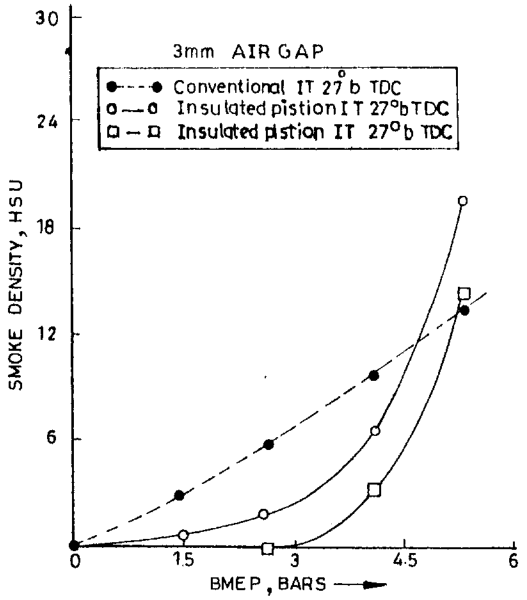

Fig. 8 Variation of smoke density with BMEP for conventional piston at 27° bTDC and insulated piston with Nimonic crow at 27° bTDC and 29.5° bTDC

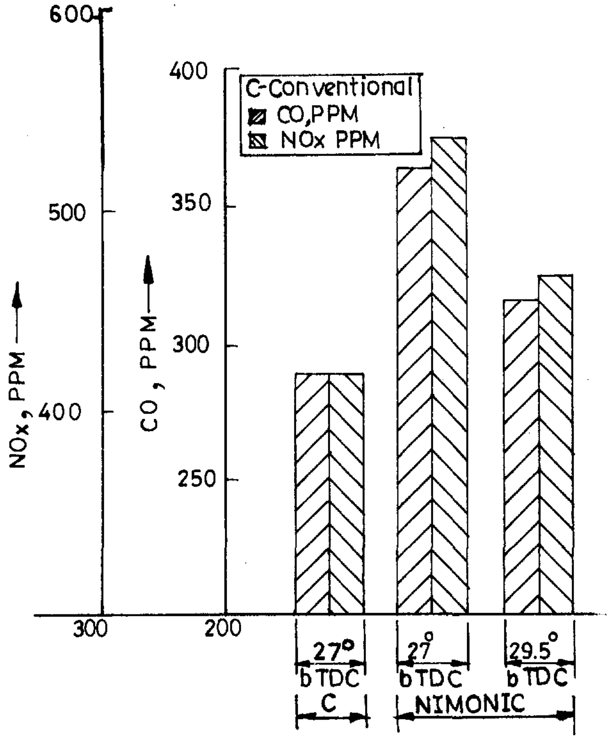

Fig. 9 Bar graphs of NOx and CO for conventional piston at 27° bTDC and insulated piston with Nimonic crown 27° bTDC and 29.5° bTDC

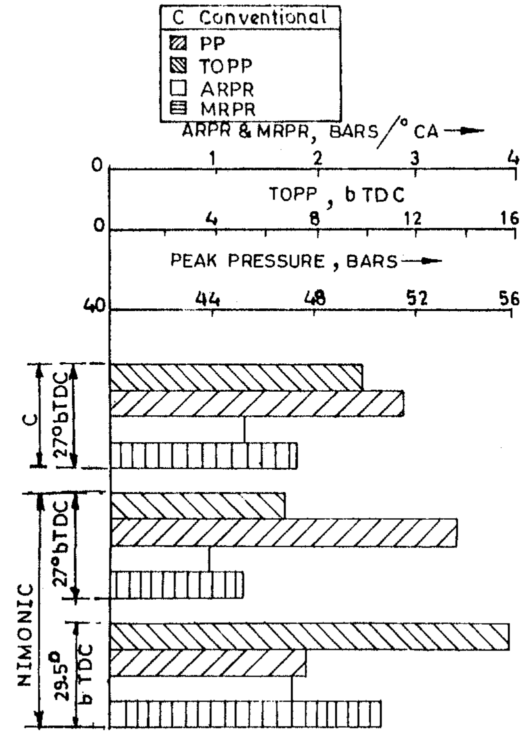

Fig. 11 Bar graphs of combustion parameters for conventional piston at 27° bTDC and insulated piston at 27° bTDC and 29.5° bTDC

Figure 9 gives the bar charts of the magnitudes of CO and NOx at full load operation of the engine. As expected, NOx increased for an insulated piston due to elevated temperatures. With advanced injection timing of 29.5° bTDC, NOx levels decreased with same insulated piston in comparison with the operation at 27° bTDC. This is because of reduction in gas temperature due to the increase in volumetric efficiency at advanced injection timings. The figure also presents data on CO emissions. One can expect that CO is not a significant pollutant in diesel engines. However, in insulated engines, many researchers presented CO emissions. Hence, the authors also measured and presented CO emissions observed in insulated engines. CO levels increased with the insulated piston because of dissosiation of CO_2 at higher temperatures.

Once again CO levels decreased with injection timing of 29.5° bTDC in comparison with the 27° bTDC on the same insulated engine. As explained earlier this is also because of reduced gas temperatures which reduced the cracking of CO_2.

(C) Combustion Parameters. Figure 10 gives the pressure-crank angle diagrams obtained from the photographs taken from the oscilloscope screen for three configurations of the conventional piston with an injection timing of 27° bTDC and insulated piston at 27 and 29.5° bTDC. Figure 11 shows the combustion parameters for the conventional piston at 27° bTDC and insulated piston with Nimonic crown at 27 and 29.5° bTDC at full load.

The peak pressures and rates of pressure rise at an injection timing of 27° bTDC were observed to be lower with the insulated piston in comparison with the conventional piston whereas peak pressures were found to occur much later from TDC. This is because the insulated piston exhibits higher temperatures of chamber walls leading to continuation of combustion, giving peak pressure away from TDC. However, this phenomenon is nullified with an injection timing of 29.5° bTDC on the same insulated piston because of reduced temperature of chamber walls thus bringing the peak pressure closure to TDC. The peak pressures and rates of pressure rise are found to be higher for the insulated piston at this injection timing.

Finite Element Analysis for Piston Temperature Distribution

Finite element analysis using the ANSYS program was adopted for estimating the temperature distribution within the conventional

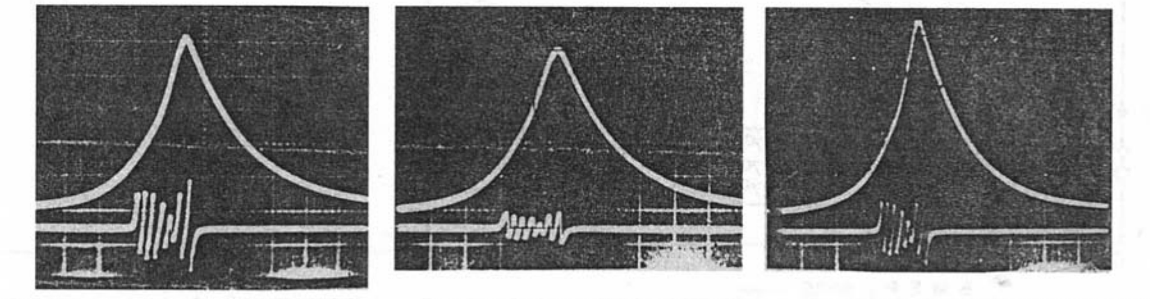

Conventional piston (IT 27° bTDC) **Insulated piston (IT 27° bTDC)** **Insulated piston (IT 29.5° bTDC)**

Fig. 10 Typical pressure-crank angle diagrams for conventional piston at 27° bTDC and insulated piston with Nimonic crown 27° bTDC and 29.5° bTDC

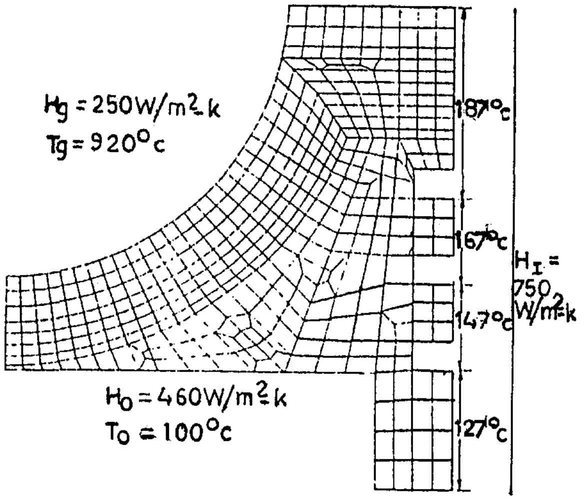

Fig. 12 Finite element mesh employed

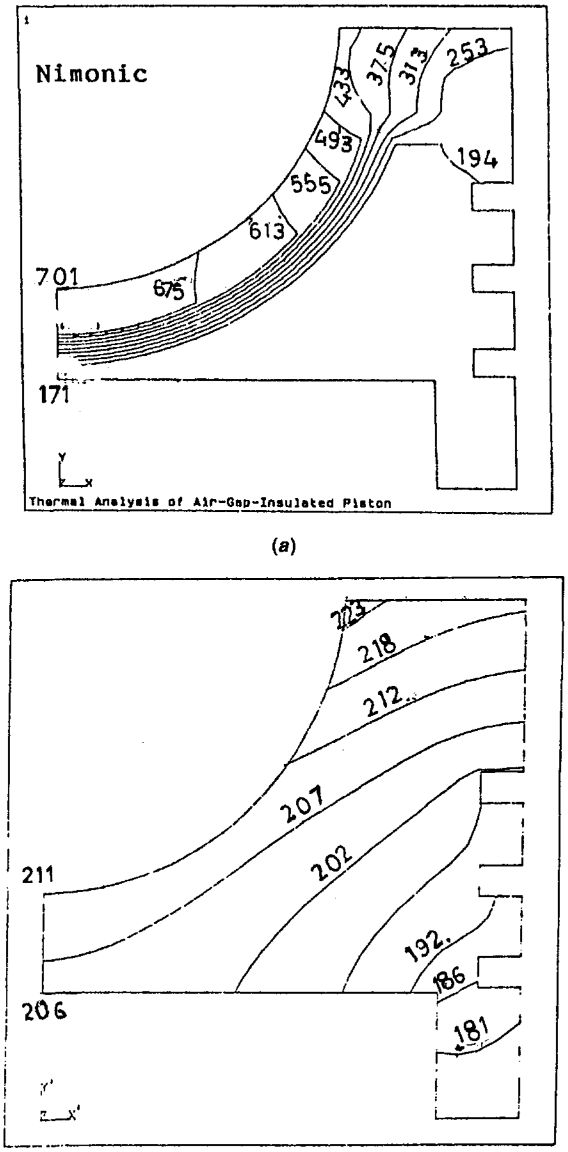

(a)

(b)

Fig. 13 (a) Isotherms in insulated piston with Nimonic crown having an air gap of 3 mm; and (b) isotherms in conventional piston

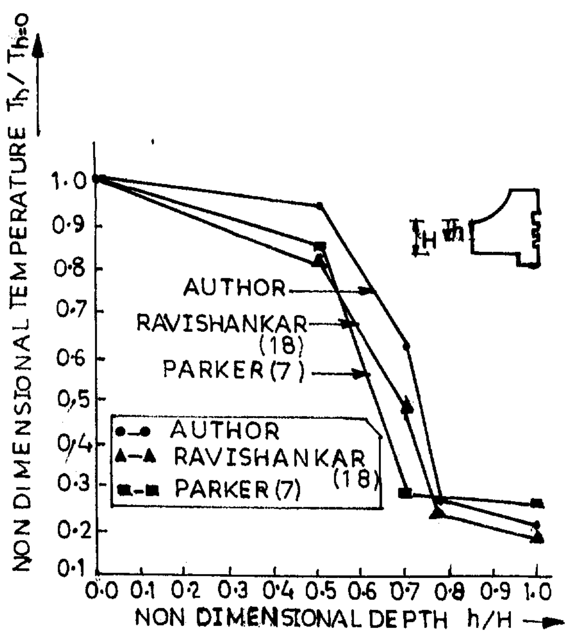

Fig. 14 Variation of nondimensional temperature with nondimensional depth with optimized insulated piston

and different configurations of the air gap insulated pistons. The mesh required for the analysis was generated using NISA software employing eight noded quadrilateral isoparametric elements. The heat transfer inside the air gap was considered to be by conduction only. Figure 12 shows the mesh generated for the present analysis along with the boundary conditions chosen (Rama Mohan et al., 1994).

Figures 13(*a*) and 13(*b*) show the distribution of isotherms in an insulated piston with an air gap of 3 mm and conventional piston, respectively. It is desirable that the temperatures and distances are nondimensionalized in order to show the trends instead of presenting the data in absolute magnitudes.

Figure 14 gives the nondimensional temperature variation along the axis of the piston with nondimensional depth for the insulated piston with Nimonic crown having 3 mm air gap, compared to the relevant data of other researchers (Parker and Donnison, 1987;

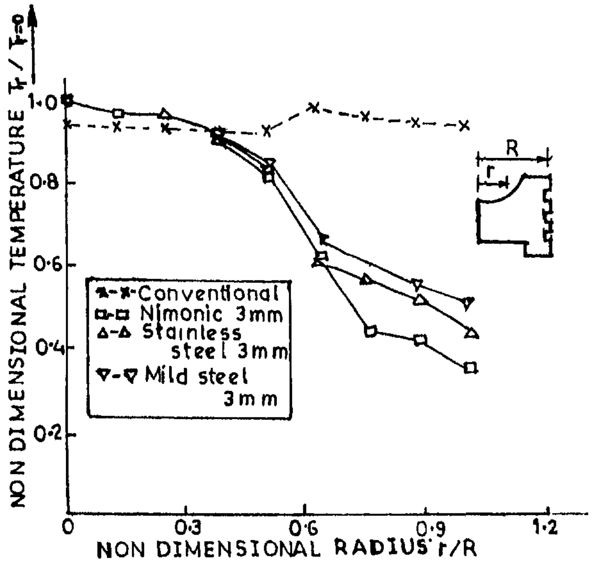

Fig. 15 Variation of nondimensional temperature with nondimensional radial distance for pistons with different crown materials having an air gap of 3 mm

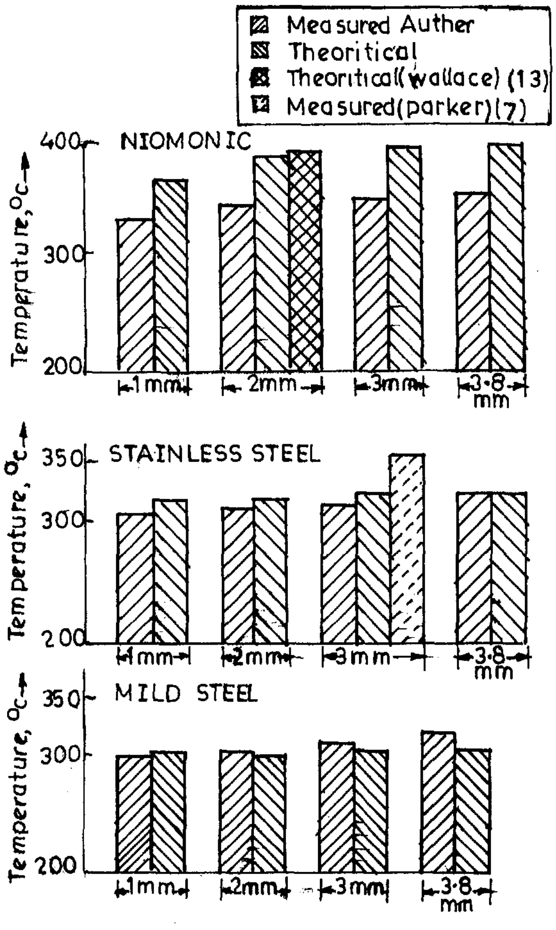

Fig. 16 Variation of air gap temperature with different air gap thicknesses obtained from theoretical and experimental evaluation

Ravishanker et al., 1989). The variation of nondimensionalized temperature with nondimensional radial distance is shown in Fig. 15 for a piston with a 3 mm air gap and different crown materials. While the temperature variation along the radial distance is negligibly small in the conventional piston due to the absence of thermal resistance, there is steep variation of temperature for an insulated piston.

Validation of the Computer Predicted Results

It is always necessary to validate the computer predictions by comparing to the results obtained from the experimental data or using the computations of the other researchers employing independent prediction techniques. Figure 16 shows the variation of air gap temperature with varying air gap thicknesses obtained theoretically and experimentally for the piston with the Nimonic crown.

The agreement between the trends of theoretical and measured values is reasonably good. However the theory predicted higher magnitudes of air gap temperatures over that of experimental results.

This is because experimental results take the average temperature of air in the air gap, while the computer predicts the average magnitudes taken from the upper and the lower isotherms of the air gap. Also, computer analysis neglected radiant and convective heat transfer effects in the air gap, so that higher magnitudes of air gap temperatures resulted. The above figure also presents the measured value of temperature in the air gap with the steel crown employed by Parker et al. (1987). The figure also gives the computer predicted values of air gap temperature estimated by Wallace et al. (1984) for a 2 mm air gap employing Nimonic crown. It is gratifying to note that the authors' results agreed exceedingly well with the data of the other researchers.

Analytical Predictions

A zero dimensional multi-zone combustion model was used to predict the performance of the low heat rejection diesel engine with air gap insulated piston. The model is a closed cycle simulation and has been divided into the following five sub models: (1) fuel injection; (2) spray penetration and air entrainment; (3) spray evaporation; (4) combustion model; and (5) heat transfer model.

Fuel Injection. The number of droplets and their Sauter mean diameter in each element are computed from the following relations (Glassman, 1977):

$$(D_{32})_{i,j} = [23.9(p_{inj} - p)^{-0.135}(\rho_a)^{0.12}]*(Q_{inj}) \tag{1}$$

$$N_{i,j} = \int_{t_i}^{t_{i+1}} Q_{inj}dt/(j*(\prod/6)(D_{32})^3_{i,j}). \tag{2}$$

Spray Penetration and Air Entrainment. The velocity of the element is found using the location of element X from the following relations (Glassman, 1977):

for $t < t_b$,

$$\frac{dX_{i,j}}{dt} = \frac{X_{i,j}}{t} \text{ for } j \geq 1. \tag{3}$$

The air entrainment into each element is obtained by momentum balance and is as shown below.

$$M_{ae_{i,j}} = M_{f_{i,j}} \frac{\{V_{inj} - 1\}}{dX_{i,j}/dt} \tag{4}$$

The entrainment of the individual species into each element is given by

$$dM_{NS_{i,j}} = Y_{NS} \frac{\{dM_{aei,j}\}}{dt}. \tag{5}$$

Spray Evaporation. The evaporation rate of a droplet in an element is computed, using Spalding's droplet evaporation relation (Ravishanker, 1989) as

$$\frac{dM_f}{dt} = 4\prod r_s\rho_s D_s \log(1 + B) \tag{6}$$

The rate of decrease of droplet radius is shown by the following expression (Ravishanker, 1989):

$$\frac{dr_s}{dt} = [\rho_s D_s/(\rho_1 r_s)] \log(1 + B) \tag{7}$$

Combustion Model. The ignition delay is obtained from,

$$\tau = 4*10^{-3}(p)^{-2.5}(phi)^{-1.04} \exp 4000/T. \tag{8}$$

The mass of air and mass of gaseous fuel determine equivalence ratio in the gaseous element is given by

$$phi = (M_{fg}/M_a)/(M_{fg}/M_a)_{st}. \tag{9}$$

Heat Transfer Model. Heat transfer to the cylinder walls is obtained using Annand's relation (Annand, 1963),

$$dQ_w/dt = aAk/D_1[F_w(\mathrm{Re})^b](T - T_w) + c(T^4 - T_w^4). \tag{10}$$

In the above equation, the total heat transfer surface is considered to be made up of different sub areas as shown below.

$$A = A_p + A_1 + A_h \tag{11}$$

In Eq. (11), the wall temperature T has to be accurately employed based on experimental data. All the earlier researchers employed the surface temperatures of the piston, liner and

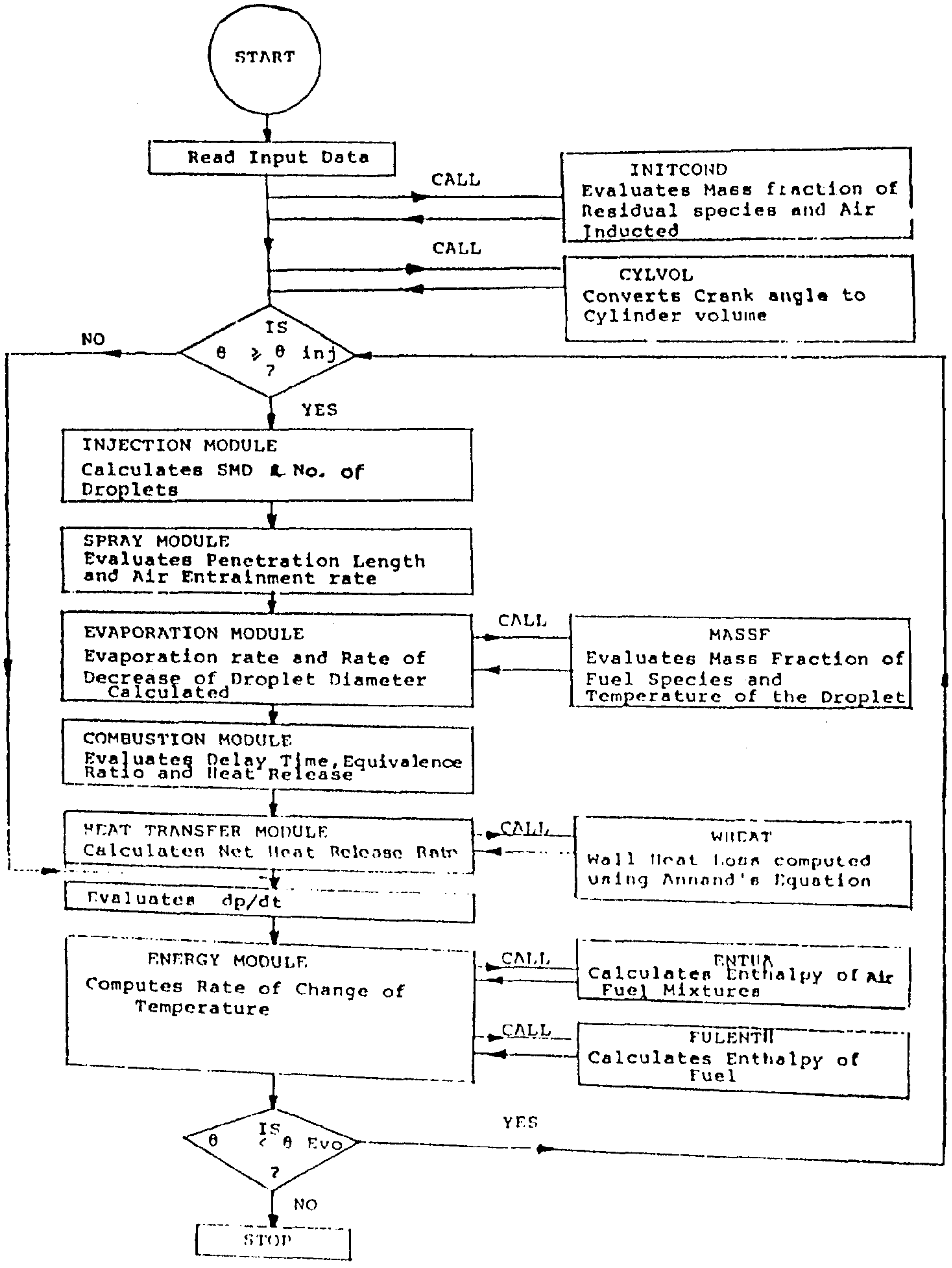

Fig. 17 Flow chart of computer model

cylinder head arbitrarily. In the present paper, though, the temperature of the liner and cylinder head are assumed to be constant, the piston temperature, however, is evaluated more accurately from the isotherms of the piston obtained using FEM analysis (Rama Mohan et al., 1994). The net heat release in an element is given by

$$\frac{dQ_{ni,j}}{dt} = \frac{dQ_{ci,j}}{dt} - \frac{dQ_{vi,j}}{dt} - \frac{dQ_{wi,j}}{dt},$$

where $dQ_{ci,j}/dt$ is the heat release rate due to combustion and $dQ_{vi,j}/dt$ is the rate of heat removal from the gas phase due to the latent heat of evaporation.

Pressure is obtained from conservation of momentum and is given by the following expression:

$$P = \left[\sum \frac{R}{C_{pij}} \{Q_n + M_{ae}(h_a - h_{ij}) - M_{ij}T_{ij}R_{ij} + M_v(h_l - h_{ij})\} + \sum M_{ij}T_{ij}R_{ij} + \sum R_{ij}T_{ij}M_{ij} - P(V - V_1) \right] \times \left[V - V_1 - \sum \frac{V_{ij}R_{ij}}{Cp_{ij}} \right].$$

The temperature of the element at any instant is obtained by applying the energy equation to each element and is given as

$$T = \frac{Q_n + VP + M_{ae}(h_a - h) + M_v(h_f - h)}{M(C_v + R)} - MTR/M(C_v + R).$$

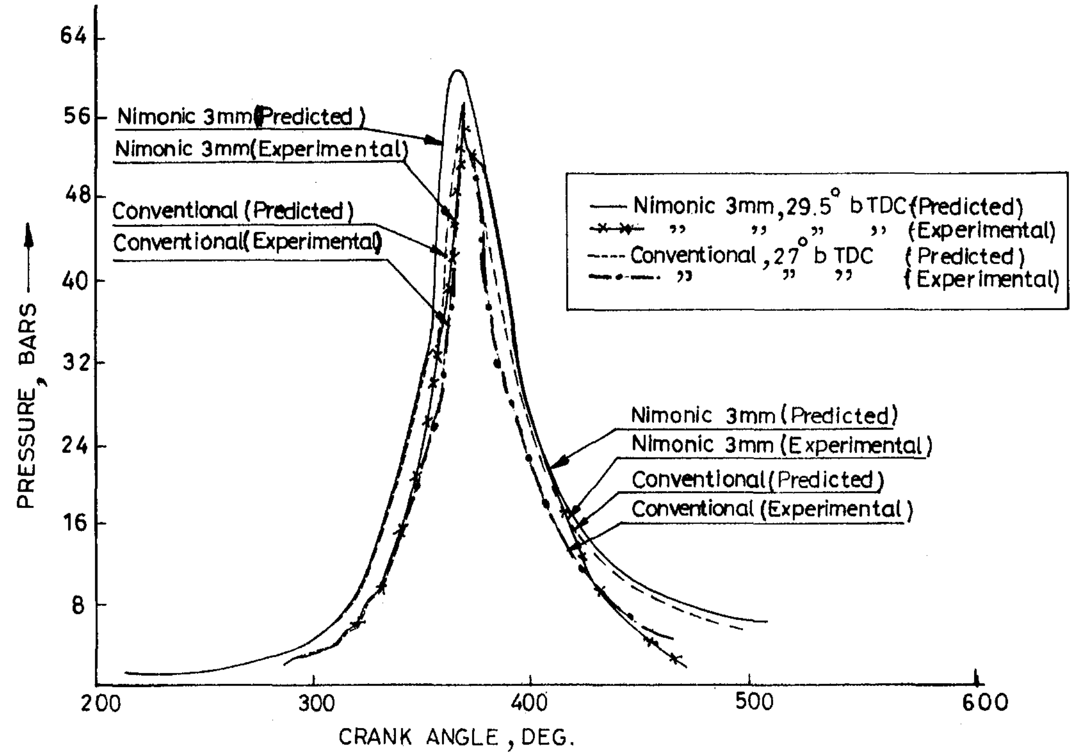

Fig. 18 Comparison to theoretical and experimental results of pressure crank angle data for the optimised piston engine and the conventional piston engine

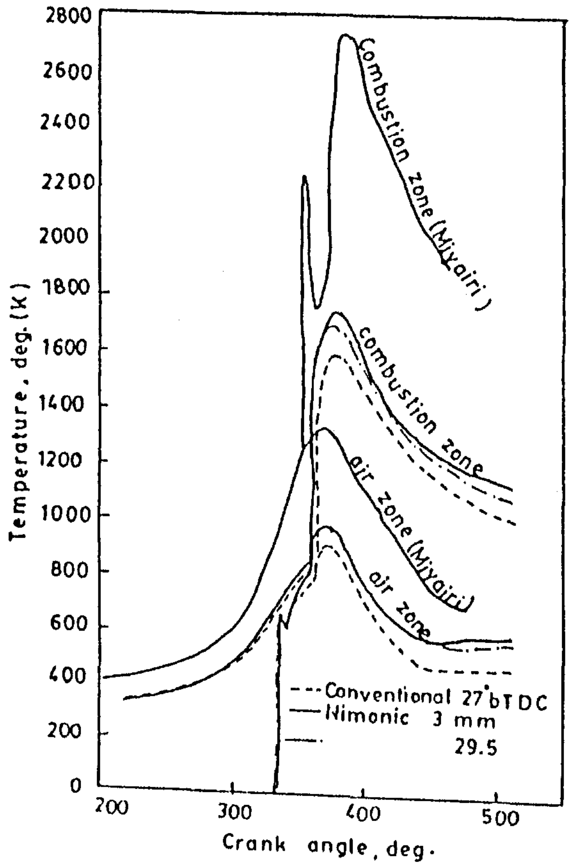

Fig. 19 Variation of temperature for conventional and optimized piston engine predicted from the combustion model

Solution Procedure

Equations (5), (6), (7), (13), and (14) form the set of governing equations which are solved using the Runge-Kutta fourth order scheme. A Fortran code has been prepared constituting the five submodels. A simplified flow chart of the computer program is shown in Fig. 17.

The heat loss to the coolant through the cylinder walls is estimated using Annand's equation (14), making use of more appropriate temperatures evaluated from the energy equation. Pressure is obtained from conservation of momentum. Figure 18 shows a comparison of the theoretical and the experimental results of pressure crank angle data for the cases of the optimized insulated piston with an injection timing of 29.5° bTDC and the conventional piston with an injection timing of 27° bTDC. The combustion model predicted higher values for both conventional and insulated piston engines in comparison with experimental results. The model also predicted higher magnitudes for the insulated piston in comparison with the conventional piston. It should also be observed that the predicted values were higher in comparison with the experimental data as the model assumes idealized combustion phenomenon.

The variation of gas and air temperatures with crank angle for the conventional piston engine with injection timing of 27° bTDC and the optimized piston engine with injection timing of 27 and 29.5° bTDC predicted from the analytical model are shown in Fig. 19. While the gas temperature has increased for the insulated engine in comparison with the 27° bTDC, there was a decrease of the gas for the insulated piston engine when the injection timing was advanced from 27° to 29.5° bTDC. The decrease in gas temperatures indicate saving of waste heat from exhaust while converting the same into useful work. This has been confirmed from the decreased BSFC observed with the advanced injection timings of the above insulated piston engine as seen from the Fig. 3. It is also observed that the insulated piston engine with an injection timing of 29.5° bTDC still exhibits higher magnitudes over the conventional piston engine at 27° bTDC.

The above results provide excellent validation for the combustion model employed. For comparison purposes, the gas and air zone temperatures predicted by Miyairi on the basis of a two zone combustion model are also presented in figure. The two zone model being less realistic in comparison with the multi zone model, Miyairi predicted very high temperatures in the air and gas zones. However the trends agreed very well.

Conclusions

1 BSFC was reduced by 12 percent at part load and 4 percent at full load at an injection timing of 29.5° bTDC with the optimized insulated piston engine with a Nimonic crown and a 3 mm air gap in comparison with a conventional engine operating at an injection timing of 27° bTDC.
2 The heat rejection to the coolant for the optimized piston decreased by 12 percent in comparison with the conventional engine, while exhaust gas temperatures increased from 420°C to 435°C.
3 The smoke density for the optimized piston reduced throught the load range in comparison to the conventional piston. NOx and CO levels at full load increased marginally with optimized piston in comparison to the conventional piston.
4 Peak pressure and rates of pressure rise increased in the optimized insulated piston engine when the engine was operated at an injection timing of 29.5° bTDC.
5 Finite element analysis predicted an increase in the peak surface temperature from 225°C for the conventional piston to 703°C for the optimized piston. The temperatures measured with an L-link mechanism provided excellent validation for the FEM results.
6 Heat flow analysis showed a reduction of about 35.8 percent in heat flow through the optimized insulated piston in comparison with the conventional piston engine.
7 The multizone combustion model predicted pressure-crank angle data which agreed closely with experimental results obtained, the deviation in peak pressure being only 7 percent.

References

Alkidas, A. C., 1987, "Experiments With an Uncooled Single Cylinder Open Chamber Diesel," SAE Paper 870020.

Annand, W. D., 1963, "Heat Transfer in the Cylinder of Reciprocating Internal Combustion Engines," Proceedings, of I. Mech., Vol. 177 No. 36, pp. 970–990.

Cheng, W. K., Wong, V. W., and Gao, F., 1989, "Heat Transfer Measurements Comparison in Insulated and Noninsulated Diesel Engines," SAE Paper 890570.

Cole, R. M., and Alkidas, A. C., 1985, "Evaluation of an Air Gap Insulated Piston in a Divided Chamber Diesel Engine," SAE Paper 850359.

Glassman, I., 1977, *Combustion,* Academic Press, Inc., San Diego, CA.

Hiroyasu, H., 1980, "Simulation Program to Predict Direct Injection Diesel Engine Efficiency and Pollutant Emissions," research report, Dept. Mech. Engg., Hiroshima University.

Jabez Dhinagar, S., Siva Rama Prasad Rao, N., Nagalingam, B., and Gopal Krishnan, K. V., 1989, "Compensating the Volumetric Efficiency Drop of an Adiabatic Diesel Engine for Improved Performance," presented at the XI National Conference on I.C. Engines and Combustion, I. I. T., Madras.

Krishnan, D. B., Raman, N., Narayanaswamy, K., and Rohatgi, P. K., 1980, "Performance of Al-Si-Graphite Particle Composie Piston in a Diesel Engine," WEAR, Vol. 60 pp. 205–215.

Miyairi, Y., 1988, "Computer Simulation of an LHR Diesel Engine," SAE Paper 880187.

Miyairi, Y., Matsuhisa, T., Ozawa, T., Oikawa, H., and Nakashima, N., 1989, "Selective Heat Insulation of Combustion Chamber Walls for a DI Diesel Engine With Monolithic Ceramics," SAE Paper 890141.

Parker, D. A., and Donnison, G. M., 1987, "The Development of an Air Gap Insulated Piston," SAE Paper 870652.

Rafiqul Islam, M. D., Subramanyam, J. P., and Gajendra Babu, M. K., 1991, "A Thermodynamic Computer Simulation Model for a Low Heat Rejection Direct Injection Diesel Engine," presented at the X National Conference on I.C. Engines and Combustion, Rajkot, India.

Ravishanker, M. S., Seetharamu, K. N., Aswathanarayana, P. A., and Ramachandrarao, V. T. V. S., 1989, "FEM Analysis of Piston Insulation in an Adiabatic Engine," presented at the 11th National Conference on I.C. Engines and Combustion, I. I. T., Madras.

Rama Mohan, K., Rama Narayana, B. L., and Vara Prasad, C. M., 1994, "Computer Prediction of Temperature Distribution of an Air Gap Insulated Piston of an I.C. Engine by FEM Technique" presented at the IX National Convention on Computers in Mechanical Engineering, The Institution of Engineers, Hydevabad, India.

Siegla, D. C., and Alkidas, A. C., 1989, "Evaluation of the Potential of a Low Heat Rejection Diesel Engine to Meet Future EPA Heavy-Duty Emission Standards," SAE Paper 890291.

Wade, W. R., Havstad, P. H., Ounsted, E. J., Trinkler, F. H., and Garwin, I. J., 1984, "Fuel Economy Opportunities With an Uncooled DI Diesel Engine," SAE Paper 841286.

Wallace, F. J., Kao, T. K., Tarabad, M., Alexander, W. D., and Cole, A., 1984, "Thermally Insulated Diesel Engines," Proceedings, I. Mech. E., Vol. 198A, No. 5.

Woschni, G., Spindler, W., and Kolesa, K., 1987, "Heat Insulation of Combustion Chamber Walls—A Measure to Decrease the Fuel Consumption of I.C. Engines," SAE Paper 870339.

Evaluating Alternative Internal Combustion Engines: 1950–1975

C. A. Amann
984 Satterlee Road,
Bloomfield Hills, MI 48304

GMR (General Motors Research Laboratories, now GM R&D Center) has long sought ways to improve automotive combustion engines. Following World War II, considerable effort was also devoted to evaluating new powerplants that embodied different operating cycles from those of the established spark-ignition and diesel engines. Two internal combustion variants receiving attention during the third quarter of the 20th century were the free-piston diesel and the gas turbine. Research on those two alternatives is reviewed. Because their shortcomings were judged to outweigh their advantages, neither has found commercial application in highway vehicles.

Introduction

Since its birth in 1920, GMR (General Motors Research Laboratories, now the GM R&D Center) has sought ways to improve the automotive combustion engine. Among the concepts spawned by that research are the light-weight two-stroke diesel engine, which was introduced at the Chicago World's Fair in 1933 (Automotive Quarterly, 1983), and the high-compression gasoline engine that emerged in 1947 (Kettering, 1947).

In the third quarter of the 20th century, considerable effort was also devoted at GMR to the search for a new combustion engine offering advantages over the established spark-ignition and diesel powerplants. Two internal-combustion engines receiving attention were the free-piston diesel and the gas turbine. Salient aspects of that search are reviewed in this paper.

Thermodynamic Cycles

The internal combustion engine (ICE) normally produces useful work by successively compressing a working medium, adding energy to elevate its temperature to some maximum level, expanding the medium to extract work from it, then returning the working medium to its original state for a repetition of the cycle. In the open-cycle ICE, this last step is accomplished by discarding combustion products and replacing them with a fresh charge.

Thermodynamics approximates engine cycles with successive ideal processes. Thus, the Otto cycle on which the spark-ignition engine is based might be characterized as the SVSV cycle. This signifies that the engine cycle consists ideally of an isentropic compression, constant-volume combustion, an isentropic expansion, and a return of the working fluid to its original state in a constant-volume process. Similarly, the ideal Diesel cycle is represented by SPSV, suggesting that combustion occurs at constant pressure rather than constant volume.

In neither of these engines does combustion actually occur isochorically (at constant volume) or isobarically (at constant pressure). Instead, combustion is more closely approximated by a combination of the two. Thus both the spark-ignition and the high-speed compression-ignition diesel engines might be more appropriately designated S(VP)SV cycles, the (VP) suggesting that combustion is more nearly represented by some combination of isochoric and isobaric heat addition.

Operation of the free-piston diesel and the gas turbine are idealized by cycles different from S(VP)SV. They are represented on a temperature-entropy plane in Fig. 1. In each case, compression occurs from (1)–(2), heat addition from (2)–(3), expansion from (3)–(4), and restoration of the original state from (4)–(1). The thermodynamic processes comprising these idealized cycles are marked P, V, or S, depending on whether they occur at constant pressure, volume, or entropy.

The free-piston diesel of Fig. 1(*a*), an ICE that was studied during the 1950s, is idealized by the S(VP)SP cycle. Release of the working gas to the environment takes place through a turbine that extracts work as the gas is expanded all the way down to ambient pressure. In principle, compared to the S(VP)SV cycle, this allows the additional work to be extracted that is normally lost at the bottom-dead-center "toe" of the pressure-volume diagram due to incomplete expansion.

The gas turbine was the subject of investigation at GMR over the entire period from 1950–1975. It operates on the SPSP cycle. As subsequently discussed, the automotive gas turbine was developed in its two-shaft form, providing an interesting parallel to the free-piston diesel. In the latter case, the free-piston machine serves as a gasifier that delivers hot, compressed gas to a turbine for conversion to output-shaft work. In the two-shaft gas turbine, the free piston is replaced by a turbo-gasifier.

Because the gas turbine involves continuous combustion, its peak cycle temperature is restricted by materials properties to a lower level than is tolerated by the intermittent-combustion free-piston machine. To compensate for the poorer thermal efficiency associated with this lower temperature, the gas turbine engine may incorporate a heat exchanger that conserves fuel by extracting heat from the turbine exhaust gas (Fig. 1(*b*), point 4) to preheat the compressor discharge air (Fig. 1(*b*), point 2) on its way to the combustor.

Free-Piston Diesel

In the early 1950s, General Motors had three diesel engine divisions. Electro-Motive Division specialized in locomotive diesels, Cleveland Diesel produced large marine engines, and Detroit Diesel built smaller engines suitable for trucks and buses. All of these engines operated on the two-stroke uniflow principle. At that time the French Navy had installed experimental free-piston engines in minesweepers. The free-piston engine is a two-stroke uniflow compound diesel. To learn more about this engine and to assess its suitability for General Motors diesel divisions, GMR purchased a large single-cylinder version with a nominal shaft rating of 1000 kW from France (Flynn, 1957). Ultimately, a much smaller two-cylinder siamesed version, known as the Hyprex, was designed, built, and installed in an

---

Contributed by the Internal Combustion Engine Division (ICE) of THE AMERICAN SOCIETY OF MECHANICAL ENGINEERS for publication in the ASME JOURNAL OF ENGINEERING FOR GAS TURBINES AND POWER.

Manuscript received by the ICE July 1, 1996; final revision received by the ASME Headquarters January 12, 1999. Associate Technical Editor: D. Assanis.

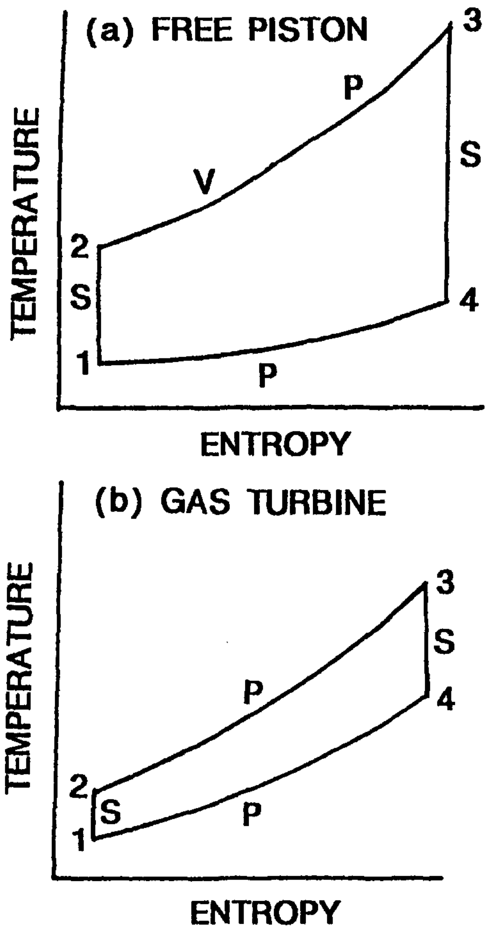

Fig. 1 Ideal temperature—entropy diagrams

automobile in 1956 for evaluation (Underwood, 1957). This vehicle, the XP-500, was the first car in the world to be powered by a free-piston engine. Six larger single-cylinder gasifiers, feeding a turbine that delivered 4475 shaft kW, were also built and installed in a converted World War II merchant vessel, the William Patterson, for the U.S. Maritime Administration (General Motors, 1969). The Patterson sailed for several years, encircling the globe before its decommissioning.

Free piston machines of the inward-compression type such as the Hyprex take the form represented schematically in Fig. 2. Identical stepped pistons reciprocate in a common cylinder, constituting a piston-supercharged opposed-piston uniflow two-stroke diesel gasifier. There is no crankshaft. Motion of the opposed pistons is synchronized through a connecting linkage, but the output from the cylinder is in the form of compressed exhaust gas. That gas is then expanded through a mechanically independent turbine that delivers the output shaft power.

Referring to Fig. 2, as the smaller power pistons move from their outer dead point (ODP) toward their inner dead point (IDP), they first move burned gas through the exhaust ports as fresh air enters through the intake ports, then compress the trapped charge once the ports are covered. Near IDP, fuel is injected into the space between the power pistons and autoignites in diesel-engine fashion. During this inward stroke of the power pistons, the larger pistons compress scavenging and charging air. When that air reaches the pressure existing in the airbox that surrounds the power cylinder, it enters the airbox through reed valves, ready for the next engine cycle. Combustion in the power cylinder forces the power pistons apart. This depresses the pressure in the compressor cylinders until it drops below ambient pressure, causing inlet reed valves to open and admit fresh air for subsequent compression. Once the power pistons uncover the exhaust ports, the burned gas exits through the duct leading to the turbine. When the intake ports are uncovered, fresh air enters from the airbox for scavenging and cylinder charging. After the pistons reach ODP, the cycle is repeated.

A bounce chamber is located at the outer extremity of travel for each piston. The bounce chambers act as air springs, storing energy in the form of compressed air during outward motion of the pistons and returning energy to the pistons once ODP is reached in order to move them inward again. Average pressure in the bounce chambers is controlled by a stabilizer allowing air exchange between the bounce chambers and the airbox. At a given fuel rate, the stabilizer is used to control IDP and ODP. ODP must always be sufficiently great to allow adequate uncovering of the intake ports in the power cylinder. At IDP the minimum space between power pistons must be greater than zero, and practically, must be sufficient to maintain acceptable peak cycle pressure and temperature.

With both ODP and IDP varying, the effective compression ratio experienced by the working fluid changes with load. It might be as high as 50 at rated power, but decreases as gasifier idle is approached. The frequency of piston oscillation is determined by Newton's Law of Motion, hence depends on piston mass as well as the gas pressures acting on the pistons and piston friction. With its 100 mm diameter power pistons and approximately 125 mm stroke, the Hyprex had a maximum frequency of 2400 strokes/min, with frequency decreasing by about 40 percent at idle.

The engine is started by moving the pistons to a point near ODP. Compressed air then introduced into the bounce chambers forces the pistons toward IDP, compressing the air in the power cylinder. Compression-ignition of injected fuel starts self-sustained operation.

A number of interesting characteristics were either confirmed or identified as a result of engine operation. First, the gasifier exhibited outstanding fuel tolerance. It was operated successfully on gasoline, crude oil, whale oil, peanut oil, and cottonseed oil. Second, despite the oscillatory motion of its sizable pistons, it was remarkably free of objectionable vibration. A nickle could easily be balanced on a horizontal surface of the operating gasifier. A large gasifier containing a pair of 520 kg pistons was never bolted to its mounting frame, yet did not move in three years of operation. Third, the turbine provided an excellent torque characteristic, with torque reaching a maximum when the turbine was locked against rotation. Although this same torque characteristic is realized by the two-shaft gas turbine, the free-piston gasifier responded to a sudden opening of the throttle from idle much faster than the turbo-gasifier, thus providing maximum torque promptly. Fourth, the turbine inlet temperature was much lower than in the gas turbine, avoiding a need for costly high-temperature alloys. The five-stage axial-flow turbine built for the Hyprex was fabricated from an exhaust-valve steel.

One disturbing trait of the free-piston engine was uncovered early in the program. The flow characteristics of a turbine resemble that of a nozzle. Flow parameter $\dot{m}\sqrt{T}/P$ (where $\dot{m}$ = mass flow rate, T = inlet absolute temperature, and P = inlet absolute pressure) is a function of the turbine pressure ratio, as illustrated in Fig. 3. For a specified pressure ratio, the turbine will accept only the value of flow parameter shown by the curve rising from unity pressure ratio. At any specified pressure ratio, the flow parameter from the gasifier can be varied only over a narrow range, also shown, by varying the pressure in the bounce chamber. Where the two characteristics intersect, the gasifier and turbine are compatible. However, at low pressure ratios, i.e., light loads, the gasifier is seen to provide more flow than the turbine can swallow.

The original way to accommodate this mismatch at light load and idle was to discard enough of the gasifier exhaust gas to

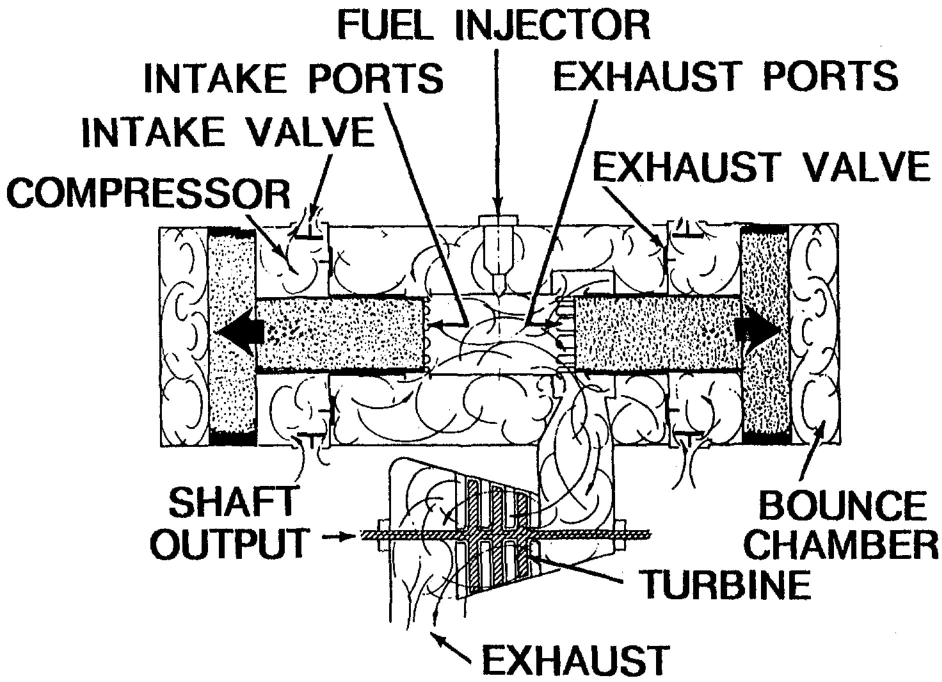

Fig. 2 Schematic of free-piston engine

satisfy the needs of the turbine. Although that practice may be tolerable in a marine application where the engine is nearly always operated at high load, the resultant penalty in fuel economy would be devastating in a passenger car, which operates most of the time at light loads. This problem was managed in the Hyprex by recirculating a fraction of the air in the airbox back to the intake of the compressor. Without such recirculation, early free-piston engines consumed about a quarter of their full-load fuel rate at idle. With recirculation, this fraction could be reduced to 8 percent.

Another difficulty encountered with the free-piston engine was intake noise. The turbine went a long way toward quieting the gasifier exhaust, but the highly unsteady flow into the air compressor was a more difficult challenge. Operating the two cylinders of the Hyprex out of phase helped, as did recirculation. Even so, the periodic gulps of air inducted by the gasifier, separated by periods of zero flow, made it difficult to match the intake noise associated with the rippling flow entering a conventional V-8.

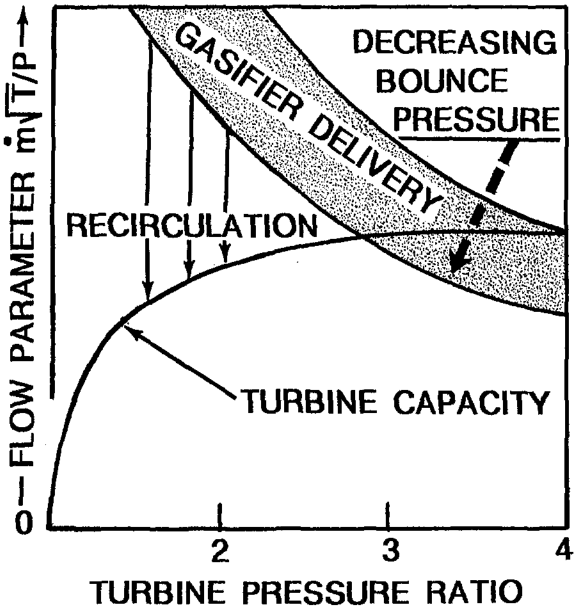

Fig. 3 Matching free-piston gasifier and turbine

Despite its several attractive features, the free-piston engine was judged to lack the competitive edge needed to succeed in the commercial market, so development was halted.

Gas Turbine

During World War II, the Allison Division of General Motors mass-produced the V-1710, a 28-L liquid-cooled V-12 spark-ignition engine, for the U.S. Air Force. In 1945 Allison began production of its first turbojet, and two years later it built its last aircraft piston engine. Understandably, the question arose of whether such a major shift in dominant aircraft engine type was conceivable for the highway-vehicle application. It fell to GMR to evaluate that possibility.

Studies identified advantages and disadvantages for the automotive gas turbine (Turunen, 1950). On the positive side, impulse-free torque delivery and insensitivity to fuel quality were anticipated. In its two-shaft version the gas turbine offered an excellent torque characteristic, with maximum torque being available at vehicle standstill. On the negative side, poor fuel economy, especially at light loads and idle, and high manufacturing cost were concerns. Such conclusions suggested that the gas turbine might be better suited to the heavy-duty application than to the passenger car. Ultimately, design and construction of the GT-300 Whirlfire engine was initiated to evaluate the potential of the automotive gas turbine.

The GT-300 was a 225-kW simple-cycle gas turbine designed to fit in the rear engine compartment of a city bus, named the Turbocruiser (Turunen, 1955). The engine had a rated pre-turbine temperature of 815°C with a compressor pressure ratio of 3.5. The rear of the Turbocruiser interior was fitted with an instrumented console to facilitate data collection during over-the-road operation. The bus was first operated with the GT-300 Whirlfire in 1953.

After design of the GT-300 was well along, plans for a gas-turbine-powered show car, to be featured at the GM Motorama

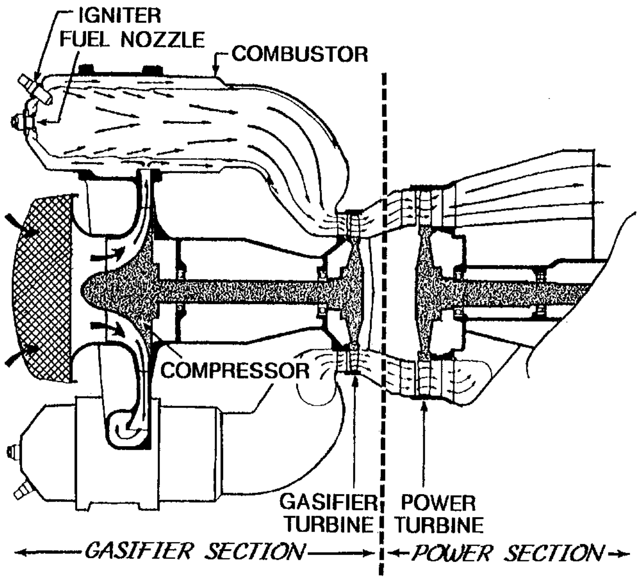

Fig. 4 Nonregenerative GT-302 gas turbine

in New York in early 1954, came to the attention of GMR. In those years it was customary to highlight the new line of GM cars at this event. Eventually named the Firebird I, the gas turbine show car built for the 1954 Motorama was a futuristic single-seater that bore intentional resemblance to a jet fighter. Unfortunately, the GT-300 had been designed with a single top-mounted combustor for ready accessibility in the rear compartment of the Turbocruiser. As a result, the GT-300 would not fit within the sleek lines of the Firebird. This led to development of a second engine, the GT-302, which was a compact version of the GT-300 that featured two combustors of reduced size, the axes of which paralleled the gasifier shaft (Turunen, 1955).

The GT-302 layout is shown in Fig. 4. The aluminum compressor rotor was driven by a single-stage axial-flow gasifier turbine. Output from the single-stage power turbine was delivered to a simple transmission offering two forward speed ratios and reverse. Operated at a slightly higher gasifier speed than the GT-300, the GT-302 was rated at 275 kW, sufficient to propel the Firebird I at a speed of 325 km/h.

Individual blades for the two turbine rotors were investment cast from GMR-235, a nickel-based high-temperature alloy developed by GMR metallurgists to replace the cobalt-based alloy then in common use in gas turbines. Following standard aircraft practice, ''fir-tree'' serrations were ground into the base of each blade for insertion into mating serrations broached into the peripheries of the turbine disks.

Following the Motorama, Firebird I made high-speed runs on airport runways around the country to demonstrate the capabilities of this new type of powerplant to the public.

Experience with the Turbocruiser and the Firebird I identified several operational concerns. First, vehicle acceleration from a standing start was sluggish. Second, the fuel economy of the vehicles was quite poor. Third, the exhaust gas was excessively hot. The upward-directed exhaust from the Turbocruiser triggered automatic sprinkler systems in indoor garages. Although the horizontally directed exhaust stream issuing from the rear of the Firebird I was tolerable at idle, behind the vehicle was not the place to stand when a full-power acceleration from a standstill was demonstrated. Fourth, the exhaust stream was a conduit for noise transmission from the turbines.

The first of these faults could be eased by decreasing the polar moments of inertia of the compressor and gasifier-turbine rotors. The remaining three could be improved by addition of a heat exchanger to the cycle. It was concluded that a much higher heat-exchanger effectiveness could be achieved in the space available by using a periodic-flow regenerator than a steady-flow recuperator. Fuel economy was subject to additional improvement through use of a higher turbine inlet temperature.

This led to design of the GT-304, a 150-kW two-shaft regenerative engine with reduced gasifier-rotor inertia and a rated pre-turbine temperature increased to 900°C (Turunen and Collman, 1957). The GT-304 was designed to fit within the Firebird II, a four-passenger show car built for the 1956 Motorama.

Lessons learned from GMR's first regenerative engine were incorporated into the GT-305, a new 170-kW engine that retained the 900°C pre-turbine temperature of the GT-304 but featured an improved regenerator and more efficient turbomachinery (Turunen and Collman, 1959). Weighing 270 kg, the GT-305 was 38 percent lighter per kW produced than its predecessor.

The GT-305 was introduced to the public at the 1958 Motorama in Firebird III. Not only did these show cars afford an opportunity to experiment with a new powerplant, but they also provided a medium for trying a variety of other vehicle concepts and technologies possessing future production potential in conventional automobiles.

The general structure of the GT-304 and GT-305 is illustrated in the schematic of Fig. 5. A pair of slowly rotating porous regenerator drums, one on either side of the engine centerline, appear in the schematic in profile as a ring. A bulkhead separates the high-pressure forward portion of the engine from the rear low-pressure portion. The high-pressure plenum, shown shaded, is bounded by the bulkhead, the gasifier-turbine nozzle diaphragm, the gasifier-shaft housing, the compressor housing and forward outer casing, all of which are represented by heavy lines, and the engine side covers and other pieces not shown in this simplified schematic. The bulkhead accommodates an upper and lower ''window frame'' on each side of the engine, through which a regenerator drum rotates. Because the pressure ratio across these openings is almost as great as the compressor pressure ratio, regenerator seals must be incorporated that minimize the leakage of high-pressure air to the low-pressure exhaust side of the engine without passing through the turbines.

As illustrated, the compressor-discharge air flowed radially inward through the regenerator drum into the portion of the high-pressure plenum falling within the drums. Within this volume, the combustors, not shown, were located. They were mounted with centerlines in a plane normal to the gasifier shaft so that the fuel nozzles were accessible from the engine side covers. In the GT-304, two combustors were mounted, one above the other, on either side of the engine. The GT-305 used only one combustor on each side.

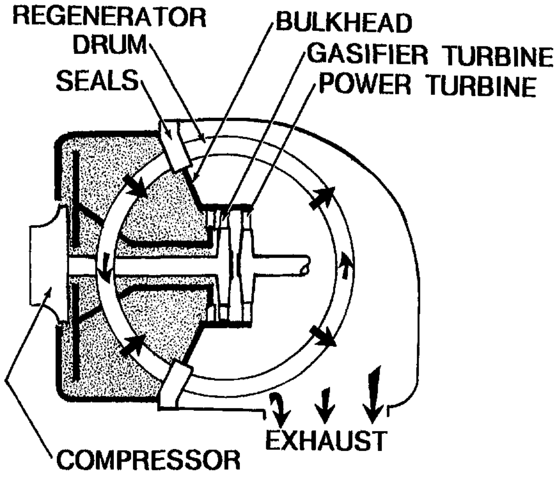

Fig. 5 Structure of regenerative gas turbine

The Allison Division made some modifications to the GT-305 design to facilitate production, designated their version the GMT-305, and supplied engines for evaluation in a tracked vehicle, an amphibious vehicle, and a wheeled tractor for the Army, and a personnel boat for the Navy (Guernsey, 1962).

Assimilation of such field experience led to the GT-309, a 210-kW regenerative engine intended specifically for heavy-duty use (Turunen and Collman, 1966). The two-shaft arrangement was retained, but a single drum regenerator was mounted at the top of the engine, rotating around a vertical axis. This led to a single vertically oriented combustor accessed from the top of the engine. Compressor pressure ratio was raised to 3.9, and pre-turbine temperature was raised to 940°C. To control manufacturing cost, the compressor rotor was cast, rather than being machined from a forged billet as previously. The expense of attaching individual turbine blades to the turbine rotors was avoided by casting the blades integrally with the rotors.

Power Transfer was introduced in the GT-309. This system allows the gasifier section to be joined to the power turbine through an accessory drive shaft and a slipping clutch. A controller regulates clutch torque. The additional load imposed on the gasifier shaft by the clutch raises turbine inlet temperature at part load to decrease fuel consumption. Additionally, Power Transfer connects the vehicle wheels to the engine compressor during deceleration to provide the engine braking that is so noticeably absent in the simple two-shaft engine. Power Transfer holds a loaded heavy-duty vehicle to a safe speed while going down any hill it is able to climb. It also provides overspeed protection so that a manual transmission can be used safely.

True to its heavy-duty intent, the GT-309 was evaluated in a GMC transit coach known as Turbocruiser II, and in two truck tractors, the GMC Astro 95 and the Chevrolet Turbo-Titan II. The GT-309 was handed off to the Detroit Diesel Division, which was merged with the Allison Division in 1970, and GMR proceeded to withdraw from the gas turbine field.

However, anticipated future light-duty emissions standards posed a new industry problem. The catalytic converter had not yet been developed sufficiently for production application, and upcoming standards could not be met by the traditional gasoline spark-ignition engine without it. Emissions tests were conducted on the GT-309 installed in a truck tractor. Introducing such data into an analytical model of a passenger-car gas turbine indicated that existing HC and CO standards could be met easily, but NOx emissions would be a problem (Wade and Cornelius, 1972). NOx emissions were decreased by up to 40 percent by modifying the existing GT-309 combustor both to decrease residence time in the high-temperature primary zone and to change the average primary zone equivalence ratio. That magnitude of reduction was insufficient to satisfy future NOx standards, however.

To extend this effort on an engine more fitting for a passenger car, design studies were initiated for a new engine. Serious consideration was given to a single-shaft gas turbine, but a complex transmission was needed to compensate for the poor torque characteristic of such an engine (Liddle et al., 1972). Various types of hydraulic torque converter, and an eight-speed geared transmission with a slipping clutch, were studied. An aerodynamic torque converter, having a centrifugal compressor as the input element and a three-stage radial-outflow turbine as the output element, was evaluated experimentally. Variable inlet guide vanes were tested on an engine compressor (Sheridan et al., 1974). These investigations only served to reaffirm the choice of a two-shaft design for automotive use.

Design of such an engine, the GT-225, was then undertaken (Collman et al., 1975). A rating of 170 kW was chosen as appropriate for the 1971 Chevrolet Impala in which it was to be installed. A design-point pre-turbine temperature of 1010°C was selected at a compressor pressure ratio of 4.5. Engine layouts considered included one with a recuperator mounted above the engine, one with two side-mounted disk regenerators, and a third with a single top-mounted disk regenerator. Component testing was completed on the recuperator and on both metal and ceramic regenerator disks. Ultimately, the layout employing a single top-mounted disk regenerator was selected.

A radial-inflow gasifier turbine was studied, but considerations of gasifier acceleration and compatibility with the downstream axial-flow power turbine led to retention of the axial-flow turbine used on previous engines. The polar moment of inertia of the monolithic cast gasifier-turbine rotor was actually made less than that of the cast aluminum compressor rotor at the opposite end of the gasifier shaft, even though the turbine alloy had triple the density of aluminum.

The power turbine was provided with variable-geometry nozzle vanes. Ability to adjust their flow angle allowed operation at higher turbine inlet temperature at part load for better fuel economy, improved engine response, provided engine braking on decelerations, decreased idle fuel rate, and decreased idle creep of the vehicle.

GMR combustion specialists joined with their counterparts at Allison to develop a low-NOx combustor. Previous effort had demonstrated that the conventional liquid fuel spray, with its resultant diffusion combustion, would not lower NOx sufficiently. A variety of concepts was assessed on the combustor test rig, backed by a model of reaction kinetics. The combustor design ultimately developed involved prevaporizing and premixing the fuel with air to form a homogeneous lean mixture ahead of the reaction zone, then introducing the remaining air into the products downstream from the reaction zone. To keep both NOx and CO emissions within bounds while avoiding flame blowout and excessive skin temperature, yet maintain low pressure drop across the combustor, programmed variable geometry was needed at both the upstream and downstream ends of the combustor. An electronic controller maintained this schedule.

The car was tested at low mileage over the 1972 Federal Test Procedure (FTP) at a mass of 2270 kg. Emissions were 0.20/2.8/6.0 g/mi HC/CO/NOx with a conventional combustor using a liquid fuel spray. With the prevaporized/premixed combustor these levels dropped to 0.18/2.0/0.38 g/mi HC/CO/NOx. This 1973 test was the first known demonstration by a gas turbine car of compliance, albeit at low mileage, with the 0.4 g/mi NOx standard that was not put in place by EPA until 1994.

Despite these encouraging emissions results, car fuel economy was still unacceptable. Although acceleration response had been improved markedly compared to earlier efforts, it was still inferior to that of a production gasoline engine. Engine durability remained unproven, and engine cost was still a concern. At this point GMR turned over further development of the automotive gas turbine to the GM Engineering Staff, redirecting its attention instead to technologies for improving conventional piston engines.

Summary

From 1950–75, two ICE alternatives to the established spark-ignition and diesel engines were investigated at GMR—the free-piston diesel and the gas turbine. Both used a gasifier-fed power turbine to deliver engine output. An intermittent-combustion opposed-piston machine served as the gasifier for the free-piston; a continuous-combustion turbo-gasifier was used by the gas turbine. Unlike the traditional piston engine, both of these alternatives offered broadened fuel tolerance, positive torque at zero output-shaft speed, freedom from engine vibration, and power delivery free of torque impulses.

The free-piston avoided the need for expensive high-temperature alloys required in the gas turbine. However, the intermittency of its air-intake pulses created a difficult noise problem.

The continuous combustion of the gas turbine limited allowable peak cycle temperature, contributing to unsatisfactory fuel economy. This was partially compensated by incorporating a regenerative heat exchanger, which also lowered the temperature of the engine exhaust and helped to silence turbine noise. Both Power Transfer and variable turbine nozzles were evaluated as means for improving fuel economy and providing engine braking. The latter feature also lowered idle fuel rate, reduced vehicle creep at idle, and improved a characteristically sluggish throttle response. A new combustor concept was demonstrated having exhaust emissions lower than possible with piston engines of that day.

Ultimately, neither of these ICEs was judged competitive over the broad spectrum of features desired from an automotive engine, e.g., size, weight, cost, fuel economy, emissions, driveability, noise and vibration—once the catalytic converter and electronic controls were perfected for the conventional engine.

References

Bailey, L.S., ed., 1983, *General Motors: The First 75 Years of Transportation Products,* Automobile Quarterly, Inc., Princeton, N.J., pp. 76–77, 94–95.

Collman, J.S., Amann, C.A., Matthews, C.C., Stettler, R.J., and Verkamp, F.J., 1975, "The GT-225—An Engine for Passenger-Car Gas-Turbine Research," SAE Transactions, Vol. 84, pp. 690–712.

Flynn, G., Jr., 1957, "Observations on 25,000 Hours of Free-Piston-Engine Operation," SAE Transactions, Vol. 65, pp. 508–515.

GM Progress of Power, 1969, Background information, General Motors, Warren, MI.

Guernsey, R.W., 1962, "Field Experience with GMT-305 Gas Turbine in Military Applications," SAE Transactions, Vol. 70, pp. 618–643.

Kettering, C.F., 1947, "More Efficient Utilization of Fuels," SAE Transactions, Vol. 1, pp. 669–676.

Liddle, S.G., Sheridan, D.C., and Amann, C.A., 1972, "Acceleration of a Passenger Car Powered by a Fixed-Geometry Single-Shaft Gas Turbine Engine," SAE Transactions, Vol. 81, pp. 133–156.

Sheridan, D.C., Nordenson, G.E., and Amann, C.A., 1974, "Variable Compressor Geometry in the Single-Shaft Automotive Turbine Engine," SAE Transactions, Vol. 83, pp. 753–764.

Turunen, W. A., 1950, "Gas Turbines in Automobiles," SAE Transactions, Vol. 4, No. 1, pp. 102–115.

Turunen, W.A., 1955, "Pinwheels or Pistons?—A Progress Report on Automotive Gas Turbines," SAE Transactions, Vol. 63, pp. 72–83.

Turunen, W.A., and Collman, J. S., 1957, "The Regenerative Whirlfire Engine for Firebird II," SAE Transactions, Vol. 65, pp. 578–587.

Turunen, W.A., and Collman, J. S., 1959, "The GT-305 Regenerative Engine in Firebird III," SAE Transactions, Vol. 74, pp. 357–373.

Turunen, W.A., and Collman, J.S., 1966, "The General Motors Research GT-309 Gas Turbine Engine," SAE Transactions, Vol. 74, Paper 650714.

Underwood, A.F., 1957, "The GMR 4-4 'Hyprex' Engine—A Concept of the Free Piston for Automotive Use," SAE Transactions, Vol. 65, pp. 377–386.

Wade, W.R., and Cornelius, W., 1972, "Emission Characteristics of Continuous Combustion Systems for Vehicular Powerplants—Gas Turbine, Steam, Stirling," *Emissions for Continuous Combustion Systems,* W. Cornelius and W.G. Agnew, ed., Plenum Press, New York, NY, pp. 375–445.

Past Experiences With Automotive External Combustion Engines

C. A. Amann
984 Satterlee Road,
Bloomfield Hills, MI 48304

GMR (General Motors Research Laboratories, now GM R&D Center) has a history of improving the internal combustion engine, especially as it relates to automotive use. During the quarter century from 1950–75, considerable effort was devoted to evaluating alternative powerplants based on thermodynamic cycles different from those on which the established spark-ignition and diesel engines are founded. Two of these, the steam engine and the Stirling engine, incorporated external combustion. Research on those two alternatives is reviewed. Both were judged to fall short of current needs for commercial success as prime movers for conventional automotive vehicles.

Introduction

Since its origin in 1920, GMR (General Motors Research Laboratories, now GM R&D Center) sought ways to improve engines responsible for vehicular propulsion, in the air and on the sea as well as on land. Most of that research was focused on internal-combustion engines (ICEs). During the third quarter of this century, however, research effort was also devoted to two external-combustion engines (ECEs)—the steam engine and the Stirling engine.

At the beginning of the 20th century, there were nearly twice as many steam cars produced in the U.S. as there were cars with spark-ignition (SI) engines. However, given the steady improvements made to both the SI engine and the fuel it consumes, steam car companies gradually withdrew from the marketplace—White in 1910, Stanley in 1925, and Doble in 1929. In the late 1960s, the lower exhaust-emissions standards promulgated by EPA encouraged re-evaluation of the external-combustion steam engine as a potentially cleaner alternative to the ubiquitous SI engine.

The Stirling engine was invented by Robert Stirling, a Scottish clergyman, in 1816. In 1937, the N. V. Philips Company in Eindhoven, Netherlands, became interested in the Stirling engine for driving a small electric generator that could supply power for Philips vacuum-tube radio equipment in remote locations lacking electricity. In 1948, several hundred copies of a Stirling engine designed to drive a 200 W generator were built in the Netherlands. However, its high cost, combined with the development of the battery-powered transistor radio, precluded its entry into the market (Flynn et al., 1960). GMR became interested in continued development of the Stirling engine for other applications because of its potential for high thermal efficiency, its quiet operation, and the fuel insensitivity afforded by its external combustion.

Thermodynamic Cycles

Thermodynamics approximates engine cycles with consecutive ideal processes. Thus, the ideal Otto cycle on which the SI engine is based is an SVSV cycle. This code signifies that the engine cycle is ideally comprised successively of an isentropic compression, the addition of heat during constant-volume combustion, an isentropic expansion, and a return of the working fluid to its original state in a constant-volume process for repetition of the cycle. Because the ICE operates on an open cycle, that return to the original state involves exchanging the combustion products for a fresh charge in some form of exhaust and intake process. Although much of the combustion gas exits the cylinder during blowdown as the piston approaches bottom dead center, in the four-stroke cycle that gas exchange actually involves an additional round trip of the piston to execute dedicated exhaust and intake strokes.

That gas exchange process is eliminated in the ECE, which operates on a closed cycle. Combustion occurs outside of the work-producing cycle and adds its heat to the working fluid through a heat-transfer process. With combustion thus separated from the working fluid, that fluid need not be chosen to support combustion. As a result, the working fluid in the steam engine is water, which undergoes a change in phase as it circumnavigates the cycle. In contrast, in the Stirling cycle the working fluid always remains in the gaseous state. The preferred fluid for the Stirling engine is hydrogen, although helium can be substituted at a slight penalty in thermal efficiency.

Ideal cycles for these two ECEs are represented on a temperature-entropy plane in Fig. 1. The thermodynamic processes comprising these cycles are marked P, V, S, or T, depending on whether they occur at constant pressure, volume, entropy, or temperature.

The steam engine operates on the Rankine cycle, characterized as an SPST cycle. It is illustrated in Fig. 1(*a*), where the dome bounding the wet-steam region is represented by the broken line. Compression occurs in the liquid state from (1)–(2) as water passes through the feedwater pump. This is advantageous to the Rankine cycle because compressing the working fluid as a liquid consumes less energy than compressing it in the gaseous state. Combustion heat is transferred into the fluid from (2)–(3), transforming it from a liquid through the wet steam condition to a superheated vapor at point 3. Then work is extracted in the expander from (3)–(4). Finally, the saturated steam at point 4 is condensed back to water from (4)–(1) in the condenser.

The ideal Stirling cycle is represented in Fig. 1(*b*). Heat is added to the cycle through external combustion during isothermal expansion from (3)–(4), and rejected to the cooler during isothermal compression from (1)–(2). Ideally, all of the heat removed from the working medium during constant-volume cooling from (4)–(1) is stored in a regenerator for return to that medium during constant-volume heating from (1)–(2). Because all the heat exchange with the surroundings thus occurs

---

Contributed by the Internal Combustion Engine Division (ICE) of THE AMERICAN SOCIETY OF MECHANICAL ENGINEERS for publication in the ASME JOURNAL OF ENGINEERING FOR GAS TURBINES AND POWER.

Manuscript received by the ICE July 1, 1996; final revision received by the ASME Headquarters January 12, 1999. Associate Technical Editor: D. Assanis.

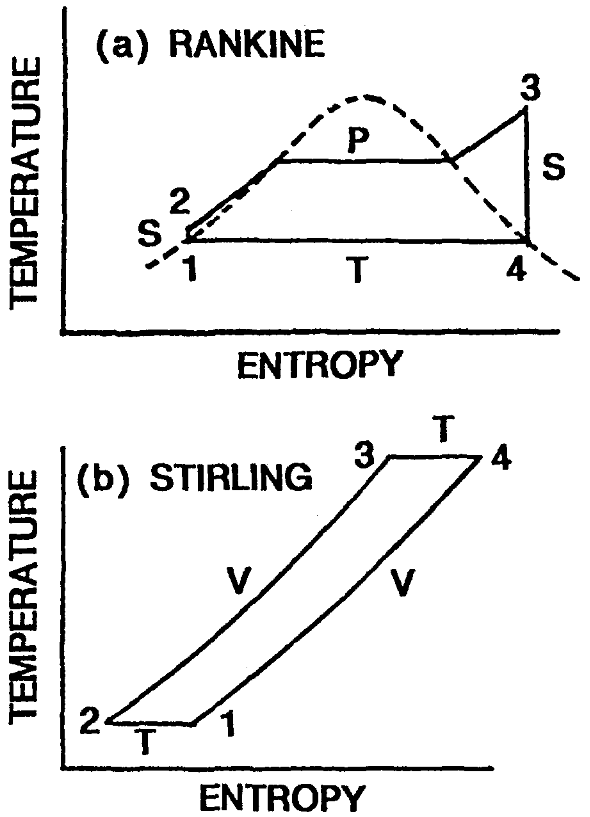

Fig. 1 Ideal temperature-entropy diagrams

isothermally, the ideal regenerative Stirling cycle has the same efficiency as a Carnot cycle operated between the same limiting temperatures. This outstanding efficiency potential is one of the factors that makes pursuit of the Stirling engine so attractive.

Steam Engine

General Motors evaluated two steam-powered buses in 1929, in the era before the diesel-powered bus, but results failed to inspire commercialization. In the late 1960s, before the catalytic converter, it was unclear that the traditional intermittent-combustion SI engine would be able to satisfy promulgated tailpipe emissions standards. Many felt that the continuous combustion of a steam engine offered greater flexibility for emissions control. In order to evaluate that possibility, GMR undertook the design of a modern steam engine, the SE-101, in 1969 (Vickers et al., 1970a).

At its rating point, the expander inlet conditions were 4.83 MPa absolute pressure and 370°C. This maximum temperature was selected in deference to the limitations of the oil used to lubricate the piston expander. The design-point condenser inlet temperature was 100°C, corresponding to an absolute pressure of 101 kPa. In the absence of losses, the steam tables project an ideal Rankine-cycle efficiency just under 30 percent for these conditions. When losses are included for expander indicated efficiency and expander friction, the steam-generator efficiency, and such engine-required auxiliaries as the combustion-air blower, condenser fan, feedwater pump, and fuel pump, losses easily cut the engine brake efficiency to half of the ideal Rankine-cycle efficiency. Because the peak efficiency of contemporary SI engines at the time exceeded 30 percent, it seemed clear from the outset that despite the opportunity for exhaust-emissions gains with the steam engine, that engine was not going to be competitive with existing production powerplants in fuel economy.

A simplified schematic of the steam engine appears in Fig. 2. Beginning at the upper left, feedwater was supplied in the SE-101 by a solenoid-controlled four-cylinder reciprocating pump.

The steam generator had three sections: the economizer (in which the water from the feedwater pump is initially heated), the evaporator (intended to boil the heated water), and the superheater (in which the vapor is heated to peak cycle temperature). Measuring 787 × 394 × 305 mm, the 90-kg steam generator contained 10.9 m of tubing, some of plain-carbon steel and some of austenitic-stainless steel. Both plain and finned tubes were used, with twisted tape being inserted into the evaporator tubes to enhance heat transfer. The steam generator earned ASME Boiler and Pressure Vessel Code certification.

The working fluid in the steam generator was heated by two 255 mm diameter stainless-steel can-type kerosene burners, each 190 mm long, providing a gas discharge temperature of 1370°C. Two burners were chosen instead of one in order to conform to underhood space limitations. Air-atomizing fuel nozzles were used for superior fuel atomization.

The four-cylinder uniflow piston expander had a displacement of 1.65 L (89 mm bore × 67 mm stroke). Steam was admitted through outward-opening poppet valves in the cylinder head, actuated through rocker arms from an overhead camshaft. Spent steam passed through exhaust ports that were uncovered by the steam pistons near bottom dead center. As illustrated in Fig. 3, the steam piston was joined to the crosshead by a piston rod. Radial clearances were adjusted to avoid contact between the steam piston and the cylinder wall, with the splash-lubricated crosshead absorbing the sidethrust. The rings on the steam piston received lubrication from a special high-temperature oil that was metered sparingly into the incoming steam. A special filtering system was introduced ahead of the condenser to remove this oil from the expander exhaust steam in order to avoid condenser fouling. This system was not developed to the point of being satisfactory for long-term use. The expander was rated at 120 gross kW at 3200 r/min. Output was controlled at part load by throttling the incoming steam.

The primary-unbalance couple inherent in a four-cylinder reciprocator with 90 deg crank spacing was counteracted by crankshaft counterweights combined with counterweights mounted at the ends of the camshaft. Because it was possible for the expander to be shut down at a crank angle where introduction of high-pressure steam on restart would cause reverse rotation of the crankshaft, an electric starter was added to initiate crankshaft rotation during starting.

Closed-cycle powerplants like the steam engine lack a stream of exhaust gas whereby heat associated with cycle inefficiency can be rejected directly to the atmosphere, as in the internal-combustion engine. Therefore, the cycle cooler—in the steam engine, the condenser—is presented with a much greater heat load than is the radiator of an internal-combustion engine. The core volume of the SE-101 condenser was approximately three

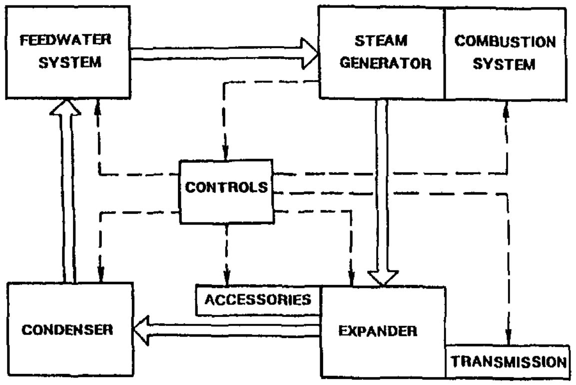

Fig. 2 Schematic of steam engine

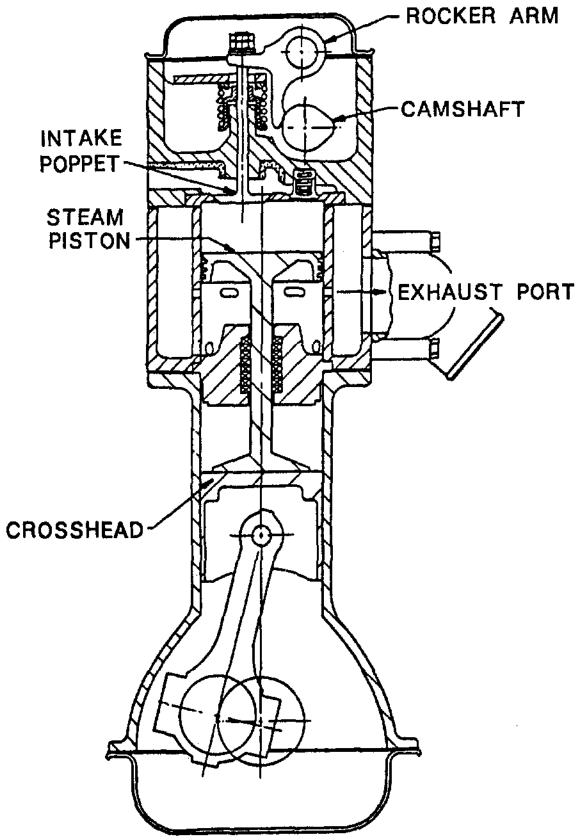

Fig. 3 Section through SE-101 steam expander

times that of a radiator for a comparable SI engine. Cooling air was supplied by two fans that, at an engine speed of 3200 r/min, consumed 15.5 kW. This amounted to a substantial fraction of the gross power available from the expander. Unevenly spaced blading on the cooling fans reduced the tonality of their noise. Because the condenser was unable to handle the heat-rejection load at high speeds up grades on hot days, a pressure relief valve was included that released steam from the condensing system when expander backpressure exceeded ambient pressure by 100 kPa. The lost water then had to be made up from a water storage tank.

At the same time the SE-101 engine was being designed and developed at GMR, a second steam engine, the SE-124, was built under contract by Besler Developments, Inc. (Vickers et al., 1970b). Besler was a veteran of the 1920s Doble steam-car era, and in 1933 was responsible for the world's first steam engine to fly in an airplane. The 2-L SE-124 expander was a compound double-acting V-2 using spool valves. Its steam generator was of the monotube type, with water/steam flowing upward through 7 m of tubing wound in a spiral coil, 292 mm high and 406 mm in diameter. Combustion air from the blower was introduced tangentially into a combustion space above the coil of tubing and spiraled downward to an exhaust opening at the bottom of the steam generator. An air-atomizing fuel nozzle was used. The brazed aluminum plate-fin condenser measured 356 × 860 mm, 76 mm thick, again large by ICE standards. Because the combustion-air blower, fuel pump and atomizing-air compressor were all run by constant-speed electric motors, the engine employed on-off control.

The SE-101 was installed in a modified Pontiac Grand Prix in which the engine compartment had to be lengthened 178 mm to fit the engine into the car. The SE-124, smaller in both size and rated power, was installed in a Chevrolet Chevelle. Both cars were subjected to extensive testing (Vickers et al., 1970b). Some results are presented in Table 1.

With a number of cars now accelerating from 0–97 km/h in 10 s or less, it is evident from Table 1 that the SE-101 produced insufficient power for acceleration of the Grand Prix in which it was installed. The lighter SE-124-powered Chevelle could not even operate on the highway at a satisfactory speed. The lack of performance in the Chevelle contributed to its much higher fuel economy, but even its fuel economy was woefully inadequate. Rankine-cycle efficiency calculations from the steam tables were indeed upheld.

The warmup times shown in Table 1 for an engine originally at room temperature are excessive. On the current federal test procedure, car acceleration begins 20 s after the cold start. These long steam-car warmup times are unacceptable to the customer, excessively decrease fuel economy in normal short-trip driving, and increase tailpipe emissions significantly.

Another matter of importance is water consumption. The SE-124 condenser essentially depended on ram air for cooling. As a result, at a level-road speed of 80 km/h on a standard day, the water consumption could actually exceed the fuel consumption. The SE-101 condenser, on the other hand, was fully condensing on a level road on a standard day over the complete vehicle speed range. At a warmer ambient temperature of 40°C, however, the SE-101 condenser had to vent some steam above 80 km/h. Venting requirements were greater for both cars on upgrades, of course.

Emissions tests run on these two steam cars are difficult to interpret because the driving schedule used for their measurement has changed substantially since 1970. It appears doubtful, however, that either could meet current standards. The SE-101 was also found to have higher-than-expected HC and CO emissions, a problem traced to premature quenching of the combustion products by the steam generator. A cure would likely require a larger burner than available space allowed.

Progress was being made with exhaust reactors on SI engines at that time, with much better fuel economy than these steam engines could provide, even with evolutionary improvement. This encouraged abandonment of the steam alternative at GMR. Federal and state governments continued sponsorship of a number of additional steam-powered vehicles with various contractors, but none proved able to provide acceptable fuel economy and/or emissions, or to overcome the problems of size, weight, and wintertime freezing of the working fluid. Gradually, serious interest in the automotive steam engine once more subsided.

Stirling Engine

The invention of the Stirling engine is attributed to Robert Stirling, a Scottish clergyman, in 1816. In 1937, the N. V. Philips Company in Eindhoven, Netherlands, became interested in the Stirling engine for driving a small electric generator that could supply power for Philips vacuum-tube radio equipment in remote locations that lacked electricity. In 1948, several hundred copies of a Stirling engine designed to drive a 200-W generator were built in the Netherlands, but its high cost, combined with development of the battery-powered transistor radio, precluded its entry into the market (Flynn et al., 1960).

In 1958 General Motors entered into a cooperative program with N. V. Philips to continue development of the Stirling engine, and soon GMR was collaborating with Philips on improved designs. From 1961–1965, GMR delivered three succes-

Table 1 Steam-car characteristics

	SE-101	SE-124
Test weight class (lb)	5500	3500
Time, 0–97 km/h (s)	37.25	∞*
Max. economy (mpg)	6.6	13.1
Warmup time (min)	2.4	5.8

* Top speed = 93 km/h

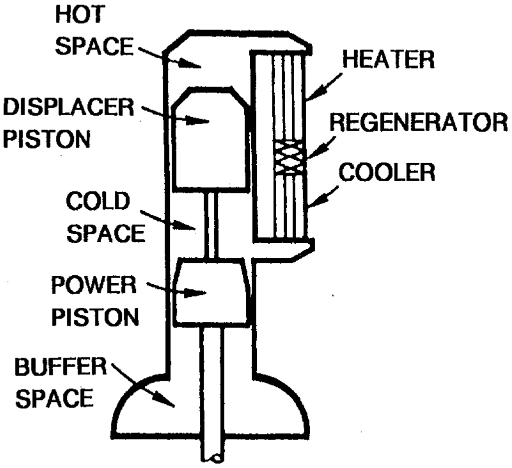

Fig. 4 Schematic of Stirling engine

sively improved models of a portable single-cylinder GPU (ground power unit) to the U.S. Army, all rated at 3 kW electrical output (Heffner, 1965). The Stirling engines in these GPUs were noted for their quietness and freedom from vibration compared to small conventional ICEs.

A schematic of the single-cylinder Stirling GPU engine is shown in Fig. 4. The cylinder contains both a power piston and a displacer piston, attached to concentric piston rods. The two pistons are reciprocated out of phase by means of a rhombic drive, not shown, that incorporates the output shaft. To the right of the cylinder in this schematic is a parallel heat-transfer path—tubular heater at the top, tubular cooler at the bottom, and metal-mesh regenerator interposed. The working gas shuttles back and forth between the cold and hot spaces. Conceptually, during compression the power piston moves upward while the displacer remains stationary, and the cooler removes heat to maintain constant temperature. Then both pistons move concurrently to transfer the compressed gas from the cold to the hot space isochorically. As the gas travels upward through the regenerator, it picks up stored heat and reaches peak cycle temperature. Next, with the displacer fixed, the power piston moves downward to extract work from the high-temperature high-pressure gas and deliver it to the output shaft. Input heat from the heater maintains isothermal expansion. Finally, the two pistons move concurrently to transfer gas from the hot to the cold space isochorically, depositing heat for storage in the regenerator in the process. This conceptualization of the cycle is, of course, an oversimplification of what occurs in the real engine, where the individual processes comprising the cycle overlap, but it serves to illustrate the principles involved.

The preferred working medium for the Stirling engine is gaseous hydrogen, although helium can be used at some sacrifice in efficiency and power. To provide a favorable specific power, the gaseous medium is pressurized. The rated mean pressure in the GMR GPUs was 6.9 MPa, although other Stirling engines have been designed for pressures as high as 18.7 MPa. Pressurization aggravates leakage of the working gas through a reciprocating seal located where the power-piston rod penetrates the wall of the buffer space in Fig. 4.

Not shown in Fig. 4 are the radiator through which the cooler heat is rejected, its fan and drive, the combustor that supplies heat to the heater tubes, the blower that delivers air to the combustor, the fuel system, and a preheater that transfers heat from the heater exhaust to the blower discharge to heat the combustor inlet air, thus decreasing the required fuel rate. All of these components are essential to the modern Stirling engine.

Also omitted is the hydrogen (or helium) storage reservoir. This engine is controlled by adjusting the mass of gas trapped in the engine loop. To increase output power, stored gas must be introduced into the engine. Similarly, to decrease power, gas must be bled from the system. For short-term fast-response power reduction, working gas can alternatively be bypassed around the power piston. In highly transient operation, as might typify city driving of a passenger car, operating the hydrogen pump to facilitate these transfers of the working gas could affect fuel economy adversely.

GMR worked with Philips and the Electro-Motive and Allison Divisions of General Motors to assess a variety of other Stirling engines. One was a 4-cylinder model rated at 270 kW, which was evaluated by the U.S. Navy. The most unusual was an auxiliary engine for the U.S. Air Force, intended for an orbiting satellite. It would be operated from solar energy transferred through a Na-K eutectic heat transfer fluid.

Concerns about closed-cycle heat rejection, and control during highly transient driving schedules, suggested that applications other than main propulsion of the passenger car held more promise initially for the Stirling engine. However, three car demonstrations were executed at GMR to highlight certain aspects of this unusual engine.

Two of these were Stirling-electric hybrids. The Stir-Lec I used an AC electric drive system (Agarwal et al., 1969), the Stir-Lec II a DC drive. The rear end of the Stir-Lec I, where the engine was located, is illustrated in Fig. 5. The engine, its radiator, and the hydrogen storage reservoir are all evident, as well as the engine-driven alternator. Cables running to and from the front end of the car communicate with the lead-acid battery pack and other required electric equipment located under the hood.

In the Stir-Lec hybrids, the engine ran most of the time at high load, supplying propulsive power to the car through what amounted to an electric transmission and charging the batteries when the engine developed more power than the vehicle needed. Engine power was insufficient for accelerations and high-speed driving. Under those circumstances, energy from the batteries augmented the engine. This system shielded the Stirling engine from excessive transient operation. Additionally, the engine could be shut down in polluted inner-city environments and the vehicle run for a limited range on stored electric energy.

Emissions tests showed low levels of HC and CO in the engine exhaust, but NOx was excessive. Substantial reductions in NOx were effected either by leaning the air-fuel ratio in the combustor or by recirculating cooled exhaust gas through the combustor, but at a modest penalty in engine efficiency (Wade and Cornelius, 1972).

The third Stirling-engine car was the Calvair, built to demonstrate the ability of the Stirling engine to operate pollution-free on stored heat (General Motors, 1969). Underwater operation of a submarine without a snorkel is a potential application for

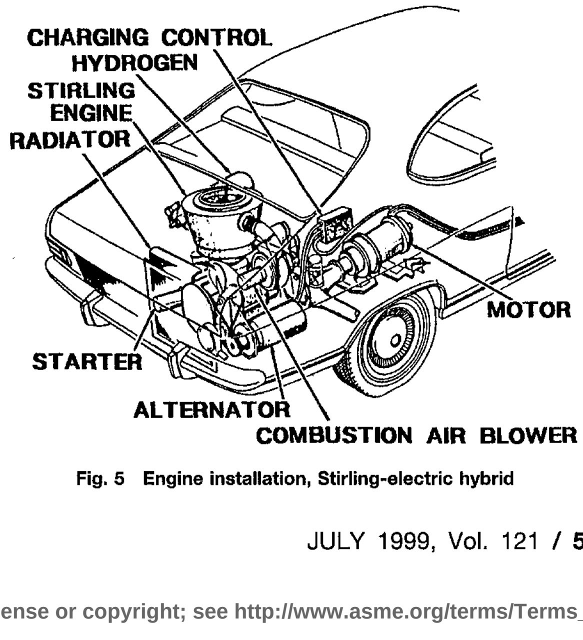

Fig. 5 Engine installation, Stirling-electric hybrid

this capability. Utilizing the latent heat of a molten salt appeared to offer a more compact energy-storage technique than storing energy electrically in a battery. Merely to demonstrate the concept, however, the Calvair was operated on energy stored in a pre-heated bed of aluminum oxide pellets housed in the front compartment of the car, beneath the hood. With the car parked, the pellets could be heated with an external natural-gas burner. To drive this zero-emission vehicle, heat was then extracted from the bed through a lengthwise tunnel in the floor of the car by a high-temperature blower, providing an engine temperature of about 650°C to the rear-mounted Stirling engine.

At the end of the 1960s, GMR suspended work on the Stirling engine to contribute to effort on another engine believed at the corporate level to have greater automotive potential—the rotary combustion engine. As a post script to the Stirling experience, however, in 1984 the Department of Energy (DOE) offered GMR the opportunity to evaluate an experimental installation of a Stirling engine in an automobile (Haverdink et al., 1984). The engine and its vehicle installation were due to Mechanical Technology Incorporated of Latham, NY, and had resulted from their long standing contract with DOE to develop an automotive Stirling engine.

The MTI engine employed four cylinders arranged in a square when viewed from the top. Weighing 263 kg, it developed 58 kW at 4000 r/min on hydrogen with a heater-head temperature of 720°C and a coolant temperature of 50°C. Maximum cycle mean pressure was 15 MPa.

The car in which the engine was installed claimed a curb weight of 1325 kg, putting it in the EPA 3250 lb TWC (test weight class). By 1984 standards, the engine was underpowered for this car. The engine might have been more appropriate for the Chevrolet Chevette then in production, but layouts revealed that the engine was so big the hood could not be closed if it had been installed in a Chevette.

Recognizing that the Stirling engine was still undergoing development, the car was tested on a chassis dynamometer as if the engine had been installed in a car of the 2500 lb Chevette TWC. This is tantamount to assuming that with continued development, the Stirling engine can be downsized to match the Chevette engine in terms of size and weight at the same rated power. With these assumptions, the experimental Stirling engine showed HC, CO, and NOx emissions that were approximately half of the 1984 standards. (Compared to current federal standards, HC was marginal and NOx excessive.) Acceleration from a standing start to 97 km/h was slightly slower than for the Chevette, but that time of around 20 s is far too slow to satisfy the current U.S. market. At highway speeds, acceleration with the Stirling engine was more deficient. Fuel economy on the federal highway driving schedule was comparable for both cars, but on the urban schedule the Stirling engine fell 20 percent short of the Chevette. This was traced to the high idle fuel rate of the Stirling engine and to the extra fuel consumed in heating an external combustion engine to its operating temperature during cold starts, an energy expenditure that is not recovered on engine shutdown.

Summary

During the third quarter of the 20th century, two different ECEs were investigated at GMR—the steam engine and the Stirling engine. Unlike the contemporary piston ICE, both were able to develop torque at zero output-shaft speed, and both were insensitive to fuel specifications. However, both were large and heavy compared to contemporary ICEs.

Both shared two other inherent traits of the ECE. First, the radiator ultimately used to reject cycle waste heat to the environment was about triple the size of a typical ICE radiator. It also involved increased cooling-fan power. Second, such an engine, when initially at room temperature, cannot develop adequate power until the heat exchanger transferring heat from the combustion gas to the working medium has achieved operating temperature. Associated with this annoying warmup time are both the loss of unrecovered fuel energy and the production of additional exhaust emissions.

In the steam car, even the oversized radiator was unable to reject all of the required heat at high engine-power output on hot days. This necessitated adding a make-up water tank to the vehicle.

In the steam car, there was no way to prevent freezing of the working fluid at wintertime temperatures. With the Stirling engine, the working-fluid problem was excessive hydrogen leakage.

Compared to contemporary automobiles, the fuel economy of the steam car was dismal. Although GMR tested the Stirling engine in a hybrid-electric vehicle and in a zero-emissions version operating on stored heat, its only experience with a more conventionally powered Stirling car came in 1984 with tests of an experimental installation on loan from a DOE contractor. Fuel economy was much better than with the steam engine but still slightly poorer than that of a production car with a SI engine. Despite their use of continuous combustion, neither ECE would satisfy emissions standards met by the SI engines with an exhaust catalyst.

References

Agarwal, P.D., Mooney, R.J., and Toepel, R.R., 1969, "Stir-Lec I, A Stirling Electric Hybrid Car," SAE Paper 690670.

Flynn, G., Jr., Percival, W.H., and Heffner, F.E., 1960, "GMR Stirling Thermal Engine, Part of the Stirling Engine Story—1960 Chapter," SAE Transactions, Vol. 68, pp. 665–683.

Haverdink, W.H., Heffner, F.E., and Amann, C.A., 1984, "Assessment of an Experimental Stirling-Engine-Powered Automobile," Proceedings, 22nd Automotive Technology Development Contractors' Meeting, SAE P-155, pp. 151–166.

Heffner, F.E., 1965, "Highlights From 6500 Hr of Stirling Engine Operation," SAE Transactions, Vol. 73, pp. 33–48.

Vickers, P.T., Amann, C.A., Mitchell, H.R., and Cornelius, W., 1970a, "The Design Features of the GM SE-101—A Vapor-Cycle Powerplant," SAE Transactions, Vol. 79, pp. 628–650.

Vickers, P.T., Mondt, J.R., Haverdink, W.H., and Wade, W.R., 1970b, "General Motors' Steam Powered Passenger Cars," SAE Transactions, Vol. 79, pp. 2099–2120.

Mixing of Multiple Jets With a Confined Subsonic Crossflow: Part II—Opposed Rows of Orifices in Rectangular Ducts

J. D. Holdeman
NASA Glenn Research Center,
Cleveland, OH 44135

D. S. Liscinsky
United Technologies Research Center,
East Hartford, CT 06108

D. B. Bain
CFD Research Corporation,
Huntsville, AL 35805

This paper summarizes experimental and computational results on the mixing of opposed rows of jets with a confined subsonic crossflow in rectangular ducts. The studies from which these results were excerpted investigated flow and geometric variations typical of the complex three-dimensional flowfield in the combustion chambers in gas turbine engines. The principal observation was that the momentum-flux ratio, J, and the orifice spacing, S/H, were the most significant flow and geometric variables. Jet penetration was critical, and penetration decreased as either momentum-flux ratio or orifice spacing decreased. It also appeared that jet penetration remained similar with variations in orifice size, shape, spacing, and momentum-flux ratio when the orifice spacing was inversely proportional to the square-root of the momentum-flux ratio. It was also seen that planar averages must be considered in context with the distributions. Note also that the mass-flow ratios and the orifices investigated were often very large (jet-to-mainstream mass-flow ratio > 1 and the ratio of orifices-area-to-mainstream-cross-sectional-area up to 0.5, respectively), and the axial planes of interest were often just downstream of the orifice trailing edge. Three-dimensional flow was a key part of efficient mixing and was observed for all configurations.

1 Introduction

Jets-in-crossflow have been extensively treated in the literature. Flows in which this is an integral constituent occur in a number of areas important in combustion and energy science and technology. In a gas turbine combustor for example, fuel and air mixing is important to combustor performance and emissions. Also, the mixing associated with arrays of jets in crossflow can play a critical role as in the dilution zone of a conventional combustor, and the mixing zone of a staged combustor such as the Rich-burn/Quick-mix/Lean-burn (RQL) combustor. Although results reported to date have all contributed additional understanding of the general problem, the information obtained in them was determined by their motivating application, and may not satisfy the specific needs of different applications.

One characteristic of jet-in-crossflow applications in gas turbine combustion chambers is that they are often confined mixing problems, with up to 80 percent of the total flow entering through the jets. The result is that the equilibrium mixing pattern and composition of the exiting flow may differ significantly from that of the entering mainstream flow.

A summary of NASA-supported research in the 1980s is given in Holdeman (1993). Reports and papers from NASA-supported studies in a cylindrical duct that were published since the previous article was presented are summarized by Holdeman et al. (1999). Recent results from rectangular and annular configurations include Bain et al. (1992–1995b), Bain et al. (1997), Blomeyer et al. (1996), Blomeyer (1997), Chiu et al., (1993), Crocker and Smith (1993), Crocker et al. (1994), Doerr and Henneke (1993), Doerr et al. (1995a, 1995b), Everson et al. (1995), Liscinsky et al. (1992), Liscinsky et al. (1993), Liscinsky et al. (1993), Liscinsky et al. (1994, 1996b), Lozano et al. (1991), Lozano et al. (1992), Krautkremer et al. (1998); Margason (1993), Margason and Tso (1993), Mungal et al. (1992), Nikjooy et al. (1993), Smith et al. (1992), and Winter et al. (1992).

2 Description of the Flowfield

Figure 1 shows a schematic of the flow in a rectangular duct with injection from opposed rows of jets on top and bottom walls. The scalar field results are often presented as plots of the temperature difference ratio, θ, where

$$\theta = \frac{(T_m - T)}{(T_m - T_j)}$$

or

$$1 - \theta = \frac{(T - T_j)}{(T_m - T_j)} \tag{1}$$

It should be noted that although T is used here, these parameters can be defined with concentrations or any conserved scalar. Also note that the jet fluid is identified by larger values of θ (i.e., $\theta = 0$ if $T = T_m$) and $\theta = 1$ if $T = T_j$. Unless noted otherwise, jet fluid will be colored white and mainstream fluid will be colored black. The equilibrium jet mass fraction for any configuration is approximately equal to the fraction of the total flow entering through the jets, $MR/(MR + 1)$.

If one averages a conserved scalar across a y-z plane downstream of the orifice trailing edge, the result is herein called C_{avg}. It has been shown by Liscinsky et al. (1993) that this value is nearly equal to the value of a fully mixed flow. Another planar averaged parameter is the variance, often called spatial unmixedness (in this paper unmixedness = spatial unmixedness). Note that this variance has been normalized by dividing by the product of C_{avg} and $(1 - C_{\text{avg}})$.

Contributed by the International Gas Turbine Institute and presented at the International Gas Turbine & Aeroengine Congress & Exhibition, Orlando, FL, June 2–5, 1997. Manuscript received by the ASME Headquarters March 15, 1997. Paper No. 97-GT-439. Associate Technical Editor: H. A. Kidd.

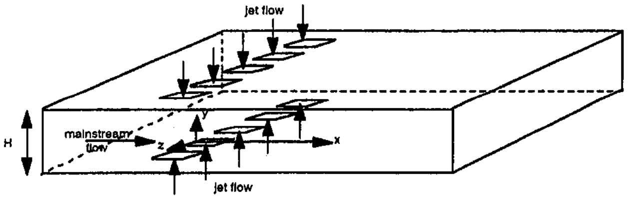

Fig. 1 Schematic of numerical mixing model (from Bain et al. (1995b))

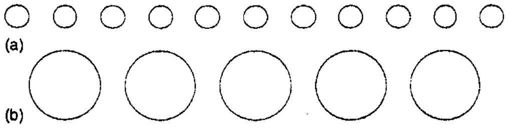

Fig. 2 Example orifice geometry: (*a*) previous dilution jet mixing; (*b*) current investigations (from Holdeman et al., 1997).

$$U_s = \frac{\frac{1}{m}\sum_{i=1}^{m}(C_i - C_{\mathrm{avg}})^2}{C_{\mathrm{avg}}(1 - C_{\mathrm{avg}})} \tag{2}$$

Although it is recognized that a uniform distribution may not always be desired, optimum is generally used herein (as in, e.g., Holdeman 1993) to identify flow and geometric conditions which lead to a uniform distribution in a minimum downstream distance. The primary independent geometric variables are the spacing between adjacent orifices, S, the orifice diameter, d, the orifice aspect ratio (long:short dimension), and the slant angle (with respect to the axial direction in the plane of the orifice). Because the objective in combustor applications is to identify configurations that provide a desired mixing pattern within a given downstream distance, locations of interest are identified in intervals of the duct height, H, rather than the orifice diameter, d. The primary independent flow variables are the jet-to-mainstream mass-flow ($MR = w_j/w_m$) and momentum-flux (J) ratios. These can be expressed as

$$J = \frac{MR^2}{(DR)(C_d)^2(A_j/A_m)^2}. \tag{3}$$

It was reported in Holdeman (1993) that jet penetration and centerplane profiles appear to be similar when the orifice spacing and the square root of the momentum-flux ratio were inversely proportional, i.e.,

$$C = (S/H)\sqrt{J}. \tag{4}$$

For single-side injection (and with $MR < .5$), the centerplane profiles were approximately centered across the duct height and approached an isothermal distribution in the minimum downstream distance when $C = 2.5$. This appeared to be independent of orifice diameter, as shown in both calculated and experimental profiles. The similarity of the profiles with the same orifice spacing but with different orifice diameters were also shown by Holdeman et al. (1973). Values of C in Eq. 4 that were a factor of 2 or more smaller or larger than the optimum corresponded to gross underpenetration or overpenetration, respectively. For opposed rows of in-line orifices, the optimum C was approximately half of the corresponding value for single-side injection; whereas, for opposed rows of staggered orifices, the optimum C was approximately doubled.

It has been recognized that what configuration is deemed "optimum" depend on the downstream location examined, so C in Eq. 4 must be a function of x/H. It has also been shown in recent studies of rectangular duct flows that C may be a function of something else too, e.g. for high mass-flow ratios the optimum C appeared to be about twice that found previously. Note that although the proportionality in Eq. 4 appears to hold for all cases, the value of the constant may vary with duct geometry, orifice shape, initial conditions and mass-flow ratio.

3 Results and Discussion

The following paragraphs describe the results from recent investigations in the context of the effects of the primary independent variables. Both experimental and computational studies were performed and are interspersed here. The work cited was performed by CFD Research Corporation, and the United Technologies Research Center. Sources are identified when results are discussed, and specifics of the calculations or experiments, as appropriate, are given in the corresponding references. Note also that the original figures often appear in color in the references.

In Fig. 1, x is the downstream coordinate, with $x = 0$ at the leading edge of the orifices. Sharp-edged orifices were considered in all cases. In the experiments, discharge coefficients were measured in separate experiments. The orifice area, A_j, was a physical dimension, so the effective area, AC_d, was $((C_d)(A_j))$. For all calculations shown herein, a uniform flow boundary was assumed for both the jets and mainstream. Since the orifice discharge coefficient, C_d, was expected to be less than unity for the jets, the area over which the uniform velocity was specified was the effective area. A_j could thus be determined as needed from the AC_d by assuming an effective discharge coefficient.

Investigations published prior to 1991 were primarily in a rectangular duct, but at significantly lower mass-flow ratios than in more recent studies. A schematic showing the relative orifice size is given in Fig. 2. Effects investigated were (1) variation of momentum-flux ratio, (J) at constant orifice shape and spacing, (2) variation of orifice spacing, S/H, at constant, J, (3) effect of orifice shape, (4) comparison of slanted slots and

Nomenclature

A_j/A_m = jet-to-mainstream area ratio
$AC_d = (A_j)(C_d)$
B = orifice blockage
$C = (S/H)\sqrt{J}$
C_{avg} = equilibrium concentration = θ_{EB}
C_d = orifice discharge coefficient
C_i = local concentration
d = orifice diameter
DR = jet-to-mainstream density ratio
H = duct height
J = jet-to-mainstream momentum-flux ratio = $(DR)(V_j/U_m)^2 = (MR)^2/((DR)(C_d)^2(A_j/A_m)^2)$
L = long dimension of orifice
L/W = orifice aspect ratio
m = number of pixels in the distribution
MR = jet-to-mainstream mass-flow ratio = $w_j/w_m = (\sqrt{DR})(\sqrt{J})(C_d)(A_j/A_m)$
S = lateral spacing between corresponding parts of adjacent orifices
T = temperature
T_j = jet exit temperature
T_m = mainstream temperature
$\theta = (T_m - T)/(T_m - T_j)$
U_m = mainstream velocity
U_s = spatial unmixedness
V_j = jet velocity
w_j/w_T = jet-to-total mass-flow ratio = $MR/(MR + 1)$
W = short dimension of orifice
x = downstream coordinate = 0 at leading edge of orifice
y = cross-stream coordinate = 0 at wall
z = lateral coordinate = 0 at centerplane

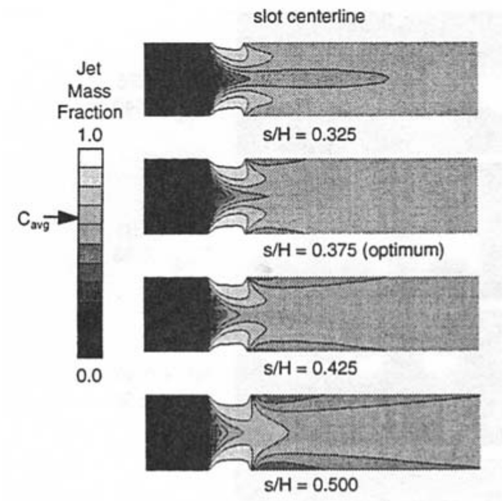

Fig. 3 Effect of varying jet spacing on calculated jet distributions for inline slots: $J = 36$; $MR = 2.0$ (data from Bain et al. (1995b)).

holes, (5) comparison of an opposed row of in-line and staggered jets, (6) effects of nonsymmetric mass addition, (7) effect of orifice blockage, and (8) variation of mass-flow ratio. These are discussed in the following sections.

3.1 Variation of Momentum-Flux Ratio. Based on previous studies which reported that the most important flow variable influencing the extent of jet mixing in a crossflow was the momentum-flux ratio, J, Liscinsky et al. (1992) performed a series of tests with $S/H = 0.5$ at two representative J values. The results reaffirmed the importance of the momentum-flux ratio in determining the downstream flowfield.

Jet penetration generally increases with increasing momentum-flux ratio, J. This can be seen in the experimental results for both slanted slots and round holes reported by Liscinsky et al. (1992). A similar effect is apparent in the calculated results of Bain et al. (1993) for a configuration with aligned slots of 4:1 aspect ratios at $S/H = 0.325$.

The planar unmixedness for both the Liscinsky et al. (1992) and Bain et al. (1994) cases suggest that it is possible to obtain low values of unmixedness at J values corresponding to overpenetration. This emphasizes that although planar averaged values are very useful and can provide insight, one should not rely on them alone, and must also assess the flowfield distributions.

3.2 Variation of Orifice Spacing. In general, the effect of decreasing the orifice spacing at constant J is similar to the effect of decreasing the momentum-flux ratio at constant S/H. This effect was shown in the computational study by Bain et al. (1993).

Figure 3 shows isotherms of the centerplane (vertical-axial plane through the geometric center of the orifice) for different spacings of 4:1 aligned slots for $J = 36$. The jet penetration increases as the spacing increases. At the smaller S/H the jets underpenetrate, allowing the approach flow to pass through the center of the duct. As S/H increases, the jets penetrate farther, beginning to pinch off the approach flow along the duct centerplane. At larger spacing, the jets have clearly overpenetrated, blocking off the approach flow near the center and forcing more of the mainstream flow adjacent to the walls and between the jets.

The optimum mixer appears to be at about $S/H = 0.375$ for $J = 36$, which agrees well with the optimum S/H that would be identified from the unmixedness plots in Fig. 4.

A similar effect is apparent in the experimental results of Liscinsky et al. (1993). Mean concentration distributions for opposed rows of round holes with centerlines opposite each other is shown in Fig. 5 for $J = 25$ at $x/H = 0.375$ and $x/H = 0.5$. In each column S/H decreases from 0.75 at the top to 0.4 at the bottom. The effect of the confinement is apparent, as these distributions show overpenetration at the largest spacing, and underpenetration at the smaller, with the "optimum" spacing depending on the axial distance of interest.

The corresponding unmixedness plots are shown in Fig. 6. $S/H = 0.5$ appears to be the best mixer, which is consistent with the configuration one would pick from Fig. 5.

3.3 Effects of Orifice Shape. The orifice shape changes the jet surface area and also affects (1) the amount of jet mass injected per unit length, and (2) the axial domain over which the mass is injected. Generally, increasing the ratio of the long to short dimension of low aspect ratio aligned slots has little effect on jet penetration. This is seen in Figs. 7 and 8 from the computational results reported by Bain et al. (1994). The planes shown in Fig. 7 are vertical-axial ones through the orifice centers, with the corresponding vertical-transverse planes at $x/H = 0.5$ shown in Fig. 8. For each case, the jets penetrate approximately one quarter of the duct height, although there are some subtle differences between these shapes. The most recognizable of these being the difference between the square and the other orifice shapes, as the jets from the square orifice appear to penetrate slightly less as shown by less mainstream fluid in the wake of the injection for the square.

Perhaps this slight effect is related to the wake width of these orifices. Figure 9 shows velocity vectors in a transverse-axial plane next to the wall. Near the wall the jets act as a bluff body to the mainstream flow. This flow then accelerates around the jet prior to separating and forming a wake. As the base area increases, the width of this region increases. Although at its diameter the circle is wider than the square, the width of the wake is less for the round hole as the approach flow remains attached beyond its maximum width. Thus, the square has the widest wake and it follows that its penetration is slightly less.

The effect of orifice shape on unmixedness is illustrated in Fig. 10. These curves are all presented at the optimum spacing for each configuration. In the near orifice region there are sizable differences between these, but aft of the orifice trailing edge all configurations essentially yield the same level of unmixedness.

The effect of orifice shape can also be seen experimentally in the results of Liscinsky et al. (1994). In Fig. 11, average jet mass fraction concentration distributions are shown for square, circle, and two-dimensional slot configurations. The concentration distributions downstream of the two-dimensional slot indicates that the mainstream fluid remains near the center of the duct while the jet fluid stays near the walls. The mixing in this case appears slower than that for either the square or circular orifices. At $x/H = 0.5$ the distributions for the latter two configurations appear quite similar.

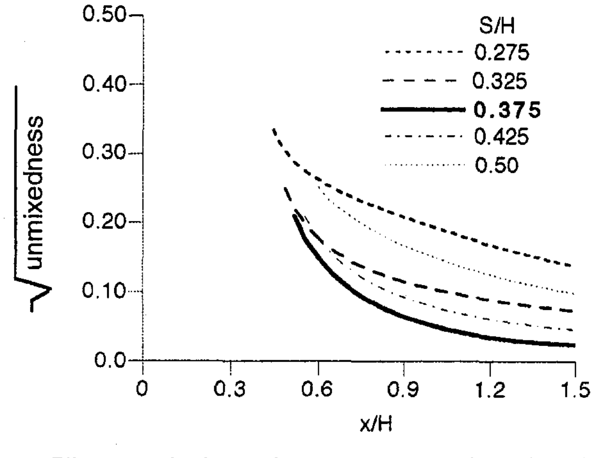

Fig. 4 Effect of varying jet spacing on unmixedness; $J = 36$ (data from Bain et al. (1995b))

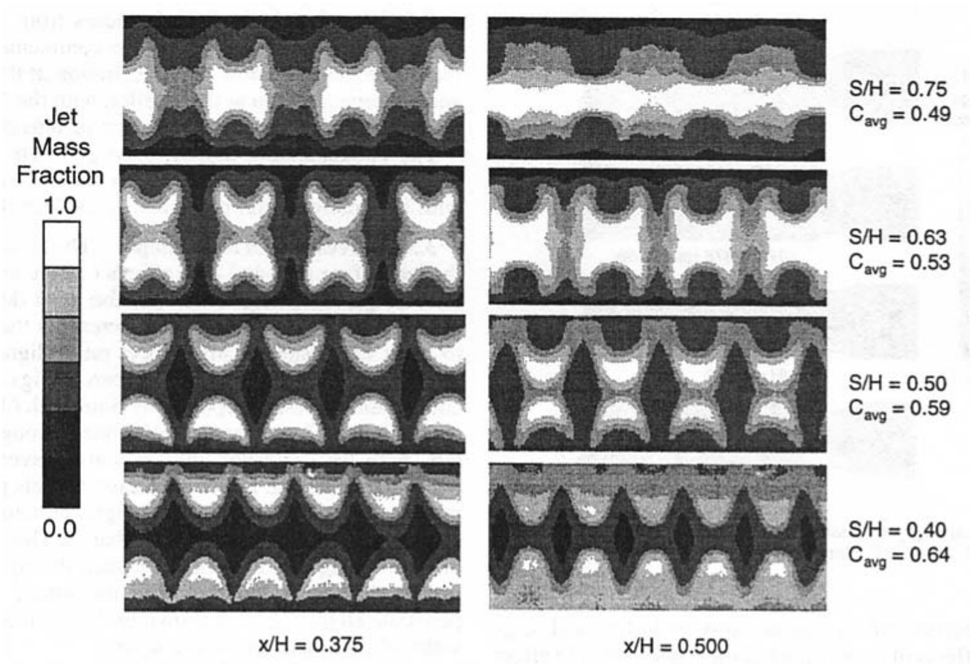

Fig. 5 Average concentration distributions for opposed inline round holes: H/d = 2.67; J = 25 (data from Liscinsky et al. (1993)).

The corresponding unmixedness for these configurations is shown in Fig. 12. These results confirm the observations above in that there is very little difference between the circle and square, and the unmixedness for the two-dimensional slot is larger than both at all downstream distances.

The data in Figs. 11 and 12 are consistent with the single jet results in Liscinsky et al. (1995, 1996) which also show little effect of orifice shape on the mean trajectory and mixing.

3.4 Comparison of Slanted Slots and Holes. Crossflow jet mixing performance is directly related to jet penetration, with optimum mixing for in-line configurations occurring when the asymptotic trajectory is near $H/4$. Previous studies (e.g., Hatch et al., 1995; Oechsle et al., 1992) showed that jet trajectory varied with orifice slant angle. Therefore, in addition to orifice spacing, slot angle can be used to modify jet penetration. The characteristics of aligned opposed rows of round holes and 45 deg slanted slots of 4:1 aspect ratio were investigated by Liscinsky et al. (1994).

Drawings of the two configurations and their corresponding concentration distributions at $x/H = 0.5$ are shown in Fig. 13. Each orifice is equal in area, however the round hole spacing was decreased to reduce jet penetration so it was equal to that for the slanted slots. Also, the gross mixing is similar for the two systems. Although the orifice shape modifies the jet concentration distribution in the vicinity of the orifice, downstream mixing appears to be independent of shape for slanted slot and round holes, when aerodynamic equivalent cases are compared.

Another experimental comparison of slanted slots and round holes is shown in Liscinsky et al. (1992). The distributions for slanted slots are given in Fig. 14 as a function of downstream distance at momentum-flux ratios (J) of 16 and 36.

The top and bottom slots slant in the same direction. In this configuration, the slanted slot jet forms a pair of counter-rotating vortices that are of unequal size and strength. The vortex formed

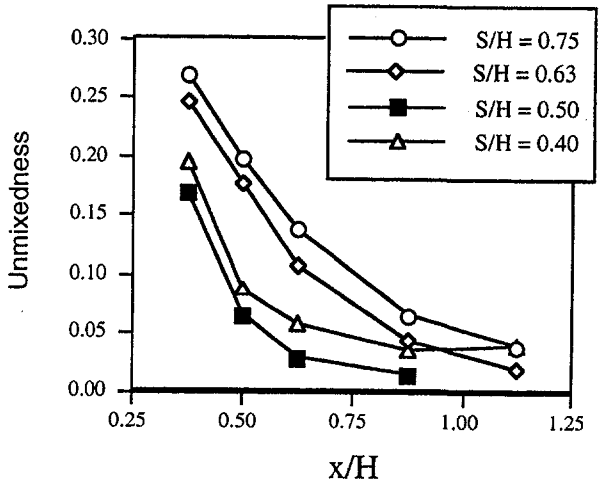

Fig. 6 Effect of orifice spacing on spatial unmixedness for inline round holes: H/d = 2.67; J = 25 (data from Liscinsky et al. (1993)).

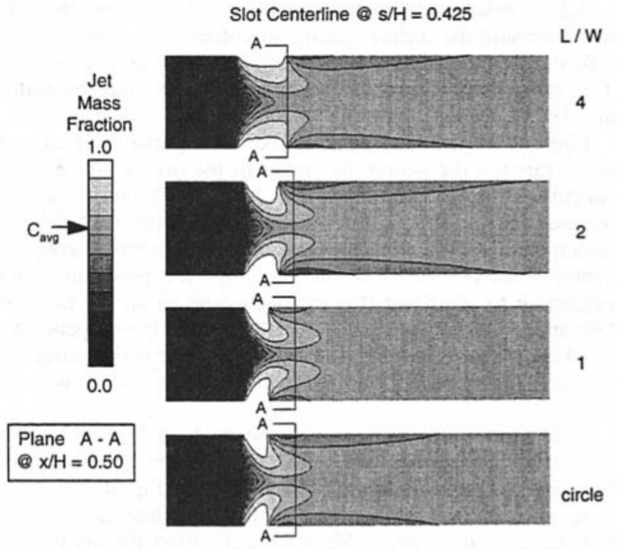

Fig. 7 Effect of orifice aspect ratio on jet penetration: J = 36; MR = 2.0 (data from Bain et al. (1994)).

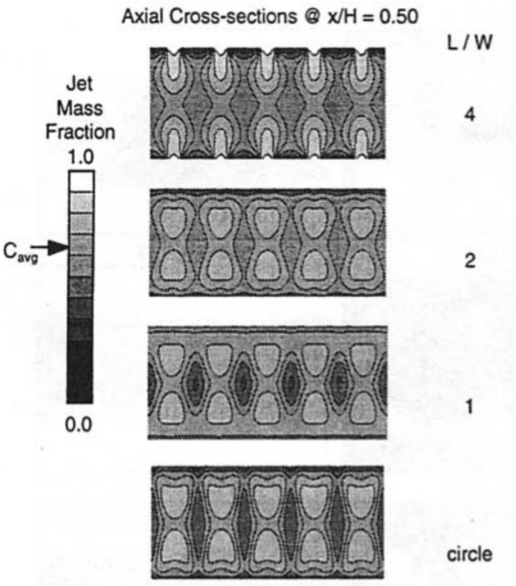

Fig. 8 Effect of orifice aspect ratio on jet penetration: $J = 36$; $MR = 2.0$ (data from Bain et al. (1994)).

at the leading edge of the orifice is larger and stronger than that formed at the trailing edge. The pair rotates so that the bulk of the jet fluid is toward the side that is upstream, thereby identifying the direction that the slot is slanted (in Fig. 14 the upstream edge of the slot is on the right).

The corresponding distributions for circular holes are shown in Fig. 15. It is obvious the vortex structure is different, and that the circular holes penetrate farther into the mainstream at each distance for each J.

The unmixedness curves are shown in Fig. 16 and confirm the previous observation that there is little difference in gross mixing between slanted slots and round holes although differences in this parameter might be expected given the difference observed in the vortex structure.

3.5 Comparison of an Opposed Row of In-Line and Staggered Jets. The effect of lateral arrangement is shown in the results of Bain et al. (1995b). Unmixedness curves for $J = 16, 36$, and 64 are given in Figs. 17, 18, and 19 respectively, where only the curves corresponding to optimum spacing are shown. In each figure, it is apparent that in-line configurations gave better initial mixing, probably due to their significantly smaller size. Farther downstream (e.g., at $x/H = 1$), in-line configurations appear better at $J = 16$, but staggered arrangements show better mixing at $J = 64$.

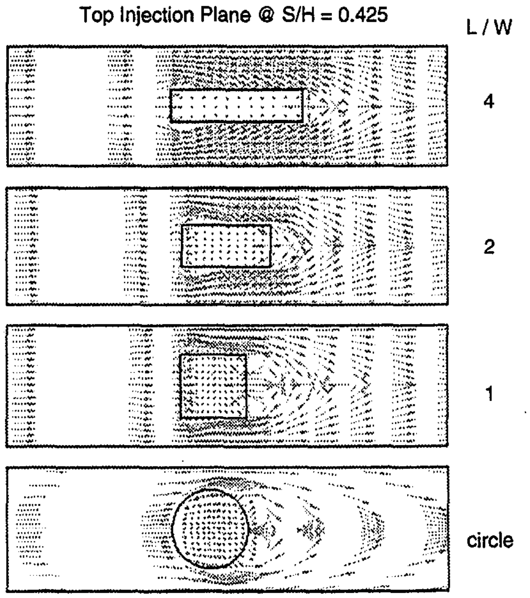

Fig. 9 Effect of orifice aspect ratio on jet wakes: $J = 36$; $MR = 2.0$ (data from Bain et al. (1994)).

Vertical-transverse distributions for $J = 36$ are shown in Fig. 20. This figure shows jet mass fraction concentrations at three downstream locations for optimum in-line and staggered configurations. It can be seen that although optimum in-line configuration offer better initial mixing, the staggered case seems to "catch up."

When experimental mixing tests are performed, only a limited number of configurations can be tested. Typically in-line arrangements are tested, followed by a lateral movement of one wall to create a staggered configuration. If an in-line configuration at a given J is optimized (upper left in Fig. 21), the corresponding staggered arrangement produced by laterally shifting one wall will produce nearly identical mixing as shown in upper right of Fig. 21.

The converse isn't true though: if a staggered arrangement is optimized (lower right in Fig. 21) at a given J, then the corresponding in-line case would produce inferior mixing (lower left of Fig. 21). Thus, optimized in-line configurations are more "tolerant" to alignment, and at low momentum-flux ratios are better mixers, so one would be inclined to choose them unless optimized staggered configurations are clearly better.

The relative insensitivity of optimized and underpenetrating in-line configurations to alignment is also shown experimentally in the results of Liscinsky et al. (1992) repeated in Fig. 22. Note that one has the option of slanting the slots in the same (parallel) or opposite (crossed) direction on opposite sides of the duct, but this makes very little difference as seem in the Fig. 22.

3.6 Effects of Nonsymmetric Mass Addition.

Variation of Orifice Sizes on Opposite Walls. In practical confined mixing applications the flow may not be symmetric about a plane parallel to and midway between opposing walls, for example in an annulus. However, most experimental and computational studies have focused on configurations that are symmetric, i.e., opposing jets are equal in area and momentum-flux ratio, J, and, therefore, mass addition is symmetric. Correlations that predict optimum mixing performance based on Eq. 4 and these data sets often assume symmetry and generally utilize duct height, H, as a nondimensionalization parameter. Besides being convenient, H is important since jet penetration is key to mixing performance. But what if mass addition is nonsymmetric? What is the correct value for the equivalent height?

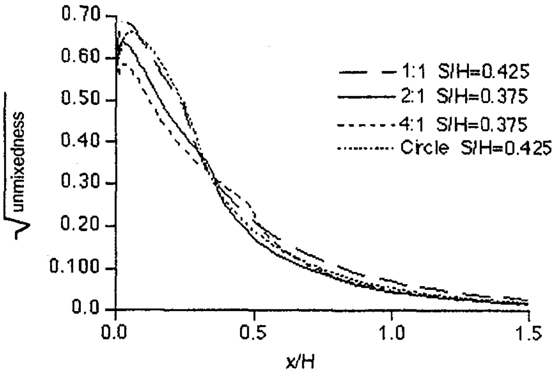

Fig. 10 Effect of orifice aspect ratio on unmixedness: $J = 36$; $MR = 2.0$ (data from Bain et al. (1994)).

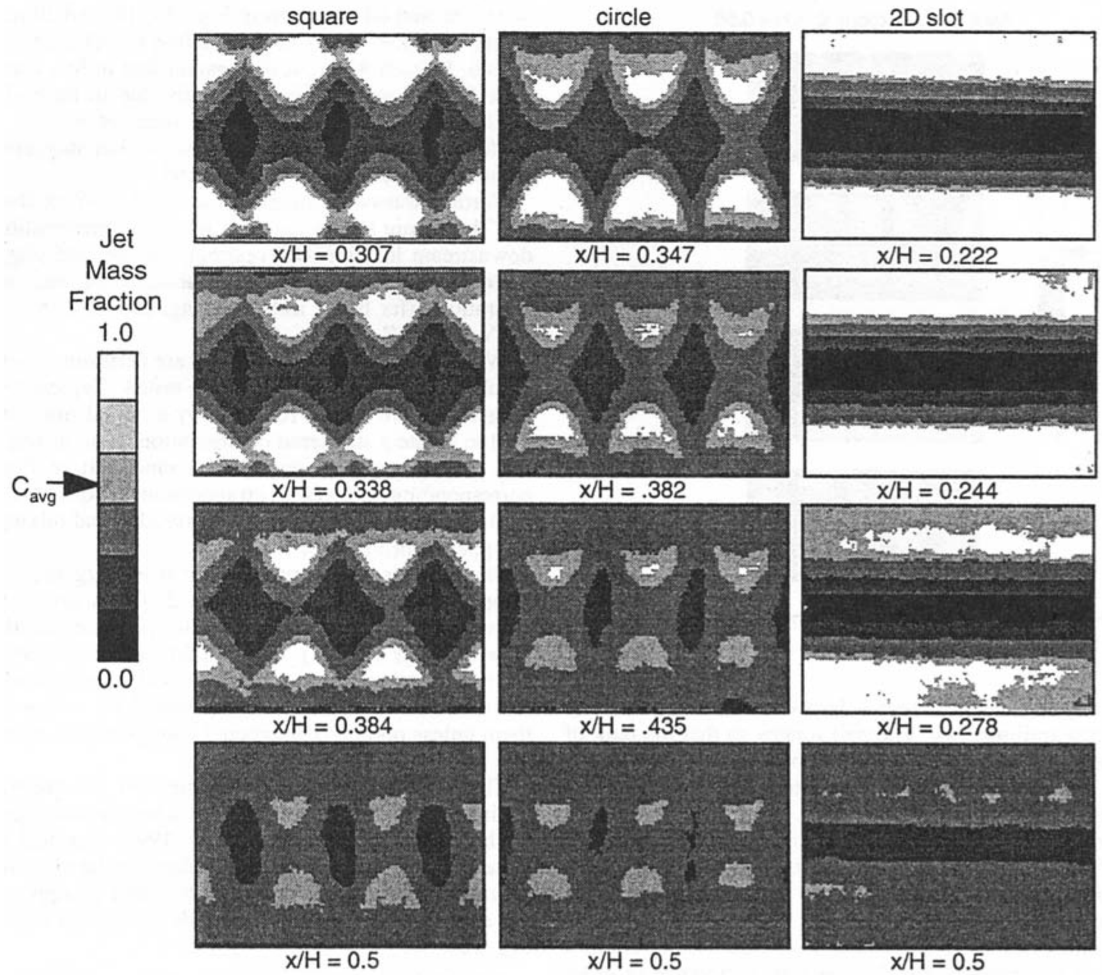

Fig. 11 Effect of Orifice Shape on Opposed Inline Orifices: $J = 48$; $MR = 2.0$; $S/H = 0.425$ (data from Liscinsky et al. (1994)).

The effect of nonsymmetric mass addition is illustrated in Fig. 23 comparing the jet mass fraction distribution at four downstream locations for tests with $H/d = 2.67$ on the top and $H/d = 4$ on the bottom, both with $S/H = 0.5$. A grayscale is used to represent contours of jet mass fraction from 0 to 1.0 (pure mainstream fluid = black and pure jet fluid = white). In each of the tests the top orifice configuration was about twice the area of the bottom orifice configuration.

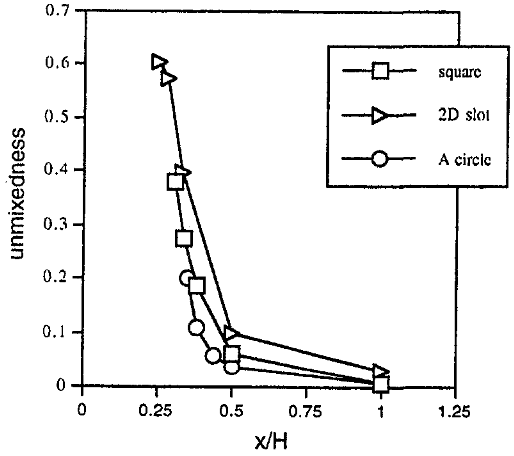

Fig. 12 Effect of orifice shape on unmixedness: $J = 48$; $MR = 2.0$; $S/H = 0.425$ (data from Liscinsky et al. (1994)).

On the left, the opposing values of J were equal but the top and bottom mass flow were not equal due to the different orifice area. The distribution shows a minimum on the duct centerline ($H/2$), which is not surprising since the jet trajectories were optimized for $H/4$ penetration using Eq. 4. On the right side the opposing mass flows were equal but the values of J were unequal so as to obtain an equal mass balance through different sized orifices. The minimum in the concentration distribution is now nearer to the top wall (the lower J side).

The effective duct height, H_{eq}, is obvious for single side injection ($H_{eq} = H$), and for opposed rows of in-line orifices with symmetric flow and geometry ($H_{eq} = (H/2)$). It is not so obvious, however, for asymmetric conditions.

Two of the H_{eq} formulations from Liscinsky et al. (1996) are plotted on Fig. 23 at the second downstream location. The solid line corresponds to the C formulation while the dashed line corresponds to a mass-flow ratio, MR, formulation.

The first of these formulation (solid line) is based on Eq. 4, where $C = (S/H)\sqrt{J}$:

$$[H_{eq}/H]_{C,\text{top}} = C_{\text{top}}/(C_{\text{top}} + C_{\text{bottom}}). \tag{5}$$

The other (dashed line) formulation is a mass-flow ratio balance:

$$[H_{eq}/H]_{MR,\text{top}} = MR_{\text{top}}/(MR_{\text{top}} + MR_{\text{bottom}}). \tag{6}$$

It follows that

$$[H_{eq}/H]_{\text{bottom}} = 1 - [H_{eq}/H]_{\text{top}}. \tag{7}$$

It appears that the better fit is obtained with the formulation

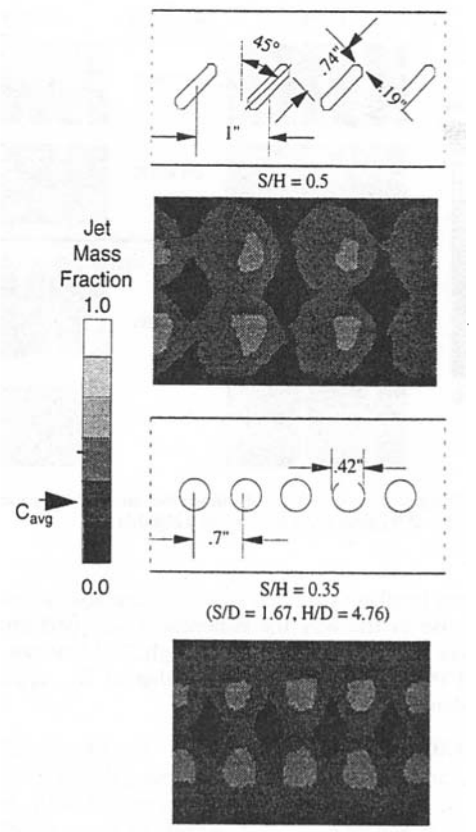

Fig. 13 Orifice configurations and concentration distributions for 45 deg 4:1 slots and round holes: $x/H = 0.5$; $J = 25$ (data from Liscinsky et al. (1994)).

based on C, i.e., the value of H_{eq} appears to depend on jet penetration which is determined by the product of S/H and the square root of J, rather than mass flow.

Variation of Momentum-Flux Ratio on Opposite Walls. Similar results were obtained by varying opposing values of J with inline circular orifices with $H/d = 8$ spaced at $S/H = 0.25$

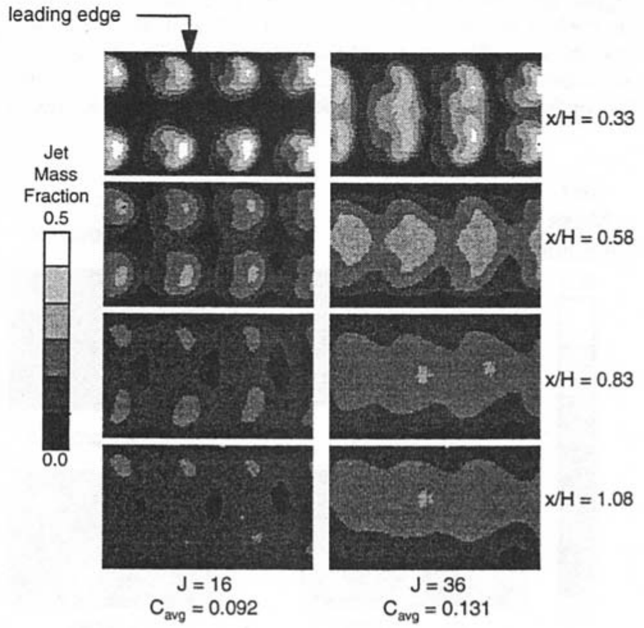

Fig. 14 Effect of momentum-flux ratio and downstream distance on the average concentration distributions of the flow through opposed inline 45 deg slanted slots (data from Liscinsky et al. (1992))

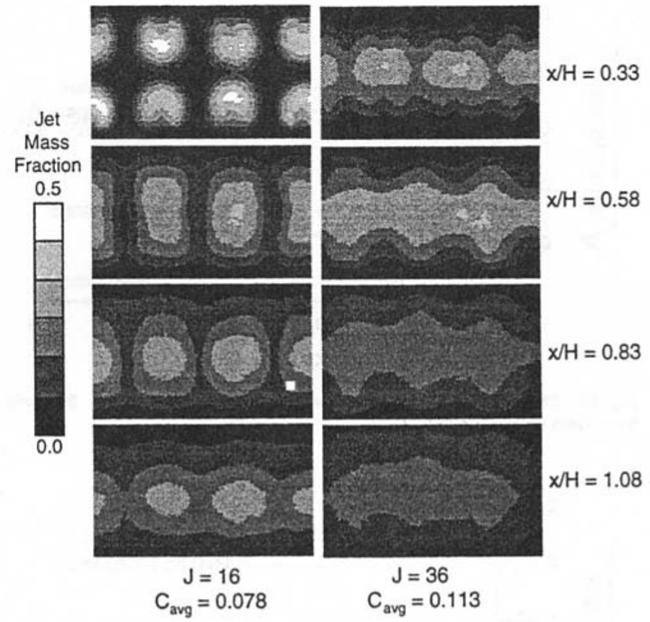

Fig. 15 Effect of momentum-flux ratio and downstream distance on the average concentration distributions of the flow through opposed inline round holes (data from Liscinsky et al. (1994))

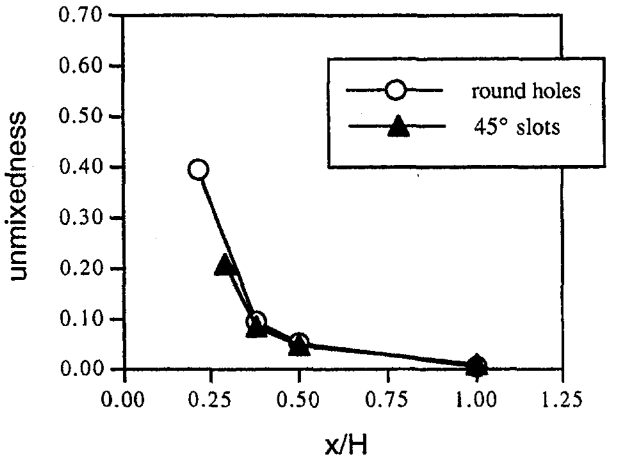

Fig. 16 Comparison of spatial unmixedness for equivalent 45 deg slot and round hole configurations at $J = 25$ (data from Liscinsky et al. 1994)

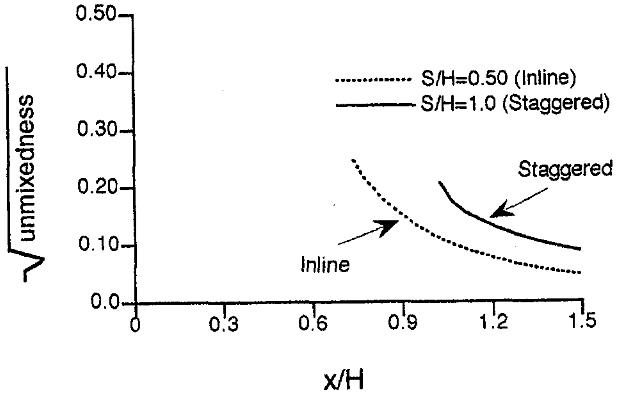

Fig. 17 Effect of lateral arrangement on unmixedness at $J = 16$ (data from Bain et al. 1995b)

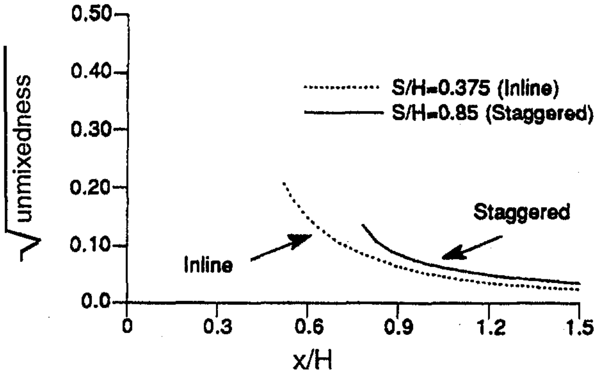

Fig. 18 Effect of lateral arrangement on unmixedness at $J = 36$ (data from Bain et al. 1995b)

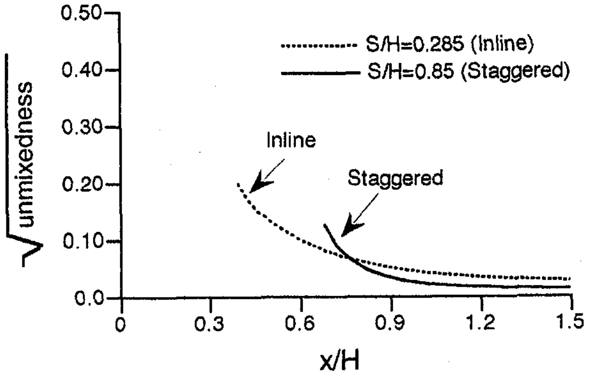

Fig. 19 Effect of lateral arrangement on unmixedness at $J = 64$ (data from Bain et al. 1995b)

in Liscinsky et al. (1994). The effect of varying opposing J values is compared to results of an empirical model (Holdeman and Srinivasan, 1986) in Fig. 24. In this experiment, the orifice plate was held constant, $H/d = 8$, with $S/H = 0.25$, while the opposing J values were varied to maintain a mass-flow ratio (MR) of 0.325. This orifice configuration was found to be an optimal in-line configuration when opposing momentum-flux ratios were equal, and also an optimal configuration for one side injection at the same MR. The concentration distributions vary as expected, in that jet penetration is proportional to $\sqrt{J}$.

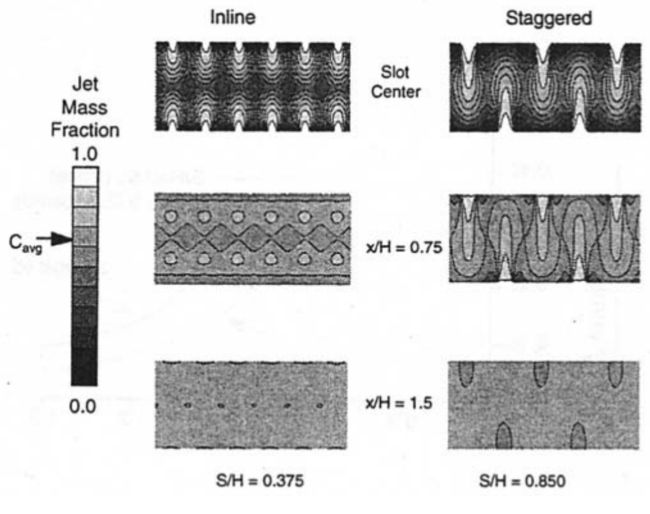

Fig. 20 Effect of lateral arrangement on mixing: $J = 36$; $MR = 2.0$ (data from Bain et al. (1995b)).

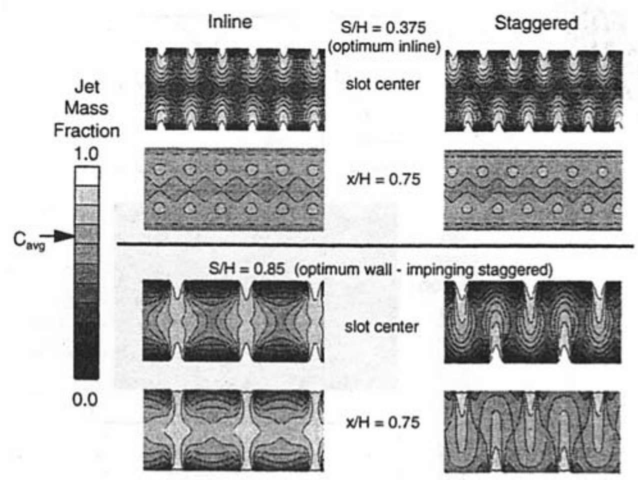

Fig. 21 Comparison of inline and staggered slots at optimum S/H and $J = 36$, $MR = 2.0$ (data from Bain et al. (1995b))

Equivalent heights (from Eq. 5 and 6) are also shown on Fig. 24 (because of the way the experiment was performed Eq. 5 and 6 give the same results). Although S/H was not varied in either of these investigations, the value of H_{eq} appears to be independent of orifice diameter.

3.7 Effect of Orifice Blockage. The inverse relation between $\sqrt{J}$ and S/H given in Eq. 4 has been shown to apply (e.g., Bain et al., 1994) when extended to typical RQL conditions of $MR > 2$ and $S/d < 2$. However, at those conditions the proportionality constant C has been found, both experimentally (Liscinsky et al., 1993) and computationally (Bain et al., 1993 & 1994), to be ~2.5 rather than the expected value of ~1.25. Thus, C appeared to be a function of something, and orifice blockage (B) was a possibility. In this summary, as in all previous studies in this program, blockage is defined as the ratio of the transverse projection of the orifice to the spacing between corresponding locations of adjacent orifices—note that $B = 1/(S/d)$ for circular holes.

To determine whether C was a discernible function of orifice blockage, a set of rectangular orifice configurations were designed and tested. A schematic of the configurations is shown in Table 1 in Liscinsky et al. (1994). A J of 36 was chosen, and the mass-flow ratio (MR) and orifice spacing (S/H) were maintained constant at $MR = 2$ and $S/H = 0.425$ for all, while the orifice blockages (B) varied substantially. The configura-

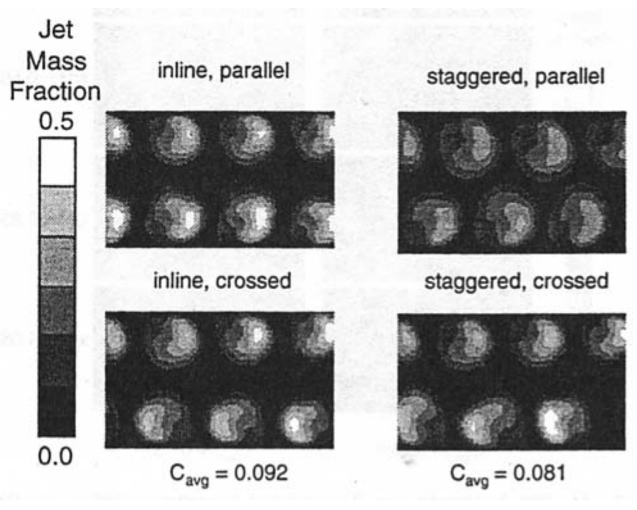

Fig. 22 Concentration distributions of opposed slanted slots at $J = 16$, $S/H = 0.5$, and $x/H = 0.33$ (data from Liscinsky et al. (1992))

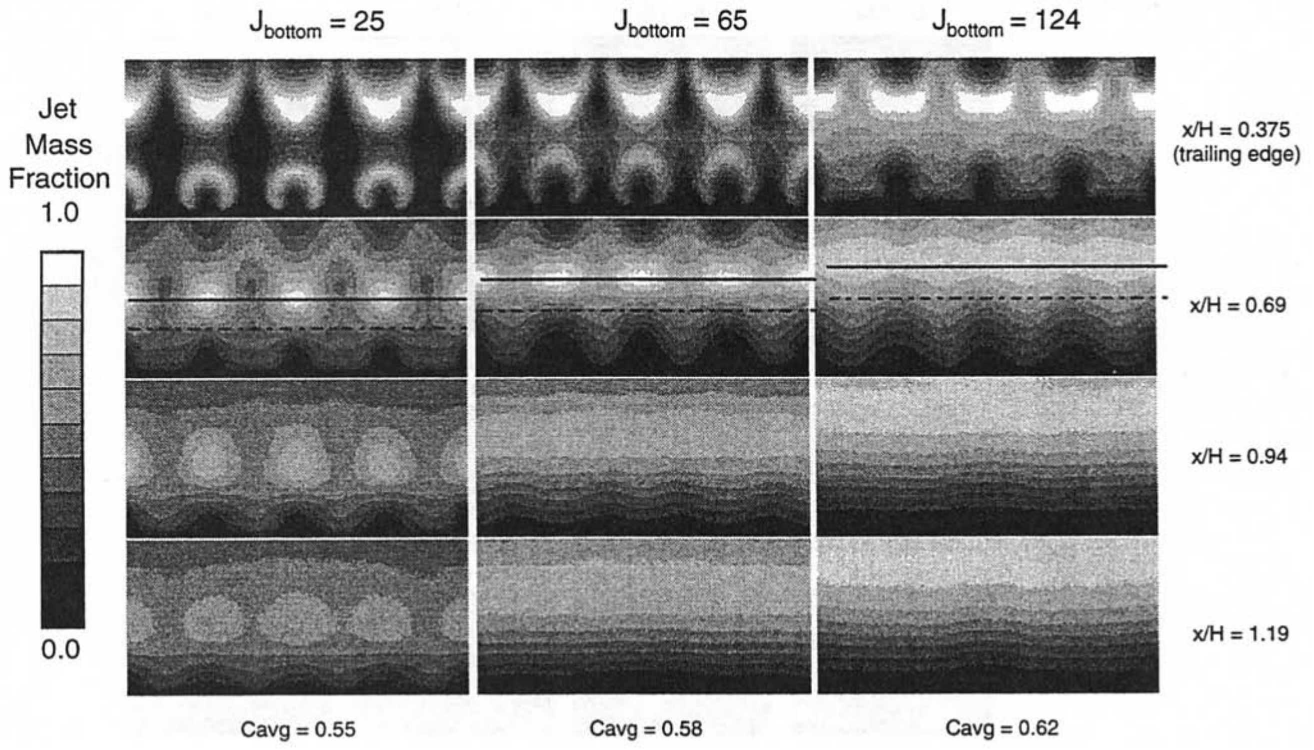

Fig. 23 Effect of nonsymmetric mass addition: $J_{top} = 25$; $H/d_{top} = 2.67$; $H/d_{bottom} = 4.0$; and $S/H = 0.5$ (data from Liscinsky et al. (1996)).

tions examined were based on a numerical study by Bain et al. (1994), in which orifice aspect ratio and shape were found to have little effect on the mixing performance of in-line configurations when a value of 2.55 was used for C in Eq. 4.

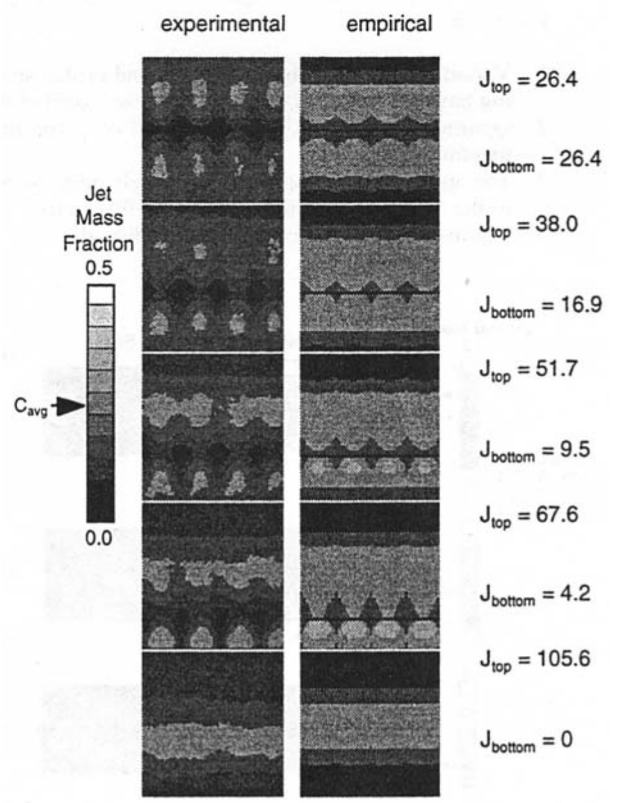

Fig. 24 Comparison of experimental and empirical results for inline round orifices when opposing J values are unequal ($S/H = 0.25$ and $x/H = 0.5$) (data from Liscinsky et al. (1994))

Average jet mass fraction distributions, perpendicular to the mainstream flow direction, are shown in Fig. 25 for blockages (B) varying from 0.59 to 0.89. Five downstream planes are shown from the trailing edge of these orifices (at the top) to a distance equal to one-half duct height downstream (at the bottom). The corresponding unmixedness curves are shown in Fig. 26. Obviously, the mixing from all these configurations is very similar, although the distance between orifices is only about 13 percent of the orifice width for the largest blockage shown.

3.8 Variation of Mass-Flow Ratio. The effect of mass-flow ratio is shown in the centerplane distributions in Fig. 27 from Bain et al. (1994). The corresponding vertical-transverse planes at $x/H = 0.5$ are shown in Fig. 28. These are all at the "optimum" spacing for each configuration. Clearly the penetration is about the same for these. Note though, that for the $MR = 2$ case the jets are still entering the flowfield at this axial location.

The unmixedness curves for these configurations are given in Fig. 29. Note that the optimum S/H is 0.375 for $MR = 2$, whereas the optimum is only $S/H = 0.25$ for $MR = 0.25$. This variation suggests that there may be a significant effect of MR on C. Although for $x/H > 0.7$ the $MR = 2$ case exhibits slightly lower unmixedness than the others, it and the $MR = 0.5$ case show higher values between $x/H = 0.3$ and $x/H = 0.7$ probably due to their larger size.

4 Design Procedure

These results suggest that for a given momentum-flux ratio and downstream distance, combustor design procedure should first identify the momentum-flux ratio, effective orifice area, and the orifice spacing required to obtain the desired penetration and profile shape. The orifice size would then be chosen to provide the required jet-to-mainstream mass-flow ratio. Some adjustments, including noncircular orifices or multiple rows, may be needed to arrive at the final design because jet penetration varies slightly with orifice size and shape, and other parameters such as the combustor pressure loss and the ratio of the

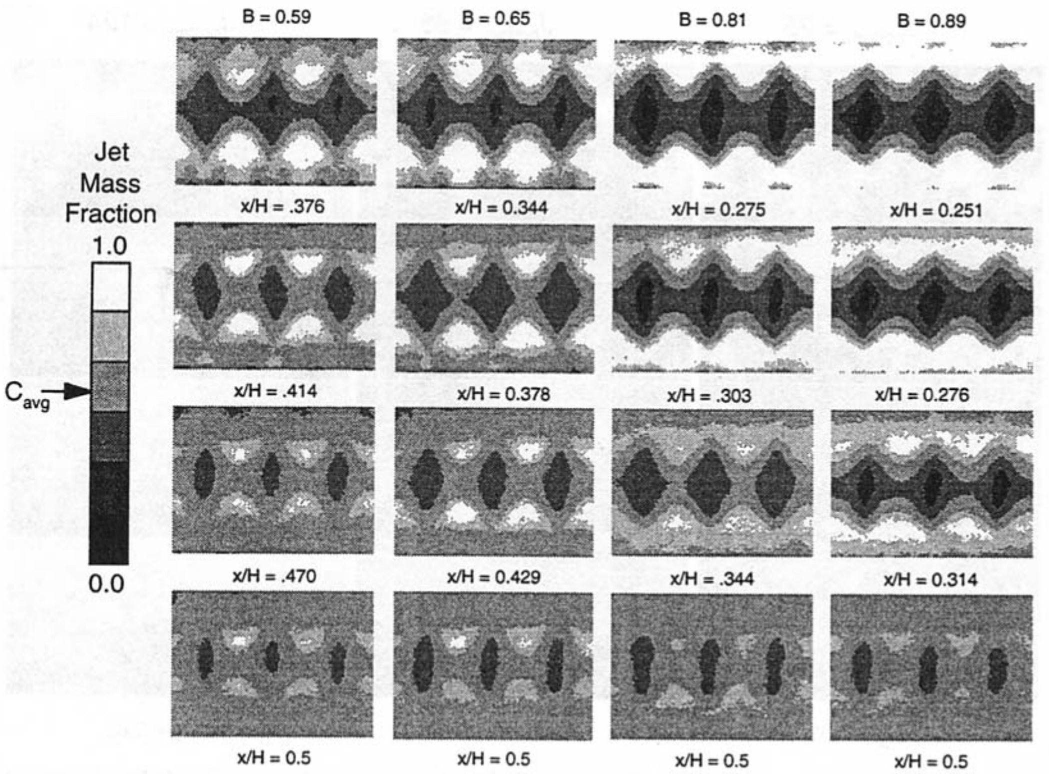

Fig. 25 Effect of orifice blockage on opposed inline rectangular orifices: ***MR*** **= 2.0;** ***S/H*** **= 0.425;** ***J*** **= 48 (data from Liscinsky et al. (1994)).**

orifice spacing to diameter must be monitored to insure that the suggested configuration is physically realistic. Also it should be noted that since jet penetration often varies with axial distance, one must consider both ''what'' and ''where'' in the optimization.

Based on these results, the suggested procedure is as follows, given mass-flow ratio, pressure drop, and channel height:

1 calculate momentum-flux ratio (J)
2 identify needed effective orifice area
3 choose desired orifice shape
4 select number of orifices for optimum penetration
5 calculate individual orifice size
6 determine blockage, fit, etc.
7 iterate to solution

Summary of Results

A Several results from recent studies are consistent with results from previous investigations. These include the following:

1 Variations in momentum-flux ratio and orifice spacing have a significant effect on the flow distribution.
2 Optimum configurations may depend on given momentum-flux ratio.
3 The optimum orifice spacing is inversely proportional to the square root of the momentum-flux ratio.
4 Optimum spacing may vary with orifice shape.

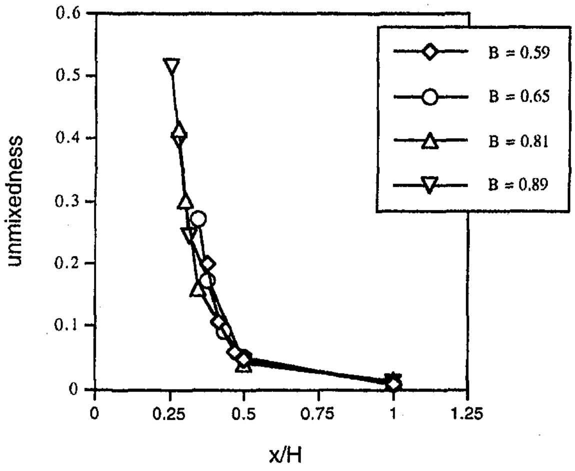

Fig. 26 Effect of orifice blockage on spatial unmixedness: ***MR*** **= 2.0;** ***S/H*** **= 0.425; and** ***J*** **= 48 (data from Liscinsky et al. (1994)).**

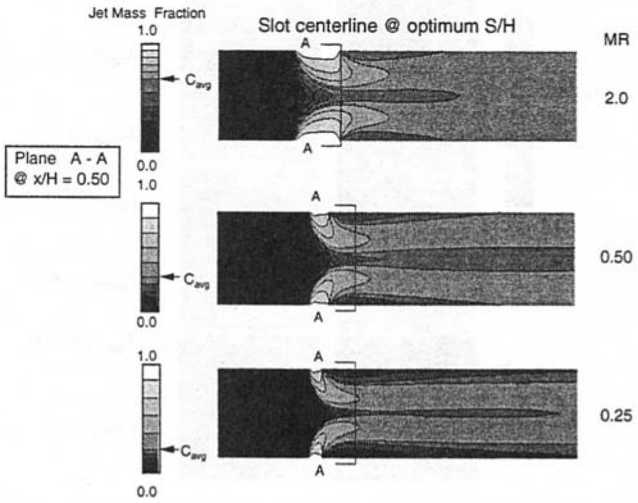

Fig. 27 Effect of jet-to-mainstream mass flow variation on jet penetration at optimum ***S/H*** **and** ***J*** **= 36,** ***L/W*** **= 4 (data from Bain et al. (1994))**

5. Similar jet penetration can be obtained, largely independent of orifice size and shape, when orifice spacing (S/H) is inversely proportional to the square-root of the momentum-flux ratio (J). Note that although orifice configurations can be optimized for any J, a shorter downstream distance is required for equivalent mixing if J is large and/or the orifice spacing is small.
6. The penetration of slanted slots is less than for equal-area circular holes.
7. For orifices that are symmetric with respect to the main flow direction, the effects of shape are significant only in the region near the injection plane. Beyond $x/H = 1$, scalar distributions were similar to those observed from equally spaced equal-area circular orifices.
8. Planar average mixing often increases monotonically with momentum-flux ratio (J). Since overpenetration cases are usually not desirable, this emphasizes the importance of perusing both the distributions and planar averages before identifying an optimum configuration.

B Conclusions that are unique to the current investigations include the following:

1. Although the current studies confirmed the inverse proportionality between orifice spacing (S/H) and the square root of the momentum-flux ratio (J), the optimum constant of proportionality for rectangular ducts at $MR > 1.0$ appears to be about twice that reported by Holdeman (1993).
2. For opposed rows of round holes with centerlines inline, mixing was similar for blockages from 0.5 to 0.90.
3. In-line configurations have better initial mixing than staggered configurations at their respective optimums.
4. For downstream mixing ($x/H > 1.5$), optimum inline configurations appear to be better mixers than staggered ones for low Js (i.e., 16), but the opposite may be true for high momentum-flux ratios (i.e., $J > 64$).
5. The vortex pattern formed by optimum in-line configurations appears to be quite different than that from optimum staggered configurations. The latter may destabilize more quickly than optimum in-line jets, so properly spaced staggered configurations may augment downstream mixing.
6. Different orifice shapes may not have the same optimum spacing for a given J, so comparison should be obtained from optimum configurations.
7. Orifice aspect ratio had little effect on jet penetration and mixing.
8. For nonsymmetric mass addition from opposite sides of the duct, an effective duct height based on the momentum-flux ratio and the orifice spacing can be used to determine the optimum mixer for opposed inline injection.

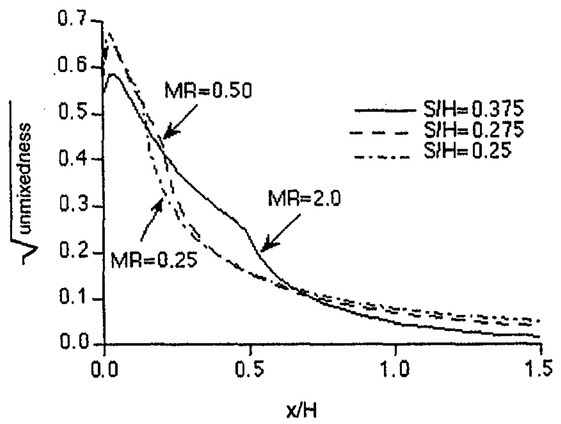

Fig. 29 Effect of jet-to-mainstream mass flow ratio on unmixedness at optimum S/H; orifice aspect ratio = 4, J = 36 (data from Bain et al. (1994))

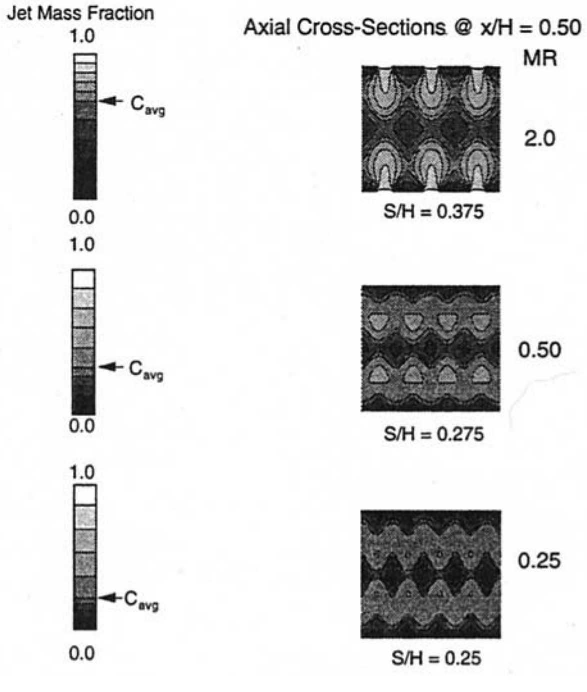

Fig. 28 Effect of jet-to-mainstream mass flow ratio on jet penetration at J = 36, MR = 2.0 (data from Bain et al. (1994))

Acknowledgments

The authors would like to acknowledge the contributions of the following: R. P. Lohmann, Pratt & Whitney Aircraft; H. C. Mongia, GE Aircraft Engines (formerly with Allison); V. L. Oechsle, Allison Advanced Development Company; G. S. Samuelsen, University of California, Irvine (UCI); C. E. Smith, CFD Research Corporation; W. A. Sowa, United Technologies Research Center (UTRC) (formerly at UCI); B. True, UTRC; A. Vranos, University of Connecticut (formerly with UTRC), and M. Winter, UTRC.

References

Bain, D. B., Smith, C. E., and Holdeman, J. D., 1992, "CFD Mixing Analysis of Jets Injected From Straight and Slanted Slots Into a Confined Crossflow in Rectangular Ducts," AIAA Paper 92-3087 (also NASA TM 105699).

Bain, D. B., Smith, C. E., and Holdeman, J. D., 1994, "CFD Assessment of Orifice Aspect Ratio and Mass Flow Ratio on Jet Mixing in Rectangular Ducts," AIAA Paper 94-0218 (also NASA TM 106434).

Bain, D. B., Smith, C. E., and Holdeman, J. D., 1995a, "Jet Mixing and Emission Characteristics of Transverse Jets in Annular and Cylindrical Confined Crossflow," AIAA Paper 95-2995 (also NASA TM 106976).

Bain, D. B., Smith, C. E., and Holdeman, J. D., 1995b, "Mixing Analysis of Axially Opposed Rows of Jets Injected into Confined Crossflow," *Journal of Propulsion and Power,* Vol. 11, No. 5, pp. 885–893 (see also AIAA Paper 93-2044 and NASA TM 106179).

Bain, D. B., Smith, C. E., Liscinsky, D. S., and Holdeman, J. D., 1996, "Flow Coupling Effects in Jet-in-Crossflow Flowfields," *Journal of Propulsion and Power,* Vol. 121, No. 1, (also AIAA Paper 96-2762; NASA TM 107257).

Blomeyer, M. M., 1997, Proceedings, Optimization of the Mixing Process in the Mixing Zone of an RQL Combustor, 13th ISABE, Chattanooga, TN.

Blomeyer, M. M., Krautkremer, B. H., and Hennecke, D. K., 1996, "Optimum Mixing for a Two-sided Injection from Opposed Rows of Staggered Jets in a Confined Crossflow," ASME Paper 96-GT-483.

Chiu, S., Roth, K. R., Margason, R. J., and Tso, J., 1993, ''A Numerical Investigation of a Subsonic Jet in a Crossflow,'' AIAA Paper 93-0870.

Chiu, S. H., Roth, K. R., Margason, R. J., and Tso, J., 1993, ''A Numerical Investigation of a Subsonic Jet in a Crossflow,'' *Computational and Experimental Assessment of Jets in Cross Flow,* AGARD Conference Proceedings 534.

Crocker, D. S., and Smith, C. E., 1993, ''Numerical Investigation of Enhanced Dilution Zone Mixing in a Reverse Flow Gas Turbine Combustor,'' ASME Paper 93-GT-129.

Crocker, D. S., and Smith, C. E., 1994, ''Numerical Investigation of Angled Dilution Jets in Reverse Flow Gas Turbine Combustors,'' AIAA Paper 94-2771.

Crocker, D. S., Smith, C. E., and Myers, G. D., 1994, ''Pattern Factor Reduction in a Reverse Flow Gas Turbine Combustor Using Angled Dilution Jets,'' ASME Paper 94-GT-406.

Doerr, T. and Henneke, D. K., 1993, ''The Mixing Process in the Quenching Zone of the Rich-Lean Combustion Concept,'' AGARD-PEP 81st Symposium of Fuels and Combustion Technology for Advanced Aircraft Engines.

Doerr, T., Blomeyer, M., and Henneke, D. K., 1995a, ''Optimization of Multiple Jets Mixing with a Confined Crossflow,'' ASME Paper 95-GT-313.

Doerr, T., Blomeyer, M., and Henneke, D. K., 1995b, ''Experimental Investigation of Optimum Jet Mixing Configurations for RQL-Combustors,'' 12th ISABE, Melborne, Australia.

Everson, R., Manin, D., Sirovich, L., and Winter, M., 1995, ''Quantification of Mixing and Mixing Rate from Experimental Observations,'' AIAA Paper 95-0169.

Hatch, M. S., Sowa, W. A., Samuelsen, G. S., and Holdeman, J. D., 1995, ''Geometry and Flow Influences on Jet Mixing in a Cylindrical Duct,'' *Journal of Propulsion and Power,* Vol. 11, No. 3, pp. 393–402, (see also ''Jet Mixing Into a Heated Cross Flow in a Cylindrical Duct: Influence of Geometry and Flow Variations,'' AIAA-92-9773 and NASA TM 105390).

Holdeman, J. D., 1993, ''Mixing of Multiple Jets With a Subsonic Crossflow,'' *Prog. Energy Combust. Sci.,* Vol. 19, pp. 31–70 (see also AIAA-91-2458 and NASA TM 104412).

Holdeman, J. D., Walker, R. E., and Kors, D. L., 1973, ''Mixing of Multiple Dilution Jets With a Hot Primary Airstream for Gas Turbine Combustors,'' AIAA Paper 73-1249 (also NASA TM X-71426).

Holdeman, J. D., Liscinsky, D. S., Oechsle, V. L., Samuelsen, G. S., and Smith, C. E., 1996, ''Mixing of Multiple Jets With a Confined Subsonic Crossflow: Part I—Cylindrical Duct Results,'' ASME Journal of Engineering for Gas Turbines and Power, Vol. 119, No. 4, pp. 852–862 (also ASME Paper 96-GT-482; NASA TM 107185).

Krautkremer, B. H., Blomeyer, M. M., and Hennecke, D. K., 1998, ''Optical Measurements of Jet-Mixing in a Swirling Crossflow of a Combustion Chamber,'' presented at the NATO RTA Symposium on Gas Turbine Engine Combustion, Emissions, and Alternate Fuels, Lisbon, Portugal, Oct. 12–16.

Liscinsky, D. S., True, B., and Holdeman, J. D., 1993, ''Experimental Investigation of Crossflow Jet Mixing in a Rectangular Duct,'' AIAA Paper 93-3090 (also NASA TM 106152).

Liscinsky, D. S., True, B., and Holdeman, J. D., 1994, ''Mixing Characteristics of Directly Opposed Rows of Jets Injected Normal to a Crossflow in a Rectangular Duct,'' AIAA Paper 94-0217 (also NASA TM 106477).

Liscinsky, D. S., True, B., and Holdeman, J. D., 1995, ''Effect of Initial Conditions on a Single Jet in Crossflow,'' AIAA Paper 95-2998 (also NASA TM 107002).

Liscinsky, D. S., True, B., and Holdeman, J. D., 1996a, ''Crossflow Mixing of Noncircular Jets,'' *Journal of Propulsion and Power,* Vol. 12, No. 1 (see also AIAA Paper 95-0732 and NASA TM 106865).

Liscinsky, D. S., True, B., and Holdeman, J. D., 1996b, ''Effect of Inlet Flow Conditions of Crossflow Jet Mixing,'' AIAA Paper 96-2881 (also NASA TM 107258).

Liscinsky, D. S., Vranos, A., and Lohmann, R. P., 1993, ''Experimental Study of Cross-Stream Mixing in Cylindrical and Rectangular Ducts,'' NASA CR 187141.

Liscinsky, D. S., True, B., Vranos, A., and Holdeman, J. D., 1992, ''Experimental Study of Crossflow Jet Mixing in a Rectangular Duct,'' AIAA Paper 92-3090 (also NASA TM 105694).

Lozano, A., Yip, B., and Hanson, R. K., 1992, ''Acetone: A Tracer for Concentration Measurements in Gaseous Flows by Planar Laser-Induced Fluorescence,'' *Experiments in Fluids,* Vol. 13, pp. 369–376.

Lozano, A., Smith, S. H., Mungal, M. G., and Hanson, R. K., 1991, ''Concentration Measurements in a Transverse Jet by Planar Laser-Induced Florescence of Acetone,'' *AIAA Journal,* Vol. 32, No. 1, pp. 218–221.

Margason, R. J., 1993, ''Fifty Years of Jet in Cross Flow Research,'' *Computational and Experimental Assessment of Jets in Cross Flow,* AGARD Conference Proceedings 534.

Margason, R. J. and Tso, J., 1993, ''Jet to Freestream Velocity Ratio Computations for a Jet in a Crossflow,'' AIAA Paper 93-4860.

Mungal, M. G., Lozano, A., and van Cruyningen, I., 1992, ''Large-Scale Dynamics in High Reynolds Number Jets and Jet Flames,'' *Experiments in Fluids,* Vol. 12, No. pp. 141–150.

Nikjooy, M., Mongia, H. C., Sullivan, J. P., and Murthy, S. N. B., 1993, Flow Interaction Experiment—Aerothermal Modeling Phase II, Vols. I and II, NASA CR 189192.

Oechsle, V. L., Mongia, H. C., and Holdeman, J. D., 1992, ''A Parametric Numerical Study of Mixing in a Cylindrical Duct,'' AIAA Paper 92-3088 (also NASA TM 105695).

Smith, S. H., Lozano, A., Mungal, M. G., and Hanson, R. K., 1992, ''Scalar Mixing in the Subsonic Jet in Crossflow,'' *Computational and Experimental Assessment of Jets in Cross Flow,* AGARD Conference Proceeding 534.

Winter, M., Barber, T. J., Everson, R., and Sirovich, L., 1992, ''Eigenfunction Analysis of Turbulent Mixing Phenomena,'' *AIAA Journal,* Vol. 30, No. 7.

Wittig, S. L. K., Elbahar, O. M. F., and Noll, B. E., 1984, ''Temperature Profile Development in Turbulent Mixing of Coolant Jets with a Confined Hot Crossflow,'' ASME Journal of Engineering for Gas Turbines and Power, Vol. 106, pp. 193ff.

Y. Nakanishi

Y. Yoshihara

K. Nishiwaki

Department of Mechanical Engineering,
Faculty of Science and Engineering,
Ritsumeikan University,
1-1-1 Nojihigashi Kusatu,
Shiga 525-8577,
Japan

T. Tanaka
Hitaci Zosen Corporation,
Ōsaka 559-0034,
Japan

Reduction of Nitric Oxide in Diesel Exhaust With the Addition of Methylamine

A chemical gas-phase process capable to reduce the nitric oxide in diesel engine exhaust was studied. In this process, monomethylamine (CH_3NH_2) was added to the exhaust gas in a molar ratio to NO varying between 1:1 and 4:1. Experiments were conducted in electrically heated quartz reactors in a temperature range of 200°C to 600°C. Diesel exhaust gas and simulated exhaust gas were used in this experiment. The results showed thorough mixing of methylamine into the exhaust effectively breaks NO down into nitrogen and water, enabling more than 80 percent NO reduction in a reactor temperature range of 400°C to 540°C and at a molar ratio of 1. On the other hand, imperfect mixing between methylamine and exhaust gases results in excess ammonia and reduced NO decomposition. Consequently, it is suggested that the mixing is a very important factor in this technique. The results also show that the coexisting gases such as carbon monoxide, carbon dioxide, hydrocarbons, and water vapor in the diesel exhaust have no effect on NO reduction by methylamine. However, the presence of oxygen in excess of 10 percent in the exhaust is needed for an 80 percent NOx reduction. Furthermore, the mechanisms of the methylamine process were discussed.

Introduction

Diesel engines are extensively used for transportation systems and industrial purposes due to fuel cost savings. However, this type of engine still has a certain environmental risk with its higher NOx emisson. By the modifying combustion process, high specific output and improved fuel efficiency can be achieved, and the exhaust emissions can also be reduced to a level within current limits. However, these levels may not be sufficient to satisfy future emission standards. Therefore, post-combustion gas treatment processes may be necessary to meet these stricter NOx regulations.

Selective catalytic reduction (SCR) systems, which are extensively used for stationary plants, have been studied as possible systems for marine diesel engines. However, SCR systems have certain problems in engine use. Some of these problems are the high initial and the operating costs of the system. Another is the emission of ammonia or ammonium compounds due to a fluctuating catalyst temperature caused by load changes.

Selective noncatalytic reduction (SNCR) systems have been extensively studied as an alternative to SCR. In these systems, ammonia or ammonium compounds such as urea and cyanuric acid may be used for NO reduction but only at temperatures higher than 700°C (Miller et al., 1981; Carton and Siebers, 1989). Accordingly, it is difficult to apply these SNCR techniques to diesel exhaust systems, in which the temperatures are normally much lower than 700°C. In these processes, NO removal takes place by a reaction with NH_2, derived from ammonia or ammonium compounds through reaction with OH and O. Since these radicals can only be generated at temperatures over 700°C, NH_2 is seldom formed in the diesel exhaust (Yoshihara et al., 1990).

Recently, the present authors proposed another SNCR technique in order to reduce NO using amines ($R\text{-}NH_2$, R: hydrocarbon radical) such as monomethylamine (Yoshihara and Tanaka, 1995). In this technique, the derivation of NH_2 from amines begins in the temperatures about 250°C to 300°C (Minkoff and Tipper, 1962). Therefore, NO reduction is achieved at temperatures which are typical for diesel exhaust.

In the present paper, NO reduction processes using monomethylamine are examined. Experiments were conducted in an electrically heated quartz reactor using diesel and simulated exhaust gas. The aim of this study is to elucidate the details of this new SNCR technique.

Experimental Apparatus and Method

Figure 1 is a schematic of the experimental apparatus. In this experiment, diesel exhaust and simulated exhaust gas were used. The exhaust gas was produced by a single cylinder, four cycle, water cooled, direct injection, 857 cm^3 stroke volume, naturally aspirated diesel engine. The diesel engine operated at an engine speed of 1800 rpm and an overall equivalence ratio of 0.64. The operating condition of the diesel engine was the same throughout experiments. A part of the diesel exhaust gas was drawn through a tube heated to 80°C to prevent the condensation of light unburned hydrocarbons. The simulated exhaust gas was prepared by a gas mixer. The compositions of the diesel and the simulated exhaust gas are given in Table 1. As pure NO and O_2 were mixed in the gas mixer to provide the simulated exhaust gas, NO_2 was formed in the simulated exhaust gas unexpectedly by the oxidation of NO.

To examine the effects of the mixing conditions between the exhaust gas and the methylamine on the NO reduction, three experiments were conducted using a 375 mm long straight reactor, having a 10.5 mm inner diameter (Fig. 2(*a*)). To minimize the surface effects on NO reduction, reactors made of quartz were used. The main variables in these experiments were the addition position of methylamine and the use of a diaphragm pump to enhance the mixing between the exhaust and the added methylamine. The conditions for gas mixing in the three experimental cases in the straight reactor are listed as case 1 to case 3 in Table 2.

To examine the catalytic effect, two more experiments were conducted. The conditions of these two catalytic experiments are listed as case 4 and case 5 in Table 2. A 105 mm long "fat reactor" having a 50 mm inner diameter (Fig. 2(*b*)) was used in these experiments. The fat reactor was filled with 7.0 mm stainless steel

---

Contributed by the Internal Combustion Engine (ICE) Division of The American Society of Mechanical Engineers for publication in the ASME Journal of Engineering for Gas Turbines and Power.

Manuscript received by ICE July 17, 1998; final revision received by the ASME Headquarters March 27, 1999. Associate Technical Editor: D. Assanis.

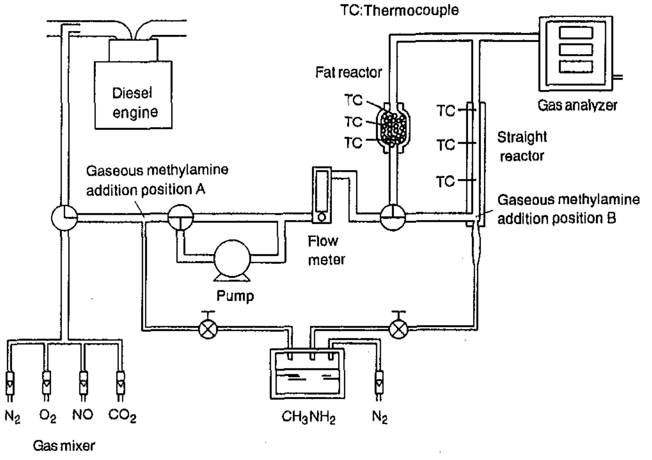

Fig. 1 Schematic of the experimental apparatus

spheres (case 4) and with cylindrical quartz pellets 7.5 mm in diameter and 7.5 mm in length (case 5).

In all cases, the flow rate was 4.5 l/min under atmospheric pressure. Each reactor was heated uniformly with an electric heater, in the range of 200 to 600°C. The reactors were designed to keep the temperature uniform along the center axis. The inside temperatures at three different locations along the center axis of the reactors (Fig. 2(*a*) and 2(*b*)) were measured with 1 mm diameter chromel/alumel thermocouple. The measured reactor temperatures showed ±5°C difference in the range of 200 to 600°C at steady state.

In the post-combustion gas treatment processes, in addition to the decomposition of NO into N_2 and H_2O in the reaction with methylamine, there is also the possibility of a decrease in NO by oxidation of NO into NO_2, because NO_2 is more stable than NO at the lower temperatures. To explore these two possibilities, both the NO and NOx removal ratios R_{NO} and R_{NOx} were measured, namely:

$$R_{NO} = 1 - [NO]_{out}/[NO]_{in} \tag{1a}$$

$$R_{NOx} = 1 - [NOx]_{out}/[NOx]_{in}. \tag{1b}$$

R_{NO} indicates the overall NO reduction ratio including both NO decomposition and NO conversion into NO_2, while R_{NOx} indicates the reduction ratio due to NO decomposition. Since the slip N_2O was very small in this process, N_2O was not take into consideration for R_{NO} and R_{NOx}. The concentration of slip N_2O will be discussed in a later section. The NO and NOx concentrations of the sample gas were measured at the reactor inlet and outlet with a NOx chemiluminescence analyzer (HORIBA MEXA 9100) and also by a Fourier transform infrared spectrometer (HORIBA MEXA-4000FT). The difference of the measured values between these gas analyses were within 4 percent which provides an estimate of the experimental error. The concentration of slip ammonia, methylamine, and other hazardous trace gases were also measured with the FTIR spectrometer.

Table 1 Composition of the diesel exhaust and the simulated exhaust gas

Constituent	Diesel exhaust *	Simulated exhaust
CO_2 (%)	9	---
O_2 (%)	11	10.0
CO (ppm)	300 - 330	---
THC (ppm)	160 - 180	---
NO (ppm)	900 - 1100	950 - 1050
NO_2 (ppm)	55 - 65	25 - 35

* Engine speed 1800 rpm, Equivalence ratio 0.64
Brake power 6.9 kW

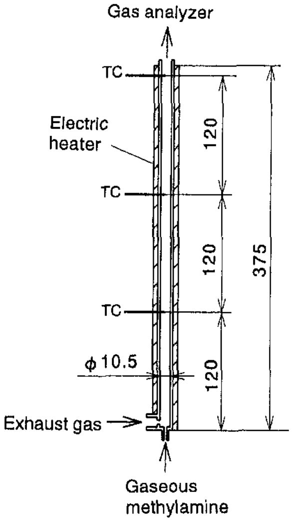

(*a*)

Fig. 2(*a*) The straight reactor

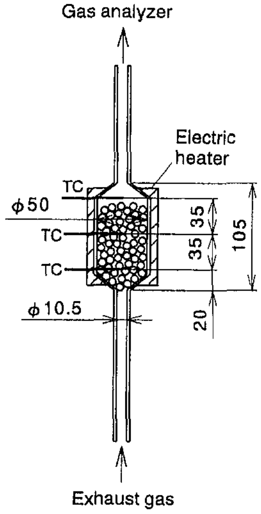

(*b*)

Fig. 2(*b*) The fat reactor

Gaseous monomethylamine was generated by supplying N_2 gas to a temperature-controlled vessel containing a 40 percent aqueous solution of monomethylamine (by volume). The quantity of the generated gaseous methylamine was controlled by adjusting the flow rate of the carrier gas. Figure 3 shows the relation between the flow rate of methylamine and that of the carrier gas N_2 under atmospheric pressure and at a temperature of 20°C. The absolute flow rate of methylamine was measured by the carbon balance

Table 2 Conditions of the experiments

Exp. case	Type of reactor	Mixing pump	Methylamine addition position	Filling
1	Straight	ON	Position A	——
2	Straight	OFF	Position B	——
3	Straight	ON	Position B	——
4	Fat	OFF	Position A	Stainless steel spheres
5	Fat	OFF	Position A	Cylindrical quartz pellets

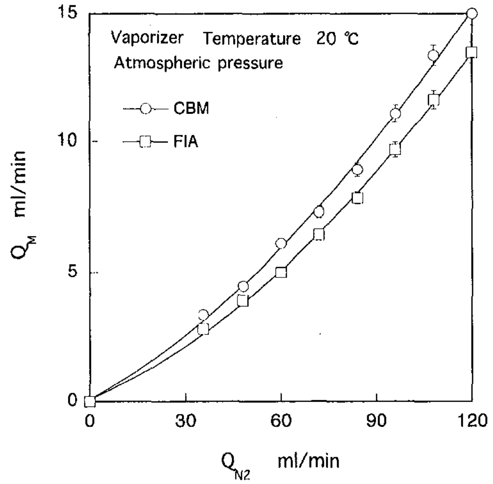

Fig. 3 Relation between flow rate of gaseous methylamine Q_M and that of carrier gas Q_{N2}

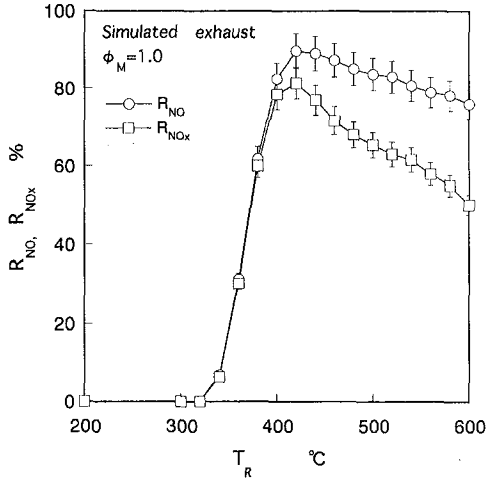

Fig. 4 Temperature effect on R_{NO} and R_{NOx} using the simulated exhaust

method (CBM), in terms of the carbonic oxide concentration of combustion flue gases of O_2-added methylamine-N_2 mixture. In each experiment, the mole number of the added methylamine vapor was monitored by taking the relative sensitivity into account through the flame ionization hydrocarbon analyzer (FIA) that indicates relative concentrations (methane equivalent). The molar ratio of added methylamine to NO in the exhaust, ϕ_M, is defined as:

$$\phi_M = [CH_3NH_2]/[NO]. \quad (2)$$

Monomethylamin is widely used in industry. Specifically, it is an important raw material for many synthetic drugs (e.g., theophylline, ephedrine), synthetic detergent, photographic chemicals (e.g., metol), acetate and vat dyes, herbicides, insecticides, and solvents. Monomethylamine is a gas at room temperature and atmospheric pressure, forming colorless liquids when cooled or compressed and manufactured by the condensation reaction of methanol and anhydrous ammonia by a zeolite catalyst. The physiological effects are generally regarded as similar to those of ammonia.

Results and Discussion

Temperature Effect on NO and NOx Reduction

The temperature dependence of the methylamine process was examined using simulated exhaust gas at $\phi_M = 1$ with the premixing system (case 1). In this case, it was thought that a sufficient mixing could be achieved. The residence time, i.e. reaction time, of the sample gas in the straight reactor was approximately 0.21 seconds at 400°C. Figure 4 shows the NO and NOx removal ratios, R_{NO} and R_{NOx}, as a function of the reactor temperature. It was found that more than 80 percent NOx removal was achieved at the temperature of 420°C. R_{NO} and R_{NOx} began increasing at a temperature of approximately 320°C and reached maximum at approximately 420°C. At temperatures of 420°C or higher, R_{NO} had a lower value than R_{NOx}, since NO_2 formed at those temperatures. Note that as NH_2 derived from methylamine reacts with and removes the NO, the methylamine process had no effect in removing NO_2. The dominant reaction for NO_2 formation is

$$NO + HO_2 \rightarrow NO_2 + OH. \quad (3)$$

Though the rate constant for this reaction has a weak negative temperature dependency, the reaction rate strongly depends on the HO_2 concentration. Therefore, the increased conversion from NO to NO_2 observed at higher temperatures might have resulted from an increased HO_2 concentration in this temperature range.

Effect of the Mixing Condition

To examine the mixing effect, an experiment was conducted using the simulated exhaust gas with the straight reactor (case 2). In this case, the diaphragm pump to enhance mixing was not used and methylamine was added at the bottom of the straight reactor. It was thought that the mixing between methylamine and the simulated exhaust gas would be less favorable compared to that of the case 1. The results using the simulated exhaust gas in the case 2 at a reactor temperature (T_R) of 400°C are shown in Fig. 5 as a function of the molar ratio of methylamine to NO (ϕ_M) along with the results of the case 1. The results suggested that the poor mixing condition (case 2) decreased R_{NO} and caused the ammonia emission. On the other hand, with the sufficient mixing condition (case 1), ammonia was not observed and more than 80 percent of the NO removal was achieved at $\phi_M = 1$. It is suggested that the mixing between methylamine and the exhaust gases is very important factor in this technique.

Further investigation of mixing effect was conducted in case 3. In this case, the diaphragm pump was used to pulse the simulated exhaust gas and methylamine was added at the bottom of the straight reactor as shown in Table 2. The R_{NO} and R_{NOx} obtained in case 3 are shown in Fig. 6, along with the results of cases 1 and 2. The pump pulsation improved the mixing between methylamine and the simulated exhaust gas which made R_{NO} and R_{NOx} in case 3 higher than those in case 2. The upstream addition of methylamine also improved the mixing between methylamine and the simulated exhaust gas. This caused R_{NO} and R_{NOx} in case 1 to be higher than

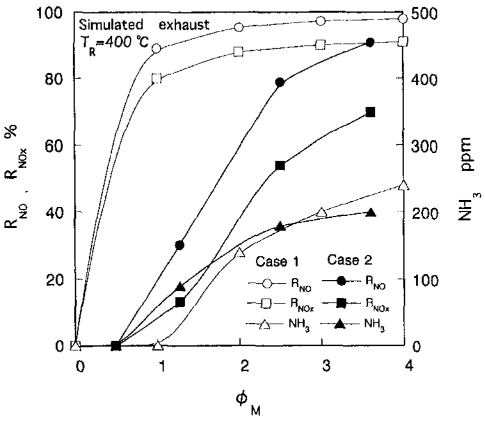

Fig. 5 Effect of mixing conditions on R_{NO}, R_{NOx}, and NH_3 concentrations using the simulated exhaust

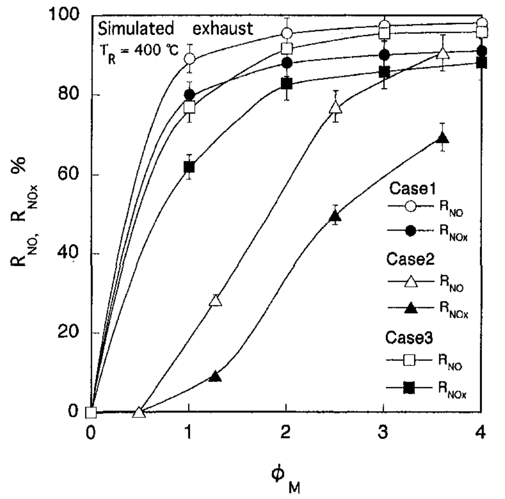

Fig. 6 Effect of mixing conditions on R_{NO}, R_{NOx} using the simulated exhaust

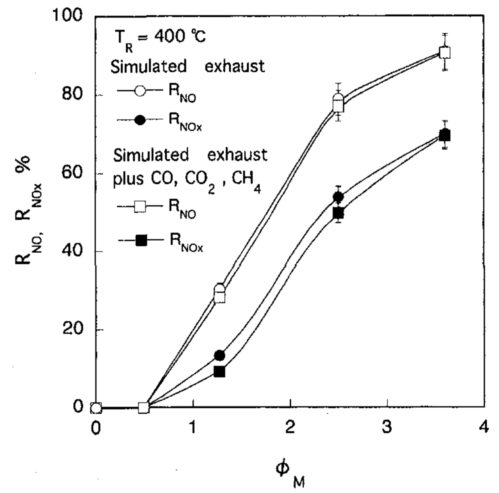

Fig. 8 Effect of the coexisting gases on R_{NO} and R_{NOx}

those in case 3. From these results, it is also suggested that the mixing is very important factor in this technique.

Figure 7 shows the measured results using diesel exhaust gas in case 2 compared with the results of case 1; the curves of R_{NO} and R_{NOx} versus ϕ_M in case 2 are now higher than those for the simulated exhaust in case 2, and are the same as those for the simulated exhaust in case 3. The possible explanation for these results is in the mixing conditions between methylamine and the sample gases. In the case of the diesel exhaust, it appeared that the mixing was enhanced by the pulsation of the exhaust, thus raising R_{NO} and R_{NOx} to the same levels as those in case 3 with the simulated exhaust. These results also show that, similar to the simulated exhaust, the enhanced mixing of case 1 increases R_{NOx}, permitting more than 80 percent NOx reduction at $\phi_M = 1$ for the diesel exhaust.

Effect of the Coexisting Gases on NO Reduction

The experiments using the diesel and the simulated exhaust gas in case 1 permitted more than 80 percent NOx reduction at $\phi_M = 1$ as show in Fig. 6 and 7. These results suggest that the coexisting gases such as CO, CO_2, THC, and H_2O, which were not included in the simulated exhaust, had no effect on NO reduction with methylamine. The effects of the coexisting gases on NO reduction were checked using the straight reactor in the case 2. All of these gases except H_2O were added to the simulated exhaust in a concentration matching that of the diesel exhaust gas as is shown in Table 1. To much THC, methane was added. The results, given in Fig. 8, confirm that these gases have no effect on NO reduction. To further investigate the effect of these coexisting gases, each gas was added to the simulated exhaust gas separately. To examine the effect of water vapor in the diesel exhaust, the partial pressure of water vapor was reduced by cooling the exhaust gas to 0°C. Even in these cases, it was found that the gases had neither positive nor negative effects on NO reduction.

Effect of Oxygen Concentration on NOx Reduction

Because the O_2 concentration in diesel exhaust varies with the load, the effect of O_2 on the methylamine process was examined. Figure 9 shows the results of experiments using the simulated exhaust gas at reaction temperatures lower than 600°C using the straight reactor with the premixing system (case 1) at $\phi_M = 1$. The data show that NO decomposition does not occur in the absence of O_2 in the simulated exhaust gas. In the case of 10 percent O_2 content, NOx was reduced by 80 percent. And in the case of 5 percent O_2 content, 75 percent NOx removal was achieved. It is thus clear that O_2 severely affects the methylamine process. The diesel exhaust usually includes at least 5 percent O_2 even at full load. Therefore, 75 percent NOx removal can be achieved. The

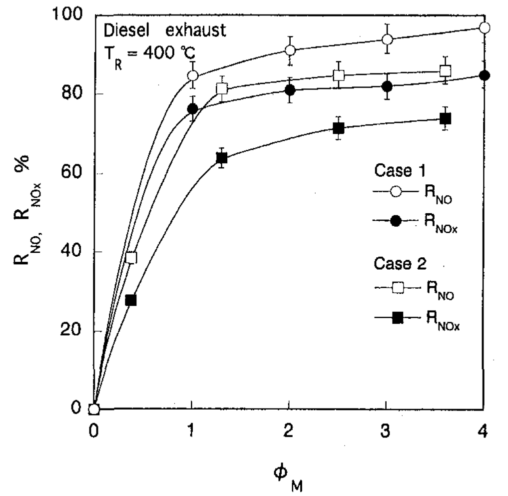

Fig. 7 Effect of mixing conditions on R_{NO} and R_{NOx} using the diesel exhaust

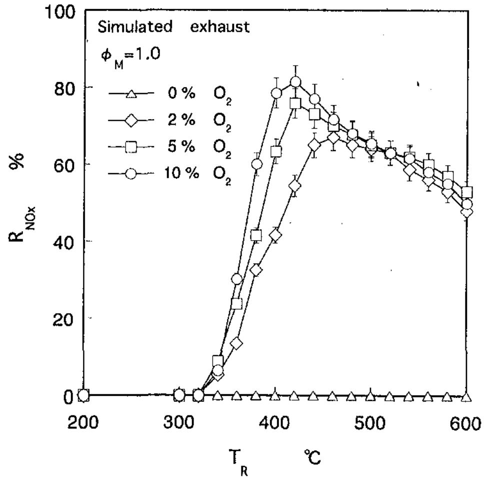

Fig. 9 Effect of oxygen concentration on R_{NOx} using the simulated exhaust

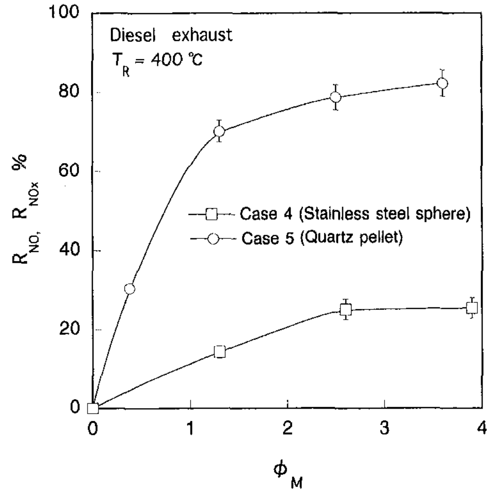

Fig. 10 Effect of stainless steel as a catalyst on R_{NOx} using the diesel exhaust

mechanism of the reaction will be discussed in the Mechanism of the Methylamine Process section.

Surface Effects

The surface effects on the chemical reaction were examined. It has been reported that steel surfaces such as Fe_2O_3 affect the processes using ammonium compounds as the reducing agent (Carton and Siebers, 1989). The present experiment was conducted using diesel exhaust at a temperature of 400 ± 5°C. Methylamine was added upstream of the fat reactor. In the first experiment, the reactor was filled with stainless steel 7.0 mm spheres to examine the catalytic effects (case 4). In the second experiment the reactor was filled with cylindrical quartz pellets 7.5 mm in diameter and 7.5 mm in length for a non-catalytic experiment (case 5). The temperature during the experiments was the same and the conditions steady. Since the reaction spaces in the reactor were set the same for the two cases, the residence (reaction) times in both cases were also the same, equal to 0.52 seconds at 400°C. Figure 10 shows the R_{NO} in cases 4 and 5. NO removal in case 4 hardly proceeded, while a 70 percent NO removal was achieved in case 5 at $\phi_M = 1$. From these results, it is found that the stainless steel surface inhibits NO breakdown by methylamine. In addition, these results suggest that the NO removal process with methylamine is not a surface interaction process but a gas phase process.

Slip of Trace Gases

The slip of trace gases such as ammonia in the methylamine process was measured with an FTIR spectrometer. This experiment was conducted using the simulated exhaust gas at a temperature of 400 ± 5°C with the very good mixing condition (case 1). In these conditions, more than 80 percent of the NO removal was achieved as shown in Fig. 6. The concentration of the slip NH_3, CH_3NH_2, CO, and N_2O in these conditions are shown in Fig. 11 as a function of ϕ_M. Ammonia and methylamine were not observed by the FTIR measurement at $\phi_M = 1$, while 270 ppm of CO were observed at $\phi_M = 1$. The results suggest that the final products of the carbon in methylamine are CO and CO_2. The molar ratio of CO to CO_2, which varies according to the conditions, is typically 0.3, based on the FTIR measurement. However, it is supposed that CO can be removed easily by current oxidation catalysts. Figure 11 also shows 30 ppm N_2O emission at $\phi_M = 1$. N_2O emission is, however, very small compared to the amount of reduced NO.

Mechanism of the Methylamine Process

NH_2 radicals, formed from ammonium compounds or amines, enable the breakdown of NO, as mentioned before. While NH_2 can only be derived from ammonium compounds at temperatures over 700°C, it is reported that the oxidation of amines begins at temperatures about 250 to 300°C and yields NH_2 as a intermediate product (Minkoff and Tipper, 1962). For this reason, NO removal with methylamine becomes possible at these temperatures. Since the presence of oxygen is essential for NO reduction with methylamine, as shown in Fig. 9, it is considered that the kinetic characteristics at relatively low temperatures of amines resemble those for the combustion of hydrocarbons at low temperatures. The reactions are as follows (Minkoff and Tipper, 1962):

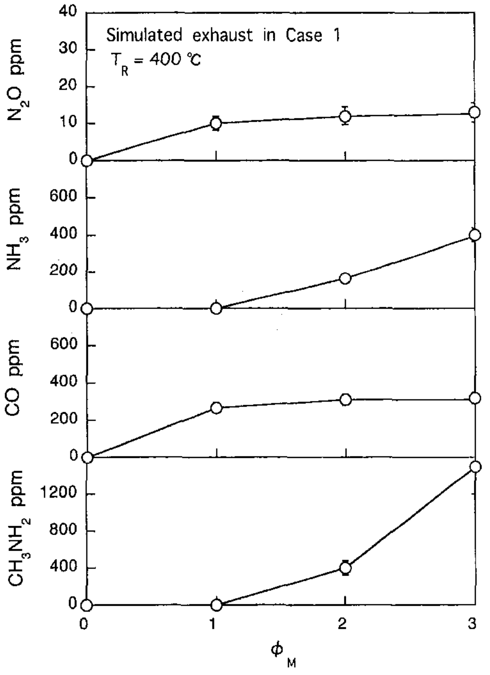

Fig. 11 The concentration of the slip NH_3, CH_3NH_2, CO, and N_2O in the case 1

$$CH_3NH_2 + O_2 \rightarrow CH_2NH_2 + HO_2 \quad (4)$$

$$CH_2NH_2 + O_2 \rightarrow CH_2NH_2OO \quad (5)$$

$$CH_2NH_2OO \rightarrow NH_3 + CO + OH \quad (6)$$

$$CH_2NH_2OO + CH_3NH_2 \rightarrow NH_2CH_2OOH + CH_2NH_2 \quad (7)$$

$$NH_2CH_2OOH \rightarrow NH_2 + CH_2O + OH \quad (8)$$

The primary initiation reaction is the abstraction of a hydrogen atom in methylamine (reaction (4)). The radicals formed from methylamine may then react with oxygen molecule, as represented in reaction (5). In reaction (6), NH_3 is formed. On the other hand, aldehyde and NH_2 radicals are produced in reactions (7) and (8). In a further oxidation, the NH_2 radical gives nitrogen oxide, the yield of which is greater if excess oxygen is present, whereas that of ammonia increases with the proportion of methylamine. In addition, a large excess of oxygen may keep the ammonia yield small and make aldehyde and NH_2 radical formation dominant. Although the NH_2 radical will often be a source of NO, as mentioned above, it acts to reduce NO if the NO concentration exceeds the equilibrium value. The equilibrium NO concentration at the temperatures of diesel exhaust is lower than 10^{-6} in mole fraction, so that the NO concentration in the exhaust, on the order of 10^{-3}, is out of equilibrium. The NH_2 mechanism is reported by Miller and Bowman (1989).

$$NH_2 + NO \rightarrow N_2 + H_2O \quad (9)$$

$$NH_2 + NO \rightarrow NNH + OH \quad (10)$$

$$NNH + NO \rightarrow HNO + N_2 \tag{11}$$

$$NNH \rightarrow N_2 + H \tag{12}$$

$$HNO + M \rightarrow NO + H + M \tag{13}$$

Since these reactions proceed rapidly at lower temperatures (Miller et al., 1981; Miller and Bowman, 1989), NH_2 radicals are consumed rapidly in the methylamine process. Therefore, aldehyde and NH_2 radical formation is much faster than ammonia formation despite the NH_2 equilibrium concentration being much lower than that of ammonia. This is the reason why the methylamine process enables more than 80 percent NO reduction with ammonia formation hardly occurring.

Further oxidation of the aldehydes gives CO and CO_2 by the following reactions:

$$CH_2O + O_2 \rightarrow CHO + HO_2 \tag{14}$$

$$CH_2O + HO_2 \rightarrow CHO + H_2O_2 \tag{15}$$

$$CH_2O + OH \rightarrow CHO + H_2O \tag{16}$$

$$CHO + O_2 \rightarrow CO + HO_2 \tag{17}$$

$$CO + OH \rightarrow CO_2 + H \tag{18}$$

$$CO + HO_2 \rightarrow CO_2 + OH \tag{19}$$

These mechanisms well explain some experimental results for the methylamine process. First, the presence of oxygen is essential for NO reduction, as shown in Fig. 9. This is because the initiation reaction should occur between methylamine and oxygen. Next, sufficient mixing between methylamine and the exhaust enables more than 80 percent NO reduction without ammonia formation. On the other hand, imperfect mixing results in the reaction under methylamine-rich conditions, which forms excess ammonia and inhibits NO decomposition as mentioned in the "Effect of the Mixing Condition" section.

Conclusions

A new, selective, noncatalytic technique for removing NO from diesel exhaust using methylamine as the reducing agent was studied. In the experiments, reactions were conducted in electrically heated quartz reactors in the temperature range of 200°C to 600°C with $[CH_3NH_2]/[NO]$ molar ratios from 1 to 4. The results showed that the addition of methylamine into the exhaust gas in the temperature range of 400°C to 540°C has the effect of breaking down NO. The reduction of more than 80 percent of NO was achieved at $\phi_M = 1$ using both diesel exhaust and simulated exhaust gas. It was also shown that sufficient mixing of the added methylamine and the exhaust gas promotes NO removal and prevents the slip of ammonia and methylamine. In addition, chemical mechanisms for the methylamine process were discussed, which can explain the obtained experimental results, and it is suggested that the NO removal processes with methylamine similar to combustion of hydrocarbons at low temperatures.

References

Carton, J. A., and Siebers, D. L., 1989, "Reduction of Nitrogen Oxides in Engine Exhaust Gases by the Addition of Cyanuric Acid," ASME *Journal of Fluids Engineering,* Vol. 111, pp. 387–393.

Miller, J. A., and Bowman, C. T., 1989, "Mechanism and Modeling of Nitrogen Chemistry in Combustion," *Progress in Energy and Combustion Science,* Vol. 15, pp. 287–338.

Miller, J. A., Branch, M. C., and Kee, R. J., 1981, "A Chemical Kinetic Model for the Selective Reduction of Nitric Oxide by Ammonia," *Combustion and Flame,* Vol. 43, pp. 81–98.

Minkoff, G. J. and Tipper, C. F. H., 1962, *Chemistry of Combustion Reactions,* Butterworth, London.

Yoshihara, Y., and Tanaka, T., 1995, "Reduction of Oxides of Nitrogen in Diesel Exhaust with Addition of Methylamine," *Transactions of the Japan Society of Mechanical Engineers,* Series B, Vol. 61-582, pp. 408–413.

Yoshihara, Y., Ikegami, M., and Mine, N., 1990, "Reduction of Oxides of Nitrogen in Diesel Exhaust with Addition of Partially Decomposed Ammonia," *Transactions of the Japan Society of Mechanical Engineers,* Series B, Vol. 56-523, pp. 845–850.

S. M. Aceves
saceves@llnl.gov

J. R. Smith

C. K. Westbrook

W. J. Pitz

Lawrence Livermore National Laboratory,
7000 East Avenue, L-641,
Livermore, CA 94551

Compression Ratio Effect on Methane HCCI Combustion

We have used the HCT (hydrodynamics, chemistry, and transport) chemical kinetics code to simulate HCCI (homogeneous charge compression ignition) combustion of methane-air mixtures. HCT is applied to explore the ignition timing, burn duration, NO_x production, gross indicated efficiency and gross IMEP of a supercharged engine (3 atm. intake pressure) with 14:1, 16:1 and 18:1 compression ratios at 1200 rpm. HCT has been modified to incorporate the effect of heat transfer and to calculate the temperature that results from mixing the recycled exhaust with the fresh mixture. This study uses a single reaction zone that varies as a function of crank angle. The ignition process is controlled by adjusting the intake equivalence ratio and the residual gas trapping (RGT). RGT is internal exhaust gas recirculation, which recycles both thermal energy and combustion product species. Adjustment of equivalence ratio and RGT is accomplished by varying the timing of the exhaust valve closure in either two-stroke or four-stroke engines. Inlet manifold temperature is held constant at 300 K. Results show that, for each compression ratio, there is a range of operational conditions that show promise of achieving the control necessary to vary power output while keeping indicated efficiency above 50 percent and NO_x levels below 100 ppm. HCT results are also compared with a set of recent experimental data for natural gas.

Introduction

The concept of homogeneous charge compression ignition (HCCI) has been described before by a number of researchers. Onishi et al. (1979) experimentally studied homogeneous charge compression ignition in a two-stroke engine and achieved low cyclic variation at idle and up to 40 percent load. Najt and Foster (1983) used a simplified kinetics scheme to correlate heat release in a Waukesha Cooperative Fuels Research (CFR) engine with modest compression ratios and high EGR. Thring (1989) used a Labeco Cooperative Lubricant Research (CLR) engine with a wedge shaped combustion chamber at 8:1 compression ratio with external mixture preparation and heating of a gasoline mixture above 640 K and EGR rates of 13 to 33 percent to map out permissible operating parameters. Thring also coined the most descriptive name of this combustion process, HCCI, which these authors will use in this work. Ryan and Callahan (1996) used a variable compression ratio engine to map operational space for HCCI using 47-cetane diesel fuel. They found that compression ratio, EGR rate and equivalence ratio were adequate for control. Nakagome et al. (1997) used early injection of diesel fuel in a DI Diesel to achieve HCCI resulting in very low NO_x (20 ppm).

Recent research and development in HCCI combustion includes the successful testing of an experimental motorcycle with a two-stroke HCCI (or activated radical combustion, ARC, as called by the authors) engine by Honda. The motorcycle participated in the Granada-Dakar rally, and placed fifth overall (Automotive Engineering, 1997). Other publications by Honda researchers (Asai et al., 1995; Ishibashi and Asai, 1996; Ishibashi and Asai, 1998) have described many technical details of the engine and motorcycle. The engine uses spark ignition for starting and for very low and very high load conditions, and an exhaust valve to regulate the amount of residual gas trapped (RGT) to achieve combustion control under HCCI combustion. Experimental testing has determined that the HCCI engine provides reduced CO and HC emissions, a 27 percent improvement in fuel economy, and a marked improvement in driveability with respect to conventional two-stroke engines.

Another recent publication has determined the fuel sensitivity of HCCI (Iida, 1997). Dimethyl ether, methanol, ethanol, methane, and propane were tested in a two-stroke, low compression ratio engine. Research for four-stroke engines (Gray and Ryan, 1997; Christensen et al., 1998) have once more demonstrated the benefits of HCCI of having a very high efficiency and low NO_x. A high IMEP has also been achieved by supercharging to 3 bar absolute pressure. These papers also indicate some drawbacks for HCCI combustion, including very sudden (and often early) heat release, and high hydrocarbons and CO emissions. Hydrocarbons and CO have been attributed by these researchers to wall wetting, wall quench, and/or crevices.

A very important issue regarding HCCI combustion is control of heat release. The HCCI process gives up the following two important control aspects: (1) the timing of the start of ignition is not directly controlled by any external event such as the beginning of injection in the standard Diesel or the sparking of the spark plug in the Otto cycle engine; and (2) the heat release rate is not controlled by either the rate and duration of the fuel injection process as in the standard Diesel or by the finite turbulent flame propagation time in the Otto cycle engine. A possibility for achieving engine control is by regulating the amount of RGT in the cylinder as a function of the engine load, and by using spark ignition for conditions where HCCI combustion is not satisfactory. This is the procedure used by Honda in the two-stroke motorcycle engine. Use of RGT can also be applied to four-stroke engines for combustion control, although its implementation is more complex than for two-stroke engines. Previous work by the authors (Smith et al., 1997) describes an active control strategy that can be applied to an engine that includes an in-cylinder pressure sensor. With this strategy, variable valve timing and equivalence ratio are used for controlling combustion. If the pressure information indicates that the previous combustion cycle occurred later than the ideal timing for maximum efficiency, the mixture equivalence ratio can be increased for the next cycle. Note that this only requires a fast response time, low-pressure injection system similar to that used in today's port injection gasoline engines. Or alternatively, if electromagnetic intake and exhaust valves are used (Theobald and Henry, 1994), the exhaust valve can be opened late to increase in-cylinder EGR

Contributed by the Internal Combustion Engine Division (ICE) of THE AMERICAL SOCIETY OF MECHANICAL ENGINEERS for publication in the ASME JOURNAL OF ENGINEERING FOR GAS TURBINES AND POWER.

Manuscript received by the ICE October 21, 1998; final revision received by the ASME Headquarters February 24, 1999. Associate Technical Editor: D. Assanis.

and initial temperature for the next cycle. Calculations show that variations in the exhaust valve timing can be used to change the charge temperature at BDC by several hundred Kelvins due to changes in the amount of trapped hot residual gases kept in the cylinder for the next cycle. An electromagnetic intake valve timing can also be used to vary the initial charge density without suffering throttling losses. Through detailed kinetic modeling, the conditions required to control the initiation of autoignition can be predicted. The calculation of the required changes to keep the combustion starting at the proper time could be used to generate a look-up table for the engine controller thus avoiding any real time detailed calculations.

Another alternative for controlling combustion consists of preheating the intake air to a temperature high enough for HCCI combustion to occur. This operating mode has often been tested in experiments (Christensen et al., 1998). This strategy could potentially be implemented in an engine by adding a heat exchanger to preheat the intake gases with the exhaust gases. This is in many respects a recycling of the exhaust thermal energy, similar to RGT. However, this methodology may be difficult to implement in vehicular applications, due to the long response time of the heat exchanger, and the extra volume and pressure drop that results from heat exchanger operation.

As an alternative to the above ignition control strategies, it is also possible to raise the temperature and the density of the charge by firing a spark plug and start a flame propagating that will further compress the unburned mixture. This would be a very slow flame in the lean, low turbulence mixture and would not have time to propagate across the chamber before conditions in the unburned gases reached the autoignition point. This type of operation, if required, would in effect be an Otto cycle engine process with "soft knock" due to the very lean operation. Yet another ignition alternative is to direct inject either near TDC or at the intake valve a small amount of high cetane fuel to promote earlier autoignition. Injection near TDC would be the equivalent to pilot injection diesel operation which has been used in some diesel dual fuel operation on natural gas (Jensen, 1994). Neither of these alternatives is as desirable due to cost and complexity, but they do exist as backups if the preferred control is too sensitive to be a robust control strategy. This paper explores only the use of externally prepared equivalence ratio and RGT as controls.

Our concept of HCCI is to use compression ignition of a homogeneous charge mixture prepared in the manifold of a very high octane (and low cetane) fuel at very lean conditions. This is contrasted to earlier work (Thring, 1989) where a 87 octane fuel was used at 8:1 compression ratio or the early direct injection studies (Nakagome et al., 1997) at 16.5:1 compression ratio using a 62 cetane fuel. In our current study we have chosen methane as the fuel with its 120 RON. Ignition is by autoignition thus relatively high compression ratios will be needed. Because the mixture is homogeneous and lean, no particulates will be formed. Thermal efficiency in an HCCI engine is likely to closely approach that of the standard diesel as was demonstrated by Thring (1989).

Computational Model

All of the modeling computations in this study were carried out using the HCT model (hydrodynamics, chemistry and transport; Lund, 1978). This model has been used in a large number of investigations over the years, and in particular was used in past studies of engine knock and autoignition (Westbrook et al., 1991; Pitz et al., 1991; Westbrook et al., 1988). The HCT code permits the use of a variety of boundary and initial conditions for reactive systems, depending on the needs of the particular system being examined. In the present case, the relevant conditions are those which describe the bulk gases in the combustion chamber.

Autoignition of a homogeneous charge is virtually identical to the knock process that can occur in the Otto cycle engine. From detailed kinetic modeling of motored engines using a homogeneous charge of a variety of fuels, it is known that the controlling parameters in the initiation of this process are the fuel components (mixtures behave differently than neat fuels), and the temperature and density history that the fuel air mixture experiences. Motored engine experiments at General Motors Research Laboratories (Curran et al., 1995) agree well with HCT simulation of this process. Thus, if the precise conditions at the start of compression are known (species, temperature, and density), the beginning of combustion can be accurately predicted.

During an engine cycle, a number of processes occur which influence the time variation of the temperature and pressure of the bulk reactive gases in the combustion chamber. Piston motion first compresses and heats the bulk gases and then expands and cools them. During this time chemical reactions release heat and change the overall composition of the gases. Fresh unreacted fuel and air are added to hot residual gases left over from the previous cycle. Residual gases from the previous engine cycles, which consist largely of water vapor, CO_2 and molecular nitrogen and oxygen, are assumed fully mixed with the fresh charge. In addition, heat losses to the engine chamber walls, blowby, fuel trapping in crevice volumes, and other processes occur. Of these, only heat transfer losses are taken into account in the current simulations.

The computational model treats the combustion chamber as a homogeneous reactor with a variable volume. The mixed temperature of the residual gases and the fresh charge is estimated by a published procedure (Heywood, 1988). Equivalence ratio is defined as that of the incoming mixture in the manifold—not the mixture in the cylinder, which can be leaner due to residual oxygen. The heat transfer submodel that we employed in the HCT code simulations uses Woschni's correlation (Woschni, 1967).

The present analysis considers a single-zone, lumped model that ignores spatial variations in the combustion chamber, treating heat loss as a distributed heat transfer rate, proportional to the temperature difference between the average gas temperature and a time-averaged wall temperature. The authors recognize that this is a great oversimplification of the actual condition within the combustion chamber. In particular, the boundary layer, which contains significant mass, must be at a lower temperature than the bulk gas near TDC. Due to the extreme temperature history sensitivity of the autoignition and heat release processes, our estimates of burn duration will be shorter than in experiments. That is, the boundary layer will always burn last and extend the heat release rate compared to this simulation. Peak cylinder pressure and rate of pressure rise are overestimated with the single-zone model, and the model cannot accurately predict CO and hydrocarbon emissions, which have been explained as depending on crevices, or wall wetting and quenching. On the other hand, predictions of start of combustion and NO, which depend on the peak temperature of the gases inside the cylinder, are expected to be accurate. These expectations are verified in a later section of this paper, where the model results are compared with recent experimental results for natural gas. The ideal computational tool for a detailed HCCI analysis would be a combination of HCT and a fluid mechanics code, such as KIVA (Amsden, 1993), where the cylinder is divided

Nomenclature

BDC = bottom dead center
CAD = crank angle degrees
DI = direct injected
EGR = exhaust gas recirculation
RGT = residual gas trapping (in-cylinder EGR)
RON = research octane number
TDC = top dead center

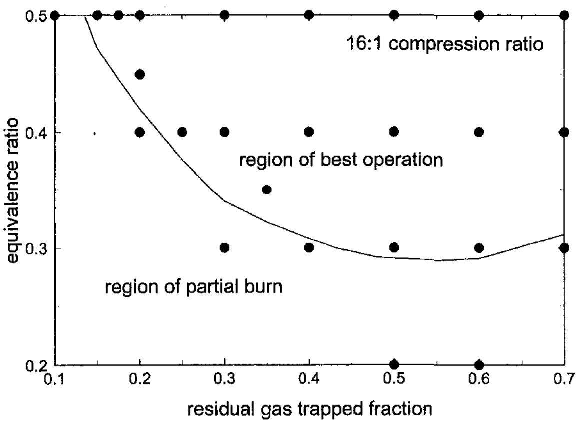

Fig. 1 Map of the regions of acceptable operation in the HCCI mode for an engine with a 16:1 compression ratio at 1200 rpm and 3 atmospheres of absolute intake pressure, running on methane. Points indicate simulations done with the HCT code.

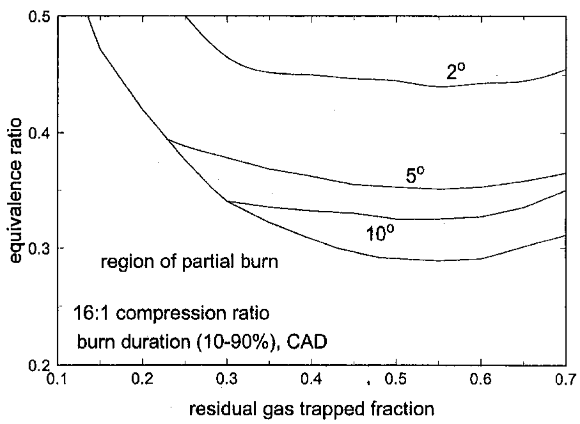

Fig. 2 Burn duration (defined as the crank angle between the points of 10 percent and 90 percent of heat release) in crank angle degrees in the region of best HCCI operation with methane at 16:1 CR, 1200 rpm, and 3 atmospheres of absolute intake pressure

into a great number of zones, each one with a different temperature history. This is, however, well beyond our current computational capabilities. KIVA has been used in the past to predict HCCI combustion, but simplified correlations for heat release have been used, instead of detailed chemical kinetics (Kong et al., 1992; Hashizume et al., 1998).

Each simulation is started at BDC. The intake gases, initially at 300 K, are compressed in a supercharger to 3 atmospheres absolute pressure and circulated through an intercooler with a 70 percent effectiveness before mixing with the trapped residuals in the cylinder. The cylinder wall, piston and head are all assumed to be at a uniform 500 K. The chemical reactions are computed explicitly in the kinetics model. Thermodynamic table values of c_p and c_v are explicitly calculated to account for enthalpy and pressure changes. The simulation is stopped at BDC and the indicated efficiency is computed. The NO values reported are those at BDC. The chemical kinetic reaction mechanisms used by the model for methane ignition and NO production have been extremely well established and are widely used. The chemical kinetic mechanism for methane was taken from Curran et al. (1995). The mechanism for nitrogen kinetics is from the Gas Research Institute mechanism version 1.2 (Frenklach et al., 1995). Other fuels can be analyzed with HCT, provided that the appropriate chemistry reaction set is available. However, the computational resources necessary for running a problem increase rapidly as the complexity of the molecules increases.

Engine Description

The engine is assumed to have a bore and stroke of 100 mm and a connecting rod length of 160 mm. Three compression ratios are analyzed: 14:1; 16:1, and 18:1, and the displacement per cylinder is 0.785 liter. The engine is assumed to have variable valve timing so as to allow quick changes in the RGT. This arrangement allows near adiabatic EGR, which means that the charge temperature rises with RGT fraction. The engine is assumed to be unthrottled at all operation points with a volumetric efficiency of 100 percent. The engine speed is 1200 rpm and the absolute intake pressure is 3 atmospheres.

Results

By making over one hundred simulation runs we have mapped the regions of acceptable operation in the HCCI mode. Most of the results presented in this section are for a 16:1 compression ratio, which was chosen as the base-case. Figure 1 shows the results in equivalence ratio versus RGT fraction parameter space. The lower left of the plot shows the region where only partial burn or no burn takes place. The boundary between partial burn and complete burn was found to be extremely sharp. The upper right region represents the region where the acceptable operation both in terms of ignition timing and maximum cylinder pressure can be achieved.

Figure 2 shows burn duration. Burn duration is defined as the crank angle between the points of 10 percent and 90 percent of heat release. All burn durations are noticeably short. We have included burn durations down to 2 CAD in the acceptable region which may be overly optimistic. Recall, however, that the single zone model used in the current simulations will, almost certainly, under predict the actual burn duration. Reasonable burn durations exist mainly for low equivalence ratios.

The gross indicated efficiency is shown in Fig. 3. The efficiency is higher than 54 percent throughout the region of best operation. This area of high efficiency is at low power levels and potentially has much higher efficiency than spark-ignited engines due primarily to the lack of throttling losses and perhaps even higher than diesels due to shorter heat release rates. The efficiency increases as the equivalence ratio and RGT are decreased. For high equivalence ratios and RGT, combustion occurs before TDC, resulting in significant negative work on the piston. Reducing the equivalence ratio and RGT delays combustion and reduces the negative work, increasing the efficiency. Efficiencies in Fig. 3 are optimistic values, since no losses due to blowby or partial combustion are considered in the analysis.

Figure 4 shows the maximum pressure inside the cylinder. Maximum cylinder pressure may be limited due to the mechanical strength of the engine. A recent publication (Christensen et al.,

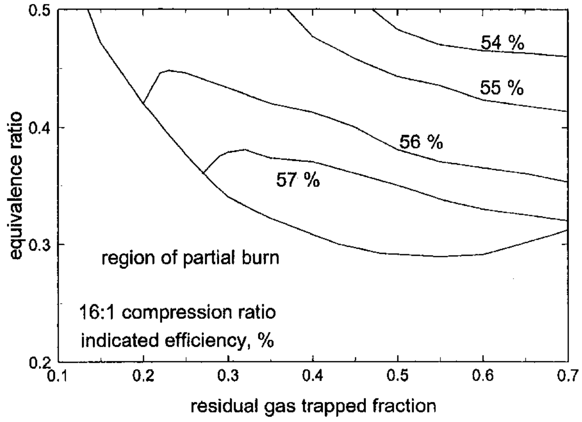

Fig. 3 Gross indicated efficiency in the best region of operation with methane at 16:1 CR, 1200 rpm, and 3 atmospheres of absolute intake pressure

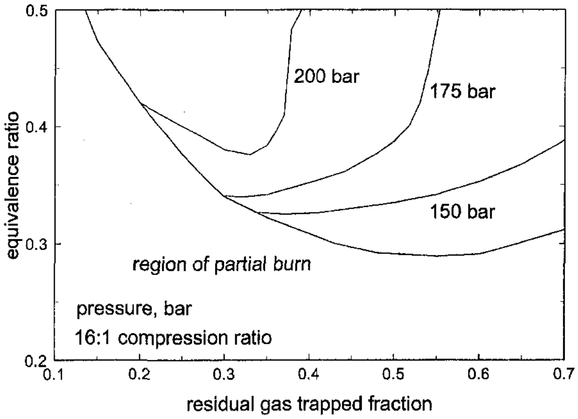

Fig. 4 Contours of maximum cylinder pressure for methane HCCI combustion at 16:1 CR, 1200 rpm, and 3 atmospheres of absolute intake pressure

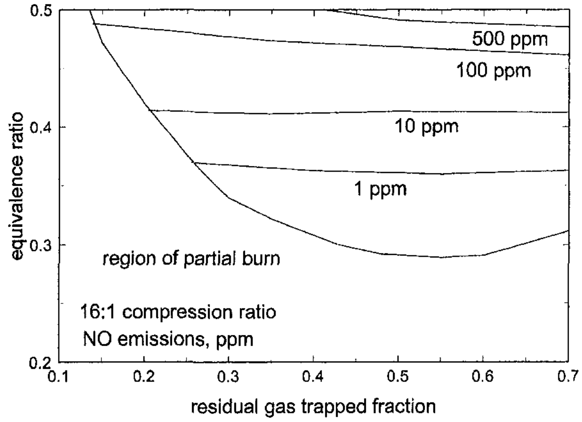

Fig. 6 Contours of NO emissions in PPM for methane HCCI combustion at 16:1 CR, 1200 rpm, and 3 atmospheres of absolute intake pressure

1998) set the maximum cylinder pressure at 250 bar. The maximum pressure is high over a large portion of the operational space, but it does not reach 250 bar, and it is therefore considered acceptable.

Figure 5 shows engine gross IMEP (indicated mean effective pressure) in bar. The maximum IMEP is high, being of the same order as the IMEP for spark-ignited engines (Heywood, 1988). Obtaining a high power out of an HCCI engine is a concern, due to the need to operate at a low equivalence ratio and a high RGT. Figure 5 shows that supercharging may provide high power when required.

The NO emissions were found to be more than 98 percent of the total NO_x emission. They are plotted in Fig. 6. As expected, when the equivalence ratio rises above 0.4, NO emissions rise quickly, and this is another reason to keep the equivalence ratio under 0.5 (in addition to a high maximum cylinder pressure and early combustion). One control strategy to produce high power without high NO could be to avoid intermediate equivalence ratios between 0.5 and stoichiometric, and go directly to stoichiometric for high power output and include a three-way catalyst to reduce NO to acceptable levels.

As the compression ratio is reduced, the peak temperature in the cylinder is lower, reducing the likelihood of fuel HCCI combustion. This is illustrated in Fig. 7, where the area of best HCCI operation is mapped as a function of equivalence ratio and RGT for an engine with a 14:1 compression ratio. Comparing Fig. 7 with Fig. 1 (for 16:1 CR) shows that the area of best operation is reduced, due to the lower temperatures and pressures reached at the 14:1 CR. Advantages of the lower CR operation include lower peak pressure, longer combustion, and an engine efficiency that is almost as high as for the 16:1 CR case. The maximum IMEP for the 14:1 engine is about 20 percent lower than for the 16:1 engine (Fig. 9).

Figure 8 shows the mapping of the area of best operation for the HCCI engine with an 18:1 compression ratio. Comparing this figure with Fig. 1 (for 16:1 CR), shows that the region of best operation extends down to lower equivalence ratios, due to the higher temperature and pressure achieved at the higher compression ratio. The figure also shows a zone in which the maximum cylinder pressure is greater than 250 bar. As previously discussed, this area may be excluded from the allowable operating area due to engine design constraints. A region is also shown in the upper right corner where combustion occurs too early (before 10° BTDC). This area may also be excluded due to the great amount of negative work done on the cylinder and also due to the potential for high stresses in the bearings and crankshaft.

Figure 8 shows that the region of excessive peak pressure appears in the operating range that produces the maximum IMEP (high equivalence ratio and low RGT). It is therefore possible that the maximum IMEP for an engine with a maximum pressure constraint may be obtained at some intermediate, optimum, compression ratio. Figure 9 illustrates this. Figure 9 shows gross IMEP as a function of maximum cylinder pressure, for the three compression ratios being analyzed. The lines are obtained assuming operating conditions in the proximity of (slightly above) the partial burn line (for smooth combustion), and IMEP is controlled by

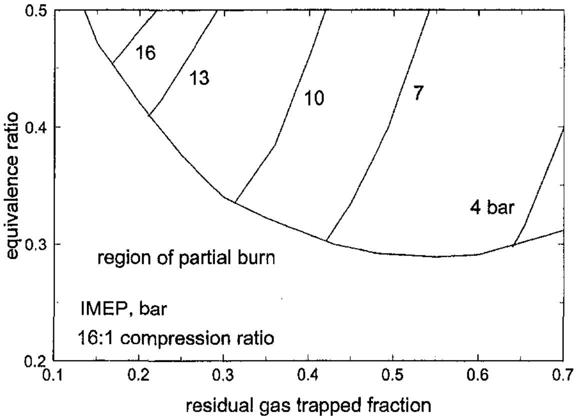

Fig. 5 Contours of engine gross IMEP (indicated mean effective pressure) in bar for methane HCCI combustion at 16:1 CR, 1200 rpm, and 3 atmospheres of absolute intake pressure

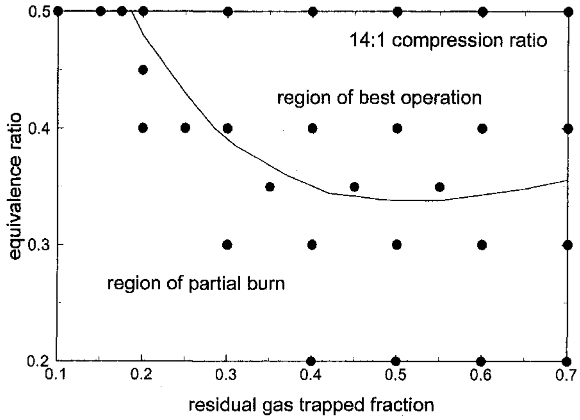

Fig. 7 Map of the regions of acceptable operation in the HCCI mode for an engine with a 14:1 compression ratio at 1200 rpm and 3 atmospheres of absolute pressure at the intake, running on methane. Points indicate simulations done with HCT code.

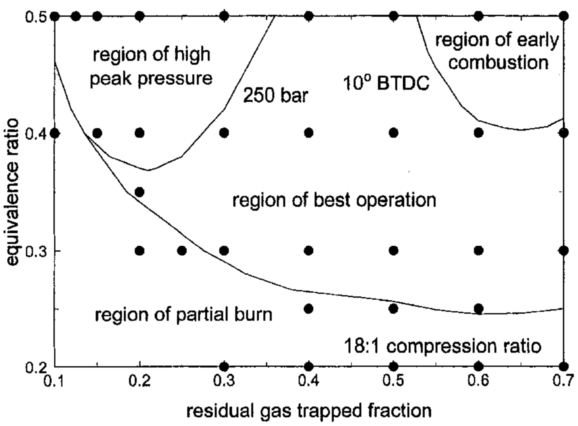

Fig. 8 Map of the regions of acceptable operation in the HCCI mode for an engine with a 18:1 compression ratio at 1200 rpm and 3 atmospheres of absolute pressure at the intake, running on methane. Points indicate simulations done with HCT code.

moving along this line. Lowest power is obtained at the right end of the partial burn line, and maximum power is obtained at the opposite (upper left) end of the partial burn line (see Figs. 1, 7, and 8). Figure 9 shows that the 250 bar restriction in the maximum pressure limits the power output from the 18:1 CR engine, so that the maximum IMEP is obtained from the 16:1 CR engine. Reducing the maximum allowable cylinder pressure results in a reduced optimum compression ratio. An engine designed for a 200 bar maximum cylinder pressure would have 14:1 as the compression ratio for maximum IMEP. This procedure can be applied to determine the compression ratio for which a maximum IMEP is obtained for a given fuel, engine, and operating conditions. An evaluation of this optimum compression ratio should help in characterizing any fuel for HCCI engine operation, although it has to be considered that engine friction varies with compression ratio, and the maximum values of BMEP and IMEP may not occur at the same compression ratio.

Figure 9 also shows lines of constant NO emissions (dotted lines). These lines may also represent a limit to engine operation, depending on the emissions standard that has to be met. As shown in the figure, NO emissions may represent an important limit at low compression ratios. For high compression ratios, the peak pressure limit is likely to be reached before NO emissions are significant.

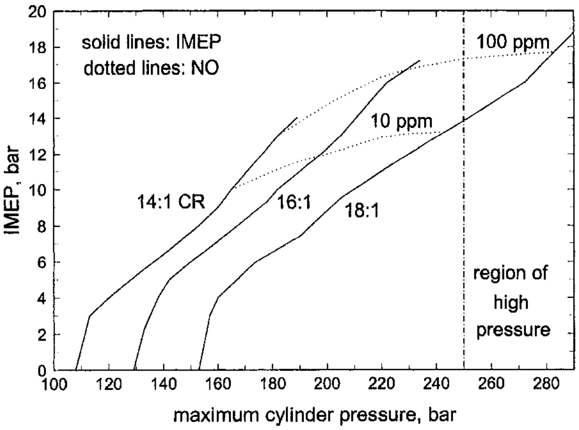

Fig. 9 Gross IMEP as a function of maximum cylinder pressure, for the three compression ratios being analyzed. The figure shows the maximum allowable cylinder pressure (250 bar), and dotted lines that indicate points of constant NO emissions.

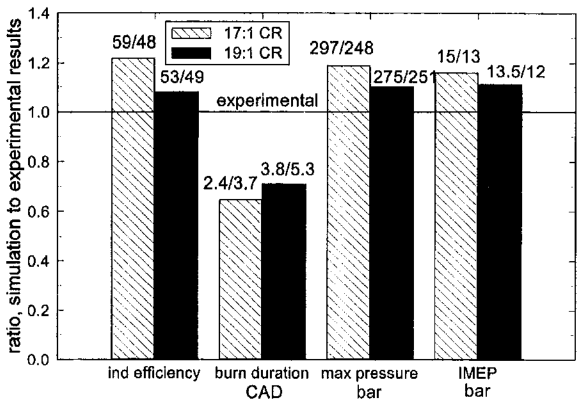

Fig. 10 Ratio of HCT simulation results to experimental results (from Christensen et al., 1998) for natural gas fuel, for four engine parameters: gross indicated efficiency, burn duration, maximum cylinder pressure, and gross IMEP, for two operating points: 17:1 compression ratio, 3 bar intake pressure, 0.31 equivalence ratio, and 70°C intake temperature, and 19:1 compression ratio, 3 bar intake pressure, 0.26 equivalence ratio, and 50°C intake temperature.

Comparison With Experimental Results

A recent paper (Christensen et al., 1998) has provided HCCI data for a four-stroke engine running on ethanol, octane, and natural gas. This section shows a comparison between the experimental results and HCT results for two of the experimental conditions. The comparison is for natural gas fuel. The volume composition of the natural gas is 91.1 percent methane, 4.7 percent ethane, 1.7 percent propane, 1.4 percent n-butane, 0.6 percent nitrogen, and 0.5 percent carbon dioxide. Only two conditions are used in the comparison, but all the results follow the same general trends. The following two conditions used in the comparison.

Condition 1. Natural gas, 17:1 trapped compression ratio, 3 bar intake pressure, 0.31 equivalence ratio, and 70°C intake temperature.

Condition 2. Natural gas, 19:1 trapped compression ratio, 3 bar intake pressure, 0.26 equivalence ratio, and 50°C intake temperature.

The comparison is complicated by the fact that the temperature at BDC before the compression stroke is not known. This temperature is higher than the intake temperature, due to heat transfer from the intake manifold, cylinder walls, and residual gases. Instead of attempting the difficult task of accurately calculating the temperature at BDC, this temperature has been used as a free parameter to match the start of combustion. It was found that adding 40°K to the intake manifold temperature results in values for BDC temperature that match the start of combustion reported in the experiments. This adjustment appears appropriate, since 40°K is a reasonable value for the temperature increase due to heat transfer and residuals.

Once the start of combustion is matched, other combustion parameters can be compared. The results are shown in Fig. 10. The figure shows the ratio of the simulation results to the experimental results, for the following four engine parameters: gross indicated efficiency, burn duration, maximum cylinder pressure, and gross IMEP, for the two operating conditions previously described (17:1 and 19:1 compression ratio). The numbers on top of the bars show the numerical and experimental results that are divided to obtain the ratio shown in the figure. For example, 59/48 on top of the first indicated efficiency bar indicates that the calculated indicated efficiency is 59 percent, and the experimental value is 48 percent.

The results are consistent with what should be expected from a single-zone model. Calculated values for indicated efficiency and IMEP are 10 to 20 percent higher than the experimental values, mainly because the single-zone model predicts that the fuel burns to completion. Multiplying these results by the combustion efficiency (reported by Christensen et al., as being about 92 percent) would result in a much better agreement between experimental and numerical results. The single-zone model also underpredicts the burn duration. As a consequence, maximum cylinder pressure is higher than the experimental result.

Conclusions

—Based on these HCT simulations there appears to be a region of acceptable engine operation using methane to achieve the HCCI combustion process.

—High indicated efficiency at low power levels should be achievable.

—NO emission levels of less than 100 ppm can be achieved without a catalyst at equivalence ratios less than 0.5.

—Equivalence ratio and residual gas trapping (RGT) are likely to be adequate controls if direct pressure feedback information is used to reduce cycle-to-cycle variation.

—Maximum cylinder pressure and NO emissions may impose upper bounds on engine IMEP. For engines with a maximum allowable cylinder pressure, an optimum compression ratio is likely to exist for which a maximum IMEP is obtained. This optimum compression ratio can be used for fuel characterization for HCCI applications.

—A comparison between simulation and experimental results has been done. The comparison shows that the single-zone model may predict well the start of combustion, but it overpredicts engine efficiency, maximum pressure and IMEP; and it underpredicts burn duration.

Acknowledgments

Work performed under the auspices of the U.S. Department of Energy by Lawrence Livermore National Laboratory under contract W-7405 ENG-48.

References

Amsden, A. A., 1993, "KIVA-3: A KIVA Program with Block-Structured Mesh for Complex Geometries," Los Alamos National Laboratory Report LA-12503-MS.

Asai, M., Kurosaki, T., and Okada, K., 1995, "Analysis of Fuel Economy Improvement and Exhaust Emission Reduction in a Two-Stroke Engine by Using an Exhaust Valve," SAE Paper 951764.

Automotive Engineering, 1997, "Honda Readies Activated Radical Combustion Two-Stroke Engine for Production Motorcycle," December, pp. 101–102.

Christensen, M., Johansson, B., Amneus, P., and Mauss, F., 1998, "Supercharged Homogeneous Charge Compression Ignition," SAE Paper 980787.

Curran, J. H., Gaffuri, P., Pitz, W. J., Westbrook, C. K., and Leppard, W. R., 1995, "Autoignition Chemistry of the Hexane Isomers: An Experimental and Kinetic Modeling Study," SAE Paper 952406.

Frenklach, M., Wang, H., Goldenberg, M., Smith, G. P., Golden, D. M., Bowman, C. T., Hanson, R. K., Gardiner, W. C., and Lissianski, V., 1995, "GRI-Mech—An Optimized Detailed Chemical Reaction Mechanism for Methane Combustion," GRI Topical Report No. GRI-95/0058.

Gray, A. W., and Ryan, T. W., 1997, "Homogeneous Charge Compression Ignition (HCCI) of Diesel Fuel," SAE Paper 971676.

Hashizume, T., Miyamoto, T., Akagawa, H., and Tsujimura, K., 1998, "Combustion and Emission Characteristics of Multiple Stage Diesel Combustion," SAE Paper 980505.

Heywood, J. B., 1988, *Internal Combustion Engine Fundamentals,* McGraw-Hill Inc., New York.

Iida, N., 1997, "Alternative Fuels and Homogeneous Charge Compression Ignition Combustion Technology," SAE Paper 972071.

Ishibashi, Y., and Asai, M., 1996, "Improving the Exhaust Emissions of Two-Stroke Engines by Applying the Activated Radical Concept," SAE Paper 960742.

Ishibashi, Y., and Asai, M., 1998, "A Low Pressure Pneumatic Direct Injection Two-Stroke Engine by Activated Radical Combustion Concept," SAE Paper 980757.

Jensen, S. P., 1994, "A Retrofit System to Convert a Locomotive to Natural Gas Operation," *Natural Gas and Alternative Fuels for Engines,* ASME ICE-Vol 21, Book No. G00830.

Kong, S. C., Ayoub, N., and Reitz, R. D., 1992, "Modeling Combustion in Compression Ignition Homogeneous Charge Engines," SAE Paper 920512.

Lund, C. M., 1978, "HCT—A General Computer Program for Calculating Time-Dependent Phenomena Involving One-Dimensional Hydrodynamics, Transport, and Detailed Chemical Kinetics," report UCRL-52504, Lawrence Livermore National Laboratory, Livermore, CA.

Najt, P. M., and Foster, D. E., 1983, "Compression-Ignited Homogeneous Charge Combustion," SAE Paper 830264.

Nakagome, K., Shimazaki, N., Niimura, K., and Kobayashi, S., 1997, "Combustion and Emission Characteristics of Premixed Lean Diesel Combustion Engine," SAE Paper 970898.

Onishi, S., Jo, S. H., Shoda, K., Jo, P. D., and Kato, S., 1979, "Active Thermo-Atmosphere Combustion (ATAC)—A New Combustion Process for Internal Combustion Engines," SAE Paper 790501.

Pitz, W. J., Westbrook, C. K., and Leppard, W. R., 1991, "Autoignition Chemistry of C4 Olefins Under Motored Engine Conditions: A Comparison of Experimental and Modeling Results," SAE Paper 912315.

Ryan, T. W., III, and Callahan, T. J., 1996, "Homogeneous Charge Compression Ignition of Diesel Fuel," SAE Paper 961160.

Smith, J. R., Aceves, S. M., Westbrook, C., and Pitz, W., "Modeling of Homogeneous Charge Compression Ignition (HCCI) of Methane," Proceedings, 1997 ASME Internal Combustion Engine Fall Technical Conference, Paper No. 97-ICE-68, ICE-Vol. 29-3, ASME, New York, pp. 85–90.

Theobald, M. A., and Henry, R., 1994, "Control of Engine Load Via Electromagnetic Valve Actuators," SAE Paper 940816.

Thring, R. H., 1989, "Homogeneous Charge Compression Ignition (HCCI) Engines," SAE Paper 892068.

Westbrook, C. K., Pitz, W. J., and Leppard, W. R., 1991, "The Autoignition Chemistry of Paraffinic Fuels and Pro-Knock and Anti-Knock Additives: A Detailed Chemical Kinetic Study," SAE Paper 912314.

Westbrook, C. K., Warnatz, J., and Pitz, W. J., 1988, "A Detailed Chemical Kinetic Reaction Mechanism for the Oxidation of iso-Octane and n-Heptane over an Extended Temperature Range and its Application to Analysis of Engine Knock," Proceedings, Twenty-Second Symposium (International) on Combustion, The Combustion Institute, Pittsburgh, PA, p. 893.

Woschni, G., 1967, "Universally Applicable Equation for the Instantaneous Heat Transfer Coefficient in the Internal Combustion Engine," SAE Paper 670931.